

GEOLOGICAL AND THERMOCHRONOLOGICAL EVOLUTION OF THE LOWER CRUST OF SOUTHERN AFRICA

by

Mark D. Schmitz

B.A. Geology
Macalester College, 1994

M.Sc. by thesis
University of Auckland, 1995

SUBMITTED TO THE DEPARTMENT OF EARTH ATMOSPHERIC AND PLANETARY SCIENCES IN PARTIAL FULFILLMENT OF THE REQUIREMENTS FOR THE DEGREE OF

DOCTOR OF PHILOSOPHY
AT THE
MASSACHUSETTS INSTITUTE OF TECHNOLOGY

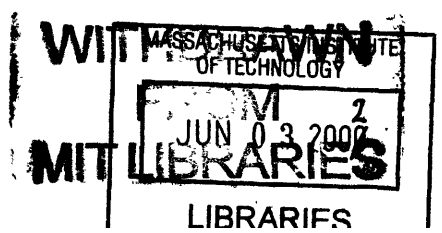
FEBRUARY 2002

2002 Massachusetts Institute of Technology. All rights reserved.

Signature of Author 
Department of Earth, Atmospheric and Planetary Sciences
November 9, 2001

Certified by 
Samuel A. Bowring
Professor of Geology
Thesis Supervisor

Accepted by
Ronald G. Prinn
TEPCO Professor of Atmospheric Chemistry
Department Head



Udger

GEOLOGICAL AND THERMOCHRONOLOGICAL EVOLUTION OF THE LOWER CRUST OF SOUTHERN AFRICA

by

Mark D. Schmitz

Submitted to the Department of Earth Atmospheric and Planetary Sciences
on November 9, 2001 in Partial Fulfillment of the Requirements for the Degree of
Doctor of Philosophy in Geochemistry

ABSTRACT

Geochronological, thermochronological and isotopic studies of kimberlite-borne crustal xenoliths have been used to elucidate the architecture and thermal evolution of the continental lithosphere of southern Africa. U-Pb accessory mineral geochronology of lower crustal xenolith assemblages illustrate the youth of granulite-facies metamorphism relative to the ancient stabilization of the craton, and demonstrate two distinct processes for their generation. Granulitic lower crust at the craton margins and in the bounding Proterozoic belts was generated during 1.1 to 1.0 Ga Namaqua-Natal orogenesis, in response to collisional crustal thickening. Ultra-high temperature granulites in the central cratonic lower crust were generated during dramatic advective perturbation of the lithosphere during 2.7 Ga Ventersdorp rifting and magmatism.

Utilizing the U-Pb systematics of titanite, apatite and rutile—minerals with closure temperatures for Pb diffusion of 650 to 400°C—the thermal evolution of the lower crust and underlying lithosphere has been constrained. Thermal relaxation times for the lithosphere following tectonothermal perturbation indicated by these data (400-600 Ma) are consistent with predictions of simple conductive cooling models, however initial cooling rates in the lithosphere are slower than predicted. Closure of the U-Pb system in rutile, heralding the establishment of cratonic geotherms in the Proterozoic belts of southern Africa by 700 Ma, demands lithospheric thickness comparable to that beneath the Archean cratons. Lower crustal thermochronology also reveals the influence of a thermal perturbation to the southern African lithosphere in the Late Mesozoic, consistent with a broad upper mantle thermal anomaly associated with southern Gondwana breakup. The patterns of lower crustal heating are spatially and temporally complex, suggesting the importance of pre-existing lithospheric structure as a control on advective focussing.

U-Pb zircon geochronology of basement lithologies from the western Kimberley domain of the Kaapvaal craton constrain a model for Neoarchean accretion of the Kimberley block to the eastern Kaapvaal shield at 2.9 Ga. The timing of this convergence through subduction beneath the western domain is correlated with a variety of Re-Os model ages for the underlying lithospheric mantle of the western craton, including peridotite depletion ages, eclogite formation ages and sulfide diamond inclusion ages, and suggests significant coupling of continental crust and lithospheric mantle formation and modification during convergent margin processes.

Thesis Supervisor: Samuel A. Bowring
Title: Professor of Geology

Acknowledgements

Over the past six years, an incredible number of people have contributed in ways great and small to the efforts which have culminated in this thesis. First and foremost, as an advisor and colleague, Sam Bowring was a daily source of inspiration, perspiration, and yes, even some exasperation, but for whom it was always a pleasure and honor to work with and learn from. As mentor to the development of my scientific thinking and professional standards, I know of no better role model. I look forward to his continued advice and ongoing collaboration as I advance in my professional career— my deepest thanks Sam.

As but a single participant in the Kaapvaal Craton Project, I am indebted to all of the other scientists comprising this diverse working group, for their hard work and scientific acumen in initiating and successfully advancing this multi-disciplinary effort. Particular thanks must be extended to the many South African colleagues who made possible this project, and particularly my thesis. Dr. Jock Robey of DeBeers Consolidated was instrumental at every stage of research in providing his time and expertise to unearthing samples of the lower crust and establishing important contacts with other scientists in South Africa. Jock also went out of his way to make my visits to South Africa memorable and pleasurable experiences with his warmth and hospitality, for which I am eternally grateful. Also at DeBeers, Drs. Herman Grutter, Chris Hatton, Kevin Quadling, George Read, Craig Smith, and Fanus Viljoen provided much aid and advice in obtaining lower crustal xenoliths from across southern Africa. Chris Hatton and his family were particularly gracious in hosting a stay in Johannesburg, introducing me to a number of colleagues at Wits and the Council for Geosciences, and showing me an amazing amount of South African geology.

At the University of Cape Town, the generosity of Prof. John Gurney in access to the Mantle Room essentially made much of my thesis possible. Similarly Prof. Maarten de Wit provided an amazing amount of time, resources, and geological insight during the course of my thesis work, and has been a primary source of inspiration in my southern African studies, for which I am extremely grateful. Dr. David Bell was also a primary source of deep insight into the geochemical and geological character of the southern African lithospheric mantle, and during his tenure as a Crosby Fellow at MIT in 2001 was an exceptional sounding board for the emerging conclusions of this thesis. And Petrus le Roux and Phillipa Notten, former grad students at U.C.T., have been kind and generous friends and colleagues since my first visit to South Africa.

Other southern African colleagues who deserve whole-hearted thanks include Dr. Henri Kampunzu of the University of Botswana for his hospitality and scientific insight, Drs. Peter Nixon and Keith Whitelock, along with Craig Smith, for organizing an amazing trip to the Northern Lesotho kimberlites following the 7th I.K.C., Drs. Jock Harmer and Bruce Eglington at the Council for Geosciences at Pretoria for their insights into southern African geology, and Drs. John Marsh and John Moore, and Martin Roberts at Rhodes University for their hospitality during a short visit to Grahamstown. Here in the U.S., scientists at the D.T.M., Carnegie Institution of Washington, including Rick Carlson, David James, Phil Janney, Steve Shirey, and Paul Silver contributed their individual insights into the architecture of the southern African lithosphere and provided an exceptional group of colleagues with which to interact and learn the ropes of multidisciplinary science.

EAPS has been an exceptional place to be a graduate student and I'd like to acknowledge all of the faculty members, and particularly Tim Grove, Fred Frey, and Kip Hodges for daily advice and aid. The staff in EAPS also deserve many thanks, particularly Garret Eastman, Kathy Keefe, and Joe Hankins in the Lindgren Library, Beverly Kozol-Tattlebaum, sorely missed in administration, Dan Burns and his successors in the Education Office, Barry Grant and Bill Olszewski, who have been my primary mentors in mass spectrometry, Kathy Keefe, Kalsoum Abbassi, and Greg Hoke, cohorts in the TIMS Lab and valued friends, and Pat Walsh, who is truly in a class of her own. But of course, the group of people who really contributed the most to my career as a graduate student at MIT were my fellow students. First in the list is Karen Viskupic— colleague, friend, partner and confidante. Special notes also go, in rough chronological order, to Dave Hawkins, C.J. Northrup, Alberto Saal, Nancy Harris, Jim van Orman, Steve Parman, Ken Koga, Eric Kirby, Kirsten Nicolaysen, Julie Baldwin, and Jenny Matzel. Of course there are many more friends and colleagues deserving of mention, but listing all of you would take up several pages and I should probably get on with it— suffice to say you all have my truest thanks.

Mark Schmitz
November 28, 2001

Table of Contents

Abstract	2
Acknowledgements	3
Table of Contents	4
Introduction	8
Chapter 1. The significance of U-Pb zircon dates in lower crustal xenoliths of the southwestern margin of the Kaapvaal craton, southern Africa	13
1. Introduction.....	14
2. High spatial resolution, high-precision dating of zircon	14
3. Regional geology.....	15
4. Analytical methods.....	17
5. Results for crustal xenoliths.....	19
5.1 Lovedale— eclogite (KX5-1).....	19
5.2 Markt— grt-cpx-plg granulite (KX4-23).....	20
5.3 Markt— grt-cpx-hbl-plg amphibolite (KX4-35)	21
5.4 Klipfontein— aegirine biotite syenite (KX12-9)	21
6. Interpretation of zircon ages in crustal xenoliths	23
6.1 Eclogitic zircon.....	24
6.2 Zircon growth at amphibolite to granulite-facies	24
6.3 Low-temperature retrograde zircon stability	25
7. Implications for the evolution of the Kaapvaal craton	26
7.1 Archean eclogite beneath the Kaapvaal craton	26
7.2 Granulite facies metamorphism at the craton margin	26
7.3 Crustal architecture of the craton boundary	27
8. Conclusions.....	28
References.....	28
Chapter 2. Lower crustal granulite formation during Mesoproterozoic Namaqua-Natal collisional orogenesis, southern Africa	31
1. Introduction.....	32
2. Geological setting and prior study	33
2.1 Eastern Namaqualand.....	33
2.2 Northern Lesotho.....	36
3. Sample Descriptions.....	38
3.1 Eastern Namaqualand.....	38
3.1.1 Markt kimberlite.....	38
3.1.2 Klipfontein kimberlite.....	40
3.1.3 Beyersfontein kimberlite.....	40
3.1.4 Witberg Pipe kimberlite.....	40
3.2 Northern Lesotho.....	40
3.2.1 Letseng-la-Terae kimberlite	41
3.2.2 Matsoku kimberlite.....	41
3.2.3 Mothae kimberlite.....	42
4. Analytical techniques.....	42
5. Analytical results.....	43
5.1 U-Pb geochronology.....	44
5.1.1 Eastern Namaqualand.....	44

5.1.2 Northern Lesotho.....	45
5.2 Sm-Nd isotopic systematics.....	47
5.2.1 Eastern Namaqualand.....	48
5.2.2 Northern Lesotho.....	51
6. Discussion.....	52
6.1 Northern Lesotho granulite formation	52
6.2 Eastern Namaqualand orogenesis and crustal structure	54
6.3 The origin of granulitic lower crust	57
6.4 Implications for lithospheric architecture, composition and evolution	58
7. Conclusions.....	59
References.....	61
Tables.....	65
Figures.....	69
Chapter 3. Ultra-high temperature metamorphism in the lower crust during Neoproterozoic Ventersdorp rifting and magmatism, Kaapvaal Craton, southern Africa	81
1. Introduction.....	82
2. Previous work and geological setting.....	85
2.1 Previous investigations.....	85
2.2 Geological and temporal setting.....	85
3. Sample descriptions.....	89
3.1 Modal mineralogy and petrography	89
3.2 Accessory mineral petrography.....	92
3.2.1 Monazite.....	92
3.2.2 Zircon.....	93
3.2.2.1 Discrete zircon grains.....	93
3.2.2.2 Zircon-rutile intergrowth	94
4. Analytical techniques.....	98
5. Analytical results.....	100
5.1 U-Pb geochronology.....	100
5.1.1 Monazite.....	100
5.1.2 Discrete zircon grains.....	102
5.1.3 Exsolved zircon lamellae	105
5.2 Sm-Nd isotopes.....	107
6. Discussion.....	109
6.1 A P-T-t path for UHT metamorphism.....	109
6.1.1 Prograde to post-peak	109
6.1.2 Constraints on zircon and monazite closure temperatures	112
6.1.3 Constraints on the cooling path: zircon exsolution from rutile	114
6.2 Constraints on mechanisms of UHT metamorphism	116
6.3 Implications for the Kaapvaal cratonic lithosphere	117
6.3.1 Thermal lithosphere perturbation	117
6.3.2 Chemical lithosphere perturbation	120
6.3.3 Thermal relaxation	121
7. Conclusions.....	123
References.....	125
Tables.....	130
Figures.....	134
Chapter 4. Constraints on the thermal evolution of continental lithosphere from U-Pb accessory mineral thermochronology of lower crustal xenoliths, southern Africa ..	145

1. Introduction.....	146
2. Pb diffusion in accessory minerals	149
3. Geological setting and character of lower crustal xenoliths	152
4. Crustal exhumation and lower crustal residence	155
5. Analytical procedures.....	157
6. Analytical results.....	158
6.1 Newlands.....	158
6.2 Free State	160
6.3 Orapa	161
6.4 Northern Lesotho.....	162
6.5 Eastern Namaqualand.....	163
7. Discussion.....	164
7.1 Thermal evolution of the Archean cratonic interior	164
7.1.1 Newlands kimberlite, western craton	164
7.1.2 Free State kimberlites, central craton	166
7.2 Thermal evolution of the cratonic margins and Proterozoic off-craton regions	169
7.2.1 Distinguishing continuous versus episodic diffusive Pb-loss	169
7.2.2 Cooling rates in the lower crust	172
7.2.3 Establishment of cratonic geotherms	174
7.2.4 Mesozoic lithospheric thermal perturbation	178
8. Conclusions.....	183
References.....	185
Tables.....	190
Figures.....	194
Chapter 5. Stabilization of the western Kaapvaal Craton: implications for Witwatersrand basin subsidence and the formation of continental lithosphere	209
1. Introduction	210
2. Archean evolution of the Kaapvaal Craton	212
2.1 Eastern Kaapvaal shield	213
2.2 Northern domain.....	216
2.3 Western domain	219
2.4 Witwatersrand basin sedimentation	220
3. Analytical techniques	222
4. Analytical results	223
4.1 U-Pb geochronology.....	223
4.1.1 Kraaipan greenstone belt	223
4.1.2 Kimberley basement.....	224
4.2 Sm-Nd isotopes.....	226
5. Discussion.....	226
5.1 Antiquity of the western domain	226
5.2 Accretion of the western domain	227
5.3 Neoproterozoic assembly of the Kaapvaal craton	229
5.4 Tectonics of Witwatersrand Supergroup deposition.....	231
5.5 Implications for the stabilization of lithospheric mantle	235
6. Conclusions.....	237
References.....	238
Tables.....	244
Figures.....	246

Chapter 6. U-Pb zircon and titanite systematics of the Fish Canyon Tuff: an assessment of high-precision U-Pb geochronology and its application to young volcanic rocks	255
1. Introduction.....	255
2. Analytical procedures.....	256
3. Results.....	256
3.1 Zircon systematics.....	256
3.2 Titanite systematics.....	260
4. Age sensitivity analysis.....	261
4.1 Instrumental detector bias and mass fractionation.....	261
4.2 Tracer calibration.....	261
4.3 Common Pb correction.....	262
4.4 Intermediate daughter product disequilibria.....	263
4.5 Concordia age.....	265
5. Discussion.....	266
5.1 FCT zircon age distributions.....	266
5.2 Intercalibration of U-Pb and $^{40}\text{Ar}/^{39}\text{Ar}$ geochronometers.....	267
5.3 Magma chamber residence time.....	268
5.4 U isotope decay constant uncertainties.....	269
6. Conclusions.....	269
References.....	270

Introduction

Kimberlite-borne crustal xenolith studies provide a window into the character and evolution of the deep crust, complementing a variety of other data sets bearing on the nature of the continental lithosphere, including studies of exposed crustal sections, mantle geochemistry and geochronology from mantle xenoliths, and seismological measurements and models of the crust and underlying mantle. Among the few direct samples of the deep crust, xenoliths provide our most detailed information on its mineralogy and composition, and provide important constraints for the interpretation of geophysical measurements ranging from heat flow to seismic velocity, and derivative models of crustal structure. Geochronological and thermochronological studies of xenoliths extend our knowledge of the spatial and temporal patterns of crustal growth and tectonothermal modification into the third dimension. By its nature as the physical link between the crust and upper mantle, the lower crust is increasingly recognized as containing a dynamic record of upper mantle phenomena and crust-mantle interaction.

Crustal xenolith studies have been pursued concomitant with the seismological, geophysical, petrologic, and mantle xenolith geochemical studies forming the Kaapvaal Seismic Experiment. This multi-disciplinary experiment seeks to elucidate the current lithospheric and upper mantle architecture of the southern African cratonic nucleus, with the goal of integrating the resulting high-resolution 3-D image with geophysical, petrologic, geochemical, and geochronological data into a genetic model for the formation and evolution of Archean cratons. Prior studies of the southern African mantle have noted the coincidence of chemically depleted and anomalously fast seismic velocity mantle tectosphere with overlying Archean crust. This spatial relationship has served to fuel speculation on the formation mechanisms of subcontinental lithospheric mantle and the possibility of secular change in mantle dynamics from the Archean to the present day. To date however, the relationships between the continental crust and its underlying mantle have been clouded by a lack of spatial and temporal resolution. To address this lack of resolution, geophysical components of the project are providing an unprecedented view of the current state and structure of the craton, while complementary geochronological studies of the crust and mantle are providing direct constraints on its evolution over time. With regard to the latter studies, a growing body of geochronological information on mantle xenoliths is commonly compared with the geological history of the craton from the surface rock record.

However the deep crust of the craton, the domain which most directly links the surface record of lithospheric evolution with that of the upper mantle, has been largely unexplored. Toward this end, the timing of formation and the subsequent tectonothermal evolution of the southern African lower crust is the particular focus of this thesis.

Abundant xenoliths of the deep crust, exhumed in Mesozoic kimberlites intruded throughout much of southern Africa, provide the necessary samples for this analysis. Prior studies have demonstrated the lower crustal provenance of the granulite xenolith suites, and hypothesized on their paragenesis. The present study focuses on the use of high-precision U-Pb accessory mineral geochronology, in concert with ancillary Sm-Nd isotopic analysis, to place precise and accurate timing constraints on the pressure-temperature paths through which these samples of the lower crust evolved. The task of interpreting these U-Pb accessory mineral isotopic systematics has been approached using petrologic and petrographic data on their paragenesis and participation in metamorphic reactions, and the kinetics of diffusion and annealing in the mineral lattices. Chapter 1 details this approach with zircon, arguably the most important crustal geochronometer, and a mineral that, because of its very high closure temperature to Pb volume diffusion, provides a high-fidelity record of growth through magmatic and metamorphic processes. Chapter 1 illustrates how, in a variety of crustal xenoliths, zircon may be tied to a wide range of metamorphic conditions, serving to clarify the interpretation of the geochronological data obtained from this mineral.

Chapter 2 examines the architecture and evolution of the southern and western margins of the Kaapvaal craton, at its boundaries with Proterozoic orogenic belts. Here U-Pb geochronology and Nd isotopic systematics of deep crustal xenoliths are used to delineate the three-dimensional geometry and age structure of the crust, and the timing of lower crustal granulite genesis. These data are used to clarify the tectonic and metamorphic history of interaction between the craton and its adjacent orogenic belts, and develop a robust crustal reference model for comparisons with geophysical observables. One of the most striking inferences of the crustal geophysical studies of the Kaapvaal project is an abrupt thickening of the crust of the Proterozoic belts relative to the Archean craton, due to the presence of a lower crustal high density, high seismic velocity layer. The lower crustal geochronology presented in Chapter 2 demonstrates that this layer comprises garnet-bearing granulites formed as the result of

crustal thickening and metamorphism of pre-existing Archean to Mesoproterozoic crust during 1.1 to 1.0 Ga collisional orogenesis along the southern and western margins of the craton, and questions the significance of magmatic underplating for the genesis of these suites of lower crustal granulites.

Cratons are defined by their apparent stability over geologic timescales. But how and when the characteristics necessary for their very stability are acquired remain unclear. In common with most Archean cratons, the Kaapvaal lithosphere underwent a number of cycles of extension and rifting following each of the convergent tectonic episodes which sutured elements of the craton together. The consequences of these episodes of rifting for the stability of the Kaapvaal craton, and its underlying lithospheric mantle keel are explored in Chapter 3, which examines a unique suite of ultra-high temperature (UHT) granulite xenoliths from the Free State kimberlites of the central Kaapvaal craton. These lower crustal xenoliths are demonstrated to have formed during dramatic metamorphism in the deep crust associated with the *ca* 2.7 Ga Ventersdorp extensional and magmatic event, which propagated across the central and western Kaapvaal craton and eventually resulted in rifting and continental breakup along the craton's western margin. It is hypothesized that this period of Neoproterozoic crustal extension dramatically altered the crustal architecture of the craton, flattening the Moho discontinuity and sharpening the velocity contrast to its present day character revealed from receiver function analysis of the Kaapvaal Seismic Array. These xenoliths record extreme advective geotherms in the mantle beneath the center of the Kaapvaal craton at 2.7 Ga, locally necessitating the removal of the thermal lithosphere, yet this event was not apparently effective at completely remobilizing the entire lithospheric mantle keel of the craton, as evidenced by the preservation of >2.9 Ga mantle xenolith and diamond inclusion ages in the western Kaapvaal lithosphere. This chapter also explores how lower crustal xenoliths provide constraints on the thermal relaxation of continental lithosphere following major tectonothermal perturbation. U-Pb thermochronological data tentatively suggest that this thermal relaxation is slower than rates predicted by simple conductive cooling models.

Chapter 4 continues to explore the application of moderate to low closure temperature U-Pb accessory mineral thermochronometers like titanite, rutile and apatite as probes of the thermal evolution of the lithosphere. Because of the low heat production and requisite shallow

temperature gradients in the lithospheric mantle compared to the crust, measurements of lower crustal paleotemperatures provide strong constraints on the thermal structure of the underlying lithosphere, particularly in the conductive regime. A particularly powerful thermochronometer in this regard is rutile, a nearly ubiquitous mineral in granulitic lower crustal rocks whose low nominal closure temperature for Pb diffusion, near 400°C, potentially constrains the time of inception of a “cratonic” geothermal state. In the simplest scenarios, crustal thermochronology may record the progressive cooling of the lithosphere following major crust-forming and crust-modifying events. Data from lower crustal xenoliths from the Proterozoic (1.1 to 1.0 Ga) orogenic belts surrounding the Kaapvaal craton are used to argue that even these terrains achieved a cratonic thermal state in the Neoproterozoic (0.8 to 0.7 Ga), which necessitates a contemporaneous lithospheric thickness of >200 km, similar to that inferred for the Archean cratonic lithosphere. It is also demonstrated from lower crustal thermochronology that the southern African lithosphere underwent a profound thermal perturbation in the Mesozoic associated with Gondwana breakup. The spatial and temporal heterogeneity of lithospheric response to this perturbation are mapped in the lower crust of the cratonic and off-craton regions, demonstrating the importance of pre-existing lithosphere-scale structures for channeling the advection of heat into the continental lithosphere.

Among the primary questions for continental lithosphere studies is to what extent the crust and mantle have been coupled to each other over their history. This relationship is particularly important to clarify as the crust is the repository of most of the geologic, structural and geochronological information available for continental lithosphere, and thus provides a vital reference for the interpretation of the geophysical and rare xenolith data from the more inaccessible lithospheric mantle. Surprisingly, there is a substantial disconnection between the available database of Kaapvaal lithospheric mantle geochemistry and geochronology, focussed in the western half of the craton, and a significant understanding of the crustal evolution of the Kaapvaal craton, restricted to the eastern craton. In order to rectify our lack of knowledge of the crustal tectonic evolution of the western half of the Kaapvaal craton, Chapter 5 examines samples of basement gneissic xenoliths sourced from the Kimberley area kimberlite mines, as well as a rhyolitic tuff from the northwestern Kraaipan greenstone belt. These samples provide important data on the age of formation and metamorphism of the crust of the western Kimberley block, and record the relatively young amalgamation of the western domain to the eastern

Kaapvaal shield at *ca* 2.9 Ga. The correspondence of the 2.9 Ga timing of subduction-convergence of the western domain with peridotite depletion ages, eclogite formation ages, and sulfide diamond inclusion encapsulation ages from the underlying lithospheric mantle demonstrates the coupling between crust and mantle during formation and modification, and suggests that the convergent margin setting is the primary site for generating the distinctive compositional characteristics of subcontinental lithospheric mantle.

Finally, Chapter 6 presents an ancillary study evaluating the precision and accuracy of the major techniques used in this thesis, U-Pb zircon geochronology, through the measurement and evaluation of a large suite of single zircon and titanite data for the Oligocene Fish Canyon Tuff of the San Juan Mountains of Colorado. As a commonly used standard in $^{40}\text{Ar}/^{39}\text{Ar}$ geochronology, the Fish Canyon Tuff has become the focus of debate regarding the accurate intercalibration of ages obtained through different radiometric decay schemes. The particular applicability of these issues to thermochronology are clear, where numerous mineral isotopic systems must be integrated to produce thermal histories for the crust. With the best available measured decay constants, and the internal consistency inherent in two independent decay schemes, the U-Pb system is the “gold standard” of geochronology, and one to which other systems may be best calibrated. The present study presents a comprehensive evaluation of the sources of analytical and systematic error in ID-TIMS U-Pb analysis in order to arrive at robust crystallization ages for the Fish Canyon Tuff zircon and titanite. These data are used to assess the importance of magmatic residence time versus systematic errors in assumed standard ages and decay constants for generating a consistent bias between U-Pb and $^{40}\text{Ar}/^{39}\text{Ar}$ geochronometers.



ELSEVIER

Chapter 1.

Chemical Geology 172 (2000) 59–76

**CHEMICAL
GEOLOGY**
INCLUDING
ISOTOPE GEOSCIENCE

www.elsevier.com/locate/chemgeo

The significance of U–Pb zircon dates in lower crustal xenoliths from the southwestern margin of the Kaapvaal craton, southern Africa

Mark D. Schmitz^{*}, Samuel A. Bowring

Massachusetts Institute of Technology, 77 Massachusetts Ave., Bldg. 54-1114 M.I.T., Cambridge, MA, USA

Abstract

The combination of high precision ID-TIMS U–Pb geochronology with cathodoluminescence (CL) imaging and spatially resolved microsampling of zircon provides a high fidelity record of the temporal evolution of samples of the middle and lower crust. A suite of xenoliths exhumed in Cretaceous kimberlites at the southwestern margin of the Kaapvaal craton, including eclogite, granulite, amphibolite, and greenschist-facies plutonic rocks, are the subject of these detailed zircon studies. CL imaging demonstrates the complexity of chemical and growth structure in single zircons, and highlights the importance of sampling on an intragrain scale to extract end-member ages for zircon growth events. For these diverse metamorphic rocks, linking the zircon chronology to geologic events and processes requires an understanding of the kinetics and thermodynamics of zircon stability during metamorphism. Using an empirical approach, we attempt to relate zircon crystallization, dissolution, and regrowth to metamorphic conditions through a detailed analysis of zircon chemical zonation patterns, mineral inclusions, and petrography. These lines of evidence indicate the crystallization of zircon under P – T conditions ranging from eclogite through greenschist facies. We discuss four examples of this approach: (1) At the lowest grade of metamorphism examined, primary igneous zircon (1900 Ma) in a syenite xenolith from the Klipfontein-08 kimberlite underwent two episodes (1015 and 964 Ma) of probable fluid-mediated resorption and reprecipitation in the greenschist facies. (2) An upper amphibolite facies xenolith from the Markt kimberlite contains two distinct populations of blocky and fir-tree sector-zoned zircon which are suggested to date prograde hornblende breakdown reactions (~ 1107 Ma) and melt infiltration under retrograde metamorphic conditions (~ 1092 Ma), respectively. (3) At granulite-facies, metamorphic zircon crystallized at ~ 1114 Ma during prograde reactions involving hornblende breakdown in a granulite xenolith also from the Markt kimberlite. Later (~ 960 Ma) zircon resorption followed by minor secondary crystallization occurred in both the amphibolite and granulite xenoliths during retrograde greenschist facies reactions, possibly enhanced by fluids. (4) In a much older episode of eclogite facies metamorphism recorded in a xenolith from the Lovedale kimberlite, zircon crystallized with the peak metamorphic mineral assemblage, or possibly early on the cooling path, in the Late Archean (~ 2630 Ma). Each of these examples provides unique information regarding the evolution of the Kaapvaal craton, while the links to metamorphic reactions and P – T conditions clarify the interpretation of zircon dates obtained from these samples of the middle to lower crust. © 2000 Elsevier Science B.V. All rights reserved.

Keywords: U–Pb geochronology; Zircon; Lower crust; Xenoliths; Kaapvaal craton; South Africa

^{*} Corresponding author. Tel.: +1-617-253-7993; fax: +1-617-253-6735.

E-mail address: mschmitz@mit.edu (M.D. Schmitz).

1. Introduction

Xenoliths erupted in kimberlites and alkaline magmas represent some of the few samples of the lower portions of the crust available for study. Yet unfortunately, the complete record of the P – T – t evolution of these samples — from primary sedimentary deposition or igneous crystallization through metamorphic recrystallization and final volcanic exhumation — is commonly obscured by the dynamic overprinting of varying conditions and processes encountered during protracted residence in the deep crust. In particular, extracting temporal information from these samples with traditional radiometric chronometers is fraught with difficulty due to open system behavior of both parent and daughter elements and the validity of assumptions pertaining to initial isotopic equilibrium.

U–Pb zircon geochronology is ideally suited for elucidating the temporal evolution of lower crustal xenoliths (e.g. Chen et al., 1994; Hanchar and Rudnick, 1995; Moser and Heaman, 1997). Zircon retains a high-fidelity record of its crystallization history due to its sluggish kinetic properties for U, Th, and Pb (Cherniak and Watson, 1999) and its refractory character during most metamorphic reactions up to and surpassing anatectic conditions (Harrison and Watson, 1983; Watson, 1996). There is also abundant evidence for the crystallization of zircon during prograde and retrograde metamorphic reactions (Vavra et al., 1996; Williams et al., 1996; Fraser et al., 1997; Roberts and Finger, 1997; Schaltegger et al., 1999). Establishing the relationships between zircon crystallization, metamorphic reactions and P – T conditions presents a significant challenge for interpreting U–Pb zircon dates from metamorphic rocks, including xenoliths.

In this study we apply high precision isotope dilution thermal ionization mass spectrometric (ID-TIMS) U–Pb geochronology to zircons from a suite of crustal xenoliths from the southwestern margin of the Kaapvaal craton of southern Africa. Zircon growth domains on intragrain scales of tens of microns were characterized by cathodoluminescence (CL) imaging, and isolated through selective micro-sampling and air-abrasion. This geochronological data is combined with imaging, mineral inclusions, zircon petrography, and geochemical evidence, in

order to infer the metamorphic grade under which zircon crystallized. We find a diversity of conditions under which zircon has grown in these xenoliths, from granulite to greenschist facies. The results provide constraints on the tectonic evolution of the Kaapvaal craton margin, and insight into the P – T – t evolution of the deep crust.

2. High spatial resolution, high-precision dating of zircon

While previous studies have analyzed the U–Pb systematics of zircon in lower crustal xenoliths, most have utilized ion probe methods (e.g. Chen et al., 1994; Hanchar and Rudnick, 1995). However, in order to link the deep crustal record of xenoliths with the surface geological framework, age constraints with the precision offered by ID-TIMS are desirable (Krogh, 1993; Moser and Heaman, 1997; Moser et al., 1996). The convergence of numerous analytical methods and technologies now allows for the analysis of increasingly small amounts of spatially characterized zircon by ID-TIMS. In particular, low laboratory blanks (~ 1 pg for Pb and U), new silica gel loading substrates (Gerstenberger and Haase, 1997), and ion-counting Daly detection now allow the analysis of as little as 10 pg of radiogenic Pb to a precision of $\geq 0.1\%$ in the $^{207}\text{Pb}/^{206}\text{Pb}$ age for Precambrian zircons. This quantity of Pb translates into ~ 100 ng of zircon with a Pb content of 100 ppm, equivalent to a sphere of zircon 35 μm in diameter, thus it is within the capability of modern ID-TIMS methods to analyze domains within single crystals.

Cathodoluminescence (CL) imaging, which has become widely used in geochemical and geochronological studies of zircons (Grauert and Wagner, 1975; Vavra, 1990; Hanchar and Miller, 1993), reveals a wealth of information on the detailed growth history of zircons which is commonly invisible by optical or back-scattered electron (BSE) imaging methods. CL is activated or suppressed by a combination of intrinsic zircon luminescence, REE (Dy) content, and radiation damage (Mariano, 1989; Koschek, 1993). Although CL does not directly image U, Th, or Pb contents, it does provide a map of spatial variation in chemical composition which serves as a proxy for crystal growth history. Recent experiments indicate

that volume diffusion rates of the REE, actinides, and Pb in zircon are so slow as to preserve micron-scale heterogeneities for these elements at lithospheric temperatures over billions of years (Cherniak and Watson, 1999; Cherniak et al., 1997). This indicates that disconformities in growth inferred from CL will also be preserved in the radiometric systems in zircon, thus for the purposes of ID-TIMS U–Pb geochronology, CL imaging provides the best means for mapping growth histories in single grains prior to micro-sampling and analysis.

Isolating discrete domains of single zircon grains is the greatest challenge in precise age determinations of various growth components. Physical methods for isolating domains include selective polishing, abrasion, fragmentation, and cutting. For example, during the course of polishing grain mounts, cores of grains can be removed leaving only thin lenses of the outer mantles of zircon. On the other hand, abrasion of grains (e.g. Krogh, 1982) removes their outer portions, concentrating the remaining sample in possible core components. Fragmentation can be used quite effectively to isolate different growth components in zircon when grains preferentially break along mechanical discontinuities corresponding to growth or resorption boundaries (e.g. Krogh, 1993). While in some cases we have been able to effectively isolate different growth phases of zircon, as demonstrated by concordant analyses at the intercepts of discordia arrays, in many cases micro-sampling is imperfect, resulting in hybrid analyses containing more than one end-member component. In the case of two components, these analyses define mixing lines in concordia space, which given high precision of individual analyses, concordancy of analyzed domains, and sufficient spread along lines can be used to derive precise end-member component ages from the intercepts with concordia.

It is important to note that the intercepts of mixing lines with concordia will only correspond to true formation ages if each analyzed sample has remained a closed system with respect to U and Pb. Zircons isolated from lower crustal xenoliths in this study, while certainly not exempt from Pb-loss, are commonly concordant or near-concordant, even without abrasion (e.g. sample KX4-23). If we subscribe to the commonly held view that the susceptibility of zircon to Pb-loss is a function of degree of radiation

damage, or metamictization (Silver and Deutsch, 1963), then the observed robustness of lower crustal zircons is a simple function of their prolonged residence above the spontaneous annealing temperature for alpha recoil damage in zircon (Murakami et al., 1991; Meldrum et al., 1998). Meldrum et al. (1998) have quantified the temperature–radiation dose dependence of metamictization; for the U and Th concentrations of the zircons in this study (<1000 ppm), the critical temperature of $\sim 150^{\circ}\text{C}$ is well below the ambient conditions of the middle to lower crust. Thus, these zircons have preserved their robust crystallinity since formation, making Pb-loss unlikely prior to entrainment in the kimberlite.

3. Regional geology

Crustal xenoliths were collected from the Cretaceous Lovedale, Markt, and Klipfontein-08 kimber-

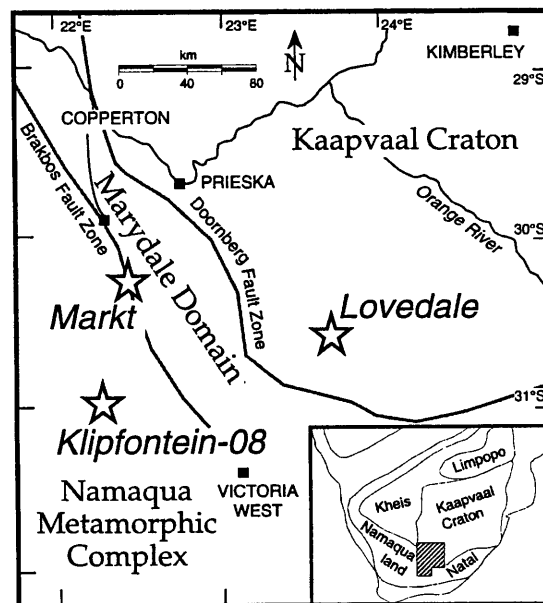


Fig. 1. Tectonic map of the southwestern margin of the Kaapvaal craton illustrating the relationships between the Kaapvaal craton, Marydale terrain, and Namaqua Metamorphic Complex (modified from Cornell et al., 1986 and de Wit et al., 1995). Traces of the Doornberg and Brakbos faults south of Prieska are inferred from aeromagnetic and gravity signatures and are drawn after the interpretation of Grütter and Apter (1998). Stars indicate the positions of the three kimberlites from which crustal xenoliths were studied.

Table 1
U–Pb isotopic data for zircons from crustal xenoliths

Sample fractions ^a	Weight (μg) ^b	Composition				Isotopic ratios								Rho	Dates (Ma)			Discordance (%) ^c
		U (ppm) ^d	Th/U ^d	Pb* (ppm) ^e	Pbc (pg) ^e	²⁰⁶ Pb*/ ²⁰⁴ Pb ^f	²⁰⁸ Pb/ ²⁰⁶ Pb ^g	²⁰⁶ Pb/ ²³⁸ U ^g	% err ^h	²⁰⁷ Pb/ ²³⁵ U ^g	% err ^h	²⁰⁷ Pb/ ²⁰⁶ Pb ^g	% err ^h		²⁰⁶ Pb/ ²³⁸ U	²⁰⁷ Pb/ ²³⁵ U	²⁰⁷ Pb/ ²⁰⁶ Pb ^h	
<i>KX5-1, Lovedale, eclogite</i>																		
z1	0.23	539	0.22	263	2.5	1483	0.0664	0.45588	(0.29)	11 18912	(0.29)	0.17801	(0.06)	0.978	2421.4	2539.0	2634.4 ± 1.0	9.7
z2	0.21	286	0.15	113	2.4	613	0.0544	0.37185	(0.91)	9.04255	(0.92)	0.17637	(0.09)	0.995	2038.1	2342.3	2619.0 ± 1.5	25.8
z3	0.15	602	0.27	296	1.8	1510	0.0848	0.45253	(0.43)	11 05411	(0.43)	0.17716	(0.06)	0.989	2406.5	2527.7	2626.5 ± 1.1	10.0
z4	0.10	437	0.09	217	1.3	1093	0.0246	0.48204	(0.29)	11.68528	(0.32)	0.17582	(0.11)	0.933	2536.1	2579.5	2613.8 ± 1.9	3.6
z5	0.20	684	0.56	381	2.3	1862	0.1638	0.48212	(0.19)	11.79389	(0.20)	0.17742	(0.05)	0.961	2536.5	2588.2	2628.9 ± 0.9	4.2
z6	0.14	531	0.13	275	1.4	1762	0.0355	0.49641	(0.20)	12.15256	(0.21)	0.17755	(0.07)	0.951	2598.4	2616.3	2630.1 ± 1.1	1.5
z7	0.10	1273	0.03	637	4.1	977	0.0090	0.48727	(0.47)	11 72996	(0.48)	0.17459	(0.07)	0.989	2558.9	2583.1	2602.2 ± 1.2	2.0
<i>KX4-23, Markt, garnet–clinopyroxene granulite</i>																		
z1	33	166	0.30	29	10.6	5504	0.0931	0.17439	(0.12)	1.78656	(0.13)	0.07430	(0.06)	0.888	1036.2	1040.6	1049.7 ± 1.2	1.4
z2, aa	31	204	0.26	38	7.9	9087	0.0782	0.18521	(0.13)	1.94627	(0.15)	0.07621	(0.08)	0.860	1095.4	1097.2	1100.7 ± 1.5	0.5
z3, aa	22	286	0.41	55	4.1	17756	0.1252	0.18600	(0.15)	1.95742	(0.17)	0.07633	(0.09)	0.863	1099.7	1101.0	1103.6 ± 1.8	0.4
z4, aa	38	184	0.28	34	3.7	21663	0.0852	0.18531	(0.08)	1.94571	(0.11)	0.07615	(0.08)	0.708	1095.9	1097.0	1099.1 ± 1.5	0.3
z5, frag	4.1	78	0.26	14	1.9	1941	0.0782	0.18065	(0.14)	1.87870	(0.19)	0.07543	(0.13)	0.758	1070.5	1073.6	1079.8 ± 2.5	0.9
z6, frag	4.1	71	0.26	13	2.3	1508	0.0792	0.18067	(0.24)	1.87893	(0.27)	0.07542	(0.11)	0.911	1070.7	1073.7	1079.8 ± 2.2	0.9
z7, frag	2.9	55	0.36	10	3.4	539	0.1119	0.17165	(0.81)	1.74663	(0.89)	0.07380	(0.33)	0.928	1021.2	1025.9	1036.1 ± 6.7	1.6
z8, frag	3.8	88	0.27	16	2.8	1434	0.0817	0.18352	(0.29)	1.92210	(0.38)	0.07596	(0.23)	0.803	1086.2	1088.8	1094.0 ± 4.5	0.8
<i>KX4-35, Markt, garnet–clinopyroxene–hornblende amphibolite</i>																		
z3, cl, aa	0.43	559	0.55	109	2.6	1082	0.1679	0.18193	(0.52)	1.89474	(0.58)	0.07554	(0.24)	0.908	1077.5	1079.2	1082.8 ± 4.8	0.5
z4, pk	1.54	656	0.25	119	3.8	3167	0.0776	0.18306	(0.18)	1.92323	(0.24)	0.07620	(0.15)	0.779	1083.6	1089.2	1100.3 ± 3.0	1.6
z6, pk, aa	0.43	489	0.31	92	2.7	973	0.0923	0.18748	(0.24)	1.97626	(0.31)	0.07645	(0.18)	0.807	1107.7	1107.4	1106.9 ± 3.7	–0.1
z7, ov, aa	2.85	275	0.62	48	1.3	6410	0.1901	0.16007	(0.07)	1.56994	(0.10)	0.07113	(0.07)	0.704	957.2	958.4	961.2 ± 1.5	0.4
z8, cl	0.33	879	0.74	179	1.1	2964	0.2252	0.18148	(0.12)	1.88598	(0.15)	0.07537	(0.09)	0.796	1075.0	1076.2	1078.5 ± 1.8	0.3
z10, cl + ov	1.37	173	0.61	33	6.5	398	0.1894	0.16485	(0.67)	1.64632	(0.69)	0.07243	(0.17)	0.968	983.7	988.1	998.0 ± 3.5	1.5
z11, pk, aa	1.11	223	0.45	43	4.2	716	0.1378	0.18400	(0.59)	1.93425	(0.63)	0.07624	(0.21)	0.943	1088.8	1093.0	1101.4 ± 4.2	1.2
z12, pk, aa	0.62	414	0.32	77	2.4	1264	0.0973	0.18457	(0.19)	1.94314	(0.24)	0.07635	(0.13)	0.841	1091.9	1096.1	1104.4 ± 2.6	1.2
z13, pk, aa	2.11	442	0.38	85	1.3	8763	0.1149	0.18667	(0.08)	1.96717	(0.11)	0.07643	(0.07)	0.711	1103.3	1104.3	1106.4 ± 1.5	0.3
z15, cl, aa	2.38	135	0.65	27	2.5	1541	0.1970	0.18462	(0.15)	1.93201	(0.18)	0.07590	(0.09)	0.858	1092.1	1092.2	1092.4 ± 1.8	0.0
z16, cl, aa	0.38	230	0.77	47	2.0	548	0.2359	0.18230	(0.60)	1.90125	(0.65)	0.07564	(0.22)	0.939	1079.6	1081.5	1085.5 ± 4.5	0.6
<i>KX12-9, Klipfontein-08, aegirine–biotite syenite</i>																		
z1, eq, aa	0.29	220	1.15	85	4.4	293	0.3648	0.29361	(1.6)	4.41981	(1.7)	0.10918	(0.34)	0.980	1659.6	1716.1	1785.7 ± 6.1	8.0
z3, el	8.6	155	0.73	34	3.3	4890	0.2531	0.18956	(0.25)	2.17862	(0.29)	0.08335	(0.14)	0.877	1119.0	1174.2	1277.5 ± 2.7	13.5
z4, el, aa	1.1	190	0.74	48	1.9	1546	0.2604	0.21793	(0.17)	2.78069	(0.21)	0.09254	(0.12)	0.815	1270.9	1350.4	1478.5 ± 2.3	15.5
z5, el, aa	10	77	0.74	17	3.5	2768	0.2583	0.19602	(0.12)	2.31152	(0.16)	0.08553	(0.09)	0.798	1153.9	1215.8	1327.5 ± 1.8	14.3
z6, eq, aa	7.5	36	0.78	7	1.3	2190	0.2366	0.17050	(0.13)	1.71742	(0.18)	0.07305	(0.11)	0.769	1014.9	1015.1	1015.4 ± 2.3	0.1
z7, el, aa	2.0	136	0.75	38	1.4	2982	0.2584	0.24009	(0.15)	3.26560	(0.16)	0.09865	(0.06)	0.917	1387.2	1472.9	1598.7 ± 1.2	14.7
z8, eq, aa	0.92	102	0.78	32	1.9	885	0.2569	0.27140	(0.35)	3.95619	(0.38)	0.10572	(0.12)	0.951	1547.9	1625.3	1726.9 ± 2.1	11.7
z9, eq, aa	0.85	90	0.99	18	1.2	694	0.3117	0.16788	(0.35)	1.71032	(0.41)	0.07389	(0.21)	0.866	1000.4	1012.4	1038.4 ± 4.1	3.9
z10, eq, aa	0.41	99	0.84	18	1.2	364	0.2638	0.16134	(0.60)	1.60448	(0.96)	0.07213	(0.70)	0.688	964.2	972.0	989.5 ± 14	2.7
z11, eq, aa	0.35	171	0.80	32	1.4	471	0.2588	0.16372	(0.60)	1.66782	(0.74)	0.07388	(0.41)	0.833	977.4	996.4	1038.3 ± 8.2	6.3

lites, which intrude the southwestern margin of the Kaapvaal craton along its abutment with the Archean to Mesoproterozoic Marydale and Namaqualand terrains (Fig. 1; Tankard et al., 1982). At the surface, three distinct crustal domains are generally recognized, separated by two major crustal discontinuities (Stowe, 1983; Grütter and Apter, 1998). From east to west, the 3.2–2.9 Ga Kaapvaal craton is separated from the 3.0–1.9 Ga Marydale domain by the Doornberg fault zone. The Marydale is in turn truncated on its western boundary by the Brakbos fault zone, which separates it from the 1.6–1.1 Ga Namaqualand Metamorphic Complex to the west. Within this broad structural framework, considerable uncertainty surrounds the age of rocks exposed at the craton margin.

Demarcation of the domains through which the studied kimberlites intrude relies on interpretation of regional aeromagnetic and gravity data, as most of the study area is covered by sedimentary rocks of the late Paleozoic Karoo basin. Of the three kimberlites studied, each is believed to intrude through different crustal domains (Grütter and Apter, 1998; H.S. Grütter, pers. comm.). The Klipfontein-08 pipe (Group 1 kimberlite; 22°10'E, 31°05'S) intrudes 40 km to the west of the Brakbos fault zone in the Namaqua terrain; the Markt kimberlite (Group 2 kimberlite; 22°22'E, 30°15'S) lies 0.5 km to the east of the Brakbos fault in the Marydale terrain; and the

Lovedale kimberlite (Group 1 kimberlite; 23°40'E, 30°35'S) lies 30 km to the east of the Doornberg fault on the Kaapvaal craton proper.

4. Analytical methods

Zircons were isolated from xenoliths by standard crushing, heavy liquid, and magnetic separation techniques, and separated into different populations based on crystal morphology, color, clarity and inclusion characteristics. From these populations, representative crystals were mounted in epoxy, polished, and imaged by back-scattered electron (BSE) and cathodoluminescence (CL) using the MIT JEOL 733 Superprobe. Both imaging techniques used an accelerating voltage of 15 keV, 10 to 30 nA beam current, and a 1 μm beam diameter. The CL image was collected with the secondary electron detector (sensitive to wavelengths of 400–600 nm) mounted in place of the optical microscope ocular. Mineral inclusions were identified by energy dispersive analysis (EDS) under the same instrumental parameters.

Certain zircons were air-abraded after the method of Krogh (1982), followed by ultrasonication in 30% HNO_3 at 50°C for 2 h. Both abraded and unabraded zircons were loaded into Teflon FEP microcapsules and washed again in 30% HNO_3 at 50°C for 2–12 h.

Notes to Table 1:

^aAll fractions were composed of single crystals of fragments of crystals; description abbreviations as follows: aa = air-abraded; frag = grain fragment, cl = colorless, pk = pink-colored, ovg = overgrowth, eq = equant, el = elongate.

^bSample weights were estimated to within 20% using measured grain dimensions ($\pm 5 \mu\text{m}$), an ellipsoidal geometry, and nominal density of 4.5 g/cm³.

^cDiscordance expressed as a percentage of the length of the chord passing through the analysis between concordia and the origin, measured from concordia.

^dExpressed as ppm U and Th and ppm radiogenic Pb: Th–U ratio calculated from the radiogenic $^{208}\text{Pb}/^{206}\text{Pb}$ ratio and the $^{207}\text{Pb}/^{206}\text{Pb}$ date of the sample assuming concordance between Th–Pb and U–Pb systems.

^ePbc and Pb* represent common Pb and radiogenic Pb respectively.

^fMeasured ratio corrected for fractionation only: Pb fractionation correction is 0.12 \pm 0.04% per a.m.u. for multicollector analyses and 0.15 \pm 0.04% per a.m.u. for single collector analysis based on repeated analyses of NBS 981.

^gMeasured ratios corrected for fractionation, spike, blank, and initial common Pb: U blank = 1 pg \pm 50%; total procedural Pb blanks averaged 1.8 \pm 0.8 (1 σ) pg ($n = 12$) during the course of this study — data were reduced using a Pb blank of 3.5 pg \pm 50% except for analyses with < 3.5 pg total common Pb, in which case this value was used as blank and the uncertainty reduced to 20%; blank composition: $^{206}\text{Pb}/^{204}\text{Pb} = 19.102$, $^{207}\text{Pb}/^{204}\text{Pb} = 15.7147$, $^{208}\text{Pb}/^{204}\text{Pb} = 38.653 \pm 0.05\%$ (1 σ); initial common Pb composition was calculated using the interpreted sample age and the two-stage terrestrial lead evolution model of Stacey and Kramers (1975).

^hNumbers in parentheses are the % errors reported at the 2 σ confidence interval; uncertainty in the $^{207}\text{Pb}/^{206}\text{Pb}$ date in Ma at the 2 σ confidence interval.

Zircons were spiked with a mixed ^{205}Pb – ^{233}U – ^{235}U tracer and dissolved in concentrated HF at 220°C for 40–60 h, followed by conversion to 6 N HCl at 180°C for 12 h. Pb and U were separated using miniaturized HCl-based ion-exchange chromatography procedures modified after Krogh (1973). Pb and U were analyzed on the MIT VG Sector 54 thermal ionization multicollector mass spectrometer. Lead isotopes were measured either dynamically with four high-mass Faraday cups and an axial ion-counting

Daly detector, peak-switching ^{205}Pb into the axial position to obtain an internal Daly–Faraday gain calibration, or by peak-switching all ion beams into the Daly detector for very small Pb beams. An ion beam of 0.5 to 1.5×10^{-13} A was maintained for ^{206}Pb during data acquisition. Uranium isotopes were measured as metal ions in static mode on three Faraday cups with an average ^{235}U ion-beam intensity of 2.5×10^{-13} A. Details of fractionation and blank corrections are given in Table 1. Ages with

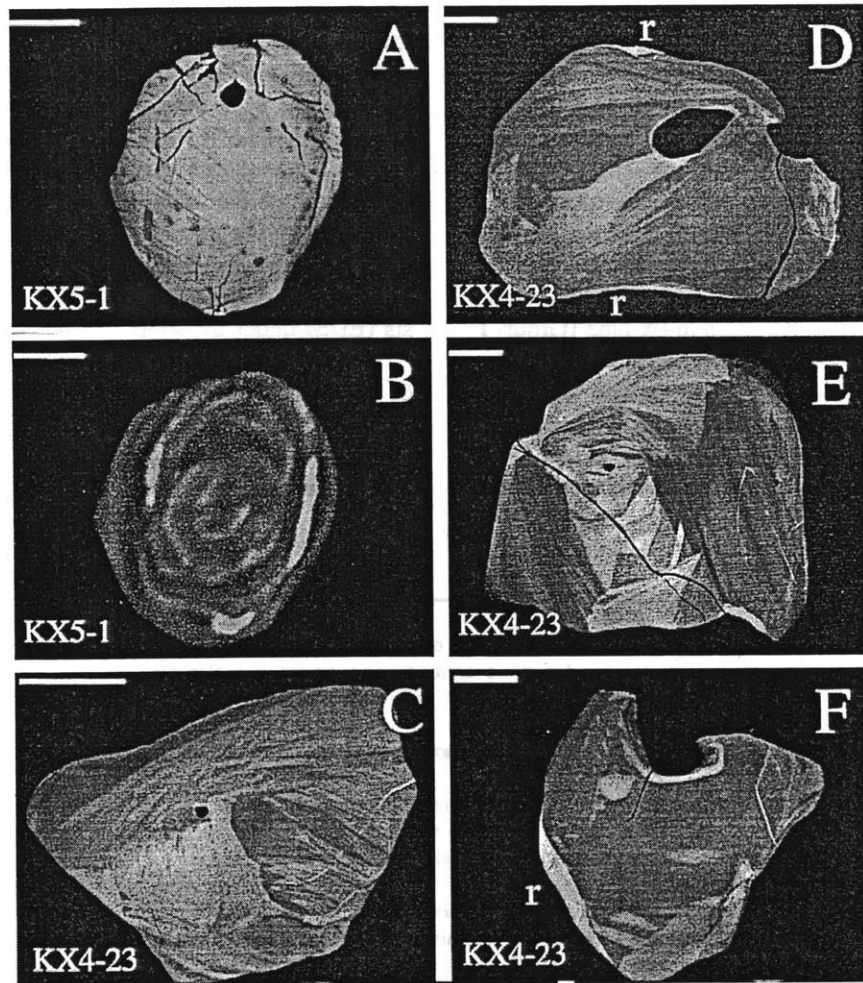


Fig. 2. Back-scattered electron (BSE) and cathodoluminescence (CL) images of polished zircons from the four xenoliths studied in this work. (A–B) BSE and CL images of an eclogitic zircon from the Lovedale xenolith; (C–F) CL images of zircon from the Markt garnet granulite xenolith, “r” bright rim overgrowths; (G–I) CL images of zircon from the Markt garnet amphibolite xenolith, “c” core, “o” overgrowth; (J–L) CL images of zircon in greenschist facies metasyenite xenolith from Klipfontein, “i” igneous phase, “b” luminescent overgrowth, “d” non-luminescent overgrowth. Scale bar is 10 μm long in A–B and 50 μm long in C–L.

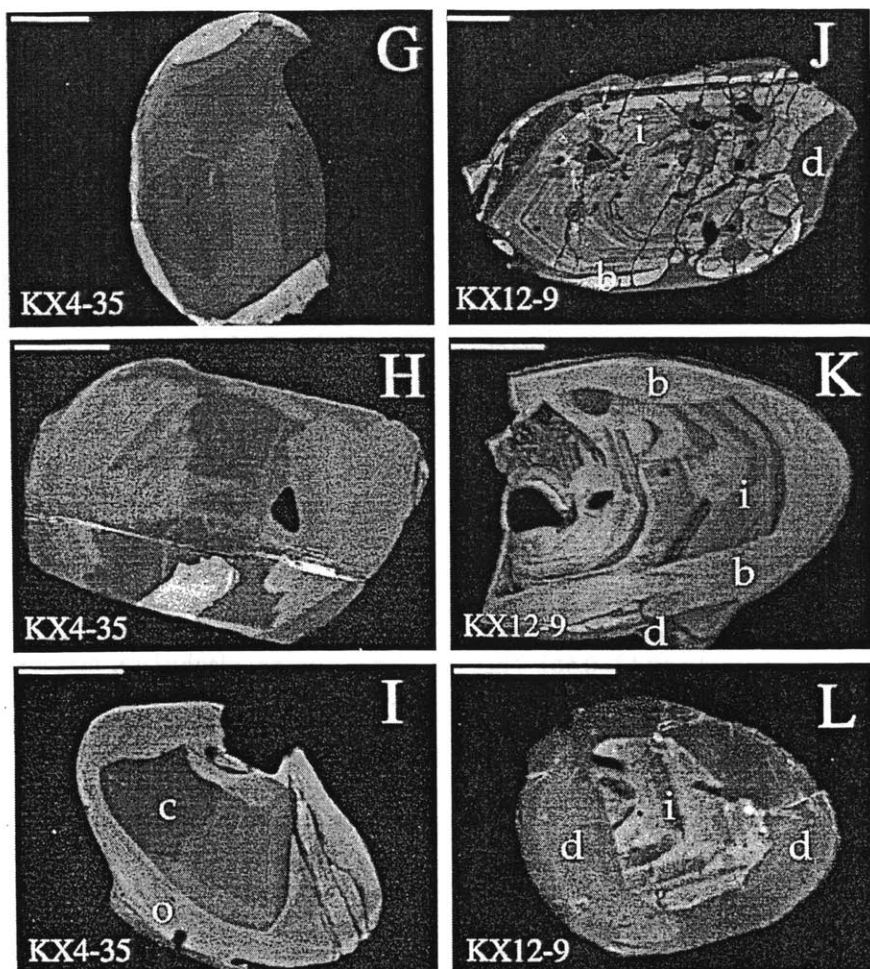


Fig. 2 (continued).

propagated uncertainties were calculated using the methodology of Ludwig (1980).

5. Results for crustal xenoliths

5.1. Lovedale — eclogite (KX5-1)

This small (8 cm dia.) coarse-grained eclogite xenolith (sample JAR-02023 of Robey (1981)) consists of granoblastic omphacitic clinopyroxene and garnet with accessory rutile and apatite, and is petrographically and chemically similar to the eclogites

studied by Pearson et al. (1995). The eclogite is non-diamondiferous and contains no graphite, and is classified as a Group II eclogite on the basis of texture and mineral compositions (McCandless and Gurney, 1989). It contains significant amounts of metasomatic phlogopite, and exhibits evidence for decompression melting during kimberlite entrainment.

Zircon was not identified in thin section, however, 18 small (10–35 μm), clear to pink, round to slightly elongate multi-faceted zircons were extracted from the xenolith. In general, the zircon is characterized by weak zonation in BSE (Fig. 2A)

and weak CL, indicating its low REE abundances, but clearly contains a set of regular, nested, multifaceted growth shells (Fig. 2B). The interiors of individual growth shells consistently trend from low to high CL intensity and some of the inner shells exhibit sector zoning. No conclusive truncations of zoning between growth shells indicating resorption could be distinguished. The zircon also contains an inclusion of omphacite (dark euhedral form in Fig. 2A).

The U–Pb systematics of seven single zircons were measured (Fig. 3). Because of their small size, the zircons were not abraded prior to dissolution. Four zircons define a discordia with an upper intercept of 2630 ± 1 Ma and a lower intercept of 84 ± 13 Ma (Fig. 3). The other three zircons cluster around this discordia to slightly higher and lower $^{207}\text{Pb}/^{206}\text{Pb}$ dates (2602 to 2634 Ma). Two zircons with younger $^{207}\text{Pb}/^{206}\text{Pb}$ dates (z4, z7) have generally lower Th/U ratios (0.03–0.09) relative to the other zircons which define the discordia (0.13–0.56). This correlation of Th/U ratio with $^{207}\text{Pb}/^{206}\text{Pb}$ date suggests that there are varying proportions of discrete growth phases present in the zircons, as will be discussed in a later Section 6.1.

5.2. Markt — *grt-cpx-plg* granulite (KX4-23)

This relatively large (20 cm) strongly foliated xenolith contains a well-developed planar fabric

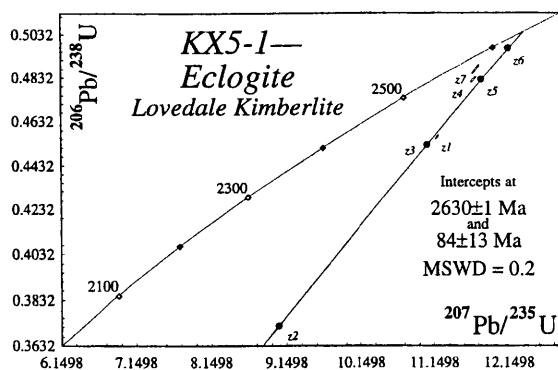


Fig. 3. U–Pb concordia diagram for the eclogite xenolith (KX5-1) from the on-craton Lovedale kimberlite; error ellipses are smaller than filled circles representing the regressed analyses z2, z3, z5, and z6; analyses z1, z4 and z7 are not included in the regression.

dominated by oriented clinopyroxene, modal layering of garnet-rich domains on millimeter to centimeter scales, and a lineation defined by streaky white felsic segregations. The mineralogy of this xenolith comprises a typical high-pressure granulite assemblage of garnet, clinopyroxene, and plagioclase, with minor rutile, magnetite, ilmenite, apatite and zircon. Overprinting this granulite facies mineralogy is a low-grade metamorphic alteration including extensive sericitization of plagioclase focussed at grain boundaries, finely intergrown actinolite–biotite coronae on clinopyroxenes, and kelyphitic rims on garnet.

Zircons occur as large (50–250 μm), anhedral, slightly pink grains with abundant mineral inclusions. They are most often in contact with or included within clinopyroxene, and less often in garnet and plagioclase. CL imaging presents compelling evidence for two episodes of zircon crystallization. The dominant phase of zircon contains inclusions of clinopyroxene, plagioclase, magnetite, and rare garnet, and exhibits a characteristic feathery or sheaf-like zonation (Fig. 2C–E), ubiquitously truncated by strong resorption along grain edges. Very thin rinds of a second phase of highly luminescent zircon occur discontinuously on the outer rims of many grains, and also on the inner surfaces of clinopyroxene inclusions which have been pseudomorphed by actinolite and biotite. On rare grains with fragments of adhering matrix, it is seen that these bright overgrowths are developed in contact with fine intergrowths of actinolite, biotite, albite, and magnetite.

The timing of these two growth episodes is constrained by the U–Pb systematics of individual grains of zircon. $^{207}\text{Pb}/^{206}\text{Pb}$ dates for eight zircon grains range from 1036 to 1104 Ma; these six analyses define a chord with upper and lower intercepts of 1114 ± 5 and 902 ± 21 Ma respectively (MSWD = 0.74; Fig. 4). This chord may be interpreted either as a Pb-loss discordia or as a mixing array between concordant domains of older core material and younger overgrowths. In light of the CL evidence for two discrete phases of zircon, we prefer the latter interpretation. Support for this view is given by experiments designed to isolate each component. As seen in Fig. 4, analyses of single grains which have been abraded to remove potential outer rinds (z2–z4) lie nearer the upper intercept of the chord, at older

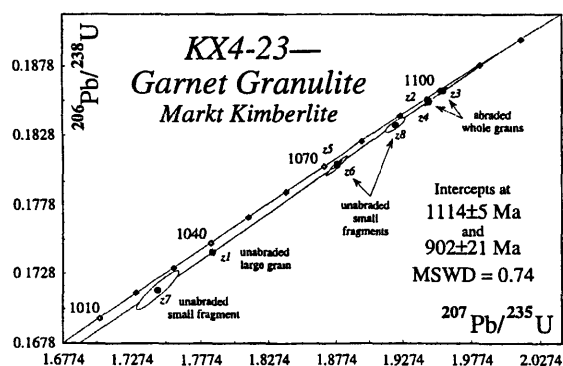


Fig. 4. U–Pb concordia diagram for all zircons from the mafic granulite xenolith (KX4-23) from the craton-marginal Markt kimberlite; linear regression is through all data points.

$^{207}\text{Pb}/^{206}\text{Pb}$ dates, than small unabraded fragments (z5, z6, z8) and a large unabraded grain (z1). Another fragment (z7) removed from the outer luminescent rind of a zircon imaged by CL (“r” in Fig. 2F) yields the youngest $^{207}\text{Pb}/^{206}\text{Pb}$ date, however is probably still a mixture of two components. Assuming that all crystal domains are concordant (as supported by the low MSWD of the mixing model), the growth ages of the two components of zircon correspond to the concordia intercepts of the chord.

5.3. Markt — *grt-cpx-hbl-plg* amphibolite (KX4-35)

This large (40 cm) xenolith of moderately foliated amphibolite is composed of medium-grained granoblastic hornblende, clinopyroxene, garnet, plagioclase and minor K-feldspar, quartz, magnetite, ilmenite, apatite and zircon. In detail, grain boundaries between clinopyroxene, garnet, and plagioclase are sharp, while hornblende grain boundaries are ragged and replacement by clinopyroxene is abundant. Distinct garnet + clinopyroxene rich zones define a millimeter scale layering. This xenolith also contains a pervasive grain boundary alteration including fine green amphibole, biotite, albite, Fe-oxides, and sulfide. Petrographic observations and CL imaging define three distinct populations of zircon in this xenolith: (1) pinkish inclusion-free subhedral ovoid grains with blocky polygonal sector zoning (Fig. 2G) and strongly resorbed margins, predominantly included

within pyroxene or in grain contact with pyroxene and amphibole (Fig. 5A); (2) colorless multi-faceted equant grains with distinctive fir-tree sector zoning (Fig. 2H) and rare inclusions of biotite, K-feldspar and quartz, which are mainly set within quartzofeldspathic domains (Fig. 5B); and (3) anhedral zircons consisting of cores of clear zircon, mantled by thin wing-like finely laminated rinds with curving zonation (Fig. 2I).

All zircons analyzed yielded near concordant U–Pb data, although abraded grains are more concordant than unabraded grains (Fig. 6). Five grains from the first population of pink zircon yield the oldest $^{207}\text{Pb}/^{206}\text{Pb}$ dates of 1100 to 1107 Ma, with Th/U ratios ranging from 0.26–0.45. The zircon with the oldest $^{207}\text{Pb}/^{206}\text{Pb}$ date is the most concordant. Four clear zircons of the second population have $^{207}\text{Pb}/^{206}\text{Pb}$ dates of 1079 to 1092 Ma and distinctly higher Th/U ratios of 0.55–0.77. Again, the most concordant zircon has the oldest $^{207}\text{Pb}/^{206}\text{Pb}$ date. To determine the age of the overgrowths observed in CL, a fragment of overgrowth from an anhedral zircon (z7) was separated from its core, and after abrasion, yielded a nearly concordant analysis with a $^{207}\text{Pb}/^{206}\text{Pb}$ date of 961 ± 2 Ma. A second grain with a small clear core and well developed overgrowth (z10) yields an analysis lying on a chord between the analyses of the clear zircons and the analysis of the overgrowth.

5.4. Klipfontein — *aegirine-biotite* syenite (KX12-9)

This xenolith of syenite with well-preserved igneous textures consists of primary aegirine, biotite, K-feldspar, and plagioclase with minor quartz, magnetite, ilmenite, sphene, apatite, and zircon. A greenschist facies assemblage of zoisite, albite, actinolite, calcite, and secondary granular sphene overprints the igneous assemblage. Two populations of colorless zircon are observed, including inclusion-rich, elongate, subhedral to prismatic crystals, and equant multi-faceted grains. CL imaging of both populations reveals three distinctive generations of zircon: (1) dominant oscillatory zoned inclusion rich cores (phase “i” in Fig. 2J–L); (2) a “bright” highly luminescent and homogeneous mantle overgrowing or replacing these truncated cores (phase “b” in Fig.

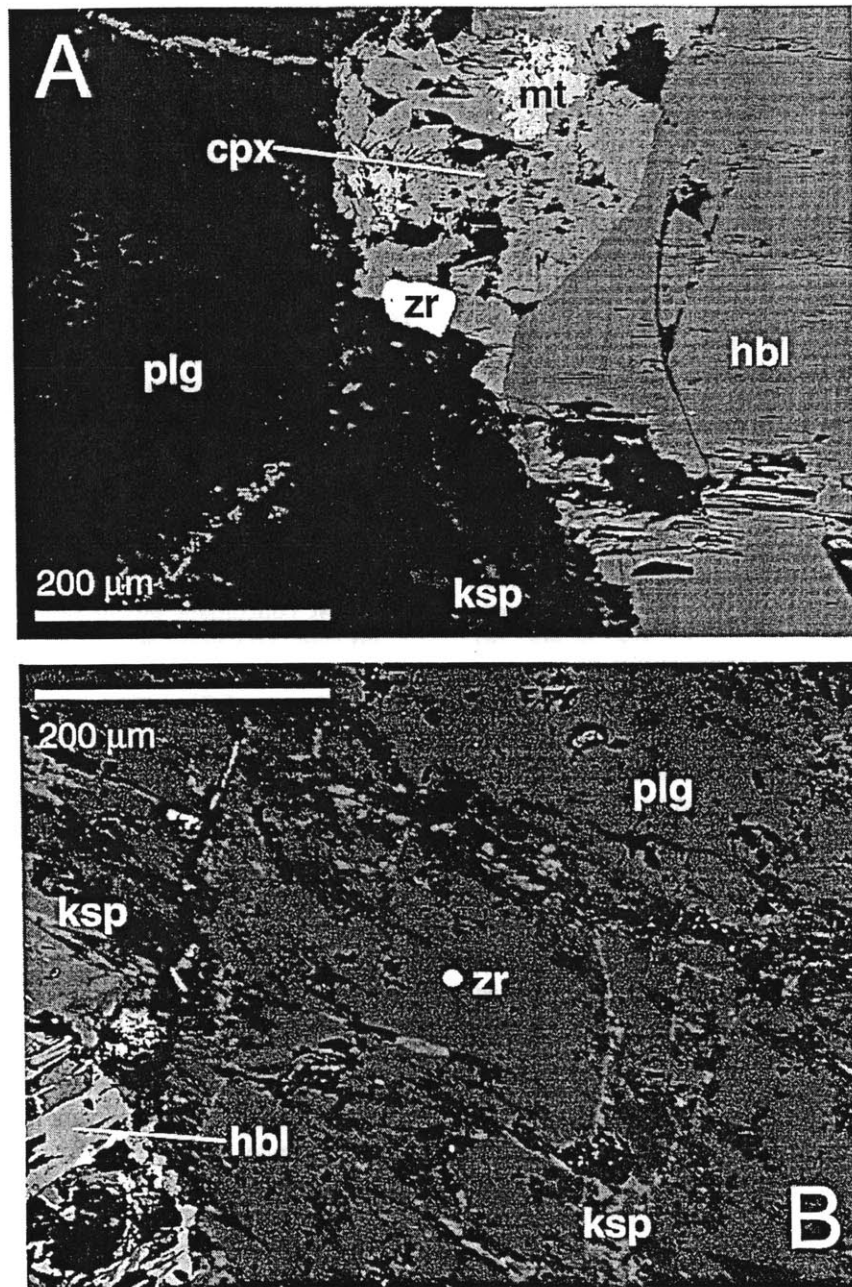


Fig. 5. BSE photomicrographs of a thin section of the garnet amphibolite xenolith (KX4-35), showing two zircons (zr) in petrographic context (cpx, clinopyroxene; hbl, hornblende; mt, magnetite; ksp, K-feldspar; plg, plagioclase). (A) pink zircon growing between clinopyroxene and plagioclase, near their contact with hornblende; (B) colorless zircon set in plagioclase.

2J–L); and (3) a “dark” weakly luminescent phase which forms rims on most zircons, occupies fractures in both prior phases and forms rinds on the inner

surfaces of breached inclusions now retrograded to a greenschist assemblage (phase “d” in Fig. 2J–L). The proportion of phases within a single grain varies

considerably, with elongate grains usually inheriting their aspect ratio from that of the primary oscillatory zoned component. In contrast, these primary cores are volumetrically variable to absent in equant grains, and thus allow the opportunity to preferentially sample overgrowths.

Single grains of both populations of zircon were abraded and analyzed, and are presented in Fig. 7. Elongate grains and three equant grains are variably discordant with $^{207}\text{Pb}/^{206}\text{Pb}$ dates ranging from 1786 to 1038 Ma, and define a chord with an upper intercept of 1898 ± 17 Ma (MSWD = 5). Near the lower intercept of the array lie a number of analyses of abraded equant grains with $^{207}\text{Pb}/^{206}\text{Pb}$ dates ranging from 1038 to 990 Ma. Based upon the CL images and petrographic observations of these grains, the discordia array exhibited by this set of zircons is easily explained as the result of mixing between the three observed phases of zircon. The upper intercept of the array is interpreted as the time of growth of the oscillatory-zoned igneous zircon component (phase “i”), and is taken to be the best estimate of the crystallization age of the syenite. The complex cluster of data at the lower intercept of the array reflects the difference in timing of growth of the two overgrowths visible in CL. The concordant date of 1015 Ma for grain z6 most likely represents the growth age of the bright overgrowth (phase “b”). This crystal has distinctly lower U, Th and Pb contents than any of the other analyses, consistent with

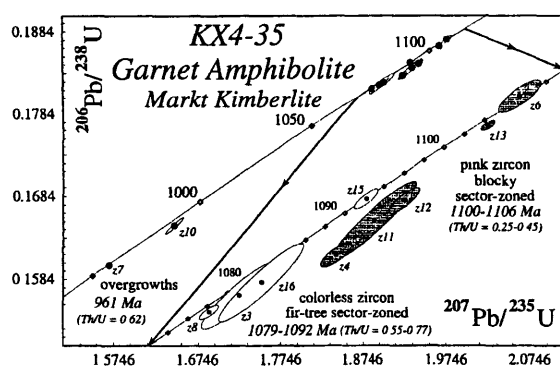


Fig. 6. U–Pb concordia diagram for the amphibolite xenolith (KX4-35) from the Markt kimberlite. Inset enlargement illustrates the two distinct arrays of data defined by the pink subhedral (shaded ellipses) and colorless equant (open ellipses) zircons.

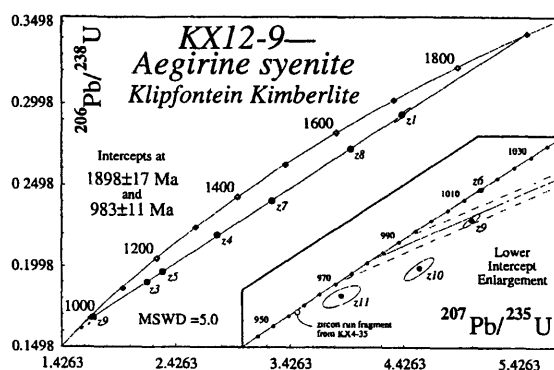


Fig. 7. U–Pb concordia diagram for the aegirine syenite xenolith (KX12-9) from the off-craton Klipfontein-08 kimberlite; linear regression (York 1) model calculated for all points denoted by filled circles in the main figure. Inset enlargement illustrates the complex systematics of zircon near the lower intercept of the data array.

the bright luminescence of this phase of zircon, as luminescence is commonly quenched by high trace element contents (Marfunin, 1979; Hoffman and Long, 1984). The younger dark overgrowth (phase “d”) has a maximum age represented by the $^{206}\text{Pb}/^{238}\text{U}$ date of 964 Ma for grain z10 (if the discordance of this analysis is due to mixing with older zircon — if the discordance is a function of recent Pb loss then the $^{207}\text{Pb}/^{206}\text{Pb}$ date of 990 Ma provides a bound on the maximum age of the overgrowth). That the array of data for this sample reflects three- and not two-component mixing may explain the poor statistical fit of the linear regression (MSWD = 5.0) to the data as due to real geological scatter.

6. Interpretation of zircon ages in crustal xenoliths

The stability of zircon during metamorphism is a function of local zirconium and silica activity. These parameters are in turn complex functions related through trace element partitioning to phase equilibria controlled ultimately by temperature, pressure, oxygen and water fugacity, and bulk composition. Because of these complexities, quantitative modelling of metamorphic zircon crystallization and/or dissolution in natural systems has not yet been achieved.

However, from an empirical approach, much information regarding zircon stability can be inferred from careful petrographic and geochemical observations of zircon in metamorphic rocks. Observations in the four xenoliths reported here indicate both crystallization and dissolution of zircon through a wide spectrum of temperatures and pressures in both prograde and retrograde metamorphic reactions.

6.1. *Eclogitic zircon*

The significance of U–Pb zircon dates in eclogites has been debated without consensus since the first eclogitic zircon was dated by Krogh et al. (1974). These zircons have been variously interpreted as dating ancient inherited components, the age of protolith magmatism, peak eclogite-facies metamorphism, or retrograde late recrystallization (Gebauer et al., 1985; Paquette et al., 1989; Creaser et al., 1997). The rare zircons present in sample KX5-1 can be linked to crystallization under eclogite-facies conditions by their minute inclusions of omphacitic pyroxene. A number of other observations can be brought to bear on their mechanism and timing of growth. The CL zonation pattern of regular nested multi-faceted shells (Fig. 2B) is indicative of episodic growth, and the broadly oscillatory (and sector) CL intensity changes within each growth band are characteristic of diffusion-limited crystal growth and/or incorporation of trace constituents (Bottinga et al., 1966; Watson and Liang, 1995). Further, the rounded, multi-faceted isometric to slightly elongate internal and external morphologies of the grains is a familiar characteristic of zircons found in rocks of high metamorphic grade and have been attributed to sub-solidus crystallization (Gebauer et al., 1985; Paquette et al., 1989; Schaltegger et al., 1999).

These characteristics of the zircons, combined with other observations on high-field strength element and accessory mineral contents of garnet and clinopyroxene are consistent with a model of zircon “exsolution” from clinopyroxene. While handicapped by a lack of direct measurements of Zr solubility in eclogite minerals, a circumstantial case can be made for this type of unmixing reaction. The recent work by Harte and Kirkley (1997) on Roberts Victor eclogites indicates that Zr is partitioned

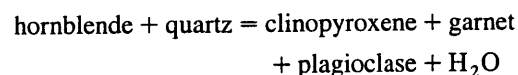
equally between omphacitic clinopyroxene and garnet, although no structural determinations were made. Tetravalent zirconium has been documented in six-fold coordination occupying the M1 site of Zr-rich sodic clinopyroxenes (Farges et al., 1994) and in the octahedral site of kimzeyite garnets (Munno et al., 1980). The structural environment of Zr is thus similar to that of tetravalent titanium, as expected from crystal chemical theory. There is abundant observational evidence for the exsolution of titanian phases from garnet and pyroxenes in eclogites, granulites, and slowly cooled plutonic rocks (Moore, 1968; Garrison and Taylor, 1981; Griffin et al., 1971; Dawson and Smith, 1987). By analogy, the potential exsolution of zircon from these minerals during slow cooling of the host rock seems plausible.

According to this model, crystal growth is not only episodic but also records early cooling. Each growth phase will have a distinct age, and each crystal will comprise a composite of ages integrating a segment of the cooling path. The dispersion of single grain ages could thus be interpreted to qualitatively constrain the cooling rate of the eclogite provided sufficient data on Zr solubility and diffusivity in clinopyroxene. More simply, this type of growth model implies that zircon dates in this xenolith do not strictly define the timing of peak metamorphism, but rather the early cooling path. Our preferred interpretation of the data is that the upper intercept date of 2630 Ma represents the age of the dominant component of zircon growth, but that episodic crystallization of zircon began as early as 2634 Ma and continued until at least 2602 Ma — an interval conservatively constrained by the $^{207}\text{Pb}/^{206}\text{Pb}$ dates of individual zircons assuming that each grain was composed only of a single growth phase.

6.2. *Zircon growth at amphibolite to granulite facies: “prograde” versus “retrograde”*

The timing and mechanisms of “metamorphic” zircon crystallization in high-grade amphibolite to granulite-facies rocks are also widely debated, with particular reference to whether U–Pb dates constrain prograde, peak, or retrograde metamorphic conditions (e.g. Fraser et al., 1997; Roberts and Finger, 1997). Zircons in the mafic granulite xenolith of this study (KX4-23) crystallized under granulite facies

conditions as evidenced by inclusions of a granulite mineral assemblage (cpx–plag–gt). In detail, clinopyroxene is the most abundant mineral inclusion in this zircon, and accompanies all other types of inclusions. This observation indicates the simultaneous crystallization of zircon and clinopyroxene, and suggests a close spatial proximity for these two phases. This is strong circumstantial evidence for crystallization of zircon triggered by a reaction involving clinopyroxene. One likely candidate is the representative breakdown reaction of hornblende (Spear, 1993):



Fraser et al. (1997) analyzed the zirconium concentrations in granulite-facies minerals and observed significant zirconium hosted only by garnet and hornblende. They conclude that breakdown reactions involving these two minerals could be potentially important zirconium sources, promoting the crystallization of new metamorphic zircon. Our observations support this suggestion for hornblende breakdown. This link between metamorphic zircon crystallization and hornblende breakdown is significant because it allows the direct correlation of the zircon age with petrologically derived P – T estimates, dating a segment of the prograde limb of the P – T path of this granulite in cases where major-element geothermobarometry records prograde P and T as faithfully as cogenetic zircon preserves its isotopic age.

Interpretation of the zircon systematics of the amphibolite xenolith (KX4-35) is not aided by abundant inclusions, however, CL patterns, Th–U ratios, and petrographic observations suggest that the difference in U–Pb dates of the pink subhedral (~ 1107 Ma) and colorless equant (~ 1092 Ma) zircon populations reflects two distinct growth ages for zircon. The pink anhedral zircons have relatively lower Th–U ratios (0.26–0.45) than the clear equant zircons (0.55–0.74), more similar in composition to the zircons in the granulite xenolith KX4-23. In CL, they have blocky sector zoning and are found preferentially included or in contact with pyroxene (e.g. Fig. 3A), which is in turn forming by hornblende breakdown. These observations lead us to tentatively conclude that this population of zircons was crystallized

during prograde hornblende breakdown reactions. The age of the oldest most concordant zircon places a minimum bound on this granulite facies reaction at 1107 Ma.

In contrast, the population of colorless zircons with younger dates exhibits different characteristics which we believe indicate crystallization on the retrograde limb of the P – T path. These zircons have ubiquitous radially symmetric fir-tree sector zoning, which has been ascribed to growth in the presence of melt (Vavra et al., 1996, 1999). These zircons are also only observed within quartzofeldspathic domains of the xenolith, and most intriguingly have rare inclusions of quartz, K-feldspar, and biotite — a comparatively retrograde mineral assemblage for this xenolith. It is suggested that this population of zircons grew in the presence of an infiltrating melt phase on the retrograde limb of the P – T path of this amphibolite. Interpreting the timing of this zircon crystallization is complicated by later low-grade zircon overgrowths discussed previously, however a minimum bound is obtained from the oldest, most concordant zircon at 1092 Ma.

6.3. Low-temperature retrograde zircon stability

Both the amphibolite and the granulite xenoliths share a common low-grade greenschist facies alteration overprint which is manifested both in hand sample and in zircon growth structure. Thin rims and anhedral overgrowths on zircons from both xenoliths are in intimate association with the greenschist metamorphic assemblage, strongly suggesting that zircon growth occurred under these low grade conditions, and approximately 130–150 Ma after high-grade metamorphism. Even more spectacular evidence for greenschist facies zircon crystallization is seen in the syenite xenolith (KX12-9). In regard to controls on zircon crystallization, two questions to be addressed are the source of zirconium and the trigger for precipitation. The nearly ubiquitous occurrence of *resorption* phenomena in all zircons from xenoliths with evidence for low-grade greenschist-facies alteration suggests that previously crystallized zircon is a major source of zirconium during retrograde metamorphism. As suggested in the literature (Ayers and Watson, 1991; Williams et al., 1996), this resorption

is most likely mediated by the presence of Zr-undersaturated fluids, and fluorine-rich fluids may be particularly effective at complexing and transporting Zr in solution (Rubin et al., 1993). The presence of fluorine-rich fluids is likely for the alkalic syenite xenolith, considering its bulk composition, and would readily explain the spectacular resorption–reprecipitation phenomena observed in its zircons. The trigger which results in precipitation of new zircon overgrowths on resorbed grains is not well-constrained, but must be related to changing zirconium solubilities in the aqueous fluid carriers. One possible candidate is the effect of temperature, whereby zircons will be dissolved by initially hotter undersaturated solutions, and then overgrown upon interaction with cooler oversaturated fluids. Fluid compositional controls such as alkalinity or silica activity, and fluid mixing might also determine zircon stability.

7. Implications for the evolution of the Kaapvaal craton

7.1. Archean eclogite beneath the Kaapvaal craton

This study presents the first high-precision U–Pb zircon data for an eclogite from the Kaapvaal craton, providing an important datum for the interpretation of lithospheric mantle dynamics and crust–mantle interaction. The mineralogy and geochemistry of sample KX5-1 was studied by Robey (1981), who determined a garnet–clinopyroxene equilibration temperature of 945–980°C (assuming $P = 10\text{--}20$ kbar) using the thermometer of Ellis and Green (1979). Assessing the $P\text{--}T$ conditions of equilibration is equivocal, however, for lack of an eclogite barometer, and depends on projection of their calculated equilibration pressures onto an appropriate crust–mantle geotherm. Pearson et al. (1995) interpreted the depth of derivation of similar eclogites from Lovedale at 10 to 20 kbar by projection onto their $P\text{--}T$ array defined by granulite thermobarometry. While these depth estimates are appropriate for equilibration of the eclogite along an elevated “oceanic” geotherm, equilibration along a cold “cratonic” geotherm would yield depths of equilibration for this eclogite of > 30 kbar. The latter thermal gradient is arguably more appropriate for the Archean

eclogite examined in this study, whose genesis and last temperature of equilibration were unrelated to the Proterozoic granulites from which the Pearson et al. (1995) geotherm was derived.

This date of eclogite formation at ~ 2630 Ma falls within a relatively sparsely constrained period in the history of the Kaapvaal craton. It remains to be clearly evidenced whether the protolith of the eclogite was substantially older than the metamorphic age we have inferred from the U–Pb zircon geochemistry. Alternatively, this eclogite may represent the high-pressure crystallization product of underplated basaltic magmas emplaced during extensional magmatism related to the latest phases of the Ventersdorp flood basalt magmatism. If so, this represents the youngest associated magmatism so far precisely dated. This date is bracketed by two reliable U–Pb zircon ages for exposed rocks: the Makwassie quartz porphyry of the Ventersdorp supergroup with a U–Pb zircon ion probe age of 2709 ± 4 Ma (Armstrong et al., 1991), and an ID-TIMS U–Pb single zircon age of 2521 ± 3 Ma for a volcanic ash 40–50 m below the contact between the Campbellrand Subgroup and the Kuruman Iron Formation of the Transvaal Supergroup (Sumner and Bowring, 1996). The intervening time period represents over 180 m.y. of rifting and Ventersdorp volcanic activity, an erosional hiatus of unknown length, followed by broad cratonic subsidence and deposition of the lower members of the Transvaal Supergroup (Tankard et al., 1982). This metamorphic age thus falls within a critical window during the evolution of the craton, at a poorly understood transition between modes of intra-cratonic rifting and broad cratonic subsidence.

7.2. Granulite facies metamorphism at the craton margin

A number of studies of the thermobarometry of crustal xenoliths have attempted to derive lithospheric paleogeotherms in a manner similar to that applied to mantle xenoliths (O’Reilly and Griffin, 1985; Pearson et al., 1995). Harte et al. (1981), however, pointed out that such reconstructions are invalid due to freezing in of mineral equilibria long prior to entrainment of the samples as xenoliths. The most direct test of the primary assumption in paleo-

geotherm reconstruction, that the P – T estimates obtained from xenoliths record the ambient temperature at depth at the time of entrainment, is the radiometric dating of mineral equilibria. The zircon data reported in this study are sufficient to invalidate that assumption for the granulites of the southwest margin of the Kaapvaal craton. Not only do these data indicate that the high P – T granulite facies assemblage was equilibrated in the Late Proterozoic at 1.1 Ga, but the dating of retrograde zircon crystallization in the greenschist facies at ~ 960 Ma demonstrates the relatively rapid cooling of mid- to lower crust from this elevated transient geotherm. Therefore, the granulite-facies mineral equilibria recorded in these xenoliths have no bearing on the thermal state of the lithosphere at the time of kimberlite eruption (Late Cretaceous).

Previous suggestions that the mafic granulite xenoliths from the craton-margin kimberlites have an Archean heritage based on Pb isotopic systematics (Cornell et al., 1986; Huang et al., 1995) are not borne out by the U–Pb zircon systematics of the xenoliths from Markt examined in this study. There is no component of zircon of Archean age in either the mafic granulite or high-grade amphibolite. Because all of the dated zircon is constrained to be metamorphic in character, this does not rule out the possibility that the protoliths to these samples are older. However, the U–Pb zircon results are consistent with Nd isotopic data for the granulites (Huang et al., 1995), and together indicate that these rocks were generated at ~ 1.1 Ga and were subsequently depleted in U at ~ 0.9 Ga, arresting Pb isotopic evolution and thus yielding artificially old Pb isotopic age systematics. We conclude that the granulites of the craton margin kimberlites are, in fact, not of Archean age, but are juvenile components of the Proterozoic Namaqua Metamorphic Complex.

7.3. Crustal architecture of the craton boundary

Considerable uncertainty in the age of rocks exposed at the southwestern Kaapvaal craton margin, combined with the increasing degree of young sedimentary cover to the south of the Copperton–Prieska line complicates tectonic models for the evolution of the margin. Data from these xenoliths provide some of the most precise and accurate geochronology

available and also extend the “ground truth” beneath the surface cover in kimberlites erupted through Karoo sediments. The presence of 1900 Ma Marydale domain syenite xenoliths in the Klipfontein kimberlite, proposed to lie to the west of the Brakbos fault in the 1.1 Ga Namaqualand Metamorphic Complex, can be used to refine the structural model for the craton margin. Two scenarios can be drawn from this occurrence: either an unrecognized splay of the Brakbos fault lies to the west of the kimberlite, requiring reinterpretation of the potential field data; or if the surface trace of the Brakbos fault does lie to the east of the Klipfontein kimberlite, then the fault surface is constrained to dip to the west, in order to accommodate eastward overthrusting of the younger Namaqua terrain over the margin of the Marydale Domain (Stowe, 1983; Pearson et al., 1995). However, additional complexity is superimposed on this simple east-vergent thrust geometry by the presence of 1.1 Ga Namaqua-aged crust in the Markt kimberlite, outcropping ostensibly within the > 1.9 Ga Marydale domain. Thus, the Brakbos fault is likely not a simple planar feature, but consists of anastomosing fault strands, which have interleaved Marydale and Namaqua crust during dextral transpression associated with juxtaposition of these disparate terrains.

Combining metamorphic histories of granulite xenoliths from the Markt kimberlite with the data from the Klipfontein syenite, we can hypothesize on the timing of juxtaposition of the Namaqua terrain with the Marydale domain and the Kaapvaal craton. While the high-grade xenoliths from Markt were metamorphosed at granulite to upper amphibolite facies from 1115 to 1092 Ma, there is no evidence of this in the Klipfontein syenite. While this metamorphic discontinuity could be the result of sampling of pieces of upper and lower crust with contrasting thermal histories, it may alternatively indicate that the two terrains were isolated during high-grade metamorphism of the Namaqualand Metamorphic Complex at 1115 to 1092 Ma. That all xenoliths record the same low-grade metamorphic overprint at 1015 to 960 is suggestive that this event estimates the age of juxtaposition of these two terrains, relatively late in the history of Kibaran orogenesis. Possible tests of these two models are available in high-grade xenoliths from the Klipfontein kimberlite

and further kimberlites straddling these three domains.

8. Conclusions

(1) Individual growth phases within single zircons can be isolated and analyzed to high precision by a combination of CL imaging, microsampling, and ID-TIMS. Zircon growth can be tied to a variety of metamorphic grades on the basis of zircon petrography, CL zonation patterns, mineral inclusions, geochemistry and U–Pb systematics.

(2) Zircon crystallization accompanying eclogite-facies metamorphism most likely occurred in the solid state during early cooling of an eclogite from the Lovedale kimberlite. This Archean (2.63 Ga) eclogite at the margin of the craton may represent continued basaltic underplating related to magmatism during the critical period between eruption of the Ventersdorp flood basalts and initiation of cratonic subsidence and deposition of the Transvaal supergroup.

(3) The crystallization of zircon in high-pressure granulite and upper-amphibolite facies rocks occurs by at least two mechanisms, including solid-state prograde breakdown reactions of hornblende, and in the presence of an infiltrating melt on the retrograde portion of the P – T path. Dating of 1.1 Ga granulite facies metamorphism in the lower crust beneath the craton margin places constraints on the antiquity of paleogeotherms inferred from these “frozen” mineral equilibria and disputes the interpretation that these granulites have an Archean heritage.

(4) There is an abundance of zircon resorption and reprecipitation phenomena in xenoliths ranging from granulites to weakly metamorphosed plutonic rocks, all of which have experienced an episode of low-grade metamorphism. Demonstrating zircon growth at greenschist conditions allows temporal constraints to be placed on the low temperature portion of the cooling path of metamorphic rocks. The common presence of low-grade zircon overgrowths on pre-existing grains also demonstrates that mixing phenomena as well as Pb-loss can play an important role in causing discordance in single zircon analyses, from weakly metamorphosed plutonic rocks to high-grade granulites. Finally, a common

greenschist facies overprint in these Proterozoic xenoliths of the Kaapvaal craton margin may date the final juxtaposition of the disparate Namaqualand, Marydale, and Kaapvaal terrains late in the history of Mesoproterozoic orogenesis.

Acknowledgements

We acknowledge support from NSF grant EAR 9526702 to S.B. and a National Defense Science and Engineering Graduate Fellowship to M.S. during this study. The authors express their gratitude to the many South African and US scientists who have contributed their expertise regarding crustal xenolith occurrences and the tectonothermal evolution of southern Africa — especially Jock Robey, Herman Grutter, Dave Bell, John Gurney, and the members of the Kaapvaal Craton Working Group. Thorough and constructive reviews by Larry Heaman and Des Moser greatly improved the manuscript. Special thanks go to Desmond Moser and Dave Scott for organizing the G.S.A. conference session and this special volume on “What are we dating?”

References

- Armstrong, R.A., Compston, W., Retief, E.A., Williams, I.S., Welke, H.J., 1991. Zircon ion microprobe studies bearing on the age and evolution of the Witwatersrand triad. *Precambrian Research* 531, 243–266.
- Ayers, J.C., Watson, E.B., 1991. Solubility of apatite, monazite, zircon, and rutile in supercritical aqueous fluids with implications for subduction zone geochemistry. *Philosophical Transactions of the Royal Society of London A* 335, 365–375.
- Bottinga, Y., Kudo, A., Weill, D., 1966. Some observations on oscillatory zoning and crystallization of magmatic plagioclase. *American Mineralogist* 51, 792–806.
- Chen, Y.D., O'Reilly, S.Y., Kinny, P.D., Griffin, W.L., 1994. Dating lower crust and upper mantle events: an ion microprobe study of xenoliths from kimberlitic pipes, South Africa. *Lithos* 32, 77–94.
- Cherniak, D.J., Hanchar, J.M., Watson, E.B., 1997. Rare-earth diffusion in zircon. *Chemical Geology* 134, 289–301.
- Cherniak, D.J., Watson, E.B., 1999. Pb diffusion in zircon. *Chemical Geology*, this volume.
- Cornell, D.H., Hawkesworth, C.J., Van Calsteren, P., Scott, W.D., 1986. Sm–Nd study of Precambrian crustal development in the Prieska–Copperton region, Cape Province. *Transactions of the Geological Society of South Africa* 89, 17–78.
- Creaser, R.A., Heaman, L.M., Erdmer, P., 1997. Timing of high-

- pressure metamorphism in the Yukon–Tanana terrane, Canadian Cordillera: constraints from U–Pb zircon dating of eclogite from the Teslin tectonic zone. *Canadian Journal of Earth Sciences* 34, 709–715.
- Ellis, D.J., Green, D.H., 1979. An experimental study of the effect of Ca on garnet–clinopyroxene Fe–Mg exchange equilibria. *Contributions to Mineralogy and Petrology* 71, 13–22.
- Farges, F., Brown, G.E. Jr., Velde, D., 1994. Structural environment of Zr in two inosilicates from Cameroon: mineralogical and geochemical implications. *American Mineralogist* 79, 838–847.
- Fraser, G., Ellis, D., Eggins, S., 1997. Zirconium abundance in granulite-facies minerals, with implications for zircon geochronology in high-grade rocks. *Geology* 25, 607–610.
- Garrison, J.R. Jr., Taylor, L.A., 1981. Petrogenesis of pyroxene-oxide intergrowths from kimberlite and cumulate rocks: co-precipitation or exsolution? *American Mineralogist* 66, 723–740.
- Gebauer, D., Lappin, M.A., Grunefelder, M., Wyttenbach, A., 1985. The age and origin of some Norwegian eclogites: a U–Pb zircon and REE study. *Chemical Geology* 52, 227–247.
- Gerstenberger, H., Haase, G., 1997. A highly effective emitter substance for mass spectrometric Pb isotope ratio determinations. *Chemical Geology* 136, 309–312.
- Grauert, B., Wagner, M.E., 1975. Age of the granulite-facies metamorphism of the Wilmington complex, Delaware–Pennsylvania piedmont. *American Journal of Science* 275, 683–691.
- Griffin, W.L., Jensen, B.B., Misra, S.N., 1971. Anomalous elongated rutile in eclogite-facies pyroxene and garnet. *Norsk Geologisk Tidsskrift* 51, 177–185.
- Grütter, H.S., Apter, D.B., 1998. Garnet xenocryst chemistries in a traverse from Eendekuil to Kimberley over the south-western margin of the Kaapvaal craton. Seventh International Kimberlite Conference. pp. 283–286, Extended Abstracts.
- Hanchar, J.M., Miller, C.F., 1993. Zircon zonation patterns as revealed by cathodoluminescence and backscattered electron images: implications for interpretation of complex crustal histories. *Chemical Geology* 110, 1–13.
- Hanchar, J.M., Rudnick, R.L., 1995. Revealing hidden structures: the application of cathodoluminescence and back-scattered electron imaging to dating of zircon from lower crustal xenoliths. *Lithos* 36, 289–303.
- Harrison, T.M., Watson, E.B., 1983. Kinetics of zircon dissolution and zirconium diffusion in granitic melts of variable water content. *Contributions to Mineralogy and Petrology* 84, 66–72.
- Harte, B., Kirkley, M.B., 1997. Partitioning of trace elements between clinopyroxene and garnet: data from mantle eclogites. *Chemical Geology* 136, 1–24.
- Harte, B., Jackson, P.M., MacIntyre, R.M., 1981. Age of mineral equilibria in granulite facies nodules from kimberlites. *Nature* 291, 147–148.
- Hoffman, J.F., Long, J.V.P., 1984. Unusual sector zoning in Lewisian zircons. *Mineralogical Magazine* 48, 513–517.
- Huang, Y.-M., Van Calsteren, P., Hawkesworth, C.J., 1995. The evolution of the lithosphere in southern Africa: a perspective on the basic granulite xenoliths from kimberlites in South Africa. *Geochimica et Cosmochimica Acta* 59, 4905–4920.
- Koschek, G., 1993. Origin and significance of the SEM cathodoluminescence from zircon. *Journal of Microscopy* 171, 223–232.
- Krogh, T.E., 1973. A low contamination method for hydrothermal decomposition of zircon and extraction of U and Pb for isotopic age determination. *Geochimica et Cosmochimica Acta* 37, 637–649.
- Krogh, T.E., 1982. Improved accuracy of U–Pb zircon ages by the creation of more concordant systems using an air abrasion technique. *Geochimica et Cosmochimica Acta* 46, 637–649.
- Krogh, T.E., 1993. High precision U–Pb ages for granulite metamorphism and deformation in the Archean Kapuskasing Structural Zone, Ontario: implications for structure and development of the lower crust. *Earth and Planetary Science Letters* 119, 1–18.
- Krogh, T.E., Mysen, B.O., Davis, G.L., 1974. A Paleozoic age for the primary minerals of a Norwegian eclogite. *Carnegie Institution of Washington Year Book* 74, 575–576.
- Ludwig, K.R., 1980. Calculation of uncertainties of U–Pb isotope data. *Earth and Planetary Science Letters* 46, 212–220.
- Marfunin, A.S., 1979. Spectroscopy, Luminescence, and Radiation Centers in Minerals. Springer, Berlin.
- Mariano, A.N., 1989. Cathodoluminescence emission spectra of rare earth element activators in minerals. In: Lipin, B.R., McKay, G.A. (Eds.), *Geochemistry and Mineralogy of Rare Earth Elements. Reviews in Mineralogy* 21. Mineralogical Society of America, pp. 339–348.
- McCandless, T.E., Gurney, J.J., 1989. Sodium in garnet and potassium in clinopyroxene: criteria for classifying mantle eclogites. In: Ross, J. (Ed.), *Kimberlites and Related Rocks: Vol. 1. Their Composition, Occurrence, Origin, and Emplacement. Geological Society of Australia Special Publication* 14. Blackwell, Australia, pp. 827–832.
- Meldrum, A., Boatner, L.A., Weber, W.J., Ewing, R.C., 1998. Radiation damage in zircon and monazite. *Geochimica et Cosmochimica Acta* 62, 2509–2520.
- Moore, A., 1968. Rutile exsolution in orthopyroxene. *Contributions to Mineralogy and Petrology* 17, 233–236.
- Moser, D.E., Heaman, L.M., 1997. Proterozoic zircon growth in Archean lower crustal xenoliths, southern Superior craton — a consequence of Matachewan ocean opening. *Contributions to Mineralogy and Petrology* 128, 164–175.
- Moser, D.E., Heaman, L.M., Krogh, T.E., Hanes, J.A., 1996. Intracrustal extension of an Archean orogen revealed using single-grain U–Pb zircon geochronology. *Tectonics* 15, 1093–1109.
- Munno, R., Rossi, G., Tadini, C., 1980. Crystal chemistry of kimzeyite from Stromboli, Aeolian Islands, Italy. *American Mineralogist* 65, 188–191.
- Murakami, T., Chakoumakos, B.C., Ewing, R.C., Lumpkin, G.R., Weber, W.J., 1991. Alpha-decay event damage in zircon. *American Mineralogist* 79, 1510–1532.
- Paquette, J.-L., Menot, R.-P., Peucat, J.-J., 1989. REE, Sm–Nd and U–Pb zircon study of eclogites from the Alpine External Massifs (Western Alps): evidence for crustal contamination. *Earth and Planetary Science Letters* 96, 181–198.
- Pearson, N.J., O'Reilly, S.Y., Griffin, W.L., 1995. The crust–

- mantle boundary beneath cratons and craton margins: a transect across the south-west margin of the Kaapvaal craton. *Lithos* 36, 257–287.
- Roberts, M.P., Finger, F., 1997. Do U–Pb zircon ages from granulites reflect peak metamorphic conditions? *Geology* 25, 319–322.
- Robey, J., 1981. Kimberlites of the central Cape Province, R.S.A. Ph.D. thesis, University of Cape Town, South Africa.
- Rubin, J.N., Henry, C.D., Price, J.G., 1993. The mobility of zirconium and other “immobile” elements during hydrothermal alteration. *Chemical Geology* 110, 29–47.
- Schaltegger, U., Fanning, C.M., Gunther, D., Maurin, J.C., Schulmann, K., Gebauer, D., 1999. Growth, annealing and recrystallization of zircon and preservation of monazite in high-grade metamorphism: conventional and in-situ U–Pb isotope, cathodoluminescence and microchemical evidence. *Contributions to Mineralogy and Petrology* 134, 186–201.
- Silver, L.T., Deutsch, S., 1963. Uranium–lead isotopic variations in zircons — a case study. *Journal of Geology* 71, 721–758.
- Spear, F.S., 1993. *Metamorphic Phase Equilibria and Pressure–Temperature–Time Paths*. Monograph Series 1. Mineralogical Society of America, Washington, DC, 799 pp.
- Stacey, J.S., Kramers, J.D., 1975. Approximation of terrestrial lead isotope evolution by a two-stage model. *Earth and Planetary Science Letters* 26, 207–221.
- Stowe, C.W., 1983. The Upington geotraverse and its implications for craton margin tectonics. *Special Publication Geological Society of South Africa* 10, 147–171.
- Sumner, D.Y., Bowring, S.A., 1996. U–Pb geochronologic constraints on deposition of the Campbellrand Subgroup, Transvaal Supergroup, South Africa. *Precambrian Research* 79, 25–35.
- Tankard, A.J., Jackson, M.P.A., Eriksson, K.A., Hobday, D.K., Hunter, D.R., Minter, W.E., 1982. *Crustal Evolution of Southern Africa: 3.8 Billion Years of Earth History*. Springer-Verlag, New York.
- Vavra, G., 1990. On the kinematics of zircon growth and its petrogenetic significance: a cathodoluminescence study. *Contributions to Mineralogy and Petrology* 106, 90–99.
- Vavra, G., Gebaur, D., Schmid, R., Compston, W., 1996. Multiple zircon growth and recrystallization during polyphase Late Carboniferous to Triassic metamorphism in granulites of the Ivrea Zone (Southern Alps): an ion microprobe (SHRIMP) study. *Contributions to Mineralogy and Petrology* 122, 337–358.
- Vavra, G., Schmid, R., Gebauer, D., 1999. Internal morphology, habit and U–Th–Pb microanalysis of amphibolite-to-granulite facies zircons: geochronology of the Ivrea Zone (Southern Alps). *Contributions to Mineralogy and Petrology* 134, 380–404.
- Watson, E.B., 1996. Dissolution, growth and survival of zircons during crustal fusion: kinetic principles, geological models and implications for isotopic inheritance. *Transactions of the Royal Society of Edinburgh: Earth Sciences* 87, 43–56.
- Watson, E.B., Liang, H., 1995. A simple model for sector zoning in slowly grown crystals: implications for growth rate and lattice diffusion, with emphasis on accessory minerals in crustal rocks. *American Mineralogist* 80, 1179–1187.
- Williams, I.S., Buick, I.S., Cartwright, I., 1996. An extended episode of early Mesoproterozoic metamorphic fluid flow in the Reynolds Range, central Australia. *Journal of Metamorphic Geology* 14, 29–47.

Chapter 2.

Lower crustal granulite formation during Mesoproterozoic Namaqua-Natal collisional orogenesis, southern Africa

Keywords: U-Pb geochronology, zircon, monazite, Nd isotopes, Kaapvaal craton, Namaqualand, Natal, granulite, xenoliths, Lesotho

Abstract— Single-grain U-Pb zircon and monazite geochronology, in concert with Sm-Nd whole-rock and monazite systematics, constrain the timing of metamorphism and protolith ages of granulitic lower crustal xenoliths from the Eastern Namaqualand and Northern Lesotho kimberlites of southern Africa. From these data, inferences regarding the Proterozoic tectonic evolution of the southern African continent, the mechanisms of lower crustal granulite formation, and the present day architecture of the lithosphere are drawn. U-Pb geochronology demonstrates that the granulitization of pre-existing Archean to Mesoproterozoic lower crust is a relatively young, 1.1 to 1.0 Ga phenomenon, resulting from tectonic activity associated with the Kaapvaal craton-bounding Proterozoic Namaqua-Natal orogenic belt. Episodic accessory mineral growth related to high-grade metamorphism of the Northern Lesotho granulites occurred at 1.10, 1.04 and 1.00 Ga, first in response to crustal thickening associated with thrust stacking of the Tugela terranes across the southern margin of the Kaapvaal craton and juxtaposition of the adjoined Mzumbe terrane at 1.10 Ga, and then by subsequent crustal accretion along an enigmatic southern convergent margin between 1.04 and 1.00 Ga. In Eastern Namaqualand, the crustal architecture of the Namaqua front is extended south beneath Phanerozoic cover by xenolith studies, comprising a narrowing band of Mesoproterozoic Gordonia subprovince lithologies wedged between the Archean Kaapvaal craton margin and a Paleoproterozoic terrane of Bushmanland subprovince affinity. Metamorphism in the lower crust again was episodic in Eastern Namaqualand, producing granulites in the margin of the Kaapvaal craton and the adjacent Gordonia subprovince lower crust at 1.10 Ga, likely related to crustal thickening associated with collision of the Bushmanland microcontinent. In the most southerly lower crustal xenoliths sourced from the Bushmanland terranes 1.00 Ga high grade metamorphism is significantly younger, and like the contemporaneous metamorphism in Northern Lesotho xenoliths, may be related to continued crustal accretion of terranes along a southern convergent margin. In both Northern Lesotho and Eastern Namaqualand, the timing and spatial patterns of

lower crustal granulite metamorphism are more consistent with models for granulite genesis involving crustal thickening related to collisional orogenesis, rather than advective heating through underplating of mafic magmas into the lower crust. With regard to the present-day crustal structure of southern Africa, crustal thickness variations across the Namaqua front at the southwestern margin of the Kaapvaal craton are related to orogenic thickening at 1.1 to 1.0 Ga; this dramatic ≥ 10 km step in crustal thickness is a likely manifestation of late stage transpressional shearing and steepening of the Archean-Proterozoic boundary, and is a long-lived feature of the southern African lithospheric architecture.

1. Introduction

Distinctive high-pressure garnet+pyroxene±kyanite granulite xenoliths in kimberlites of the Cape Province of South Africa were noted as early as the first geological surveys of Du Toit (1908). Over the last several decades, these granulites have been the subject of occasional study, including the work of Jackson and Harte (1977), Rogers (1977), Griffin et al. (1979), and Robey (1981), who demonstrated the nature of granulites in the Northern Lesotho and Eastern Namaqualand kimberlites as components of the lower crust. Because of its intrinsic inaccessibility, these and similar suites of granulitic xenoliths of the lower crust have become an invaluable sampling of this lithospheric reservoir, from which inferences are made regarding the mineralogy, composition, seismic properties, and evolution of the continental crust (McCulloch et al., 1982; Griffin and O'Reilly, 1987; Rudnick, 1990; Rudnick and Fountain, 1995).

In order to accurately assess the nature of the lower crust, its evolution, and processes of formation, it is crucial to establish the timing of both protolith generation and subsequent high-grade metamorphism. Previous geochronological studies of southern African granulite xenoliths relying on whole rock and mineral Rb-Sr, Sm-Nd, and common Pb systematics have been hampered by the lithological diversity of the lower crust and an apparently complex and long-lived metamorphic history (Rogers and Hawkesworth, 1982; van Calsteren et al., 1986; Huang et al., 1995). Over the last decade the increasingly apparent accuracy and precision of single-grain U-Pb zircon geochronology for elucidating the evolution of high-grade metamorphic rocks has led several workers to examine granulites from various exhumed terranes and crustal xenolith suites (Krogh, 1993; Chen et al., 1994; Hanchar and Rudnick, 1995; Moser and Heaman, 1997), and demonstrated the utility of the technique for revealing a long-lived dynamic evolution of the

lower crust. Surprisingly, such high-precision U-Pb geochronological studies have not been previously pursued in the lower crustal xenoliths of southern Africa.

This paper presents single grain U-Pb zircon and monazite geochronological data for the craton-margin granulite suites of Eastern Namaqualand and Northern Lesotho, along with new whole rock Sm-Nd isotopic analyses. In concert, these data provide a temporal framework for the protolith formation and high-grade metamorphism of these samples of the lower crust, from which inferences regarding the Proterozoic tectonic evolution of the southern African continent, the mechanisms of lower crustal granulite formation, and the architecture of the deep lithosphere may be derived.

2. Geological setting and prior study

2.1 Eastern Namaqualand

Drawing heavily upon reviews by Hartenady et al. (1986), Stowe (1986), and Thomas et al. (1994), we summarize the present understanding of the geological evolution of the Proterozoic Namaqualand terrains in order to provide a framework for interpretation of the geochronology and isotopic systematics of the lower crustal granulites from the Eastern Namaqualand kimberlites. From west to east, the Proterozoic crust of Namaqualand may be divided into a number of distinct, discontinuity-bounded domains, or subprovinces. The largest of these domains is the Bushmanland subprovince, in southern and central Namaqualand. The Bushmanland subprovince is also the most poorly exposed and least understood of the domains of southern Namaqualand, with modern geochronological studies restricted to the western regions of the Okiep Copper District (OCD) and near Garies on the western coast. In western Bushmanland, SHRIMP U-Pb zircon studies of Robb et al. (1999) demonstrate that the basement of the region consists of amphibolite to granulite grade Paleoproterozoic (1.8 to 2.0 Ga) supracrustals (Aggeneys Sequence) and intrusive gneissic granitoids (Gladkop Suite), which have been subsequently intruded by a younger suite of ~1.2 Ga gneissic granitoids (Little Namaqualand Suite) and finally a number of late to post-tectonic 1.03 to 1.06 Ga plutons (Spektakel Suite). Although at higher metamorphic grade, the basement of western Bushmanland is similar in age to that of the northern Richtersveld subprovince, which hosts 1.9 to 2.0 Ga low-grade mafic to felsic volcanic sequences with minor interbedded sediments

(Orange River Sequence), intruded by 1.9 to 1.7 granitoids (Vioolsdrif Suite) (Reid, 1997). Nd depleted mantle model ages for both provinces range from 2.0 to 2.5 Ga. The transition between the Richtersveld and Bushmanland subprovinces is defined by the Groothoek Thrust, a major north-dipping mylonite zone along which the Richtersveld domain was thrust over the Bushmanland subprovince. The similarity of basement crystallization and model ages suggests that the Richtersveld and Bushmanland subprovinces comprise a Paleoproterozoic microcontinent which was subsequently accreted to the southern African cratonic nucleus during Namaqualand orogenesis.

East of the Bushmanland subprovince, the Gordonia subprovince comprises a central domain of volcano-plutonic amphibolite complexes of arc-like affinity (Archeap Group, including the Jannelspan Formation) separating a western granitoid-dominated high-grade Kakamas Terrane, from the eastern Upington Terrane (Figure 2). The latter comprises a complex, faulted stratigraphy of arenitic metasediments of poorly constrained age (~1.35 to 1.92 Ga), and overlying 1.35 Ga volcanoclastic sediments and greenstones of the Wilgenhoutsdrif Group. A correlative of the Archeap Group, the volcano-sedimentary Copperton Formation outcrops at the southern limit of exposure, near Copperton. Cornell et al. (1990) reported a zircon evaporation age of 1.285 ± 0.014 Ga for the Smouspan Gneiss Member of the Copperton Formation and interpreted this as the eruption age of its metadacitic volcanic protolith. Voluminous syn- to post-tectonic plutons of the Keimos Suite intrude the Archeap Group and gneisses of the Kakamas Terrane, and have been dated at *ca* 1.15 by conventional bulk zircon analysis (Geringer et al., 1988). The southwest boundary of the Gordonia subprovince with the Bushmanland subprovince is an south-west verging reverse structure, the Waterval Thrust, while the eastern boundary with the Kheis province is similarly a zone of convergence, which in the north resulted in east-directed thrusting of the Upington terrane over the Paleoproterozoic Kheis terrane along the Dabep Fault and related structures. Farther south, the thrust boundary between the Gordonia and Kheis subprovinces has been steepened by late dextral transpression into the subvertical Trooilspan and Brakbos shear zones.

The Kheis and Gordonia subprovinces progressively narrow to the south, converging into a thin belt of higher grade schists and gneisses near the town of Marydale, south of which lies the enigmatic Marydale Terrain (Figure 2). The nature of this terrain, bounded by the eastern Doornberg Fault and the western Brakbos Fault, is specifically clouded by a lack of precise

geochronology, as well as the higher degrees of deformation seen in these rocks compared with those to the north. The Marydale Terrain includes essentially three distinct lithostratigraphic packages: eastern Archean granitoids and mafic volcanics and interbedded metasediments of the Marydale Group; a western suite of diverse supracrustal metasediments of poorly known age, the Spioenkop Formation; and unconformable quartzites and subordinate sericite schists of the Uitdraai Formation. Age relationships between the Marydale Group and the Spioenkop Formation remain unclear; while Moen (1999) correlates the Spioenkop Formation with the northerly Dagbreek Formation based on lithological similarities, Cornell et al. (1986) interpret the Spioenkop as a formation of the Archean Marydale Group based on Sm-Nd isotopic systematics. We tentatively follow the conclusions of these authors in considering the Marydale Terrain as severely reworked but intrinsically Archean cratonic basement flooring unconformable and/or allochthonous Proterozoic supracrustal sequences. While the age of its constituent members is still controversial, the Marydale Terrain is clearly bounded to the west by the Brakbos Fault, which separates it from high-grade supracrustal metavolcanics and metasediments and intrusives of the southerly extension of the Gordonia subprovince. Cornell et al. (1986) demonstrated that a significant isotopic discontinuity exists across this fault, with a transition from Archean Nd depleted mantle model ages east of the fault to Paleoproterozoic model ages in the western Copperton Formation of the Gordonia subprovince. On this basis, the Brakbos Fault is considered synonymous with the southern Namaqua Front.

First described by Du Toit in the first decade of the 20th century (Du Toit, 1908; Rogers and Du Toit, 1909), abundant granulitic crustal xenoliths are exhumed in the kimberlites straddling the southwestern margin of the Kaapvaal craton with the bounding Namaqua orogen (Figure 2). The geologic setting of these Eastern Namaqualand kimberlite-borne xenolith occurrences is however, substantially obscured by late Paleozoic to early Mesozoic sediments of the Karoo Basin. Surface outcrop of the crystalline basement of the craton and bounding orogen ends at approximately 30°S; most kimberlites, including those sampled for this study outcrop 100 to 200 km south of this point. The continuation of lithologies and major crustal structures beneath the Phanerozoic cover must be inferred from geophysical data, including magnetic and gravity measurements. The dashed lines in Figure 2 represent linear magnetic anomalies which coincide with faults and shear zones exposed in the basement. From these lineaments we may infer the continuation of the two major crustal breaks along the Namaqua front, the eastern

Brakbos Fault separating the Gordonia subprovince from the Marydale Terrane and Kaapvaal Craton, and the western Waterval Thrust separating the Gordonia and Bushmanland subprovinces. Within this framework, kimberlite-borne upper crustal xenoliths provide important ground-truth to geophysical inferences, while lower crustal xenoliths provide information on the geometry of the bounding structures at depth.

The Eastern Namaqualand granulite xenoliths were not examined in detail until the pioneering work of Robey (1981), who first established their mineralogy, petrography, mineral chemistry and thermobarometric characteristics. These granulites were demonstrated to be unlike low-P, high-T granulites and charnockites exposed in the Namaqua Front, and to have pressures of equilibration consistent with metamorphism in the lower crust. Subsequent detailed petrological and thermobarometric studies of Pearson et al. (1995) focussed on the nature of the granulite to eclogite transition recorded in these xenoliths, and expanded on the observation, first noted by Robey (1981), that granulites from just on the Kaapvaal craton generally preserve higher pressures (13-18 kbar) of equilibration for a given temperature than off-craton kimberlites (10-13 kbar). Huang et al. (1995) examined the whole rock and mineral Sm-Nd and U-Pb isotopic systematics of granulite xenoliths from the off-craton Markt kimberlite and the on-craton Britstown Group kimberlites, and noted that whole-rock granulite samples generally scattered about a *ca* 1.2 Ga reference line in a Sm-Nd isotope correlation diagram, while internal mineral isotopic systematics of single xenoliths preserved *ca* 0.6 to 0.9 Ga errorchrons. Nd model ages range from Meso- to Paleoproterozoic, however on the basis of whole-rock and mineral Pb systematics, Huang et al. (1995) inferred a Mesoarchean heritage for the Markt granulites. If correct this suggests that the Gordonia subprovince in the south is a relatively shallow allochthonous domain above Archean cratonic lower crust; this hypothetical geometry is re-examined in light the U-Pb geochronology and Nd isotopic systematics present below.

2.2 Northern Lesotho

The nearest exposed crystalline basement to the Northern Lesotho kimberlites lies 200km to the east, where Mesoproterozoic rocks of the Natal province have overthrust the southeastern margin of the Kaapvaal craton along the north-directed Tugela Front and related reverse faults (Figure 3). Following the synthesis of Thomas et al. (1994), the Natal province comprises three major fault-bounded domains, the Tugela, Mzumbe, and Margate terranes, each of which

contains a unique deformational and metamorphic evolution. The northern Tugela terrane comprises an allochthonous thrust stack of continental passive margin sediments and ~1.2 Ga mafic volcanic and shallow plutonic rocks, interpreted as a partial ophiolite complex obducted across the southern margin of the Kaapvaal craton at ~1.14 Ga (Matthews, 1972; Jacobs et al., 1997; Thomas et al., 1999). The Tugela Front delineates the remnant northern line of thrusting, while the southern boundary of the Tugela terrane is denoted by the sinistral Lilani-Matigulu shear zone. This major shear zone is interpreted to represent the southern extent of the Kaapvaal Craton beneath the allochthonous Tugela Terrane, based on gravity modeling (De Beer and Meyer, 1984; Barkhuizen and Matthews, 1990). South of the Lilani-Matigulu shear zone, the Mzumbe terrane is composed of a ~1.23 Ga suite of low-P (<4 kbar) amphibolite to granulite grade layered gneisses of intermediate volcanic and volcano-sedimentary protolith (Thomas et al., 1999), intruded by an older suite of 1.20 Ga orthogneisses, and a younger suite of 1.06 to 1.03 Ga syn- to post-tectonic granitoids (Thomas et al., 1993; Thomas et al., 1996). Deformation in the Mzumbe terrane is polyphase, with subhorizontal D1 reverse structures overprinted by a pervasive sinistral D2 shearing along multiple steep ENE trending shear zones. The Mzumbe terrane stretches for nearly 200 km to the Melville Thrust, its southern boundary with the predominantly granulite-facies Margate Terrane, which shares a similar intrusive and deformation record (Thomas et al., 1990).

Surface exposure of the Natal terranes ends near 32°E, however reactivation of the Proterozoic thrusts and shear zones as normal faults during Gondwana rifting reveals their position beneath the younger cover sequences. These faults may also be traced as lineaments in aeromagnetic maps of the region as far west as the border with Lesotho before they are obscured by the Stormberg lavas of the highlands (Figure 3). This extrapolation is particularly important for the purposes of inferring the nature of the crust underlying the volcanic highlands of Lesotho, which was sampled by the Northern Lesotho kimberlites. Fig. 3 shows the extrapolated extension of the Lilani-Matigulu shear zone through central Lesotho, demarcating the edge of the Archean craton. To the north, the Tugela Front may be extrapolated from its strong aeromagnetic signature nearly due west to the northern tip of Lesotho, past which it must curve to the southwest. The position of the Tugela Front as it passed through northern Lesotho is probably also delineated by the surface heat anomaly noted by Jones (1992), which is defined by a near step function from values of $q < 50 \text{ mW/m}^2$ to the north and $q > 50 \text{ mW/m}^2$ to the south.

This abrupt gradient in heat flow may be explained by a thickened high heat production crustal section south of the Tugela Front related to Mesoproterozoic orogenesis— a hypothesis further explored later in the paper. From Figure 3, it is readily observed that the location of the Northern Lesotho kimberlites places them between Tugela Front and the Lilani-Matigulu shear zone, and thus within the bounds of the allochthonous Tugela Terrane.

The Northern Lesotho kimberlite pipes contain abundant garnet-bearing granulites of mafic to felsic bulk composition which have been described in detail by Jackson and Harte (1977), Rogers (1977) and Griffin et al. (1979). These granulites comprise garnet + cpx + plag ± opx ± kyanite assemblages which have equilibrated at 10-15 kbar and elevated crustal geotherms. Two bulk zircon U-Pb measurements yielded $^{207}\text{Pb}/^{206}\text{Pb}$ dates of 1.1 and 1.5 Ga (Davis, 1977), indicating Proterozoic zircon crystallization in these rocks. Rogers and Hawkesworth (1982) presented geochemical and Sr and Nd isotopic data for granulites mainly from the Matsoku kimberlite, and argued for a cogenetic cumulate origin; a 1.4 Ga whole rock errorchron was interpreted to represent the protolith age of the basic igneous rocks from which the granulites were derived by high-grade metamorphism during the Namaqua-Natal orogeny. Since these early studies, however, the potential for these granulite xenoliths to elucidate the tectonic evolution of the Natal belt, and modification of the underlying lithosphere, has lain dormant.

3. Sample Description

3.1 Eastern Namaqualand

The kimberlites of Eastern Namaqualand comprise a diverse set of hundreds of kimberlites spread across the southwestern margin of the craton and extending into the bounding Proterozoic Kheis and Namaqualand mobile belts. In this area, Group 1 and 2 varieties are spatially and temporally associated over several hundred square kilometers, with emplacement ages ranging from 143 to 74 Ma. Crustal xenoliths were collected and examined from the Markt (Group 2, 117 ± 1 Ma, Smith et al., 1994), Witberg Pipe (Group 1, 108 ± 1 Ma, Smith et al., 1994), Beyersfontein (Group 1, 82 ± 2 Ma, Smith et al., 1994), and Klipfontein-08 pipes (Group 1, no age data available).

3.1.1 Markt kimberlite

Garnet+kyanite+clinopyroxene mafic granulite (KX4-18): This sample is a fine grained, exceptionally large xenolith (30 cm diameter) with granoblastic texture and mafic mineralogical character. The mineral assemblage is dominated by garnet and clinopyroxene with nearly complete replacement of plagioclase by kyanite and quartz. Accessory minerals include rutile and apatite. Garnets also contain an abundance of kyanite inclusions. All grains are small, less than 0.5 mm in diameter with the exception of a few clinopyroxene grains which can reach 1-2 mm.

Garnet+clinopyroxene mafic granulites (KX4-21/KX4-23/KX4-35/KX4-36): KX4-21 and KX4-23 are large (20 cm) xenoliths comprising a medium grained (1-2 mm) granoblastic assemblage of garnet, clinopyroxene and plagioclase with very minor hornblende, and accessory rutile (KX4-21) or ilmenite (KX4-23), apatite, and zircon. Garnet and clinopyroxene occur as discrete isolated grains, or more commonly in irregular aggregates which can reach over 1 cm in diameter. KX4-23 has a well-developed planar fabric dominated by oriented clinopyroxene and hornblende, modal layering of garnet-rich domains on millimeter to centimeter scales, and a lineation defined by streaky white felsic segregations. KX4-35 and KX4-36 are very similar large (40 cm), moderately foliated, and layered xenoliths composed of granoblastic clinopyroxene, garnet, hornblende and plagioclase with minor Fe-Ti oxides, sulfide, apatite and zircon. KX4-36 is slightly coarser-grained and has less modal hornblende than KX4-35, but like the latter xenolith has compositional layering controlled by the modal proportion of amphibole. In hornblende poor zones, grain boundaries between clinopyroxene, garnet, and plagioclase are sharp, while hornblende grain boundaries are ragged and reaction to or from clinopyroxene is apparent. In hornblende rich layers, garnet and to a lesser extent clinopyroxene are corroded, indicating that some of the amphibole growth is retrograde. A pervasive grain boundary alteration in sample KX4-35 is less well developed or absent throughout most of KX4-36.

Garnet+biotite+muscovite granitic gneiss (KX4-28): Sample KX4-28 is a 12 cm diameter xenolith of strongly foliated felsic quartzofeldspathic gneiss containing garnet and biotite with rare muscovite. Plagioclase and K-feldspar have cusped grain boundaries, interlocking with quartz grains into a recrystallized mosaic texture. Garnet porphyroblasts are 1-5 mm in diameter,

contain inclusions of quartz, biotite and unidentified minute minerals, and are strongly fractured in parallelism with the foliation. The foliation itself is defined by oriented mica flakes and trails of comminuted quartz crystals. Accessory minerals include apatite, monazite, and zircon.

3.1.2 Klipfontein kimberlite

Garnet+clinopyroxene mafic granulite (KX12-7): The 10 cm diameter xenolith KX12-7 contains a granuloblastic assemblage of 3-6 mm garnets in a matrix of 1-2 mm clinopyroxene, plagioclase, rare potassium feldspar and Fe-Ti oxides, minor hornblende, and accessory apatite and zircon. Garnets contain large inclusion of red-brown titanian phlogopite and minute oriented needles of rutile, however no mica or rutile is observed in the matrix.

3.1.3 Beyersfontein kimberlite

Garnet+clinopyroxene mafic granulite (KX13-2): Sample KX13-2 is a 20 cm diameter medium-grained granuloblastic textured xenolith, comprising a simple mineralogy of garnet, clinopyroxene and plagioclase, with accessory rutile, apatite and zircon and a few flakes of red-brown titanian phlogopite. All crystals of the major phases range from 1-3 mm in diameter, with an isotropic granuloblastic texture.

3.1.4 Witberg Pipe kimberlite

Two-pyroxene mafic granulite (KX10-4): Sample KX10-4 is a 10 cm diameter fine-grained granuloblastic textured two-pyroxene granulite xenolith lacking garnet or amphiboles; accessory minerals include apatite and very rare zircon. Pyroxenes are <1 mm in diameter homogeneously distributed grains and aggregates of grains within a matrix of 1-2 mm plagioclase grains. A foliation is defined by alignment of pyroxene aggregates.

3.2 Northern Lesotho

The Northern Lesotho kimberlites comprise a geographically restricted set of intrusions on the volcanic plateau highlands of Lesotho. All are of Group 1 affinity, and geochronological measurements have been restricted to U-Pb zircon megacrysts, with a zircon age of 87.1 Ma reported for the Mothae pipe by Davis (1977), and an unpublished zircon age of 94.6 Ma (also

by Davis, reported in Allsopp et al., 1989) for the Letseng-la-Terae pipe. Crustal xenoliths were obtained from the Letseng-la-Terae, Matsoku, and Mothae kimberlites.

3.2.1 Letseng-la-Terae kimberlite

Garnet+kyanite±orthopyroxene mafic granulite (KX20-1/KX20-2): Samples KX20-1 and KX20-2 are very similar 10-12 cm diameter mafic (<45 wt.% SiO₂, >25 wt.% Al₂O₃) metapelitic granulites xenoliths comprising coarse-grained (5-10 mm) garnets, kyanite laths, and smaller (1-2 mm) crystals of plagioclase, K-feldspar, Fe-Ti oxides, rare orthopyroxene, and accessory rutile, apatite, zircon, and monazite.

Garnet+kyanite±clinopyroxene felsic granulite (KX20-3/KX20-5): Samples KX20-3 and KX20-5 are relatively small, 5 cm diameter, felsic granulite (>60 wt.% SiO₂) xenoliths comprising a network of 1-2 mm interlocking cusped quartz and minor plagioclase grains with distributed kyanite lathes and garnet porphyroblasts. KX20-5 contains minor amounts of diopside associated with garnet, while KX20-3 lacks pyroxene; the extremely quartz-rich, feldspar-poor character of KX20-3 and its lack of ferromagnesian components other than garnet may indicate an impure quartzitic protolith. A well developed foliation is defined by flattened quartz grains, and kyanite lathes. Kyanite tends to concentrate near garnet porphyroblasts, which contain inclusions of quartz. Rutile is the dominant accessory mineral, found as inclusions in all major minerals, and is accompanied by monazite, apatite, and zircon.

Garnet+clinopyroxene mafic granulite (KX20-4/KX20-8): Samples KX20-4 and KX20-8 are 5-8 cm diameter, mafic granulites (<50 wt.% SiO₂) comprising 2-3 mm granoblastic garnet, clinopyroxene and plagioclase. Minor deep brown amphibole is found in KX20-4 at the cores of pyroxene grains, and also in proximity to plagioclase. Contacts between plagioclase and amphibole are ragged. Large 2-3 mm grains of Fe-Ti oxide are abundant in KX20-4 but lacking in KX20-8, while accessory minerals include common rutile, apatite, zircon.

3.2.2 Matsoku kimberlite

Garnet+clinopyroxene mafic granulite (KX21-1/KX21-2/KX21-3): All three xenoliths are 8-10 cm diameter medium-grained granuloblastic-textured mafic granulites (<45 wt.% SiO₂) comprising 2-3 mm garnet and clinopyroxene grains in a matrix of calcic plagioclase, with accessory Fe-Ti oxides, rutile and apatite. Sample KX21-2 differs slightly in containing minor hornblende and titanian phlogopite, and accessory titanite, likely stabilized by high bulk rock CaO content (>20 wt.%).

Garnet+biotite granitic gneiss (KX21-7): Sample KX21-7 is an altered felsic gneissic granulite consisting of altered plagioclase, quartz, K-feldspar, and biotite, with 2-3mm garnet porphyroblasts. Accessory minerals include Fe-Ti oxides, apatite, monazite and zircon.

3.2.3 Mothae kimberlite

Garnet+biotite +sillimanite granulite (KX23-3): Sample KX23-3 is a severely altered metapelitic granulite comprising garnet porphyroblasts in a matrix of coarse red-brown mica, sillimanite, plagioclase and K-feldspar. Accessory minerals include rutile, apatite, monazite, and zircon.

4. Analytical Techniques

Zircon and monazite were isolated from xenoliths by standard crushing, heavy liquid, and magnetic separation techniques, and separated into different populations based on crystal morphology, color, and grain size. From these populations representative crystals were reserved for photomicrography. Grains were mounted in epoxy, polished, carbon-coated, and imaged by back-scattered electrons (BSE) and cathodoluminescence (CL) at the MIT JEOL 733 Superprobe electron microprobe facility. Both imaging techniques used an accelerating voltage of 15 keV, 10 nA beam current, and a 1 μ m beam spot size. High resolution gray-scale CL images were collected with the secondary electron detector mounted in place of the optical microscope ocular.

Zircons were air-abraded with pyrite after the method of Krogh (1982), and acid rinsed in warm 3M HNO₃ for 12 hours, followed by ultrasonication. All mineral fractions underwent ultrasonication in ethanol for two hours followed by rinsing in double-distilled acetone. Accessory mineral fractions were loaded into Teflon FEP microcapsules and washed again in

3M HNO₃ (zircon) or high-purity water (monazite) at 50°C for 2-4 hours, followed by rinsing with several capsule volumes of water. Samples were spiked with a mixed ²⁰⁵Pb-²³³U-²³⁵U tracer and dissolved in 28M HF at 220°C for 48-120 hours (zircon), or 12M HCl at 180°C for 48 hours (monazite), followed by conversion to 6M HCl at 180°C for 18-24 hours. Pb and U were separated from the resulting mineral solutions using miniaturized HCl-based anion exchange chromatography procedures modified after Krogh (1973).

Pb and U were analyzed on the MIT VG Sector 54 thermal ionization multicollector mass spectrometer. Lead was loaded on single Re filaments with a dilute silica gel-0.1M H₃PO₄ emitter solution and measured either dynamically with four high-mass Faraday cups and an axial ion-counting Daly detector, peak-switching ²⁰⁵Pb into the axial position to obtain an internal Daly-Faraday gain calibration, or by peak-switching all ion beams into the Daly detector for very small amounts of lead. An ion beam of >0.1x10⁻¹³ A was maintained for ²⁰⁷Pb during data acquisition. Uranium was loaded on single Re filaments either with colloidal graphite and measured as metal ions, or with silica gel and measured as UO₂⁺ ions by one of two methods: in static mode on three Faraday cups for ²³⁸U⁺ (²³⁸U¹⁶O₂⁺) ion-beam intensities of >0.5x10⁻¹³ A, or by peak switching all ion beams into the Daly detector for smaller amounts of uranium. Details of fractionation and blank corrections are given in Table 1. Ages with propagated uncertainties were calculated using the methodology of Ludwig (1980).

For Sm-Nd isotopic analyses, single crystals of monazite, or 50-100 mg of powdered whole rock samples were spiked with a mixed ¹⁴⁹Sm-¹⁵⁰Nd tracer and completely dissolved with 12M HCl or HF-HNO₃ respectively, in teflon pressure vessels at 220°C for two or five days, followed by conversion to 6M HCl and fluxing at 120°C for 24 hours. The separation and purification of Sm and Nd were accomplished with a standard two-stage cation exchange-HDEHP reverse chromatography procedure. Sm was loaded on single Ta filaments with 1 μl of 1M H₃PO₄ and analyzed as metal ions in static multicollector mode with a ¹⁵²Sm ion beam of 2.5x10⁻¹¹ A. Nd was loaded on triple Re filaments with 1 μl of 0.1M H₃PO₄ and analyzed as metal ions in dynamic multicollector mode with a ¹⁴⁴Nd ion beam of 1.5x10⁻¹⁰ A. Sm and Nd data were fractionation corrected with an exponential law, normalizing to ¹⁵²Sm/¹⁴⁷Sm = 1.783 and ¹⁴⁶Nd/¹⁴⁴Nd = 0.7219 respectively. Details of data internal and external reproducibility are given in the caption to Table 2.

5. Analytical Results

5.1 U-Pb geochronology

5.1.1 Eastern Namaqualand

KX12-7 (Klipfontein-08): Zircon is very abundant in this granulite, and several dozen zircons were imaged by CL (Figure 4), revealing the presence of complex planar zoned cores extensively resorbed, veined and overgrown by secondary zircon. From these imaged grains, four single zircons (including those pictured in Figure 4) were selected, abraded and analyzed. Despite our attempt to isolate different growth components, these four zircons are variably discordant (Figure 5), and define a linear discordia with upper and lower intercepts of 1859 ± 7 and 991 ± 6 Ma (MSWD=0.1). The upper intercept is considered to represent the protolith age of this granulite, while the lower intercept is interpreted as the time of growth of the overgrowing metamorphic zircon. By reference to the well-preserved peak granulite assemblage in this rock, this metamorphic zircon is inferred to have grown during high-grade conditions.

KX10-4 (Witberg Pipe): Of approximately twenty very small, clear, colorless, round zircons extracted from this sample, three of the largest single zircons yielded essentially identical concordant data with a weighted mean $^{207}\text{Pb}/^{206}\text{Pb}$ date of 1100 ± 3 Ma (MSWD=0.1; Figure 6). These zircons are interpreted to date high grade metamorphism of this two-pyroxene granulite.

KX4-28 (Markt): Optical examination and CL images of euhedral elongate prismatic zircon from this foliated peraluminous, micaceous granitic gneiss show common small resorbed cores mantled by a dominant phase of oscillatory zoned high-U zircon (variably metamict). No overgrowths characteristic of metamorphism are observed either in CL images of the zircons or BSE images of monazite, which are exceptionally homogeneous. From their morphology and zoning character, both monazite and zircon are interpreted to be igneous in character. From the clearest most non-magnetic zircons without visible cores, four abraded zircons yielded variably discordant dates (Figure 6). Two grains have similar $^{207}\text{Pb}/^{206}\text{Pb}$ dates of 1150 and 1153 ± 2 Ma, while two other grains have similar but slightly younger $^{207}\text{Pb}/^{206}\text{Pb}$ dates of 1146 ± 2 Ma. A similar bimodal distribution of ages is illustrated by three blocky subhedral monazite grains, with $^{207}\text{Pb}/^{206}\text{Pb}$ dates of 1153, 1151, and 1147 ± 1 Ma. These data define two discordia arrays with

upper intercepts of 1148 ± 3 and 1152 ± 5 Ma. The cause of this bimodality remains unclear, but may represent the intimate mixture of two slightly different-aged igneous precursors during ductile deformation of this gneiss. The 1150 ± 3 Ma upper intercept of a discordia fit to all grains is identical to the weighted mean of the $^{207}\text{Pb}/^{206}\text{Pb}$ dates, and is considered to represent the mean crystallization age of the granitic protoliths to this gneiss.

5.1.2 Northern Lesotho

KX23-3 (Mothae): Both zircon and monazite were examined from this metasedimentary granulite, and yield systematics that reveal aspects of the timing of both protolith formation and metamorphism. In CL, the abundant rounded prism and ovoid zircons from this granulite are seen to contain resorbed cores with complex oscillatory and/or planar zoning (Figure 5a-b), which have been overgrown by variable thickness rims of secondary metamorphic zircon, exhibiting more evenly-zoned but varying CL intensity. Considering the likely sedimentary origin of this granulite, the cores of these grains likely represent detrital components. Four single abraded zircons yielded data with highly discordant U-Pb dates, and $^{207}\text{Pb}/^{206}\text{Pb}$ dates ranging from 1489 to 1769 Ma (Figure 8). Given the evidence from imaging, this discordance is attributed to mixing of radiogenic Pb derived from older cores of grains, with that in overgrowing younger metamorphic zircon. If we assume a metamorphic age of 1.05 Ga (as justified by the monazite systematics below), the approximate ages of the detrital zircon cores range from Neoproterozoic to Paleoproterozoic.

In BSE, the abundant monazites from KX23-3 exhibit broadly sector-zoned cores (Figure 5c-d), with a brighter mantling rim of more Th-rich monazite. Slight truncation of the original sector zoning by the homogeneous rim may indicate episodic growth of monazite. Three grains of monazite analyzed without prior imaging (m2-m4) yielded near concordant U-Pb dates with $^{207}\text{Pb}/^{206}\text{Pb}$ dates of 1020 to 1027 ± 1 Ma. Subsequent to imaging, four additional grains were removed from the mount and analyzed after selection on the basis of zoning patterns, yielding near concordant U-Pb systematics. Grain m6 appeared to have essentially no Th-rich overgrowth from the section polished through the grain, and accordingly yielded a substantially older $^{207}\text{Pb}/^{206}\text{Pb}$ date of 1045 ± 2 Ma. Grains m5, m7, and m8 were smaller grains, homogeneous in BSE with relatively bright emission, suggesting that they comprise dominantly the Th-rich

overgrowth component. Their $^{207}\text{Pb}/^{206}\text{Pb}$ dates are correspondingly younger than the first monazites, ranging from 1010 to 1001 ± 2 Ma. From this grain-specific sampling it may be inferred that there are two growth components in the monazites of KX23-3— an older sector-zoned growth phase with a minimum crystallization age of 1045 ± 2 Ma, and a younger unzoned growth phase with a maximum age of 1001 ± 2 Ma. The monazite grains with intermediate dates represent mixtures of these phases and their $^{207}\text{Pb}/^{206}\text{Pb}$ dates do not represent geologically meaningful growth ages.

KX20-3 (Letseng-la-Terae): When imaged in CL, single zircons from this felsic garnet+kyanite granulite display resorbed oscillatory-zoned cores of likely primary igneous zircon, overgrown by thick mantles of more homogeneous patchy-zoned metamorphic zircon (Figure 7e-f). Similar to KX23-3, single zircons from this sample yield highly discordant U-Pb systematics, with $^{207}\text{Pb}/^{206}\text{Pb}$ dates ranging from 1064 to 1468 Ma (Figure 8). Excluding fraction z2, the four remaining zircons define a discordia array with an upper and lower intercepts of 2636 ± 70 and 1050 ± 4 Ma respectively (MSWD=0.17). A number of fractions from KX23-3 also fall on this discordia array; the upper intercept of this array may indicate the protolith age of a predominant igneous detrital component in both of these inferred metasedimentary xenoliths. The lower intercept of *ca* 1050 Ma is interpreted as the time of crystallization of the metamorphic zircon overgrowth, and is similar to the older monazite crystallization age in KX23-3.

KX20-1 and KX20-2 (Letseng-la-Terae): When imaged in CL, single zircons from this garnet+kyanite+opx granulite display complex nested, multifaceted, broadly-zoned internal structure which is likely recording metamorphic crystallization. Diffuse dark zones at the center of some grains may represent volumetrically minor inherited cores; all grains exhibit some subsequent resorption, and are overgrown by thin mantles of homogeneous less-luminous zircon (Figure 7g-h). Three abraded fractions of zircon yield near concordant U-Pb systematics with $^{207}\text{Pb}/^{206}\text{Pb}$ dates of 1017 to 1000 Ma (Figure 9), indicating the general time of metamorphic zircon crystallization. In contrast, two single monazites from KX20-1 are concordant at 1098 ± 3 Ma and a reversely discordant analysis has a $^{207}\text{Pb}/^{206}\text{Pb}$ of 1034 Ma, indicating at least two periods of older metamorphic monazite crystallization. These two ages of monazite crystallization are broadly supported by the data for two single monazites from the lithologically similar granulite, KX20-2, which yield ages of 1104 ± 2 and 1044 ± 1 Ma.

KX20-4, KX20-5 and KX20-8 (Letseng-la-Terae): Of the three remaining granulite xenoliths, two abraded zircon fractions from the felsic granulite, KX20-5, yield near-concordant U-Pb dates of 997 ± 6 Ma, and a slightly discordant analysis with a $^{207}\text{Pb}/^{206}\text{Pb}$ date of 983 ± 1 Ma, the former suggesting a similar period of metamorphic zircon growth to that observed in KX20-1. Zircon is not abundant in the mafic granulite KX20-4, and forms anhedral and droplet shaped grains; a single grain of zircon from this granulite yielded a very young and nearly concordant date of 948 ± 4 Ma. By contrast, the mafic granulite KX20-8 contains extremely abundant zircon. In CL, these zircons have a distinctive complexly resorbed planar-zoned interior (Figure 7i-j) replaced and overgrown by rinds of more evenly zoned zircon. Two abraded zircon fractions yield slightly discordant U-Pb systematics and $^{207}\text{Pb}/^{206}\text{Pb}$ dates of 1099 and 1092 ± 2 Ma, demonstrating an older zircon growth component than seen in other granulites from Letseng.

KX21-2 and KX21-7 (Matsoku): Zircon is not abundant in any mafic granulite from Matsoku and only a few dozen small ($< 50\ \mu\text{m}$), clear, colorless ellipsoidal grains were obtained from KX21-2. Two of the largest abraded single grains yielded near concordant systematics with $^{207}\text{Pb}/^{206}\text{Pb}$ dates of 1099 and 1034 Ma, which based on the morphology of these grains likely indicate one or more periods of metamorphic zircon growth. Despite its felsic composition, the garnet-biotite gneiss KX21-7 from Matsoku similar did not yield abundant zircon. Optically two populations of grains are separable: clear to slightly turbid rounded prismatic grains, and strongly pink colored anhedral to spheroidal grains. The latter pink phase of zircon overgrows the former colorless grains in some crystals. Single grains of the pink zircon (z5, z8) yield the youngest near-concordant dates of 995 to 997 Ma. In contrast, five of the rounded prismatic grains yield a range of near-concordant dates between 1008 and 1080 Ma (note fraction z9 is imprecise and reversely discordant because of its low radiogenic to common Pb ratio, and for this reason the $^{206}\text{Pb}/^{238}\text{U}$ date of 1080 Ma, which is the least sensitive to the common Pb correction, is taken as the best estimate of the age of the zircon). Given the rounding of these prismatic grains, and demonstrable overgrowth of younger pink zircon on some examples, this range of dates is interpreted as indicating mixing of *ca* 1000 Ma zircon overgrowths on older protolith zircons with a minimum crystallization age of *ca* 1080 Ma.

5.2 Sm-Nd isotopic systematics

5.2.1 Eastern Namaqualand

The Sm-Nd isotopic systematics of four mafic garnet-clinopyroxene granulites of the Markt kimberlite have nearly identical unradiogenic present-day ϵ_{Nd} of -9.0 to -10.2 (Table 2), with a wider range of subchondritic $^{147}\text{Sm}/^{144}\text{Nd}$. ϵ_{Nd} values at the age of granulite-facies metamorphism (1.1 Ga) range from -1.5 to 0.4 , while Nd model ages vary between 1.1 to 1.3 Ga (t_{CHUR}) and 1.7 to 2.1 Ga (t_{DM}). The Markt granitic gneiss has very similar systematics, with ϵ_{Nd} at its 1.15 Ga crystallization age of -1.4 , and t_{CHUR} and t_{DM} model ages of 1.3 and 1.9 Ga respectively. Isotopic systematics of two single monazites from the granitic gneiss closely reproduce the whole rock data suggesting that dynamic amphibolite-facies recrystallization of the granitic gneiss did not affect the Sm-Nd systematics. The only sample from the Markt kimberlite exhibiting different systematics is the single kyanite-bearing mafic granulite, which has a higher Sm/Nd ratio and more radiogenic ϵ_{Nd} , evolving on a shallower trajectory with a resultantly older $t_{\text{DM}} = 2.4$ Ga.

Two samples from the more southerly Klipfontein-08 kimberlite, a lower crustal garnet granulite and an upper crustal greenschist-facies syenite (Schmitz and Bowring, 2001; Chapter 1), yield similar systematics with less radiogenic present day ϵ_{Nd} of -19.7 to -20.7 , and older model ages of 2.1 to 2.3 (t_{CHUR}) and 2.6 to 2.7 Ga (t_{DM}). These older Nd model ages are consistent with the indications from zircon systematics of a *ca* 1.9 Ga protolith for both of these rocks. A single garnet granulite from the nearby Beyersfontein kimberlite has a similar t_{DM} model age of 2.8 Ga, although this sample has evolved with a near chondritic Sm/Nd ratio, resulting in significant uncertainty in the model age extrapolation.

In Figure 10a, we plot on a f - $\epsilon_{\text{Nd}}^{(t)}$ diagram the Sm-Nd isotopic systematics for lower crustal granulite and mid-crustal granitic gneissic xenoliths from the Eastern Namaqualand kimberlites, including the data of Harris et al. (1987) and Huang et al. (1995). In this variant of the isotope correlation diagram, the Sm/Nd and Nd isotopic compositions of the granulites are recalculated at 1.1 Ga, the time of high-grade metamorphism, and normalized to the synchronous values of the chondritic uniform reservoir (CHUR) to yield f (enrichment factor) and $\epsilon_{\text{Nd}}^{(t)}$ (Shirey and Hanson, 1986). This normalization generates a convenient geometry of elemental fractionation, and serves to expand small changes in the isotopic composition due to radiogenic ingrowth as a function of time. As illustrated in the inset to Figure 10a, isochronous systems

with the same initial isotopic composition, which undergo an instantaneous change in Sm/Nd ratio, move vertically up or down the ordinate axis producing a depletion/enrichment chord; subsequent ingrowth of radiogenic ^{143}Nd causes clockwise rotation of the chord. Rotation about the centerpoint is not required; reservoirs with differing initial enrichment factor (f) and isotopic composition will evolve along parallel chords (see for example the evolution of the depleted mantle denoted by the intersection of the “ t_{DM} ” chords in both panels of Figure 10).

In addition to allowing comparison between suites of cogenetic samples evolving through time, this presentation also allows easy visualization of the effects of metamorphism on samples. For example, as illustrated in the inset to Figure 10b, partial melt extraction during reactions leading to granulite-facies metamorphism, particularly in the presence of garnet, will instantaneously deplete the whole rock in LREE, increasing the Sm/Nd ratio (and f), and moving points vertically upward. This process will introduce corresponding scatter in the ordinate onto any isochronous array of samples. A further advantage of this isotope ratio space is that because the plotted ratios have the same denominator, mixing arrays are straight lines.

In Figure 10a, it is immediately apparent that the Eastern Namaqualand xenolith data define two clusters, one at only slightly negative $\epsilon_{\text{Nd}}^{(1.1\text{Ga})}$ comprising granulites and gneisses exclusively from the Markt kimberlite, and the second, at more negative $\epsilon_{\text{Nd}}^{(1.1\text{Ga})}$, comprising granulites from both the Markt kimberlite and the more southerly Klipfontein-08, Hebron, and Uintjiesberg kimberlites. These clusters have fairly similar ranges in f , although some samples with near chondritic $\epsilon_{\text{Nd}}^{(1.1\text{Ga})}$ have f near -0.1 . While numerous interpretations of the data are possible depending on the initial isotopic compositions of the mantle reservoirs from which they were extracted, all require an older heritage for the more unradiogenic cluster of samples and their separation from a mantle source > 2.0 Ga. The more radiogenic cluster of data can be derived a number of ways, including derivation from a relatively enriched reservoir immediately preceding metamorphism with small amounts of mixing with an older component, or derivation from a depleted reservoir in the Paleoproterozoic with superposed mixing and/or metamorphic LREE-depletion at 1.1 Ga. If we assume that the two clusters of data represent crust derived from a depleted mantle reservoir at 2.5 and 1.7 Ga (see reference isochrons in Figure 10a), then variable degrees of LREE depletion during metamorphism are indicated for different lower crustal granulites from the Markt kimberlite.

When the Sm-Nd isotopic data are combined with geologic and geochronologic constraints, certain patterns are revealed in the data. The geography of the data clustering is particularly striking in that xenoliths from kimberlites piercing the southernmost crustal domains (Klipfontein-08, Beyersfontein, Uintjiesberg, Hebron) are exclusively characterized by unradiogenic Nd isotopic compositions necessitating time-integrated LREE-enrichment since the Paleoproterozoic. This isotopic character is consistent with the presence of 1.9 Ga protolith zircons in xenoliths from Klipfontein-08, and confirms that the crust of the southern domain is part of the larger Paleoproterozoic Bushmanland subprovince exposed to the northwest. On the other hand, xenoliths from the more northerly Markt kimberlite fall into both clusters Nd isotopic composition. By comparison with the southern kimberlite xenoliths, the unradiogenic Markt granulites could represent older crust from the Paleoproterozoic Bushmanland terrane, while the more radiogenic granulites were derived from more juvenile crust, similar to that of the Mesoproterozoic Gordonia terranes. Such a scenario is geologically consistent with the fact that the Markt kimberlite lies within a few kilometers of the inferred boundary between the Gordonia and Bushmanland terranes, and thus may easily have sampled both types of crust.

Huang et al. (1995) proposed a Mesoarchean age for the Markt granulites, and by extension the underlying lower crust, based on their Pb isotopic systematics. The geological implication of this interpretation was that, at depth, the Archean Kaapvaal craton extends further to the southwest than observed in the near surface. As this has implications for mantle lithospheric structure, it is worth re-evaluating this interpretation. We have demonstrated using U-Pb accessory mineral geochronology that granulite-facies metamorphism in these rocks occurred at 1.1 to 1.0 Ga, which invalidates any inference that the 2.9 Ga internal metamorphic mineral “isochrons” obtained for two Markt granulites represent the time of metamorphism. Further, the demonstrated bimodality in Nd isotopic characteristics and model ages of the Markt granulites argues against inferring geochronological information from the whole rock isotopic systematics of this granulite suite. Any apparent correspondence of whole rock systematics to a linear array in a lead isotope correlation diagram must be an artifact, or a mixing line between broadly defined crustal end-members. Finally, the suggestive evidence that melt extraction during granulite metamorphism was sufficient to modify the Sm/Nd ratio of some mafic granulites seems to argue against robust preservation of whole rock U-Pb systematics during the same event, given the much greater difference in partitioning behavior during melting between U

and Pb compared with the rare earth elements. Modification of the U-Pb system during metamorphism is in fact the likely means of developing the mineral Pb isotopic systematics measured by Huang and coworkers. As they note, the Markt granulite Pb systematics could be explained by depletion of *ca* 2.5 Ga protoliths in U during *ca* 1.2 Ga metamorphism, with a correspondingly retarded isotopic evolution; although rejected at the time, this scenario is consistent with the geological and geochronological data now available for the Markt granulites. We conclude that at this time, there is no xenolith evidence to suggest an Archean component in the lower crust beneath the Markt kimberlite.

5.2.2 Northern Lesotho

Of the six granulite xenoliths examined from Letseng-la-Terae, all have relatively unradiogenic present-day Nd isotopic compositions of ϵ_{Nd} of -6.88 to -19.4 , over a wide range of $^{147}\text{Sm}/^{144}\text{Nd}$ between 0.09 and 0.18. Model ages range from 1.3 to 1.6 Ga (t_{CHUR}) and 1.9 to 2.4 Ga (t_{DM}) for samples with relatively low $^{147}\text{Sm}/^{144}\text{Nd}$; a garnet-cpx granulite and a garnet-kyanite-opx granulite having higher $^{147}\text{Sm}/^{144}\text{Nd}$ yield older model ages due to their retarded evolution. The felsic granulite, KX20-3, which has evidence of *ca* 2.7 zircon inheritance, has a complementary *ca* 2.4 Ga t_{DM} . Three granulites from Matsoku have present-day values of ϵ_{Nd} of -6.0 to $+3.7$, that are generally correlated with $^{147}\text{Sm}/^{144}\text{Nd}$; t_{DM} model ages are 1.7 to 2.0 Ga ($t_{\text{CHUR}} = 0.8$ to 1.0) for samples with subchondritic $^{147}\text{Sm}/^{144}\text{Nd}$. The more LREE-enriched biotite gneiss from Matsoku has correspondingly unradiogenic neodymium isotopic ratio, and yields a similar t_{DM} of 2.0 Ga. The final garnet-biotite-sillimanite metapelitic granulite from Mothae has the most unradiogenic Nd of any sample from N. Lesotho, and correlated LREE-enrichment resulting in a t_{DM} of 2.7 Ga, comparable again to the demonstrated zircon inheritance age from this metasediment.

In Figure 10b, we plot the Northern Lesotho granulite data on a f - ϵ_{Nd} diagram normalized to the time of metamorphism at 1.0 Ga. It may also be noted on this diagram that samples like KX23-3 and KX20-3, with demonstrable Archean components in the form of zircon cores, generally conform to a crude linear array whose slope yields a Neoproterozoic date, suggesting that these granulites, which are likely metasedimentary based on their bulk composition, were predominantly derived from the Archean cratonic crust. On the other hand, some mafic

granulites have more radiogenic compositions consistent with Proterozoic mantle affinity, and are more similar to juvenile crustal material represented in the nearby Natal terranes. The rest of the data exhibit significant scatter, likely highlighting the importance of both metamorphic segregation and/or mixing processes. Several granulites from Matsoku have suprachondritic f values, and it is tentatively suggested that these samples may represent residua from partial melt extraction during metamorphism. The scatter of the data between the two depleted mantle isochrons in Figure 10b may also, in part, be the result of mixing between more radiogenic, juvenile crust, and evolved unradiogenic Archean crustal components. This type of scenario may be particularly relevant to some of the more intermediate to felsic granulites if they represent crustal melts generated and emplaced into the lower crust in response to crustal thickening during and following obduction and collision of the Proterozoic Natal terranes with the Archean Kaapvaal craton.

6. Discussion

6.1 Northern Lesotho granulite formation

In Northern Lesotho lower crustal granulites, metamorphic zircon and monazite growth spans a period between 1.1 and 1.0 Ga, and thus unequivocally relates granulite-facies metamorphism to tectonothermal events associated with the Natal orogeny. This metamorphism affected lithologies with an Archean heritage, specifically what are likely metasediments with detrital igneous zircons >2.6 Ga in age, and also mafic to intermediate composition rocks with relatively juvenile, Proterozoic Nd systematics. This mixture of protoliths is broadly consistent with the inferred geologic setting of the Northern Lesotho lower crust, in that the hosting kimberlites pierce crust within the extrapolated confines of the Tugela Terrane, which is known to comprise juvenile Proterozoic oceanic arc terranes obducted onto the Archean cratonic margin. Interleaving of Proterozoic and Archean crust during this obduction is supported by the mixed “provenance” of the Northern Lesotho granulites.

The growth of metamorphic zircon and monazite appears to have occurred episodically at 1.10, 1.04, and 1.00 Ga, and by inference high grade metamorphism of these granulites was polyphase and episodic. In order to understand the mechanisms of lower crustal granulite formation, an attempt may be made to correlate the timing of these metamorphic accessory

mineral growth phases to the geological evolution of the Natal terranes inferred from surface exposures to the east. Monazite growth in metasedimentary granulites (KX20-1, KX20-2) and zircon growth in mafic (KX21-2, KX20-8) to felsic (KX21-7) metaigneous granulites occurred at *ca* 1.10 Ga. This growth slightly post-dates the inferred timing of obduction of the Tugela terrane onto the Kaapvaal craton at *ca* 1.15 Ga (Jacobs et al., 1997; Arima and Johnston, 2001), and as such is consistent with initial metamorphism in response to crustal thickening by stacking of Tugela thrusts along the cratonic margin. Convergence of the southerly Mzombe terrane was apparently synchronous with obduction of the Tugela terrane, and provides a further mechanism of crustal thickening as this arc collided with the craton margin.

The *ca* 1.04 Ga growth of metamorphic monazite and zircon in metasedimentary granulites (KX20-1, KX20-3, KX23-3) and metaigneous mafic to intermediate granulites and gneisses (KX21-2, KX21-7), may be correlated with major transtensional deformation, amphibolite- to granulite-facies mid-crustal metamorphism, and the intrusion of voluminous granitoids throughout the Mzombe and Margate terranes between 1.06 and 1.03 Ga. The cause of the rejuvenation of the Natal terranes and the lower crust of Northern Lesotho at this time is not well constrained, but likely is related to continued subduction-convergence of arc terranes further to the south, which generated the distinctive Beattie magnetic anomaly. The abundance of A-type granitoid magmagenesis during this event has been taken to indicate significant lower crustal melting in the Natal terranes (Thomas et al., 1993), and has further been correlated with identical granitoid emplacement and low-P, high-T mid-crustal metamorphism in western Namaqualand (Thomas et al., 1996; Robb et al., 1999). A significant component of advective heating associated with the emplacement of mafic magmas at the base of the crust is generally deemed necessary to generate mid-crustal granulites (Waters, 1990; De Yoreo et al., 1991). Interestingly however, no granites of this age are recognized at surface in the Tugela Terrane and by inference in Northern Lesotho. Mafic magmatic underplating is thus of questionable relevance in this region unless such granitoids remained stalled in the middle to lower crust, in which case some of the Lesotho metaigneous granulites lacking evidence for pre-1.05 Ga zircon or monazite could represent mafic underplated materials. Interaction of these magmas with Archean cratonic crust could then explain some of the scattering of the Northern Lesotho data between the Proterozoic and Archean depleted mantle source isochrons in Figure 10b.

The significant metamorphic zircon and monazite growth at ca 1.00 Ga in nearly every granulite and gneiss xenolith from Northern Lesotho post-dates the youngest plutonism known in the Natal belt (1.026 ± 0.003 Ga; Thomas et al., 1993) by 20-30 million years. By comparison however, 1.00 to 0.97 Ga ages are consistently obtained from the $^{40}\text{Ar}/^{39}\text{Ar}$ systematics of hornblende in mylonite zones throughout the Mzumbe and Margate terranes, which are interpreted to date deformation induced recrystallization (Jacobs et al., 1997). Metamorphism in the lower crust of Northern Lesotho at 1.0 Ga is thus synchronous with and coupled to continued deformation throughout the southern Natal terranes. It is tentatively suggested that both this last episode of metamorphism in the lower crust and middle crustal transcurrent shearing, are a response to crustal thickening associated with terminal convergence of the southernmost (obscured) domains of the Namaqua-Natal belt. As will be shown in the next discussion, a similar metamorphic age for the most southerly lower crustal granulites in Eastern Namaqualand, and for dextral transcurrent shearing along the major crustal boundaries of that region, support the same model.

6.2 Eastern Namaqualand orogenesis and crustal structure

The metamorphic zircon and monazite geochronology for granulites and gneisses presented above, in concert with the data for the Markt and Klipfontein granulites presented in Chapter 1, provide new constraints on the nature and timing of the Namaquan orogeny in the vicinity of the southwestern margin of the Kaapvaal craton. As the crystalline basement of the Namaqua orogen is obscured by younger sediments in this region, the first application of kimberlite-borne crustal xenoliths is for constraining the crustal structure. In this regard, data for upper to middle crustal xenoliths confirm inferences from geophysics of the nature of the basement in the near surface of the region. The granitic gneiss from the Markt kimberlite has a primary crystallization age of 1152 ± 2 Ma based on igneous zircon and monazite, which is comparable with the ages of Keimos suite granites throughout the exposed Gordonia subprovince to the north, and thus confirms that a narrow domain of Gordonia basement extends along the margin of the craton, as depicted in Figure 2. Similarly, the ca 1898 ± 17 Ma igneous crystallization age for an upper crustal syenite xenolith from the southerly Klipfontein-08 kimberlite, reported in Chapter 1, confirms that the basement to the south of the inferred

continuation of the Waterval Thrust is similar in age to that of the exposed Paleoproterozoic Bushmanland subprovince in the north.

At depth, the fact that a mafic granulite also from the Klipfontein-08 kimberlite contains primary igneous zircon with an age of 1859 ± 7 Ma, very similar to the protolith age of the upper crustal syenite, confirms the Paleoproterozoic nature of the lower crust in the south of the study area. Unfortunately primary protolith-aged zircon is not common in the mafic granulites of other kimberlites, however the Sm-Nd systematics of these granulites can be used to infer the protolith age of the lower crust. As described in Section 5.2.1, granulites from the southern domain kimberlites, those south of the inferred Waterval thrust, consistently yield unradiogenic Sm-Nd isotopic systematics with model ages from 2.0 to 2.5 Ga, including those samples which have *ca* 1.9 Ga protolith zircon crystallization ages. Likewise a subgroup of granulites from the Markt kimberlite yield the same general systematics and model ages (Figure 10a, Table 2). However, other granulites from Markt have more juvenile radiogenic systematics more like those characterizing the Gordonia subprovince terranes (Harris et al., 1987). As previously noted the Markt kimberlite lies just northeast of the inferred continuation of the Waterval Thrust, which separates the Gordonia and Bushmanland subprovinces (Figure 2). The Waterval is an east-dipping structure where it is exposed to the north, and a similar geometry would allow the sampling of both subprovince lithologies by the vertically propagating Markt kimberlite. The Gordonia subprovince thus likely narrows at depth in the crust.

U-Pb zircon geochronology also serves to clarify the timing of metamorphism, and generation of granulites in the lower crust of Eastern Namaqualand. Zircon growth during high grade metamorphism of the two-pyroxene granulite from the Witberg Pipe occurred at 1100 ± 3 Ga. This metamorphic age fits within the framework of high grade metamorphism established from the Markt kimberlite granulites reported in Chapter 1, where it was demonstrated that garnet granulites record prograde metamorphic zircon growth at *ca* 1107 to 1114 Ma, and retrograde zircon crystallization at *ca* 1092 Ma. The timing of this metamorphism is intriguing in that it post-dates the age of deformation and middle to upper crustal plutonism in the adjacent and overlying Gordonia terranes, as constrained by syn-tectonic granitoid intrusion at 1.15 Ga and deposition of the non-deformed 1.17 Ga Koras Group volcanics in the foreland of the Namaqua front (Geringer et al., 1988; Gutzmer et al., 2000), by approximately 70 to 40 million years. Lower crustal granulite formation is apparently decoupled from this phase of

Namaqualand evolution, commonly termed the Kibaran event (Robb et al., 1999), which placed the terranes of the Gordonia Subprovince against, and over the margin of the Kaapvaal craton. Instead, it is tentatively inferred that 1.12 to 1.09 Ga lower crustal granulite genesis was not initiated until the subsequent convergence of the Bushmanland microcontinent with the adjoined Gordonia subprovince and Kaapvaal craton. Granulite-facies conditions were thus generated in the lower crust in response to crustal thickening related to continental collision. This hypothesis is supported by the fact that 1.12 to 1.09 Ga metamorphism affects granulites of both Bushmanland and Gordonia 'provenance' at Markt.

Moving further outboard, the garnet granulite from the Klipfontein-08 kimberlite contains metamorphic zircon which grew at 1.00 Ga. As previously noted, this granulite shows no evidence of retrogression and thus this phase of metamorphic zircon is interpreted to date high-grade metamorphic conditions. We also note that the timing of granulite facies metamorphism in the lower crust at Klipfontein-08 is synchronous with low grade metamorphism in the upper crust as recorded in the accompanying upper greenschist-facies syenite from the Klipfontein kimberlite (Chapter 1). The cause of this younger metamorphism within the eastern Bushmanland subprovince is enigmatic. Low-P, high-T granulite conditions in western Namaqualand, which are thought to be due to an influx of mantle-derived magmatic heat during the 'Namaquan' orogeny (Waters, 1990), are well-dated at between 1.06 and 1.03 Ma (Robb et al., 1999), and resolvably older than the metamorphism in southeastern Namaqualand. Also, the voluminous granites which accompany this Namaquan metamorphic episode in both Natal and western Namaqualand are not apparent in eastern Namaqualand. As discussed for the Northern Lesotho granulites, which display a similarly young metamorphic episode, this 1.00 Ga metamorphism is best correlated with the age of transcurrent shearing on both the southeastern Natal and southwestern Namaqualand cratonic margins (Jacobs et al., 1997). This transcurrent shearing is a component of the partitioned strain response to oblique transpressional crustal thickening during continued convergence of terranes along the southern margin of the growing continental mass, a margin which is remotely sensed by the Beattie magnetic anomaly. Again it is tentatively suggested that the last 1.0 Ga episode of metamorphism in the lower crust of Eastern Namaqualand is a similar response to terminal convergence of the southernmost (obscured) domains of the Namaqua-Natal orogen.

6.3 *The origin of granulitic lower crust*

Recognizing the origins of lower crustal granulites is important for understanding the tectonomagmatic context of high-grade metamorphism in the crust, and the dramatically different implications of differing tectonic regimes on the subsequent structure of the lithosphere. Two models are generally put forth to explain granulite-facies metamorphism. One model relates high geothermal gradients to advective heat addition from the mantle through magmatic fluxing (De Yoreo et al., 1991). Ponding of mafic melts beneath the more buoyant crust is termed magmatic underplating (Drummond and Collins, 1986). The second model for granulite genesis invokes crustal thickening associated with collisional orogenesis to generate high thermal gradients in the crust due to thickening of a higher radiogenic heat production layer and upward advection of heat during subsequent erosional isostatic re-equilibration (England and Thompson, 1984).

The role of magmatic underplating to form high-seismic velocity, high-density lower crust observed in many Proterozoic crustal provinces has been suggested in numerous studies (Drummond and Collins, 1986; Durrheim and Mooney, 1994). Waters (1990) proposed that a ~30 kilometer thick mafic underplate was necessary to generate the conditions of low-P, high-T metamorphism observed in western Namaqualand terrain. In its simplest form, the underplating model states that garnet granulites in the lower crust are the products of mafic magmatic addition to the deep crust crystallized at granulite-facies conditions. Generalizing the role of underplating in the Precambrian lithosphere, Durrheim and Mooney (1994) interpreted the generally observed difference in crustal thickness between Archean and Proterozoic crust as due to differential magmatic underplating from more fertile Proterozoic mantle compared with depleted Archean mantle lithosphere. Those authors went on to hypothesize that this underplating model explained the crustal thickness variation across the Archean-Proterozoic boundary between the Kaapvaal craton and Namaqua orogen, and that the abundant granulites xenoliths exhumed in Namaqualand kimberlites represent this magmatic underplate.

The geochronological and isotopic data presented above test this model of granulite genesis by magmatic underplating. U-Pb zircon geochronology constrains the timing of granulite facies metamorphism to 1.1-1.0 Ga; by the underplating model these granulites should have isotopic systematics consistent with derivation from the lithospheric mantle at this time. In fact, few mafic granulite samples have Nd isotopic systematics consistent with derivation from either

lithospheric or depleted convecting mantle at 1.1 Ga; instead their Nd systematics, and in one case protolith zircon U-Pb systematics, suggest crustal residence times in excess of several hundred million years. In detail, the timing of lower crustal granulite formation in the lower crust beneath eastern Namaqualand and Northern Lesotho also does not correlate well with demonstrable periods of magmatism during the 1.2 to 1.0 Ga interval of Namaqua-Natal orogenesis. For example the 1.06 to 1.03 Ga period of granite genesis and middle crustal granulite metamorphism apparent in western Namaqualand and the southern Mzumbe and Margate terrane of Natal is only poorly represented in the lower crustal metamorphic record in northern Lesotho, and not at all in eastern Namaqualand. 1.12 to 1.09 Ga lower crustal granulite genesis in eastern Namaqualand also apparently post-dates 1.15 Ga arc magmatism and associated middle-crustal charnockitization and low-pressure granulite metamorphism in the Gordonia subprovince terranes to the north.

The U-Pb zircon geochronology and Nd isotopic data rather demonstrate that granulite-facies metamorphism affected pre-existing Archean to Mesoproterozoic lower crust at the southern (Northern Lesotho) and western (Eastern Namaqualand) craton. Tentatively, the timing of metamorphism is better correlated with episodes of major terrane accretion, including the juxtaposition of the Natal terranes to the southeastern margin of the craton at 1.10 Ga, the Bushmanland microcontinent to the southwestern margin of the craton again at 1.10 Ga, and an enigmatic crustal domain south of the Beattie magnetic anomaly at 1.00 Ga. From these data it is suggested that the thermal effect of compressional crustal thickening was a more important process for generating lower crustal granulite-facies metamorphism, at least in these regions of the southern African lithosphere, than magmatic advection and underplating.

6.4 Implications for lithosphere architecture, composition and evolution

A few words on the implications of these lower crustal granulite ages for larger scale lithospheric structure and evolution are warranted. Of particular relevance to this discussion are the granulites of eastern Namaqualand, as this region lies within the array of the recently deployed Kaapvaal Seismic Experiment, whose goal is to establish the present architecture of the lithosphere beneath southern Africa. One aspect of these seismic studies is the computation and correlation of seismic receiver functions, from which inferences on the depth and velocity contrast of the Moho discontinuity have been derived (Nguuri et al., 2001). The inferred crustal

thickness for the Kaapvaal craton is uniformly thin (Figure 11), averaging approximately 35 kilometers depth to the Moho (cf. Hales and Sacks, 1959; Durrheim and Green, 1992), and the seismic velocity contrast across the crust-mantle boundary is very sharp and high, with a fairly slow inferred lower crustal V_p seismic velocity of approximately 6.8 km/s consistent with an amphibolitic or intermediate composition lower crust. In contrast, the crustal thickness beneath the southwestern Proterozoic orogenic belts is substantially greater, from 45-50 kilometers, and both receiver functions and seismic refraction studies (Green and Durrheim, 1990) indicate a substantial thickness of high seismic velocity lower crust ($V_p > 7.0$ km/s) underlying the region. Closely spaced stations along the Kaapvaal Seismic Array indicate that the transition between these domains takes place within <50 km. This abrupt transition is in accord with geological observations of a meter to kilometer scale, lithological and deformational boundary between the Archean and Proterozoic terranes (the Brakbos Fault), characterized in its later history by predominantly dextral transpressive movement .

The garnet-pyroxene granulite xenoliths of the Eastern Namaqualand kimberlites have densities, seismic velocities and depths of equilibration appropriate to their representing the underlying high-velocity lower crustal layer in Namaqualand. The geochronology presented here demonstrates that the formation of these granulites occurred at 1.1 to 1.0 Ga from pre-existing crust, during the Namaqua-Natal orogeny. In this region of southern Africa then, high-velocity lower crust was generated through the stabilization of garnet-bearing lithologies by processes of crustal thickening during collisional orogenesis, rather than the emplacement of a mafic underplate. This differs from other lower crustal sections, for example in southeast Australia, where mafic magmatism was clearly an important mechanism, and highlights the importance of elucidating the temporal and tectonic setting of lower crustal granulite genesis through xenolith studies in concert with seismological inferences of crustal architecture. Finally, it is notable that in the southern African lithosphere this step function in crustal thickness across the Archean-Proterozoic transition has been maintained as long-lived topography on the Moho since 1.0 Ga, reflecting the strong rheology of granulitic lower crust.

7. Conclusions

Single-grain U-Pb zircon and monazite geochronology has constrained the timing of metamorphism, and, in concert with Sm-Nd systematics, the protolith ages of granulitic lower

crustal xenoliths from the Eastern Namaqualand and Northern Lesotho kimberlites. In Northern Lesotho lower crustal granulites, episodic metamorphic zircon and monazite growth at 1.10, 1.04, and 1.00 is explained by a model of crustal thickening in the westward continuation of the Tugela terrane by initial thrust stacking of Mesoproterozoic juvenile arc-crust over the southern margin of the Kaapvaal craton and accretion of the Mzumbe terrane to the south at *ca* 1.10 Ga, followed by further dynamothermal reworking of the lower crust correlated with major sinistral transpression deformation, mid-crustal metamorphism, and intrusion of the Oribi Gorge suite of plutons throughout the Mzumbe and Margate terranes at 1.06 to 1.03 Ga. High grade metamorphism in the lower crust of Northern Lesotho (and by inference the terranes to the south) continued, or was punctuated by a final event at 1.00 Ga which is correlated with continued transpressional deformation but postdates known magmatism in the Natal belt. The later *ca* 1.04 and 1.00 Ga events are likely related to continued subduction accretion outboard and south of the exposed Natal terranes, leading to development of the Beattie magnetic anomaly.

In Eastern Namaqualand, the structure of the various subsurface Proterozoic terranes inferred from geophysics is largely confirmed by the geochronological and isotopic systematics of crustal xenoliths, with a narrow band of Mesoproterozoic Gordonia subprovince crust wedged between the Archean craton on the northeast and the Paleoproterozoic Bushmanland subprovince to the southwest. Shallow and lower crustal xenoliths in the most southerly Eastern Namaqualand kimberlites have protolith zircon ages of *ca* 1.9 Ga and Nd isotopic model ages >2.0 Ga, similar to rocks in the Bushmanland terranes exposed to the northwest. In contrast, an isotopically bimodal lower crustal xenolith suite in the Markt kimberlite, outcropping with the Gordonia subprovince and just east of the inferred continuation of the Waterval thrust, is consistent with the geometry of the latter structure as an east dipping boundary thrust which places Gordonia lithologies over the Bushmanland terranes. There is as yet no xenolith data from the Markt kimberlite which necessitates a cratonic Archean component, suggesting that the craton boundary, as represented by the Brakbos fault to the northeast, is a steep structure throughout the crust.

Granulite facies metamorphism in the Eastern Namaqualand and bounding Kaapvaal cratonic lower crust was episodic. Initial high grade metamorphism affecting the craton margin and the lower crust as far south as the Waterval Thrust occurred between 1.12 and 1.09 Ga. This

dynamothermal metamorphism in the lower crust post-dates magmatism and deformation in the northern Gordonia terranes by 50-70 million years, suggesting that significant crustal thickening (and granulite genesis) was delayed, perhaps until collisional accretion of the Bushmanland subprovince. Zircon in both upper and lower crustal xenoliths of the more southerly Klipfontein-08 kimberlite record younger metamorphism at 1.00 to 0.96 Ga. This younger metamorphism may be correlated with contemporaneous metamorphism in the Northern Lesotho granulites to the east, and while apparently correlative with transpressional shearing in both Namaqualand and Natal, post-dates known Namaquan or Natal magmatism by 20-30 million years. As in the Northern Lesotho lower crustal xenoliths, this younger ca 1.00 Ga metamorphism may be explained by continued crustal thickening and dynamic metamorphism related to southerly outboard accretion of terranes along a subduction zone now represented by the Beattie anomaly.

These geochronological and isotopic data for lower crustal xenoliths from Eastern Namaqualand and Northern Lesotho demonstrate that the granulitization of the lower crust is a relatively young 1.1 to 1.0 Ga phenomenon affecting preexisting Archean to Mesoproterozoic crust. In both regions, the timing and spatial patterns of lower crustal granulite metamorphism are more consistent with models for granulite genesis involving crustal thickening related to collisional orogenesis, rather than advective heating through underplating of mafic magmas into the lower crust. Recently imaged crustal thickness variations across the Namaqua front at the southwestern margin of the Kaapvaal craton are clearly genetically related to orogenic thickening at 1.1 to 1.0 Ga; this dramatic ≥ 10 km step function in crustal thickness is a likely manifestation of late stage transpressional shearing and steepening of the Archean-Proterozoic boundary, and is a long-lived feature of the southern African lithospheric architecture.

References

- Allsopp, H.L., Bristow, J.W., Smith, C.B., Brown, R., Gleadow, A.J.W., Kramers, J.D., Garvie, O.G., 1989. A summary of radiometric dating methods applicable to kimberlites and related rocks. *In: Kimberlites and Related Rocks, Vol. 1: Their Composition, Occurrence, Origin, and Emplacement.* Ross, J. (Ed.), Geological Society of Australia Special Publication 14, Blackwell Scientific Publishers, Carlton, Victoria, Australia, 343-357.
- Arima, M., Johnston, S.T., 2001. Crustal evolution of the Tugela Terrane, Natal Belt, South Africa. *Gondwana Research* 4, 563-564.
- Barkhuizen, J.G., Matthews, P.E., 1990. Gravity modeling of the Natal Thrust Front: a mid-Proterozoic crustal suture in southeastern Africa. *Ext. Abstr. Geocongress '90, Geological Society of South Africa, Cape Town, 32-35.*
- Chen, Y.D., O'Reilly, S.Y., Kinny, P.D., Griffin, W.L., 1994. Dating lower crust and upper mantle events: an ion microprobe study of xenoliths from kimberlitic pipes, South Australia. *Lithos* 32, 77-94.

- Cornell, D.H., Hawkesworth, C.J., Van Calsteren, P., Scott, W.D., 1986. Sm-Nd study of Precambrian crustal development in the Prieska-Copperton region, Cape Province. *Transactions of the Geological Society of South Africa* 89, 17-78.
- Cornell, D.H., Kroner, A., Humphreys, H., Griffin, G., 1990. Age of origin of the polymetamorphosed Copperton Formation, Namaqua-Natal Province, determined by single grain zircon Pb-Pb dating. *South African Journal of Geology* 93, 709-716.
- Cornell, D.H., Thomas, R.J., Bowering, S.A., Armstrong, R.A., Grantham, G.H., 1996. Protolith interpretation in metamorphic terranes: a back-arc environment with Besshi-type base metal potential for the Quha Formation, Natal Province, South Africa. *Precambrian Research* 77, 243-271.
- Davis, G.L., 1977. The ages and uranium contents of zircons from kimberlites and associated rocks. *Carnegie Institute of Washington Yearbook* 76, 631-635.
- De Beer, J.H., Meyer, R., 1984. Geophysical characteristics of the Namaqua-Natal belt and its boundaries, South Africa. *Journal of Geodynamics* 1, 473-494.
- De Yoreo, J.J., Lux, D.R., Guidotti, C.V., 1991. Thermal modeling in low-pressure/high-temperature metamorphic belts. *Tectonophysics* 188, 209-238.
- Drummond, B.J., Collins, C.D.N., 1986. Seismic evidence for underplating of the lower continental crust of Australia. *Earth and Planetary Science Letters* 79, 361-372.
- Du Toit, A.L., 1908. The kimberlite and allied pipes and fissures in Prieska, Britstown, Victoria West and Carnarvon. *Annual Report of the Geological Commission, Cape of Good Hope* 13, 121-127.
- Durrheim, R.J., Green, R.W.E., 1992. A seismic refraction investigation of the Archean Kaapvaal Craton, South Africa, using mine tremors as the energy source. *Geophysical Journal International* 108, 812-832.
- Durrheim, R.J., Mooney, W.D., 1994. Evolution of the Precambrian lithosphere: seismological and geochemical constraints. *Journal of Geophysical Research* 99, 15359-15374.
- England, P.C., Thompson, A.B., 1984. Pressure-temperature-time paths of regional metamorphism I. Heat transfer during the evolution of regions of thickened continental crust. *Journal of Petrology* 25, 894-928.
- Geringer, G.J., Botha, B.J.V., Slabbert, M.J., 1988. The Keimos Suite- a composite granitoid batholith along the eastern margin of the Namaqua mobile belt, South Africa. *South African Journal of Geology* 91, 465-476.
- Green, R.W.E., Durrheim, R.J., 1990. A seismic refraction investigation of the Namaqualand Metamorphic Complex, South Africa. *Journal of Geophysical Research* 95, 19927-19932.
- Griffin, W.L., O'Reilly, S.Y., 1987. The composition of the lower crust and the nature of the continental Moho—xenolith evidence. *In: Mantle Xenoliths*. Nixon, P.H. (Eds.), Wiley-Interscience, Chichester, U.K., 411-430.
- Griffin, W.L., Carswell, D.A., Nixon, P.H., 1979. Lower crustal granulites and eclogites from Lesotho, southern Africa. *In: The Mantle Sample: Inclusions in Kimberlites and other Volcanics*. Boyd, F.R., Meyer, H.O.A. (Eds.), *Proceedings of the 2nd International Kimberlite Conference* 2, American Geophysical Union, Washington, D.C., 59-86.
- Gutzmer, J., Beukes, N.J., Pickard, A., Barley, M.E., 2000. 1170 Ma SHRIMP age for Koras Group bimodal volcanism, Northern Cape Province. *South African Journal of Geology* 103, 32-37.
- Hales, A.L., Sacks, I.S., 1959. Evidence for an intermediate layer from crustal seismic studies in the Eastern Transvaal. *Geophysical Journal of the Royal Astronomical Society* 2, 15-33.
- Hanchar, J.M., Rudnick, R.L., 1995. Revealing hidden structures: the application of cathodoluminescence and back-scattered electron imaging to dating of zircon from lower crustal xenoliths. *Lithos* 36, 289-303.
- Harris, N.B.W., Hawkesworth, C.J., Van Calsteren, P., McDermott, F., 1987. Evolution of continental crust in southern Africa. *Earth and Planetary Science Letters* 83, 85-93.
- Hartnady, C., Joubert, P., Stowe, C., 1985. Proterozoic crustal evolution in southwestern Africa. *Episodes* 8, 236-244.
- Huang, Y.-M., Van Calsteren, P., Hawkesworth, C.J., 1995. The evolution of the lithosphere in southern Africa: a perspective on the basic granulite xenoliths from kimberlites in South Africa. *Geochimica et Cosmochimica Acta* 59, 4905-4920.
- Jackson, P.M., Harte, B., 1977. The nature and conditions of formation of granulite facies xenoliths from the Matsoku kimberlite pipe. *Ext. Abstr., 2nd International Kimberlite Conference*.
- Jacobs, J., Falter, M., Thomas, R.J., Kunz, J., Jebberger, E.G., 1997. ⁴⁰Ar/³⁹Ar thermochronological constraints on the structural evolution of the Mesoproterozoic Natal Metamorphic Province, SE Africa. *Precambrian Research* 86, 71-92.
- Jones, M.Q.W., 1992. Heat flow anomaly in Lesotho: implications for the southern boundary of the Kaapvaal craton. *Geophysical Research Letters* 19, 2031-2034.
- Kretz, R., 1983. Symbols for rock-forming minerals. *American Mineralogist* 68, 277-279.

- Krogh, T.E., 1973. A low contamination method for hydrothermal decomposition of zircon and extraction of U and Pb for isotopic age determination. *Geochimica et Cosmochimica Acta* 37, 485-494.
- Krogh, T.E., 1982. Improved accuracy of U-Pb zircon ages by the creation of more concordant systems using an air abrasion technique. *Geochimica et Cosmochimica Acta* 46, 637-649.
- Krogh, T.E., 1993. High precision U-Pb ages for granulite metamorphism and deformation in the Archean Kapuskasing structural zone, Ontario: implications for structure and development of the lower crust. *Earth and Planetary Science Letters* 119, 1-18.
- Ludwig, K.R., 1980. Calculation of uncertainties of U-Pb isotope data. *Earth and Planetary Science Letters* 46, 212-220.
- Matthews, P.E., 1972. Possible Precambrian obduction and plate tectonics in southeastern Africa. *Nature* 240, 37-39.
- McCulloch, M.T., Arculus, R.J., Chappell, B.W., Ferguson, J., 1982. Isotopic and geochemical studies of nodules in kimberlite have implications for the lower continental crust. *Nature* 300, 166-169.
- Moen, H.F.G., 1999. The Kheis Tectonic Subprovince, southern Africa: a lithostratigraphic perspective. *South African Journal of Geology* 102, 27-42.
- Moser, D.E., Heaman, L.M., 1997. Proterozoic zircon growth in Archean lower crustal xenoliths, southern Superior craton- a consequence of Matachewan ocean opening. *Contributions to Mineralogy and Petrology* 128, 164-175.
- Nguuri, T.K., Gore, J., James, D.E., Webb, S.J., Wright, C., Zengeni, T.G., Gwavava, O., Snoke, J.A., Kaapvaal Seismic Group, 2001. Crustal structure beneath southern Africa and its implications for the formation and evolution of the Kaapvaal and Zimbabwe cratons. *Geophysical Research Letters* 28, 2501-2504.
- Pearson, N.J., O'Reilly, S.Y., Griffin, W.L., 1995. The crust-mantle boundary beneath cratons and craton margins: a transect across the south-west margin of the Kaapvaal craton. *Lithos* 36, 257-287.
- Reid, D.L., 1997. Sm-Nd age and REE geochemistry of Proterozoic arc-related igneous rocks in the Richtersveld Subprovince, Namaqua mobile belt, Southern Africa. *Journal of African Earth Sciences* 24, 621-633.
- Robb, L.J., Armstrong, R.A., Waters, D.J., 1999. The history of granulite-facies metamorphism and crustal growth from single zircon U-Pb geochronology: Namaqualand, South Africa. *Journal of Petrology* 40, 1747-1770.
- Robey, J., 1981. Kimberlites of the central Cape Province, R.S.A.. Unpublished Ph.D. thesis, University of Cape Town.
- Rogers, A.W., Du Toit, A.L., 1909. Geological Survey of parts of Kenhardt, Prieska, and Carnarvon. Annual Report of the Geological Commission, Cape of Good Hope 14, 98-103.
- Rogers, N.W., 1977. Granulite xenoliths from Lesotho kimberlites and the lower continental crust. *Nature* 270, 681-684.
- Rogers, N.W., Hawkesworth, C.J., 1982. Proterozoic age and cumulate origin for granulite xenoliths, Lesotho. *Nature* 299, 409-413.
- Rudnick, R.L., 1990. Nd and Sr isotopic compositions of lower-crustal xenoliths from north Queensland, Australia: implications for Nd model ages and crustal growth processes. *Chemical Geology* 83, 195-208.
- Rudnick, R.L., Fountain, D.M., 1995. Nature and composition of the continental crust: a lower crustal perspective. *Reviews of Geophysics* 33, 267-309.
- Schmitz, M.D., Bowring, S.A., 2001. The significance of U-Pb zircon dates in lower crustal xenoliths from the southwestern margin of the Kaapvaal craton, southern Africa. *Chemical Geology* 172, 59-76.
- Shirey, S.B., Hanson, G.N., 1986. Mantle heterogeneity and crustal recycling in Archean granite-greenstone belts: evidence from Nd isotopes and trace elements in the Rainy Lake area, Superior Province, Ontario, Canada. *Geochimica et Cosmochimica Acta* 50, 2631-2651.
- Smith, C.B., Clark, T.C., Barton, E.S., Bristow, J.W., 1994. Emplacement ages of kimberlite occurrences in the Prieska region, southwest border of the Kaapvaal Craton, South Africa. *Chemical Geology* 113, 149-169.
- Stowe, C.W., 1986. Synthesis and interpretation of structures along the north-eastern boundary of the Namaqua tectonic province, South Africa. *Transactions of the Geological Society of South Africa* 89, 185-198.
- Thomas, R.J., Agenbacht, A.L.D., Cornell, D.H., Moore, J.M., 1994. The Kibaran of southern Africa: tectonic evolution and metallogeny. *Ore Geology Reviews* 9, 131-160.
- Thomas, R.J., Cornell, D.H., Armstrong, R.A., 1999. Provenance age and metamorphic history of the Quha Formation, Natal Metamorphic Province: a U-Th-Pb zircon SHRIMP study. *South African Journal of Geology* 102, 83-88.
- Thomas, R.J., De Beer, C.H., Bowring, S.A., 1996. A comparative study of the Mesoproterozoic late orogenic prophyritic granitoids of southwest Namaqualand and Natal, South Africa. *Journal of African Earth Sciences* 23, 485-508.

- Thomas, R.J., Eglington, B.M., Kerr, A., 1990. The geology and geochronology of the Belmont pluton and microgranite dykes from the Margate area— the search for Pan-African magmatism in southern Natal. *South African Journal of Geology* 93, 766-775.
- Thomas, R.J., Eglington, B.M., Bowring, S.A., 1993. Dating the cessation of Kibaran magmatism in Natal, South Africa. *Journal of African Earth Sciences* 16, 247-252.
- Van Calsteren, P.W.C., Harris, N.B.W., Hawkesworth, C.J., Menzies, M.A., Rogers, N.W., 1986. Xenoliths from southern Africa: a perspective on the lower crust. *In: The Nature of the Lower Continental Crust*. Dawson, J.B., Carswell, D.A., Hall, J., Wedepohl, K.H. (Eds.), Geological Society Special Publication 24, Oxford University Press, London, 351-362.
- Waters, D.J., 1990. Thermal history and tectonic setting of the Namaqualand granulites, southern Africa: clues to Proterozoic crustal development. *In: Granulites and Crustal Evolution*. Vielzeuf, D., Vidal, Ph. (Eds.), Kluwer Academic Publishers, Netherlands, 243-256.

Table 1. Zircon and monazite U-Pb isotopic data, Eastern Namaqualand and Northern Lesotho crustal xenoliths

# ^a	Frac ^a	Wt. (μg) ^b	Composition					Isotopic Ratios						corr. coef.	Dates (Ma)			±		
			[U] (ppm)	[Pb] (ppm)	Th ^c U	Pb* ^d Pbc	Pbc ^d (pg)	²⁰⁶ Pb ^e / ₂₀₄ Pb	²⁰⁸ Pb ^f / ₂₀₆ Pb	²⁰⁶ Pb ^g / ₂₃₈ U	% err ^g	²⁰⁷ Pb ^f / ₂₃₅ U	% err ^g		²⁰⁷ Pb ^f / ₂₀₆ Pb	% err ^g	²⁰⁶ Pb ^h / ₂₃₈ U		²⁰⁷ Pb ^h / ₂₃₅ U	²⁰⁷ Pb ^h / ₂₀₆ Pb
Eastern Namaqualand																				
<i>KX10-4: Witberg Pipe kimberlite, Two-pyroxene granulite</i>																				
1	z1	2.96	111	24	0.834	18.8	3.7	1074	0.253	0.185525	(.44)	1.94865	(.47)	0.076178	(.14)	0.955	1097.1	1098.0	1099.8	2.8
2	z2	0.82	89	22	0.698	2.3	6.5	148	0.211	0.186074	(1.84)	1.95364	(1.99)	0.076148	(.69)	0.939	1100.1	1099.7	1099.0	14
3	z3	0.34	134	28	0.516	2.3	3.9	157	0.155	0.186816	(3.11)	1.95880	(3.51)	0.076046	(1.44)	0.912	1104.1	1101.5	1096.3	29
<i>KX12-7, Klipfontein-08 kimberlite, Garnet-clinopyroxene mafic granulite</i>																				
4	z1	13.8	87	23	0.600	163	2.0	9362	0.204	0.239709	(.06)	3.22258	(.08)	0.097503	(.05)	0.728	1385.2	1462.6	1576.9	1.0
5	z2	6.58	173	43	0.489	182	1.6	10815	0.168	0.229870	(.05)	3.01207	(.08)	0.095035	(.06)	0.632	1333.8	1410.7	1528.8	1.2
6	z3	4.39	108	26	0.699	29.6	3.8	1662	0.243	0.209654	(.28)	2.58082	(.30)	0.089280	(.10)	0.944	1227.0	1295.2	1410.2	1.9
7	z4	1.44	143	31	0.770	15.6	2.9	887	0.262	0.189198	(.27)	2.14531	(.34)	0.082238	(.20)	0.802	1117.0	1163.5	1251.2	4.0
<i>KX4-28, Markt kimberlite, Garnet-biotite gneiss</i>																				
8	z1	0.70	1182	209	0.026	42.2	3.5	2927	0.008	0.189153	(.13)	2.03287	(.16)	0.077946	(.08)	0.862	1116.8	1126.6	1145.5	1.6
9	z2	0.90	1580	266	0.036	98.0	2.4	6753	0.012	0.179845	(.07)	1.93735	(.13)	0.078128	(.11)	0.549	1066.1	1094.1	1150.1	2.1
10	z6	0.72	488	90	0.049	14.3	4.4	988	0.015	0.192651	(.41)	2.07819	(.43)	0.078237	(.13)	0.957	1135.7	1141.6	1152.9	2.5
11	z7	0.49	248	56	0.282	3.0	7.8	203	0.087	0.189969	(1.09)	2.04178	(1.28)	0.077951	(.62)	0.874	1121.2	1129.6	1145.6	12
12	m2	5.00	18309	13459	10.84	1449	46	23244	3.299	0.193930	(.22)	2.09004	(.22)	0.078165	(.04)	0.983	1142.6	1145.5	1151.1	0.8
13	m4	6.58	2470	1734	10.18	174	65	2897	3.158	0.190543	(.10)	2.05545	(.11)	0.078237	(.05)	0.901	1124.3	1134.1	1152.9	1.0
14	m5	11.4	1239	995	12.11	106	107	1565	3.703	0.192233	(.11)	2.06710	(.12)	0.077989	(.06)	0.879	1133.5	1138.0	1146.6	1.1
Northern Lesotho																				
<i>KX21-2: Matsoku kimberlite, Garnet-clinopyroxene mafic granulite</i>																				
15	z1	0.93	92	18	0.174	2.3	6.2	169	0.053	0.173852	(1.74)	1.76686	(1.88)	0.073709	(.64)	0.941	1033.3	1033.4	1033.5	13
16	z2	0.69	55	10	0.066	1.8	3.6	143	0.020	0.184211	(3.84)	1.93387	(4.13)	0.076140	(1.36)	0.945	1089.9	1092.9	1098.8	27
<i>KX21-7: Matsoku kimberlite, Garnet-biotite gneiss</i>																				
17	z1	1.11	2027	322	0.032	186	1.9	12868	0.010	0.170777	(.07)	1.73475	(.09)	0.073673	(.06)	0.753	1016.4	1021.5	1032.5	1.2
18	z2	1.45	2934	457	0.007	486	1.4	33878	0.002	0.168672	(.06)	1.69474	(.08)	0.072872	(.04)	0.821	1004.8	1006.6	1010.4	0.9
19	z3	1.32	759	125	0.119	146	1.1	9831	0.037	0.172081	(.10)	1.76188	(.14)	0.074258	(.10)	0.728	1023.6	1031.5	1048.5	2.0
20	z5	3.39	780	120	0.030	186	2.2	12928	0.009	0.166185	(.09)	1.65671	(.11)	0.072302	(.06)	0.849	991.1	992.1	994.5	1.1
21	z7	0.22	4054	646	0.020	22.3	6.2	1525	0.006	0.168675	(.19)	1.69262	(.33)	0.072779	(.25)	0.648	1004.8	1005.8	1007.8	5.2
22	z8	0.21	702	110	0.039	21.3	1.1	1492	0.012	0.167922	(.16)	1.67636	(.19)	0.072403	(.10)	0.850	1000.7	999.6	997.3	2.0
23	z9	0.25	847	398	0.084	0.5	66	53	0.025	0.182469	(.70)	1.87371	(5.94)	0.074475	(5.44)	0.748	1080.5	1071.8	1054.4	110
24	m1	1.14	5025	3137	10.51	227	16	3779	3.213	0.167786	(.12)	1.68043	(.16)	0.072638	(.10)	0.799	999.9	1001.1	1003.8	1.9
25	m2	5.76	2626	1906	12.53	1144	9.6	16758	3.826	0.171054	(.15)	1.72838	(.16)	0.073283	(.05)	0.939	1017.9	1019.1	1021.8	1.1
26	m3	11.0	1679	1550	16.89	1508	11	17250	5.176	0.170479	(.08)	1.72280	(.09)	0.073293	(.04)	0.881	1014.8	1017.1	1022.0	0.9

Table 1 (con't).

# ^a	Frac ^a	Composition						Isotopic Ratios						Dates (Ma)						
		Wt. (μg) ^b	[U] (ppm)	[Pb] (ppm)	Th ^c U	Pb* ^d Pbc	Pbc ^d (pg)	$\frac{^{206}\text{Pb}^e}{^{204}\text{Pb}}$	$\frac{^{208}\text{Pb}^f}{^{206}\text{Pb}}$	$\frac{^{206}\text{Pb}^f}{^{238}\text{U}}$	% err ^e	$\frac{^{207}\text{Pb}^i}{^{235}\text{U}}$	% err ^e	$\frac{^{207}\text{Pb}^l}{^{206}\text{Pb}}$	% err ^e	corr. coef.	$\frac{^{206}\text{Pb}^h}{^{238}\text{U}}$	$\frac{^{207}\text{Pb}^h}{^{235}\text{U}}$	$\frac{^{207}\text{Pb}^h}{^{206}\text{Pb}}$	±
Northern Lesotho (con't)																				
<i>KX20-1: Letseng-la-terae kimberlite, Garnet-kyanite-orthopyroxene granulite</i>																				
27	zhf1	38.8	201	40	0.237	4.9	13	321	0.074	0.165964	(.20)	1.66488	(.30)	0.072756	(.20)	0.725	989.8	995.2	1007.1	4.1
28	zhf2	42.1	253	46	0.154	7.5	11	491	0.047	0.165390	(.23)	1.65297	(.28)	0.072486	(.15)	0.845	986.7	990.7	999.6	3.0
29	zhf3	30.7	192	47	0.283	2.3	21	160	0.086	0.171060	(.13)	1.72452	(.75)	0.073117	(.68)	0.573	1017.9	1017.7	1017.2	14
30	m1	2.61	2406	2387	18.02	406	15	4506	5.351	0.177970	(.20)	1.80883	(.22)	0.073714	(.10)	0.903	1055.9	1048.7	1033.6	1.9
31	m2	1.65	1041	1101	17.74	46	39	517	5.376	0.185650	(.13)	1.94849	(.22)	0.076121	(.17)	0.641	1097.8	1097.9	1098.3	3.3
<i>KX20-2: Letseng-la-terae kimberlite, Garnet-kyanite-orthopyroxene granulite</i>																				
32	m1	2.24	675	281	4.950	154	4.1	4446	1.498	0.186744	(.11)	1.96522	(.14)	0.076324	(.09)	0.798	1103.7	1103.7	1103.6	1.7
33	m2	8.57	1669	2059	23.11	554	32	4817	7.073	0.174540	(.07)	1.78332	(.08)	0.074103	(.05)	0.814	1037.1	1039.4	1044.3	1.0
<i>KX20-3: Letseng-la-terae kimberlite, Garnet-kyanite felsic granulite</i>																				
34	z1	1.11	228	45	0.310	26.4	1.9	1670	0.111	0.190430	(.21)	2.24939	(.29)	0.085670	(.18)	0.792	1123.7	1196.6	1330.7	3.4
35	z2	1.85	129	22	0.455	18.6	2.2	1151	0.155	0.160173	(.29)	1.65292	(.36)	0.074845	(.22)	0.804	957.7	990.7	1064.3	4.4
36	z3	1.34	234	43	0.268	31.3	1.8	2027	0.089	0.182512	(.21)	1.99472	(.26)	0.079266	(.14)	0.837	1080.7	1113.7	1178.8	2.8
37	z4	0.62	271	62	1.125	8.6	4.3	461	0.363	0.180089	(.94)	1.92425	(.97)	0.077495	(.21)	0.977	1067.5	1089.5	1134.0	4.2
38	z5	0.55	345	116	1.504	4.1	13.1	195	0.575	0.198643	(.71)	2.52050	(.77)	0.092026	(.27)	0.938	1168.0	1278.0	1467.9	5.1
<i>KX20-4: Letseng-la-terae kimberlite, Garnet-clinopyroxene mafic granulite</i>																				
39	z3	10.0	13	2	0.988	16.2	1.5	897	0.304	0.157021	(.60)	1.52985	(.64)	0.070663	(.20)	0.952	940.2	942.4	947.7	4.0
<i>KX20-5: Letseng-la-terae kimberlite, Garnet-kyanite-clinopyroxene felsic granulite</i>																				
40	zhf1	74.1	468	83	0.601	36.9	8.1	2083	0.190	0.158631	(.26)	1.57279	(.27)	0.071909	(.06)	0.976	949.2	959.5	983.3	1.2
41	zhf2	81.4	422	95	0.627	4.1	76	247	0.191	0.167090	(.28)	1.66765	(.41)	0.072386	(.27)	0.747	996.1	996.3	996.8	5.5
<i>KX20-8: Letseng-la-terae kimberlite, Garnet-clinopyroxene mafic granulite</i>																				
42	zhf1	91.8	205	48	1.053	15.5	13	801	0.320	0.184906	(.19)	1.94117	(.23)	0.076139	(.13)	0.832	1093.7	1095.4	1098.8	2.5
43	zhf2	113	132	32	1.103	11.7	14	603	0.338	0.182754	(.09)	1.91211	(.12)	0.075883	(.08)	0.787	1082.0	1085.3	1092.0	1.5
<i>KX23-3: Mothae kimberlite, Garnet-biotite-sillimanite granulite</i>																				
44	z4	1.23	250	58	0.134	37.3	1.9	2463	0.046	0.235952	(.13)	3.12430	(.16)	0.096035	(.09)	0.815	1365.6	1438.7	1548.5	1.7
45	z5	0.48	1271	252	0.082	20.2	5.9	1329	0.031	0.201084	(.43)	2.57953	(.43)	0.093038	(.07)	0.986	1181.1	1294.8	1488.6	1.4
46	z7	0.60	246	50	0.064	8.0	3.7	551	0.024	0.210559	(.87)	2.75564	(.90)	0.094918	(.21)	0.971	1231.8	1343.6	1526.4	4.0
47	z8	1.70	271	59	0.047	24.8	4.0	1653	0.019	0.224324	(.30)	3.34526	(.33)	0.108156	(.12)	0.933	1304.7	1491.7	1768.6	2.2

Table 1 (con't).

# ^a	Frac ^a	Composition						Isotopic Ratios						Dates (Ma)						
		Wt. (μg) ^b	[U] (ppm)	[Pb] (ppm)	Th ^c U	Pb* ^d Pbc ^d	Pbc ^d (pg)	²⁰⁶ Pb ^e / ₂₀₄ Pb	²⁰⁸ Pb ^f / ₂₀₆ Pb	²⁰⁶ Pb ^l / ₂₃₈ U	% err ^g	²⁰⁷ Pb ^f / ₂₃₅ U	% err ^g	²⁰⁷ Pb ^f / ₂₀₆ Pb	% err ^g	corr. coef.	²⁰⁶ Pb ^h / ₂₃₈ U	²⁰⁷ Pb ^h / ₂₃₅ U	²⁰⁷ Pb ^h / ₂₀₆ Pb	±
Northern Lesotho (con't)																				
<i>KX23-3: Mothae kimberlite, Garnet-biotite-sillimanite granulite (con't)</i>																				
48	m2	11.7	1305	2057	31.34	511	47	3394	9.588	0.170342	(.11)	1.71931	(.12)	0.073204	(.05)	0.921	1014.0	1015.8	1019.6	0.9
49	m3	4.90	917	1453	31.34	911	7.8	6151	9.612	0.170964	(.07)	1.73076	(.09)	0.073423	(.05)	0.801	1017.4	1020.0	1025.6	1.1
50	m4	3.66	1202	2046	33.89	903	8.3	5673	10.395	0.171113	(.07)	1.73311	(.09)	0.073459	(.06)	0.779	1018.2	1020.9	1026.6	1.2
51	m5	1.71	2037	3567	35.65	1077	5.7	6543	10.915	0.168503	(.08)	1.69234	(.10)	0.072842	(.06)	0.821	1003.9	1005.6	1009.5	1.1
52	m6	8.00	321	475	28.35	238	16	1759	8.633	0.175426	(.11)	1.79264	(.16)	0.074114	(.12)	0.683	1041.9	1042.8	1044.6	2.4
53	m7	2.29	3834	6072	32.16	438	32	2853	9.817	0.167455	(.14)	1.67448	(.16)	0.072524	(.08)	0.873	998.1	998.9	1000.7	1.6
54	m8	2.74	5749	8269	28.79	850	27	6101	8.798	0.167978	(.19)	1.68296	(.20)	0.072664	(.06)	0.954	1001.0	1002.1	1004.6	1.2

^a # corresponds to label on concordia diagrams; all fractions composed of single grains except those with zhf modifiers which comprised 3-5 abraded grains.

^b Sample weights were estimated to within 40% using measured grain dimensions and a nominal density of 5.0 g/cm³ for monazite and 4.5 g/cm³ for zircon.

^c Th contents calculated from radiogenic ²⁰⁸Pb and the ²⁰⁷Pb/²⁰⁶Pb date of the sample, assuming concordance between U-Th-Pb systems.

^d Pb* and Pbc represent radiogenic Pb and common Pb respectively.

^e Measured ratio corrected for fractionation and spike contribution; Pb fractionation was 0.12 ± 0.04 %/a.m.u. for Faraday detector or 0.15 ± 0.04 %/a.m.u. for Daly detector analysis, based on daily analysis of NBS-981.

^f Measured ratios corrected for fractionation, spike, blank, and initial common Pb; nominal U blank = 0.1 pg ± 50% (2σ); nominal Pb blank = 3.5 pg ± 50% (2σ) or where lower, the total common Pb of the analysis ± 10% (2σ); measured laboratory blank composition: ²⁰⁶Pb/²⁰⁴Pb = 19.10, ²⁰⁷Pb/²⁰⁴Pb = 15.72, ²⁰⁸Pb/²⁰⁴Pb = 38.65 ± 0.01 (2σ); initial Pb composition from model of Stacy and Kramers (1972) at the nominal age of the fraction (i.e. 1.0 or 1.1 Ga).

^g Numbers in parentheses are the % errors reported at the 2σ confidence interval, propagated using the algorithms of Ludwig (1980).

^h Isotopic ages calculated using the decay constants of Jaffey et al. (1971): λ(²³⁵U) = 9.8485x10⁻¹⁰ yr⁻¹ and λ(²³⁸U) = 1.55125x10⁻¹⁰ yr⁻¹; error in ²⁰⁷Pb/²⁰⁶Pb date reported at the 2σ confidence interval.

Table 2. Sm-Nd isotopic data for Eastern Namaqualand and Northern Lesotho crustal xenoliths

Sample ^a	Lith. ^a	[Sm] ^a	[Nd] ^a	$\frac{^{147}\text{Sm}}{^{144}\text{Nd}}^{\text{b}}$	$\frac{^{143}\text{Nd}}{^{144}\text{Nd}}^{\text{c}}$	\pm	$\epsilon_{\text{Nd}}^{\text{c}}$	$\epsilon_{\text{Nd(i)}}^{\text{c}}$	$t_{\text{CHUR}}^{\text{c}}$	t_{DM}^{d}
KX4-18	gt-ky-cpx	4.48	15.68	0.1726	0.512409	±6	-4.47	-1.07	1.45	2.73
KX4-21	gt-cpx	0.47	2.08	0.1364	0.512145	±8	-9.62	-1.12	1.25	1.98
KX4-23	gt-cpx	6.02	25.32	0.1437	0.512177	±7	-9.00	-1.53	1.33	2.11
KX4-28	gneiss	12.93	62.20	0.1257	0.512053	±10	-11.41	-1.41	1.26	1.90
KX4-28 m	“	18971	105721	0.1085	0.511906	±7	-14.28	-1.86	1.27	1.80
KX4-28 m	“	21622	121698	0.1074	0.511890	±7	-14.59	-2.02	1.28	1.80
KX4-35	gt-cpx	3.69	16.14	0.1383	0.512174	±15	-9.04	-0.81	1.21	1.97
KX4-36	gt-cpx	2.89	14.44	0.1211	0.512114	±10	-10.23	0.42	1.06	1.70
KX12-7	gt-cpx	9.82	49.39	0.1202	0.511575	±7	-20.74	-9.99	2.12	2.56
KX12-9	syenite	5.86	27.35	0.1295	0.511627	±11	-19.71	-10.28	2.30	2.74
KX13-2	gt-cpx	3.78	12.67	0.1805	0.512545	±6	-1.82	0.47	0.88	2.77
KX20-1	gt-ky-opx	6.85	31.97	0.1295	0.511930	±10	-13.82	-5.24	1.61	2.20
KX20-2	gt-ky-opx	5.66	18.76	0.1823	0.512285	±10	-6.88	-5.04	3.74	4.16
KX20-3	gt-ky	33.36	130.62	0.1544	0.512212	±9	-8.32	-2.91	1.54	2.40
KX20-4	gt-cpx	5.21	19.00	0.1659	0.512279	±6	-7.01	-3.08	1.78	2.77
KX20-5	gt-cpx	7.32	48.34	0.0915	0.511643	±6	-19.41	-5.96	1.45	1.88
KX20-8	gt-cpx	5.06	24.44	0.1252	0.512042	±8	-11.62	-2.47	1.27	1.90
KX21-1	gt-cpx	0.92	3.64	0.1532	0.512377	±7	-5.10	0.47	0.92	2.00
KX21-1 dup	“	0.94	3.65	0.1553	0.512380	±8	-5.03	0.27	0.95	2.05
KX21-2	gt-cpx	2.72	8.43	0.1953	0.512826	±6	3.67	3.87	---	2.67
KX21-3	gt-cpx	2.34	10.03	0.1410	0.512333	±6	-5.95	1.18	0.84	1.71
KX21-7	gneiss	4.86	31.75	0.0926	0.511530	±6	-21.61	-8.31	1.63	2.03
KX23-3	gt-bt-sil	6.64	34.50	0.1164	0.511403	±6	-24.10	-13.85	2.35	2.72
KX23-3 dup	“	6.55	34.36	0.1153	0.511385	±10	-24.44	-14.05	2.35	2.72

^a “dup” identifier indicates duplicate analysis of whole rock powder, while “m” identifier signifies analysis of single monazite crystal; further descriptions of lithology are summarized in the text; concentrations in ppm, as determined by isotope dilution.

^b Internal errors in measured $^{147}\text{Sm}/^{144}\text{Nd}$ are $\leq 0.1\%$ (2σ s.d.).

^c Measured $^{143}\text{Nd}/^{144}\text{Nd}$ with absolute internal error (2σ s.e.); long-term reproducibility of Nd isotopic standards is ≤ 20 ppm (2σ s.d.)— analyses ($n=12$) of USGS standard BCR-1 during the course of the study yielded $^{143}\text{Nd}/^{144}\text{Nd} = 0.512643 \pm 9$ and $^{147}\text{Sm}/^{144}\text{Nd} = 0.1383 \pm 3$ (2σ s.d.), which propagate into a conservative reproducibility for $\epsilon_{\text{Nd(i)}}$ of approximately ± 0.5 epsilon units; present-day ϵ_{Nd} and t_{CHUR} (Ga) calculated with $(^{147}\text{Sm}/^{144}\text{Nd})_{\text{CHUR}} = 0.1967$ and $(^{143}\text{Nd}/^{144}\text{Nd})_{\text{CHUR}} = 0.512638$; $\epsilon_{\text{Nd(i)}}$ calculated at 1.1 Ga (E. Namaqualand) or 1.0 Ga (N. Lesotho) age of granulite-facies metamorphism.

^d t_{DM} (Ga) = $(1/\lambda_{147}) * \ln[(((^{143}\text{Nd}/^{144}\text{Nd})_{\text{sample}} - (^{143}\text{Nd}/^{144}\text{Nd})_{\text{DM}}) / ((^{147}\text{Sm}/^{144}\text{Nd})_{\text{sample}} - (^{147}\text{Sm}/^{144}\text{Nd})_{\text{DM}})) + 1]$; present-day $(^{143}\text{Nd}/^{144}\text{Nd})_{\text{DM}} = 0.513151$, $(^{147}\text{Sm}/^{144}\text{Nd})_{\text{DM}} = 0.2137$.

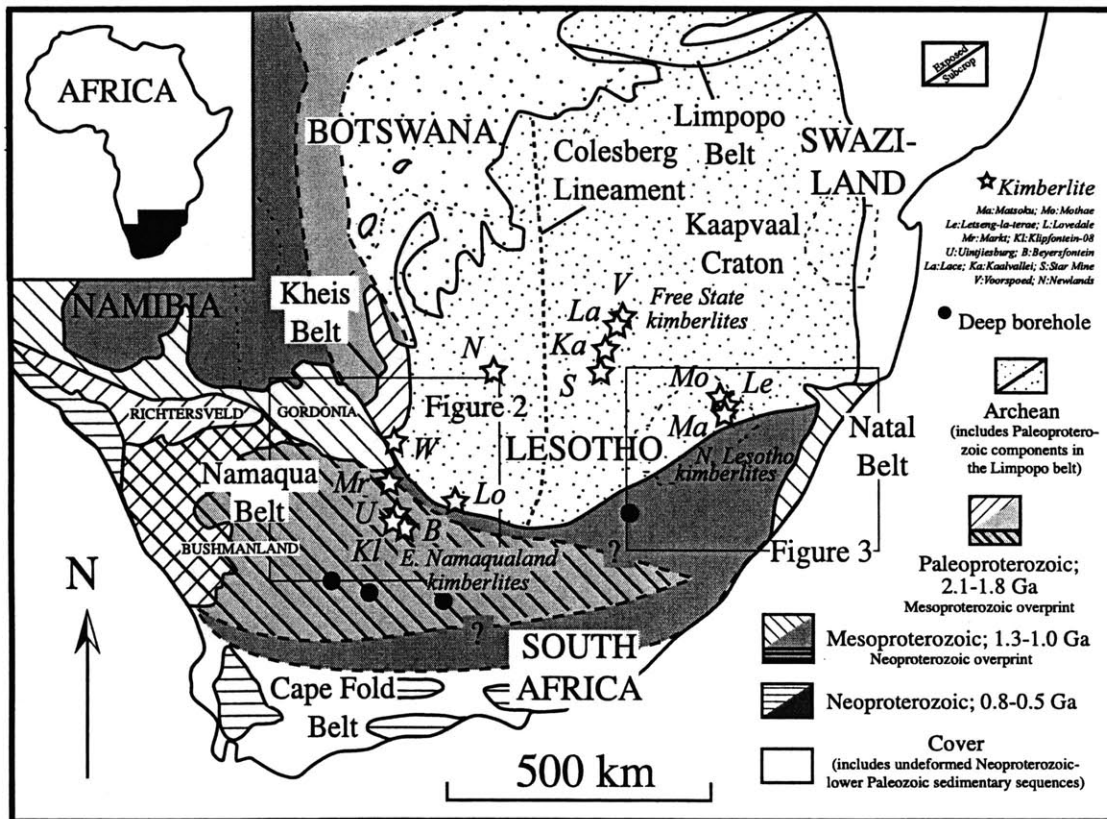


Figure 1. Tectonic map of southern Africa illustrating the distribution of Archean and Proterozoic crust, bounding tectonic structures, and the distribution of kimberlite fields within which significant quantities of lower crustal granulites are recovered. The majority of high-pressure garnet-clinopyroxene granulite xenoliths are exhumed in the craton-bounding Eastern Namaqualand and Northern Lesotho kimberlite suites.

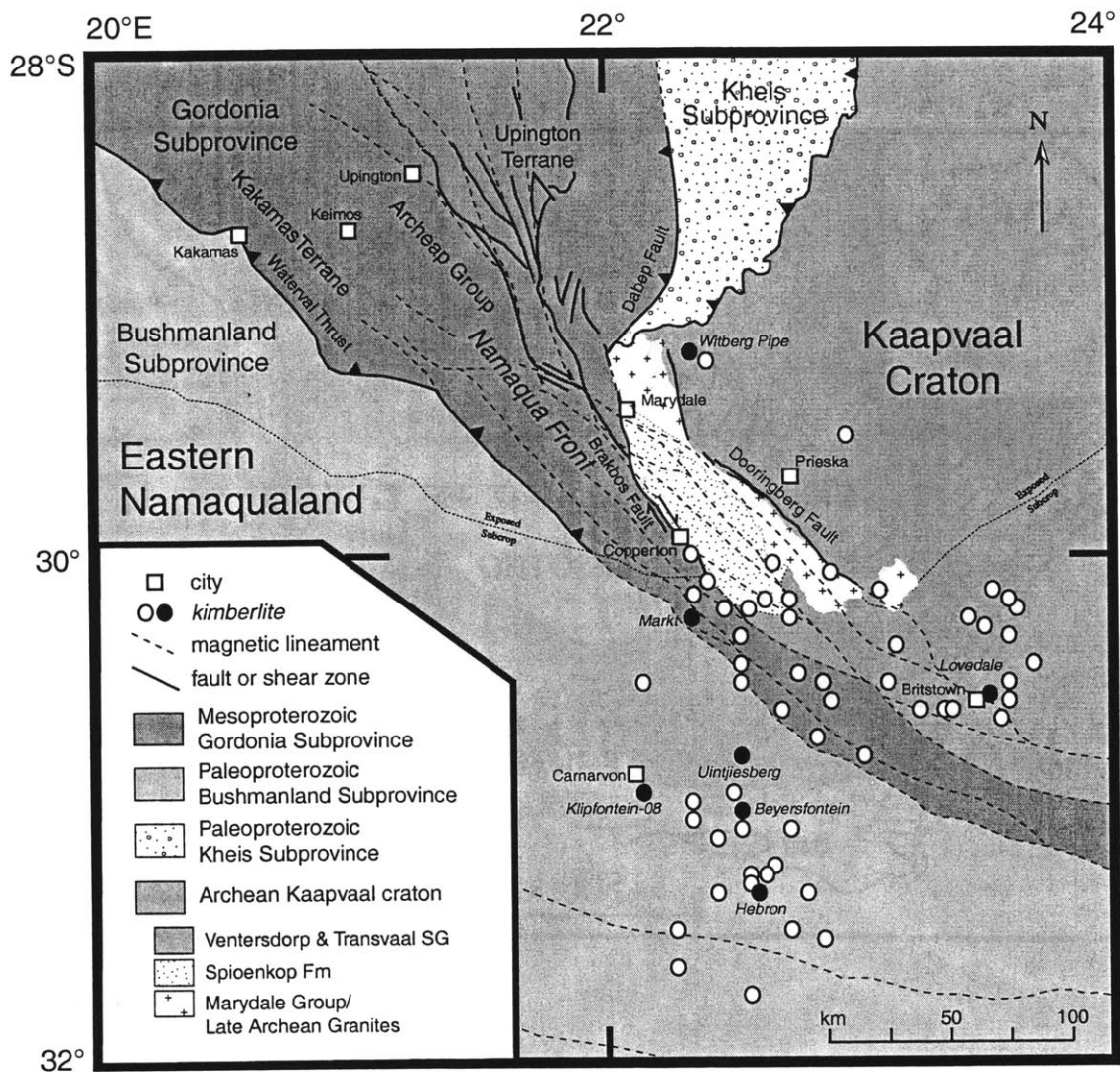


Figure 2. Simplified geologic map of the southwestern margin of the Kaapvaal Craton with the bounding Proterozoic Kheis and Namaqualand orogenic belts. The predominantly juvenile Mesoproterozoic Gordonia subprovince terranes are juxtaposed between the Archean Kaapvaal Craton and the Paleoproterozoic Bushmanland subprovince. Surface outcrop of crystalline basement ends at approximately 30°S; mapped subprovince bounding structures are inferred to continue beneath Phanerozoic cover from aeromagnetic lineaments. Kimberlites are shown as circles; filled circles indicate kimberlites referred to in the text.

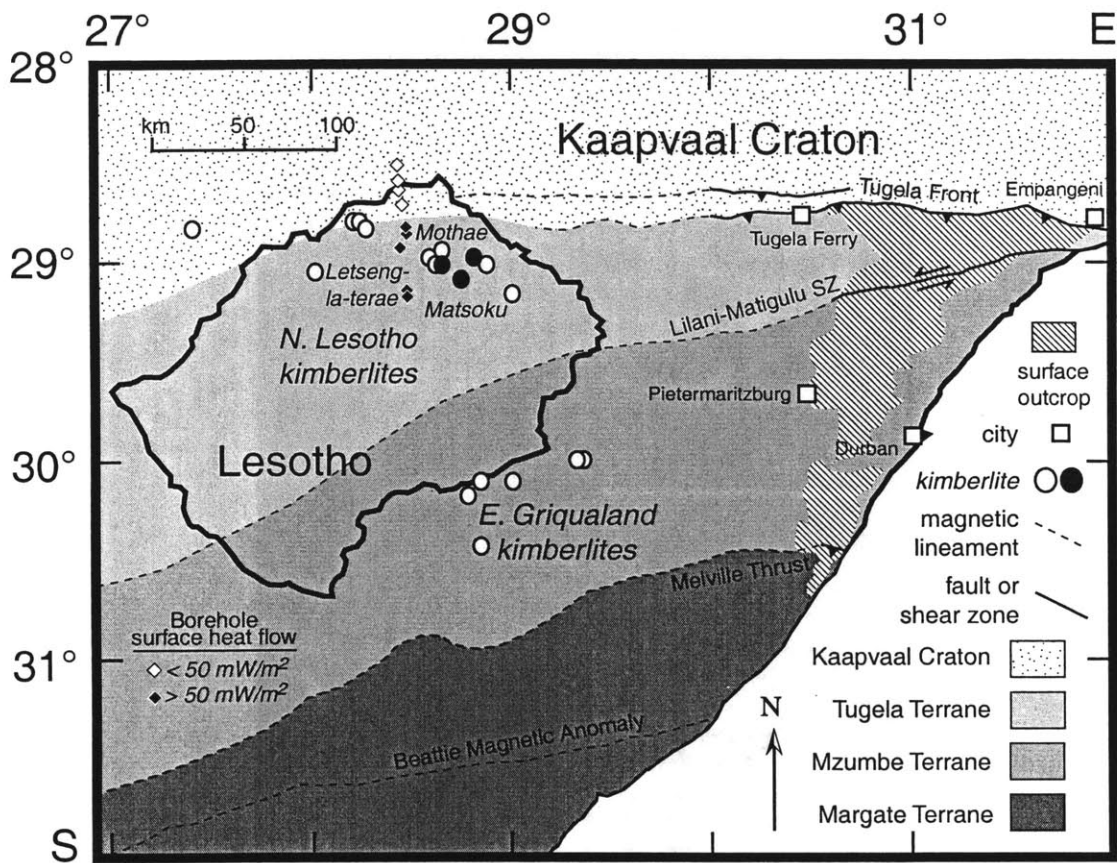


Figure 3. Simplified geologic map of the southeastern margin of the Kaapvaal craton with the bounding Natal Province, west to the vicinity of Lesotho. Mapped expressions of the Tugela, Lilani-Matigulu, and Melville faults and/or shear zones may be traced to the west through aeromagnetic signatures, and the presence of a heat flow anomaly associated with crustal thickening along the Tugela front in northern Lesotho; diamonds on map are boreholes defining this heat flow anomaly from Jones (1992). Kimberlites of northern Lesotho and east Griqualand denoted by circles; filled circles indicate kimberlites referred to in text.

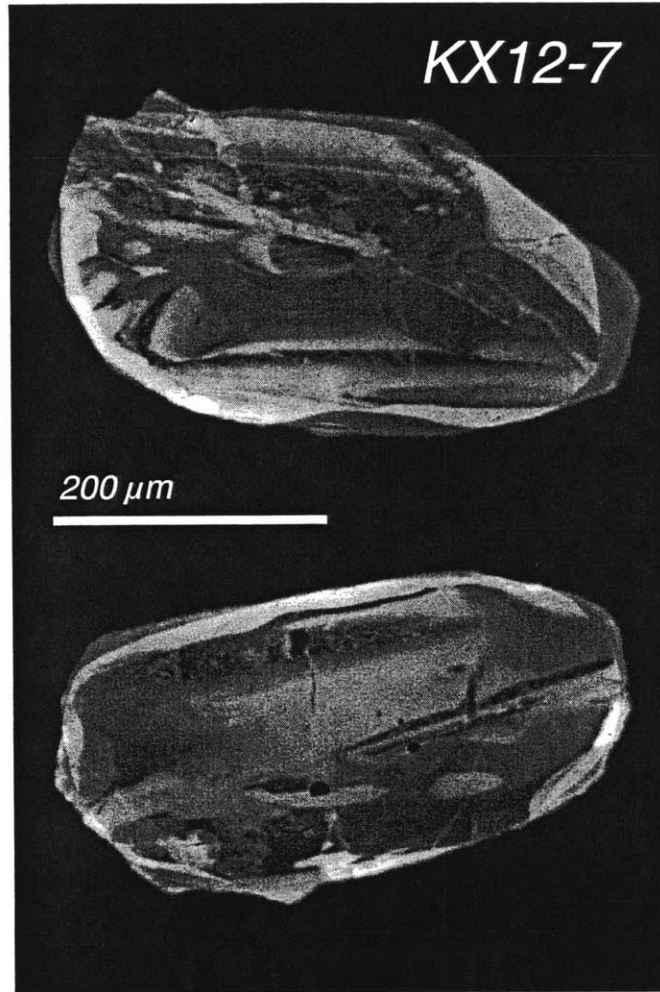


Figure 4. Cathodoluminescence (CL) images of zircon from a mafic granulite of the Klipfontein-08 kimberlite, Eastern Namaqualand.

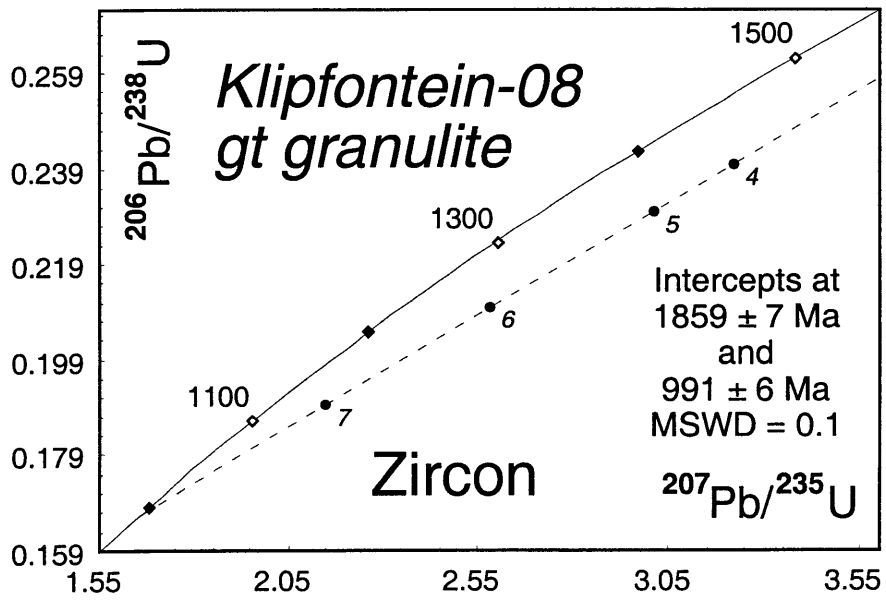


Figure 5. U-Pb concordia diagram for zircon from a mafic garnet + cpx granulite of the Klipfontein-08 kimberlite, Eastern Namaqualand. Point labels are keyed to numbers in first column of Table 1. Dashed line is discordia fit to the four single zircons.

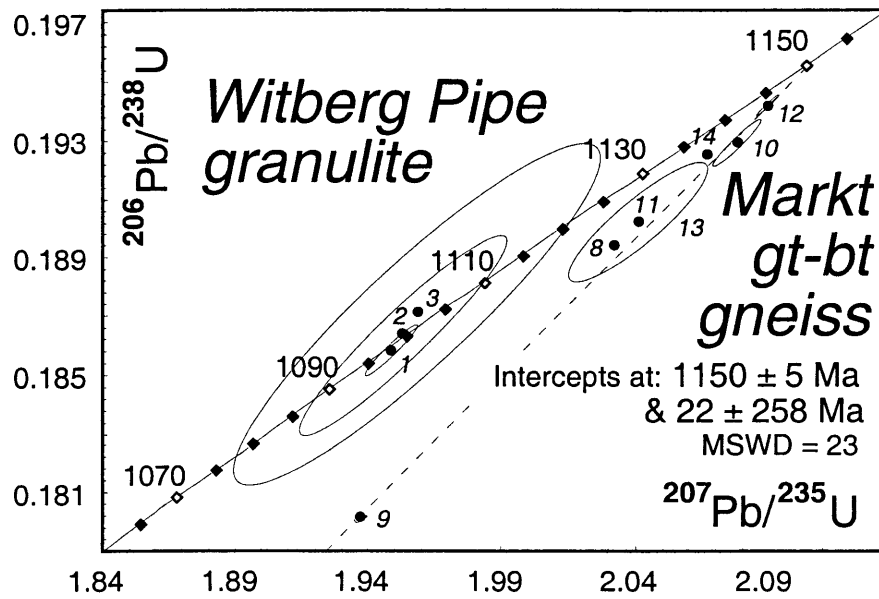


Figure 6. Concordia diagram for zircon from a mafic two-pyroxene granulite of the Witberg Pipe kimberlite, and for zircon and monazite from a granitic gneiss from the Markt kimberlite, Eastern Namaqualand. Point labels are keyed to numbers in first column of Table 1. Dashed line is discordia fit to the all fractions from the Markt granitic gneiss.

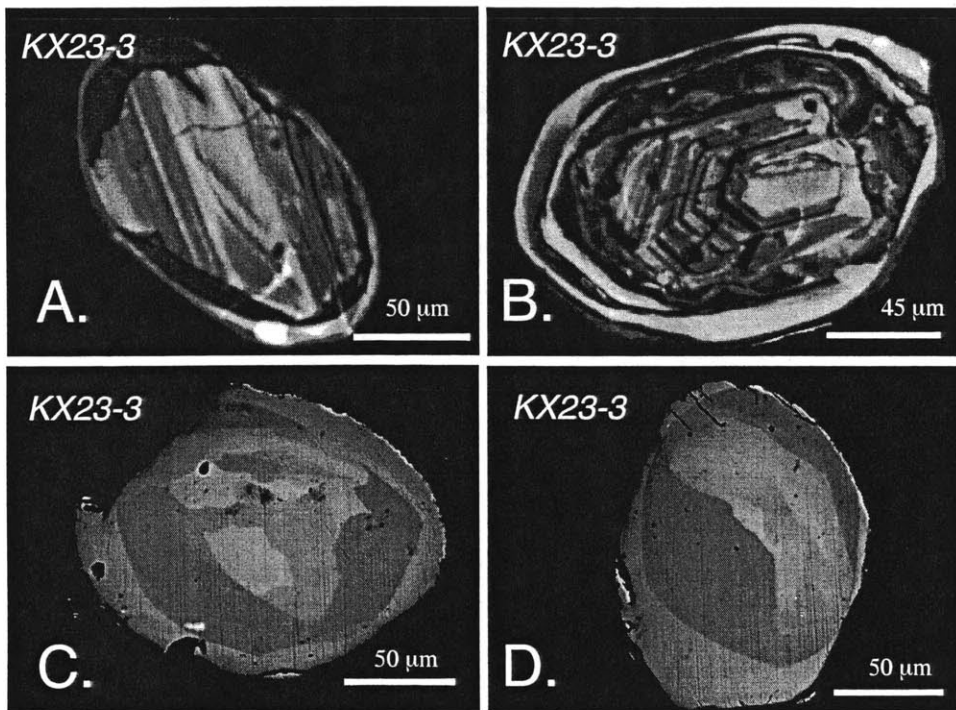


Figure 7.

CL images of zircon and BSE images of monazites from granulites of the Northern Lesotho kimberlites: a-b) Zircons from a metapelitic granulite of the Mothae kimberlite illustrating oscillatory zoned cores with metamorphic overgrowths; c-d) Monazites from the same Mothae granulite showing sector zoned cores overgrown by Th-rich mantles.

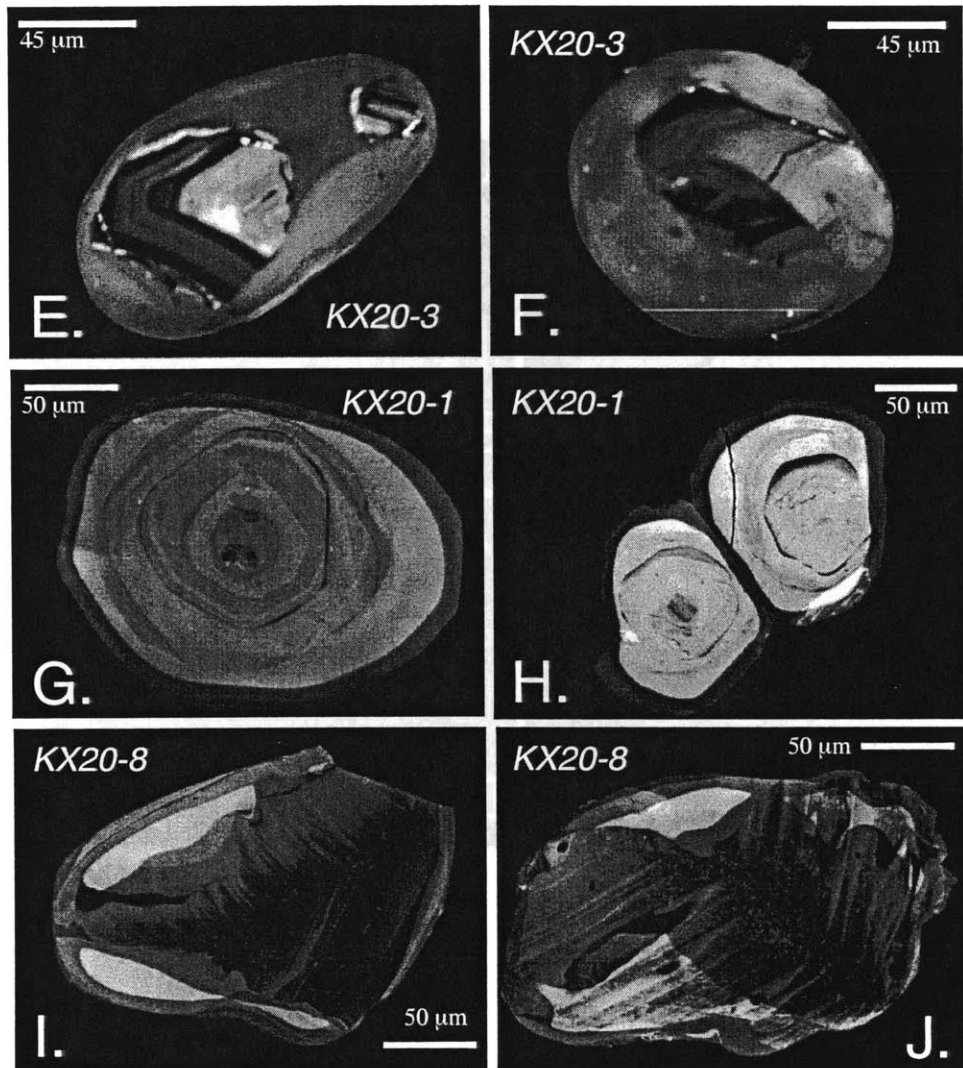


Figure 7 (con't). e-f) Zircons from a felsic gt+kyanite granulite of the Letseng-la-terae kimberlite comprising resorbed oscillatory-zoned cores with homogeneous metamorphic mantles; g-h) Zircons from a gt+ky+opx granulite from Letseng, illustrating nested multifaceted growth with thin weakly-luminescent rims, which have fused together two grains in (h); i-j) Zircons from a garnet+cpx granulite from Letseng, illustrating complex planar zoning with resorption and overgrowth of new more evenly zoned zircon.

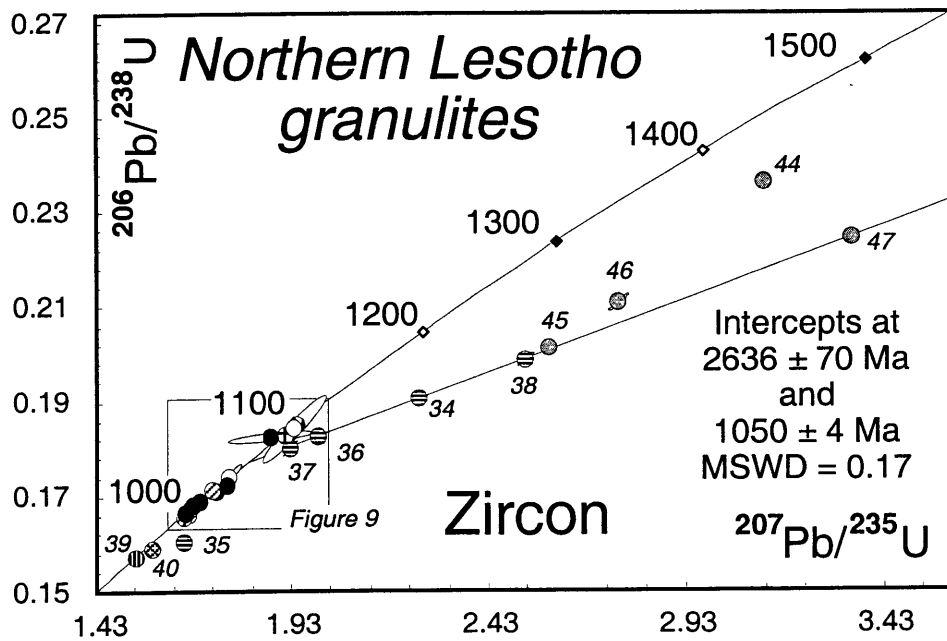


Figure 8. U-Pb concordia diagram for all zircon and monazite from granulites of the Northern Lesotho kimberlites, highlighting the systematics of zircon from KX23-3 and KX20-3. Inset is shown in Figure 9. Dashed line indicates discordia fit to four zircons from KX20-3.

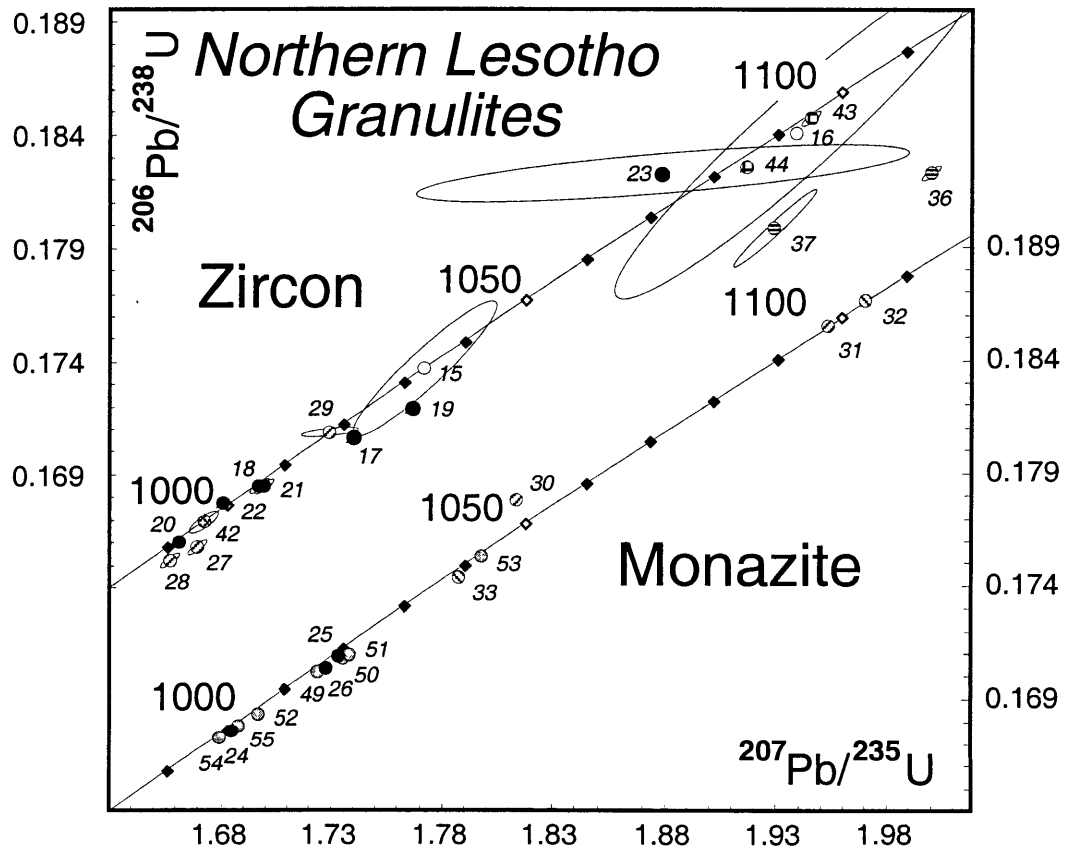


Figure 9. Enlarged composite U-Pb concordia diagram illustrating metamorphic zircon and monazite systematics from all granulites from Northern Lesotho. Point labels are keyed to numbers in first column of Table 1.

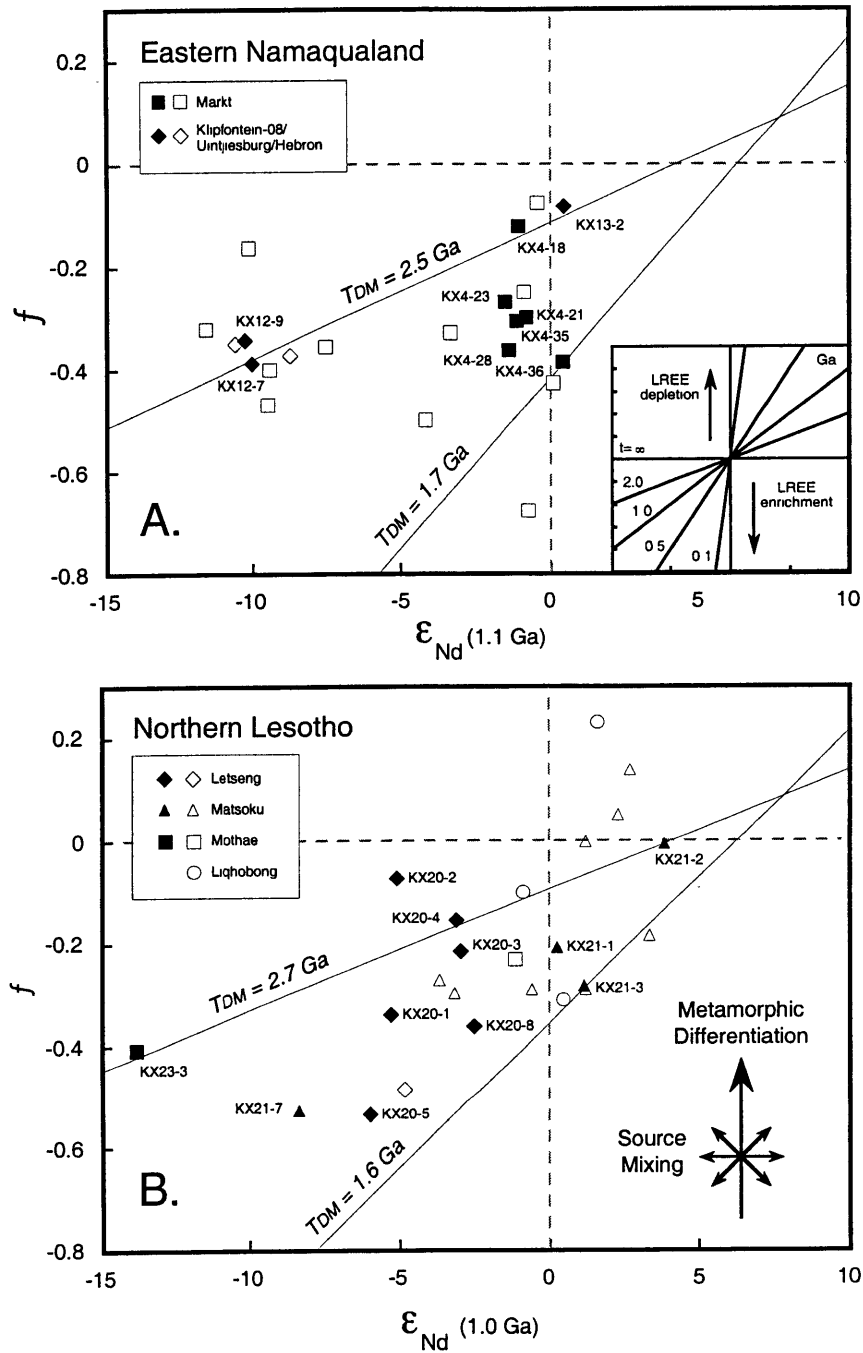


Figure 10. $f_{Sm/Nd}$ versus ϵ_{Nd} at the time of metamorphism, for xenoliths from the a) Eastern Namaqualand, and b) Northern Lesotho kimberlites. Inset in (a) illustrates the behaviour of systems subject to relative LREE-enrichment or depletion (by partial melting or metamorphism) as they evolve through time. Inset to (b) illustrates general vectors for processes of metamorphic segregation (instantaneous change in Sm/Nd), and source mixing (straight lines in this ratio space).

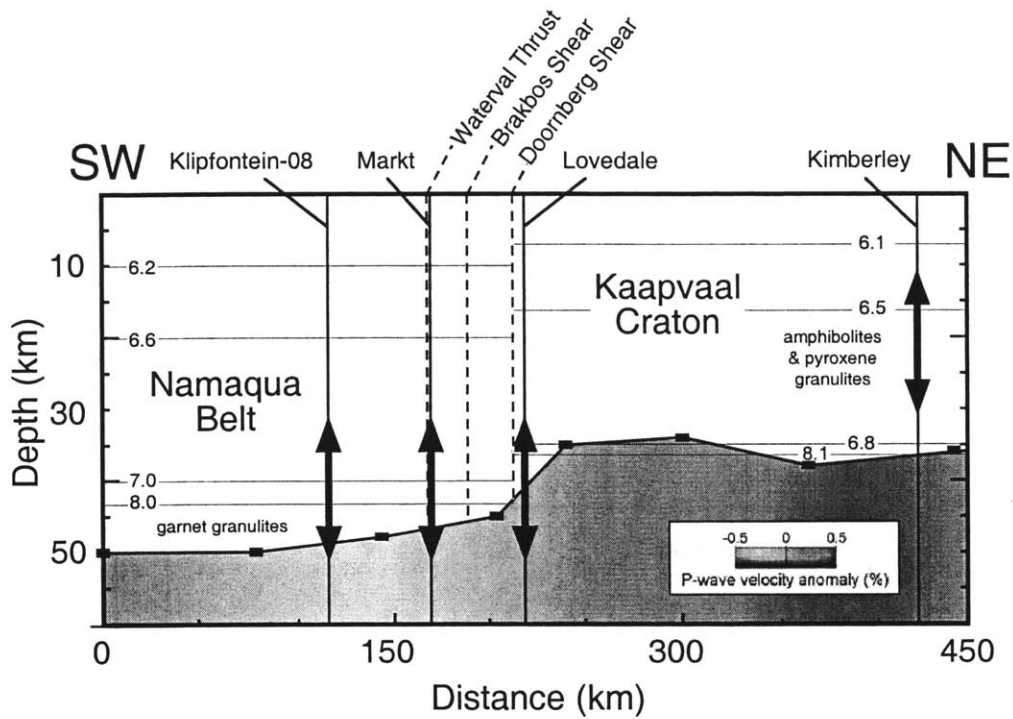


Figure 11. Schematic cross-section representing the seismic crustal thickness, seismic velocities, and lithological variation across the southwestern margin of the Kaapvaal craton into the Eastern Namaqualand orogenic belt, based on integrated studies of Ps receiver functions (Nguuri et al., 2001), seismic refraction data (Green and Durrheim, 1990; Durrheim and Green, 1992), and lower crustal xenolith petrography and isotopic geochronology (this study; Huang et al., 1995; Rogers and Hawkesworth, 1982). Section runs approximately from upper right to lower left-hand corners of Figure 2.

Chapter 3.

Ultra-high temperature metamorphism in the lower crust during Neoproterozoic Ventersdorp rifting and magmatism, Kaapvaal Craton, southern Africa

Keywords: U-Pb geochronology, rutile, zircon, monazite, UHT metamorphism, sapphirine, granulite, lower crust, Ventersdorp Supergroup, Kaapvaal craton, rifting

Abstract— A diverse suite of ultra-high temperature (UHT) granulite xenoliths from kimberlites of the Free State, South Africa, record the deep crustal manifestation of Neoproterozoic Ventersdorp extensional tectonics and magmatism within the central Kaapvaal Craton. Isobarically cooled UHT (>1000°C) garnet + quartz + sapphirine and related assemblages from the Lace kimberlite (Dawson et al., 1997) are described from other Free State kimberlites, suggesting the regional extent of metamorphism. U-Pb geochronological data for petrographically characterized metamorphic zircon and monazite from a number of UHT granulites are used to elucidate the pressure-temperature-time path of metamorphism. Prograde metamorphic growth of zircon and monazite indicate ramping of lower crustal temperatures ~25 Ma prior to peak UHT metamorphic conditions; preservation of prograde monazite dates through the UHT event support very high closure temperatures for this mineral, equivalent to those for zircon (>1000°C). Peak UHT metamorphism is dated by both zircon and monazite at *ca* 2720 to 2715 Ma. The subsequent early cooling path of the UHT granulites is established by dating of retrograde 2690 Ma zircon in kyanite-rich leucosomes, suggesting initial cooling rates of $\geq 8^\circ\text{C}/\text{Ma}$ following peak metamorphism.

The UHT granulites also contain a unique reaction texture of zircon exsolution from rutile. A model of subsolvus unmixing of zircon from compositionally heterogeneous (Zr,Si)-bearing rutile solid solutions is proposed to explain the diverse topology of exsolution phenomena, including heterogeneous nucleation and variable diffusive coarsening. Direct dating of individual zircon exsolution lamellae yield a wide range in integrated growth ages of *ca* 2.60 to 2.30 Ga which support slow cooling of the UHT granulites. Combined with available kinetic data for Zr diffusion in rutile, the lamellae ages and length scales of diffusive coarsening are used to place constraints on the cooling path of the UHT granulites. This analysis indicates integrated cooling rates of $\sim 1^\circ\text{C}/\text{Ma}$ at the base of the crust, and a thermal relaxation time constant for the Kaapvaal lithosphere of 400-600 Ma, consistent with a lithospheric thickness of

>250 km. However, the maintenance of relatively higher temperatures in the lower crust than those predicted from simple conductive cooling models for several hundred million years following disturbance remains enigmatic.

The 5-10 m.y. duration of UHT metamorphism in the lower crust is directly correlated with high advective lithospheric heat flux during rapid eruption of the Klipriviersberg Group flood basalts through the central Kaapvaal craton at 2714 ± 8 Ma (Armstrong et al., 1991). The dramatic lithospheric thermal gradients necessitated by these UHT lower crustal granulites demand a complete, if transient, removal of the thermal lithosphere localized along the NNE-trending axis of the Ventersdorp rift at 2.72 Ga, but contemporaneous maintenance of a coherent lithospheric keel with “cratonic” thermal gradients distal to the rift, in order to preserve ancient diamonds. Having demonstrated the first link between the surface geology and deeper lithospheric manifestations of Ventersdorp magmatism and extension, it is further argued on geological and geochronological grounds, that the flat seismic Moho of the central and western Kaapvaal craton recently imaged by the Kaapvaal Seismic Experiment (Nguuri et al., 2001) is a lower crustal rheological response to Ventersdorp rifting. The contrast between the broad geography of upper crustal extension/ lower crustal flow and the more restricted localization of thermal effects in the lithospheric mantle embodies a profound crust-mantle decoupling during 2.7 Ga intracratonic Ventersdorp rifting.

1. Introduction

For decades, researchers have noted the paucity of high-pressure granulitic lower crustal xenoliths from kimberlites erupted through the central Archean Kaapvaal craton, relative to the abundant granulitic assemblages from the southern and western cratonic margins and bounding Proterozoic Namaqua-Natal orogenic belts (Rickwood et al., 1969; Rogers, 1977; Griffin et al., 1979; Van Calsteren et al., 1986) (Figure 1). This dichotomy in the nature of the lower crust is unlikely to be an artifact of differential sampling, but rather emphasizes distinctive differences in the composition and metamorphic grade of the lower crust beneath different regions of southern Africa. Recent high-precision U-Pb zircon and monazite geochronology of the high-pressure granulite xenoliths of the craton-margin Northern Lesotho and Eastern Namaqualand kimberlite provinces (Chapter 2), have demonstrated that these high grade lower crustal assemblages were generated by crustal thickening during the 1.1 to 1.0 Ga Natal and Namaquan orogenic events,

related to the collisional accretion of juvenile Mesoproterozoic and older Paleoproterozoic crust onto the southern and western margins of the Kaapvaal craton (Hartenady et al., 1985; Stowe, 1986; Thomas et al., 1994). The imprint of this episode of crustal thickening is still evident in the architecture of the southern African lithosphere, as revealed by variations in crustal heat production and surface heat flow between the Proterozoic belts and the craton (Jones, 1992), as well as recent direct seismic receiver function mapping of crustal thickness variations across the Kaapvaal Seismic Experiment array (Nguuri et al., 2001).

The correlation between the presence of 10-15 kbar granulitic lower crustal xenoliths in the craton-margin and off-craton kimberlites, and current crustal thicknesses of 40-50 km with high lower crustal seismic velocities in the same regions is compelling. A *lack* of high-pressure granulite xenoliths from kimberlites within the craton is also generally consistent with the remarkably uniform and thinner crust of the central and western craton. A higher seismic velocity contrast across the Moho beneath the craton also demands on average a more intermediate, hydrous character for the cratonic lower crust (Durrheim and Green, 1992; Nguuri et al., 2001). Whether this current character of the cratonic crustal section is a primary feature of formation and assembly, or has resulted from subsequent tectonomagmatic modification has been unclear. Paramount to our further understanding of the evolution of the crustal architecture of the Kaapvaal is a closer examination of the rare deep crustal samples available in kimberlites from within the craton.

A singular exception to the general lack of cratonic lower crustal granulites is the description of garnet-bearing assemblages as xenoliths from the Lace kimberlite, located in the Free State province of South Africa, in the central craton (Dawson and Smith, 1987) (Figure 1,2). These unique xenoliths are dominated by a suite of garnet + sapphirine + quartz granulites which record “ultra-high temperature” (UHT) metamorphism under extreme crustal thermal conditions (Harley, 1998). Peak temperatures in excess of 1000°C, at pressures of 10 kbar have been estimated for these rocks (Dawson et al., 1997), suggesting a dramatic, if transient period of advective heat transport to the base of the crust, and posing an intriguing conundrum regarding the formation and stability of the thick cold lithospheric mantle keel presently developed beneath the Archean craton.

A combined isotopic and U-Pb geochronological study of these samples was initiated, in order to constrain the age and thermal evolution of this unique metamorphic assemblage. The

overreaching goal of this study was to determine the relationship of UHT metamorphism in the lower crust to the geological and tectonic evolution of the craton, and examine the consequences of this metamorphism for the architecture and evolution of the Kaapvaal craton. A more general application of the resulting geochronological data is to elucidating the tempo and causal mechanisms of UHT metamorphism, as it is increasingly encountered in exposed high-grade continental crustal terrains (Harley, 1998). Finally, with regard to the specific systematics and applications of U-Pb accessory mineral geochronology, the extreme conditions of UHT metamorphism in these rocks provide a unique natural laboratory for examining the kinetics of trace element diffusion in a number of accessory minerals, including zircon, monazite, and rutile.

The present study began with examination of the abundant sapphirine-bearing assemblages of the Lace kimberlite. During this examination, two important discoveries shaped the course of subsequent investigations: first was the discovery of a unique reaction texture within the UHT assemblages of zircon exsolution from rutile. This phenomenon has only previously been described from similar UHT sapphirine-bearing assemblages from the Snowbird Zone of northern Saskatchewan (Snoeyenbos et al., 1995), and in the diverse lower crustal granulite and eclogite xenolith suites of southern Africa, is only known from this UHT granulite suite of the Free State kimberlites. This reaction texture was found not only in garnet-quartz-sapphirine assemblages, but also in less refractory ternary feldspathic garnet-bearing granulites, and became a convenient fingerprint of this consanguineous suite of UHT xenoliths.

Second, examination of garnet-bearing granoblastic-textured xenoliths from the nearby Voorspoed kimberlite revealed a suite of very similar UHT mineral assemblages to those from the Lace kimberlite. These included sapphirine-bearing assemblages, as well as sapphirine-free rocks dominated by a garnet + quartz + antiperthite + sillimanite (kyanite) + rutile; all of these assemblages contained the unique rutile-zircon exsolution textures. To determine the regional extent of these UHT mineral assemblages in the lower crust, very small rare granulite xenoliths from the Kaalvallei and Star Mine kimberlites were also obtained. These xenoliths have not been previously described, but were found to have very similar mineral assemblages, including the key reaction texture involving zircon exsolution from rutile unique to the better documented UHT assemblages from Lace. U-Pb geochronological data presented in this paper will document that all of these xenoliths were generated during the same UHT metamorphic event. Most importantly, the discovery of these UHT granulites in widely dispersed kimberlites of the Free

State demonstrates the regional nature of this event in the lower crust of the central craton, and thus highlights the importance of establishing the tectonomagmatic impetus for this dramatic crustal metamorphism.

2. Previous work and geological setting

2.1 Previous investigations

Dawson and Smith (1987) first described the occurrence of high-Mg, high-Al, graphitic sapphirine-bearing metamorphic mineral assemblages in granulite xenoliths from the Lace kimberlite of the central Free State of South Africa. Dawson et al. (1997) extended the mineralogy and mineral chemical investigations of these rocks to refine the P-T conditions of equilibration and retrograde reaction. The diagnostic peak ultra-high temperature (UHT) assemblage of quartz + sapphirine + garnet + sillimanite ± orthopyroxene, in the absence of cordierite, or coexisting orthopyroxene and sillimanite, was deduced from FMAS and KFMASH petrogenetic grids to indicate equilibration conditions of >1000°C and 9-11 kbar. Coronal reactions involving garnet + sillimanite and minor garnet + cordierite also further interpreted to indicate near-isobaric cooling of these rocks, in agreement with the comparative results of core-rim garnet-orthopyroxene geothermobarometry. Although kyanite was noted as a minor phase in some of the samples studied by Dawson and Smith (1987), the occurrence of this mineral was de-emphasized in subsequent work; the significance of coexisting kyanite and sillimanite for constraining the P-T-t path the UHT granulites is substantial, and an understanding of the relationship between the aluminosilicates was one of the primary goals of this study. The first indication of the antiquity of the UHT assemblages was provided by SHRIMP analysis of a single zircon grain from one of the sapphirine-bearing granulites studied by Dawson et al. (1997), which because of the low U content, yield relatively imprecise data with a weighted mean $^{207}\text{Pb}/^{206}\text{Pb}$ date of 2.590 ± 0.080 Ma. Interpreting this zircon as a metamorphic mineral, the Neoproterozoic age was inferred to represent the timing of high grade metamorphism, although no attempt was made to relate this age to the geological and tectonic evolution of the Kaapvaal craton.

2.2 Geological and temporal setting

The Free State kimberlites stretch over 120 km in a northeasterly array erupted through the Mesoarchean crust of the central Kaapvaal craton (Figure 2). These volcanics comprise both Group 1 and 2 kimberlites, and were erupted asynchronously between 132 Ma (Lace, Voorspoed; Phillips et al., 1999), 124 Ma (Star Mine; McIntyre and Dawson, 1974), and 88 Ma (Kaalvallei; Viljoen, 1989). The Lace (Crown) and Voorspoed kimberlites are located within a few kilometers of each other, approximately 100 km southwest of Johannesburg, and approximately 50 km to the west of the Vredefort Dome. The Kaalvallei pipe is located some 70 kilometers to the south, near Welkom, while the Star Mine is located in a kimberlite dike another 50 km further south, near Theuniessen. All of these pipes outcrop in within the confines of the Witwatersrand basin, and specifically proximal to the bounding faults of the De Bron Horst, a 2.7 Ga Ventersdorp extensional feature. These kimberlites are located well within the craton, and east of the Colesburg magnetic lineament, the inferred major crustal suture separating 3.5-3.1 Ga crust of the eastern Kaapvaal shield from 3.2-2.9 Ga accreted terrains of the western Kimberley block. An overview of the relevant Neoproterozoic geological evolution of the central craton and vicinity is presented to set the stage for possible tectonomagmatic mechanisms for the production of the Free State UHT granulites, with emphasis on the character and development of the 2.72 to 2.67 Ga volcanosedimentary Ventersdorp Supergroup. For details of Ventersdorp stratigraphy, volcanology and sedimentology, the reader is referred to excellent summaries by Winter (1976), Buck (1980), Burke et al. (1985), and van der Westhuizen et al. (1991).

Following stabilization of the eastern Kaapvaal shield at ca 3.2 Ga, and subsequent rifting and deposition of the Dominion Group in the western sector of the shield between 3.087 and 3.074 Ga (Robb et al., 1991; de Wit et al., 1992), amalgamation of the western Kimberley block to the eastern craton through continental collision was accomplished simultaneously with Witwatersrand basin subsidence and deposition between 2.97 to 2.82 Ga (Robb et al., 1995; Chapter 5). Broad subaerial exposure and peneplanation of the craton between ca 2.82 and ca 2.72 Ga is indicated by the extensive unconformity developed on the upper Central Rand Group and older Archean crystalline basement prior to eruption and deposition of the Ventersdorp Supergroup (Winter, 1976; Hall et al., 1997). Intercalated with lowermost Venterspost Formation conglomerates are the first lavas of the Ventersdorp Supergroup, the Meredale Member of the Westonia Formation, Klipriviersberg Group (SACS, 1980). As the first of three subdivisions of the Ventersdorp, the Klipriviersberg Group comprises approximately 2000

meters of mantle-derived tholeiitic mafic to ultramafic flood basalt flows and associated intrusive sills and dikes with a presently recognized outcrop distribution of over 155,000 km², but generally confined to the eastern central craton in the vicinity of the older Witwatersrand Basin (Van der Westhuizen et al., 1991; Marsh et al., 1992). The age of extrusion of the Klipriviersberg is constrained by a SHRIMP U-Pb zircon age of 2.714±0.008 Ga for a lava of the Alberton Porphyry Formation (Armstrong et al., 1991). The lack of interflow sediments or weathering horizons indicates rapid eruption of this volcanic package, while extensional fault control on formational thicknesses demonstrates eruption in a initiating rift setting (Tyler 1979), although the most significant block-faulting post-dates Klipriviersburg eruption. Geographically, the Free State kimberlites appear to trend approximately parallel to inferred N-S bounding faults of the De Bron horst, which were eastern loci of magmatism and extension during the initial Klipriviersberg stage of the Ventersdorp event (Figure 2). This observation gives the first indication that this 2.72 Ga magmatism may play an important causative role in the formation of the UHT granulite suite.

The Klipriviersberg Group is succeeded by the overlying Platberg Group, which itself comprises coarse immature clastic sediments of the lower Kameelsdorn Formation, overlying intermediate felsic volcanics including the Makwassie Quartz Porphyry Formation, and the uppermost mixed volcanosedimentary Rietgat Formation. Together the formations of the Platberg Group have preserved accumulations of >2000 meters thickness. The sediments of the Kameeldoorns Formation were deposited as fanglomerate and alluvial fan wedges prograding into and filling rapidly subsiding half-grabens formed by N-S and E-W striking normal faults across >200,000 km² of the central and western craton (Burke et al., 1985). In contrast to the underlying Klipriviersburg Group, the lower Platberg Group sediments and succeeding lavas of the Makwassie Formation extend in outcrop further to the west, likely to the very margin of the craton (Tinker, 2001), illustrating the broad scope of extensional tectonism across the central and western Kaapvaal (Figure 2). The Makwassie Formation andesites and rhyolites have been interpreted as partially crustally-derived melts, and are dated by U-Pb SHRIMP zircon age of 2.709±0.004 Ga (Armstrong et al., 1991), demonstrating the relatively rapid extrusion of the Klipriviersberg and lower Platberg Group volcanics over approximately 5-10 million years and a similarly rapid tempo for crustal extension. The overlying Rietgat Formation mixed volcanics

and sediments record a decline in both volcanism and extension through the sequence (Buck, 1980; Burke et al., 1985).

The Bothaville Formation of the final Pneil Sequence of the Ventersdorp unconformable overlies the Platburg Group, and differs from it in its maturity and lack of rapid facies changes (Winter, 1976). It is interpreted to record deposition by southward flowing meandering stream networks on an alluvial plain undergoing marine transgression from the south. Bothaville deposition was abruptly terminated by a renewed phase of ultramafic to mafic continental flood basalt volcanism comprising the Allanridge lavas, which reach an accumulated thickness of ~750 meters in a present outcrop pattern of similar broad extent to the underlying Platberg Group. Interpretation of seismic reflection profiles across the western margin of the craton have revealed the presence of substantial thicknesses (>5 km) of Platberg and Pneil-equivalent sediments and volcanics as a west-facing depositional wedge in the subsurface (Tinker, 2001), which may represent a rifted passive margin sequence. Although the Allanridge Formation has not been directly dated, correlative lavas of the Witrandfontein Formation of the Buffelsfontein Group in northern South Africa and southern Botswana have been dated at 2.664 ± 0.002 Ga (Barton et al., 1995), suggesting that Pneil Sequence volcanism post-dated the initial pulse of Klipriviersberg and Platburg magmatism by as much as 40 million years.

The end of Ventersdorp Supergroup deposition is defined by an erosional unconformity upon which the Black Reef Quartzite Member of the Transvaal Supergroup is deposited. Minor volcanics immediately overlying the unconformity (Vryberg Formation) have been dated at 2.642 ± 0.002 Ga (Walraven and Martini, 1995). The overlying lower Transvaal Supergroup sequences comprise a platformal sequence of approximately four kilometers of carbonate and banded iron formation recording gradual subsidence of the craton. An ash bed near the top of the lower Transvaal sequence (near the base of the Griquatown Iron Formation) has yielded an age of 2.432 ± 0.031 Ma establishing a minimum of 200 million years of subsidence. Above an unconformity, the base of the overlying ~8 km thick upper Transvaal sequence is tentatively dated by a Pb-Pb whole rock isochron age of 2.222 ± 0.013 Ma for the Ongeluk Andesite Formation of the Griqualand West sequence, correlated with the Hekpoort Andesite of the Pretoria Group to the east. Lacking a precise and accurate U-Pb zircon age however, it is difficult to place the upper Transvaal within a temporal framework; latest deposition of the entire

Transvaal Supergroup of bracketed by the 2.060 ± 0.002 Ga age of the Rooiberg Felsites (Walraven, 1997).

A final note should be made regarding the geometry of Ventersdorp strata and rifting. Based mainly on outcrop distribution and relatively abundant borehole sampling in the vicinity of the Witwatersrand basin, the Ventersdorp has been historically considered as a NNE-trending intracratonic rift zone approximately 200 km wide passing through the central Kaapvaal (Figure 2; van der Westhuizen et al., 1991). To a large degree this geometry is inferred from the thinning of the Ventersdorp strata in the northwest in the vicinity of the Kraaipan basement uplifts and the lack of further pre-Transvaal strata outcropping to west of these basement highs. Recent interpretation of upper and middle crustal seismic reflection profiles across the northwestern margin of the craton has however revealed a dramatic wedge of Ventersdorp strata in the subsurface, which may be tentatively correlated with both Pneil sequence and Platberg Group volcanics and sediments (Tinker, 2001). This wedge thickens dramatically from east to west with accumulations of Ventersdorp strata estimated at >10 km— much greater than their manifestations on the craton. These new correlations fundamentally change our perception of the geometry of the Ventersdorp depository and interpretations of the evolution of rifting and extension across the western craton. From the accumulation of Ventersdorp, and succeeding Transvaal Supergroup strata, is apparent that the western margin of the craton achieved full fledged continental breakup and passive margin status as a culmination of 2.72 to 2.67 Ga rifting. In this light, the western block of the Kaapvaal craton is bounded on both east and west by either abortive or mature rift sequences.

3. Sample Descriptions

3.1 Modal mineralogy and petrography

KX1-1 (Lace): Sample KX1-1 is a 20 cm diameter xenolith, comprising a primary mineral assemblage of garnet, sapphirine, and quartz with subordinate rutile, sillimanite, graphite, and sulfide, and accessory kyanite, corundum, zircon, and monazite. The xenolith displays a coarse granoblastic texture with grain sizes of 2-5 mm for garnet and quartz, and 1-3 mm for sapphirine. Details of the petrography of this xenolith mimic those reported by Dawson and Smith (1987) and Dawson et al. (1997). Garnets are extensively fractured and have well developed

kelyphitization along these boundaries. Inclusions of quartz are common, concentrated toward the center of grains. Sapphirine is most commonly in grain contact with garnet, although it can be completely occluded by quartz. Quartz grains show patchy extinction, with the development of discrete subgrain domains separated by crenulated boundaries. Quartz is also unique in exhibiting strong planar fractures in some grains, while most grains also contain parallel planar concentrations of minute inclusions, in addition to ubiquitous oriented rutile needles. Rutile is found in two distinct settings: as elongate acicular micron-scale needles in garnet, sapphirine and quartz; and as larger rounded prisms and anhedral grains included in all major phases and on grain boundaries. The first morphology of rutile is crystallographically controlled, and best developed in quartz, where needles oriented on three planes can coarsen up to several microns in thickness and tens of microns length. The second form of rutile is the phase analyzed for U-Pb isotopic composition. When occluded by other minerals, these discrete rutile grains exhibit a euhedral rounded prismatic morphology. The rutile in this, and all of the Free State UHT granulites, contain a unique reaction texture involving the exsolution of zircon from the rutile lattice. Because of the semi-opaque red-brown to black coloration of rutile, this phenomenon is difficult to observe in thin section, possibly explaining why previous workers overlooked this dramatic microstructure. However in very thin sections of rutile, fine needles oriented along three crystallographic directions may be observed. In back-scattered electron (BSE) imaging of rutile, this microstructure is easily observed and the exsolved phase identified as zircon by energy dispersive X-ray analysis. Further details of the development and morphology of the zircon-rutile reaction texture are discussed in a following section.

KX1-2 (Lace): Sample KX1-2 is a 7 cm diameter xenolith which is slightly more altered than KX1-1, with the development of secondary phlogopite grains as well as pervasive grain boundary alteration. The mineralogy of sample KX1-2 is identical to that of KX1-1, namely comprising garnet, sapphirine and quartz with minor rutile, sillimanite, sulfide and graphite, and accessory kyanite, corundum, zircon and monazite. Unlike KX1-1, garnet in this sample forms thin rims between some sapphirine and quartz crystals. KX1-2 is also coarser-grained, with garnets reaching over 1 cm in diameter and sapphirine up to 5 mm. This sample may contain slightly more modal garnet than KX1-1.

KX1-8 (Lace): Sample KX1-8 is a 10 cm diameter xenolith with an unaltered primary mineralogy more diverse than that of the previous sapphirine-bearing samples. In addition to garnet, sapphirine, quartz and rutile, this xenolith contains abundant sillimanite and rarer plagioclase feldspar grains. Textures are also more complex, with common reaction boundaries and 'fingerprint' intergrowths involving sapphirine, garnet, sillimanite and quartz. Similar to those described by Dawson et al., these textures comprise single or double rinds of sillimanite±garnet developed between primary sapphirine-quartz contacts, with sillimanite preferentially crystallized next to sapphirine and garnet next to quartz. Sillimanite rims sometimes merge into coarsely bladed crystals. Garnet is homogeneously distributed throughout the xenolith, with grain sizes of 3-7 mm, and the xenolith has an overall granoblastic texture. Accessory minerals include rutile, graphite, sulfide, corundum, zircon, and monazite. Rutile follows the same morphologies and habit as the previously described xenoliths, and zircon is tentatively identified as inclusions in garnet and sapphirine.

KX2-1 (Voorspoed): Sample KX2-1 is a 15 cm diameter composite xenolith comprising a medium grained garnet + quartz + sapphirine-bearing domain, and a coarse-grained felsic domain dominated by milky white quartz and antiperthitic feldspar. Large garnets growing in the felsic domain exceed 1 cm in diameter, and are idiomorphic in contact with feldspar and quartz. Other minerals include abundant sillimanite and kyanite, in addition to minor rutile, titanian phlogopite, graphite, and sulfide. Accessory minerals include corundum, zircon, and monazite. The antiperthitic feldspar forms large 1-5 mm grains with pervasive micron-scale lamellae of K-feldspar. Sillimanite forms large grains or clusters of smaller interlocking grains, which often include euhedral rutile grains. Coexisting kyanite is a second, and clearly retrograde aluminosilicate, forming large blades, agglomerates of smaller crystals, and sheaf-like crystal sprays at the expense of sillimanite. A dramatic indication of kyanite's late appearance is its relationship to rutile, which is commonly cleaved and disaggregated by clusters of small kyanite grains which have replaced formerly occluding sillimanite. Rutile is also occluded by primary garnet, quartz, and feldspar, and forms anhedral interstitial grains. A second type of rutile is present in the form of oriented micron-scale needles in garnet and quartz. High relief inclusions tentatively identified as zircon or monazite are present in the aluminosilicates, garnet, and sapphirine.

KX2-2 (Voorspoed): Sample KX2-2 is a 7 cm diameter xenolith consisting of equigranular granoblastic-textured submillimeter quartz, antiperthite and sillimanite with evenly distributed 2-3 cm porphyroblasts of garnet, and subordinate kyanite blades, euhedral rutile grains, red-brown titanian phlogopite tablets, graphite flakes, and sulfide blebs. While this sample does not contain sapphirine, it does contain the same unique rutile-zircon exsolution textures, which warrants placing this sample in the same UHT category. Orange-brown spinel is found as rare inclusions in the cores of some garnets, with quartz and sillimanite. Exsolved rutile needles are present in garnet and quartz. Rutile is found as discrete grains occluded by garnet but more commonly within the quartz and feldspar domains. High-relief inclusions tentatively identified as zircon are observed in garnet, feldspar, sillimanite and quartz.

KX27-1 (Star Mine): Sample KX27-1 is an 8 cm diameter xenolith comprising a mineral assemblage dominated by garnet and quartz with minor plagioclase and sillimanite, and accessory graphite, sulfide, rutile, corundum, and rare zircon. The xenolith lacks a ferromagnesian phase other than garnet, and no monazite was obtained from mineral separates. Garnets range from 1-10 mm, with inclusion rich cores and relatively inclusion-free outer mantles. Quartz grains include large 3-5 mm crystals exhibiting patchy to undulose extinction, as well as smaller submillimeter interlocking grains with uniform extinction making up mosaic textured domains between larger crystals, along with plagioclase. Both garnet and quartz contain oriented rutile needles, and quartz has abundant trails of unidentified inclusions. Discrete rutile is the most abundant minor constituent, included in garnet and quartz and as interstitial grains.

KX18-2 (Kaalvallei): Sample KX18-2 is a very small, 3 cm diameter nodule comprising garnet, an unidentified altered ferromagnesian phase, antiperthitic feldspar, quartz, phlogopite, sillimanite and rutile, with accessory corundum, sulfide, zircon and monazite. Garnet forms dispersed 3-5 mm porphyroblasts within a matrix of 5-10 mm feldspar and 1-3 mm quartz crystals. Rutile is present as discrete grains included in all major minerals and as interstitial crystals.

3.2 Accessory mineral petrography

3.2.1 Monazite

The abundance of monazite varies in the UHT granulites, however no more than several dozen monazites were separated from each xenolith. In thin sections of sample KX1-2, monazite is found as discrete grains included in garnet, quartz and sapphirine, and at grain boundaries; monazite is presumed to occupy similar positions in the other granulites although few grains were observed petrographically. Optically, monazites are pale to strongly colored yellow grains, typically rounded to lenticular in shape. Larger grains are more subhedral to anhedral than smaller crystals. Back-scattered electron (BSE) imaging of monazites reveals fairly weak zonation (Figure 3a), suggesting that any variations in Th and U content are likely anticorrelated. However discrete domains and core-rim relationships are observed, which may indicate episodic growth of this accessory mineral.

3.2.2 Zircon

The zircon populations of the various UHT granulites, when examined in detail, display a systematic set of characteristics, resulting in a classification on the basis of morphology, color, and cathodoluminescence (CL)-derived growth zonation patterns. Five distinctive types of zircon are recognized in the UHT granulites, both from mineral separates and from thin section observation. Three of these types comprise a subgroup of zircons found as components of discrete grains found as mineral inclusions and interstitial crystals. The other two types of zircon form a second subgroup distinguished by an intimate association with rutile.

3.2.2.1 Discrete zircon grains

Type 1 is the least common phase of zircon, forming rare colorless anhedral discrete grains in sample KX1-1, and small resorbed cores within some composite spheroidal grains in samples KX1-1 and KX1-8. Type 1 zircon is most clearly distinguished by its oscillatory zoning pattern in CL, and it is on this basis that the whole anhedral grains (Figure 3b) and small cores in composite grains (Figures 3c-d) are correlated. The irregular margins of Type 1 zircon indicate that a period of zircon resorption occurred following its crystallization.

Type 2 zircon, which predominates in all samples of UHT granulite, comprises populations of colorless, spheroidal to ellipsoidal or football-shaped zircons ranging from >20 to approximately 200 microns in diameter. In CL, Type 2 zircon display a distinctive zonation

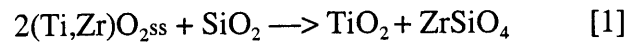
consisting of numerous polyhedra of even luminescence within a meshwork of brighter zircon, together forming a mosaic texture (Figure 3c-f). This pattern is the result of sector zonation during the growth of ellipsoidal multi-faceted crystals. Type 2 zircon also contains rare inclusions of sapphirine (Figure 3f). As previously noted, fairly rare grains (<5% of those imaged) comprise a small resorbed core of oscillatory-zoned Type 1 zircon surrounded by mantling sector-zoned Type 2 zircon (Figure 3c-d). These grains provide important constraints on the relative ages of older Type 1 versus younger Type 2 zircon. The spheroidal morphology of Type 2 zircons is sometimes modified by irregular corroded margins (Figure 3c), and internal zonation patterns are commonly truncated, suggesting that a period of resorption followed Type 2 crystallization.

Type 3 zircon, which is only found in a subset of UHT granulites, is notable for its pink coloration, and forms both optically discernable anhedral or onion-skin overgrowths on colorless grains, as well as anhedral to subhedral whole grains in a single sample, KX2-1. In CL, Type 3 zircon displays a relatively bright intensity of emission, but only weak, wispy zonation (Figure 3f-h). These CL images, in accord with optical observations, show that this Type 3 zircon forms overgrowths on resorbed Type 2 grains (Figure 3f-g), thus Type 3 zircon is demonstrably the youngest growth phase of zircon. The abundance of Type 3 zircon varies according to sample; it is not commonly observed in separates of KX1-1, KX1-2 or KX18-2, but is particularly abundant as very large pink anhedral grains and grain fragments in sample KX2-1. In KX2-1, Type 3 discrete zircon grains have been observed to contain zones with dispersed inclusions of brown rutile.

3.2.2.2 Zircon-rutile intergrowths

The second subgroup of zircon types are intimately associated with rutile, and represents only the second known natural occurrence of extensively developed reaction textures between these two accessory minerals (see Snoeyenbos et al., 1995 for the only recorded occurrence). Type 4 zircon is a component in graphic intergrowth with rutile (Fig. 4a-c), extensively developed only in sample KX2-1. Under high magnification, these intergrowths are resolved as crystallites of rutile several microns in diameter set within an interconnected matrix of zircon (Fig. 4b). The margins of these intergrowths with the hosting rutile are generally enriched in zircon, and intergrowth-host rutile contacts have a cusped-lobate morphology (Figure 4a,c).

These intergrowths are situated exclusively at the margins of larger rutile grains (Figure 4a,c); in some instances, the intergrowths appear to wedge into the hosting rutile over distances of several hundred microns. These characteristics are consistent with a replacement texture whereby a zirconium-bearing rutile solid solution reacts with silica to form zircon + rutile:

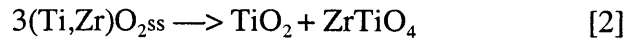


Unfortunately, no experimental sub-solidus phase equilibria have been determined for the ternary system $\text{ZrO}_2\text{-TiO}_2\text{-SiO}_2$. However, some insight into hypothetical phase relations may be gained by examination of the corresponding binary systems. In the system $\text{ZrO}_2\text{-TiO}_2$, significant solubility of zirconium in rutile at temperatures exceeding 1000°C is indicated by experimental phase equilibria (Brown and Duwez, 1954; Coughanour et al., 1954) as well as measurements of mantle derived eclogitic rutile (Vlassopoulos et al., 1993). A poorly defined solvus is also present in this system whereby Zr-rich rutile solid solutions may exsolve a zirconium titanate (ZrTiO_4) upon cooling. In the presence of silica, it may be hypothesized that the subsolidus stability of this titanate is compromised in favor of an expanded zircon primary phase volume. The quantity of zircon produced, and localization of the zircon-rutile graphic intergrowths at grain boundaries suggests an extrinsic source of silica for the replacement reaction. In this case of surface reaction, the extent of reaction is limited not only by the degree of undercooling below the solvus of the Zr-rutile solid solution, but by the availability of silica. As with other types of graphic intergrowth, the participation of a fluid or melt phase is probably necessary to promote this type of localized replacement reaction over simple coronal overgrowth. This idea is substantiated by the observation that these zircon-rutile graphic intergrowths are best developed in sample KX2-1, which contains significant quantities of what is interpreted as the residue of an infiltrating melt phase in the form of coarse-grained quartz + antiperthite-rich domains.

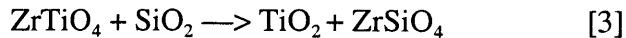
Type 5 zircon is also intimately associated with rutile, and takes the unique form of lamellar needles and plates within hosting rutile grains (Figure 4c-g). A spectrum of lamellae morphology and topology is exhibited, ranging from dispersed sub-micron to micron scale needles (Figure 4c-e) to condensed elongate tabular plates of zircon tens of microns in length (Figure 4f-g). As fine needles, zircon is present in three crystallographic orientations (Fig. 4c-e), developed parallel to, and at approximately 45° to $[001]$. These orientations are consistent with

heterogeneous nucleation of lamellae on the {110} cleavage and {011} twin planes. In cross section, zircon needles have a rhomboidal or diamond shape (Figure 4f). More dense concentrations of coarse needles, and larger plates of zircon are consistently developed parallel to [001] and tend to be near the center of grains (Figure 4f-g). Large plates appear to be the result of coarsening and eventual intergrowth of many aligned needles. Support for coarsening of zircon lamellae is found in CL images of individual lamellae, which illustrate fine-scale roughly symmetric growth zonation of the plates parallel to the elongation direction (Figure 4h).

The phase equilibria governing the unmixing of zircon from rutile are unclear. Exsolved zircon and host rutile are the only observed phases. No free silica is found in the rutile or associated with the zircon lamellae. Similarly, the stable titanate observed in the $\text{ZrO}_2\text{-TiO}_2$ binary system, ZrTiO_4 has not been found, nor has ZrO_2 . As previously discussed, the qualitative solubility and insolubility of zirconium and silicon respectively, in rutile, have been established from examination of binary systems. From the binary systems, and the compelling evidence for exsolution, the presence of a relatively steep solvus in the ternary system in the vicinity of the TiO_2 end member is inferred. In the absence of silica, cooling through the solvus would result in the unmixing of the solid solution into stoichiometric rutile and zirconium titanate:



No titanate is observed in the samples, however, thus we must assume sufficient silica activity that the titanate, if formed, undergoes the exchange:



Alternatively, the phase equilibria may be such that the zirconium titanite has no stable primary phase volume in the ternary system at the temperatures under consideration, and the unmixing is one of two reactions depending on the extrinsic or intrinsic role of silica:



The siting and participation of silica is problematic, and unlike the graphic Type 4 zircon-rutile intergrowths, reaction with extrinsic silica is less obvious, lacking the unlikely scenario of nucleation of all exsolution lamellae at grain boundaries. At the P-T conditions of these granulites, there is no experimental evidence to support abundant substitution of tetrahedral silicon into the octahedral cation site of rutile. Experiments in the $\text{TiO}_2\text{-SiO}_2$ binary system between 1500°C and 1800°C (DeVries et al., 1954) found no perceptible solid solution of SiO_2 in rutile as measured by X-ray diffraction methods. On the other hand, minor quantities of silica, up to 1 wt.% are commonly reported in analyses of crustal rutile grains (Rumble, 1976) suggesting some capacity for silica in rutile by poorly understood substitutional mechanisms. Electron microprobe analyses of both rutile and zircon from the UHT granulites were undertaken to determine whether any rutile crystals preserved *in situ* silica. These data reveal that while there is minor substitution of Al, Cr, Fe, and Nb, there is presently no detectable (<200 ppm) silica in any of the hosting rutile crystals. However, there was also no detectable zirconium present in any rutile grain, which underscores the fact that the unmixing of both components from the initial rutile solid solution went to completion. We cannot then infer the initial silica contents from the present measurements.

Regardless of the exact mechanism of unmixing, a model for the progress of the reaction may be constructed taking into account the observed compositional and morphological characteristics of the exsolved and host phases. The present lack of *in situ* zirconium in the host rutiles (from electron microprobe analysis) indicates that the amount of zircon developed in a rutile grain is essentially equivalent to the initial concentration of zirconium in the rutile solid solution, thus rutile grains containing large plates had correspondingly higher initial zirconium concentrations. Image analysis reveals that grains with large plates contain the most zircon by volume and this zircon is concentrated on {110} cleavage planes, while rutile grains with dispersed small needles, roughly equally distributed between {110} and {011} planes, contain less zircon. Qualitatively, these differences in the topology of exsolution in different grains may be explained by slow cooling of crystals with initial contrasts in bulk composition through a solvus. Upon cooling, rutile with higher initial Zr contents encountered the sloping limb of the hypothetical solvus earlier and at higher temperatures, promoting heterogeneous nucleation on {110}. Subsequent undercooling was slow enough to allow coarsening of lamellae by diffusive

transport of zirconium (and silica) to the lamellae interface. In contrast, rutile grains with lower initial concentrations of zirconium encountered the solvus later, and at lower temperatures, thus producing smaller amounts of fine zircon needles which were less restricted in their nucleation sites, although still apparently heterogeneously nucleated. There are also rutile which presently have no measurable Zr or Si, *and* no exsolved zircon, which must represent initially Zr and Si free grains. The fact that no host rutile presently contains *in situ* Zr or Si demands that the exsolution reactions essentially went to completion.

The opportunity to test this model of zircon exsolution, and quantify the cooling rate of these granulites arises from our ability to date the growth of the zircon lamellae using their U-Pb systematics. The abundance of exsolution, the striking degree of lamellae coarsening, and the evidence that the transformation essentially reached completion in all rutile grains is strong evidence that these deep crustal samples underwent relatively slow cooling following peak UHT conditions. As in a slow cooling model the large plates of zircon result from progressive growth and coarsening of early nucleated lamellae, we would predict that the measured ages of the large plates, which integrate this crystallization, will scatter over some finite amount of time. A further prediction is that, finer lamellae of zircon will yield younger ages than thick plates. As detailed below, these predictions are in large part met by the available U-Pb data and confirm slow cooling rates.

4. Analytical Techniques

Zircon and monazite were isolated from xenoliths by standard crushing, heavy liquid, and magnetic separation techniques, and separated into different populations based on crystal morphology, color, and grain size. From these populations representative crystals were reserved for photomicrography. Grains were mounted in epoxy, polished, carbon-coated, and imaged by back-scattered electrons (BSE) and cathodoluminescence (CL) at the MIT JEOL 733 Superprobe electron microprobe facility. Both imaging techniques used an accelerating voltage of 15 keV, 10 nA beam current, and a 1 μm beam spot size. High resolution gray-scale CL images were collected with the secondary electron detector mounted in place of the optical microscope ocular. Quantitative analysis of rutile was accomplished by wavelength-dispersive X-ray spectrometry utilizing the same beam characteristics, ZAF corrections, and natural and synthetic oxide and silicate standards.

For U-Pb analysis, zircons were air-abraded with pyrite after the method of Krogh (1982), and acid rinsed in warm 3M HNO₃ for 12 hours, followed by ultrasonication. All mineral fractions underwent ultrasonication in ethanol for two hours followed by rinsing in double-distilled acetone. Accessory mineral fractions were loaded into Teflon FEP microcapsules and washed again in 3M HNO₃ (zircon) or high-purity water (monazite) at 50°C for 2-4 hours, followed by rinsing with several capsule volumes of water. Samples were spiked with a mixed ²⁰⁵Pb-²³³U-²³⁵U tracer and dissolved in 28M HF at 220°C for 48-120 hours (zircon), or 12M HCl at 180°C for 48 hours (monazite), followed by conversion to 6M HCl at 180°C for 18-24 hours. Pb and U were separated from the resulting mineral solutions using miniaturized HCl-based anion exchange chromatography procedures modified after Krogh (1973).

Pb and U were analyzed on the MIT VG Sector 54 thermal ionization multicollector mass spectrometer. Lead was loaded on single Re filaments with a dilute silica gel-0.1M H₃PO₄ emitter solution and measured either dynamically with four high-mass Faraday cups and an axial ion-counting Daly detector, peak-switching ²⁰⁵Pb into the axial position to obtain an internal Daly-Faraday gain calibration, or by peak-switching all ion beams into the Daly detector for very small amounts of lead. An ion beam of >0.1x10⁻¹³ A was maintained for ²⁰⁷Pb during data acquisition. Uranium was loaded on single Re filaments either with colloidal graphite and measured as metal ions, or with silica gel and measured as UO₂⁺ ions by one of two methods: in static mode on three Faraday cups for ²³⁸U⁺ (²³⁸U¹⁶O₂⁺) ion-beam intensities of >0.5x10⁻¹³ A, or by peak switching all ion beams into the Daly detector for smaller amounts of uranium. Details of fractionation and blank corrections are given in Table 1. Ages with propagated uncertainties were calculated using the methodology of Ludwig (1980).

Whole rock rare earth element concentrations were obtained by solution ICP-MS on the VG PQ 2+S at M.I.T. Fifty milligrams of each sample powder were completely dissolved in a mix of HF-HNO₃, in pressure vessels at 220°C for 5 days, converted to 7M HNO₃, spiked with internal standards of Se, In, and Bi, diluted, and analyzed in triplicate. Following internal and external instrumental drift corrections, blank and isobaric interference corrections, concentrations were calibrated against the USGS whole rock standards and are inferred to be accurate and precise to ± 2% based on replicate analyses of blind standards. For Sm-Nd isotopic analyses, single crystals of monazite, or 50-100 mg of powdered whole rock samples were spiked with a mixed ¹⁴⁹Sm-¹⁵⁰Nd tracer and completely dissolved with 12M HCl or HF-HNO₃

respectively, in teflon pressure vessels at 220°C for two or five days, followed by conversion to 6M HCl and fluxing at 120°C for 24 hours. The separation and purification of Sm and Nd were accomplished with a standard two-stage cation exchange-HDEHP reverse chromatography procedure. Sm was loaded on single Ta filaments with 1 μ l of 1M H₃PO₄ and analyzed as metal ions in static multicollector mode with a ¹⁵²Sm ion beam of 2.5x10⁻¹¹ A. Nd was loaded on triple Re filaments with 1 μ l of 0.1M H₃PO₄ and analyzed as metal ions in dynamic multicollector mode with a ¹⁴⁴Nd ion beam of 1.5x10⁻¹⁰ A. Sm and Nd data were fractionation corrected with an exponential law, normalizing to ¹⁵²Sm/¹⁴⁷Sm = 1.783 and ¹⁴⁶Nd/¹⁴⁴Nd = 0.7219 respectively. Details of data internal and external reproducibility are given in the caption to Table 2.

5. Analytical Results

5.1 U-Pb geochronology

5.1.1 Monazite

KX1-1 (Lace): Seven single monazite crystals yield variably discordant U-Pb dates, with ²⁰⁷Pb/²⁰⁶Pb dates ranging from 2686 to 2562 Ma. These data are highly discordant (3-13%) in comparison with data from other UHT granulites, as highlighted in Figure 5A. These seven analyses scatter along a discordia array with upper and lower intercepts of *ca* 2.72 Ga and 1.2 Ga. The poor fit of the data to this discordia (MSWD=80) apparently indicates geological scatter caused by diachronous crystallization of monazite; episodic crystallization of monazite is also supported by BSE images showing core-rim relationships (Figure 3a). Also because of the leveraging of the data toward the upper intercept of the discordia, this episodic high-temperature growth is considered more likely to produce the scatter than variability in age of the mechanism generating the lower intercept of the discordia. Regarding this mechanism, the greater degree of discordance in monazites of this sample compared with those from other UHT granulites with similar U and Th contents, which ostensibly underwent the same thermal history, argues against thermally-activated volume diffusive Pb-loss to explain the discordance. Alternatively, the variability in monazite discordance could be due to different extents of Mesoproterozoic chemical alteration and/or recrystallization, or the growth of new monazite at *ca* 1.2 Ga. In situ analysis has not been carried out to test this mechanisms. As a final note, the discordia line defined by the KX1-1 monazites bracket nearly all the other monazite data, which fall to the

right of the chord; this can be interpreted as constraining the minimum age of the bulk of monazite crystallization in the UHT granulites, which will become important in later discussions of their paragenesis.

KX18-2 (Kaalvallei): Six monazites from granulite KX18-2 yield generally more concordant data than that from KX1-1, and define the oldest monazite ages from the suite of UHT granulites. Two monazites are concordant at an age of 2767 ± 1 Ma. Two other grains with ~4% discordant U-Pb dates have $^{207}\text{Pb}/^{206}\text{Pb}$ dates of 2722 ± 1 Ma, and when combined with the two concordant analyses generate the discordia illustrated by the dashed line in Figure 5b, which is notable for its ca 1.3 Ga lower intercept, similar to that generated by the KX1-1 monazite discordia illustrated by the solid line in both panels of Figure 5. This discordia also serves to bound all of the monazite data for the UHT granulites, suggesting that the 2767 Ma grains in KX18-2 are recording the oldest episode of monazite crystallization in the UHT granulites. Two further monazite grains from KX18-2 yield a concordant analysis at 2743 ± 4 Ma and a discordant analysis with a $^{207}\text{Pb}/^{206}\text{Pb}$ date of 2722 ± 2 Ma. These grains indicate a younger episode of monazite crystallization with a maximum age of 2743 Ma in this UHT granulite, although whether the concordant grain accurately dates this crystallization, or represents a mixture of a 2767 Ma core and <2743 Ma overgrowth cannot be presently evaluated.

KX2-1 (Voorspoed): Six monazite crystals, including two fragments from the same grain (#39 and #40), were analyzed and yielded a range of $^{207}\text{Pb}/^{206}\text{Pb}$ dates from 2723 to 2648 Ma, correlated with degree of discordance. If compared with the discordia drawn through the monazite data for KX1-1, these monazites are substantially less discordant, and while some grains generally conform to this discordia others plot to the right suggesting older crystallization ages. Forcing a chord from 1.2 Ga through the least discordant analysis from KX2-1 yields an upper intercept of 2738 Ma, which is similar to the date for the young concordant monazite of KX18-2. Regarding the two grain fragments analyzed from the same crystal, the fragment broken from the crystal rim (#39) does yield a younger, more discordant date than the remaining monazite fragment including the core of the grain, suggesting that the cause of discordance is correlated with the surface of the grain, however this experiment is insufficient to further clarify the discordance mechanism.

KX2-2 (Voorspoed): Two monazite crystals from KX2-2 were analyzed, yielding 2-3% discordant analyses with $^{207}\text{Pb}/^{206}\text{Pb}$ dates of 2740 and 2704 Ma. The older analysis falls very near the discordia defined by the oldest grains from KX18-2 (Figure 5b).

In summary, the monazite data for the UHT granulites exhibit variable, and sometimes substantial Mesoproterozoic discordance from primary Neoproterozoic crystallization ages of ca 2717 to 2767 Ma. Multiple episodes of high-temperature crystallization of monazite is supported by core-rim relationships in BSE images, and is bracketed by discordia arrays defined by individual UHT granulite samples. Tentatively, the majority of monazite crystallization particularly in the sapphirine-bearing UHT granulites (KX1-1 and KX2-1), took place at the younger end of the spectrum, around 2717 Ma, while older monazite crystallization at 2767 Ma is better recorded in the more felsic sapphirine-free UHT assemblages KX2-2 and KX18-2.

5.1.2 Discrete zircon grains

KX1-1 (Lace): Four spheroidal to ellipsoidal colorless single grains of zircon were dissolved without abrasion, and yielded variably discordant (0.2 to 2.2%) U-Pb data. Three of the four zircons have identical $^{207}\text{Pb}/^{206}\text{Pb}$ dates, within uncertainty, of 2721 ± 1 Ma. A fourth grain, z4, yields an older $^{207}\text{Pb}/^{206}\text{Pb}$ date of 2733 ± 2 Ma. These grains were not imaged, thus it is not possible to uniquely determine whether these grains specifically represent Type 1 or 2 zircon. Imaging of other grains from this sample however, indicates a preponderance of Type 2 sector zoned zircon comprising the morphological type grains analyzed, and thus it is inferred that the dominant age of 2721 Ma likely represents the timing of growth of Type 2 zircon in this sample. The anomalously older zircon could represent a core of Type 1 zircon, which would then indicate a minimum age of 2733 Ma for the growth of this phase. To test this speculation, a large anhedral grain with Type 1 oscillatory zonation (Figure 3b) was removed from the mount and fragmented along the mechanical boundary between the relatively homogeneous interior and the oscillatory-zoned mantle. These two fragments were abraded to the ellipsoidal volumes schematically illustrated in Figure 3b, and analyzed. Both fragments yielded concordant or near-concordant analyses, the core with a $^{207}\text{Pb}/^{206}\text{Pb}$ date of 2743 ± 1 Ma and the oscillatory mantle with a $^{207}\text{Pb}/^{206}\text{Pb}$ date of 2730 ± 1 Ma, similar to the prior older zircon. These data confirm the older age of Type 1 zircon relative to Type 2, and suggest a minimum age of ca 2730 and a maximum age of ca 2743 Ma for crystallization of this growth phase of zircon.

KX1-2 (Lace): Two multi-grain fractions (four grains each) of zircon from KX1-2 were analyzed following abrasion to remove approximately 20% of the outer portion of each grain. Both fractions consisted of colorless, subhedral, spheroidal to ellipsoidal grains. One fraction yielded a 5% discordant analysis with a $^{207}\text{Pb}/^{206}\text{Pb}$ date of 2690 ± 10 Ma; fraction zhf2 however yielded a concordant analysis with a $^{207}\text{Pb}/^{206}\text{Pb}$ date of 2714 ± 1 Ma. CL imaging of other grains from this sample indicate, as is sample KX1-1, a preponderance of Type 2 zircon, thus this concordant date is interpreted to approximate the growth age of this phase of zircon in this xenolith.

KX1-8 (Lace): Three unabraded colorless or pale pink spheroidal to ellipsoidal single zircons from KX1-8 were analyzed. The larger pale pink grain yielded the youngest, concordant analysis with a $^{207}\text{Pb}/^{206}\text{Pb}$ date of 2691 ± 2 Ma; this zircon is tentatively interpreted to date crystallization of Type 3 zircon. By comparison, two colorless zircons were slightly discordant with $^{207}\text{Pb}/^{206}\text{Pb}$ dates of 2698 and 2730 Ma, the latter suggestive of dates for Type 1 zircon from KX1-1. In these grains there is a tentative correlation between Th/U content of the zircon and age, consistent with mixing of young, low Th/U and older, high Th/U domains. This scenario is further evidenced by CL images of the KX1-8 illustrating overgrowths of Type 3 zircon on both Type 1 and Type 2 zircon cores (Figure 3e).

KX2-1 (Voorspoed): Two unabraded, colorless to pale pink, slightly flattened spheroidal single grains yielded slightly discordant data, with $^{207}\text{Pb}/^{206}\text{Pb}$ dates of 2687 and 2710 Ma. The younger grain has a lower Th/U of 0.08 relative to the older grain with a Th/U of 0.25. Two multi-grain fractions of zircon were also abraded and analyzed. Fraction zfh1 consisted of 20 colorless spheroidal to ellipsoidal grains which yielded a concordant analysis with a $^{207}\text{Pb}/^{206}\text{Pb}$ date of 2715 ± 2 Ma. CL imaging of other grains of this type in this sample indicate a dominant population of Type 2 zircon, thus this concordant date is interpreted as the time of growth of Type 2 zircon in this sample, identical to that in sample KX1-2. Fraction zhf2 consisted of a single very large anhedral pink grain (Figure 3h), and also yielded a concordant analysis with a $^{207}\text{Pb}/^{206}\text{Pb}$ date of 2691 ± 1 Ma. Its morphology, color, and CL pattern indicate that this grain represents Type 3 zircon, and thus the concordant date is interpreted to estimate the timing of Type 3 zircon growth in this sample. This date for Type 3 crystallization is consistent with that inferred from KX1-8. It is also noteworthy that this fraction was drawn from a population which includes crystals with numerous small rutile inclusions. This may indicate a link between

crystallization of Type 3 zircon and Type 4 zircon-rutile graphic intergrowths; both of these phases of zircon are much more abundant in this sample than in any other.

KX18-2 (Kaalvallei): Spheroidal zircons with Type 2 CL patterns predominated in this UHT granulite. Several such grains were abraded to remove approximately 20% by volume, subsequently yielded variably discordant data with nearly identical $^{207}\text{Pb}/^{206}\text{Pb}$ dates of 2714 ± 2 Ma. By their CL patterns, these zircons are considered to date crystallization of Type 2 zircon; this date of ca 2714 is essentially identical to those for Type 2 zircon from KX1-2 and KX2-1.

KX27-1 (Star Mine): Only 6 zircons were separated from this sample of felsic granulite, including several large spheroidal pink grains and three colorless slightly ellipsoidal grains. Two of the former and one of the latter grains were air abraded, during which time the spheroidal grains fragmented. The colorless ellipsoidal grain, after abrasion, yielded the oldest concordant $^{207}\text{Pb}/^{206}\text{Pb}$ date of 2738 Ma. Among the abraded fragments of the spheroidal grains, two fragments were analyzed, also yielding concordant data. A curved shard apparently representing a portion of a spherical shell fragmented from a larger grain yielded the youngest concordant analysis with a $^{207}\text{Pb}/^{206}\text{Pb}$ dates of 2691 Ma. A larger rounded fragment yielded a third concordant analysis with an intermediate $^{207}\text{Pb}/^{206}\text{Pb}$ date of 2699 Ma. By correlating appearance with the age systematics, the first ellipsoidal colorless grain is interpreted to represent the equivalent of the Type 3 growth phase of zircon in this sample. The shell-like pink fragment represents a younger overgrowth of zircon, identical in age to Type 3 zircon in other samples, while the third larger pink zircon is interpreted as a mixture of an older core with substantial overgrowth of younger zircon. This interpretation of two growth components is supported by the chemistry of the zircons. The two younger grains have distinctly lower Th/U of 0.08, relative to the older grain (Th/U = 0.33). This trend of lower Th/U in younger, more strongly pink colored zircon is seen in other UHT granulite xenolith zircon systematics.

In summary, the U-Pb isotopic systematics of the three types of discrete phase zircon confirm the relative ages inferred from CL zonation patterns. Type 1 oscillatory-zoned zircon is the oldest phase, crystallizing between ca 2743 and 2730 Ma. Subsequent dissolution of this phase of zircon was extensive, with Type 1 zircon mainly surviving as small cores subsequently mantled by Type 2 sector-zoned zircon. Type 2 zircon crystallized as abundant discrete grains in all granulites between ca 2721 and 2714 Ma. Similarly, this phase of zircon underwent variable

resorption, and subsequent overgrowth by *ca* 2690 Ma Type 3 zircon. Sample KX2-1 contains the most abundant quantities of Type 3 zircon, suggesting a correlation with the unique felsic leucosomal textures developed in this xenolith. Type 3 zircon in KX2-1 also contains discrete inclusions of rutile, and on this basis a tentative link between this discrete zircon type and the Type 4 zircon-rutile graphic intergrowths is made. Further discussion of this correlation follows in Section 6.x.

5.1.3 Exsolved zircon lamellae

KX1-1 (Lace): Six individual lamellar plates of exsolved zircon separated from host rutile were analyzed from sample KX1-1, yielding variably discordant U-Pb dates, with $^{207}\text{Pb}/^{206}\text{Pb}$ dates ranging from 2596 to 2450 Ma. The oldest lamellae are nearly concordant, while the younger $^{207}\text{Pb}/^{206}\text{Pb}$ dates are generally correlated with the degree of discordance. A simple discordia fit the six lamellae yields upper and lower intercepts of 2552 ± 88 Ma and 1220 ± 350 Ma respectively, but with an exceptionally poor fit (MSWD=406). The purpose of this discordia is primarily to emphasize the correlation of the Mesoproterozoic lower intercept with that observed from discordant monazite data in the same sample; this correlation suggests that the discordancy mechanisms responsible for both sets of data had a similar timing of *ca* 1.2 to 1.3 Ga. It is clear however, that the individual lamellae do not conform to a simple discordia, and because of the leverage of the data toward the upper intercept of the array, it is suggested that the scatter from the discordia is a function of asynchronous crystallization of lamellae. Such episodic growth is a prediction of the subsolvus crystallization model put forth in Section 3.2.2.2, and is consistent with the coarsening of zircon lamellae in rutile, and the internal zonation patterns of these lamellar plates (Figure 4h). If this interpretation is correct, then the near-concordant analysis at 2596 Ma provides a constraint on the integrated age of this growth in a single lamellar plate. Similarly, if chords originating from 1.2 to 1.3 Ga are constrained to pass through the variously discordant data for other lamellae from KX1-1, integrated growth ages from 2595 Ma to as young as 2510 Ma are obtained.

KX1-2 (Lace): Four individual lamellae yielded discordant data similar to that of KX1-1, with $^{207}\text{Pb}/^{206}\text{Pb}$ dates ranging from 2512 to 2399 Ma. Mesoproterozoic Pb-loss is suggested by the topology of the data, and by the same justification noted for KX1-1, forcing chords from 1.2 to

1.3 Ga through individual points results in upper intercept dates of 2670 to 2470 Ma, a similar although slightly wider range than that obtained for single lamellae from KX1-1.

KX2-1 (Voorspoed): Ten individual exsolution lamellae were analyzed from this sample, and are notably distinct from lamellae from the Lace xenoliths in their lack of substantial normal discordance. This is again similar to the systematics of monazite from these UHT granulites, where Lace samples have greater discordance than the Voorspoed samples. $^{207}\text{Pb}/^{206}\text{Pb}$ dates range from 2581 Ma for thick plates of zircon to as young as 2462 and 2314 Ma for a very thin needles of zircon. Similar to our analysis of lamellae in KX1-1 and KX1-2, when chords through 1.3 to 1.2 Ga are constrained to pass through the individual data points, a range of integrated growth ages between 2581 and 2310 Ma are obtained. A few lamellae exhibit reverse discordance, which is not well understood, but is unlikely to result from laboratory-induced fractionation given the reproducibility of sample-spike equilibration demonstrated for the dissolution techniques used, the fact that reversely discordant lamellae were obtained in two separate dissolution batches, and the fact that we recover concordant systematics in other lamellae and discrete zircon grains dissolved in the same batch of samples. It may be hypothesized that Pb-U fractionation took place during the sampling of these lamellae by mechanisms similar to those proposed by Williams et al. (1984), McLaren et al. (1994) and Hawkins and Bowring (1997), whereby radiogenic Pb is implanted over sub-micron distances from high-U zones into adjacent regions. Subsequent loss of the high-U zones during sampling results in unsupported Pb and reversely discordant analyses. In addition, the very fine, micron-scale microstructure of lamellar growth in these zircons may have been particularly susceptible to redistribution of Pb during the Mesoproterozoic event which caused the development of normal discordance in other lamellae and the nearly complete isotopic resetting of U-Pb systematics in host rutile grains (Chapter 4). Regardless of the exact mechanism causing reverse discordance in these few zircon lamellae, their $^{207}\text{Pb}/^{206}\text{Pb}$ dates may be interpreted as maximum ages, and their concordia intercepts for chords fit through *ca* 1.3 Ga as minimum ages for their integrated crystallization.

In summary, both concordant U-Pb dates, and dates inferred from upper intercepts of chords fit between discordant data and 1.3 to 1.2 Ga lower intercepts, yield a range of results which may be interpreted to represent integrated growth ages spanning a wide range between

2670 and 2310 Ma for individual lamellae. Most large platy lamellae yield integrated growth ages between *ca* 2600 and 2500 Ma, while finer needles from all three samples yield consistently younger integrated growth ages from 2484 to 2310 Ma. This general trend is illustrated by the photomicrographs of eight lamellae from KX2-1 shown in Figure 8 with their corresponding $^{207}\text{Pb}/^{206}\text{Pb}$ dates (near concordant analyses). The differential in the ages of thick platy lamellae versus smaller needle-shaped lamellae is consistent with the proposed model of progressive bulk compositional-dependent subsolvus exsolution of zircon from rutile, with coarsening of early formed lamellae into larger plates. Comparison of the U-Pb data to the exsolution model is further explored in Section 6.1.3.

5.2 Sm-Nd isotopes

The whole rock Sm-Nd isotopic systematics of the UHT granulites record time-integrated variable enrichment to extreme depletion in light rare earth elements (LREE). Whole rock $^{147}\text{Sm}/^{144}\text{Nd}$ ratios range from 0.137 to 0.5672, and are correlated with present day $^{143}\text{Nd}/^{144}\text{Nd}$ ratios of 0.511383 to 0.519517 ($\epsilon_{\text{Nd}} = -24.5$ to $+134.2$) (Table 3). The whole rock data do not however form an isochronous relationship, as indicated by the very high MSWD of the errorchron fit plotted in Figure 9a. Isotopic ratios are also correlated with lithology: sapphirine-bearing, feldspar-poor granulites (e.g. Lace, Star Mine samples) exhibit the highest Sm/Nd ratios and super-chondritic $^{143}\text{Nd}/^{144}\text{Nd}$ isotopic compositions. The Voorspoed composite sapphirine-bearing granulite (KX2-1) with feldspar-rich leucosomal domains exhibits slightly sub-chondritic Sm/Nd and Nd isotopic ratios, while the sapphirine-free, feldspar-rich granulite from Voorspoed (KX2-2) is LREE-enriched and has a correspondingly lower $^{143}\text{Nd}/^{144}\text{Nd}$. The extremely super-chondritic Nd isotopic ratios in some of these UHT lithologies are the result of time-integrated LREE-depletion in these granulites as the likely the result of severe melt depletion, and is the most compelling indicator of the restitic character of these xenoliths.

Values of ϵ_{Nd} recalculated to the time of high grade metamorphism at 2.7 Ga ($\epsilon_{\text{Nd}}^{2.7\text{Ga}}$) range from -3.9 for the most LREE-enriched granulite, KX2-2, to $+10.2$ for the sapphirine-bearing granulite KX1-1 (Table 3). The extremely depleted sapphirine-bearing lithologies all have positive $\epsilon_{\text{Nd}}^{2.7\text{Ga}}$, and span a wide range of values from $+1.6$ to $+10.2$. This spread in $\epsilon_{\text{Nd}}^{2.7\text{Ga}}$ would demand highly heterogeneous, relatively juvenile sedimentary protoliths to these samples, with extraction from a similarly heterogeneously depleted source, or a relatively long prehistory

of time-integrated depletion. Alternatively, the LREE-depleted character and low Nd concentrations of these restitic lithologies raises the possibility that their Sm/Nd ratios are highly sensitive to later addition of rare earth elements, for example during subsequent crustal metasomatism or from contaminating kimberlite. Subsequent addition of LREE to an initially highly depleted composition is supported by the whole rock rare earth patterns of the highly depleted UHT granulites (Figure 9b), which illustrate sigmoidal patterns with flat to gently sloping HREE, systematic depletion through the MREE through Nd, and substantial enrichments in La, Ce, and Pr. Such patterns are unlikely to be caused by melt depletion and are indicative of metasomatic re-enrichment processes.

To obtain an independent measure of the initial Nd isotopic composition of these granulites at 2.7 Ga, the Sm-Nd isotopic systematics of high-grade monazite grown at 2.7 Ga were analyzed. As a refractory accessory mineral rich in rare earth elements, monazites are less susceptible to alteration of the Sm/Nd ratio, and will provide a more robust estimate of initial ϵ_{Nd} , assuming that these monazites inherit the isotopic composition of the host rock at the time of metamorphic crystallization. This assumption that the metamorphic monazites capture the composition of the host rock is probably well-founded given the extremely high-T, anhydrous conditions of metamorphism during monazite crystallization. Two single monazite grains from KX2-1 were analyzed, and yielded highly reproducible isotope ratios, with calculated $\epsilon_{Nd}^{2.7Ga}$ of -2.6 to -2.8 . This compares favorably with the result from the whole rock analysis of KX2-1 ($\epsilon_{Nd}^{2.7Ga} = -0.18$) considering the near chondritic Sm/Nd ratio of the whole rock and subsequent uncertainty introduced into back-calculation of initial ratio. The monazite initial ϵ_{Nd} for this sample is also similar to the whole rock value for the other granulite from Voorspoed, KX2-2 ($\epsilon_{Nd}^{2.7Ga} = -3.2$).

Two single monazite grains from KX1-1 were also analyzed, and again yielded highly reproducible isotope ratios, with calculated $\epsilon_{Nd}^{2.7Ga}$ of -2.1 to -2.3 . The similarity of this result with that of the Voorspoed granulites suggests that this in fact is the appropriate isotopic composition of the protolith to the UHT granulite at 2.7 Ga. In contrast to the agreement between monazite and whole rock systematics in the Voorspoed granulite, the monazite from KX1-1 is significantly more enriched than the whole rock $\epsilon_{Nd}^{2.7Ga}$ value of $+10.2$. This result appears to confirm that the present Sm/Nd ratio of the whole rock does not represent the time-

integrated value since 2.7 Ga, but rather has been lowered. By the lever rule, a lesser degree of modification of the Sm/Nd ratio is allowable for young, e.g. kimberlitic LREE metasomatism, while a larger change is permissible for ancient metasomatism. A similar variable lowering of the Sm/Nd ratio in the other depleted sapphirine bearing samples would explain the variation in calculated $\epsilon_{\text{Nd}}^{2.7\text{Ga}}$, and also may explain the substantial scatter in whole rock isochron relationship between the UHT granulites. Relatively recent lowering of Sm/Nd ratios in the most depleted samples is also compatible with the steepening of the whole rock isotopic array, producing the slightly older whole rock “errorchron” date of *ca* 2.92 Ga, relative to the age of UHT metamorphism as dated by zircon and monazite at *ca* 2.72 Ga.

The slightly enriched values of $\epsilon_{\text{Nd}}^{2.7\text{Ga}} \sim -2$ to -3 obtained for these UHT granulites are consistent with the metasedimentary character of the protoliths and some period of crustal residence prior to UHT metamorphism. An indication of this residence is given by the tDM and tCHUR Nd model ages of the UHT granulites. Several hundred million years of residence are indicated by the 3.0 to 3.4 Ga model ages of these rocks. The 3.2 to 3.4 Ga model ages of KX2-2 are particularly robust because of the slope of the evolution line of this sample. Similarly, as monazites have Sm/Nd ratios generally lower than crustal rock compositions, the calculated *ca* 3.0 Ga model ages of the monazites from the two UHT granulites are robust *minimum* crustal residence ages of their protoliths. These results are in accord with measurements of zircon U-Pb crystallization ages and Nd model ages for crystalline basement rocks exposed at the surface of the craton in the nearby Vredefort dome (Hart et al., 1990, 1999). In summary, the Nd isotopic data are interpreted to indicate that the protoliths of the UHT granulites comprised sedimentary lithologies emplaced into the lower crust prior to *ca* 3.1 Ga, which were subsequently metamorphosed at 2.7 Ga.

6. Discussion

6.1 A P-T-t path for UHT metamorphism

6.1.1 Prograde to post-peak

From the zircon petrography and U-Pb systematics presented above, there is compelling evidence that the bulk of metamorphic zircon crystallization, in the form of Type 2 zircon contained within all UHT granulite samples, took place over a restricted time interval between

2720 and 2715 Ma (Figure 6). The characteristics of Type 2 zircon, including its spherical to multi-faceted morphology and sector zoning, are consistent with solid-state high-grade metamorphic crystallization in the absence of an abundant melt phase. In addition, the presence of rare inclusions of sapphirine in Type 2 zircon strengthens the interpretation that this phase of zircon grew during UHT conditions and thus dates the peak of metamorphic conditions. Similarly, much of the monazite data for the UHT granulites scatter around a discordia with an upper intercept at ca 2715 Ma (Figure 5), and thus may also be interpreted to have grown at peak metamorphic conditions. While compelling in their own right, these systematics are also in excellent agreement with independent geological evidence for very high advective heat flux through the lithosphere, namely the synchronous eruption of the Klipriviersberg flood basalts at 2714 ± 8 Ma. This correlation will be further detailed in Section 6.2.

The duration of peak conditions and the tempo of subsequent cooling are important parameters for interpreting the tectonic scenario and mechanism of heat flux responsible for the sustainment of extreme UHT conditions. The highly consistent and restricted ages of peak metamorphic Type 2 zircon crystallization between 2715 and 2720 Ma may be used to argue that the interval of peak conditions was no more than five million years. Further constraints on the post-peak time-temperature path are provided by correlations between retrograde kyanite crystallization and Type 3 zircon ages. Kyanite is a trace phase found in all UHT granulites of this study, and was described as a modal mineral (1%) comprising prismatic grains in one sample of the suite studied by Dawson and Smith (1987). In our samples, kyanite is most abundant in sample KX2-1, a composite sample which appears to represent a depleted garnet-quartz-sapphirine assemblage infiltrated by an alkali- and alumina-rich leucosome. Kyanite is particularly abundant in the “leucosomal” sector of this composite xenolith, but also occurs in the more mafic sapphirine-bearing sector of the xenolith, where it grows at the expense of sillimanite. Its late retrograde character is emphasized by the manner in which it fractures and disrupts previously formed rutile grains within sillimanite aggregates. Importantly, the stability of kyanite places an upper temperature limit of approx. $825 \pm 25^\circ\text{C}$ (at 10 ± 1 kbar) on ambient conditions during the infiltration and crystallization of this leucosome (Bohlen et al., 1990).

We have previously noted two unique features of the zircon petrography of KX2-1, namely the presence of Type 4 zircon-rutile graphic intergrowths and the abundance of Type 3 zircon in this xenolith. It was also noted that some Type 3 zircon grains have abundant

inclusions of rutile, suggesting a possible genetic relationship between the two types of zircon. Four basic observations are reiterated with regard to the modal and accessory mineral petrography of sample KX2-1: the presence of a leucosomal infiltration of the xenolith; kyanite stability during infiltration and crystallization of this leucosome; the presence of unique graphic zircon-rutile replacement textures of primary rutile, likely requiring the presence of a silicate melt; and the abundance of Type 3 zircon which has been dated at 2690 ± 1 Ma. In combination, these observations suggest that Type 3 (and Type 4?) zircon are dating the infiltration of this kyanite-bearing melt phase under retrograde P-T conditions at 2690 ± 1 Ma. By reference to kyanite stability, this episode of zircon crystallization occurred at maximum temperatures of 825°C , assuming isobaric cooling of the UHT assemblages. This point on the P-T-t path of the UHT granulites is illustrated in panel A of Figure 10. Panel B displays these thermal and geochronological constraints in T-t space; from this figure we may infer that cooling following peak UHT conditions initially proceeded fairly rapidly, at $\geq 8^{\circ}\text{C}/\text{Ma}$.

With regard to the prograde path of the UHT metamorphism, it is apparent from Figure 5b that much of the monazite data lie to the right of the *ca* 2715 Ma discordia, and thus must have grown prior to peak metamorphic conditions. Monazite growth as old as 2768 ± 3 Ma is demanded by the consistent data for KX18-2. Other monazite geochronological data cluster around a chord to *ca* 2740 Ma, including a concordant point at 2743 Ma, and while this date could be an artifact of intragrain mixing of 2767 and 2715 Ma components, it could also reveal a discrete episode of monazite crystallization. Support for the latter interpretation is derived from the systematics of Type 1 zircon, which yield essentially identical concordant ages at 2743 and 2738 Ma. Thus it is suggested that both monazite and Type 1 zircon are recording reactions on the prograde path leading to the UHT granulite paragenesis. Monazite has been previously documented as growing during prograde amphibolite-facies hydrous mineral breakdown reactions in para- and orthogneisses (Smith and Barreiro, 1990; Hawkins and Bowring, 1997, 1999; Bingen and van Breeman, 1998; Pyle and Spear, 1999; Rubatto et al., 2001). Smith and Barreiro (1990), among other workers have demonstrated initiation of metamorphic crystallization at or above the staurolite isograd, at temperatures $\geq 525\pm 25^{\circ}\text{C}$. Thus we suggest this as a minimum temperature of formation for the prograde monazite in the UHT granulites. Another circumstantial line of evidence for the metamorphic conditions during the *ca* 2740 Ma accessory mineral growth is the nature of fine-scale oscillatory zonation in Type 1 zircon, which

most commonly believed to indicate growth in the presence of melt (Bottinga et al., 1966). This observation suggests that thermal conditions at 2743 Ma exceeded the wet granite solidus, or approximately 650°C at the pressures of interest. From these inferences, the *ca* 2768 and 2740 Ma monazite and zircon data suggests that UHT metamorphic conditions followed a ramping of lower crustal temperatures over 25-50 million years (Figure 10b), or alternatively were superimposed upon lower crustal protoliths possessing a prior *ca* 2.77 to 2.74 Ga upper amphibolite- to granulite-facies metamorphic history which is only cryptically preserved in these accessory mineral systematics.

6.1.2 Constraints on zircon and monazite closure temperature

Very slow volume diffusion rates of Pb and U in zircon have been clearly established by tracer diffusion experiments (Lee et al., 1997; Cherniak and Watson, 2000), which indicate a nominal closure temperatures to Pb diffusion of >1000°C for zircon, consistent with the preservation of inherited radiogenic Pb in zircon during crustal anatexis (Black et al., 1986; Watson, 1996). By contrast, the rate of Pb volume diffusion in monazite has been the subject of considerable debate over the past decade. Early estimates of Pb closure temperatures based on field studies of monazites in granitic and metamorphic rocks ranged from 650 to 750°C (Koppel and Grunenfelder, 1975; Koppel et al., 1980; Kingsbury et al., 1993; Copeland et al., 1988). Similarly low closure temperatures were inferred from modeling of purported Pb diffusion gradients in natural monazites as measured by electron microprobe analysis (Suzuki, 1994), and in-diffusion laboratory experiments on nature monazite (Smith and Giletti, 1997). These studies have led to the common attribution and modeling of discordance in monazite U-Pb systematics as resulting from diffusive Pb loss mechanisms (Parrish, 1990; Grove and Harrison, 1999).

The last several years however, have seen the demonstration of inherited Pb preservation in natural monazites subjected to granulite-facies metamorphic conditions in excess of 750°C (Spear and Parrish, 1996; Schaltegger et al., 1999)—necessitating the possibility of a higher closure temperature for volume diffusion in the light rare earth phosphate. Just as importantly, the increased use of imaging techniques and high-spatial resolution electron microprobe chemical mapping and dating of monazite have demonstrated that age discordance in single monazites is more often due to recrystallization and or new growth of younger monazite on older

grains (Hawkins and Bowring, 1997, 1999; Crowley and Ghent, 1999; Williams et al., 1999). Sharp contrasts in intragrain age structure at the micron-scale in such monazites offer compelling evidence that volume diffusion was inconsequential for homogenizing Pb isotopic signatures. Finally, the most recent laboratory diffusion experiments for monazite (Cherniak et al., 2000), have measured a very high activation energy for Pb volume diffusion in monazite compared with previous experiments, and indicate a nominal closure temperature for monazite similar or *higher* than that of zircon.

The extreme crustal thermal conditions achieved during the UHT metamorphism of these granulites provides a unique natural experiment with regard to Pb diffusion in both zircon and monazite. The boundary conditions of this experiment are fairly clearly established in that the assemblages under consideration were essentially anhydrous, while oxygen fugacity was buffered by graphite. The UHT mineral assemblages demand minimum temperatures of 1040°C, at pressures of *ca* 10 kbar, while the Type 2 zircon data presented above indicate that peak metamorphic temperatures persisted for 1-5 million years between 2720 and 2715 Ma.

The preservation of reproducible concordant U-Pb ages for Type 2 zircon, and older concordant ages for Type 1 zircons in the same UHT rocks, confirms the slow Pb volume diffusion rates and high closure temperatures for zircon anticipated from laboratory experimental data and previous field investigations. Similarly the lack of any distinguishable blurring of CL zonation patterns even at the micron-scale (Figure 3b) supports equally slow diffusion of CL-activating rare earth elements. In fact, given the extreme conditions of the metamorphism, some blurring or homogenization of the isotopic and chemical zoning in the zircons might have been expected given the laboratory kinetic data. The fact that this loss of resolution is not observed in the UHT granulites suggests that even these slow experimental diffusivities may be maxima.

With regard to Pb diffusion in monazite, the fundamental observation we make is that despite metamorphism at >1040°C for 1-5 Ma and sustained temperatures >850°C for possibly another 25 Ma, nearly all monazite data for the UHT granulites are synchronous with or *predate* peak metamorphic conditions. Prograde growth ages at *ca* 2767 and 2740 Ma are reproducibly preserved in individual monazite grains, and are in the latter case identical to U-Pb ages of prograde Type 1 zircons. These are some of the most compelling empirical data with which to argue for very high closure temperatures of >1000°C for Pb volume diffusion in monazite. They appear to substantiate similar inferences from granulites of less extreme paragenesis (Spear and

Parrish, 1996; Schaltegger et al., 1999), as well as the most recent laboratory experiments (Cherniak et al., 2000), that closure temperatures for Pb volume diffusion in monazite meet or exceed those of zircon.

6.1.3 Constraints on the cooling path: zircon exsolution from rutile

In Section 6.1.1 we presented evidence that cooling to a maximum temperature of 850°C had occurred within 25 million years of peak metamorphism, suggesting initial cooling rates of $\geq 8^\circ\text{C}/\text{Ma}$. This cooling rate cannot be maintained indefinitely, and a reasonable lower bound to steady-state temperatures at 10 kbar depth of 350°C is given by models of cratonic surface heat flow (Chapman and Pollack, 1977; Jones, 1988). Establishing the appropriate time constant for the cooling path may be realized by measurements of time-temperature pairs in the intervening temperature range. The exsolution of zircon from rutile in these UHT granulites may provide such time-temperature pairs and allow a unique analysis of the cooling path of these samples.

Of obvious use in this analysis would be data on the T-X relations of the $\text{TiO}_2\text{-ZrSiO}_4$ solvus; unfortunately appropriate subsolidus experiments have not been done in the $\text{TiO}_2\text{-SiO}_2\text{-ZrO}_2$ ternary system. Similarly no experimental data are available for the nucleation kinetics of zircon in rutile solid solutions. Nonetheless, the qualitative observations regarding the nucleation and coarsening of zircon lamellae in the UHT rutile set forth in Section 3.2.2.2, combined with the U-Pb geochronological data for individual zircon lamellae described in Section 5.1.3, provide the basis for a testable model of the kinetics of this transformation.

Zircon exsolution is hypothesized to have occurred upon cooling of (Zr,Si)-rich rutile through an inferred rutile-zircon solvus. A spectrum in the initial variable [Zr,Si] content of individual UHT rutile crystals is warranted by the variable quantity of zircon exsolved from different grains (coupled with the lack of measurable *in situ* Zr or Si presently in the rutile). We argue that slow cooling of rutile grains of variable [Zr,Si] content through a steeply sloping solvus can explain the observed topology of zircon exsolution. Upon initial cooling from peak UHT conditions, relatively [Zr,Si]-rich rutile first encountered the solvus, whereupon heterogeneous nucleation of the first zircon lamellae on {110} cleavage planes occurred. Cooling rates in the UHT granulites in this initial interval of exsolution were sufficiently slow to allow coarsening of early formed lamellae by diffusive transport of Zr (and Si) to the lamellar interface during continued undercooling. This model predicts that large plates will have the

oldest ages of the various lamellar morphologies, and because they integrate growth during coarsening, will exhibit a spread in ages for individual plates. This is in fact exactly what is observed in the U-Pb systematics of analyzed lamellae. Large plates have individual ages spanning a very large range from *ca* 2670 to 2500 Ma, slightly to substantially younger than peak metamorphism.

Extending the hypothesized exsolution model further, rutile grains with initial lower concentrations of [Zr,Si] encountered the rutile-zircon solvus later and at lower temperatures, and realized heterogeneous nucleation of fine lamellae on both {110} cleavage planes and {011} parting. While still heterogeneous, the less specific partitioning of lamellae on both {110} and {011} planes, and corresponding dispersion of fine lamellae throughout such grains (e.g. Figure 3c), are consistent with nucleation in these grains occurring at lower temperatures, and greater degrees of undercooling, which augments the potency of the {011} planes as sites of nucleation. These grains illustrate the influence of slowing nucleation kinetics on the topology of exsolution. Temperatures at which this latter exsolution took place were also apparently insufficient to allow diffusive coarsening of fine lamellae. While the separation and analysis of these micron-scale needles was not feasible, an indication of the maximum time at which this latter exsolution took place may be given by the measured ages of the thinnest individual lamellae, which do indeed yield generally younger ages than thick platy lamellae, from *ca* 2500 to as young as 2310 Ma. The finest zircon needles, like those shown in Figure 3c-e, may thus be even younger than 2300 Ma.

To first order, the observation that exsolution of zircon from rutile went essentially to completion in all rutile grains implies slow cooling rates. Similarly, the wide range in individual ages of the exsolution lamellae over at least 400 Ma would also appear to demand remarkably slow cooling rates. A possible key to further understanding of the cooling rates necessitated by the zircon exsolution textures lies in the kinetics of Zr diffusion in rutile. There is a clear transition recorded in exsolution lamellae morphology from early nucleated and significantly coarsened plates on {110} to more distributed, later nucleated needles which did not significantly coarsen. This dichotomy is most easily explained by the inhibitive effects of cooling on temperature-dependent diffusive transport of Zr to the lamellar interface to promote coarsening. The former large plates were apparently nucleated at temperatures high enough for diffusion of Zr through rutile to efficiently remove that component from the host to the interface

with a small number of early nucleated lamellae. On the other hand, temperatures were apparently too low during nucleation of the later small needles to allow diffusion of Zr across even small distances to allow lamellar coarsening.

The kinetics of Zr volume diffusion in synthetic rutile ($E_a = 288$ kJ/mol; $D_0 = 8.384 \times 10^{-7}$ m²/s) were measured in experiments by Sasaki et al. (1985) and provide the necessary data to place tentative bounds on the minimum temperatures necessary for diffusive coarsening of zircon lamellae. In Figure 11, curves of Zr diffusion length scales as a function of temperature are plotted for various durations. Two constraints may be derived from these curves and observations of lamellae in the UHT rutile. First, as illustrated in Figure 3g, coarsening of thick central lamellar plates of zircon demand that Zr was able to diffuse ~100 microns through the rutile to the lamellae interfaces. We also know from the age of these plates, ranging from 2670 to 2500 Ma, that a maximum of approximately 200 Ma was available for diffusion to take place. Combined, these measurements indicate that temperatures must have exceeded approximately 570-600°C during coarsening of these lamellae. Second, as illustrated in Figure 3c, diffusion was apparently insufficient to transport Zr across distances as small as five microns following later nucleation of fine lamellae. Again considering time scales of several hundred million years, temperatures could not have exceeded approximately 450° at the time of exsolution of these lamellae which must have been ≤ 2300 Ma considering the measured ages of the youngest lamellae.

These two somewhat speculative constraints on the cooling path of the UHT granulites are plotted in Figure 10b. Cooling rates apparently slowed considerably between 2.69 and 2.5 Ga with an integrated linear cooling rate of approximately 1.5°C/Ma. Cooling rate continued to decrease after 2.5 Ga, to less than 1°C/Ma, as the limit of conductive steady state was approached some time after 2.3 Ga. The slow integrated linear cooling rate of <1°C/Ma in the lower crust between ca 800 and 400°C is, in fact, comparable with that revealed in similar studies of isobarically cooled granulite terrains (Mezger et al., 1991; Hodges et al., 1994; Holm and Dahl, 1997; Moller et al., 2000; Willigers et al., 2001), as well as our own estimates from lower crustal granulite titanite, apatite and rutile thermochronology for cooling of the southern African lithosphere following Mesoproterozoic orogenesis (Chapter 4).

6.2 Constraints on mechanisms of UHT metamorphism

The zircon and monazite data for the Free State granulites presented above establish these rocks as among the chronologically best-constrained examples of UHT metamorphism. These data may be fit within an equally detailed framework for the tectonic and magmatic evolution for the Kaapvaal craton, in order establish the operative processes responsible for the attainment of UHT conditions in the lower crust at *ca* 2.72 Ga. The relevant geological and temporal setting of the central Kaapvaal craton in the Neoproterozoic was set forth in Section 2.2. An immediate and primary correlation may be made between the timing of peak lower crustal UHT metamorphism at 2720 to 2715 Ma, and the initiation of the Klipriviersberg flood basalt magmatic phase of the Ventersdorp Supergroup rift sequence at 2714±8 Ma (Armstrong et al., 1991). The spatial distribution of the Klipriviersberg Group in the east central craton, centered on the precursor Witwatersrand basin is similarly consistent with the localization of UHT granulites within the Free State kimberlites, which are roughly distributed about the bounding faults of the De Bron horst, a known locus of Klipriviersberg magmatism. The Klipriviersberg Group represents more than 300,000 km³ of basaltic magma, fluxed through the Kaapvaal lithosphere over a very short period of 5-10 million years; this duration of magmatic advection is also consistent with that inferred for peak UHT metamorphism. Regarding the consequences of UHT metamorphism, the necessary melt extraction from the lower crust to produce the restitic character of the lower crustal granulites is clearly manifested in the felsic crustal melts of the middle Platberg Group (Makwassie porphyries and rhyolites), which rapidly follow on the heels of the Klipriviersburg Group, within ≤5 million years.

6.3 Implications for the Kaapvaal cratonic lithosphere

6.3.1 Thermal lithosphere perturbation

The 3.2-2.9 Ga age of stabilization of the Kaapvaal crust (de Wit et al., 1992), preservation of similarly aged geochemical signatures in lithospheric mantle peridotites and eclogites (Carlson et al., 1999; Shirey et al., 2001), and the existence of 3.2 to 2.9 Ga diamonds (Richardson et al., 1984, 2001) provide a strong case for the maintenance of a thick lithospheric mantle keel beneath the Kaapvaal craton since at least 2.9 Ga. On the other hand, UHT metamorphic conditions in the lower crust, on an arguably regional scale, clearly necessitate severely perturbed geothermal gradients in the central Kaapvaal cratonic lithosphere at 2.72 to 2.71 Ga. Correlation of this metamorphism with the initiation of Ventersdorp flood basalt

magmatism and extension demonstrates that this rifting is the mechanism for the necessary heat flux through the lithosphere, and deepens the enigma of this intracratonic rifting event.

To achieve the requisite temperatures of the UHT granulites at their recorded pressures of 10 kbar, essentially requires the effective removal of the conductive boundary layer, or *thermal* lithosphere, and the propagation of adiabatic mantle thermal gradients to very near the base of the crust. At face value, a complete thermal reactivation of the lithosphere is difficult to reconcile with the preservation of the pre-existing mantle keel beneath the central Kaapvaal craton. However by removal of the thermal lithosphere, we are not necessarily implying replacement of the lithospheric chemical boundary layer with convecting mantle. In fact, all Ventersdorp mafic lavas have a clear signature of ancient enriched lithospheric mantle in their trace element and isotopic systematics (Marsh et al., 1992; Nelson et al., 1992), which argues strongly for their interaction with a pre-existing Kaapvaal mantle keel, but also indicates that the older lithosphere was not replaced wholesale by depleted asthenosphere during generation of the Ventersdorp melts.

We suggest that magmatic advection of heat through the lithosphere, rather than lithospheric replacement with convecting asthenosphere, was sufficient to generate the requisite thermal anomaly in the lithosphere. We would emphasize that the distribution of UHT granulites mimics the localization of extension and magmatism during Klipriviersberg and early Platberg times along a NNE-SSW trending corridor in the east-central craton, and specifically along the trend of the De Bron horst bounding faults. By comparison, similar granulites have not been found, for example, in the kimberlites piercing craton further to the west, although both Platberg and Pneil sequence volcanics extend to and substantially thicken along the western rifted margin of the craton (Tinker, 2001). Until such granulites are found, this suggests a focussed linear localization of *ca* 2.72 Ga magmatic advection in a discrete rift zone, similar to modern analogues like the Rio Grande rift of North America (Perry et al., 1987), or the East African rifts along the Tanzanian craton (Ritsema et al., 1998). This geometry, as well as the transience of the thermal perturbation, perhaps allows the preservation of a thick lithospheric mantle keel even relatively proximal to the locus of rifting.

If we posit even a localized 2.72-2.67 Ga linear rift zone through the central craton, aligned roughly along the outcrop occurrence of UHT granulites, and possibly another localized zone on the western margin of the craton which developed into a full-fledged oceanic rifted

margin (Tinker, 2001), then the implications of these thermal perturbations for the temperature structure of the intervening cratonic block comprising the western cratonic domain, or Kimberley block, must be addressed. The obvious manifestation of these thermal perturbations at the surface is the upper crustal extension and volcanism which took place relatively quickly in Platberg times, within 5-15 million years following peak UHT metamorphism at 2715 Ma, and over essentially the entire central and western craton, from just west of Johannesburg to the present craton margin. There are indications that the architecture of the lower crust also reflects dramatic modification by the Ventersdrop event. Although deep seismic reflection profiles are not presently available for the craton, recent teleseismic receiver function analysis across the Kaapvaal Craton Seismic Experiment array has generated a detailed crustal thickness map across much of the western craton, as well as estimates for the Poisson's ratio of the crust and the coherence of the Moho transition (Nguuri et al., 2001). A primary observation of this analysis is the remarkably flat and high velocity contrast seismic Moho, and relatively thin crust (<35 km) of the western Kaapvaal craton. A flattened Moho transition is commonly attributed to modification, usually by magmatism and/or extensional tectonics (Meissner et al., 1987; Kusznir and Matthews, 1988). For the Kaapvaal craton, we know that any modification must be younger than the age of accretion and stabilization of the western craton with the eastern Kaapvaal shield by 2.88 Ga (de Wit et al., 1992; Chapter 5). Similarly, Moho flattening must predate various later modifications, including a step function induced in Moho transition depth by 1.1 to 1.0 Ga Namaqua-Natal orogenesis (Chapter 2), and deflection of the Moho by the 2.06 Ga Bushveld Complex (Cawthorn and Webb, 2001). A further constraint may be derived from the Moho discontinuities induced by the Limpopo orogen, specifically an offset interpreted as due to the retrocharriage of the Southern Marginal Zone onto the northern Kaapvaal craton at *ca* 2.67 Ga (De Beer and Stettler, 1988; De Wit et al., 1992). From these constraints, it seems quite compelling that if the flat Moho discontinuity is a modification of the primary crust-mantle boundary, then this flattening must have occurred during the Ventersdorp event.

The implication then is that some type of middle to lower crustal flow operated across the entire western craton to erase primary variation in Moho topography, simultaneous with Ventersdorp extension and volcanism in the upper crust. However, the 3.2 to 2.9 Ga diamonds from the western craton kimberlites apparently demand the preservation of an intact lithospheric keel extending into the diamond stability field through this same 2.72 Ga heating episode. The

necessary localization of thermal reactivation in the lithospheric mantle compared with the much broader manifestation of thermal effects in the overlying crust, is a clear embodiment of crust-mantle decoupling. Tentatively, this decoupling may be attributed to the differential rheological structure and the prediction of a weak lower crust in the strength profiles of the lithosphere (Kusznir and Park, 1986; Ranalli, 1997). We hypothesize that during the lateral propagation of the Ventersdorp thermal perturbation into the surrounding lithosphere, crustal melting combined with a weaker intrinsic rheology promoted preferential heating and strain localization in the lower crust relative to lithospheric mantle. This hypothesis warrants further testing with analytical and numerical models combining heat transport and crustal rheology. The geochronological and petrological constraints on the nature of the thermal perturbation derived from the UHT granulites and analysis of the geological evolution of the craton may serve to set the boundary and initial conditions for such modeling.

A final point with regard to the 2.72 Ga thermal perturbation to the Kaapvaal lithosphere concerns the presence of diamonds in the same kimberlites which bear the UHT granulites. While heterogeneous thermal transport within the cratonic lithosphere may allow the preservation of diamonds distal from the loci of rifting, it is difficult to envision that the mantle directly beneath the Free State kimberlites was not completely expunged of diamonds during the Ventersdorp thermal perturbation. The relatively abundant diamonds in these kimberlites then, it is argued, must be younger than this event. This is a testable hypothesis; however, to our knowledge no diamond inclusion geochronology has been attempted from these kimberlites. Such studies would complement and refine the model for the thermal effects of Ventersdorp rifting on the lithosphere.

6.3.2 Chemical lithosphere perturbation

While the rheological coherence of the Kaapvaal lithospheric mantle was apparently sufficient to accommodate thermal reactivation along the strike of the Ventersdorp rift without wholesale replacement by asthenosphere, the chemical consequences of the magmatic flux through, and even partial melting of the lithosphere beneath the rift zone must have been substantial. Unfortunately, the Mesozoic kimberlites piercing this sector of the craton (which bear the UHT granulites) do not yield abundant large mantle xenoliths, and so the lithospheric mantle of this region has not been so extensively studied as that for example beneath the

Kimberley area. We suggest that analysis of the chemical and isotopic systematics of the lithospheric mantle beneath the Ventersdorp rift zone, perhaps from mantle xenocrysts concentrates, should reveal anomalies related to 2.7 Ga modification of the lithosphere by ascending mafic magmas, correlated with the manifestation of UHT metamorphism in the lower crust.

Another predicted modification of the lithosphere during the Ventersdorp event is the intraplating of ascending mafic magmas as eclogitic or pyroxenitic components. Eclogites are an integral component of the Kaapvaal lithospheric mantle, and are relatively abundant in the Lace and Kaalvallei kimberlites of the Free State. Many of these eclogites may be predicted to be ca 2.7 Ga in age. Affirmatively, Moser (1998) report a tentative U-Pb zircon age for a coesite eclogite from the Lace kimberlite of ca 2.7 Ga; similarly, our own ongoing geochronological investigations of eclogites from Lace have found zircons dating from 2.78 to 2.76 Ga (manuscript in prep.). An eclogite from the Lovedale kimberlite at the western margin of the craton contains zircon with ages of 2.65 Ga (Schmitz and Bowring, 2001), suggesting correlation of this eclogite with Pneil sequence magmatism. There are additional suggestive indications of ca. 2.7 Ga eclogites from other regions of the western craton. Based on early studies at the Roberts Victor kimberlite, mantle eclogites are generally subdivided into Type 1 and Type 2 categories, which are texturally and compositionally distinct. Shirey et al. (2001) have demonstrated that while the Re-Os systematics of Type 1 eclogites indicate older derivation at ≥ 2.9 Ga, many Type 2 eclogites have younger model ages and plot nearer a ca 2.7 Ga reference line. Further analysis to clarify the potential origins of a subgroup of the Kaapvaal lithospheric mantle eclogites during Ventersdorp magmatism is an important line of future inquiry.

6.3.3 Thermal relaxation

Generally, the shape of the cooling curve for the lower crust following UHT metamorphism at 2.72 Ga appears to be compatible with conductive cooling from a lithospheric scale thermal perturbation. The amount of time necessary to reestablish conductive steady state geotherms through the Kaapvaal lithosphere can be generally deduced at approximately 400 to 600 Ma, from the ages and modeled kinetics of the zircon exsolution phenomena in rutile. This is in good agreement with estimates from perturbation models (Vitarello and Pollack, 1980; Morgan, 1987), which arrive at similar thermal relaxation time constants for conductive

relaxation of ~ 250 km thick continental lithosphere suffering tectonothermal reactivation. Indirectly, this observation supports the inferences above that the Kaapvaal cratonic lithosphere was not physically replaced by convecting aesthenospheric mantle during rifting, as the thermal relaxation time constant of such physically thinned lithosphere would be substantially shorter (Morgan and Sass, 1984).

In detail, however, discrepancies arise between our thermochronological data and simple conductive models of thermal relaxation. Following Vitorello and Pollack (1980) we generated a forward model of conductive cooling of a 250 km thick lithosphere following a “triangular” thermal perturbation from a cratonic steady state geotherm, with a maximum ΔT of 850° at 50 km, and a no heat flux lower lithosphere boundary condition; this perturbation generates the requisite initial UHT conditions at 35 km. The curve plotted in Figure 10b represents the conductive cooling curve at a depth of 35 km, comparable with the depth of isobaric cooling of the UHT granulites. It is immediately apparent that the modeled conductive cooling of the lithosphere proceeds much faster than the rates measured or inferred from the lower crustal thermochronology. The discrepancy in rates is particularly egregious at timescales of 100-200 millions years following peak metamorphism: while the inferred temperatures of 2.6 to 2.5 Ga exsolution and coarsening of the zircon lamellae in rutile are >570°C, the conductive cooling model predicts temperatures of ~450°.

An obvious means of rectifying these measured and modeled cooling paths is to reject the available laboratory data for Zr diffusion in rutile, and postulate a much lower activation energy and faster diffusivity at a given temperature, such that the coarsening phenomena observed in the UHT rutiles could occur at relatively low temperatures. For example, lowering the activation energy for Zr diffusion to that of Ti self diffusion in rutile would allow coarsening to proceed at temperatures as low as 450°C. However, doing so would make it very difficult to explain the lack of coarsening of fine zircon needles also observed in the UHT granulites— at these faster diffusivities, coarsening on length scales of tens of microns would occur within tens of millions of years at steady-state lower crustal temperatures of ~350°C. Lacking further experimental constraints on Zr diffusion in rutile, we consider the available data robust and move on to examine possible geological means of explaining the cooling rate discrepancy.

High temperatures in the crust could be maintained by continued advection of heat from the mantle. Maintenance of relatively high lower crustal temperatures for approximately 40

million years following peak UHT by continued thermal advection is geologically warranted given the inferred age of the upper Platberg volcanics and particularly the 2.664 Ga Pniel sequence flood basalts. However this advective maintenance is difficult to prolong to much younger ages due to the lack of abundant volcanism associated with the succeeding Transvaal basin.

The platformal sediments of the Transvaal Supergroup are generally attributed to thermal subsidence of the craton following Ventersdorp rifting (Hunter, 1974; Clendenin et al., 1988; Martin et al., 1998), and demonstrate thermal densification of the lithosphere after 2.642 Ga. A fruitful line of further inquiry regards whether the subsidence history of the Transvaal basin is consistent with cooling rates and thermal densification predicted from the simple conductive models, or the apparent lower crustal thermochronologically-derived cooling rates. Such an analysis awaits better absolute chronological constraints on Transvaal Supergroup deposition rates.

Thermal subsidence following rifting is generally associated with crustal cooling and the lowering of lithospheric geotherms. As such, the effects of subsidence-driven sedimentation have generally been modeled as shortening the thermal relaxation time constant of the lithosphere (Morgan, 1987), essentially by advection of geotherms downward with the upper boundary condition. Such thermal behavior obviously only exacerbates the problem of maintaining elevated middle to lower crustal temperatures over extended periods. Recently however, Sandiford et al. (1998) have put forth a model promoting *heating* of the middle crust during thermal subsidence by the burial of moderate- to high-heat production upper crust during sedimentation. While reserving judgement for the ability of such models to generate the necessary conditions of high-T, low-P metamorphism, it is relevant to the problem of lower crustal temperature maintenance that such models similarly predict much slower cooling in the lower crust, due to the thermal blanketing effect of the buried high heat production crustal layer. We tentatively suggest that such thermal models incorporating crustal heat production and changing boundary conditions may predict the slow cooling rates observed in the UHT granulite thermochronology, and should be the subject of further analysis.

7. Conclusions

The age, duration, and tempo of UHT metamorphism in the lower crust of the central Kaapvaal craton have been established through high precision U-Pb zircon and monazite geochronology. The peak of metamorphism, which exceeded 1000°C at 10 kbar pressures—equivalent to the current base of the crust, is dated by both metamorphic zircon and monazite to a short interval between 2720 to 2715 Ma, following a cryptic ramping of crustal temperatures over ca 25 million years, as recorded by prograde monazite and zircon. The preservation of prograde monazite ages through this UHT metamorphism places one of the firmest field-based constraints on the very slow Pb diffusivity and high closure temperature for monazite, comparable to that of zircon. Peak UHT metamorphic conditions in the lower crust correlate exactly with the timing of very high advective heat flux through the cratonic lithosphere associated with the rapid eruption of the Klipriviersburg flood basalts of the Ventersdorp Supergroup at 2714±8 Ma. This link provides the basis for one of the first mechanistic models for the general phenomenon of UHT crustal metamorphism.

Following peak metamorphism, retrograde zircon growth indicates initial isobaric cooling rates of $\geq 8^\circ\text{C}/\text{Ma}$, to temperatures below the kyanite-sillimanite phase boundary by 2690 Ma. Additional geochronological information on the cooling path of the UHT granulites is obtained from a unique reaction texture of zircon exsolution from rutile. The topology of this phenomenon is consistent with a subsolvus unmixing model incorporating heterogeneous nucleation and diffusive coarsening; direct dating of individual zircon lamellae yield ages of 2.60 to 2.30 Ga indicating to first order the slow cooling of the UHT granulites in the lower crust. These ages, combined with the topology of exsolution and coarsening, and kinetic data for Zr diffusion in rutile, tentatively constrain a T-t path indicating slow cooling rates of $\sim 1^\circ\text{C}/\text{Ma}$, and a thermal relaxation time constant for the Kaapvaal lithosphere of 400 to 600 Ma. While these rates and timescales are generally consistent with the predictions of conductive thermal relaxation models for 250-300 km thick lithosphere, in detail the data indicate maintenance of higher temperatures for longer times in the lower crust than the models, and may indicate the influence of crustal heat production and moving boundary conditions on the tempo of lithospheric thermal relaxation.

The dating of UHT metamorphism in the lower crust at 2.72 Ga provides the first tangible link between the surface manifestations of intracratonic Ventersdorp magmatism and extension, and extreme transient thermal regimes in the underlying cratonic lithosphere.

Effective removal of the thermal lithosphere beneath the Ventersdorp rift zone was apparently sufficiently localized to maintain a cold diamondiferous lithospheric mantle keel beneath the western craton. This thermomechanical localization in the lithospheric mantle, when compared with the much broader manifestation of crustal extension and partial melting across the entire western craton— including an apparently profound flattening of the Moho by lower crustal flow— epitomizes a significant crust-mantle decoupling at 2.72 Ga.

Acknowledgements— The authors wish to particularly thank Dr. George Read for introducing us to the Lace kimberlite, and for his enthusiasm regarding geochronological studies of the unique crustal xenoliths of this kimberlite. Drs. K.S. Viljoen and J. Stiefenhofer are thanked for access to crustal nodules from the Kaalvallei kimberlite, and Prof. J.J. Gurney for access to crustal samples in the Mantle Room of the Dept. of Geological Sciences, University of Cape Town. Drs. David Bell and Maarten de Wit are thanked for numerous discussions on the integration of surface geology, lower crustal geochronology and the lithospheric mantle record. This research was conducted under the auspices of a National Defense Science and Engineering Fellowship, U.S. Army Research Office grant DAAH049510560 to MDS, and by NSF Continental Dynamics Program grant EAR9526702 to SAB.

References

- Armstrong, R.A., Compston, W., Retief, E.A., Williams, I.S., Welke, H.J., 1991. Zircon ion microprobe studies bearing on the age and evolution of the Witwatersrand triad. *Precambrian Research* 53, 243-266.
- Barton, J.M., Jr., Blignaut, E., Salnikova, E.G., Kotov, A.B., 1995. The stratigraphical position of the Buffelsfontein Group based on field relationships and chemical and geochronological data. *South African Journal of Geology* 98, 386-392.
- Bingen, B., van Breemen, O., 1998. U-Pb monazite ages in amphibolite- to granulite-facies orthogneisses reflect hydrous mineral breakdown reactions: Sveconorwegian Province of SW Norway. *Contributions to Mineralogy and Petrology* 132, 336-353.
- Black, L.P., Williams, I.S., Compston, W., 1986. Four zircon ages from one rock: the history of a 3939 Ma old granulite from Mt. Sones, Enderby Land, Antarctica. *Contributions to Mineralogy and Petrology* 94, 427-437.
- Bohlen, S.R., Montana, A., Kerrick, D.M., 1991. Precise determinations of the equilibria kyanite-sillimanite and kyanite-andalusite and a revised triple point for Al_2SiO_5 polymorphs. *American Mineralogist* 76, 677-680.
- Bottinga, Y., Kudo, A., Weill, D., 1966. Some observations on oscillatory zoning and crystallization of magmatic plagioclase. *American Mineralogist* 51, 792-806.
- Brown, F.H., Duwez, P., 1954. The zirconia-titania system. *Journal of the American Ceramics Society* 37, 129-132.
- Buck, S.G., 1980. Stromatolite and ooid deposits within the fluvial and lacustrine sediments of the Precambrian Ventersdorp Supergroup of South Africa. *Precambrian Research* 12, 311-330.
- Burke, K., Kidd, W.S.F., Kusky, T., 1985. Is the Ventersdorp rift system of southern Africa related to a continental collision between the Kaapvaal and Zimbabwe Cratons at 2.64 Ga ago? *Tectonophysics* 115, 1-24.
- Carlson, R.W., Pearson, D.G., Boyd, F.R., Shirey, S.B., Irvine, G., Menzies, A.H., Gurney, J.J., 1999. Re-Os systematics of lithospheric peridotites: implications for lithosphere formation and preservation. *In: The*

- J.B.Dawson Volume: Proceedings of the 7th International Kimberlite Conference, Volume 1. Gurney, J.J., Gurney, J.L., Pascoe, M.D., Richardson, S.H. (Eds.), Red Roof Design, Cape Town, S.A., 99-108.
- Cawthorn, R.G., Webb, S.J., 2001. Connectivity between the western and eastern limbs of the Bushveld Complex. *Tectonophysics* 330, 195-209.
- Chapman, D.S., Pollack, H.N., 1977. Regional geotherms and lithospheric thickness. *Geology* 5, 265-268.
- Cherniak, D.J., Watson, E.B., 2000. Pb diffusion in zircon. *Chemical Geology* 172, 5-24.
- Cherniak, D.J., Watson, E.B., Harrison, T.M., Grove, M., 2000. Pb diffusion in monazite: a progress report on a combined RBS/SIMS study [abs.]. *EOS (Transactions, American Geophysical Union)* 82, S232.
- Clendenin, C.W., Charlesworth, E.G., Maske, S., 1988. An early Proterozoic three-stage rift system, Kaapvaal Craton, South Africa. *Tectonophysics* 145, 73-86.
- Copeland, P., Parrish, R.R., Harrison, T.M., 1988. Identification of inherited radiogenic Pb in monazite and its implications for U-Pb systematics. *Nature* 333, 760-763.
- Coughanour, L.W., Roth, R.S., DeProse, V.A., 1954. Phase equilibrium relations in the systems lime-titania and zirconia-titania. *Journal of Research of the National Bureau of Standards* 52, 37-41.
- Crowley, J.L., Ghent, E.D., 1999. An electron microprobe study of the U-Th-Pb systematics of metamorphosed monazite; the role of Pb diffusion versus overgrowth and recrystallization. *Chemical Geology* 157, 285-302.
- Dawson, J.B., Harley, S.L., Rudnick, R.L., Ireland, T.R., 1997. Equilibration and reaction in Archaean quartz-sapphirine granulite xenoliths from the Lace kimberlite pipe, South Africa. *Journal of Metamorphic Geology* 15, 253-266.
- Dawson, J.B., Smith, J.V., 1987. Reduced sapphirine granulite xenoliths from the Lace Kimberlite, South Africa: implications for the deep structure of the Kaapvaal Craton. *Contributions to Mineralogy and Petrology* 95, 376-383.
- De Beer, J.H., Stettler, E.H., 1988. Geophysical characteristics of the southern African continental crust. *In: Oceanic and Continental Lithosphere: Similarities and Differences*. Menzies, M.A., Cox, K.G. (Eds.), *Journal of Petrology, Special Volume*, Oxford University Press, London, 163-184.
- de Wit, M.J., Roering, C., Hart, R.J., Armstrong, R.A., de Ronde, C.E.J., Green, R.W.E., Tredoux, M., Peberdy, E., Hart, R.A., 1992. Formation of an Archaean continent. *Nature* 357, 553-562.
- DeVries, R.C., Roy, R., Osborn, E.F., 1954. 27. The system TiO_2 - SiO_2 . *Transactions of the British Ceramics Society* 53, 525-540.
- Durrheim, R.J., Green, R.W.E., 1992. A seismic refraction investigation of the Archean Kaapvaal Craton, South Africa, using mine tremors as the energy source. *Geophysical Journal International* 108, 812-832.
- Griffin, W.L., Carswell, D.A., Nixon, P.H., 1979. Lower crustal granulites and eclogites from Lesotho, southern Africa. *In: The Mantle Sample: Inclusions in Kimberlites and other Volcanics*. Boyd, F.R., Meyer, H.O.A. (Eds.), *Proceedings of the 2nd International Kimberlite Conference 2*, American Geophysical Union, Washington, D.C., 59-86.
- Grove, M., Harrison, T.M., 1999. Monazite Th-Pb age depth profiling. *Geology* 27, 487-490.
- Hall, R.C.B., Els, B.G., Mayer, J.J., 1997. The Ventersdorp Contact Reef: final phase of the Witwatersrand Basin, independent formation, or precursor to the Ventersdorp Supergroup?. *South African Journal of Geology* 100, 213-222.
- Harley, S.L., 1998. On the occurrences and characterization of ultrahigh-temperature crustal metamorphism. *In: What Drives Metamorphism and Metamorphic Reactions?*. Treloar, P.J., O'Brien, P.J. (Eds.), *Geological Society Special Publications* 138, Geological Society of London, London, 81-107.
- Hart, R., Moser, D., Andreoli, M., 1999. Archean age for the granulite facies metamorphism near the center of the Vredefort structure, South Africa. *Geology* 27, 1091-1094.
- Hartnady, C., Joubert, P., Stowe, C., 1985. Proterozoic crustal evolution in southwestern Africa. *Episodes* 8, 236-244.
- Hawkins, D.P., Bowring, S.A., 1997. U-Pb systematics of monazite and xenotime: case studies from the Paleoproterozoic of the Grand Canyon, Arizona. *Contributions to Mineralogy and Petrology* 127, 87-103.
- Hawkins, D.P., Bowring, S.A., 1999. U-Pb monazite, xenotime, and titanite geochronological constraints on the prograde to post-peak metamorphic thermal history of Paleoproterozoic migmatites from the Grand Canyon, Arizona. *Contributions to Mineralogy and Petrology* 134, 150-169.
- Hodges, K.V., Hames, W.E., Bowring, S.A., 1994. $^{40}Ar/^{39}Ar$ age gradients in micas from a high-temperature-low-pressure metamorphic terrain: evidence for very slow cooling and implications for the interpretation of age spectra. *Geology* 22, 55-58.

- Holm, D.K., Dahl, P.S., 1997. $^{40}\text{Ar}/^{39}\text{Ar}$ evidence for Middle Proterozoic (1300-1500 Ma) slow cooling of the southern Black Hills, South Dakota, midcontinent, North America: implications for Early Proterozoic P-T evolution and posttectonic magmatism. *Tectonics* 16, 609-622.
- Hunter, D.R., 1974. Crustal development in the Kaapvaal Craton, II. The Proterozoic. *Precambrian Research* 1, 295-326.
- Jones, M.Q.W., 1988. Heat flow in the Witwatersrand Basin and environs and its significance for the South African shield geotherm and lithosphere thickness. *Journal of Geophysical Research* 93, 3243-3260.
- Jones, M.Q.W., 1992. Heat flow anomaly in Lesotho: implications for the southern boundary of the Kaapvaal craton. *Geophysical Research Letters* 19, 2031-2034.
- Kingsbury, J.A., Miller, C.F., Wooden, J.L., Harrison, T.M., 1993. Monazite paragenesis and U-Pb systematics in rocks of the eastern Mojave Desert, California, U.S.A.: implications for thermochronometry. *Chemical Geology* 110, 147-167.
- Koppel, V., Grunefelder, M., 1975. Concordant U-Pb ages of monazite and xenotime from the Central Alps and the timing of the high temperature Alpine metamorphism, a preliminary report. *Schweizerische Mineralogische und Petrographische Mitteilungen* 55, 129-132.
- Koppel, V., Gunthert, A., Grunefelder, M., 1980. Patterns of U-Pb zircon and monazite ages in polymetamorphic units of the Swiss Central Alps. *Schweizerische Mineralogische und Petrographische Mitteilungen* 61, 97-119.
- Kretz, R., 1983. Symbols for rock-forming minerals. *American Mineralogist* 68, 277-279.
- Krogh, T.E., 1973. A low contamination method for hydrothermal decomposition of zircon and extraction of U and Pb for isotopic age determination. *Geochimica et Cosmochimica Acta* 37, 485-494.
- Krogh, T.E., 1982. Improved accuracy of U-Pb zircon ages by the creation of more concordant systems using an air abrasion technique. *Geochimica et Cosmochimica Acta* 46, 637-649.
- Kusznir, N.J., Matthews, D.H., 1988. Deep seismic reflections and the deformational mechanics of the continental lithosphere. *In: Oceanic and Continental Lithosphere: Similarities and Differences*. Menzies, M.A., Cox, K.G. (Eds.), *Journal of Petrology, Special Volume*, Oxford University Press, London, 63-87.
- Kusznir, N.J., Park, R.G., 1986. Continental lithosphere strength: the critical role of lower crustal deformation. *In: The Nature of the Lower Continental Crust*. Dawson, J.B., Carswell, D.A., Hall, J., Wedepohl, K.H. (Eds.), *Geological Society Special Publication* 24, Oxford University Press, London, 79-93.
- Lee, J.K.W., Williams, I.S., Ellis, D.J., 1997. Pb, U and Th diffusion in natural zircon. *Nature* 390, 159-162.
- Ludwig, K.R., 1980. Calculation of uncertainties of U-Pb isotope data. *Earth and Planetary Science Letters* 46, 212-220.
- MacIntyre, R.M., Dawson, J.B., 1974. Age significance of some South African kimberlites. 4th Euro. Collog. Geochron. *Cosmochron. Isotope Geol.*, 66.
- Maphalala, R.M., Kroner, A., 1993. Pb-Pb single zircon ages for younger Archean granitoids of Swaziland, southern Africa. *Ext. Abst. 16th Colloquium on African Geology, Mbabane, Swaziland.* pp. 201-206.
- Marsh, J.S., Bowen, M.P., Rogers, M.W., Bowen, T.B., 1992. Petrogenesis of Late Archean flood-type basic lavas from the Klipriviersberg Group, Ventersdorp Supergroup, South Africa. *Journal of Petrology* 33, 817-847.
- Martin, D.McB., Clendenin, C.W., Krapez, B., McNaughton, N.J., 1998. Tectonic and geochronological constraints on late Archean and Paleoproterozoic stratigraphic correlation within the between the Kaapvaal and Pilbara Cratons. *Journal of the Geological Society of London* 155, 311-322.
- McLaren, A.C., Fitzgerald, J.D., Williams, I.S., 1994. The microstructure of zircon and its influence on the age determination from Pb/U isotopic ratios measured by ion microprobe. *Geochimica et Cosmochimica Acta* 58, 993-1005.
- Meissner, R., Wever, Th., Fluh, E.R., 1987. The Moho in Europe— implications for crustal development. *Annales Geophysicae* 5B, 357-364.
- Mezger, K., Rawnsley, C.M., Bohlen, S.R., Hanson, G.N., 1991. U-Pb garnet, sphene, monazite, and rutile ages: implications for the duration of high-grade metamorphism and cooling histories, Adirondack Mts., New York. *Journal of Geology* 99, 415-428.
- Moller, A., Mezger, K., Schenk, V., 2000. U-Pb dating of metamorphic minerals: Pan-African metamorphism and prolonged slow cooling of high pressure granulites in Tanzania, East Africa. *Precambrian Research* 104, 123-146.
- Moser, D.E., Hart, R.J., 1998. Neoarchean and Paleoproterozoic re-activation of the crust-mantle transition beneath the central Kaapvaal craton, Lace kimberlite. *Extended Abstracts, 7th International Kimberlite Conference, University of Cape Town, South Africa*, 609-611.
- Nelson, D.R., Trendall, A.F., de Laeter, J.R., Grobler, N.J., Fletcher, I.R., 1992. A comparative study of the geochemical and isotopic systematics of late Archean flood basalts from the Pilbara and Kaapvaal Cratons. *Precambrian Research* 54, 231-256.

- Nguuri, T.K., Gore, J., James, D.E., Webb, S.J., Wright, C., Zengeni, T.G., Gwavava, O., Snoke, J.A., Kaapvaal Seismic Group, 2001. Crustal structure beneath southern Africa and its implications for the formation and evolution of the Kaapvaal and Zimbabwe cratons. *Geophysical Research Letters* 28, 2501-2504.
- Parrish, R.R., 1990. U-Pb dating of monazite and its application to geological problems. *Canadian Journal of Earth Sciences* 27, 1431-1450.
- Perry, F.V., Baldrige, W.S., DePaolo, D.J., 1987. Role of asthenosphere and lithosphere in the genesis of late Cenozoic basaltic rocks from the Rio Grande Rift and adjacent regions fo the Southwestern United States. *Journal of Geophysical Research* 92, 9193-9213.
- Phillips, D., Machin, K.J., Kiviets, G.B., Fourie, L.F., Roberts, M.A., Skinner, E.M.W., 1999. A petrographic and ⁴⁰Ar/³⁹Ar geochronological study of the Voorspoed kimberlite, South Africa: implications for the origin of Group II kimberlite magmatism. *South African Journal of Geology* 101, 299-306.
- Pyle, J.M., Spear, F.S., Rudnick, R.L., McDonough, W.F., Horn, I., 1999. Involvement of monazite and xenotime in pelite reactions [abs.]. *Geological Society of America Abstracts with Programs* 31, 39.
- Ranalli, G., 1997. Rheology of the lithosphere in space and time. *In: Orogeny Through Time*. Burg, J.P., Ford, M. (Eds.), Geological Sociey Special Publication 121, Geological Society of London, London, 19-37.
- Richardson, S.H., Gurney, J.J., Erlank, A.J., Harris, J.W., 1984. Origin of diamonds in old enriched mantle. *Nature* 310, 198-202.
- Richardson, S.H., Shirey, S.B., Harris, J.W., Carlson, R.W., 2001. Archean subduction recorded by Re-Os isotopes in eclogitic sulfide inclusions in Kimberley diamonds. *Earth and Planetary Science Letters* 191, 257-266.
- Rickwood, P.C., Gurney, J.J., White-Cooper, D.R., 1969. 17. The nature and occurrences of eclogite xenoliths in the kimberlites of southern Africa. *In: The Upper Mantle Project*. Geological Society of South Africa Special Publication 2, , 371-393.
- Ritsema, J., Nyblade, A.A., Owens, T.J., Langston, C.A., VanDecar, J.C., 1998. Upper mantle seismic velocity structure beneath Tanzania, East Africa; implications for the stability of cratonic lithosphere. *Journal of Geophysical Research* 103, 21201-21213.
- Robb, L.J., Charlesworth, E.G., Drennan, G.R., Gibson, R.L., Tongu, E.L., 1997. Tectono-metamorphic setting and paragenetic sequence of Au-U mineralization in the Archean Witwatersrand Basin, South Africa. *Australian Journal of Earth Sciences* 44, 353-371.
- Robb, L.J., Davis, D.W., Kamo, S.L., 1991. Chronological framework for the Witwatersrand Basin and environs: towards a time-constrained depositional model. *South African Journal of Geology* 94, 86-95.
- Robb, L.J., Meyer, F.M., 1995. The Witwatersrand Basin, South Africa: Geological framework and mineralization processes. *Ore Geology Reviews* 10, 67-94.
- Rogers, N.W., 1977. Granulite xenoliths from Lesotho kimberlites and the lower continental crust. *Nature* 270, 681-684.
- Rubatto, D., Williams, I.S., Buick, I.S., 2001. Zircon and monazite response to prograde metamorphism in the Reynolds Range, central Australia. *Contributions to Mineralogy and Petrology* 140, 458-468.
- Rumble, D., III, 1976. Oxide minerals in metamorphic rocks. *In: Oxide Minerals: Petrologic and Magnetic Significance*. Lindsley, D.H., Ribbe, P.H. (Eds.), *Reviews in Mineralogy* 3, Mineralogical Society of America, R1-R20.
- Sandiford, M., Hand, M., McLaren, S., 1998. High geothermal gradient metamorphism during thermal subsidence. *Earth and Planetary Science Letters* 163, 149-165.
- Sasaki, J., Peterson, N.L., Hoshino, K., 1985. Tracer impurity diffusion in single-crystal rutile (TiO_{2-x}). *Journal of Physics and Chemistry of Solids* 46, 1267-1283.
- Schaltegger, U., Fanning, C.M., Gunther, D., Maurin, J.C. Schulmann, K., Gebauer, D., 1999. Growth, annealing and recrystallization of zircon and preservation of monazite in high-grade metamorphism: conventional and in-situ U-Pb isotope, cathodoluminescence and microchemical evidence. *Contributions to Mineralogy and Petrology* 134, 186-201.
- Schmitz, M.D., Bowring, S.A., 2001. The significance of U-Pb zircon dates in lower crustal xenoliths from the southwestern margin of the Kaapvaal craton, southern Africa. *Chemical Geology* 172, 59-76.
- Shirey, S.B., Carlson, R.W., Richardson, S.H., Menzies, A., Gurney, J.J., Pearson, D.G., Harris, J.W., Weichert, U., 2001. Archean emplacement of eclogitic components into the lithospheric mantle during formation of the Kaapvaal craton. *Geophysical Research Letters* 28, 2509-2512.
- Smith, H.A., Barreiro, B., 1990. Monazite U-Pb dating of staurolite grade metamorphism in pelitic schists. *Contributions to Mineralogy and Petrology* 105, 602-615.
- Smith, H.A., Giletti, B.J., 1997. Lead diffusion in monazite. *Geochimica et Cosmochimica Acta* 61, 1047-1055.

- Snoeyenbos, D.R., Williams, M.L., Hanmer, S., 1995. Archean high-pressure metamorphism in the western Canadian Shield. *European Journal of Mineralogy* 7, 1251-1272.
- South African Committee for Stratigraphy (SACS), 1980. Stratigraphy of South Africa. Part 1. Lithostratigraphy of the Republic of South Africa, South West Africa/Namibia, and the Republics of Bophuthatswana, Transkei and Venda. Kent, L.E. (Ed.), Geological Survey of South Africa Handbook 8, 690 p.
- Spear, F.S., Parrish, R.R., 1996. Petrology and cooling rates of the Valhalla Complex, British Columbia, Canada. *Journal of Petrology* 37, 733-765.
- Stowe, C.W., 1986. Synthesis and interpretation of structures along the north-eastern boundary of the Namaqua tectonic province, South Africa. *Transactions of the Geological Society of South Africa* 89, 185-198.
- Suzuki, K., Adachi, M., Kajizuka, I., 1994. Electron microprobe observations of Pb diffusion in metamorphosed detrital monazites. *Earth and Planetary Science Letters* 128, 391-405.
- Thomas, R.J., Agenbacht, A.L.D., Cornell, D.H., Moore, J.M., 1994. The Kibaran of southern Africa: tectonic evolution and metallogeny. *Ore Geology Reviews* 9, 131-160.
- Tinker, J., 2001. Unpublished M.Sc. thesis, University of Cape Town, South Africa.
- Tyler, N., 1979. Stratigraphy, geochemistry and correlation of the Ventersdorp Supergroup in the Derdepoort area, west-central Transvaal. *Transactions of the Geological Society of South Africa* 82, 133-147.
- Van Calsteren, P.W.C., Harris, N.B.W., Hawkesworth, C.J., Menzies, M.A., Rogers, N.W., 1986. Xenoliths from southern Africa: a perspective on the lower crust. *In: The Nature of the Lower Continental Crust*. Dawson, J.B., Carswell, D.A., Hall, J., Wedepohl, K.H. (Eds.), Geological Society Special Publication 24, Oxford University Press, London, 351-362.
- Van der Westhuizen, W.A., De Bruijn, H., Meintjes, P.G., 1991. The Ventersdorp Supergroup: an overview. *Journal of African Earth Sciences* 33, 83-105.
- Viljoen, K.S., 1989. Unpublished Ph.D. thesis, University of the Witwatersrand, South Africa.
- Vitarello, I., Pollack, H.N., 1980. On the variation of continental heat flow with age and the thermal evolution of continents. *Journal of Geophysical Research* 85, 983-995.
- Vlassopoulos, D., Rossman, G.R., Haggerty, S.E., 1993. Coupled substitution of H and minor elements in rutile and the implications of high OH contents in Nb- and Cr-rich rutile from the upper mantle. *American Mineralogist* 78, 1181-1191.
- Walraven, F., 1997. Geochronology of the Rooiberg Group, Transvaal Supergroup, South Africa. *Economic Geology Research Unit Information Circular* 316, University of the Witwatersrand, Johannesburg, 21 p.
- Walraven, F., Martini, J., 1995. Zircon Pb-evaporation age determinations of the Oak Tree Formation, Chuniespoort Group, Transvaal Sequence: implications for Transvaal-Griqualand West basin correlations. *South African Journal of Geology* 98, 58-67.
- Watson, E.B., 1996. Dissolution, growth and survival of zircons during crustal fusion: kinetic principles, geological models and implications for isotopic inheritance. *Transactions of the Royal Society of Edinburgh: Earth Sciences* 87, 43-56.
- Williams, I.S., Compston, W., Black, L.P., Ireland, T.R., Foster, J.J., 1984. Unsupported radiogenic Pb in zircon; a case of anomalously high Pb-Pb, U-Pb and Th-Pb ages. *Contributions to Mineralogy and Petrology* 88, 322-327.
- Williams, M.L., Jercinovic, M.J., Terry, M.P., 1999. Age mapping and chemical dating of monazite using the electron microprobe: deconvoluting multistage tectonic histories. *Geology* 27, 1023-1026.
- Willigers, B.J.A., Krogstad, E.J., Wijbrans, J.R., 2001. Comparison of thermochronometers in a slowly cooled terrain: Nagssugtoqidian Orogen, West Greenland. *Journal of Petrology* 42, 1729-1749.
- Winter, H. de la R., 1976. A lithostratigraphic classification of the Ventersdorp succession. *Transactions of the Geological Society of South Africa* 79, 31-48.

Table 1. Zircon and monazite U-Pb isotopic data for Free State UHT granulites

#	Frac ^a	Composition						Isotopic Ratios						Dates (Ma)						
		Wt. (μg) ^b	[U] (ppm)	[Pb] (ppm)	Th ^c U	Pb* ^d Pbc	Pbc ^d (pg)	$\frac{^{206}\text{Pb}^e}{^{204}\text{Pb}}$	$\frac{^{208}\text{Pb}^f}{^{206}\text{Pb}}$	$\frac{^{206}\text{Pb}^f}{^{238}\text{U}}$	% err ^g	$\frac{^{207}\text{Pb}^f}{^{235}\text{U}}$	% err ^g	$\frac{^{207}\text{Pb}^f}{^{206}\text{Pb}}$	% err ^g	corr. coef.	$\frac{^{206}\text{Pb}^h}{^{238}\text{U}}$	$\frac{^{207}\text{Pb}^h}{^{235}\text{U}}$	$\frac{^{207}\text{Pb}^h}{^{206}\text{Pb}}$	±
Zircon discrete grains																				
<i>KX1-1: Lace kimberlite, Garnet-quartz-sapphirine-sillimanite-kyanite-rutile granulite</i>																				
1	z1,ii	0.40	525	337	0.156	5.3	22	290	0.0433	0.522303	(.33)	13.4970	(.36)	0.187419	(.12)	0.940	2708.9	2715.1	2719.6	2.0
2	z2,ii	2.00	304	182	0.371	18	20	895	0.1048	0.513534	(.15)	13.2925	(.17)	0.187731	(.07)	0.914	2671.7	2700.6	2722.4	1.1
3	z4,ii	3.80	284	166	0.288	44	14	2310	0.0801	0.525506	(.11)	13.6966	(.12)	0.189031	(.04)	0.923	2722.5	2729.0	2733.7	0.7
4	z5,ii	1.30	356	214	0.264	14	19	746	0.0733	0.523604	(.20)	13.5376	(.21)	0.187516	(.06)	0.961	2714.4	2717.9	2720.5	0.9
5	z12,i	2.18	188	113	0.446	75	3.3	4273	0.1232	0.530090	(.15)	13.8897	(.15)	0.190038	(.05)	0.952	2741.8	2742.2	2742.5	0.8
6	z13,i	2.16	197	117	0.445	161	1.6	9166	0.1232	0.526180	(.07)	13.6824	(.08)	0.188594	(.04)	0.848	2725.3	2728.0	2729.9	0.7
<i>KX1-2: Lace kimberlite, Garnet-quartz-sapphirine-sillimanite-kyanite-rutile granulite</i>																				
7	zhf-1,ii	32.6	130	80	0.411	19	6.4	948	0.1135	0.523870	(.33)	13.4933	(.34)	0.186807	(.08)	0.973	2715.6	2714.8	2714.2	1.3
8	zhf-2,iii	31.4	116	83	0.482	3.6	28	185	0.1410	0.490409	(1.01)	12.4409	(1.19)	0.183989	(.58)	0.875	2572.4	2638.3	2689.2	9.5
<i>KX1-8: Lace kimberlite, Garnet-quartz-sapphirine-sillimanite-kyanite-rutile granulite</i>																				
9	z1,ii	0.25	694	468	0.417	5.2	19	273	0.1172	0.518496	(.39)	13.4835	(.44)	0.188606	(.18)	0.912	2692.8	2714.1	2730.0	2.9
10	z2,ii	0.41	475	270	0.260	20	5.3	1162	0.0720	0.518225	(.29)	13.1595	(.31)	0.184170	(.09)	0.953	2691.6	2691.2	2690.8	1.6
11	z3,iii	0.18	457	260	0.384	19	2.6	1090	0.1080	0.511555	(.24)	13.0497	(.26)	0.185015	(.10)	0.929	2663.3	2683.3	2698.4	1.6
<i>KX2-1, Voorspoed kimberlite, Garnet-quartz-sapphirine-antiperthitic feldspar-sillimanite-kyanite-rutile granulite</i>																				
12	zhf1,ii	24.4	235	140	0.169	14	11	732	0.0466	0.523787	(.32)	13.4989	(.33)	0.186914	(.08)	0.971	2715.2	2715.2	2715.2	1.3
13	zhf2,iii	67.6	95	75	1.362	7.6	29	321	0.3771	0.517952	(.27)	13.1518	(.29)	0.184159	(.09)	0.950	2690.5	2690.6	2690.7	1.5
14	z1,ii	0.40	694	385	0.247	44	3.5	2653	0.0694	0.513457	(.17)	13.1940	(.18)	0.186367	(.07)	0.924	2671.4	2693.6	2710.4	1.2
15	z3,ii	0.40	348	182	0.078	28	2.6	1784	0.0220	0.504327	(.16)	12.7807	(.18)	0.183798	(.08)	0.903	2632.4	2663.6	2687.4	1.3
<i>KX18-2, Kaalvallei kimberlite, Garnet-quartz-antiperthitic feldspar-sillimanite-rutile granulite</i>																				
16	z1,ii	0.74	157	87	0.139	31	2.1	1905	0.0385	0.521849	(.23)	13.4429	(.25)	0.186830	(.08)	0.946	2707.0	2711.3	2714.5	1.3
17	z2,ii	0.74	122	66	0.087	26	1.9	1656	0.0240	0.523708	(.42)	13.4875	(.44)	0.186785	(.10)	0.972	2714.9	2714.4	2714.1	1.7
18	z3,ii	0.74	132	71	0.090	21	2.5	1306	0.0253	0.515236	(.43)	13.2573	(.45)	0.186616	(.11)	0.968	2678.9	2698.1	2712.6	1.9
<i>KX27-1, Star Mine kimberlite, Garnet-quartz-plagioclase-sillimanite-rutile granulite</i>																				
19	z1,iii	0.55	501	269	0.082	40	3.7	2495	0.0227	0.518098	(.22)	13.1551	(.23)	0.184154	(.09)	0.923	2691.1	2690.8	2690.6	1.5
20	z2,ii	0.95	414	224	0.085	103	2.1	6409	0.0235	0.520554	(.08)	13.2865	(.10)	0.185116	(.06)	0.832	2701.5	2700.2	2699.2	0.9
21	z3,ii	0.55	1157	676	0.328	89	4.2	5055	0.0905	0.529359	(.11)	13.8330	(.13)	0.189523	(.06)	0.863	2738.8	2738.3	2738.0	1.1

Table 1 (con't).

# ^a	Frac ^a	Composition						Isotopic Ratios						Dates (Ma)						
		Wt. (μg) ^b	[U] (ppm)	[Pb] (ppm)	Th ^c U	Pb* ^d Pbc	Pbc ^d (pg)	$\frac{^{206}\text{Pb}^e}{^{204}\text{Pb}}$	$\frac{^{208}\text{Pb}^f}{^{206}\text{Pb}}$	$\frac{^{206}\text{Pb}^f}{^{238}\text{U}}$	% err ^g	$\frac{^{207}\text{Pb}^f}{^{235}\text{U}}$	% err ^g	$\frac{^{207}\text{Pb}^f}{^{206}\text{Pb}}$	% err ^g	corr. coef.	$\frac{^{206}\text{Pb}^h}{^{238}\text{U}}$	$\frac{^{207}\text{Pb}^h}{^{235}\text{U}}$	$\frac{^{207}\text{Pb}^h}{^{206}\text{Pb}}$	±
Monazite																				
<i>KX1-1: Lace kimberlite, Garnet-quartz-sapphirine-sillimanite-kyanite-rutile granulite</i>																				
22	m1	3.40	1548	7458	36.35	2751	9.2	14786	11.2159	0.448414	(.48)	10.7905	(.48)	0.174527	(.08)	0.986	2388.2	2505.3	2601.5	1.3
23	m2	3.70	4589	15394	22.93	10897	5.2	98072	6.5907	0.498125	(.17)	12.6151	(.18)	0.183675	(.04)	0.973	2605.7	2651.3	2686.3	0.7
24	m3	1.90	3601	19289	41.74	3504	10	15857	13.4301	0.423185	(.99)	9.9477	(1.00)	0.170486	(.08)	0.997	2274.9	2429.9	2562.4	1.3
25	m4	10.0	194	933	35.90	1963	4.8	11513	10.9054	0.459614	(.12)	11.2075	(.13)	0.176854	(.05)	0.926	2437.9	2540.5	2623.6	0.8
26	m5	2.20	375	10630	227.4	7973	2.9	8764	66.4625	0.482943	(.10)	11.9683	(.13)	0.179736	(.08)	0.776	2540.1	2601.9	2650.4	1.4
27	m6	2.10	342	7883	189.5	3713	4.5	4314	60.4709	0.431456	(.15)	10.3067	(.18)	0.173254	(.11)	0.799	2312.3	2462.7	2589.3	1.8
28	m7	1.20	1120	9875	68.4	1424	8.3	4376	20.6906	0.464849	(.17)	11.4487	(.18)	0.178626	(.05)	0.955	2460.9	2560.4	2640.2	0.9
<i>KX18-2, Kaalvallei kimberlite, Garnet-quartz-antiperthitic feldspar-sillimanite-rutile granulite</i>																				
29	m1	0.48	3074	12079	25.53	26	216	210	7.0564	0.529803	(.13)	13.8905	(.29)	0.190153	(.22)	0.672	2740.6	2742.3	2743.5	3.6
30	m2	0.37	2498	7962	20.84	77	37	706	5.8782	0.514755	(.11)	13.3174	(.17)	0.187636	(.12)	0.750	2676.9	2702.4	2721.5	1.9
31	m3	0.43	1118	4733	27.40	23	84	179	7.5602	0.535737	(.20)	14.2555	(.28)	0.192988	(.18)	0.772	2765.6	2766.9	2767.8	3.0
32	m4	13.7	897	3087	23.10	196	215	1579	6.6707	0.503025	(.31)	13.0181	(.32)	0.187697	(.06)	0.979	2626.8	2681.0	2722.1	1.1
33	m5	5.44	1071	6040	39.61	435	75	2275	10.9152	0.536358	(.34)	14.2672	(.35)	0.192922	(.06)	0.984	2768.2	2767.6	2767.2	1.0
34	m6	2.74	749	3867	36.62	119	89	647	10.6137	0.500917	(.31)	12.9595	(.32)	0.187638	(.08)	0.965	2617.7	2676.7	2721.6	1.4
<i>KX2-1, Voorspoed kimberlite, Garnet-quartz-sapphirine-antiperthitic feldspar-sillimanite-kyanite-rutile granulite</i>																				
35	m2	10.0	810	6610	61.30	7326	9.0	25896	17.6645	0.499289	(.23)	12.7393	(.24)	0.185052	(.04)	0.984	2610.7	2660.6	2698.7	0.7
36	m3	0.50	72416	149864	12.23	9399	8.0	136585	3.4427	0.516356	(.34)	13.3741	(.34)	0.187851	(.04)	0.993	2683.7	2706.4	2723.4	0.7
37	m4	0.50	3958	13535	23.23	1129	6.0	10063	6.5586	0.509593	(.08)	12.9967	(.09)	0.184973	(.04)	0.866	2654.9	2679.4	2698.0	0.7
38	m5	1.50	3429	13956	28.80	3270	6.4	23080	8.5225	0.483877	(.11)	12.2540	(.11)	0.183671	(.04)	0.932	2544.1	2624.1	2686.3	0.7
39	m6a	0.80	4265	9387	13.97	1073	7.0	13904	4.0726	0.483821	(.24)	11.9728	(.24)	0.179477	(.05)	0.974	2543.9	2602.3	2648.0	0.9
40	m6c	1.30	4749	9311	11.74	3178	3.8	51268	3.3584	0.498845	(.07)	12.5955	(.08)	0.183125	(.04)	0.860	2608.8	2649.9	2681.4	0.7
<i>KX2-2, Voorspoed kimberlite, Garnet-quartz-antiperthitic feldspar-sillimanite-kyanite-rutile granulite</i>																				
41	m3	9.07	3460	6956	11.93	973	65	13400	3.4045	0.505468	(.55)	12.9420	(.55)	0.185697	(.04)	0.997	2637.3	2675.4	2704.4	0.7
42	m4	3.23	1442	5721	26.99	279	66	2010	7.6228	0.517764	(.40)	13.5423	(.41)	0.189697	(.09)	0.976	2689.7	2718.2	2739.5	1.5
Zircon exsolution lamellae																				
<i>KX1-1: Lace kimberlite, Garnet-quartz-sapphirine-sillimanite-kyanite-rutile granulite</i>																				
43	z6,v	4.11	59	44	2.542	67	2.7	2637	0.7339	0.455038	(.15)	10.1720	(.18)	0.162127	(.10)	0.842	2417.6	2450.5	2478.0	1.7
44	z7,v	1.03	220	83	0.018	38	2.2	2510	0.0057	0.381305	(.14)	7.9386	(.15)	0.150998	(.06)	0.915	2082.4	2224.1	2357.3	1.0
45	z8,v	1.76	64	29	0.107	32	1.6	1995	0.0326	0.436725	(.13)	9.8964	(.17)	0.164349	(.10)	0.799	2336.0	2425.2	2500.9	1.7
46	z9,v	1.32	95	48	0.527	11	5.7	575	0.1621	0.427392	(.53)	9.5608	(.54)	0.162243	(.09)	0.986	2294.0	2393.4	2479.2	1.5
47	z10,v	0.31	151	76	0.188	3.3	6.3	201	0.0577	0.421907	(1.39)	9.2756	(1.45)	0.159450	(.34)	0.973	2269.1	2365.6	2449.8	5.7
48	z11,v	0.29	145	231	0.732	0.5	46	38	0.2061	0.490242	(.96)	11.7569	(1.49)	0.173932	(.98)	0.761	2571.7	2585.2	2595.8	16.4

Table 1 (con't).

# ^a	Frac ^a	Composition						Isotopic Ratios						corr. coef.	Dates (Ma)			±		
		Wt. (μg) ^b	[U] (ppm)	[Pb] (ppm)	Th ^c U	Pb* ^d Pbc	Pbc ^d (pg)	²⁰⁶ Pb/ ²⁰⁴ Pb ^e	²⁰⁸ Pb/ ²⁰⁶ Pb ^f	²⁰⁶ Pb/ ²³⁸ U ^f	% err ^g	²⁰⁷ Pb/ ²³⁵ U ^f	% err ^g		²⁰⁷ Pb/ ²⁰⁶ Pb ^f	% err ^g	²⁰⁶ Pb/ ²³⁸ U ^h		²⁰⁷ Pb/ ²³⁵ U ^h	²⁰⁷ Pb/ ²⁰⁶ Pb ^h
Zircon exsolution lamellae (con't)																				
<i>KX1-2: Lace kimberlite, Garnet-quartz-sapphirine-sillimanite-kyanite-rutile granulite</i>																				
49	z1,v	7.40	11	4	0.230	28	1.2	1735	0.0793	0.372364	(.28)	8.0582	(.29)	0.156952	(.07)	0.972	2040.5	2237.6	2423.1	1.2
50	z2,v	2.94	29	15	0.482	26	1.6	1519	0.1418	0.453266	(.20)	10.3440	(.21)	0.165514	(.07)	0.935	2409.8	2466.0	2512.8	1.3
51	z3,v	1.83	22	10	0.159	6.5	2.8	423	0.0474	0.426547	(.58)	9.0997	(.64)	0.154724	(.22)	0.939	2290.1	2348.1	2398.8	3.7
52	z4,v	1.44	19	8	0.390	7.5	1.6	455	0.1259	0.393857	(.52)	8.4245	(.56)	0.155133	(.17)	0.953	2140.7	2277.8	2403.3	2.9
<i>KX2-1, Voorspoed kimberlite, Garnet-quartz-sapphirine-antiperthitic feldspar-sillimanite-kyanite-rutile granulite</i>																				
53	z4,v	0.77	475	244	0.020	20	9.2	1143	0.0055	0.492916	(.17)	11.4067	(.20)	0.167836	(.09)	0.883	2583.3	2557.0	2536.2	1.6
54	z5,v	1.23	320	160	0.007	29	6.6	1752	0.0019	0.490039	(.25)	11.1281	(.25)	0.164698	(.06)	0.975	2570.8	2533.9	2504.5	1.0
55	z7,v	1.32	291	133	0.009	41	4.2	2590	0.0027	0.455701	(.18)	10.0906	(.19)	0.160596	(.06)	0.944	2420.6	2443.1	2461.9	1.1
56	z8,v	0.69	480	208	0.010	35	4.1	2217	0.0027	0.436324	(.28)	8.8560	(.30)	0.147206	(.10)	0.946	2334.2	2323.3	2313.7	1.7
57	z9,v	1.65	223	110	0.011	41	4.4	2531	0.0030	0.487997	(.33)	11.4865	(.33)	0.170715	(.06)	0.982	2562.0	2563.5	2564.7	1.1
58	z10,v	1.86	94	49	0.006	18	4.9	1134	0.0017	0.503301	(.34)	11.9623	(.36)	0.172379	(.10)	0.959	2628.0	2601.5	2580.9	1.7
59	z11,v	1.54	248	124	0.005	148	1.3	9461	0.0013	0.498814	(.09)	11.7494	(.11)	0.170835	(.05)	0.878	2608.7	2584.6	2565.8	0.8
60	z12,v	1.03	134	65	0.019	35	1.9	2276	0.0053	0.482587	(.16)	11.1808	(.18)	0.168034	(.08)	0.899	2538.5	2538.3	2538.2	1.3
61	z13,v	1.48	202	94	0.011	60	2.3	3851	0.0032	0.467419	(.09)	10.4840	(.11)	0.162674	(.05)	0.858	2472.2	2478.5	2483.6	0.9
62	z14,v	4.44	72	37	0.207	45	3.6	2764	0.0578	0.490385	(.36)	11.6127	(.37)	0.171749	(.05)	0.992	2572.3	2573.7	2574.8	0.8

^a # corresponds to label on concordia diagrams; all fractions composed of single grains, roman numeral identifiers for zircon indicate type as defined in text.

^b Sample weights were estimated to within 40% using measured grain dimensions and a nominal density of 5.0 g/cm³ for monazite and 4.5 g/cm³ for zircon.

^c Th contents calculated from radiogenic ²⁰⁸Pb and the ²⁰⁷Pb/²⁰⁶Pb date of the sample, assuming concordance between U-Th-Pb systems.

^d Pb* and Pbc represent radiogenic Pb and common Pb respectively.

^e Measured ratio corrected for fractionation and spike contribution; Pb fractionation was 0.12 ± 0.04 %/a.m.u. for Faraday detector or 0.15 ± 0.04 %/a.m.u. for Daly detector analysis, based on daily analysis of NBS-981.

^f Measured ratios corrected for fractionation, spike, blank, and initial common Pb; nominal U blank = 0.1 pg ± 50% (2σ); nominal Pb blank = 3.5 pg ± 50% (2σ) or where lower, the total common Pb of the analysis ± 10% (2σ); measured laboratory blank composition: ²⁰⁶Pb/²⁰⁴Pb = 19.10, ²⁰⁷Pb/²⁰⁴Pb = 15.72, ²⁰⁸Pb/²⁰⁴Pb = 38.65 ± 0.01 (2σ); initial common Pb composition from model of Stacy and Kramers (1972) at 2.9 Ga.

^g Numbers in parentheses are the % errors reported at the 2σ confidence interval, propagated using the algorithms of Ludwig (1980).

^h Isotopic ages calculated using the decay constants of Jaffey et al. (1971): λ(²³⁵U) = 9.8485x10⁻¹⁰ yr⁻¹ and λ(²³⁸U) = 1.55125x10⁻¹⁰ yr⁻¹; error in ²⁰⁷Pb/²⁰⁶Pb date reported at the 2σ confidence interval.

Table 2. Sm-Nd isotopic data for selected Free State UHT granulite whole rocks and monazite

Sample ^a	[Sm] ^a	[Nd] ^a	$\frac{^{147}\text{Sm}^b}{^{144}\text{Nd}}$	$\frac{^{143}\text{Nd}^c}{^{144}\text{Nd}}$	ϵ_{Nd}^c	$\epsilon_{\text{Nd}(2.7)}^c$	t_{CHUR}^c	t_{DM}^d
KX1-1m1	6083	95868	0.0384	0.509692 ± 8	-57.48	-2.05	2.85	2.99
KX1-1m2	8156	103545	0.0476	0.509847 ± 7	-54.44	-2.26	2.86	3.01
KX2-1m1	15414	115829	0.0805	0.510409 ± 5	-43.49	-2.81	2.93	3.11
KX2-1m2	15594	116711	0.0808	0.510427 ± 6	-43.12	-2.56	2.92	3.10
KX1-1w	3.679	6.124	0.3632	0.516122 ± 14	67.96	10.16	3.20	3.01
KX1-2w	3.736	3.982	0.5672	0.519517 ± 9	134.18	5.46	2.84	2.73
KX1-8w	2.759	5.987	0.2787	0.514178 ± 8	30.05	1.58	2.87	2.40
KX2-1w	5.230	16.324	0.1937	0.512576 ± 7	-1.21	-0.18	3.19	4.34
KX2-2w	3.829	16.859	0.1373	0.511383 ± 7	-24.48	-3.87	3.23	3.50
KX27-1w	3.382	6.093	0.3356	0.515360 ± 6	53.11	4.88	3.00	2.75

^a “w” identifier indicates analysis of whole rock powder, “m” identifier signifies analysis of single monazite crystal; concentrations in ppm, as determined by isotope dilution.

^b Internal errors in measured $^{147}\text{Sm}/^{144}\text{Nd}$ are ≤ 0.1% (2σ s.d.).

^c Measured $^{143}\text{Nd}/^{144}\text{Nd}$ with internal error (2σ s.e.); long-term reproducibility of Nd isotopic standards is ≤ 20 ppm (2σ s.d.)— analyses (n=12) of USGS standard BCR-1 during the course of the study yielded $^{143}\text{Nd}/^{144}\text{Nd} = 0.512643 \pm 9$ and $^{147}\text{Sm}/^{144}\text{Nd} = 0.1383 \pm 3$ (2σ s.d.), which propagate into an average reproducibility for $\epsilon_{\text{Nd}(t)}$ of approximately ± 0.5 epsilon units; present-day ϵ_{Nd} and t_{CHUR} (Ga) calculated with $(^{147}\text{Sm}/^{144}\text{Nd})_{\text{CHUR}} = 0.1967$ and $(^{143}\text{Nd}/^{144}\text{Nd})_{\text{CHUR}} = 0.512638$; $\epsilon_{\text{Nd}(t)}$ calculated at age of UHT metamorphism.

^d t_{DM} (Ga) = $(1/\lambda_{147}) * \ln[((^{143}\text{Nd}/^{144}\text{Nd})_{\text{sample}} - (^{143}\text{Nd}/^{144}\text{Nd})_{\text{DM}}) / ((^{147}\text{Sm}/^{144}\text{Nd})_{\text{sample}} - (^{147}\text{Sm}/^{144}\text{Nd})_{\text{DM}}) + 1]$; present-day $(^{143}\text{Nd}/^{144}\text{Nd})_{\text{DM}} = 0.513151$, $(^{147}\text{Sm}/^{144}\text{Nd})_{\text{DM}} = 0.2137$.

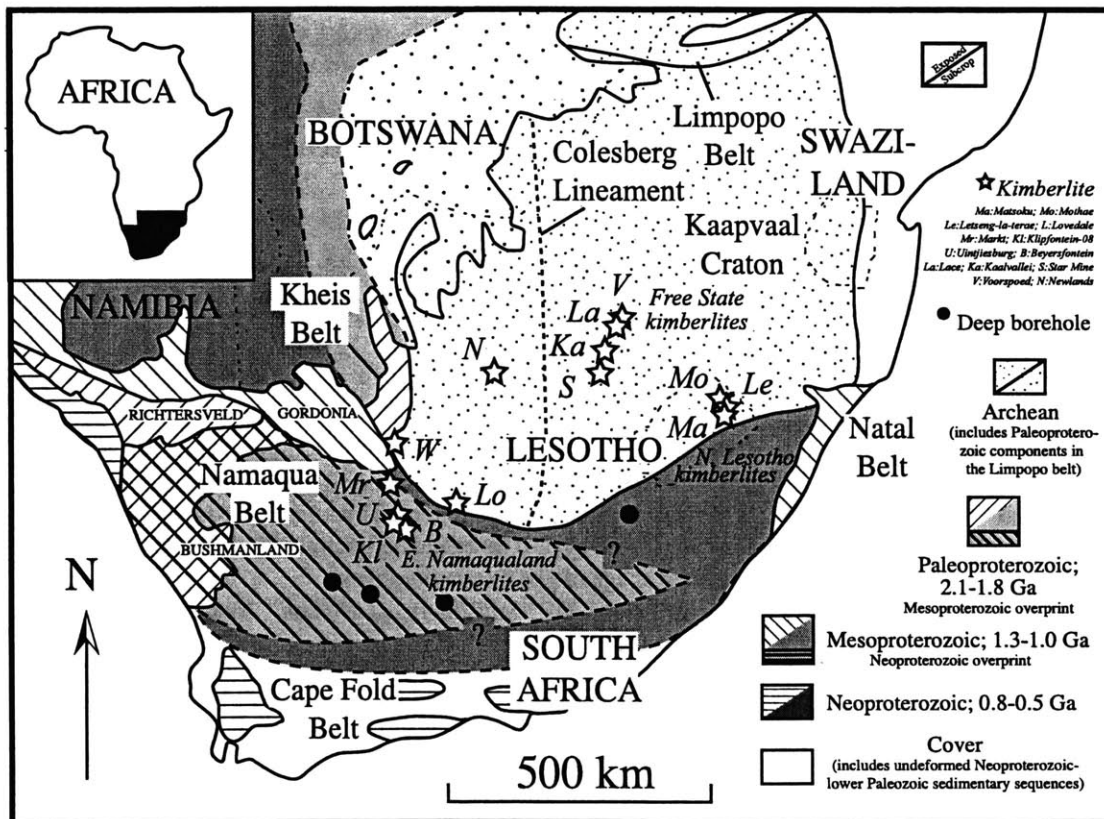


Figure 1. Tectonic map of southern Africa illustrating the distribution of Archean and Proterozoic crust, bounding tectonic structures, and the distribution of kimberlite fields within which significant quantities of lower crustal granulites are recovered. The Free State kimberlites represent the only group within the craton where abundant garnet-bearing granulites are exhumed.

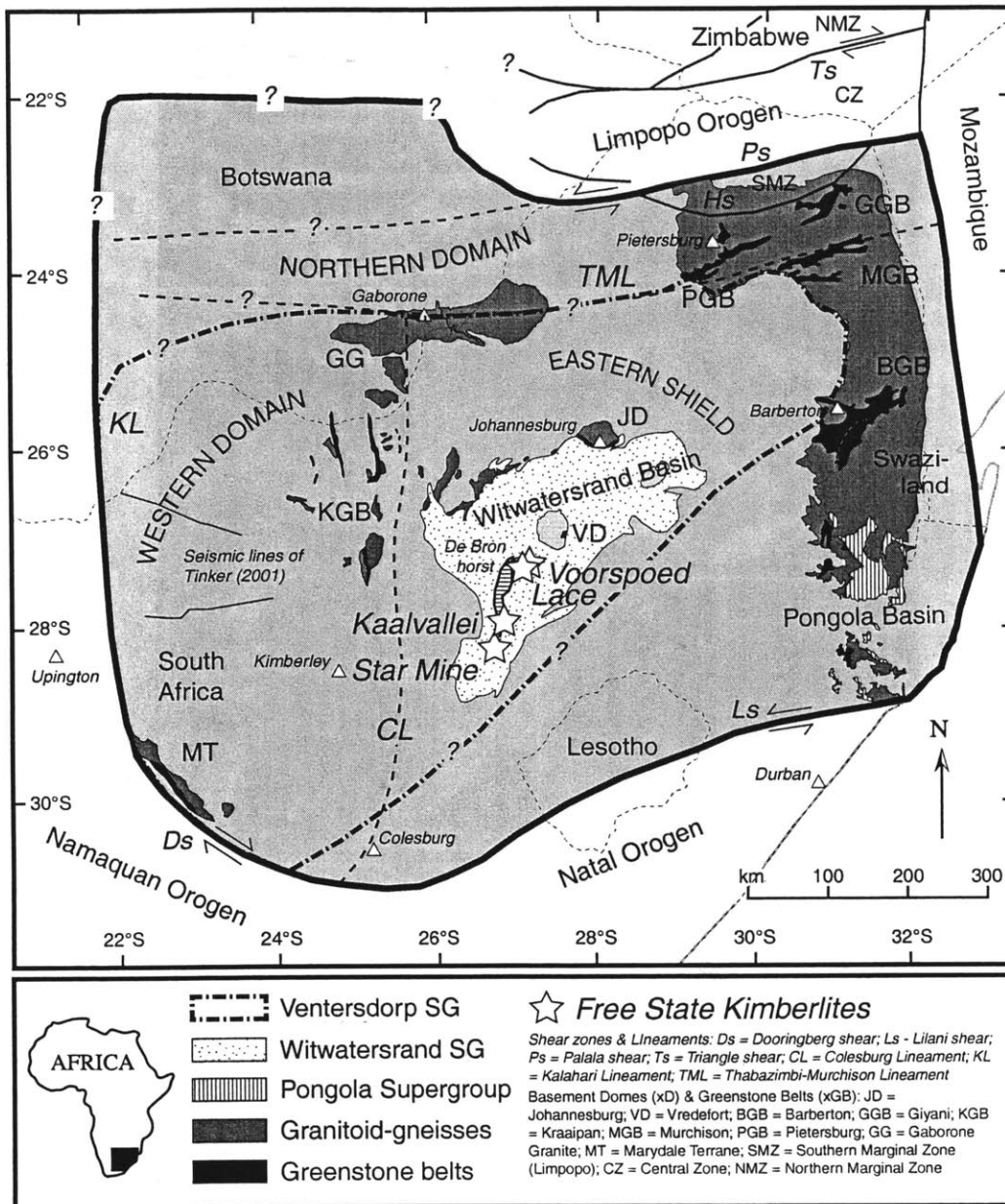


Figure 2. Simplified geologic map of the Kaapvaal craton, showing the location of the Free State kimberlites relative to the locations of exposed Paleo- to Neoproterozoic crystalline basement throughout the Kaapvaal craton, major tectonic boundaries, and the present distributions of sediments and volcanics of the Mesoproterozoic to Neoproterozoic Pongola, Witwatersrand, and Ventersdorp basins. The Free State kimberlites erupted in the Late Mesozoic to the east of the ca 2.9 Ga Colesburg Lineament (CL), separating the eastern Kaapvaal shield from a western domain, and in the vicinity of the De Bron Horst, a 2.7 Ga Ventersdorp extensional structure.

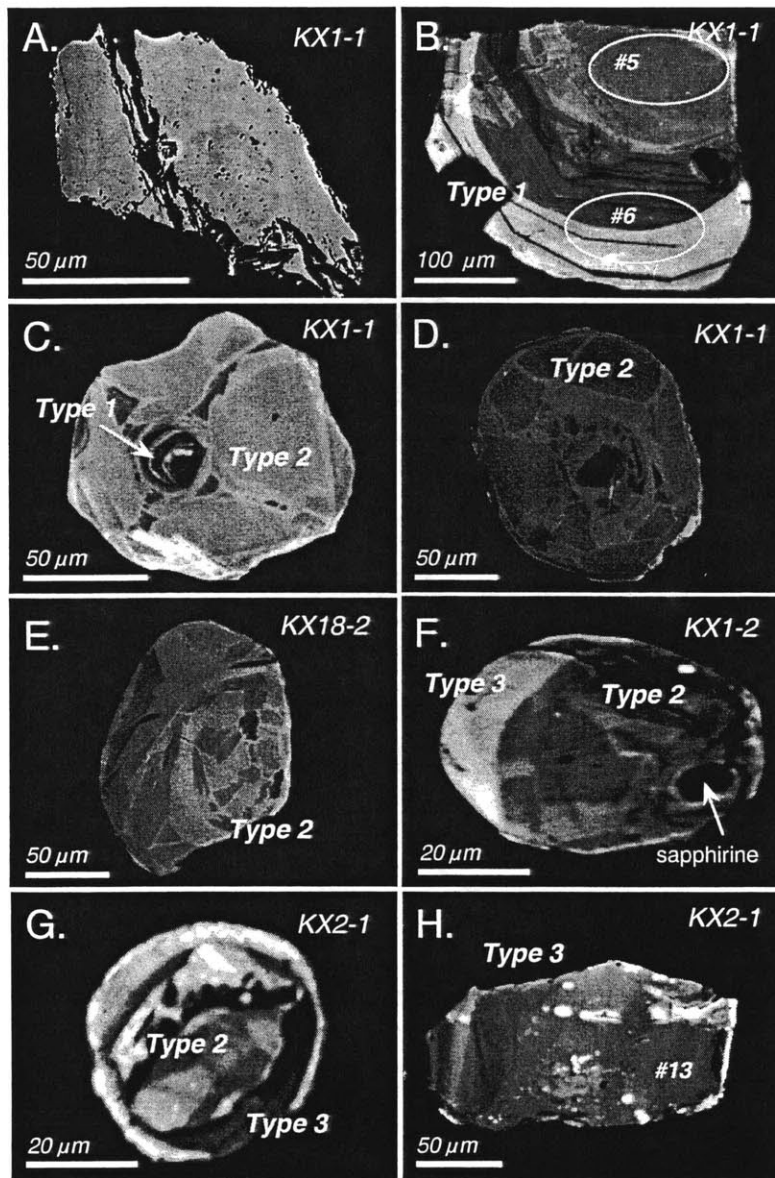


Figure 3. Back-scattered electron (BSE) image of monazite and cathodoluminescence (CL) images of zircon from UHT granulites of the Free State kimberlites. A) monazite grain exhibiting weak zonation with a dark Th-poor core and bright Th-rich rim; B) Type 1 discrete zircon grain illustrating a monotonous core with an oscillatory zoned mantle, ellipses with numbers indicate sampled domains within grain; C-D) Type 2 sector-zoned zircon with small resorbed cores of Type 1 zircon; E) sector-zoned Type 2 zircon; F-G) Type 2 sector-zoned zircon showing resorption and overgrowth by Type 3 zircon, Type 2 zircon in F contains a rare inclusion of sapphire; H) anhedral wispy-zoned Type 3 zircon from abundant population in KX2-1 (bright spots are artifacts of surface charging), this grain was extracted, abraded and analyzed as analysis #13.

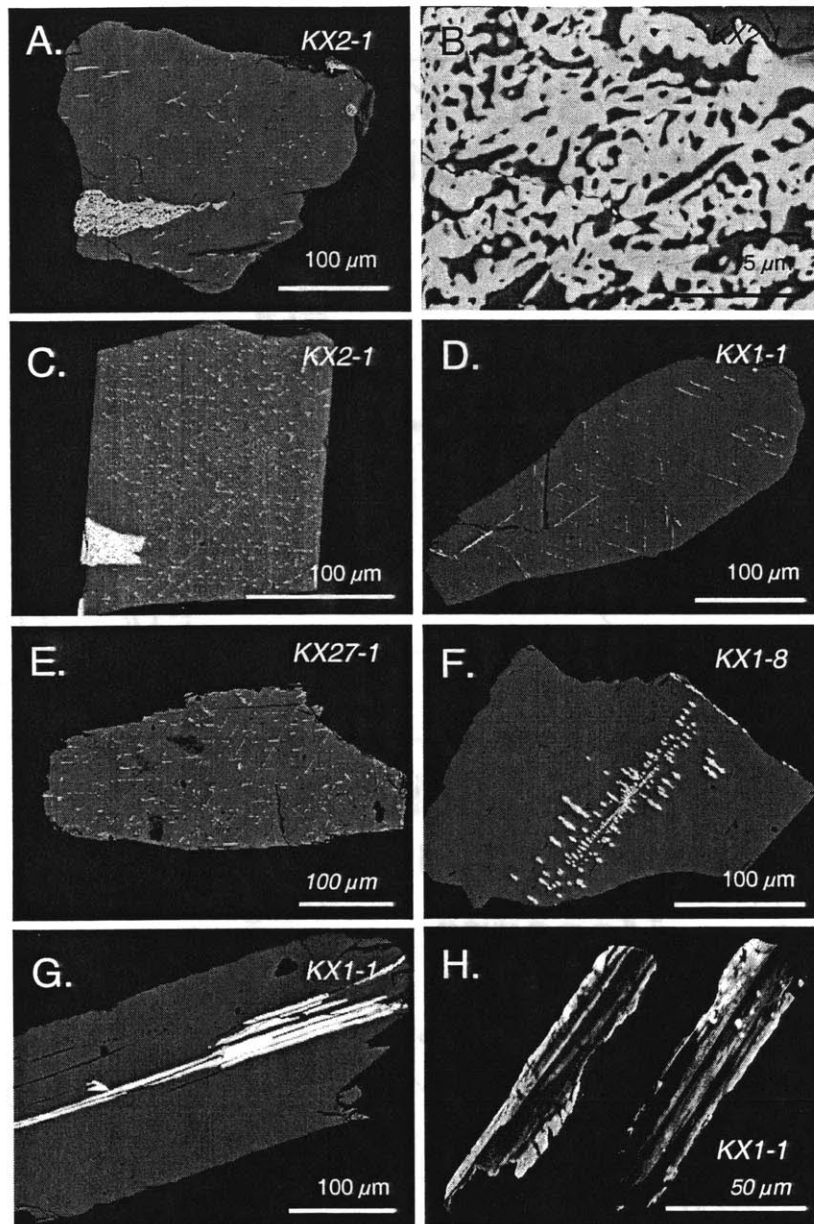


Figure 4. BSE and CL images of rutile grains (dark phase) from the Free State kimberlite UHT granulites, illustrating a variety of reaction textures with zircon (bright phase). A) acicular Type 5 zircon lamellae and Type 4 "graphic" zircon-rutile intergrowth within a host rutile crystal; B) close up of Type 4 graphic intergrowth; C-E) rutile grains with dispersed needle-shaped lamellae oriented on {011} and {110}, C also contains a Type 4 graphic intergrowth; F) thicker lamellar plates with diamond-shaped cross sections, illustrating merging of individual lamellae into thicker plates; G) thick platy lamellae restricted to center of grain and along {110}, note in both F and G host rutile is free of fine acicular lamellae; H) CL images of two lamellae fragments illustrating fine zonation parallel to elongation direction.

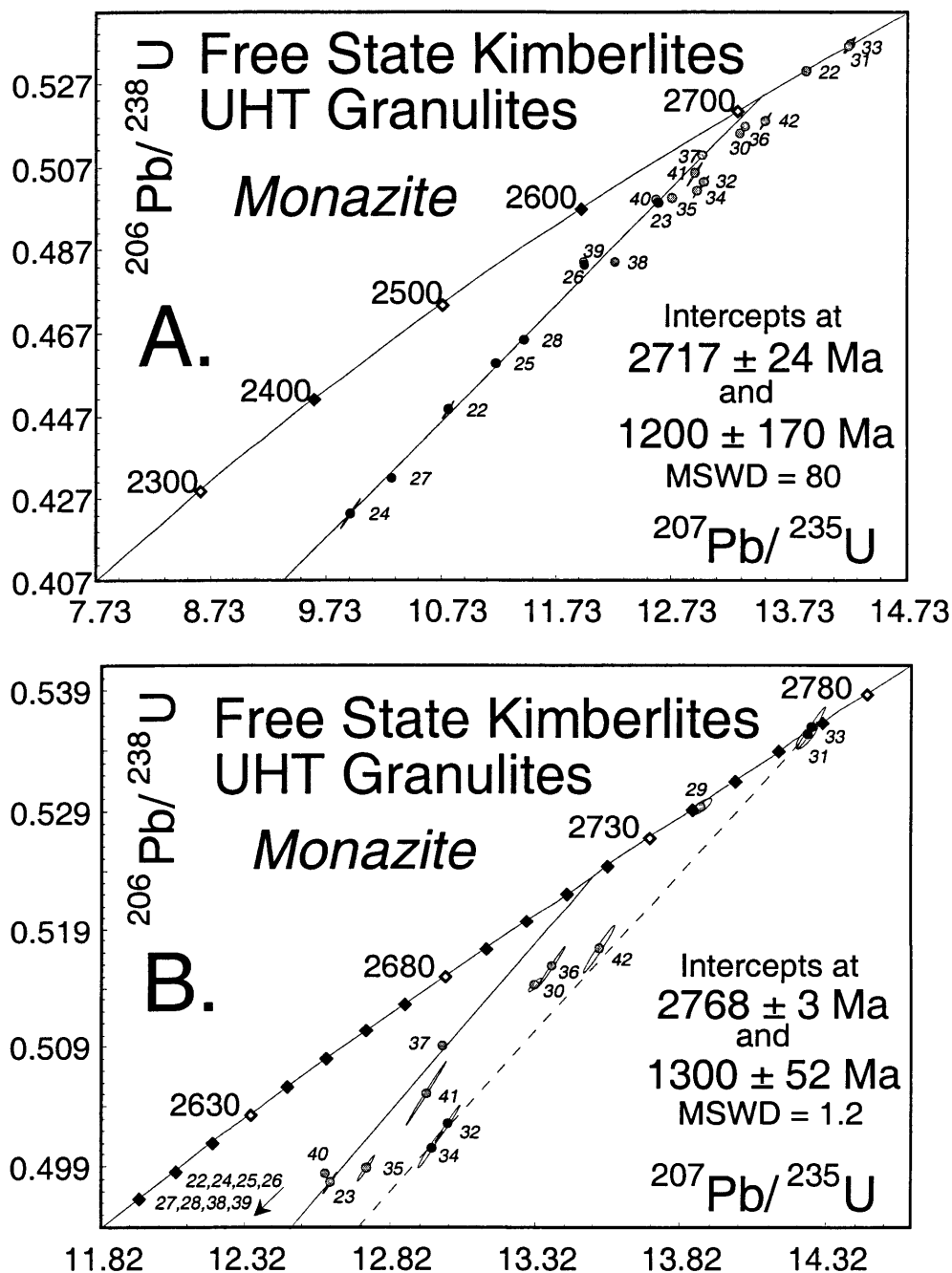


Figure 5. U-Pb concordia diagram illustrating data for monazite grains from four samples of UHT granulite. Numbers labeling each sample ellipse are referenced to Table 1. A) All monazite data for UHT granulites, note significant discordance of KX1-1 monazites, to which the plotted discordia line is fit, and the Mesoproterozoic lower intercept of the discordia; B) enlargement of A, solid line is discordia for KX1-1 monazites, while dashed line is discordia fit to four oldest monazites from KX18-2.

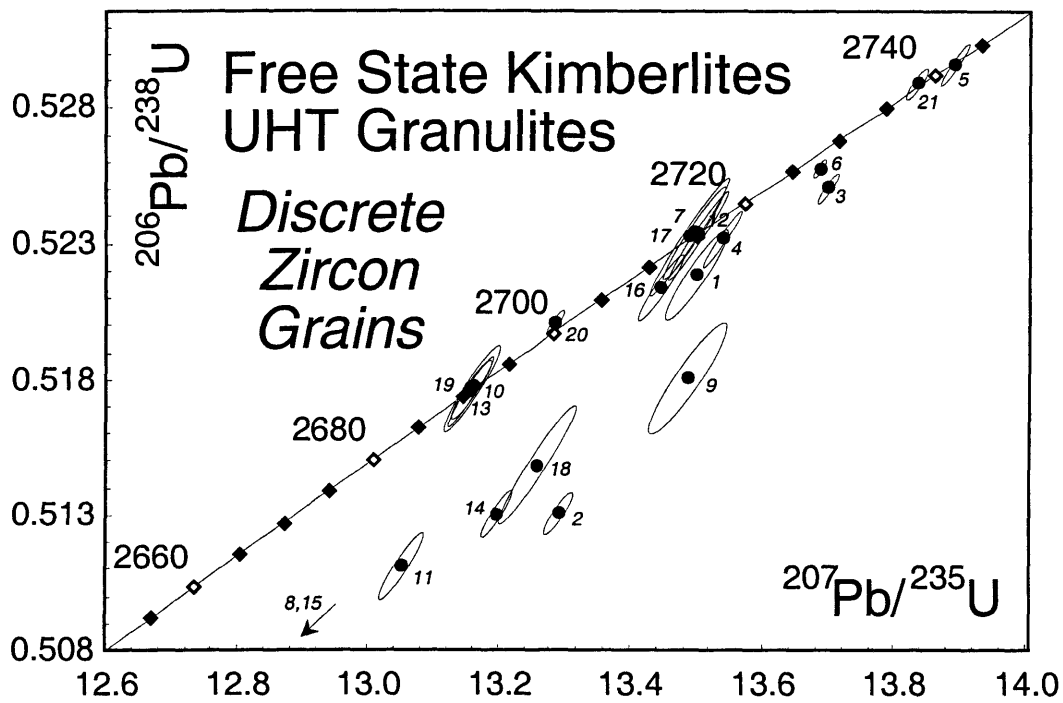


Figure 6. U-Pb concordia diagram illustrating data for discrete zircon grains from six samples of UHT granulite. Numbers labeling each sample ellipse are referenced to Table 1.

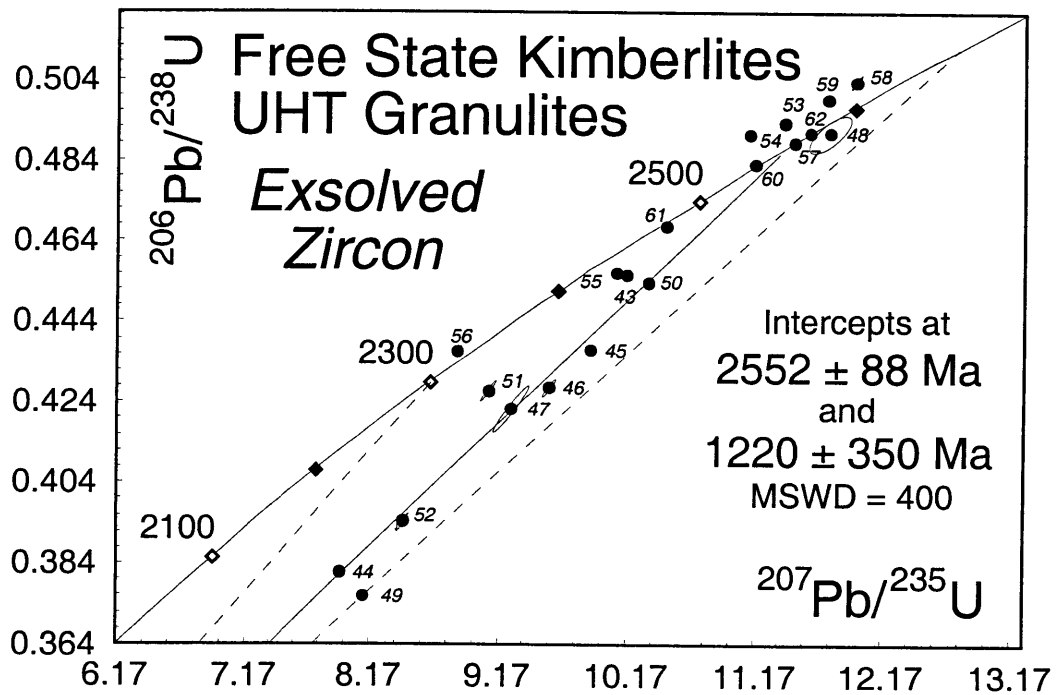


Figure 7. U-Pb concordia diagram illustrating data for zircon exsolution lamellae in rutile from three samples of UHT granulite. Numbers labeling each sample ellipse are referenced to Table 1. Solid line is discordia fit to lamellae from KX1-1, note the Mesoproterozoic lower intercept. Dashed lines are reference discordias from 1.2 Ga through bracketing lamellae.

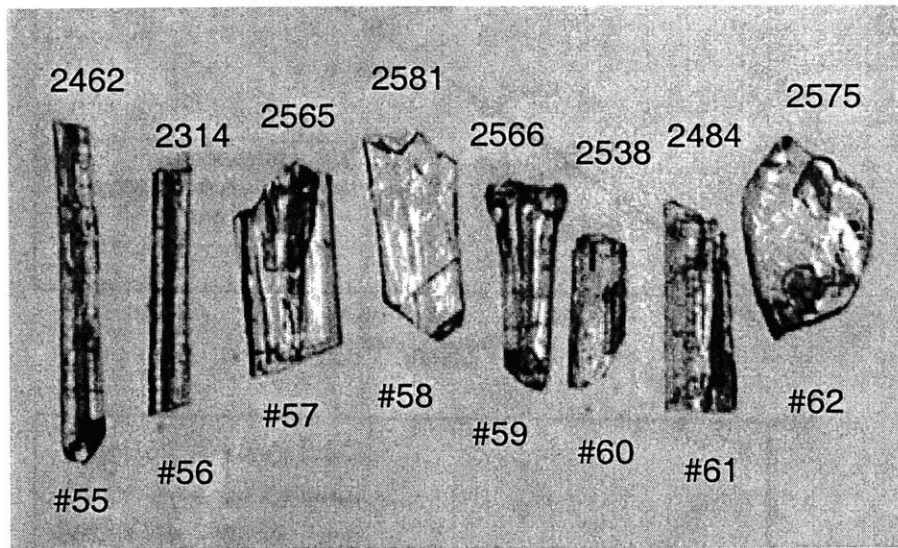


Figure 8. Photomicrograph of individual zircon lamellae prior to analysis, with resulting $^{207}\text{Pb}/^{206}\text{Pb}$ dates above each grain, illustrating the generally older dates for thick platy lamellae and younger dates for thinner needles.

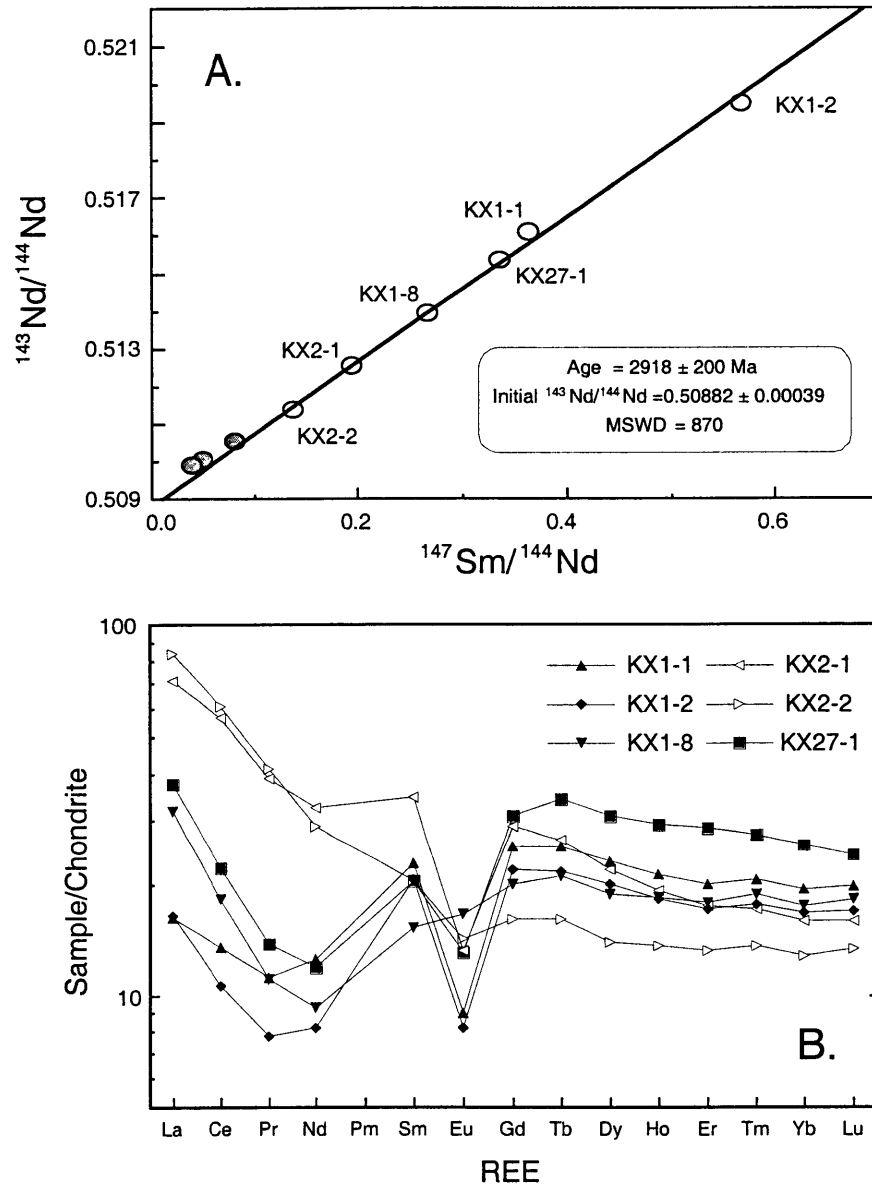


Figure 9. A) Sm-Nd isotope correlation diagram for monazite (shaded) and whole rock (open) UHT granulite samples; B) chondrite-normalized rare earth element patterns for UHT granulites.

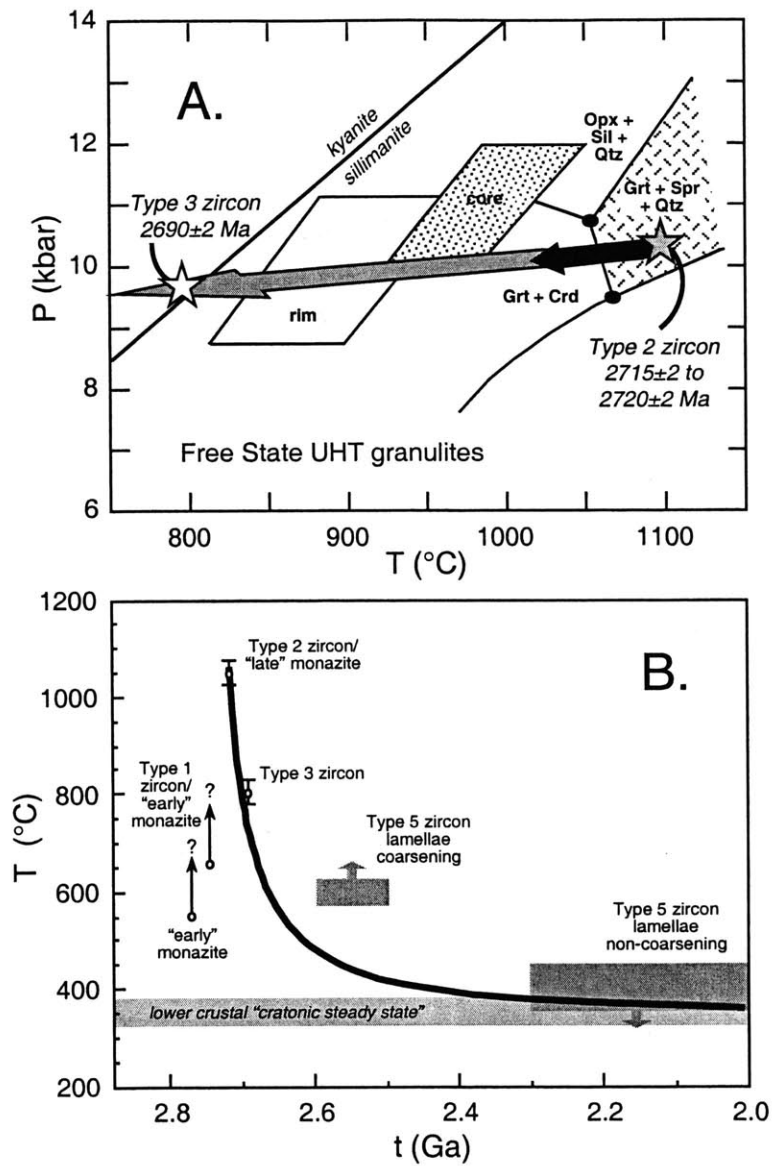


Figure 10. A) Pressure-temperature diagram for sapphirine granulites, redrawn from Dawson et al., 1997. FMAS stability fields from Bertrand et al. (1991); rhombic fields represent garnet-orthopyroxene core and rim equilibration conditions based on Al-solubility geothermobarometer of Harley & Green (1982). Shaded star indicates age constraint on UHT conditions from Type 2 zircon and late monazite, open star indicates age constraint from Type 3 zircon associated with kyanite-bearing leucosomes; B) Temperature-time diagram illustrating the accessory mineral geochronological constraints relative to temperature estimates for their crystallization. Direction of arrow on some points indicates maximum or minimum temperature constraint. Curve is the modeled cooling path at 35 km predicted from conductive relaxation of a "triangular" perturbation to 250 km thick lithosphere ($\Delta T=850^{\circ}\text{C}$ at 50 km) which generates temperatures of $>1000^{\circ}\text{C}$ at 10 kbar (Vitarello and Pollack, 1980).

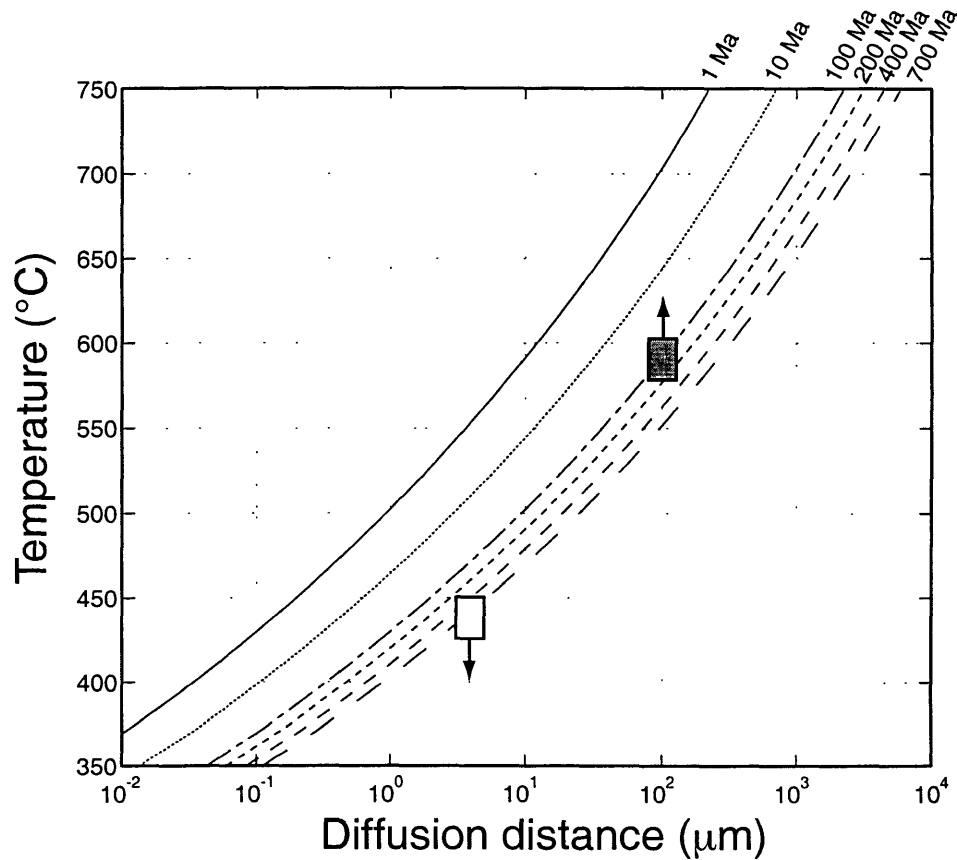


Figure 11. Curves of Zr diffusion length scale in rutile as a function of temperature for various diffusion times. Kinetic data for Zr diffusion in rutile ($E_a=288$ kJ/mol; $D_0=8.38 \times 10^{-7}$ m²/s) from Sasaki et al. (1985). Filled box indicates minimum temperatures required for Zr to diffuse 100 μm on time scales of 100-200 million years as appropriate to the measured ages of coarsened platy rutile lamellae. Open box indicates maximum temperatures allowable for limiting Zr diffusion to <5 μm over time scales >200 million years, as appropriate to preserving fine lamellar needles of zircon in some rutile.

Chapter 4.

Constraints on the thermal evolution of continental lithosphere from U-Pb accessory mineral thermochronology of lower crustal xenoliths, southern Africa

Keywords: lower crust, xenoliths, rutile, apatite, titanite, U-Pb, geochronology, thermochronology, Kaapvaal Craton, southern Africa, continental geotherms, Proterozoic, Archean

Abstract—U-Pb isotopic thermochronometry of rutile, apatite and titanite from lower crustal granulite xenoliths has been used to constrain the thermal evolution of Archean cratonic and Proterozoic off-craton lithosphere beneath southern Africa. The relatively low closure temperature of the U-Pb rutile thermochronometer (~400°C) allows its use as a particularly sensitive recorder of the establishment of “cratonic” lithospheric geotherms, as well as subsequent thermal perturbations to the lithosphere. Contrasting lower crustal thermal histories are revealed between cratonic and off-craton regions. Lower crustal granulites exhumed in the Jurassic to Cretaceous kimberlites of the central Kaapvaal Craton contain rutile grown under Neoproterozoic granulite-facies conditions, but which yield much younger and discordant U-Pb ages, indicative of at least two episodes of Paleoproterozoic and Mesoproterozoic isotopic resetting by thermal perturbations apparently affecting the deep crust of much of the cratonic nucleus. In contrast, rutile from Mesoproterozoic granulite xenoliths at the craton margins and bounding Natal, Namaqua, and Magondi orogenic belts define discordia arrays with Neoproterozoic upper intercepts and lower intercepts equivalent to the eruption age of the host kimberlite. When combined with U-Pb data for co-existing titanite (near concordant dates of 870 to 890 Ma) and apatite (discordant Neoproterozoic dates), these results may be modeled and interpreted as a record of slow cooling through titanite, apatite and rutile closure intervals at a consistent rate of approximately 1°C/m.y. following Mesoproterozoic high-grade metamorphism, followed by variable Pb loss in the apatite and rutile systems during a thermal perturbation to the lower crust in the Mesozoic. Modeling of this latter Pb loss during a square pulse Mesozoic heating event constrains the temperature and duration of this heating to ≤550°C for >100 k.y. to tens of millions of years. This result indicates that the thermal perturbation is not solely related to kimberlite magmatism but is a broader manifestation of heating related to mantle upwelling and rifting of Gondwana during the Late Jurassic to Cretaceous.

The implications of this lower crustal thermochronology are two-fold. First, as closure of the rutile thermochronometer in the lower crust signals the establishment of a “cratonic” conductive geotherm, the fact that “off-craton” Proterozoic lower crust reached temperatures $<400^{\circ}\text{C}$ requires that the deeper lithospheric profile was essentially cratonic from the Neoproterozoic through to the Late Jurassic. A cratonic geotherm in these “off-craton” regions necessitates similar lithospheric thickness and potential for diamond stability beneath *both* Proterozoic and Archean domains of southern Africa. Higher surface heat flow in the Proterozoic terrains is not due to a thinner lithospheric boundary layer, but is instead the result of heterogeneously elevated crustal radiogenic heat production, and possible transient thermal effects related to the aforementioned Mesozoic heating of the lithosphere. Second, the late partial thermal resetting of U-Pb rutile systematics in off-craton lower crustal xenoliths is independent evidence of a transient thermal modification of the lithosphere of southern Africa in the Mesozoic. The manifestation of this thermal pulse in the lower crust is spatially and temporally correlated with both anomalously elevated Cretaceous paleogeotherms (with respect to a cratonic geotherm) defined by mantle xenoliths from the off-craton Proterozoic orogenic belts, as well as kinked paleogeotherms and evidence for metasomatic modification in cratonic mantle peridotite suites. It is argued that most of the geographic differences in lithospheric thermal structure inferred from mantle xenolith thermobarometry are due to the heterogeneous propagation of a broad upper mantle thermal anomaly into the southern African lithosphere. The heterogeneous manifestation of heating between cratonic margin and cratonic interior implies a similar heterogeneity in heat transport through the continental lithosphere, and is perhaps indicative of the importance of advective heat transport along pre-existing lithosphere-scale discontinuities. It is suggested that kimberlite magmatism is a similarly complex manifestation of the spatial and time-dependent response to this Late Mesozoic thermal perturbation.

1. Introduction

The thermal structure of continental lithosphere can be only indirectly modeled from measurement of surface heat flow and models of lithospheric thermal conductivity structure and the distribution of radiogenic heat producing elements (Chapman and Pollack, 1977; Morgan, 1984; Rudnick et al., 1998). Such models are subject to the steady-state assumption, and while they may provide a snapshot of the present thermal state of the lithosphere, they specifically fail

to capture time-dependent phenomena. Inferences on the thermal *evolution* of the deeper continental lithosphere are most commonly drawn from the construction of paleogeotherms from quantitative thermobarometry of volcanically erupted mantle xenoliths (Boyd, 1973; Finnerty and Boyd, 1987). However, mantle xenolith thermobarometry also relies upon the assumption that the samples analyzed are open systems in steady-state thermal equilibrium until their quenching upon eruption, and thus recover the thermal state of the lithosphere at the time of volcanic entrainment. Again, this technique provides a single, albeit ancient, snapshot of the lithospheric thermal state, and one which is potentially altered by the very thermal event which brings the mantle-derived samples to the surface.

By contrast, the technique of radiogenic isotope thermochronology, a synthesis of isotopic geochronology, petrology, and kinetic theory (Dodson, 1973), is predicated upon non-steady-state kinetic phenomenon, and can provide quantitative constraints on the time-temperature paths of samples of the lithosphere which have passed through the closure temperatures of various mineral-isotopic chronometers. Thermochronological methods have been successfully applied for decades to upper and middle crustal rocks, particularly to develop an understanding of the evolution of orogenic belts from the Phanerozoic to the Archean (Hodges, 1991; Harrison et al., 1993; Spear and Parrish, 1996; Corfu and Easton, 2000). Thermochronology has also been used to examine the evolution of exposed high grade granulite terrains, to establish the mechanisms of granulite-facies metamorphism and subsequent exhumation (Mezger et al., 1993; Cox et al., 1998; Möller et al., 2000; Willigers et al., 2001). Yet despite its potential, radiometric thermochronology has only rarely been applied to xenolithic samples of the lower crust, which have the potential to record a prolonged lithospheric thermal evolution prior to later volcanic entrainment and eruption (see Davis, 1997 for an exception).

Such information on the thermal evolution of the lower crust serves as a vital link between the evolution of the continental crust and the underlying mantle lithosphere. Because of the low heat production and requisite shallow temperature gradients in the mantle lithosphere compared to the crust, measurements of lower crustal paleotemperatures provide strong constraints on the thermal structure of the underlying lithosphere, particularly in the conductive regime (Figure 1). In simple scenarios, lower crustal thermochronology may record the progressive cooling of the lithosphere following major tectonomagmatic events, placing

constraints on the timescales of establishment of the shallow geotherms which typify the cratonic interiors of continents. In regions of more complex thermal history, lower crustal thermochronology may reveal spatial and temporal heterogeneity in the response of the lithosphere to heat transfer from the convecting mantle.

Of the available mineral-isotopic thermochronometers, the U-Pb system in accessory minerals has unique advantages in lower crustal rocks. A variety of U-rich accessory minerals, including zircon, monazite, titanite, apatite and rutile, are stable at the high grade metamorphic conditions which are typical of the formation of the lower crust. These accessory minerals in turn have a wide range of nominal closure temperatures for Pb volume diffusion (Figure 2), ranging from $>1000^{\circ}\text{C}$ for zircon and monazite, to approximately 400°C for rutile. This dynamic range is uniquely appropriate to elucidating the thermal evolution of the deep crust, as temperatures of formation of lower crustal assemblages are typically slightly lower than those of zircon and monazite closure, such that these accessory minerals record their time of growth at high grade metamorphic conditions. On the other hand, temperatures on the order of 350 to 400°C are predicted for the base of the crust in steady-state cratonic thermal regimes where surface heat flow is as low as 40 mW/m^2 ; thus isotopic closure of minerals like apatite and rutile should be attained in this end member lithospheric thermal state (Figure 1).

In addition to the uniquely suited kinetic properties of these accessory minerals, the advantages of the coupled U-Pb decay schemes can be brought to bear in these minerals. Assessment of the U-Pb isotopic concordance of mineral systems not only quantifies the accuracy of the inferred growth or cooling ages, but also serves to reveal and distinguish between continuous versus punctuated thermal histories (as detailed in Section 7.1). Continuously cooled systems preserve near-concordance, and can be integrated to yield detailed cooling histories for the deep lithosphere. Systems affected by punctuated thermal events undergo episodic Pb loss, which is manifested as discordant isotopic systematics. Careful examination of the patterns of discordance, however, allow us to “see through” thermal events late in the history of such samples to the earlier cooling history of the lower crust. At the same time, by the application of suitable kinetic parameters, modeling of these discordant U-Pb data can provide details of the magnitude and duration of the late thermal perturbations affecting the lower crust.

The southern African continent provides a unique opportunity to map the thermal evolution of Archean to Proterozoic lithosphere through lower crustal thermochronology, due to

the abundant sampling of the lower crust by kimberlite magmatism in the Late Mesozoic. High pressure granulite xenoliths from geographically diverse regions of the Archean craton and bounding Proterozoic orogenic belts have been examined using U-Pb accessory mineral geochronology, to establish their timing of formation and subsequent cooling history. This contribution focuses on the systematics of lower temperature thermochronometers, and the valuable information on the thermal history of the deep crust which these minerals preserve.

2. Pb diffusion in accessory minerals

In order to use the U-Pb systematics of various accessory minerals as thermochronometers, it is necessary to develop an understanding of the thermally-activated diffusivities of U and Pb in these structures. Both empirical field studies and experimental data yield constraints on rates of volume diffusion of parent and daughter atoms in these minerals, and where the results of these two methods agree, a high degree of confidence may be assumed for a given mineral-isotopic thermochronometer. The majority of cation diffusion experiments on accessory minerals have been accomplished in a single laboratory by D. Cherniak and coworkers over past decade, leading to a high quality database of diffusion parameters for zircon (Cherniak and Watson, 2001), monazite (Cherniak et al., 2000), titanite (Cherniak, 1993), apatite (Cherniak et al., 1991), and rutile (Cherniak, 2000). Using the methodology of Dodson (1973), these diffusion parameters may be transformed for a given linear cooling rate, geometry, and diffusion dimension, into an isotopic closure temperature (T_c) for Pb diffusion. The closure age of a mineral-isotopic system is similarly defined as the time of passage through its closure temperature. Two caveats to these experimental studies are whether induced concentration gradients in experiments represent volume diffusive phenomena, and also the applicability of the commonly-used synthetic, or gem-quality megacrystic mineral specimens, for reproducing natural mineral-isotopic systems.

In complement to experimental data, comparative and semi-quantitative estimates of accessory mineral U-Pb closure temperatures have been inverted from geochronological and thermometric data for rocks of known cooling history (Mezger, 1989; Heaman and Parrish, 1991). These field-based empirical studies have developed a consistent accessory mineral Pb diffusivity series: zircon, monazite, titanite, apatite, rutile. Zircon and monazite exhibit the highest T_c for Pb diffusion; as a result these minerals often crystallize below their closure

temperatures, thus recording crystallization ages in their U-Pb systematics. The accessory minerals titanite, apatite, and rutile commonly manifest their progressively lower closure temperatures through correspondingly younger closure ages in coexisting slowly cooled mineral suites (Mattinson, 1978; Willigers et al., 2001). Caveats to these field-based studies include whether the minerals studied crystallized above their closure temperature, whether Pb loss was due to thermally-activated volume diffusion, and if cooling rate was slow enough to generate analytically discernable age differences between minerals of differing closure temperature.

There is substantial agreement between field and experimental estimates of T_c for Pb volume diffusion in most accessory minerals. Experimental studies (Cherniak et al., 2000; Cherniak and Watson 2001) have demonstrated the very low diffusivities of Pb in zircon and more recently monazite, with estimates of nominal closure temperatures of $>1000^\circ\text{C}$ for these minerals. These closure temperatures are consistent with the preservation of ancient radiogenic Pb in zircons and monazites incorporated into crustal melts with temperatures in excess of 800 to 900°C and in protolithic crystals exposed to high-grade metamorphism in excess of the same temperatures. The new experimental results for monazite in particular resolve a outstanding debate regarding its closure temperature. Former measurements of relatively fast Pb diffusivity in monazite (Suzuki, 1994; Smith and Giletti, 1997) with a corresponding closure temperature of $\sim 700^\circ\text{C}$, were at odds with the recognition of anomalously old monazite ages in high temperature granulites— ages at times older than coexisting zircon (Spear and Parrish, 1996; Crowley and Ghent, 1999; Schaltegger et al., 1999)— suggesting a much higher closure temperature for the light rare earth phosphate.

The mineral titanite was demonstrated from field studies to have a range of U-Pb T_c from 550 to 650°C (Hanson et al., 1971; Tucker et al., 1986; Mezger et al., 1991). These estimates are in excellent agreement with the experiment results of Cherniak (1993), whose Pb diffusivities predict the same closure temperatures for diffusive radii ranging from 50 to 500 μm in slowly cooled rocks (Figure 2). Similarly, U-Pb geochronological studies of a variety of occurrences of apatite (Krogstad and Walker, 1994; Corfu and Stone, 1998; Chamberlain and Bowring, 2001) infer a range of closure temperatures for Pb diffusion in apatite from 450 to 550°C , which agrees well with the predictions of the experimental kinetic data of Cherniak et al. (1991) for diffusive radii from 50 to 500 μm . Empirical and experimental closure temperatures for titanite and apatite are also consistent with those predicted from theoretical considerations of crystal

chemistry and ionic porosity (Dahl, 1997). Figure 2 presents curves of bulk T_c as a function of diffusive radius for a variety of U-Pb and K-Ar ($^{40}\text{Ar}/^{39}\text{Ar}$) mineral-isotopic thermochronometers, assuming a slow cooling rate of $1^\circ\text{C}/\text{Ma}$ and utilizing the available experimental kinetic data (see references in Figure 2 caption). To the right of those curves we plot the ranges in applicable T_c for common grain sizes of the various minerals in metamorphic rocks. Rather than relying upon a singular nominal closure temperature, this method of presentation emphasizes the range in potential T_c exhibited by various minerals; we consider this emphasis important due to the enhanced sensitivity of T_c to the diffusive radius for slow cooling rates (Dodson, 1973), such as are commonly inferred for isobarically cooled granulite terrains and xenoliths. The closure temperatures for titanite, apatite, and hornblende referred to in later discussions are extracted from these curves and the appropriate grain sizes of the minerals under consideration (Table 1).

Estimates of Pb diffusivity in rutile present the only striking experimental versus empirical conundrum. An overwhelming number of field-based empirical studies of rutile thermochronological systematics from slowly cooled terrains demonstrate younger rutile ages relative to coexisting titanite (Schärer et al., 1986; Mezger et al., 1989; Corfu and Easton, 1995; Cox et al., 1998; Christofel et al., 1999; Connelly et al., 2000; Norcross et al., 2000; Möller et al., 2000; Bibikova et al., 2001; De Wit et al., 2001). Rare published instances where concordant titanite and rutile ages are apparently preserved are in rapidly cooled terranes (e.g. Santos Zalduegui et al., 1996), and even in these instances it is unclear whether titanite did not grow below its closure temperature. Mezger et al. (1989) inferred a grain-size dependent closure temperature of $380\text{-}420^\circ\text{C}$ for granulite-facies metamorphic rutile (see “field” dots in Figure 2), by comparison to cooling curves defined by other U-Pb, Rb-Sr, and K-Ar ($^{40}\text{Ar}/^{39}\text{Ar}$) thermochronometers. A survey of the literature reveals that rutile systematically yields ages similar or slightly younger than K-Ar and $^{40}\text{Ar}/^{39}\text{Ar}$ ages for hornblende, which has a range of compositionally dependent closure temperatures from 450 to 550°C (Figure 2; Harrison, 1981). On the other hand, rutile U-Pb ages are older than K-Ar and $^{40}\text{Ar}/^{39}\text{Ar}$ cooling ages for biotite (Mezger et al., 1989; Moller et al., 2000), a mineral-isotopic system with a compositionally-dependent range in closure temperature from 300 to 400°C (Giletti, 1974; Dahl, 1996; Grove and Harrison, 1996).

In contrast, recent experiments by Cherniak (2000) recover kinetic data suggesting Pb diffusivity in rutile comparable, or even slower than in titanite (“experimental” curve in Figure

2). Corresponding closure temperatures predicted from these data lie in the range of 600 \pm 50°C— much higher than the field based estimates of 400 \pm 20°C. The causes of the substantial disagreement between experiment and observation remain unclear. Compositional dependence of Pb diffusion rates was tentatively tested by Cherniak, who demonstrated similar diffusivities for two synthetic and natural samples of differing composition. There remains however considerable uncertainty regarding the lattice diffusion mechanisms for Pb transport through the rutile structure. As a result, the effects of water on Pb diffusivity are essentially unknown, as are the role of defect distributions in natural samples, neither of which were directly examined in the experiments of Cherniak (2000). Also, the possibility of diffusive anisotropy for Pb in rutile, as is observed for smaller cations, requires further examination. These issues appear to compromise the applicability of the current experimental rutile Pb diffusivity parameters to natural samples.

Until the causes of incongruity between laboratory and field estimates of Pb diffusivity in rutile are resolved, we feel compelled to rely on well-bracketed field-based closure temperature estimates (Figure 2). The form of the T_c curve for rutile is assumed to be subparallel to the other mineral T_c functions, and is constrained to pass through the rutile “field” estimates. Bracketing of the rutile T_c also allows us to define proxies for Pb diffusivity in rutile based on comparison with other thermochronometers. A lower-limiting proxy is the diffusivity of Ar in phlogopite, which yields very similar or only slightly lower closure temperatures in experimental and thermochronological studies (Giletti, 1979; Jenkin et al., 2001). Another possible upper-limiting proxy is Pb diffusion in apatite (Figure 2), which does demonstrate self-consistency between field and laboratory data and, as will be shown in this study, yields cooling ages only slightly older than rutile. Finally, a third proxy for Pb diffusion in rutile are experimentally measured coefficients for Ti self-diffusion in rutile (Freer, 1980), which yield a T_c function consistent with the field-based estimates of Pb closure temperature (dashed curve in Figure 2). We use the Ti self-diffusion constants as the preferred estimators of Pb diffusion in rutile in Section 7.2.4, for quantitative modeling of the rutile systematics of lower crustal granulites from the craton-margins and off-craton regions of southern Africa.

3. Geological setting and character of lower crustal xenoliths

U-Pb accessory mineral thermochronological data were obtained from suites of lower crustal granulite xenoliths entrained in Late Jurassic to Late Cretaceous kimberlites from the Archean Kaapvaal Craton and bounding Proterozoic orogenic belts of southern Africa. On-craton Archean granulite suites include those from the Newlands kimberlite of the Barkly West cluster (Kimberley region), and the Lace, Voorspoed, Kaalvallei, and Star kimberlites of the Free State province. Proterozoic off-craton and craton-margin suites include xenoliths from the Orapa kimberlite in the Magondi belt of north-central Botswana (north of the Kaapvaal craton and west of the Zimbabwe craton); the Letseng-la-Terae, Matsoku, and Mothae kimberlites of Northern Lesotho, at the southern boundary of the Kaapvaal craton with the Natal orogenic belt; and the Markt, Lovedale, Klipfontein-08, Beyersfontein, and Uintjiesberg kimberlites on the western boundary of the Kaapvaal with the eastern Namaqualand orogenic belt (Figure 3).

The Group 2, 114 Ma Newlands kimberlite (Smith et al., 1985) erupted through Mesoarchean crust of the Kimberley block of the Kaapvaal Craton, west of the Colesberg lineament, an inferred epicratonic lithospheric suture between younger western and older eastern crustal blocks. Terminal deformation and metamorphism accompanying the accretion of these blocks occurred at around 2.93 Ga, while later metamorphism related to intracratonic extension and eruption of the Ventersdorp Supergroup lavas affected the lower crust over a protracted interval between 2.74 and 2.69 Ga (Chapter 3). Metapelitic granulites from the Newlands kimberlite contain the assemblage $gt + bt + ky + sil + ksp + pl + qtz$ with accessory metamorphic zircon and monazite, which record both of these metamorphic perturbations to the lower crust. These granulites also contain ubiquitous rutile, which is found as inclusions in the major metamorphic minerals and as euhedral to subhedral, idiomorphic grains at mineral triple junctions, pointing to its crystallization during one or both of these Archean high grade metamorphic events.

The Free State kimberlites stretch over 150 km in a northeasterly array erupted through Mesoarchean crust east of the Colesberg lineament, in the central Kaapvaal craton. These volcanics comprise both Group 1 and 2 kimberlites, and were erupted asynchronously over tens of millions of years from 132 Ma (Lace, Voorspoed; Phillips et al., 1999) and 124 Ma (Star; McIntyre and Dawson, 1974) to 88 Ma (Kaalvallei; Viljoen, 1989). All of these kimberlites have entrained to the surface a unique and diverse suite of ultra-high temperature (UHT) $gt + qtz + sil +/- ky +/- opx +/- antiperthite +/- sapphirine$ granulites, which have been inferred to record

equilibration conditions of $>1000^{\circ}\text{C}$ and 10-12 kbar (Dawson and Smith, 1987; Dawson et al., 1997). Minor retrograde reactions in these xenoliths demonstrate essentially isobaric cooling, indicating their prolonged residence in the lower crust. The extreme metamorphic conditions recorded in these granulites are a lower crustal thermal response to Ventersdorp magmatism at 2.74 to 2.69 Ga, as dated by metamorphic zircon and monazite (Chapter 3). Rutile is an abundant accessory mineral in these samples, and is clearly a part of the UHT assemblage, being included in all major phases, particularly garnet, and residing as interstitial crystals at well-equilibrated grain triple junctions. Rutile from the UHT granulites also contains a unique reaction texture involving the exsolution of zircon; separated zircon lamellae yield ages of ~ 2.5 Ga (Chapter 3), which demands an Archean age for the host rutile and confirms its growth during the UHT metamorphic event.

In northern Botswana, the Orapa cluster comprises several Group 1, *ca* 93 Ma kimberlites (Davis, 1977), which erupted through inferred Archean Zimbabwe craton basement, subsequently reactivated during Magondi orogenesis at 2.0 Ga (Mapeo et al., 2001; Majaule et al., 2001). Lower crustal metaigneous $\text{gt} + \text{cpx}$ granulites and metapelitic $\text{gt} + \text{bt} + \text{ky} + \text{ksp} + \text{plag} + \text{qtz}$ granulites contain abundant metamorphic zircon and monazite which record high grade metamorphism at 2.0 Ga, as well as a poorly understood lower crustal event at 1.24 Ga, which may be related to outboard early Kibaran orogenesis (Ramokate et al., 2000). Rutile in these assemblages include large red equant idiomorphic grains of a range of sizes, demonstrably a component of the Paleoproterozoic high grade metamorphic assemblage, residing as inclusions in garnet and feldspar, and as equilibrated interstitial grains.

At the southern margin of the Kaapvaal craton, south of the inferred extension of the Tugela front beneath the Karoo lavas of the Lesotho highlands, and tens of kilometers north of the inferred suture between the craton and the Mesoproterozoic Natal orogenic belt at the Mzumbe lineament, the Group 1 Northern Lesotho kimberlites erupted between 95 Ma (Letsteng-la-Terae) and 87 Ma (Mothae) (Davis, 1977). These kimberlites entrained abundant lower crustal granulite xenoliths, including metaigneous $\text{gt} + \text{cpx} + \text{pl}$ granulite, and metapelitic $\text{gt} + \text{bt} + \text{aluminosilicate}$ assemblages. High grade metamorphic conditions for these granulites have been estimated at 800 to 900°C and 10-13 kbar (Griffin et al., 1979), while limited retrograde reactions indicate essentially isobaric cooling. Timing of the granulite-facies metamorphism of these samples is constrained by metamorphic zircon and monazite, which

record growth between 1.1 and 1.0 Ga (Chapter 2), demonstrating the link between lower crustal granulite genesis and crustal thickening during Natal collisional orogenesis. Rutile, and in some samples coexisting apatite and titanite, are found in these samples as inclusions in the major metamorphic minerals, and/or as interstitial grains, and are inferred to have grown during Mesoproterozoic granulite facies metamorphism.

At the western margin of the Kaapvaal craton, along its contact with the Paleoproterozoic to Mesoproterozoic Kheis and Namaquan orogenic belts, the informally termed Eastern Namaqualand kimberlites comprise an abundant, compositionally diverse, and temporally complex magmatic province, with coeval Group 1 and 2 magmatism spanning a period from 143 Ma to 80 Ma (Skinner et al., 1992; Smith et al., 1994). The composition, mineral chemistry, and thermobarometry of abundant $gt + cpx + pl$ granulitic lower crustal xenoliths entrained in these kimberlites have been previously studied (Robey, 1981; Pearson et al., 1995), and yield estimates of peak metamorphic conditions of 800-900°C and 10-13 kbar, as well as inferences of essentially isobaric cooling from mineral zonation and coronal reactions. The composition, density, seismic properties, and depth of derivation of these granulites are consistent with the nature of the present day lower crust inferred from seismic studies (Green and Durrheim, 1990; Nguuri et al., 2001), supporting the notion that these granulites resided in the lower crust until their Cretaceous volcanic entrainment. Recent U-Pb dating of metamorphic monazite and zircon from these granulites indicate their high-grade metamorphism at 1120 to 1080 Ma (Schmitz and Bowring, 2001; Chapter 2), providing a link with crustal thickening during Namaquan collisional orogenesis. Rutile is the most abundant accessory mineral in these lower crustal granulites, and as it is included in all major metamorphic phases as well as residing interstitially in well-equilibrated textures, the rutile is inferred to have grown during Mesoproterozoic high-grade metamorphism.

4. Crustal exhumation and lower crustal residence

Of prime importance to the interpretation of lower crustal xenolith thermochronological data is establishing the exhumation history of the crust. Many of the inferences regarding the thermal structure of the lithosphere which can be made from lower crustal thermochronology depend upon the assumption that the examined xenoliths resided near the base of the crust for most of their history prior to volcanic entrainment. We may look to evidence both in the

xenoliths themselves, and in the geological evolution of the overlying crust to establish this history. The following discussion focuses on the exhumation of the southern and western craton-margin and off-craton regions, which host kimberlites and xenoliths from which many of the conclusions of this paper are drawn.

Looking first at the xenoliths, quantitative thermobarometric data give estimates of the peak or near-peak temperatures and pressures of equilibration at 10-15 kbar, establishing initial depths of 30-45 km for the samples at the time of metamorphism. The first line of evidence which may establish the subsequent record of exhumation is the development of retrograde mineral reactions following peak metamorphism. For the granulite xenoliths of this study, all examples show evidence for essentially isobaric cooling following peak metamorphism (Dawson et al., 1997; Griffin et al., 1979; Pearson et al., 1995) indicating minimal exhumation through the closure temperatures of the studied barometric reactions. Similarly, in the overlying crust, coronal reaction textures indicative of isobaric cooling through ~600°C have been developed in the high-T, low-P granulite terrains of Namaqualand (Humphreys and Cornell, 1989; Waters, 1990; Cornell et al., 1992) and Natal (Grantham et al., 1993), suggesting that exhumation of these exposed shallow middle crustal rocks significantly post-dated high grade metamorphism.

On the other hand, the present erosional level of the Proterozoic orogenic belts lies at between 6-10 km, indicating the minimum amount of exhumation of the crust between high-grade metamorphism and the present. Geological constraints on the timing of this exhumation include the age of overlying sedimentary basins. In western Namaqualand, sediments of the Nama group unconformably overlie Namaquan basement, indicating that exhumation predated 550 Ma (Grotzinger et al., 1995). Similarly the Natal Group comprises a foreland basin deposit on the eastern seaboard whose deposition constrains the minimum age of exhumation of the Natal terranes to approximately 490 Ma (Jacobs et al., 1997). The preservation of these Neoproterozoic basement-cover unconformities indicates essentially no further exhumation of the crust through the Phanerozoic.

Direct geochronological constraints on the time of uplift of the Natal terranes come from fission track dating of titanite by Jacobs et al. (1997), which consistently yield ages of approximately 550 Ma in rocks of the Natal belt. These data indicate that the exhumation of these middle crustal rocks occurred during the Pan-African orogeny, only slightly pre-dating foreland basin development. A similar scenario is indicated for Namaqualand, where $^{40}\text{Ar}/^{39}\text{Ar}$

dating of feldspar from the Okiep district in western Namaqualand, and the Jannelspan amphibolites in eastern Namaqualand, yield inverse isochron dates of *ca* 570 Ma at closure temperatures of 100° to 150°C (Onstott et al., 1986). These data again support exhumation of middle crustal amphibolites and granulites simultaneous with early Pan-African orogenesis. It should also be noted that the Namaqua-Natal terrains show little or no magmatic or metamorphic expression of the Pan-African event, which occurred substantially outboard of the southern African foreland. It is therefore very unlikely that significant cryptic intracrustal vertical motions took place since final stabilization of the Namaqua-Natal terrains just after 1 Ga.

These data strongly suggest that the xenolith samples from the Eastern Namaqualand and Northern Lesotho kimberlites remained at the base of the crust, near their recorded depths of equilibration, until at least 570 Ma, subsequent to undergoing exhumation of ~5 km to their structural level prior to kimberlite eruption. Although not quantified, a similar exhumational history is suggested for the lithosphere of northern Botswana, which was subjected to the same Meso- and Neoproterozoic events as the more southerly Proterozoic terranes. From this evidence, inferences regarding the cooling path of the lower crust and the deeper lithosphere from these samples are not subject to significant uncertainty in the depth of residence of the studied xenoliths.

5. Analytical procedures

Accessory minerals were isolated from xenoliths by standard crushing, heavy liquid, and magnetic separation techniques, and separated into different populations based on crystal morphology, color, and grain size. Fractions of accessory minerals comprising both single grains and multi-grain fractions were carefully picked to yield consistent grain sizes, which were measured and recorded by digital photography. Zircons were air-abraded with pyrite after the method of Krogh (1982), and acid rinsed in warm 3M HNO₃ for 12 hours, followed by ultrasonication. Certain rutile fractions were air-abraded in an alumina ceramic abrasion device, without pyrite, and all mineral fractions underwent ultrasonication in ethanol for two hours followed by rinsing in double-distilled acetone. Accessory mineral fractions were loaded into Teflon FEP microcapsules and washed again in 3M HNO₃ (zircon) or high-purity water (monazite, rutile, apatite, titanite) at 50°C for 2-4 hours, followed by rinsing with several capsule volumes of water. Samples were spiked with a mixed ²⁰⁵Pb-²³³U-²³⁵U tracer and dissolved in

28M HF at 220°C for 48-120 hours (zircon, rutile and titanite), or 12M HCl at 180°C for 48 hours (monazite, apatite), followed by conversion to 6M HCl at 180°C for 18-24 hours. Pb and U were separated from all mineral solutions using miniaturized HCl (zircon, monazite) or HBr/HCl-based (titanite, rutile, apatite) anion exchange chromatography procedures modified after Krogh (1973). Hand picked potassium feldspar or plagioclase mineral separates (20 to 100 mg) from several xenoliths were also sequentially leached in Savillex beakers with 1 ml each of 7M HNO₃, 6M HCl, and five aliquots of 2M HF, for 30 minutes at 100°C, rinsing three times with deionized water in between each acid leach step. Pb was separated from each of the final three leaches using standard HBr-based anion exchange chromatography.

Pb and U were analyzed on the MIT VG Sector 54 thermal ionization multicollector mass spectrometer. Lead was loaded on single Re filaments with a dilute silica gel-0.1M H₃PO₄ emitter solution. Feldspar common Pb isotopic compositions were measured by static multicollecion on four Faraday cups with a ²⁰⁷Pb ion beam of >5x10⁻¹¹ A. Radiogenic Pb was measured either dynamically with four high-mass Faraday cups and an axial ion-counting Daly detector, peak-switching ²⁰⁵Pb into the axial position to obtain an internal Daly-Faraday gain calibration, or by peak-switching all ion beams into the Daly detector for very small amounts of lead. An ion beam of >0.1x10⁻¹³ A was maintained for ²⁰⁷Pb during data acquisition. Uranium was loaded on single Re filaments either with colloidal graphite and measured as metal ions, or with silica gel and measured as UO₂⁺ ions by one of two methods: in static mode on three Faraday cups for ²³⁸U⁺ (²³⁸U¹⁶O₂⁺) ion-beam intensities of >0.5x10⁻¹³ A, or by peak switching all ion beams into the Daly detector for smaller amounts of uranium. Details of fractionation and blank corrections are given in Table 1. Ages with propagated uncertainties were calculated using the methodology of Ludwig (1980).

6. Analytical results

6.1. Newlands

No geochronological data has been previously published for the small metapelitic granulite xenoliths discovered at the Newlands kimberlite. In order to constrain the timing of high grade metamorphism which produced the granulite mineral assemblage in these samples, both metamorphic zircon and monazite were analyzed from sample KX3-7. Six single zircons

yielded consistent slightly discordant data with a wide range of $^{207}\text{Pb}/^{206}\text{Pb}$ dates from 2790 to 2825 Ma (Table 1; Figure 4a). Four single monazite crystals were similarly slightly discordant, but yielded older ages over a range from 2840 to 2870 Ma. These data could be interpreted as indicating progressive growth of monazite over 30 Ma, followed subsequently by progressive growth of zircon over 35 Ma. An alternative, and favored explanation of this data is that both zircon and monazite grains consist of intergrowths of phases which grew during two periods of metamorphism. The consistent discordance of the analyses supports this alternative interpretation, as does cathodoluminescence imaging of zircons from this granulite (Fig. 5a-c), which reveals the presence of distinct primary sector-zoned cores, which are truncated and subsequently overgrown by onion-skin rinds of a secondary luminescent phase of zircon. Maximum and minimum ages for these postulated two episodes of metamorphism are given by the youngest and oldest single grain ages of 2.79 and 2.87 Ga respectively. Alternative bounds on the timing of these two metamorphic events may be obtained by a linear regression of the zircon and monazite data, which yields lower and upper intercepts of 2.73 and 2.92 Ga, respectively (MSWD = 1.65). These latter estimates are, in fact, in excellent geological agreement with the timing of terminal collision of the Kimberley block to the Kaapvaal craton nucleus (Chapter 5) and the timing of extension and magmatism associated with the Ventersdorp rifting and flood basalt event (Armstrong et al., 1991; Chapter 3), which implies that these are the causative events for metamorphism and accessory mineral growth in these lower crustal xenoliths at Newlands.

Eight rutile fractions from two samples of Newlands metapelitic granulite were also analyzed (Figure 4b). All analyses were moderately unradiogenic, and the isotopic composition of potassium feldspar from one of the granulites (KX3-9; Table 2) was used to correct for initial common Pb. Rutile is sparse in sample KX3-7, and thus only two multigrain fractions were separated and subjected to air-abrasion to remove outer reaction rims of picroilmenite; these two fractions yielded, within error, nearly identical discordant data with $^{206}\text{Pb}/^{238}\text{U}$ dates of 1381 and 1387 Ma, and $^{207}\text{Pb}/^{206}\text{Pb}$ dates of 1567 and 1596 Ma. From the more abundant rutile in sample KX3-9, six fractions of rutile were selected and analyzed without abrasion. These fractions consisted of either anhedral single grain fragments or in two cases pooled smaller grain fragments of similar size. The resultant data exhibit varying degrees of discordance, with $^{206}\text{Pb}/^{238}\text{U}$ dates ranging from 1626 to 1078 Ma, and $^{207}\text{Pb}/^{206}\text{Pb}$ dates ranging from 1651 to 1109

Ma. Within this wide spectrum of data, the oldest and youngest grain fragments of rutile are also the most nearly concordant of the analyses. A linear regression to all of the data yield upper and lower concordia intercepts at 1.8 and 1.0 Ga, albeit with a poor fit (MSWD = 30). The upper intercept is less well constrained due to the spread in $^{207}\text{Pb}/^{235}\text{U}$ dates for a given $^{206}\text{Pb}/^{238}\text{U}$ date for some of the data points. The comparative significance of the rutile U-Pb data is their substantially younger age than the postulated periods of high grade metamorphism at 2.73 and 2.92 Ga defined by the coexisting zircon and monazite data. The implications for the thermal evolution of the cratonic interior are discussed in Section 7.1.1.

6.2 Free State

Twenty-eight rutile fractions, consisting of single grains or small populations of grains, were analyzed from eight different xenoliths from four different Free State kimberlites, and are illustrated in the concordia diagram of Figure 6. The properties of the rutile are described in Table 1; multi-grain fractions consisting of smaller grains were chosen from euhedral elongate prismatic grains. Single grain fractions included medium sized crystals which were carefully chosen for their euhedral, idiomorphic to subidiomorphic character, and some of the largest grains in the sample which were commonly subhedral to anhedral in shape.

Although it may be demonstrated petrographically that the rutile grew during Archean ultra-high grade metamorphism at ~2.7 Ga (dated by metamorphic zircon and monazite, Chapter 3), the U-Pb systematics of all rutile yield variably discordant data with Proterozoic $^{207}\text{Pb}/^{206}\text{Pb}$ dates ranging from 1905 to 1163 Ma. Rutile from all xenoliths also show consistent, if complex patterns of discordance, such that the data fall within a triangular region of concordia space bounded by apices at 2.0 Ga, 1.2 Ga, and 0.1 Ga. To first order, the rutile data clearly indicate open system behavior and partial Pb-loss from this mineral over a protracted interval of time, as is consistent with the lower closure temperature for Pb volume diffusion in rutile. The data do not however lie on a simple discordia as might be formed by single stage Pb loss following initial cooling through the rutile closure interval, suggesting that the Free State rutile systematics result from a more complex thermal history. Resolving the details of that history requires a closer look at the U-Pb systematics of the entire rutile data set; different models to explain the topology of the rutile data set in concordia space are discussed in Section 7.2.2.

6.3 Orapa

Metapelitic granulites from the Orapa kimberlite have had no prior geochronological investigation. Metamorphic zircon is abundant in these granulites as round to multi-faceted grains. In cathodoluminescence, these zircons reveal predominant cores of highly luminescent weakly sectorized zoned zircon, which are weakly resorbed and then overgrown by relatively thin rims of finely laminated weakly luminescent zircon (Figure 5d-f). Rare grains have very small, highly resorbed cores of oscillatory zoned, likely inherited igneous or detrital, zircon which is mantled by the two previously described phases. Eight single zircons were analyzed from two metapelitic xenoliths. These zircons yield variably discordant data with $^{207}\text{Pb}/^{206}\text{Pb}$ dates ranging from 1875 to 2031 Ma (Figure 7a). Seven of the eight zircons define a discordia array with upper and lower intercepts of 2019 and 1223 Ma respectively (MSWD = 0.2). The eighth zircon lies significantly to the right of the discordia. When interpreted in light of the cathodoluminescence imagery, the upper and lower intercepts of the discordia may represent the time of metamorphic growth of the luminescent sector zoned interior zircon and the mantling laminated rim zircon respectively. The single grain lying off the discordia could be influenced by a small inherited core, as is seen in some images. It is noteworthy that the intercept ages of the Orapa zircon array may be correlated with known geological events in the evolution of the region; the age of 2019 Ma is correlative with manifestations of the Magondi orogen of western Zimbabwe and north-central Botswana, as well as with high-grade metamorphism in the Limpopo belt to the south and east. The lower intercept of the Orapa zircon array is similar to the age of a Mesoproterozoic orogenic belt approximately 100 kilometers to the west of the Orapa kimberlite locale.

Five rutile fractions from three Orapa metapelites, including those from which zircon was analyzed, yielded substantially younger isotopic systematics (Fig. 7b). The five fractions were composed of small numbers of subhedral reddish-brown translucent rutile grains of similar dimension, and yielded variably discordant data with $^{206}\text{Pb}/^{238}\text{U}$ dates ranging from 114 to 255 Ma. The youngest grains are the most concordant, such that the analyses define a discordia array with upper and lower intercepts of 864 and 104 Ma (MSWD = 1.2). The Cretaceous lower intercept is only slightly older than the eruption age of the Orapa kimberlite (93 ± 2 Ma; Davis, 1977); the Neoproterozoic upper intercept does not however correspond to any known geological event in the region. Its significance is discussed in Section 7.3.

6.4 Northern Lesotho

Titanite, rutile and apatite were analyzed from six granulite xenoliths from four different kimberlite pipes from Northern Lesotho, and are plotted together in Figure 8. All three coexisting minerals were analyzed from a mafic-intermediate garnet-clinopyroxene granulite from the Matsoku pipe (KX21-2). Five fractions of titanite from this xenolith yielded near concordant data with $^{207}\text{Pb}/^{206}\text{Pb}$ dates of 875 to 893 Ma. The largest and smallest grain size fractions yielded the oldest and youngest ages respectively, suggesting that diffusive gradients, developed during slow cooling, exist within grains. That the titanite dates represent cooling ages is consistent with the high peak metamorphic temperatures of $\sim 850^\circ\text{C}$ recorded in these granulites (Griffin et al., 1979). Two fractions of apatite from KX21-2 yielded relatively unradiogenic Pb compositions; using the Stacey and Kramers (1975) model Pb composition at 1.0 Ga to correct for initial common Pb results in slightly discordant data with $^{206}\text{Pb}/^{238}\text{U}$ ages of 349 and 393 Ma. A single fraction of rutile from KX21-2 was also analyzed, and with the same model initial Pb, yields discordant U-Pb ratios with a $^{206}\text{Pb}/^{238}\text{U}$ date of 165 Ma.

Apatite and rutile were analyzed from a metapelitic garnet-biotite granulite xenolith from the Mothae kimberlite. Using the Pb isotopic composition of K-feldspar in this xenolith to correct for initial common Pb, two fractions of apatite yielded discordant U-Pb systematics, with $^{206}\text{Pb}/^{238}\text{U}$ dates of 410 and 435 Ma. Four fractions of rutile of varying grain size also yielded variably discordant data, with the smallest grain sizes giving near concordant dates of ~ 87 Ma, and more discordant larger grains having $^{206}\text{Pb}/^{238}\text{U}$ dates of 90 to 137 Ma.

Apatite from a mafic garnet-clinopyroxene granulite (KX20-4) from the Letseng-la-Terae kimberlite, corrected for initial common Pb with leached plagioclase feldspar Pb data, yields discordant data with a $^{206}\text{Pb}/^{238}\text{U}$ date of 569 Ma. Two rutile grains from a second garnet-clinopyroxene granulite (KX20-8) yielded slightly discordant data with $^{206}\text{Pb}/^{238}\text{U}$ dates of 96 and 100 Ma. Seven fractions of rutile from two metasedimentary garnet-kyanite granulites (KX20-1 and KX20-3) from the same kimberlite were also analyzed, yielding variably discordant data. The smallest grain size fraction of rutile yielded near concordant data with a $^{206}\text{Pb}/^{238}\text{U}$ date of 93 Ma, while larger grain size fractions yielded increasingly discordant data with $^{206}\text{Pb}/^{238}\text{U}$ dates from 107 to 170 Ma. The largest single grain analyzed yielded the oldest $^{206}\text{Pb}/^{238}\text{U}$ date of 365

Ma. Most of the rutile data from these Letseng-la-Terae granulites are radiogenic enough to be relatively insensitive to the choice of initial common Pb composition.

Significant patterns emerge when all of the data for the northern Lesotho granulites are examined together (Figure 8). First, there is a systematic younging of accessory mineral $^{206}\text{Pb}/^{238}\text{U}$ dates from titanite (881 to 856 Ma) through apatite (569 to 349 Ma) to rutile (365 to 87 Ma). As discussed in Section 2, this order is in accord with the relative field-derived U-Pb closure temperatures for these minerals, which suggests that these minerals are recording thermally-activated diffusion-dependent ages. Second, the data for accessory minerals from granulite xenoliths in all three Northern Lesotho kimberlites define similar systematics, indicating that these thermochronometers are recording a regional thermal evolution. Third, while titanite data are nearly concordant, both apatite and rutile data exhibit substantial degrees of discordance. The sensitivity of the apatite dates, and particularly the $^{207}\text{Pb}/^{235}\text{U}$ date, to the common Pb correction limits their detailed interpretation, however the apatite analyses clearly exhibit older ages and a lesser degree of discordance than the rutile data. The more robust rutile data define a linear array in concordia space (Figure 8b), with a lower intercept of approximately 90 Ma pinned by near-concordant analyses of small grain size fractions, and more discordant large grains pointing to an upper intercept of approximately 650 Ma. The significance of this discordia and the upper and lower intercepts of the array are discussed in Section 7.3.

6.5 Eastern Namaqualand

Sixteen rutile fractions from seven granulite xenoliths in five kimberlites from eastern Namaqualand were analyzed. The resulting data from most of these kimberlites record variably discordant Cretaceous $^{206}\text{Pb}/^{238}\text{U}$ dates (Fig. 9a). A single rutile fraction from a garnet-clinopyroxene granulite xenolith in the Markt kimberlite yielded a slightly discordant analysis with a $^{206}\text{Pb}/^{238}\text{U}$ date of 123 Ma. Five fractions of rutile from two eclogites and a garnet-clinopyroxene granulite from the Lovedale kimberlite also yield variably discordant, Cretaceous $^{206}\text{Pb}/^{238}\text{U}$ dates between 94 and 133 Ma. Two rutile fractions from a garnet-clinopyroxene granulite from the Uintjiesberg kimberlite yield a concordant analysis at 99 Ma and a slightly discordant analysis with a $^{206}\text{Pb}/^{238}\text{U}$ date of 102 Ma. Two rutile fractions from a gt-cpx granulite xenolith in the Beyersfontein kimberlite yield slightly discordant analyses with $^{206}\text{Pb}/^{238}\text{U}$ dates of 112 and 115 Ma. While the near-complete isotopic resetting in these Eastern Namaqualand

granulitic rutiles is similar to that observed in the Northern Lesotho and Orapa granulite suites, viewed as a whole, these data do not conform to a linear discordia array (Figure 9a), but rather scatter along or slightly displaced to the right of the concordia curve. This phenomenon is in large part a function of the variable age of the kimberlites from which these granulitic rutiles were sampled, compared with the singular ages of the Orapa kimberlite as well as most of the Northern Lesotho suite. For example, in Eastern Namaqualand samples, the oldest near concordant rutile is from a granulite of the Markt kimberlite, which has the oldest eruption age (117 ± 2 Ma) of the pipes examined (Smith et al., 1994). Similarly, $^{206}\text{Pb}/^{238}\text{U}$ dates of the other granulitic rutiles fall in the same relative descending order as the inferred ages of the host kimberlite: Markt, Uintjiesberg, Beyersfontein, Lovedale. Such correlations suggest that these granulitic rutiles were losing radiogenic Pb as they resided in the lower crust, until their quenching upon eruption in the kimberlite.

A garnet-clinopyroxene granulite from the Klipfontein-08 kimberlite also contains rutile with variably discordant Phanerozoic systematics, however the $^{206}\text{Pb}/^{238}\text{U}$ dates of these rutile are considerably older, ranging from 225 to 400 Ma. A clear and reproducible grain size dependence to these rutile systematics is present—two fractions composed of grains with a minimum radius of ~ 75 μm yield the youngest $^{206}\text{Pb}/^{238}\text{U}$ dates of 225 and 238 Ma. A further two fractions composed of the largest grains in the sample with a radius of ~ 125 μm yield older $^{206}\text{Pb}/^{238}\text{U}$ dates of 314 and 315 Ma. Two final fractions of these sample large grains which were abraded to remove approximately 10% of the outermost portions of the crystals yielded even older $^{206}\text{Pb}/^{238}\text{U}$ dates of 394 and 401 Ma. Together these six fractions of rutile, and those from the other Eastern Namaqualand granulites, define a discordia array with lower and upper intercepts of ~ 90 and ~ 740 Ma (Figure 9b). As with the Northern Lesotho and Orapa rutile data, the significance of the upper and lower intercepts of this discordia array are discussed in Section 7.2.

7. Discussion

7.1 *Thermal evolution of the Archean cratonic interior*

7.1.1 Newlands kimberlite, western craton

The primary significance of the Proterozoic rutile dates from the Newlands granulites is that this low-closure temperature mineral did in fact close to quantitative Pb diffusion, and

accumulate radiogenic Pb since approximately 1 Ga. This observation is important for two reasons. First, it offers an initial indication of the robust nature of the rutile thermochronometer to transient thermal effects associated with kimberlite entrainment and eruption. There is no quantifiable Mesozoic Pb-loss in the systematics of the Newlands granulite rutile, despite the fact that the xenoliths from which they were extracted were only a few centimeters in diameter, and exhibited significant alteration of primary feldspar and micas, presumably due to reaction with kimberlitic magmatic fluids. This lack of a kimberlitic thermal imprint is perhaps not surprising considering the very transient nature of the heating associated with volcanic entrainment and eruption (Canil and Fedortchouk, 1999; Kelley and Wartho, 2000). In Section 7.2.4, quantitative modeling of partially reset rutiles in other craton-margin xenoliths will further demonstrate the inadequacy of kimberlite entrainment for disturbing rutile U-Pb systematics.

Second, closure of the rutile thermochronometer necessitates temperatures of $<400^{\circ}\text{C}$, and thus the data from the Newlands granulites places a robust constraint on the maximum temperature of the lower crust. Steady-state conductive geotherms which reproduce the low surface heat flow of Archean cratons ($\sim 40 \text{ mW/m}^2$) similarly predict temperatures of $350\text{--}400^{\circ}\text{C}$ at the base of the crust (Figure 1). Thus lower crustal rutile thermochronology effectively confirms these steady-state conductive geotherms for cratonic lithosphere, independent of models of surface heat flow or mantle xenolith thermobarometry, and their associated assumptions; these issues are explored further in Section 7.2.3. More importantly, rutile records the time at which these conditions were established in the lithosphere. For Newlands, the conclusion that a cratonic geotherm was established in the underlying lithosphere since at least the Mesoproterozoic is of course not surprising, as it is consistent with the present low surface heat flow of the craton (Jones, 1988), mantle xenolith Cretaceous paleothermobarometry, and the presence of diamond xenocrysts of Archean age in the Newlands kimberlite (Menzies, 1999).

The comparative significance of Proterozoic rutile U-Pb dates from the Newlands granulites is that they are substantially younger than the timing of episodic high grade metamorphism at 2.9 and 2.7 Ga defined by the coexisting zircon and monazite data (Figure 4a). They are also substantially younger than cooling ages of 2.4 to 2.3 Ga which might be expected even with very slow cooling of the lower crust at $\sim 1^{\circ}\text{C/Ma}$. The Proterozoic rutile ages suggest that, due to its low closure temperature for Pb diffusion, rutile was sensitive to Pb loss during thermal perturbations of the lower crust from established steady-state cratonic conditions. The

discordance patterns of the rutile also demand that this Pb loss history was complex. The rutile data do not define a linear discordia, and so cannot be modeled by single-stage Pb-loss following initial isotopic closure. Multiple episodes of partial Pb-loss generate a polygonal topology of U-Pb data in concordia space, whose apices with concordia correspond to the various times of closure of the rutile system from excursions to higher temperatures during thermal perturbations. Such multi-stage Pb loss is the likely explanation for the Newlands data. From their systematics, the time of initial rutile closure is poorly defined, while two Proterozoic episodes of variable Pb-loss are approximated by the intercepts of the linear regression of the data at ~ 1.0 and ~ 1.8 Ga. Despite the scatter of the data, it is striking that both intercepts of the rutile discordia array broadly correspond to two episodes of collisional orogenesis (the Kheis and Namaquan events) which occurred approximately 150 km to the west of the Newlands site (Thomas et al., 1994; Cornell et al., 1998). These craton margin events were apparently of sufficient thermal impetus to perturb the temperature profiles in the base of the crust well into the cratonic foreland. The U-Pb rutile thermochronometer in lower crustal rocks appears to be a sensitive recorder of these minor thermal perturbations to the lithosphere, undergoing repetitive partial isotopic resetting over the long history of the craton.

7.1.2 Free State kimberlites, central craton

A large amount of rutile U-Pb data has been generated for the *ca* 2.7 Ga granulites of the Free State kimberlites, which show complicated, discordant U-Pb systematics. Like the rutile data from the Newlands kimberlite xenoliths, the Free State rutile data preserve Proterozoic ages, indicating the ancient establishment of cratonic geotherms in the underlying lithosphere. Also like the samples from Newlands, the Free State rutile do not conform to a simple linear discordia, but instead lie within the apices of a triangular region of concordia. This topology may be indicative of multiple episodes of partial Pb-loss during a series of thermal perturbations to the lower crust. It should be noted however that these rutile from the Free State UHT granulites are the same crystals which contain a unique reaction texture involving the exsolution of zircon from the rutile structure, as described by Schmitz and Bowring (Chapter 3). This zircon exsolution has been demonstrated to have occurred over a protracted interval between 2.6 and 2.3 Ga by dating individual zircon lamellae, with the majority of exsolution occurring prior to 2.5 Ga. The

effects of this exsolution on the isotopic evolution of these two-phase systems must be evaluated in order to interpret the host U-Pb rutile systematics.

Estimates of the volume of zircon exsolved from rutile grain have been made based upon back-scattered electron images of polished sections through rutile grains, and result in estimates of <0.1% exsolved zircon by volume in typical host rutile crystals. Radiogenic Pb concentrations in the exsolved zircons range from approximately 50 to 100 ppm, while radiogenic Pb contents in analyzed rutiles range from 0.5 to 1 ppm. Mass balance thus requires that less than 10% of the radiogenic Pb in the total rutile analysis can be attributed to Pb residing in exsolved zircon. Mixing of radiogenic Pb hosted in rutile versus zircon is explored in Figure 10a. The dark shaded field with white gridding represents mixing lines from exsolved zircon with an age of 2.5 Ga extrapolated through the range of analyzed rutile compositions. Simple mixing of U and Pb separately hosted in exsolved zircon and host rutile would demand that near-concordant rutile components span a range of ages over 900 million years, between ~0.7 and 1.6 Ga; mixing of 0-20% exsolved zircon and 100-80% host rutile of various ages is required to explain the scatter of data. Besides necessitating an unrealistic span of “concordant” rutile closure ages, the simple zircon-rutile mixing model also overestimates the amount of radiogenic Pb hosted in exsolved zircon compared to estimates based on volume and Pb concentration of analyzed zircon exsolution lamellae; for these reasons the simple mixing model may be rejected with some confidence.

Figure 10b explores the effects of superimposing various Pb loss histories on the Free State rutiles to explain their present-day U-Pb systematics. The medium shaded field with black gridding represents Pb loss trajectories lines resulting from single stage episodic loss at the time of kimberlite eruption, ~0.1 Ga. Extrapolation of these trajectories through the entire array of data points would necessitate initial concordant age systematics of individual rutile grains ranging over 700 million years, from 1.2 to 1.9 Ga, with up to 40% Pb loss at 0.1 Ga, to explain the available data. Again, this model is rejected as necessitating an unrealistic span of initial rutile cooling ages. The next logical step is to create more complex multi-stage models to explain the array of Free State rutile data. One such model combines mixing between exsolved zircon and host rutile, and kimberlite-aged Pb loss, and is visualized in Figure 10c by the overlap of the two previously defined fields, highlighted in light shading. This two-stage model can reproduce the array of data if the host rutile exhibited initial concordant U-Pb systematics

ranging over 400 million years, from 1.2 to 1.6 Ga. Mixing of the host rutile component with an exsolved zircon component (again, up to 20% of the latter) then drives the data points upward and to the right of concordia, while subsequent Pb loss at 0.1 Ga (up to 40%) would drive individual data points downward along chords towards 0.1 Ga. Again such a model demands initial concordant rutile cooling ages between 1.2 and 1.6 Ga, probably unrealistic even given slow cooling rates in the deep crust.

The final model to be considered concerns the effects of multiple episodes of Pb-loss on the Free State rutile systematics. As noted previously, simply defining a triangular field in which all the data reside, results in apices at 0.1, 1.2 and 2.0 Ga. The entire array of rutile data could be explained by near-complete resetting of the rutile U-Pb systematics at ~2.0 Ga, followed by partial to complete resetting (20-100%) at ~1.2 Ga, and then a superimposed further partial resetting (0-40%) at 0.1 Ga. Within this model small amounts (<10%) of mixing of host rutile with ~2.5 Ga exsolved zircon would cause an allowable degree of scattering of the data. One of the appeals of such a model is that each of these proposed episodic Pb-loss events has some geological significance in the evolution of the central craton, the first being the general timing of both Bushveld magmatism and the Vredefort impact, the second being a (prolonged but episodic) period of intracontinental alkaline and tholeiitic magmatism (Verwoerd et al., 1992; Reimold et al., 2000) and collisional orogenesis along the southern cratonic margin (Thomas et al., 1993), and the last being the time of Karoo magmatism and kimberlite eruption (Duncan et al., 1997).

A further appeal of this model is that it constrains the nature of the ~1.2 Ga end member as being due to an episodic Pb-loss event, rather than a protracted passage through the rutile closure interval. The episodic nature of this 1.2 Ga event is supported by other U-Pb systematics in the UHT granulites. For example, there is a distinct ~1.2 Ga Pb-loss signature in the analyzed zircon exsolution lamellae (Chapter 3). Similarly, monazites from the UHT granulites exhibit a remarkable degree of discordance, with a lower intercept of 1.2 Ga, which may be due to Pb-loss at this time, or to the growth of new monazite as thin rims on primary ~2.7 Ga grains. For these reasons this final model is favored to explain the rutile systematics of the Free State UHT granulites.

Again, as in the Newlands granulite suite, the U-Pb rutile thermochronometer in lower crustal granulites from the Free State kimberlites appears to yield a sensitive record of numerous transient thermal perturbations to the cratonic lithosphere over its long history. However unlike

the Newlands suite, one apex of the Free State rutile data triangle, though poorly defined, appears to be quite young, and potentially corresponds to the time of kimberlite entrainment and eruption. The maximum Pb-loss associated with this young thermal perturbation amounts to several tens of percent. These data provide the first evidence for an episode of transient heating of the Archean southern African cratonic lithosphere in the Late Mesozoic; the greater magnitude of this event at the craton margins and in the bounding Proterozoic belts is examined in Section 7.2.4.

7.2 Thermal evolution of the cratonic margins and Proterozoic off-craton regions

7.2.1 Distinguishing continuous versus episodic diffusive Pb-loss

U-Pb isotopic data for rutile in the Archean cratonic granulites display complex patterns of discordance, which can be only qualitatively ascribed to multiple episodes of Pb-loss over a protracted history. In contrast, rutile data for Mesoproterozoic granulites of the craton margins and bounding orogenic belts display apparently simpler systematics characterized by linear discordias, with data leveraged toward lower intercepts approximating the times of kimberlite eruption. These apparently simpler systematics may be amenable to more rigorous interpretation and quantitative modeling, in order to constrain the thermal evolution of the underlying lithosphere. Of prime importance to the further interpretation and modeling of these data is a clear understanding of the U-Pb thermochronological systematics predicted for a variety of lower crustal cooling histories. Two end member scenarios are continuous cooling versus punctuated heating, and associated with these different temperature-time (T-t) paths are consequent phenomena of continuous versus episodic thermally-activated isotopic exchange. Unique among isotopic systems, the coupled U-Pb decay schemes allow the quantification of diffusive parent and/or daughter loss. The differential decay rates of the two uranium isotopes, which generate curvature in the concordia function, allow us to not only identify Pb loss, but distinguish between continuous loss during progressive cooling, versus episodic loss in discrete punctuated heating events.

This phenomenon is best illustrated in Fig. 11a, which shows the systematics of model systems undergoing these two end-member thermal histories. The dashed and dotted lines represents the Pb-loss functions of systems of identical diffusivity and geometry, but differing

radii, which, following initial isotopic closure at τ_1 (or τ_2), underwent diffusive Pb loss in a single discrete thermal pulse at τ_3 . Because of the episodic nature of the diffusive Pb loss, these functions exhibit discordancy, plotting as *linear* chords between τ_1 (or τ_2) and τ_3 (Wetherill, 1956). The degree of discordance of individual systems is dependent upon the amount of Pb loss (U diffusion is assumed to be negligible), itself a function of the magnitude and duration of heating, and the diffusive characteristics of the system; systems with smaller radii are reset to a greater extent than those with larger radii.

Systems undergoing continuous diffusion display a different topology in U-Pb concordia space. Tilton (1960) presented an analytical solution to the problem of coupled radiogenic daughter accumulation and simultaneous loss by continuous (and constant) diffusion, specifically applied to the U-Pb systems in zircon. Under the restriction of constant diffusivity, the resultant Pb-loss functions are the solid curves represented in Figure 11a, displaced beneath the concordia curve and approximating straight lines near their upper intercept with concordia (the time of initiation of daughter product accumulation), but rapidly changing slope on approach to their lower intersection (the time of cessation of diffusive loss). Wasserburg (1963) explored the topology of loss trajectories in concordia space for a variety of functions for the bulk diffusivity of Pb, demonstrating how time-dependent diffusivity affects the curvature of the Pb-loss function. When the bulk diffusivity increases with time, the curvature of the Pb-loss function decreases, approaching the linear discordia associated with episodic Pb-loss. When the bulk diffusivity decreases with time, as is the case for cooling systems, then the curvature of the Pb-loss function will increase, resulting in an arcuate trajectory subparallel to concordia. In the context of isotopic closure (e.g. Dodson, 1973), the upper and lower intersections of the continuous diffusive Pb-loss function with concordia represent the time of entry (τ_1 or τ_2) and exit (τ_3) through the *closure interval* of the mineral-isotopic system, that is, the intervening period between complete loss and complete retainment of the daughter isotope.

It is important to realize that this effective closure interval for most mineral-isotopic systems over a variety of cooling rates is generally no more than a few tens of degrees (Dodson, 1983), such that even for slow cooling, the times of entry and exit through the closure interval are at most ≤ 100 million years apart, and the resulting continuous Pb loss trajectories followed by these systems are only slightly distinguishable from concordia. In Figure 10b, this phenomenon is illustrated by the open square symbols, which represent spherical systems with

identical Pb diffusivity but contrasting radii, undergoing continuous diffusive Pb loss during linear cooling from high temperatures through their respective closure intervals. The isotopic ratios of these systems were determined numerically by first calculating the gradient in closure temperature within each diffusive system (Dodson, 1983), transforming the closure temperature function into a related function for closure age assuming an initial temperature and cooling rate, and then integrating the isotopic ratios corresponding to these closure ages over the volume of the system. It is apparent that even for the relatively slow cooling rate of 1°C/Ma assumed in this model, the passage through the closure interval for each of these systems is sufficiently brief so as to assure near concordance of their U-Pb isotopic systematics. It is only in the special case where the systems reside for several hundred million years at near-constant temperature within the closure interval, that the Pb-loss profile could approach the type of continuous diffusion curves illustrated in Figure 10a. Even in this extreme case, continuous versus episodic Pb-loss functions are distinctly different at their lower intercept with concordia, i.e. at the time of quenching or thermal perturbation respectively, and are readily distinguished in sets of U-Pb data if near complete loss has occurred near τ_3 . The inset in Figure 10a illustrates the asymptotic approach of continuous Pb-loss curves at their lower intercepts with concordia, compared with the oblique intersection of episodic Pb-loss lines.

The rutile data presented for the craton-margin and off-craton suites of xenoliths (Eastern Namaqualand, Northern Lesotho, Orapa) all illustrate young, discordant U-Pb systematics conforming to linear discordia chords, with most data proximal to the discordia lower intercepts, which reproduce the age of kimberlite eruption (Figures 7b, 8b, 9b). Comparing these systematics with the predictive Pb-loss models of Figure 10, it is apparent that they do not simply conform to the concordant systematics predicted from continuous cooling models (compare to the open squares in Figure 10b). Neither do they conform to the extreme model of steady state residence in the closure interval, which would place the data on the asymptotic curves of the inset to Figure 10a, rather than the actual oblique linear discordias which they define. We are left with the result that the rutile data for the craton-margin and off-craton granulite suites can only be explained by an episodic Pb-loss event late in their history, immediately prior to their entrainment and quenching upon kimberlitic eruption. A thermally activated diffusive-loss mechanism is supported by the grain-size dependency of the loss systematics in at least some of the rutiles, as noted in Section 6. The thermal perturbation

responsible for this Pb-loss must have been of sufficient duration and magnitude to nearly completely reset many of the rutile systems; modeling of the necessary perturbation is explored in Section 7.2.4.

An important consequence of the episodic Pb-loss mechanism is the interpretation of the upper intercept of the rutile discordia lines for the various granulite suites. This upper intercept is, in an episodic loss model, necessarily the time of prior isotopic closure of the rutile thermochronometers, and is mainly leveraged by the largest (and least disturbed) diffusive systems. Thus the upper intercepts of the rutile discordias allow us to essentially “see through” the late thermal perturbation of the rutile thermochronometers to the initial cooling ages of the lower crust. The implications of these Neoproterozoic rutile cooling ages are discussed below.

7.2.2 Cooling rates in the lower crust

As the continental lithosphere relaxes from the high temperatures and steep advective thermal gradients associated with crust formation and aggregation, the lower crust experiences dramatic cooling from initial metamorphic temperatures of 800 to 1000°C, to temperatures as low as 350 to 400°C, as predicted by steady-state conductive geotherms for old stable cratons (Figure 1). In fact, it is in the lower crust that the most dramatic changes in temperature occur, and thus these samples provide us with the most leverage for constraining lithospheric cooling. However, while the magnitude of this cooling is clear, very little data regarding the *rate* of cooling of the lithosphere, particularly in its deeper portions, are available. Such data may be extracted from the U-Pb accessory mineral thermochronometry of lower crustal granulites in the following manner.

The craton margin Northern Lesotho, Eastern Namaqua, and Orapa granulite xenoliths have well defined Mesoproterozoic ages of high grade metamorphism, as defined by their metamorphic zircon and monazite U-Pb systematics. If these ages are assumed to represent the timing of peak metamorphic conditions recorded in the granulitic mineral geothermometers, then when combined with data for lower closure temperature systems, they may be used to derive a maximum integrated linear cooling rate for the lower crust following Proterozoic orogenesis around the craton margins. This exercise is best undertaken for the granulite assemblages of the Northern Lesotho and the Eastern Namaqua kimberlites, whose peak temperatures have been

previously assessed at 700 to 800°C (Griffin et al., 1979; Pearson et al., 1995), and which have been dated at 1.1 to 1.0 Ga by zircon and monazite geochronology (Chapter 2).

Titanite provides a valuable intermediate closure temperature system (530 to 580°C for the grain sizes investigated). Unfortunately, only a single granulite from Northern Lesotho contains titanite, coexisting with rutile (which is the more common Ti-bearing accessory mineral in these granulites). However, the near concordant ages of 870 to 890 Ma for titanite from this granulite yield the first indication of the relevant cooling rates, on the order of 1 to 2°C/m.y., in the lower crust of Northern Lesotho following Natal orogenesis (Figure 12). For the Northern Lesotho lower crust, an additional point on the cooling curve is available in the form of a K-Ar age of 715 Ma for hornblende from a granulite from Matsoku pipe (Harte et al., 1981). As hornblende has a nominal closure temperature of 480°C, this data is also consistent with the ~1°C/Ma cooling rate inferred from the U-Pb titanite data (Figure 12). With a nominal closure temperature of 400°C, rutile greatly extends the cooling interval under investigation. While the rutile from all of the craton margin xenolith suites has been shown to be variably discordant, the understanding of discordant U-Pb systematics during episodic diffusive loss gained in the previous section suggests that the upper intercepts of the discordia arrays defined by craton margin rutile suites represent the timing of initial closure of the rutile thermochronometers. For the Northern Lesotho suite, the upper intercept age of approximately 650 Ma again indicates an integrated linear cooling rate in the lower crust of approximately 1°C/Ma.

While there are presently fewer mineral-isotopic thermochronometers available to define the cooling path of the lower crust sampled by the Orapa and Eastern Namaqua kimberlites, the combination of the ubiquitous rutile systematics with high grade metamorphic monazite and zircon systematics are sufficient to infer integrated linear cooling rates. For the Orapa granulite samples, numerous rutile analyses fall along a discordia array with an upper intercept of approximately 850 Ma. As peak metamorphic temperatures estimated at 800°C occurred at 1240 Ma, these data are again consistent with slow cooling on the order of 1°C/Ma in the deep crust beneath Orapa (Fig. 8). In the case of rutile from granulites of the Eastern Namaqua kimberlites at the southwestern margin of the craton, most analyses approximate the age of the kimberlite eruption, indicating near complete late Mesozoic isotopic setting. However, rutile from a mafic granulite from the Klipfontein-08 kimberlite yield only partially reset data, defining a discordia array with an upper intercept of approximately 700 Ma. Once again a

consistent integrated linear cooling rate of $\sim 1^\circ\text{C}/\text{Ma}$ is derived upon comparison of this Neoproterozoic, $\sim 400^\circ\text{C}$ cooling age with the timing of $\sim 800^\circ\text{C}$ peak metamorphism at 1080 to 1120 Ma recorded in metamorphic monazite and zircon from numerous Eastern Namaqua granulite xenoliths (Fig. 8).

The remarkable consistency of cooling rates between different suites of lower crustal samples of different ages suggest that slow cooling rates are a distinctive characteristic of the relaxation of continental geotherms following collisional orogenic activity involving previously formed crustal material. The rates inferred from this study are very similar with those determined for slowly cooled mid- to lower-crustal granulite terrains of a variety of ages, including the Paleoproterozoic Nagssugtoqidian Orogen of West Greenland (Willigers et al., 2001), the Paleoproterozoic orogen of the southwestern U.S.A. (Hodges et al., 1994), the Adirondack Highlands of the Mesoproterozoic Grenville Orogen (Mezger et al., 1993), and the Neoproterozoic Mozambique belt of East Africa (Moller et al., 2000).

7.2.3 Establishment of cratonic geotherms

Cratonic regions of the continents, which have been stable and isolated from plate margin processes for several hundred to thousands of millions of years, commonly exhibit the lowest surface heat flow on Earth ($\sim 40 \text{ mW}/\text{m}^2$). When modeled to take into account the thermal conductivity structure and the distribution of radiogenic heat sources in the lithospheric column, resulting steady-state conductive geothermal gradients in the lithospheric mantle are extremely low ($\sim 5\text{-}6^\circ\text{C}/\text{km}$) and indicate thermal lithospheric thicknesses on the order of several hundred kilometers (Figures 1). As was intimated in Section 7.1.1, lower crustal thermochronology may be used to examine three inter-related questions pertinent to the establishment of cratonic geotherms. The first use of lower crustal thermochronology is as an independent test of the predictions of surface-heat flow based lithospheric geotherms. In this regard the closure temperature of the U-Pb system in rutile, approximately 400°C , is similar or only slightly higher than the temperatures at the base of the crust predicted by cratonic conductive geothermal models (Fig. 1). It follows that in “cratonic” thermal regimes, lower crustal rutile grains should close to Pb diffusion, retain radiogenic Pb, and yield ancient cooling ages. We have seen that, positively, rutile in granulite xenoliths from the Newlands and Free State kimberlites, within the

Kaapvaal craton, do indeed yield Proterozoic ages, consistent with the ancient establishment of a “cratonic” thermal state in the Kaapvaal lithosphere.

This introduces the second use of lower crustal thermochronology as a unique and direct recorder of the time of establishment of cratonic geotherms. The thermal boundary conditions of the lithosphere, namely surface cooling with internal and basal heating, and the contrast in thermal conductivity and radiogenic heat production between continental crust and lithospheric mantle, result in a situation whereby equilibrium temperature gradients in the lithosphere decrease continuously with depth. Thus, as a straightforward consequence of these lithospheric boundary conditions and properties, measurements of lower crustal *temperatures* necessarily also constrain the deeper lithospheric mantle thermal structure. This is particularly true as the lithosphere approaches a conductive steady state, but also applies to partially advective systems. As a corollary, U-Pb rutile cooling ages in lower crustal granulites directly estimate the *time* of conductive cratonic geotherm establishment, not only in the lower crust, but also in the lithospheric mantle. This dating of the establishment of cratonic geotherms has direct bearing on understanding ancient lithospheric architecture; temperatures of 400°C in cratonic lower crust demand a minimum conductive lithospheric mantle thickness of approximately 200 km in order to sufficiently insulate the crust from the convecting mantle (Davies and Strebeck, 1982; Chapman, 1986; Morgan and Sass, 1984).

A third application for lower crustal thermochronology is the evaluation of the steady state condition. More explicitly, can it be demonstrated that regions with higher present-day surface heat flow and/or steeper mantle xenolith paleogeotherms, relative to “cratonic” values and gradients, are reflecting steady-state lithospheric thermal conditions? This question is particularly pertinent to comparisons between the Archean and Proterozoic domains within the southern African continent, where studies of both surface heat flow and mantle xenolith thermobarometry have revealed distinctive differences in the thermal structure of these regions, and interpreted them in terms of secular differences in lithospheric properties. As illustrated in Fig. 13, the current paradigm for southern African lithosphere is one of contrast between the inferred low heat flow thermal state beneath the Archean Kaapvaal cratonic areas and elevated heat flow in the “off-craton” Proterozoic orogenic belts (Ballard and Pollack, 1987; Jones, 1987, 1988). This contrast is apparently also reflected in mantle xenolith thermobarometry, with peridotites from the off-craton regions (Namaqualand, Namibia, East Griqualand) displaced to

higher temperatures for a given depth relative to cratonic mantle xenoliths (Boyd and Nixon, 1979; Boyd and Gurney, 1986; Finnerty and Boyd, 1987). Assuming that the surface heat flow models and mantle xenolith thermobarometry capture a conductive steady-state, these data have been interpreted as indicative of differences in lithospheric thickness: greater beneath Archean cratons and thinner beneath Proterozoic belts (Boyd and Gurney, 1986; Durrheim and Mooney, 1994). Thinner Proterozoic lithosphere, restricted to the graphite stability field, has further been suggested as the explanation for the barren (non-diamondiferous) nature of off-craton kimberlites (Boyd and Gurney, 1986).

The steady-state assumption inherent to this comparison is directly tested by lower crustal rutile thermochronology. The elevated geothermal gradients inferred for Proterozoic terrains from surface heat flow models (Jones, 1987) predict temperatures at the base of the crust of $>500^{\circ}\text{C}$, well above the U-Pb rutile closure temperature. If this was the steady-state condition, off-craton lower crustal rutile should not have closed to Pb diffusion, and thus their U-Pb systematics should capture concordant ages equivalent to the time of kimberlite eruption. As first noted in Section 7.2.1, this is not the case for the measured granulite rutiles from both craton-margin and off-craton regions, which rather fall on discordia arrays with lower intercepts of kimberlite age, but Neoproterozoic upper intercepts. The topology of these data necessitate that the rutile thermochronometers closed to Pb diffusion in the Neoproterozoic, and by inference a “cratonic” thermal state was developed within the Proterozoic lithosphere at this time. At some later time, likely in the Mesozoic, the rutile thermochronometers experienced episodic Pb loss which was apparently ongoing until the time of quenching upon kimberlite entrainment and eruption. These systematics are unequivocal evidence for a transient, non-steady-state condition in the southern African lithosphere in the Late Mesozoic.

As noted earlier, temperatures of 400°C at the base of the crust require a mantle lithospheric thickness on the order of 200-250 km in order to sufficiently insulate the upper lithosphere from the convecting mantle. The establishment of a cratonic thermal profile in the Proterozoic lithosphere of southern Africa by *ca* 600 Ma is consistent with simple models of the thermal relaxation times for *ca* 200 km thick continental lithosphere following tectonothermal reactivation (Vitarello and Pollack, 1980; Morgan, 1984;). Lower crustal rutile thermochronology indicates that a differential lithospheric thickness between Proterozoic and Archean domains of southern Africa, at least from the Neoproterozoic until early Gondwana

breakup in the Late Jurassic, is unsupported. Under this new paradigm, the elevated temperatures recorded in the off-craton mantle xenolith record must instead represent transient thermal effects. Direct support for the transient nature of the higher thermal gradients in the Proterozoic lithospheric mantle comes from examination of peridotites from neighboring kimberlites in Eastern Namaqualand. The 154 Ma Melton Wold kimberlite contains garnet peridotites falling along a well defined “cratonic” 40 mW/m² geotherm (Figure 13), however peridotites of the younger 100-70 Ma kimberlites, like the nearby Hebron pipe, have notably higher equilibration temperatures (Robey, 1981; Finnerty and Boyd, 1987). This secular change in the state of the lithosphere between the Late Jurassic and Cretaceous has numerous manifestations in the mantle, which are further documented in Section 7.2.5.

Another significant implication of these results is that the lithospheric mantle beneath the Proterozoic mobile belts extended well into the diamond stability field, at least until the onset of thermal perturbation in the Late Jurassic. Thus the apparent diamond infertility of the southern African Proterozoic orogenic belts compared to the Archean Kaapvaal craton is not simply a consequence of an insufficiently thick Proterozoic mantle keel, or of differential thermodynamic diamond stability in hotter Proterozoic lithosphere (Kennedy and Kennedy, 1976). Other causal mechanisms for the diamond fertility contrast between Archean and Proterozoic lithosphere in southern Africa must be sought; these causes may likely include compositional distinctions (Boyd and Gurney, 1982, 1986), as well as the differential tectonic evolution of these mantle domains.

Returning to present day surface heat flow, either of two explanations could be responsible for the higher flux through the Proterozoic belts relative to the craton. The first and likely influential mechanism is heterogeneous radiogenic heat production and crustal thickness. Crustal heat production clearly plays an important role in explaining heat flow anomalies on the craton. Higher heat flow through the Witwatersrand basin is due to HPE enrichment in its sedimentary strata (Jones, 1988). Jones (1992) noted a dramatic heat flow anomaly at the southern margin of the craton in Northern Lesotho, where heat flow values climb from values of ~40 mW/m² to values as high as 80 mW/m² from north to south. This step function in heat flow occurs on cratonic lithosphere, from which diamonds were derived by Late Cretaceous kimberlites, and is clearly correlated with crustal thickening due to overthrusting of the allochthonous Natal terrane over the craton edge; crustal heat production is much more likely

than higher mantle heat flux for explaining this anomaly. Examining the specific heat flow data in Namaqualand and northern Lesotho (Jones, 1987, 1992), as well as regional compilations (Ballard and Pollack, 1987), it is apparent that the Proterozoic regions of southern Africa are more accurately characterized as not just having a higher *average* heat flow, but also a wider *dispersion* in heat flow, from values similar to those for craton ranging up to much higher values. This is clearly evidence for more heterogeneous crustal heat production in off-craton regions. As noted by Jones (1987) an average of $2 \mu\text{W}/\text{m}^3$ higher heat production in the Proterozoic belts relative to that of the Archean craton could explain the higher average heat flow in the former. Unfortunately, current models of regional crustal composition and heat production, particularly at depth, are inadequate to evaluate this hypothesis, and are an important avenue of further research.

The second possible contribution to the higher heat flow in off-craton regions invokes residual heat flux from the Mesozoic transient thermal perturbation to the lithosphere. The obvious causal mechanism for this perturbation in southern Africa is Late Jurassic to Cretaceous mantle upwelling and magmatism associated with the breakup of Gondwana. If a significant thickness of the lithosphere was perturbed during this disturbance, then simple models of thermal relaxation require several hundred million years to return to cratonic steady state (Vitarello and Pollack, 1980; Morgan, 1984). Some of the regional variation in heat flow in southern Africa could then be due to residual heat from Gondwana break-up. One prediction of this mechanism is that geographic variations in heat flow should correlate with heterogeneous manifestations of Mesozoic heating in the deep lithosphere— such correlations are explored in the next discussion.

7.2.4 Mesozoic lithospheric thermal perturbation

As previously demonstrated, the U-Pb age discordancy of the rutile data in nearly all lower crustal xenolith suites in southern Africa necessitates a pervasive, but heterogeneous Mesozoic thermal perturbation of the continental lithosphere. This perturbation is most evident in the U-Pb isotopic systematics of rutile from the craton-margin and off-craton Northern Lesotho, Eastern Namaqua, and Orapa granulite xenolith suites, which have been partially to completely reset to the age of the host kimberlite eruption. A fuller exploration of the magnitude and duration of this lithospheric heating is warranted considering its implications for the

chemical and thermal modification of the lithospheric mantle, the origins of kimberlite magmatism, and the present thermal structure of southern Africa.

The discordant age systematics of the craton margin lower crustal rutile and titanite can be inverted to yield estimates of the magnitude and duration of the Mesozoic thermal perturbation affecting the southern African lithosphere. Prior to this exercise, the requisite assumption that volume diffusion is the primary mechanism of the Pb-loss in the accessory minerals must be evaluated. First, there is no petrographic indication of rutile or titanite nucleation and growth in the host granulites subsequent to Mesoproterozoic metamorphism, inclusive of *ca* 960 retrograde metamorphic reactions documented in some granulites from both Northern Lesotho and Eastern Namaqualand (Schmitz and Bowring, 2001; Chapter 2). A fairly common phenomenon observed in the rutile crystals of some xenoliths is a replacive reaction of rutile to ilmenite, both on grain boundaries and also as exsolution lamellae within crystals. Although predominantly a replacive transformation (Frost, 1991), this reaction likely involves some minor degree of recrystallization of rutile, which could promote some component of the observed Pb loss and isotopic resetting if mediated by oxidizing fluids associated with Mesozoic heating. Alternatively, if the reaction is ancient, for example during Proterozoic cooling and equilibration, then the development of internal exsolution lamellae of ilmenite in rutile grains is more important for establishing short-circuit pathways for Pb diffusion through the crystal, which essentially decreases the volume diffusion dimension of the rutile from that of the grain size to smaller and more varied radii. This short-circuiting will complicate simple grain size versus age correlations which are common diagnostics of volume diffusion in mineral-isotopic systems. Fortunately, ilmenite oxy-exsolution is easily identified, and affected grains have been avoided for detailed diffusion modeling of rutile U-Pb systematics.

As an example, in granulite suites of the Eastern Namaqualand kimberlites, most analyzed rutile grains exhibit some degree of ilmenite oxyexsolution, and as predicted, the majority of analyzed crystals are nearly completely reset to their entrainment ages, regardless of their grain radii, which ranged from 80 to 200 μm (Fig. 9a). In contrast to most samples, however, the mafic granulite KX12-8 from the Klipfontein-08 kimberlite contains abundant rutile free of reaction to ilmenite. Analysis demonstrates that these rutile exhibit only partial Pb loss, with a clear grain size dependence (Fig. 9b), suggesting that the diffusive radius approaches grain size in these rutile. Duplicate fractions of carefully size rutile from this sample reproduce

the same characteristic discordancy. Further, when large rutile grains from this sample are carefully abraded to remove approximately 5% of their radius, the resulting analyses are substantially and reproducibly less discordant, demonstrating that these rutile contain radially symmetric intra-grain age gradients, consistent with predictions of volume diffusive loss.

To further model these rutile data, we have combine a simple square pulse heating schedule with the Arrhenius relations for volume diffusion for both rutile and titanite (Crank, 1975; McDougall and Harrison, 1999). As discussed in Section 2, we chose the experimental kinetic parameters of Ti self-diffusion in rutile as the best available proxies for Pb tracer diffusion, given similar calculated closure temperature functions. Figure 14a illustrates one set of modeled fractional loss curves, as a function of duration of heating at 450°C, for diffusive radii of 50, 75, and 125 μm . Plotted for comparison as horizontal lines are the observed degrees of fractional Pb-loss for grains of 125 and 75 μm radius from the Klipfontein-08 granulite, and a line for rutile grains from other Eastern Namaqualand granulites whose internal ilmenite exsolution likely reduce their diffusion dimension to <50 μm . It is readily observed that these three predicted and observed sets of curves intersect at along an isochron at 7 Ma, represented by the vertical gray bar, which is the necessary relationship for a volume diffusion mechanism for Pb-loss.

Confident from this analysis that volume diffusion is the operative mechanism for Pb-loss in the rutile grains, we may use similar, if more general model constraints to bracket the possible conditions of temperature versus duration of heating which reproduce the fractional loss characteristics of the analyzed rutile, apatite and titanite. In Figure 14b, the plotted curves represent the modeled loci of given degrees of Pb-loss in various minerals (50 μm diffusion radius) for a given magnitude and duration of heating. Constraints on the degree of fractional Pb-loss observed in these minerals allow us to define an allowable T-t space. The first general constraint is the near concordancy (<3% discordant) of the systematics of all grain sizes of titanite; this observation allows us to eliminate all space to the right of the titanite 3% loss curve as inappropriate for the T-t conditions of heating. Similarly we can eliminate all space to the *left* of the 3% loss in apatite and rutile curves, as tangible Pb-loss has occurred in these minerals. The allowable heating domain is greatly reduced when we take into consideration the near complete Pb-loss induced in all rutile grains <50 μm in diffusion radius, which obviates all space to the left of the 99% loss in rutile curve. On the other hand, apatite data from the Northern

Lesotho granulites exhibits partial, but not complete Pb-loss, therefore we are constrained to space to the left of the apatite 99% loss curve. The remaining allowable T-t space is highlighted as the white field in Figure 14b. The most important observation from this modeling is that, because of the intersection of the rutile and titanite curves, heating cannot have exceeded $\sim 600^{\circ}\text{C}$ and cannot have occurred for less than $\sim 10,000$ years. It should also be emphasized that in choosing to use Ti self-diffusion as a conservative proxy for Pb-diffusion in rutile, the size of the allowable heating field is also conservatively defined. If Pb diffusivities are slower in rutile than Ti self-diffusion, this will shift the 99% loss curve to the right, narrowing the allowable heating field to lower temperatures and longer duration.

Immediately, this analysis eliminates very transient, high temperature heating during kimberlite entrainment for causing the isotopic resetting of the thermochronometers. This supports previous qualitative inferences from the preservation of Proterozoic ages in granulitic rutiles from cratonic kimberlites (Section 7.1.1). The remaining allowable T-t field demands that heating of the lower crust was a more prolonged, but relatively moderate temperature perturbation. We consider it significant that the allowable thermal perturbation includes low-temperature heating for tens of millions of years to as much as 100 Ma. This type of thermal transient has the appropriate timescale of a causal mechanism related to Gondwanide rifting and initiation of southern Indian Ocean opening by the voluminous 180 Ma Karoo magmatic event. Similarly, southern Atlantic opening at 120 Ma was accompanied by mantle upwelling and magmatism to produce the Etendeka-Parana magmatic province, superposing a second thermal perturbation on the southern African lithosphere. These magmatic outpourings may also be punctuated events in a broader episode of upwelling and anomalously high temperatures in the upper mantle beneath southern Africa, whether induced by, or driving continental breakup.

In Section 7.2.3 it was demonstrated that a cratonic thermal state had to have been established within *both* on- and off-craton lithospheric mantle by the Neoproterozoic; the associated 40 mW/m^2 conductive geotherm serves to define the lower surface of nearly all of the southern African mantle xenolith P-T data. Figure 13 further shows that the requisite transient temperatures of 450 to 550°C in the lower crust inferred for the Late Mesozoic thermal perturbation are consistent with temperatures predicted by conductive geotherms based on a surface heat flow of $\text{ca } 55 \text{ mW/m}^2$ (Jones, 1987), and that this same geotherm also serves to define the upper surface of the envelope of mantle xenolith P-T data from both on-and off-craton

southern African kimberlites. Together these two lower crustal thermochronological constraints very simply demonstrate that all of the dispersion and inflection in mantle xenolith P-T arrays can be explained by a thermal perturbation, lasting for several tens of millions of years, sufficient to raise the temperature of much of the lithosphere by 200 to 300°. The idea that southern African mantle xenolith chemical and thermobarometric systematics record transient phenomena is not a new one. Boyd (1973) introduced the concept of a kinked mantle xenolith geotherm as a record of lithospheric thermal transience. Robey (1981) originally pointed out the previously noted P-T incongruities between Jurassic and Cretaceous kimberlite-borne peridotites in Eastern Namaqualand, which Finnerty and Boyd (1986) suggested as recording thermal effects related to Karoo magmatism. The major contribution of lower crustal thermochronology is to extend and quantify the timescales of these transient thermal effects beyond the brief magmatic timescales of kimberlite generation and eruption, to the plate tectonic timescales of continental breakup and the thermal re-equilibration of the entire lithosphere.

As with the lithospheric mantle record, the lower crustal manifestation of this Mesozoic thermal perturbation is spatially and temporally heterogeneous. No evidence of it is seen in granulites exhumed from the western craton at 114 Ma in the Newlands kimberlite. However a few tens of percent Pb-loss is documented in lower crustal rutile from the Free State kimberlites, exhumed 30 million years earlier from the central craton. Only once you move to the margins of the craton do you find evidence for more substantial thermal effects in the lower crust beneath Orapa, Eastern Namaqualand, and Northern Lesotho. In Eastern Namaqualand heating is manifested as early as 117 Ma (Markt) and continues through to the Late Cretaceous. Thermal effects are fully manifested in the lower crust by 90 Ma in Northern Lesotho. This spatial and temporal heterogeneity in the response of the lithosphere to thermal perturbation suggests a similar differential advective focussing of heat transport through the lithosphere. The common thread connecting these spatial and temporal patterns of thermal perturbation may be the presence of pre-existing lithospheric structure. It is striking that the regions where lower crustal thermal effects are the most developed are along the ancient boundaries between Archean and Proterozoic terrains (Figure 3). There was an apparent similar focussing of 180 Ma magmatism in some of these same regions, for example the vents and plateau basalts of the Lesotho region, and the Botswana dike swarm (Figure 15).

Finally, we note that kimberlite magmatism is another clearly heterogeneous spatial and temporal phenomena in southern Africa (Dawson, 1989) which must be a similarly complex response of the lithosphere to thermal perturbation. Further efforts toward establishing the high-precision geochronology of kimberlite eruptions in southern Africa may shed more light on this response. In a holistic manner, examining the mantle lithospheric record in kimberlites, xenoliths, and megacrysts in light of this model of pervasive Mesozoic thermal re-equilibration, and establishing further correlations between lower crustal thermal effects, mantle chemical and thermal perturbations, and lithospheric structure and tectonics will be fruitful avenues of future research into the evolution of the southern African continental lithosphere.

8. Conclusions

U-Pb rutile and titanite thermochronology of lower crustal granulite xenoliths constrain the thermal evolution of the southern African continental lithosphere by recording progressive cooling of the lithosphere following tectonothermal perturbation, and thermal reactivation of the lithosphere during transient heating events. Within the Archean Kaapvaal craton, U-Pb rutile isotopic closure, corresponding to cooling of the deep lithosphere through approximately 400°C, last occurred in the Mesoproterozoic (~1000 Ma), following numerous thermal perturbations correlative with marginal orogenesis and intraplate magmatism. In lower crustal xenoliths of the craton-marginal Mesoproterozoic Namaqua, Natal, and Magondi orogenic belts, U-Pb titanite, apatite, and rutile data consistent cooling rates in the deep lithosphere of approximately 1°C/Ma following collisional orogenesis, which culminated in Neoproterozoic (650 to 850 Ma) cooling through rutile U-Pb isotopic closure and the establishment of cratonic geotherms throughout the lithospheric mantle of the Proterozoic orogenic belts. These cratonic thermal gradients in the Proterozoic regions necessitate a thick, >200 km lithospheric mantle keel extending into the diamond stability field at least prior to Late Jurassic Gondwana breakup. Concepts of thinner Proterozoic lithosphere restricted the graphite stability field, or thermodynamic diamond stability in hotter Proterozoic lithosphere are untenable in light of the lower crustal data, and other causes (composition, tectonic evolution) for the diamond fertility contrast between Archean and Proterozoic lithosphere in southern Africa must be explored.

A widespread thermal reactivation of the southern African lithosphere in the Late Mesozoic is also recorded in the U-Pb systematics of lower crustal rutile. While absent, or only

mildly affecting the Kaapvaal cratonic nucleus, this heating event caused partial to complete isotopic resetting of rutile systems in the lower crust of the craton margins and bounding Proterozoic orogenic belts. Modeling of the partial resetting of rutile systematics, combined with the absence of isotopic resetting in the titanite thermochronometer, indicate that this heating event was of modest magnitude, ~450 to 550°C, but prolonged duration, from tens of thousands to tens of millions of years, and was most likely related to the same upper mantle dynamics which Gondwana breakup between 180 and 120 Ma.

These conditions of heating in the lower crust are consistent with the geothermal gradients in the deeper lithosphere inferred from thermobarometry of mantle xenoliths from the same craton-margin and off-craton kimberlite provinces. “Off-craton” geotherms, which are elevated with respect to cratonic gradients, are thus indicative of transient thermal conditions rather than steady-state conditions of heat flow through a thinner lithosphere. The clear record of Neoproterozoic cooling of the Proterozoic off-craton lower crust through rutile U-Pb closure to cratonic thermal gradients demands comparable lithospheric thicknesses of greater than 250 km, well into the diamond stability field, at least prior to Late Jurassic magmatism and rifting. Finally, the spatial and possible temporal heterogeneity in the manifestation of this thermal perturbation in the lower crust and underlying mantle lithosphere may result from conductive and/or advective focussing along pre-existing lithospheric structures like the Proterozoic-Archean cratonic sutures. Similar spatial and temporal heterogeneity in kimberlite magmatism across the southern African continent may represent another reflection of the progressive thermal reactivation of the continental lithosphere during the Late Mesozoic.

Acknowledgements— The authors would like to thank Dr. Jock Robey for his insight into the distribution and significance of lower crustal granulites in southern Africa, and invaluable assistance in procuring samples of the deep crust. Fruitful discussions with Dr. David Bell revealed the rich and complementary patterns of chemical and thermal transience in the southern African lithospheric mantle. This research was conducted under the auspices of a National Defense Science and Engineering Fellowship, U.S. Army Research Office grant DAAH049510560 to MDS, and by NSF Continental Dynamics Program grant EAR9526702 to SAB.

References

- Armstrong, R.A., Compston, W., Retief, E.A., Williams, I.S., Welke, H.J., 1991. Zircon ion microprobe studies bearing on the age and evolution of the Witwatersrand triad. *Precambrian Research* 53, 243-266.
- Ballard, S., Pollack, H.N., 1987. Diversion of heat by Archean cratons: a model for southern Africa. *Earth and Planetary Science Letters* 85, 253-264.
- Bibikova, E., Skiold, T., Bogdanova, S., Gorbatshev, R., Slabunov, A., 2001. Titanite-rutile thermochronometry across the boundary between the Archean craton in Karelia and the Belomorian mobile belt, eastern Baltic Shield. *Precambrian Research* 105, 315-330.
- Boyd, F.R., 1973. A pyroxene geotherm. *Geochimica et Cosmochimica Acta* 37, 2533-2546.
- Boyd, F.R., Gurney, J.J., 1982. Low-calcium garnets: keys to craton structure and diamond crystallization. *Carnegie Institute of Washington Yearbook* 81, 261-267.
- Boyd, F.R., Gurney, J.J., 1986. Diamonds and the African lithosphere. *Science* 232, 472-477.
- Boyd, F.R., Nixon, P.H., 1979. Garnet ilmenite xenoliths from the kimberlites of East Griqualand, South Africa. *Carnegie Institute of Washington Yearbook* 78, 488-492.
- Canil, D., Fedortchouk, Y., 1999. Garnet dissolution and the emplacement of kimberlites. *Earth and Planetary Science Letters* 167, 227-237.
- Chamberlain, K.R., Bowring, S.A., 2000. Apatite-feldspar U-Pb thermochronometer: a reliable, mid-range (~450°C), diffusion-controlled system. *Chemical Geology* 172, 173-200.
- Chapman, D.S., 1986. Thermal gradients in the continental crust. *In: The Nature of the Lower Continental Crust*. Dawson, J.B., Carswell, D.A., Hall, J., Wedepohl, K.H. (Eds.), Geological Society Special Publication 24, Oxford University Press, London, 63-70.
- Chapman, D.S., Pollack, H.N., 1977. Regional geotherms and lithospheric thickness. *Geology* 5, 265-268.
- Cherniak, D.J., 1993. Lead diffusion in titanite and preliminary results on the effects of radiation damage on Pb transport. *Chemical Geology* 110, 177-194.
- Cherniak, D.J., 2000. Pb diffusion in rutile. *Contributions to Mineralogy and Petrology* 139, 198-207.
- Cherniak, D.J., Lanford, W.A., Ryerson, F.J., 1991. Lead diffusion in apatite and zircon using ion implantation and Rutherford Backscattering techniques. *Geochimica et Cosmochimica Acta* 55, 1663-1673.
- Cherniak, D.J., Watson, E.B., 2001. Pb diffusion in zircon. *Chemical Geology* 172, 5-24.
- Cherniak, D.J., Watson, E.B., Harrison, T.M., Grove, M., 2000. Pb diffusion in monazite: a progress report on a combined RBS/SIMS study [abs.]. *EOS (Transactions, American Geophysical Union)* 82, S232.
- Christofell, C.A., Connelly, J.N., Ahall, K.L., 1999. Timing and characterization of recurrent pre-Sveconorwegian metamorphism and deformation in the Varberg-Halmstad region of SW Sweden. *Precambrian Research* 98, 173-195.
- Connelly, J.N., van Gool, J.A.M., Mengel, F.C., 2000. Temporal evolution of a deeply eroded orogen: the Nagssugtoqidian Orogen, West Greenland. *Canadian Journal of Earth Sciences* 37, 1121-1142.
- Corfu, F., Easton, R.M., 1995. U-Pb geochronology of the Mazinaw terrane, an imbricate segment of the Central Metasedimentary Belt, Grenville Province, Ontario. *Canadian Journal of Earth Sciences* 32, 959-976.
- Corfu, F., Easton, R.M., 2000. U-Pb evidence for polymetamorphic history of Huronian rocks within the Grenville front tectonic zone east of Sudbury, Ontario, Canada. *Chemical Geology* 172, 149-171.
- Corfu, F., Stone, D., 1998. The significance of titanite and apatite U-Pb ages: constraints for the post-magmatic thermal-hydrothermal evolution of a batholithic complex, Berens River area, northwestern Superior Province. *Geochimica et Cosmochimica Acta* 62, 2979-2995.
- Cornell, D.H., Armstrong, R.A., Walraven, F., 1998. Geochronology of the Proterozoic Hartley Basalt Formation, South Africa: constraints on the Kheis tectogenesis and the Kaapvaal Craton's earliest Wilson Cycle. *Journal of African Earth Sciences* 26, 5-27.
- Cornell, D.H., Humphreys, H., Theart, H.F.J., Scheepers, D.J., 1992. A collision-related pressure-temperature-time path for Prieska Copper Mine, Namaqua-Natal tectonic province, South Africa. *Precambrian Research* 59, 43-71.
- Cox, R.A., Dunning, G.R., Indares, A., 1998. Petrology and U-Pb geochronology of mafic, high-pressure, metamorphic coronites from the Tshenukutish domain, eastern Grenville Province. *Precambrian Research* 90, 59-83.
- Crank, J., 1975. *The Mathematics of Diffusion*, 2nd ed. Clarendon Press, Oxford, 414 p.
- Crowley, J.L., Ghent, E.D., 1999. An electron microprobe study of the U-Th-Pb systematics of metamorphosed monazite; the role of Pb diffusion versus overgrowth and recrystallization. *Chemical Geology* 157, 285-302.
- Dahl, P.S., 1996. The crystal-chemical basis for Ar retention in micas: inferences from interlayer partitioning and implications for geochronology. *Contributions to Mineralogy and Petrology* 123, 22-39.

- Dahl, P.S., 1997. A crystal-chemical basis for Pb retention and fission-track annealing systematics in U-bearing minerals, with implications for geochronology. *Earth and Planetary Science Letters* 150, 277-290.
- Davies, G.F., Strebeck, J.W., 1982. Old continental geotherms: constraints on heat production and thickness of continental plates. *Geophysical Journal of the Royal Astronomical Society* 69, 623-634.
- Davis, G.L., 1977. The ages and uranium contents of zircons from kimberlites and associated rocks. *Carnegie Institute of Washington Yearbook* 76, 631-635.
- Davis, W.J., 1997. U-Pb zircon and rutile ages from granulite xenoliths in the Slave province: evidence for mafic magmatism in the lower coincident with Proterozoic dike swarms. *Geology* 25, 343-346.
- Dawson, J.B., 1989. Geographic and time distribution of kimberlites and lamproites: relationships to tectonic processes. *In: Kimberlites and Related Rocks Vol.1: Their Composition, Occurrence, Origin, and Emplacement.* Ross, J. (Eds.), Geological Society of Australia Special Publication 14, Blackwell Scientific Publishers, Carlton, Victoria, Australia, 323-342.
- Dawson, J.B., Harley, S.L., Rudnick, R.L., Ireland, T.R., 1997. Equilibration and reaction in Archaean quartz-sapphirine granulite xenoliths from the Lace kimberlite pipe, South Africa. *Journal of Metamorphic Geology* 15, 253-266.
- Dawson, J.B., Smith, J.V., 1987. Reduced sapphirine granulite xenoliths from the Lace Kimberlite, South Africa: implications for the deep structure of the Kaapvaal Craton. *Contributions to Mineralogy and Petrology* 95, 376-383.
- De Wit, M.J., Bowring, S.A., Ashwal, L.D., Randriansolo, L.G., Morel, V.P.I., Rambelison, R.A., 2001. Age and tectonic evolution of Neoproterozoic ductile shear zones in southwestern Madagascar, with implications for Gondwana studies. *Tectonics* 20, 1-45.
- Dodson, M.H., 1973. Closure temperature in cooling geochronological and petrological systems. *Contributions to Mineralogy and Petrology* 40, 259-274.
- Dodson, M.H., 1986. Closure profiles in cooling systems. *Materials Science Forum* 7, 145-154.
- Duncan, R.A., Hooper, P.R., Rahecek, J., Marsh, J.S., Duncan, A.R., 1997. The timing and duration of the Karoo igneous event, southern Gondwana. *Journal of Geophysical Research* 102, 18127-18138.
- Durrheim, R.J., Mooney, W.D., 1994. Evolution of the Precambrian lithosphere: seismological and geochemical constraints. *Journal of Geophysical Research* 99, 15359-15374.
- Finnerty, A.A., Boyd, F.R., 1987. Thermobarometry for garnet peridotites: basis for the determination of thermal and compositional structure of the upper mantle. *In: Mantle Xenoliths.* Nixon, P.H. (Eds.), pp. 381-402 Wiley-Interscience, Chichester, U.K..
- Freer, R., 1980. Bibliography: self diffusion and impurity diffusion in oxides. *Journal of Materials Science* 15, 803-824.
- Frost, B.R., 1991. Stability of oxide minerals in metamorphic rocks. *In: Oxide Minerals: Petrologic and Magnetic Significance.* Lindsley, D.H., Ribbe, P.H. (Eds.), *Reviews in Mineralogy* 25, Mineralogical Society of America, 469-488.
- Giletti, B.J., 1974. Studies in diffusion: I. Argon in phlogopitic mica. *In: Geochemical Transport and Kinetics.* Hofmann, A.W., Giletti, B.J., Yoder, H.S., Yund, R.A. (Eds.), Carnegie Institute of Washington, Carnegie Institute of Washington, 107-115.
- Grantham, G.H., Thomas, R.J., Eglinton, B.M., de Bruin, D., Atanasov, A., Evans, M.J., 1993. Corona textures in Proterozoic olivine melanorites of the Equeefa Suite, Natal Metamorphic Province, South Africa. *Mineralogy and Petrology* 49, 91-102.
- Green, R.W.E., Durrheim, R.J., 1990. A seismic refraction investigation of the Namaqualand Metamorphic Complex, South Africa. *Journal of Geophysical Research* 95, 19927-19932.
- Griffin, W.L., Carswell, D.A., Nixon, P.H., 1979. Lower crustal granulites and eclogites from Lesotho, southern Africa. *In: The Mantle Sample: Inclusions in Kimberlites and other Volcanics.* Boyd, F.R., Meyer, H.O.A. (Eds.), *Proceedings of the 2nd International Kimberlite Conference 2*, American Geophysical Union, Washington, D.C., 59-86.
- Grotzinger, J.P., Bowring, S.A., Saylor, B.Z., Kaufman, A.J., 1995. Biostratigraphic and geochronologic constraints on early animal evolution. *Science* 270, 598-604.
- Grove, M., Harrison, T.M., 1996. ⁴⁰Ar* diffusion in Fe-rich biotite. *American Mineralogist* 81, 940-951.
- Hanson, G.N., Catanzaro, E.J., Anderson, D.H., 1971. U-Pb ages for sphene in a contact metamorphic zone. *Earth and Planetary Science Letters* 12, 231-237.
- Harrison, T.M., Copeland, P., Hall, S.A., Quade, J., Burner, S., Ojha, T.P., Kidd, W.S.F., 1993. Isotopic preservation of Himalayan/Tibetan uplift, denudation, and climatic histories of two molasse deposits. *Journal of Geology* 101, 157-175.

- Harte, B., Jackson, P.M., Macintyre, R.M., 1981. Age of mineral equilibria in granulite facies nodules from kimberlites. *Nature* 291, 147-148.
- Heaman, L., Parrish, R., 1991. U-Pb geochronology of accessory minerals. *In: Applications of Radiogenic Isotope Systems to Problems in Geology*. Heaman, L., and Ludden, J.N. (Eds.), Short Course Handbook 19, Mineralogical Association of Canada, Toronto, 59-102.
- Hodges, K.V., 1991. Pressure-temperature-time paths. *Annual Reviews of Earth and Planetary Sciences* 19, 207-236.
- Hodges, K.V., Hames, W.E., Bowring, S.A., 1994. $^{40}\text{Ar}/^{39}\text{Ar}$ age gradients in micas from a high-temperature-low-pressure metamorphic terrain: evidence for very slow cooling and implications for the interpretation of age spectra. *Geology* 22, 55-58.
- Humphreys, H.C., Cornell, D.H., 1989. Petrology and geochronology of low-pressure mafic granulites in the Marydale Group, South Africa. *Lithos* 22, 287-303.
- Jacobs, J., Falter, M., Thomas, R.J., Kunz, J., Jebberger, E.G., 1997. $^{40}\text{Ar}/^{39}\text{Ar}$ thermochronological constraints on the structural evolution of the Mesoproterozoic Natal Metamorphic Province, SE Africa. *Precambrian Research* 86, 71-92.
- Jenkin, G.R.T., Ellam, R.M., Rogers, G., Stuart, F.M., 2001. An investigation of closure temperature of the biotite Rb-Sr system: the importance of cation exchange. *Geochimica et Cosmochimica Acta* 65, 1141-1160.
- Jones, M.Q.W., 1987. Heat flow and heat production in the Namaqua Mobile Belt, South Africa. *Journal of Geophysical Research* 92, 6273-6289.
- Jones, M.Q.W., 1988. Heat flow in the Witwatersrand Basin and environs and its significance for the South African shield geotherm and lithosphere thickness. *Journal of Geophysical Research* 93, 3243-3260.
- Jones, M.Q.W., 1992. Heat flow anomaly in Lesotho: implications for the southern boundary of the Kaapvaal craton. *Geophysical Research Letters* 19, 2031-2034.
- Kelley, S.P., Wartho, J.-A., 2000. Rapid kimberlite ascent and the significance of Ar-Ar ages in xenolith phlogopites. *Science* 289, 609-611.
- Kennedy, C.S., Kennedy, G.C., 1976. The equilibrium boundary between graphite and diamond. *Journal of Geophysical Research* 81, 2467-2470.
- Krogh, T.E., 1973. A low contamination method for hydrothermal decomposition of zircon and extraction of U and Pb for isotopic age determination. *Geochimica et Cosmochimica Acta* 37, 485-494.
- Krogh, T.E., 1982. Improved accuracy of U-Pb zircon ages by the creation of more concordant systems using an air abrasion technique. *Geochimica et Cosmochimica Acta* 46, 637-649.
- Krogstad, E.J., Walker, R.J., 1994. High closure temperatures of the U-Pb system in large apatites from the Tin Mountain pegmatite, Black Hills, South Dakota, USA. *Geochimica et Cosmochimica Acta* 58, 3845-3853.
- Ludwig, K.R., 1980. Calculation of uncertainties of U-Pb isotope data. *Earth and Planetary Science Letters* 46, 212-220.
- MacIntyre, R.M., Dawson, J.B., 1974. Age significance of some South African kimberlites. 4th Euro. Collog. Geochron. *Cosmochron. Isotope Geol.*, 66.
- Majaule, T., Hanson, R.E., Key, R.M., Singletary, S.J., Martin, M.W., Bowring, S.A., 2001. The Magondi Belt in northeast Botswana: regional relations and new geochronological data from the Sua Pan area. *Journal of African Earth Sciences* 32, 257-267.
- Mapeo, R.B.M., Armstrong, R.A., Kampunzu, A.B., 2001. SHRIMP U-Pb zircon geochronology of gneisses from the Gweta borhole, northeast Botswana: implications for the Paleoproterozoic Magondi Belt in southern Africa. *Geological Magazine* 138, 299-308.
- Mattinson, J.M., 1978. Age, origin, and thermal histories of some plutonic rocks from the Salinian block of California. *Contributions to Mineralogy and Petrology* 67, 233-245.
- McDougall, I., Harrison, T.M., 1999. *Geochronology and Thermochronology by the $^{40}\text{Ar}/^{39}\text{Ar}$ Method*, 2nd ed. Oxford University Press, New York, 269 pp.
- Menzies, A.H., Carlson, R.W., Shirey, S.B., Gurney, J.J., 1999. Re-Os systematics of Newlands peridotite xenoliths: implications for diamond and lithosphere formation. *In: The P.H. Nixon Volume: Proceedings of the 7th International Kimberlite Conference, Volume 2*. Gurney, J.J., Gurney, J.L., Pascoe, M.D., Richardson, S.H. (Eds.), pp. 566-573 Red Roof Design, Cape Town, S.A..
- Mezger, K., Essene, E.J., van der Pluijm, B.A., Halliday, A.N., 1993. U-Pb geochronology of the Grenville Orogen of Ontario and New York: constraints on ancient crustal tectonics. *Contributions to Mineralogy and Petrology* 114, 13-26.
- Mezger, K., Hanson, G.N., Bohlen, S.R., 1989. High-precision U-Pb ages of metamorphic rutile: application to the cooling history of high-grade terranes. *Earth and Planetary Science Letters* 96, 106-118.

- Mezger, K., Rawnsley, C.M., Bohlen, S.R., Hanson, G.N., 1991. U-Pb garnet, sphene, monazite, and rutile ages: implications for the duration of high-grade metamorphism and cooling histories, Adirondack Mts., New York. *Journal of Geology* 99, 415-428.
- Möller, A., Mezger, K., Schenk, V., 2000. U-Pb dating of metamorphic minerals: Pan-African metamorphism and prolonged slow cooling of high pressure granulites in Tanzania, East Africa. *Precambrian Research* 104, 123-146.
- Morgan, P., 1984. The thermal structure and thermal evolution of continental lithosphere. *Physics and Chemistry of the Earth* 15, 107-193.
- Morgan, P., Sass, J.H., 1984. Thermal regime of the continental lithosphere. *Journal of Geodynamics* 1, 143-166.
- Nguuri, T.K., Gore, J., James, D.E., Webb, S.J., Wright, C., Zengeni, T.G., Gwavava, O., Snoke, J.A., Kaapvaal Seismic Group, 2001. Crustal structure beneath southern Africa and its implications for the formation and evolution of the Kaapvaal and Zimbabwe cratons. *Geophysical Research Letters* 28, 2501-2504.
- Norcross, C., Davis, D.W., Spooner, E.T.C., Rust, A., 2000. U-Pb and Pb-Pb age constraints on Paleoproterozoic magmatism, deformation and gold mineralization in the Omai area, Guyana Shield. *Precambrian Research* 102, 69-86.
- Onstott, T.C., Hargraves, R.B., Joubert, P., 1986. Constraints on the tectonic evolution of the Namaqua Province II: reconnaissance paleomagnetic and $^{40}\text{Ar}/^{39}\text{Ar}$ results from the Namaqua Province and Kheis Belt. *Transactions of the Geological Society of South Africa* 89, 143-170.
- Pearson, N.J., O'Reilly, S.Y., Griffin, W.L., 1995. The crust-mantle boundary beneath cratons and craton margins: a transect across the south-west margin of the Kaapvaal craton. *Lithos* 36, 257-287.
- Phillips, D., Machin, K.J., Kiviets, G.B., Fourie, L.F., Roberts, M.A., Skinner, E.M.W., 1999. A petrographic and $^{40}\text{Ar}/^{39}\text{Ar}$ geochronological study of the Voorspoed kimberlite, South Africa: implications for the origin of Group II kimberlite magmatism. *South African Journal of Geology* 101, 299-306.
- Ramokate, L.V., Mapeo, R.B.M., Corfu, F.J., Kampunzu, A.B., 2000. Proterozoic geology and regional correlation of the Ghanzi-Makunda area, western Botswana. *Journal of African Earth Sciences* 30, 453-466.
- Reimold, W.U., Pybus, G.Q.J., Kruger, J.F., Layer, P.W., Koeberl, C., 2000. The Anna's Rust Sheet and related gabbroic intrusions in the Vredefort Dome-Kibaran magmatic event on the Kaapvaal Craton and beyond? *Journal of African Earth Sciences* 31, 499-521.
- Robey, J., 1981. Kimberlites of the central Cape Province, R.S.A.. Unpublished Ph.D. thesis, University of Cape Town.
- Rudnick, R.L., McDonough, W.F., O'Connell, R.J., 1998. Thermal structure, thickness and composition of continental lithosphere. *Chemical Geology* 145, 395-411.
- Santos Zalduegui, J.F., Scharer, U., Gil Ibarguchi, J.I., Girardeau, J., 1996. Origin and evolution of the Paleozoic Cabo Ortegal ultramafic-mafic complex (NW Spain): U-Pb, Rb-Sr and Pb-Pb isotope data. *Chemical Geology* 129, 281-304.
- Schaltegger, U., Fanning, C.M., Gunther, D., Maurin, J.C., Schulmann, K., Gebauer, D., 1999. Growth, annealing and recrystallization of zircon and preservation of monazite in high-grade metamorphism: conventional and in-situ U-Pb isotope, cathodoluminescence and microchemical evidence. *Contributions to Mineralogy and Petrology* 134, 186-201.
- Schärer, U., Krogh, T.E., Gower, C.F., 1986. Age and evolution of the Grenville Province in eastern Labrador from U-Pb systematics in accessory minerals. *Contributions to Mineralogy and Petrology* 94, 438-451.
- Schmitz, M.D., Bowring, S.A., 2001. The significance of U-Pb zircon dates in lower crustal xenoliths from the southwestern margin of the Kaapvaal craton, southern Africa. *Chemical Geology* 172, 59-76.
- Singletary, S.J., 1999. Geochronology and regional tectonic significance of isolated Proterozoic basement outcrops and drill cores in the Kalahari Desert, Botswana. M.Sc. thesis, Texas Christian University, 99 p.
- Skinner, E.M.W., Viljoen, K.S., Clark, T.C., Smith, C.B., 1992. The petrography, tectonic setting and emplacement ages of kimberlites in the southwestern border region of the Kaapvaal Craton, Prieska area, South Africa. *In: Kimberlites, Related Rocks and Mantle Xenoliths: Proceedings of the 5th International Kimberlite Conference.* Meyer, H.O.A., Leonardos, O.H. (Eds.), Special Publication 92/1, CPRM (Companhia Pesquisa Recurs. Miner.), Brasilia, 80-97.
- Smith, C.B., Allsopp, H.L., Kramers, J.D., Hutchinson, G., Roddick, J.C., 1985. Emplacement ages of Jurassic-Cretaceous South African kimberlites by the Rb-Sr method on phlogopite and whole-rock samples. *Transactions of the Geological Society of South Africa* 88, 249-266.
- Smith, C.B., Clark, T.C., Barton, E.S., Bristow, J.W., 1994. Emplacement ages of kimberlite occurrences in the Prieska region, southwest border of the Kaapvaal Craton, South Africa. *Chemical Geology* 113, 149-169.
- Smith, H.A., Giletti, B.J., 1997. Lead diffusion in monazite. *Geochimica et Cosmochimica Acta* 61, 1047-1055.

- Suzuki, K., Adachi, M., Kajizuka, I., 1994. Electron microprobe observations of Pb diffusion in metamorphosed detrital monazites. *Earth and Planetary Science Letters* 128, 391-405.
- Thomas, R.J., Agenbacht, A.L.D., Cornell, D.H., Moore, J.M., 1994. The Kibaran of southern Africa: tectonic evolution and metallogeny. *Ore Geology Reviews* 9, 131-160.
- Thomas, R.J., Von Veh, M.W., McCourt, S., 1993. The tectonic evolution of southern Africa: an overview. *Journal of African Earth Sciences* 16, 5-24.
- Tilton, G.R., 1960. Volume diffusion as a mechanism for discordant lead ages. *Journal of Geophysical Research* 65, 2933-2945.
- Tucker, R.D., Raheim, A., Krogh, T.E., Corfu, F., 1986. Uranium-lead zircon and titanite ages from the northern portion of the Western Gneiss Region, south-central Norway. *Earth and Planetary Science Letters* 81, 203-211.
- Verwoerd, W.J., Weder, E.E.W., Harmer, R.E., 1992. The Stukpan Carbonatite in the Orange Free State goldfield. *South African Journal of Geology* 96, 108-118.
- Viljoen, K.S., 1989. Unpublished Ph.D. thesis, University of the Witwatersrand, Johannesburg.
- Vitarello, I., Pollack, H.N., 1980. On the variation of continental heat flow with age and the thermal evolution of continents. *Journal of Geophysical Research* 85, 983-995.
- Wasserburg, G.J., 1963. Diffusion processes in lead-uranium systems. *Journal of Geophysical Research* 68, 4821-4846.
- Waters, D.J., 1990. Thermal history and tectonic setting of the Namaqualand granulites, southern Africa: clues to Proterozoic crustal development. *In: Granulites and Crustal Evolution*. Vielzeuf, D., Vidal, Ph. (Eds.), Kluwer Academic Publishers, Netherlands, 243-256.
- Wetherill, G.W., 1956. Discordant uranium-lead ages, I. *Transactions of the American Geophysical Union* 37, 320-326.
- Willigers, B.J.A., Krogstad, E.J., Wijbrans, J.R., 2001. Comparison of thermochronometers in a slowly cooled terrain: Nagssugtoqidian Orogen, West Greenland. *Journal of Petrology* 42, 1729-1749.

Table 1. U-Pb isotopic data for accessory minerals from lower crustal xenoliths

#	Xeno-lith	Frac-tion ^a	Prop-erties ^a	Diam (μm) ^b	Wt. (mg) ^b	Composition					Isotopic Ratios					corr. coef.	Dates (Ma)					
						[U] (ppm)	Th ^c U	[Pb] (ppm)	Pb ^{*d} Pbc	Pbc ^d (pg)	²⁰⁶ Pb ^e / ²⁰⁴ Pb	²⁰⁸ Pb ^f / ²⁰⁶ Pb	²⁰⁶ Pb ^f / ²³⁸ U	% err ^g	²⁰⁷ Pb ^f / ²³⁵ U		% err ^g	²⁰⁷ Pb ^f / ²⁰⁶ Pb	% err ^g	²⁰⁶ Pb ^h / ²³⁸ U	²⁰⁷ Pb ^h / ²³⁵ U	²⁰⁷ Pb ^h / ²⁰⁶ Pb
Free State Kimberlites																						
<i>Lace (KX1)</i>																						
1	KX1-1	r1	7,bl,e,l	100	0.081	4.80	2.30	1.86	35.8	3.37	118.1	1.118	0.16183	(1.08)	2.11342	(1.23)	0.09472	(.50)	0.914	966.9	1153.2	1522.4
2		r2	4,rd,e,l	100	0.079	4.77	0.09	0.79	18.9	2.55	172.7	0.039	0.13342	(1.42)	1.44666	(1.53)	0.07864	(.42)	0.962	807.4	908.5	1163.0
3		r7	10,bl,s,r	200	1.640	6.73	0.02	1.23	131.7	14.3	887.0	0.007	0.18106	(.29)	2.21523	(.33)	0.08874	(.16)	0.882	1072.8	1185.9	1398.5
4		r14	1,bl,e,r	400	0.480	7.29	0.04	1.58	63.4	11.0	687.3	0.014	0.21105	(.19)	2.51117	(.26)	0.08630	(.17)	0.763	1234.4	1275.3	1344.8
5		r15	2,bl,s,q	400	0.719	2.10	0.09	0.49	72.2	3.99	254.6	0.032	0.19870	(.26)	2.37950	(.30)	0.08685	(.14)	0.885	1168.3	1236.5	1357.3
6		r16	4,bl,f	500	1.021	5.47	0.02	1.10	58.3	18.3	1121	0.010	0.20023	(.12)	2.74352	(.14)	0.09938	(.07)	0.875	1176.5	1340.3	1612.4
7	KX1-2	r1	1,br,s,l	300	0.421	2.44	0.05	0.59	49.4	4.10	264.4	0.018	0.20701	(.36)	2.54862	(.42)	0.08929	(.20)	0.885	1212.9	1286.0	1410.5
8		r2	2,br,s,l	300	0.652	1.83	0.14	0.44	96.8	2.03	131.7	0.068	0.16421	(.37)	2.16985	(.59)	0.09584	(.42)	0.704	980.1	1171.4	1544.6
9		r3	4,br,s,l	300	1.441	2.54	0.05	0.42	66.5	8.11	502.7	0.026	0.15363	(.53)	1.91198	(.88)	0.09026	(.67)	0.654	921.3	1085.3	1431.1
10	KX1-8	r1	1,bl,s,r	280	0.358	1.99	0.06	0.45	11.1	13.9	882.7	0.022	0.22348	(.48)	3.16866	(.50)	0.10283	(.11)	0.974	1300.3	1449.6	1675.9
11		r3	4,br,f	300	1.035	2.02	0.05	0.51	65.8	7.14	441.5	0.020	0.23239	(.20)	3.33759	(.23)	0.10416	(.11)	0.875	1347.0	1489.9	1699.6
12		r4	1,bl,e,l	300	0.101	2.12	0.06	0.57	7.0	7.99	528.4	0.022	0.26881	(1.31)	4.00064	(1.33)	0.10794	(.19)	0.990	1534.8	1634.3	1765.0
13		r6	1,bl,e,r	220	0.114	2.05	0.26	0.51	4.1	14.4	907.7	0.104	0.23841	(.46)	3.67219	(.48)	0.11171	(.14)	0.959	1378.4	1565.3	1827.4
<i>Voorspoed (KX2)</i>																						
14	KX2-1	r1	12,bl,f	150	0.369	12.6	0.00	2.96	65.5	15.8	971.5	0.000	0.23451	(.15)	3.43940	(.21)	0.10637	(.15)	0.716	1358.1	1513.4	1738.1
15		r2	1,bl,e,q	250	0.092	14.2	0.00	3.95	18.2	19.3	1204	0.000	0.28071	(.24)	4.37760	(.27)	0.11310	(.11)	0.910	1594.9	1708.1	1849.9
16		r3	2,bl,e,q	250	0.166	13.5	0.03	2.96	133.1	2.72	181.4	0.013	0.17169	(.22)	1.94780	(.45)	0.08228	(.37)	0.584	1021.4	1097.7	1252.2
17		r4	4,br,f	250	0.297	13.6	0.04	2.95	30.4	28.0	1728	0.014	0.22174	(.14)	2.91434	(.15)	0.09532	(.07)	0.896	1291.1	1385.6	1534.5
18		r5	5,br,e,l	80	0.047	13.6	0.01	2.24	10.2	9.81	646.6	0.005	0.16589	(.71)	2.10578	(.75)	0.09206	(.20)	0.965	989.4	1150.7	1468.7
19		r6	7,bl,e,l	80	0.064	11.8	0.01	2.04	7.8	16.5	1097	0.005	0.17914	(.57)	2.27512	(.58)	0.09211	(.10)	0.986	1062.3	1204.6	1469.6
20		r7	1,bl,e,l	150	0.049	16.3	0.01	3.55	4.9	35.6	2447	0.004	0.23124	(.19)	3.02797	(.21)	0.09497	(.08)	0.929	1341.0	1414.7	1527.5
21		r8	1,bl,e,r	200	0.050	12.3	0.01	3.19	15.0	9.87	629.4	0.004	0.25285	(.49)	3.79098	(.52)	0.10874	(.16)	0.950	1453.1	1590.8	1778.4
22		r9	1,bl,e,r	200	0.027	13.4	0.00	4.07	4.1	26.6	1800	0.000	0.31541	(.23)	5.07304	(.25)	0.11665	(.07)	0.959	1767.3	1831.6	1905.6
<i>Kaalvallei (KX18)</i>																						
23	KX18-1	r1	1,bl,s,r	300	0.144	0.53	1.02	0.76	93.0	0.23	25.7	0.366	0.22079	(2.18)	2.88798	(5.26)	0.09487	(4.34)	0.592	1286.1	1378.8	1525.4
24	KX18-2	r1	1,bl,s,q	450	0.324	0.41	0.07	0.13	19.3	1.39	98.5	0.036	0.20441	(2.69)	3.28608	(2.75)	0.11660	(.44)	0.987	1199.0	1477.8	1904.7
		r2	1,bl,s,q	300	0.086	0.89	0.63	0.77	56.4	0.27	28.8	0.259	0.16902	(3.11)	2.00987	(4.02)	0.08624	(2.06)	0.864	1006.7	1118.8	1343.6
<i>Star Mine (KX27)</i>																						
25	KX27-1	r4	1,bl,s,q	400	0.307	0.41	0.08	0.11	13.6	1.77	124.6	0.034	0.19660	(2.88)	2.72219	(2.97)	0.10042	(.43)	0.989	1157.0	1334.5	1631.9
26	KX27-7	r1	1,bl,s,r	350	0.146	0.20	0.63	0.19	25.5	0.28	29.4	0.283	0.19872	(7.41)	2.88649	(8.07)	0.10535	(2.18)	0.964	1168.4	1378.4	1720.4
27		r2	1,bl,s,q	250	0.105	0.25	0.75	0.29	29.6	0.21	25.8	0.309	0.19368	(7.43)	2.56516	(10.0)	0.09606	(5.54)	0.839	1141.3	1290.8	1548.9
Newlands Kimberlite																						
28	KX3-7	z1	1,p,a		0.0199	114	0.49	71.4	0.8	1739	97460	0.134	0.54799	(.05)	15.07836	(.06)	0.19956	(.04)	0.771	2816.8	2820.2	2822.6
29		z2	1,p,a		0.0099	126	0.49	79.2	0.8	925	51761	0.136	0.54896	(.09)	15.14574	(.10)	0.20010	(.04)	0.912	2820.8	2824.4	2827.0
30		z3	1,p,a		0.0067	145	0.58	92.1	1.2	516	28431	0.159	0.54332	(.07)	14.79125	(.08)	0.19745	(.04)	0.859	2797.3	2801.9	2805.2
31		z4	1,p,a		0.0057	72	0.61	45.9	0.7	383	20982	0.168	0.54104	(.11)	14.59555	(.12)	0.19565	(.05)	0.908	2787.8	2789.2	2790.3
32		z5	1,p,f		0.0012	83	0.50	52.3	1.1	56.1	3153	0.139	0.54576	(.13)	14.93717	(.16)	0.19850	(.08)	0.848	2807.5	2811.2	2813.9
33		z6	1,p,f		0.0012	126	0.42	78.8	4.3	21.0	1166	0.117	0.54717	(.41)	15.06003	(.42)	0.19962	(.09)	0.979	2813.4	2819.0	2823.1
34		z7	1,p,f		0.0014	247	0.48	153.5	1.9	111	6266	0.133	0.54295	(.16)	14.74546	(.17)	0.19697	(.05)	0.956	2795.8	2799.0	2801.3
35		m1	1,y,e		0.0041	2189	15.03	5590	33.9	677	7936	4.148	0.55059	(.48)	15.31964	(.48)	0.20180	(.04)	0.996	2827.6	2835.3	2840.8
36		m2	1,y,e		0.0041	1886	11.58	4007	14.0	1173	17199	3.181	0.55928	(.31)	15.83030	(.31)	0.20529	(.04)	0.990	2863.7	2866.6	2868.7
37		m3	1,y,e		0.0015	2500	13.76	6034	94.3	92.7	1162	3.789	0.55293	(.24)	15.42357	(.26)	0.20231	(.11)	0.906	2837.4	2841.8	2844.9
38		m4	1,y,e		0.0007	3688	14.59	9390	94.7	63.8	771.6	4.006	0.55625	(.17)	15.60524	(.18)	0.20347	(.07)	0.916	2851.1	2852.9	2854.2

Table 1 (cont.)

#	Xeno-lith	Frac-tion*	Prop-erties*	Diam (μm) ^b	Wt. (mg) ^b	Composition					Isotopic Ratios					corr. coef.	Dates (Ma)					
						[U] (ppm)	Th ^c U	[Pb] (ppm)	Pb ^{e,d} Pbc	Pbc ^d (pg)	²⁰⁶ Pb ^c / ₂₀₄ Pb	²⁰⁸ Pb ^f / ₂₀₆ Pb	²⁰⁶ Pb ^f / ₂₃₈ U	% err ^g	²⁰⁷ Pb ^f / ₂₃₅ U		% err ^g	²⁰⁷ Pb ^f / ₂₀₆ Pb	% err ^g	²⁰⁶ Pb ^h / ₂₃₈ U	²⁰⁷ Pb ^h / ₂₃₅ U	²⁰⁷ Pb ^h / ₂₀₆ Pb
Newlands Kimberlite (con't)																						
39	KX3-7	r1	12,rd,f,a	100	0.085	0.87	0.66	0.83	55.9	0.36	32.3	0.223	0.24002	(1.36)	3.20931	(2.23)	0.09697	(1.53)	0.742	1386.8	1459.4	1566.7
40		r2	7,rd,f,a	150	0.089	0.53	2.02	1.40	111.7	0.16	19.9	0.699	0.23894	(1.43)	3.24442	(6.27)	0.09848	(5.52)	0.606	1381.2	1467.8	1595.5
41	KX3-9	r1	1,rd,f	500	0.157	0.73	1.01	0.66	69.4	0.57	39.4	0.306	0.28306	(.88)	3.95988	(1.75)	0.10146	(1.36)	0.652	1606.8	1626.0	1651.0
42		r2	2,rd,f	300	0.195	0.79	0.46	0.48	61.0	0.60	44.3	0.163	0.22081	(1.09)	2.86903	(2.05)	0.09424	(1.61)	0.625	1286.1	1373.8	1512.9
43		r3	4,rd,f	200	0.102	1.69	0.19	1.26	93.6	0.43	39.2	0.058	0.23723	(1.33)	2.95736	(2.00)	0.09041	(1.17)	0.829	1372.3	1396.7	1434.3
44		r4	1,rd,f	400	0.256	1.96	0.13	0.51	50.4	1.71	111.5	0.040	0.17928	(.42)	1.89178	(.57)	0.07653	(.31)	0.850	1063.0	1078.2	1109.0
45		r5	1,rd,f	400	0.256	0.71	0.26	0.32	47.3	0.81	57.7	0.091	0.20752	(.84)	2.58195	(1.24)	0.09024	(.73)	0.816	1215.6	1295.5	1430.6
46		r6	1,rd,f	350	0.196	0.31	0.36	0.16	25.6	0.44	38.4	0.121	0.18265	(2.63)	2.01217	(5.96)	0.07990	(4.71)	0.647	1081.5	1119.6	1194.5
Northern Lesotho Kimberlites																						
<i>Letseng-la-terae (KX20)</i>																						
47	KX20-1	r1	1,bl,s,q	450	0.324	29.4	0.00	1.64	31.2	16.2	1108	0.002	0.05821	(.16)	0.48078	(.24)	0.05990	(.17)	0.700	364.8	398.6	600.0
48		r2	70,bl,e,r	70	0.110	30.8	1.20	1.02	33.6	2.49	136.3	0.435	0.01932	(1.02)	0.14773	(1.22)	0.05546	(.61)	0.866	123.3	139.9	430.9
49		r4	1,bl,s,r	400	0.461	44.8	0.16	1.09	168.8	2.00	145.1	0.054	0.01719	(.21)	0.12191	(1.41)	0.05143	(1.31)	0.498	109.9	116.8	260.3
50	KX20-3	r1	12,bl,e,l	90	0.176	45.1	0.06	1.33	97.4	1.46	113.5	0.021	0.01939	(.45)	0.14218	(.99)	0.05318	(.84)	0.526	123.8	135.0	336.3
51		r2	45,bl,e,l	50	0.950	5.83	0.08	0.14	65.6	1.14	92.4	0.025	0.01459	(.77)	0.09960	(1.24)	0.04951	(.92)	0.670	93.4	96.4	172.2
52		r3	1,bl,s,q	300	0.115	17.2	0.11	0.53	35.0	0.89	75.6	0.039	0.01686	(1.80)	0.12293	(2.04)	0.05287	(.84)	0.911	107.8	117.7	323.3
53		r4	1,bl,s,q	300	0.115	20.6	0.20	1.61	129.4	0.47	46.9	0.071	0.02669	(.77)	0.20512	(1.34)	0.05573	(1.03)	0.641	169.8	189.5	441.8
54	KX20-4	a1	165,cl,e,q	100	0.050	4.0	2.95	4.78	207.5	0.18	22.4	1.230	0.09226	(1.18)	0.82051	(5.63)	0.06450	(5.17)	0.475	568.9	608.3	758.1
55	KX20-8	r1	1,bl,s,q	450	0.292	14.3	0.14	0.55	106.0	0.56	52.8	0.047	0.01506	(1.10)	0.10208	(2.16)	0.04915	(1.77)	0.576	96.4	98.7	155.1
56		r2	1,bl,s,q	300	0.173	10.1	0.11	0.25	23.1	1.11	90.1	0.037	0.01570	(1.54)	0.10771	(1.71)	0.04975	(.68)	0.918	100.4	103.9	183.5
<i>Matsoku (KX21)</i>																						
57	KX21-2	a1	160,cl,e,q	50	0.683	1.6	0.83	0.69	395.7	0.20	26.3	0.476	0.05562	(.24)	0.46583	(2.70)	0.06074	(2.55)	0.667	348.9	388.3	630.1
58		a2	28,cl,e,q	200	0.191	3.4	1.18	1.56	241.1	0.26	27.5	0.682	0.06284	(.74)	0.54747	(2.64)	0.06319	(2.39)	0.466	392.9	443.3	714.5
59		r1	6,bl,s,q	300	0.504	7.00	0.12	0.39	117.8	0.73	64.4	0.042	0.02590	(.61)	0.19287	(1.01)	0.05400	(.76)	0.665	164.9	179.1	370.9
60		s1	2,y,s,q	150	0.096	43.5	3.58	12.53	55.6	20.7	689.1	1.115	0.14641	(.13)	1.38919	(.16)	0.06882	(.08)	0.861	880.8	884.4	893.3
61		s2	4,y,s,q	50	0.004	176.5	3.32	55.70	46.9	4.18	158.0	1.035	0.14321	(.63)	1.34711	(.69)	0.06822	(.27)	0.924	862.8	866.3	875.3
62		s3	1,y,s,q	170	0.013	88.3	2.80	26.65	71.4	3.96	161.5	0.871	0.14600	(.40)	1.38443	(.48)	0.06877	(.24)	0.868	878.5	882.3	892.0
63		s4	3,y,s,q	100	0.006	124.7	3.18	34.45	20.0	9.15	332.1	1.008	0.14238	(.73)	1.34642	(.76)	0.06858	(.20)	0.965	858.1	866.0	886.2
64		s5	3,y,s,q	130	0.031	47.5	3.31	13.69	46.0	8.22	292.2	1.050	0.14203	(.35)	1.34222	(.38)	0.06854	(.14)	0.930	856.1	864.2	884.9
<i>Mothae (KX23)</i>																						
65	KX23-3	a1	60,cl,s,q	70	0.036	27.5	0.52	31.50	1066	0.07	21.1	0.221	0.06565	(.43)	0.52951	(7.13)	0.05850	(6.75)	0.886	409.9	431.5	548.4
66		a2	7,cl,s,q	200	0.102	10.4	0.41	10.62	1010	0.08	21.9	0.182	0.06982	(.48)	0.57901	(6.73)	0.06015	(6.34)	0.822	435.1	463.8	608.8
67		r1	1,bl,s,r	300	0.037	47.9	0.00	0.61	3.8	5.88	438.3	0.001	0.01404	(.93)	0.09596	(1.08)	0.04957	(.53)	0.870	89.9	93.0	174.7
68		r2	1,bl,s,r	300	0.038	50.6	0.00	0.69	7.9	3.00	230.1	0.000	0.01360	(2.77)	0.09021	(2.88)	0.04812	(.81)	0.959	87.1	87.7	105.0
69		r3	15,bl,s,r	150	0.216	11.2	0.08	1.03	192.4	0.18	29.4	0.027	0.01551	(.87)	0.10451	(3.24)	0.04887	(3.00)	0.409	99.2	100.9	141.6
70		r4	1,bl,s,q	500	0.480	9.28	0.02	0.40	111.5	0.78	70.5	0.006	0.02146	(.60)	0.15308	(1.01)	0.05174	(.77)	0.640	136.9	144.6	273.9
Eastern Namaqua Kimberlites																						
<i>Marka (KX4)</i>																						
71	KX4-21	r1	34,rd,e,r	160	0.490	5.94	0.08	0.41	156.5	0.33	39.5	0.027	0.01923	(.81)	0.13232	(3.5)	0.04990	(3.2)	0.432	122.8	126.2	190.5
<i>Lovedale (KX5)</i>																						
72	KX5-1	r1	1,bl,s,r	400	0.293	1.39	0.22	0.05	13.7	0.44	44.2	0.073	0.01528	(9.33)	0.10711	(11.8)	0.05085	(5.17)	0.905	97.7	103.3	233.9
73		r2	33,br,f	200	1.881	1.49	0.57	0.13	179.0	0.36	34.6	0.219	0.02082	(.82)	0.17068	(2.4)	0.05946	(2.2)	0.485	132.8	160.0	583.8
74	KX5-3	r1	35,br,f	250	2.515	5.60	0.08	0.11	94.9	2.00	142.1	0.027	0.01462	(.34)	0.09647	(.57)	0.04786	(.43)	0.668	93.6	93.5	92.4
75	KX5-7	r1	36,br,s,r	180	0.566	4.41	0.17	0.17	63.8	0.59	52.1	0.058	0.01591	(1.41)	0.11429	(3.9)	0.05210	(3.4)	0.498	101.8	109.9	289.8
76		r4	110,br,s,r	180	1.964	3.39	0.44	0.25	377.7	0.31	33.0	0.150	0.01694	(.65)	0.11957	(3.6)	0.05119	(3.4)	0.417	108.3	114.7	249.2

Table 1 (cont.)

#	Xeno-lith	Frac-tion ^a	Prop-erties ^a	Diam (μm) ^b	Wt. (mg) ^b	[U] (ppm)	Composition					Isotopic Ratios					Dates (Ma)					
							Th ^c U	[Pb] (ppm)	Pb* ^d (pg)	Pbc ^d (pg)	²⁰⁶ Pb/ ²⁰⁴ Pb ^e	²⁰⁸ Pb/ ²⁰⁶ Pb ^f	²⁰⁶ Pb/ ²³⁸ U ^f	% err ^g	²⁰⁷ Pb/ ²³⁵ U ^f	% err ^g	²⁰⁷ Pb/ ²⁰⁶ Pb ^f	% err ^g	corr. coef.	²⁰⁶ Pb/ ²³⁸ U ^h	²⁰⁷ Pb/ ²³⁵ U ^h	²⁰⁷ Pb/ ²⁰⁶ Pb ^h
<i>Umjiesberg (KX6)</i>																						
77	KX6-1	r3	24,bl,s,q	300	2.452	1.56	0.27	0.11	216.0	0.31	36.1	0.089	0.01757	(.63)	0.12013	(2.2)	0.04958	(2.0)	0.436	112.3	115.2	175.2
78		r4	120,bl,f	200	2.764	1.42	0.32	0.12	267.9	0.26	33.1	0.109	0.01799	(.55)	0.12764	(2.6)	0.05146	(2.4)	0.424	114.9	122.0	261.4
<i>Klipfontein-08 (KX12)</i>																						
79	KX12-8	r1	35,rd,s,q	250	3.811	8.92	0.01	0.49	312.0	4.99	348.4	0.005	0.04997	(.25)	0.42202	(.29)	0.06125	(.13)	0.894	314.3	357.5	648.1
80		r2	30,rd,s,q	250	5.267	9.67	0.01	0.56	587.9	3.99	281.2	0.007	0.05012	(.13)	0.42305	(.23)	0.06122	(.18)	0.626	315.2	358.2	647.1
81		r3	6,rd,s,a	250	0.680	10.1	0.01	0.68	70.2	5.62	391.8	0.004	0.06300	(.47)	0.53617	(.48)	0.06172	(.10)	0.979	393.9	435.9	664.5
82		r4	22,rd,s,r	150	0.346	8.00	0.03	0.59	111.0	0.87	74.2	0.022	0.03758	(.69)	0.30746	(.93)	0.05933	(.59)	0.777	237.8	272.2	579.3
83		r5	51,rd,s,r	150	0.375	8.27	0.03	0.60	127.8	0.80	69.7	0.026	0.03555	(.56)	0.29217	(.79)	0.05960	(.52)	0.751	225.2	260.3	589.2
84		r6	10,rd,s,a	250	0.384	9.02	0.02	0.65	48.6	4.20	296.6	0.008	0.06411	(.60)	0.54689	(.64)	0.06187	(.21)	0.945	400.6	443.0	669.6
<i>Beyersfontein (KX13)</i>																						
85	KX13-2	r1	56,bl,s,r	300	6.450	1.62	0.00	0.15	843.5	0.17	29.1	0.000	0.01589	(.54)	0.11277	(7.8)	0.05146	(7.4)	0.794	101.6	108.5	261.5
86		r2	60,bl,s,r	200	3.072	1.74	0.00	0.15	405.2	0.17	29.5	0.000	0.01550	(.45)	0.10112	(4.0)	0.04731	(3.8)	0.515	99.2	97.8	65.0
<i>Orapa Kimberlite</i>																						
87	KX9-1	r1	7,br,s,q	200	0.280	13.6	0.00	1.34	239.9	0.58	56.0	0.001	0.04034	(.44)	0.34116	(1.15)	0.06134	(1.02)	0.474	254.9	298.1	651.2
88		r2	8,bl,s,r	250	0.348	8.66	0.07	0.34	73.6	0.67	61.6	0.023	0.01776	(1.04)	0.12274	(1.52)	0.05012	(1.04)	0.731	113.5	117.6	200.5
89	KX9-2	r1	3,rd,s,q	250	0.192	17.9	0.00	0.80	75.7	1.10	91.1	0.000	0.02662	(.69)	0.20878	(1.11)	0.05688	(.83)	0.675	169.4	192.5	486.8
90		z1	1,cl,a	0.0005	642.1	0.30	275.5	18.2	6.27	367.3	0.088	0.36468	(.29)	6.22374	(.31)	0.12378	(.10)	0.951	2004.3	2007.8	2011.4	
91		z2	1,cl,a	0.0003	149.4	1.32	68.19	2.5	7.98	413.4	0.390	0.35040	(.99)	5.87631	(1.04)	0.12163	(.31)	0.955	1936.5	1957.7	1980.3	
92		z3	1,cl,a	0.0002	308.4	0.34	110.7	2.9	8.78	556.6	0.102	0.34144	(.73)	5.64863	(.80)	0.11998	(.30)	0.924	1893.6	1923.6	1956.0	
93		z4	1,cl,a	0.0002	700.8	0.16	237.8	4.0	9.97	643.7	0.050	0.33156	(.82)	5.72162	(.85)	0.12516	(.21)	0.970	1845.9	1934.6	2031.0	
94	KX9-3	z1	1,cl,a	0.0005	154.0	0.73	64.38	5.3	5.36	304.3	0.220	0.34091	(1.17)	5.63892	(1.27)	0.11997	(.42)	0.945	1891.0	1922.1	1955.7	
95		z2	1,cl,a	0.0006	209.8	0.22	73.44	4.6	9.59	606.0	0.066	0.33512	(.65)	5.48402	(.72)	0.11869	(.28)	0.919	1863.2	1898.1	1936.5	
96		z3	1,cl,a	0.0003	657.8	0.57	257.4	4.3	15.04	869.2	0.170	0.34785	(.48)	5.80740	(.50)	0.12108	(.11)	0.974	1924.3	1947.5	1972.3	
97		z4	1,cl,a	0.0003	245.6	0.45	92.17	6.3	4.39	265.0	0.139	0.31590	(1.05)	4.99431	(1.32)	0.11466	(.72)	0.839	1769.7	1818.4	1874.6	
98		r1	2,rd,s,q	250	0.240	2.89	0.06	0.24	49.6	0.25	33.8	0.021	0.01929	(2.97)	0.13446	(4.17)	0.05054	(2.66)	0.773	123.2	128.1	220.0
99		r2	4,rd,s,q	180	0.108	9.26	0.00	1.93	192.2	0.11	24.7	0.000	0.02396	(1.08)	0.18576	(4.7)	0.05622	(4.33)	0.440	152.7	173.0	461.0

^a Properties: # of grains in fraction; bl=black, br=brown, rd=red, y=yellow, cl=colorless, p=pink, e=euhedral, s=subhedral, f=fragment, a=abraded, l=elongate prismatic, r=rounded prismatic, q=equant.

^b Minimum consistent diameter of grains in fraction; sample weights were estimated to within 40% using measured grain dimensions, an ellipsoidal geometry, and nominal density of 5.0 g/cm³ for monazite, 4.5 g/cm³ for zircon, 4.2 g/cm³ for rutile, 3.5 g/cm³ for titanite, and 3.2 g/cm³ for apatite.

^c Th contents calculated from radiogenic ²⁰⁸Pb and the ²⁰⁷Pb/²⁰⁶Pb or ²⁰⁶Pb/²³⁸Pb date of the sample, assuming concordance between U-Th-Pb systems; λ(²³²Th) = 4.9475x10⁻¹¹ yr⁻¹.

^d Pb* and Pbc represent radiogenic Pb and common Pb respectively.

^e Measured ratio corrected for fractionation and spike contribution; Pb fractionation correction is 0.12 ± 0.04 % per a.m.u. for multicollector analyses or 0.15 ± 0.04 % per a.m.u. for single collector analyses based on repeated daily analysis of NBS-981.

^f Measured ratios corrected for fractionation, spike, blank, and initial common Pb; nominal Pb blank = 5 pg ± 50% (2σ) for titanite, rutile and apatite, or 3.5 pg ± 50% (2σ) for zircon and monazite; nominal U blank = 0.1 pg ± 50% (2σ); measured laboratory blank composition: ²⁰⁶Pb/²⁰⁴Pb = 19.10, ²⁰⁷Pb/²⁰⁴Pb = 15.72, ²⁰⁸Pb/²⁰⁴Pb = 38.65 ± 0.01 (2σ); initial common Pb composition from leached feldspars or model of Stacy and Kramers (1972), as noted in text.

^g Numbers in parentheses are the % errors reported at the 2σ confidence interval, propagated using the algorithms of Ludwig (1980).

^h Isotopic ages calculated using the decay constants of Jaffey et al. (1971): λ(²³⁵U) = 9.8485x10⁻¹⁰ yr⁻¹ and λ(²³⁸U) = 1.55125x10⁻¹⁰ yr⁻¹.

Table 2. Pb isotopic composition of leached feldspar separates for lower crustal xenoliths

Sample	Mineral	$\frac{^{206}\text{Pb}^a}{^{204}\text{Pb}}$	$\frac{^{207}\text{Pb}^a}{^{204}\text{Pb}}$	$\frac{^{208}\text{Pb}^a}{^{204}\text{Pb}}$
KX3-9	K-feldspar	13.489	14.583	33.228
KX4-21	plagioclase	17.303	15.492	37.306
KX20-4	plagioclase	16.943	15.526	37.048
KX23-3	K-feldspar	17.312	15.668	37.166

^a Error in isotopic ratios estimated at $\pm 0.3\%$ (2σ), limited by reproducibility of mass fractionation, $0.12 \pm 0.03\%$ per a.m.u., as determined by replicate analysis of NBS-981.

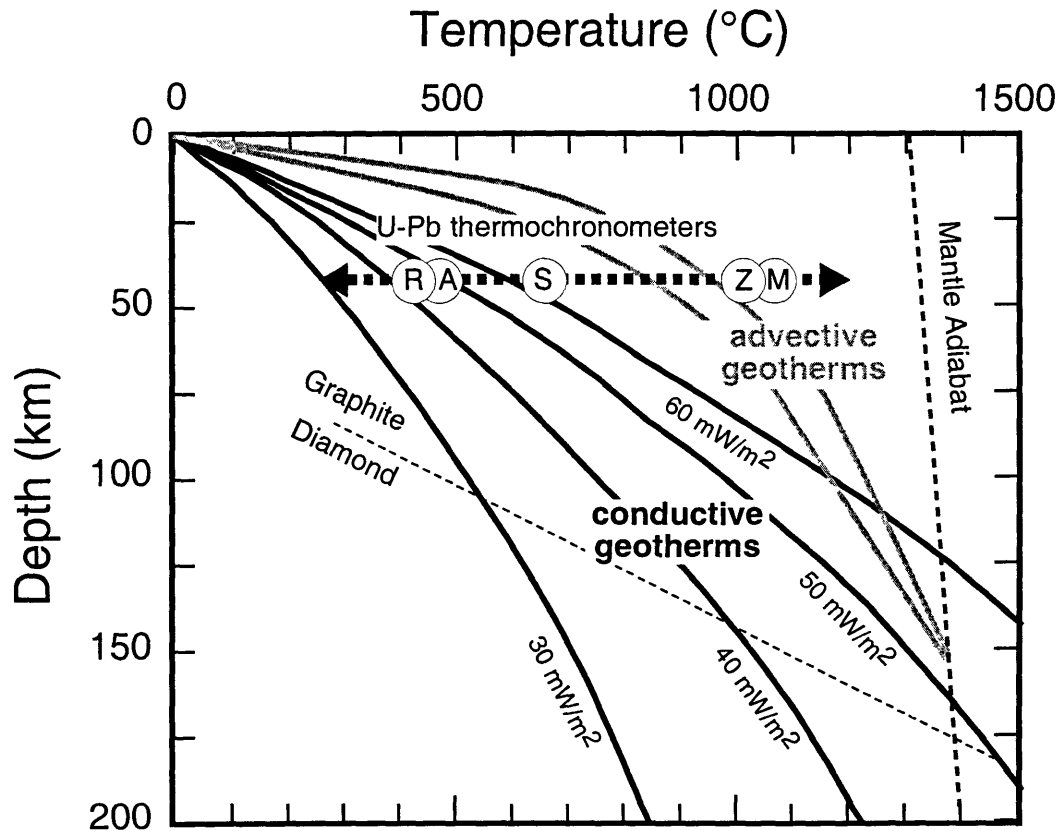


Figure 1. Pressure-temperature diagram for continental lithosphere, illustrating model lithospheric geotherms for a number of conductive and advective thermal regimes, and the closure temperature of various U-Pb accessory mineral thermochronometers intervals (lettered circles: R=rutile, A=apatite, S=titanite, Z=zircon, M=monazite). The sensitivity of the temperature at the base of the crust to inferred lithospheric geotherms is apparent, as is the potential of the U-Pb rutile thermochronometer for elucidating the establishment of “cratonic” or “shield” geotherms, as commonly approximated by a 40 mW/m² surface heat flow conductive geotherm.

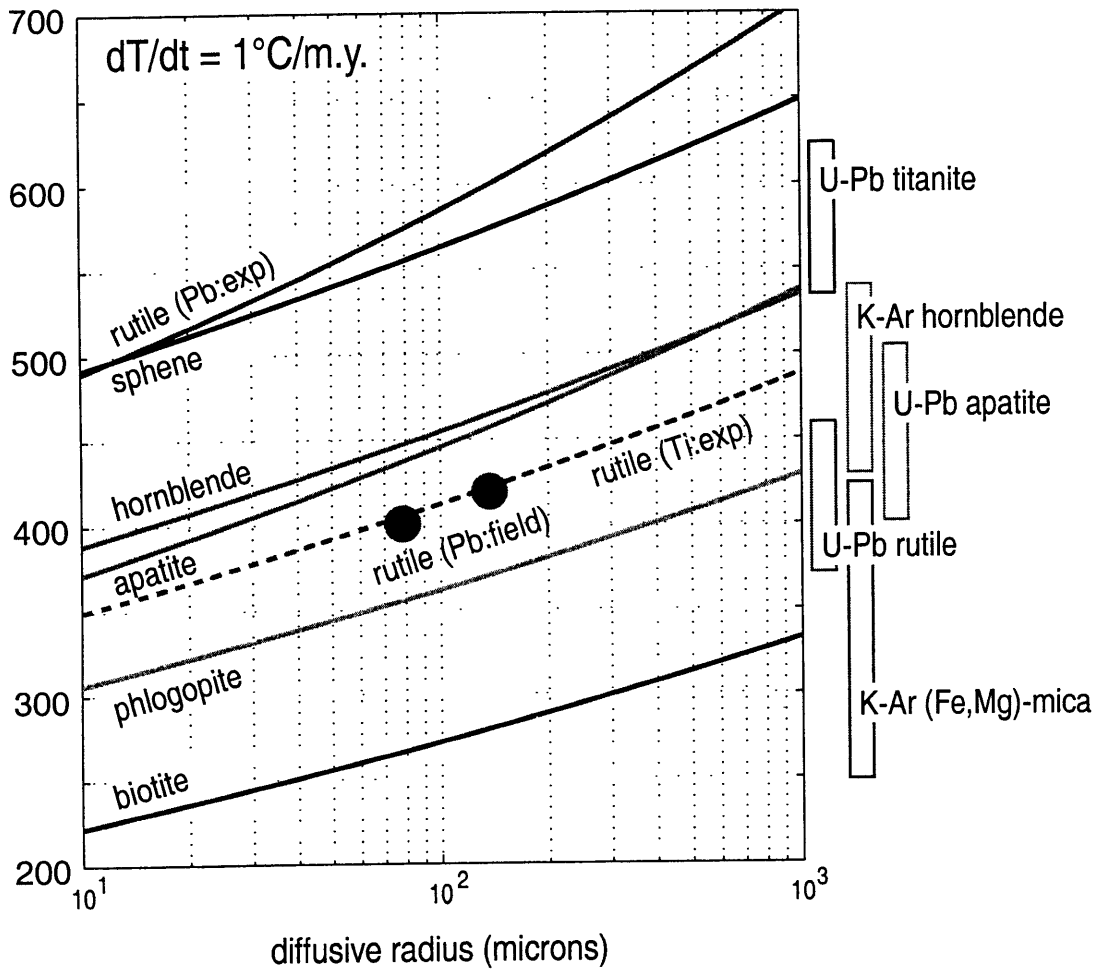


Figure 2. Closure temperature for Pb or Ar diffusion as a function of effective diffusive radii, at a cooling rate of 1°C/Ma , for a variety of U-rich accessory minerals and K-rich rock-forming minerals. All curves are based on experimentally determined diffusivity parameters. Solid and dashed lines for rutile represent closure temperatures calculated from Pb and Ti diffusivity data respectively. The two points labeled "rutile (Pb:field)" represent field-based estimates of rutile closure temperature from Mezger (1989).

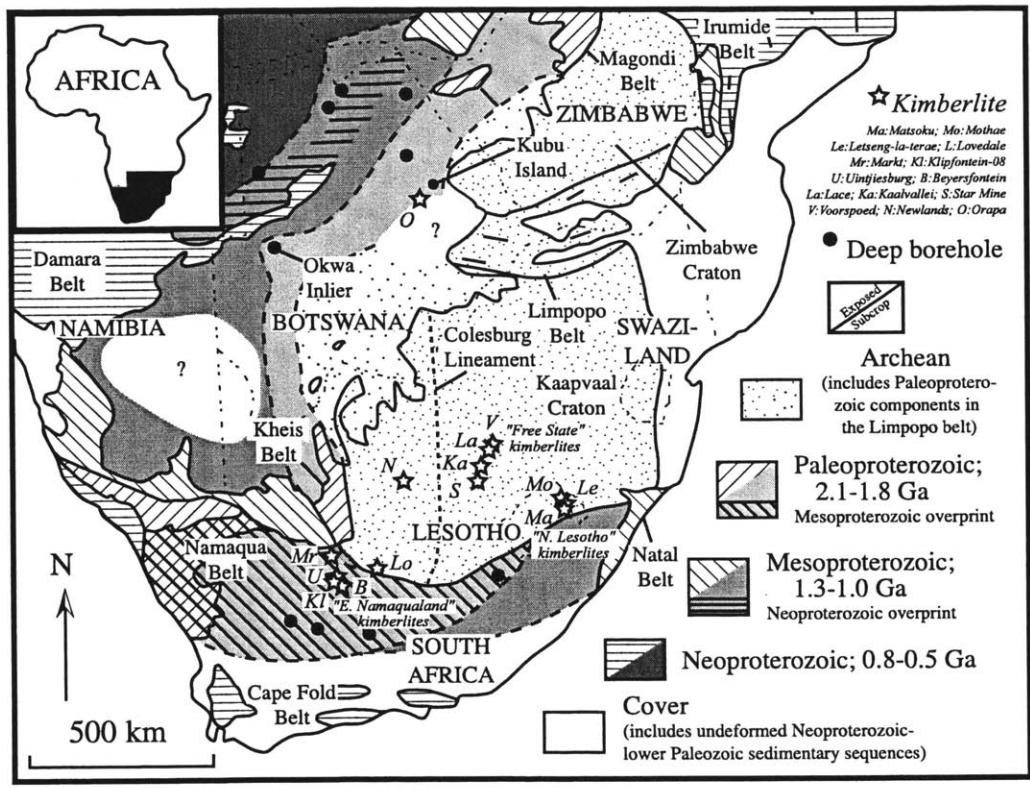


Figure 3. Geological sketch map of southern Africa (after Singletary, 1999) indicating the age of basement stabilization and subsequent reworking, and the location of Mesozoic kimberlites from which lower crustal xenolith collections were obtained and analyzed.

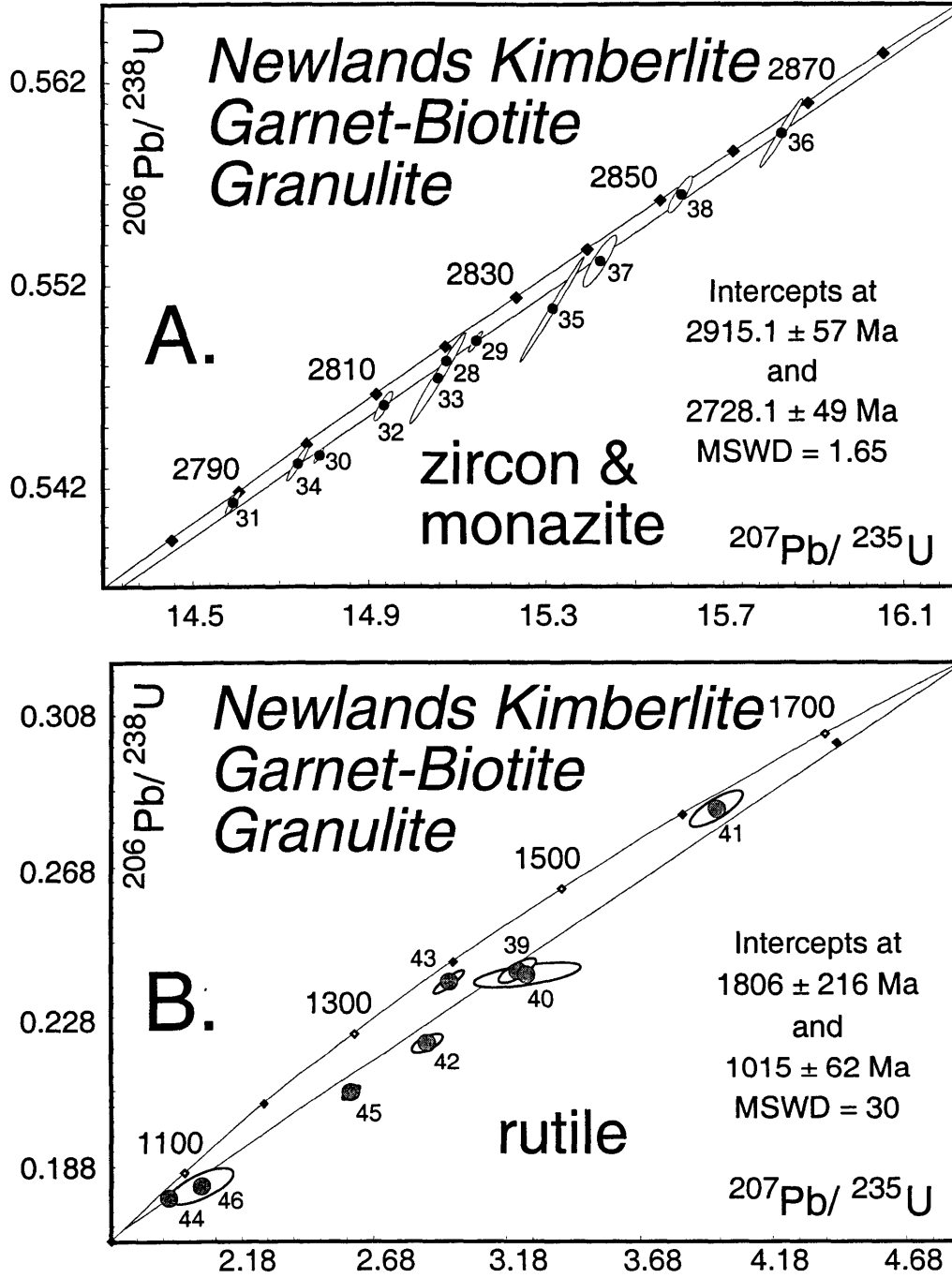


Figure 4. Concordia diagrams for: A) zircon and monazite; and B) rutile from the Newlands kimberlite, in the Kimberley block of the western Kaapvaal craton.

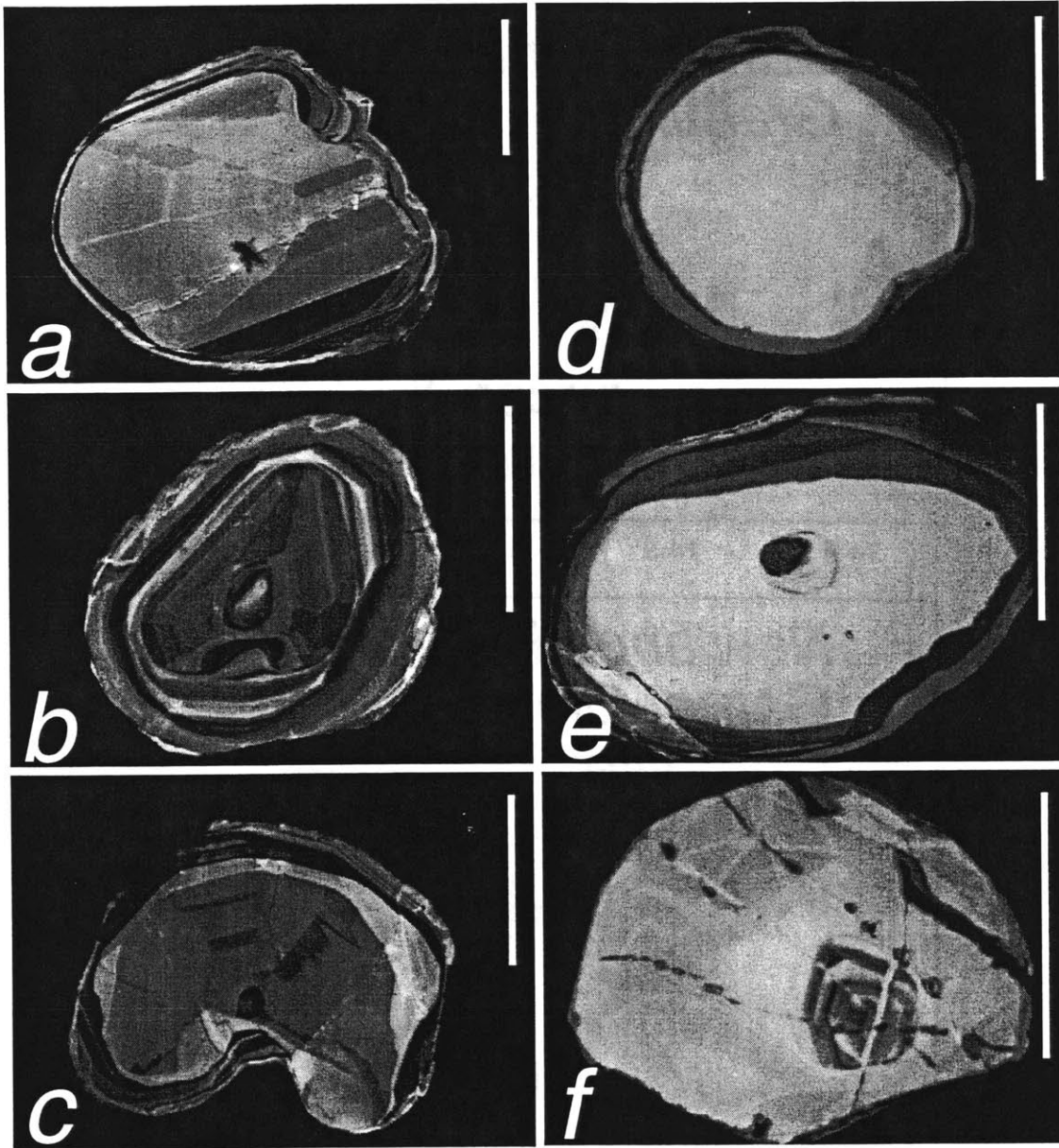


Figure 5. Cathodoluminescence images of zircon from metapelitic granulite xenoliths from: A-C) the Newlands kimberlite of the Barkley West region, western Kaapvaal craton; and D-F) the Orapa kimberlite of central Botswana.

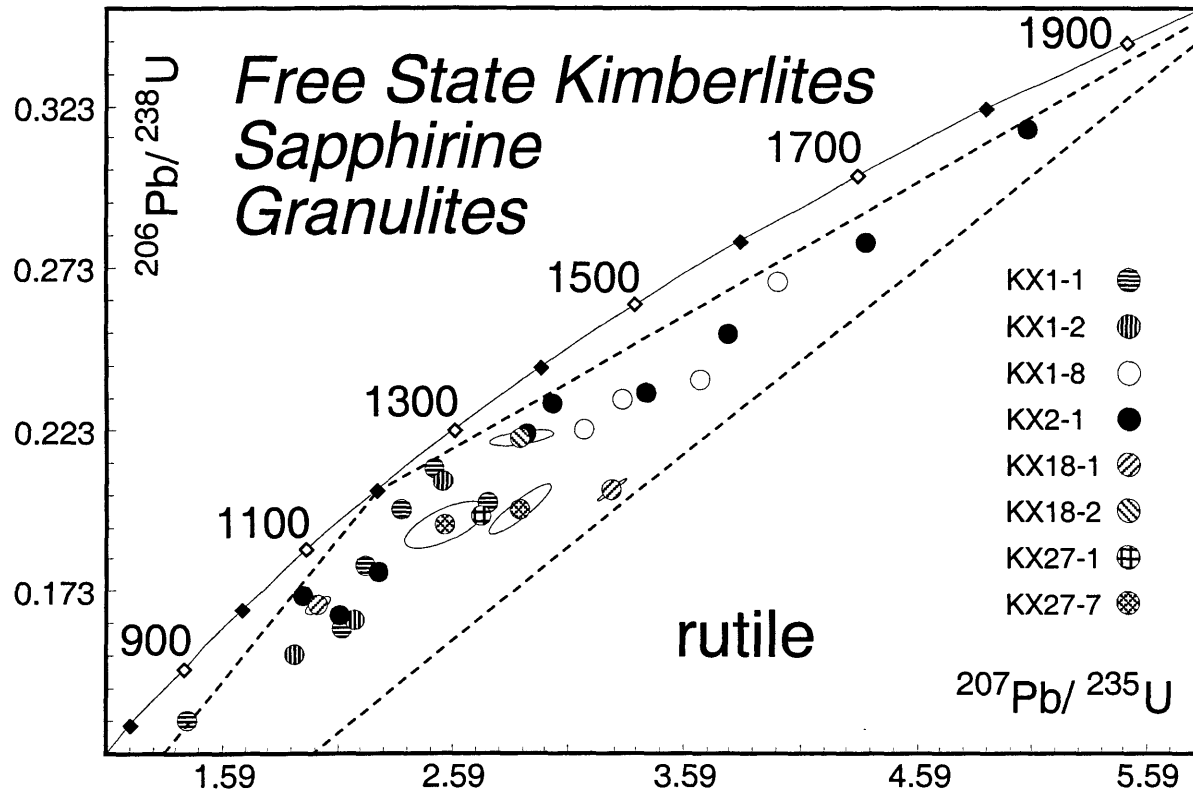


Figure 6. Concordia diagram of rutile analyses from the Lace, Voorspoed, Kaalvallei, and Star Mine kimberlites of the Free State, South Africa.

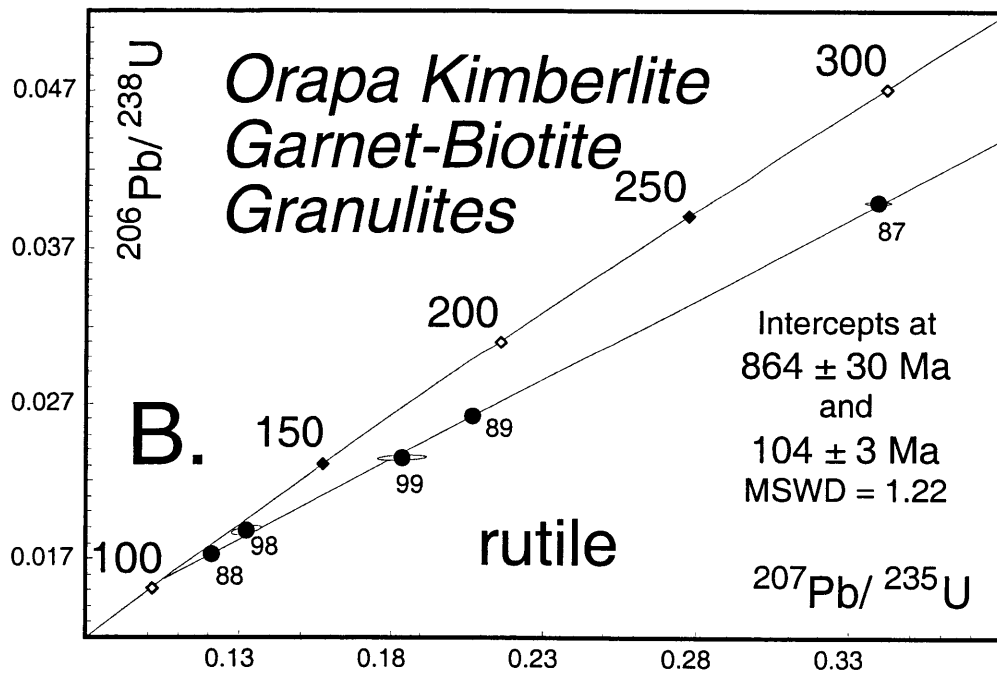
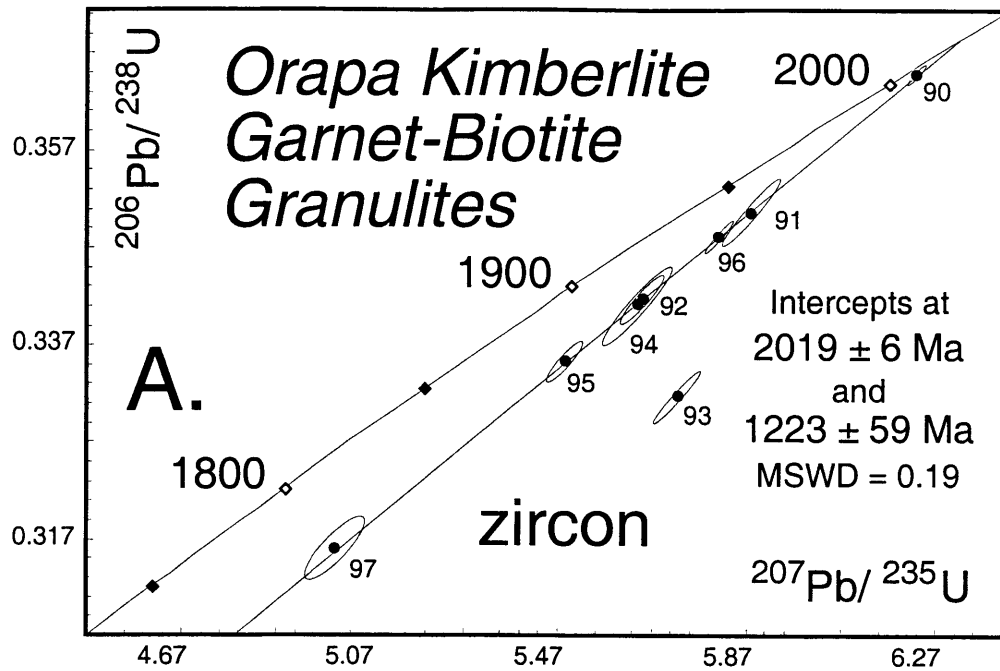


Figure 7. Concordia diagrams for A) zircon from two granulites from the Orapa kimberlite of central Botswana; and B) rutile from three granulites of the Orapa kimberlite.

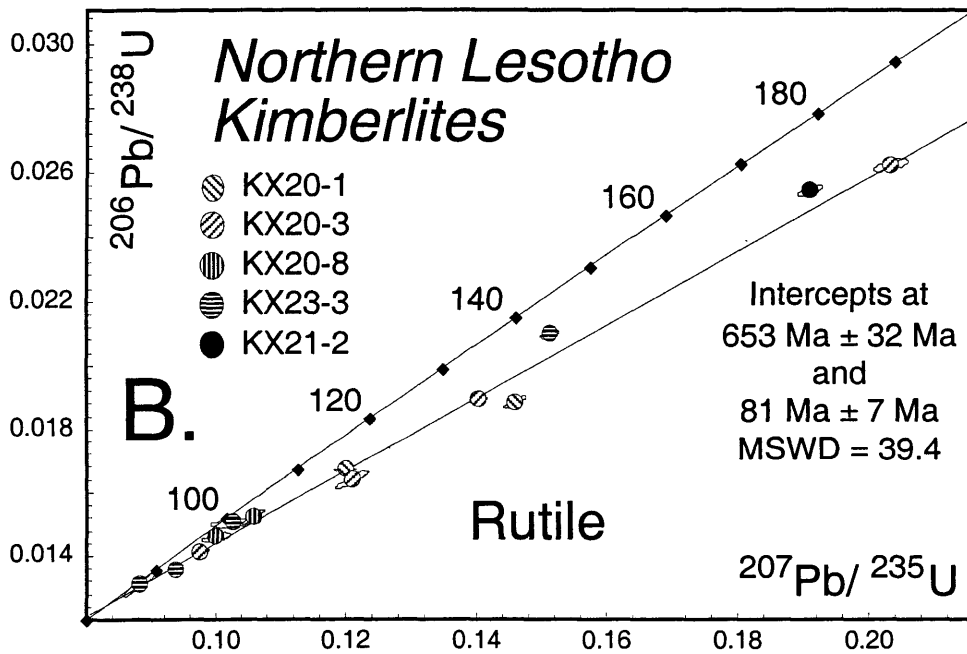
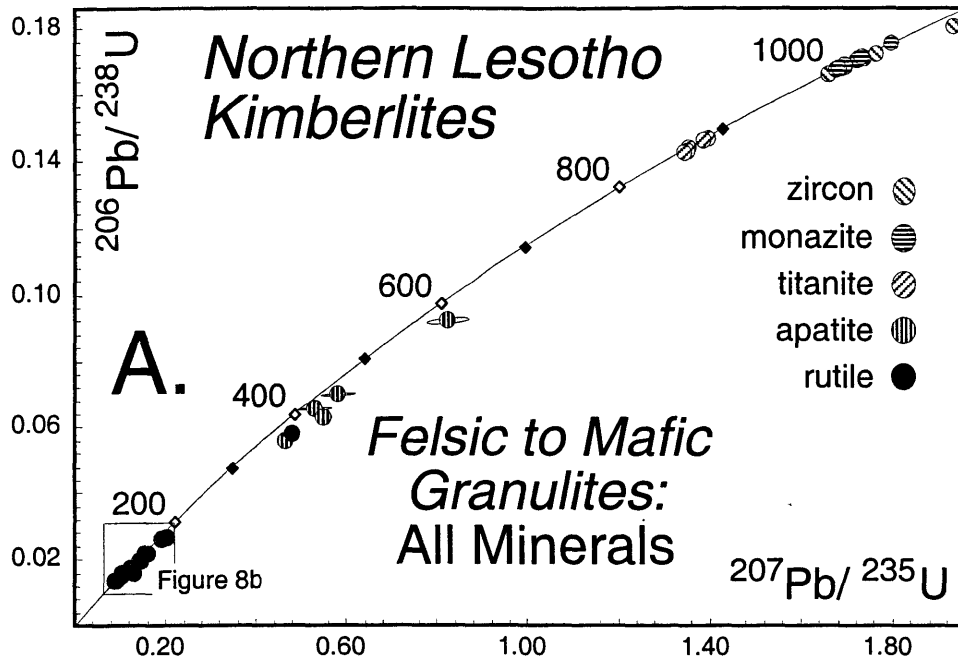


Figure 8. Concordia diagrams for: A) metamorphic zircon, monazite, titanite, apatite, and rutile data from the Northern Lesotho kimberlites; B) shows an enlargement of the rutile data which approach concordia near the age of kimberlite eruption [93 Ma, Davis (1977)].

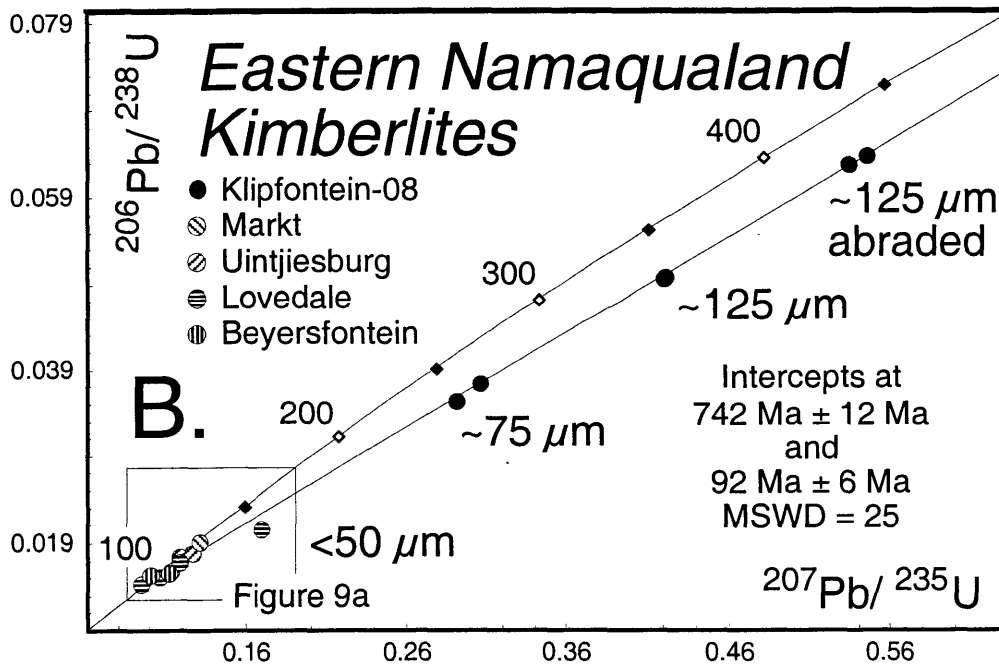
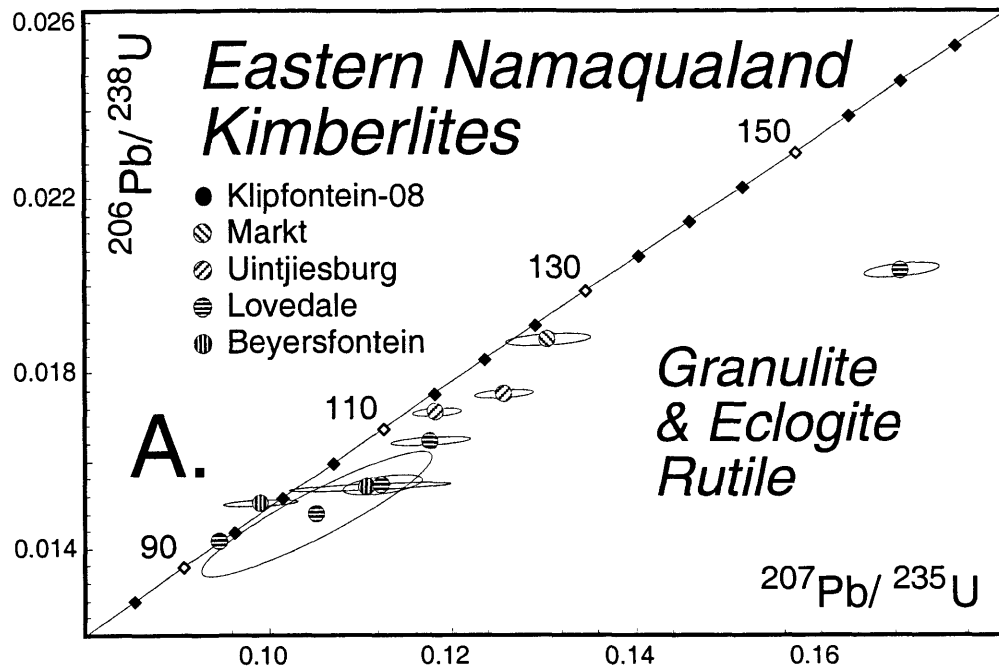


Figure 9. A) Concordia diagram for metamorphic rutile from the Eastern Namaqua kimberlites; most rutile dates approach the age of the kimberlite eruption. B) Concordia diagram for Eastern Namaqualand granulitic rutile, including data from the garnet-clinopyroxene granulite of the Klipfontein-08 kimberlite. Labels represent measured grain radii of analyzed fractions, “125 μm abraded” fraction radius is measured prior to abrasion.

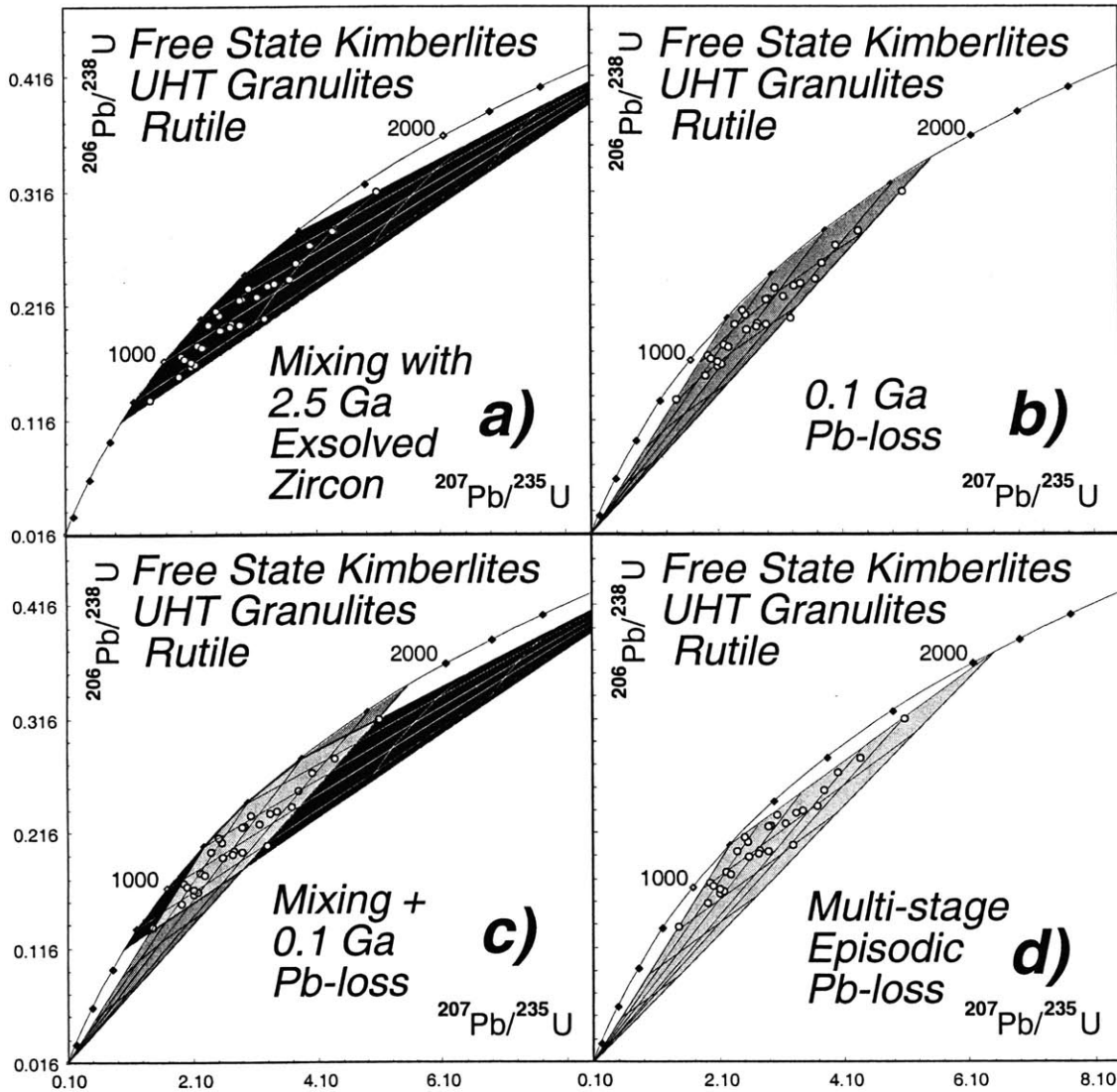


Figure 10. Concordia diagrams illustrated possible models to explain the topology of discordance of rutile U-Pb isotopic data from the Free State kimberlites: A) mixing between an average 2.5 Ga growth age of exsolved zircon and cooling ages of host rutile; B) single-stage kimberlite eruption age (~0.1 Ga) Pb-loss from rutile with a range of initial Proterozoic cooling ages; C) 0.1 Ga Pb loss superimposed on mixing with Archean exsolved zircon; D) multi-stage episodic Pb loss at 2.0, 1.2, and 0.1 Ga.

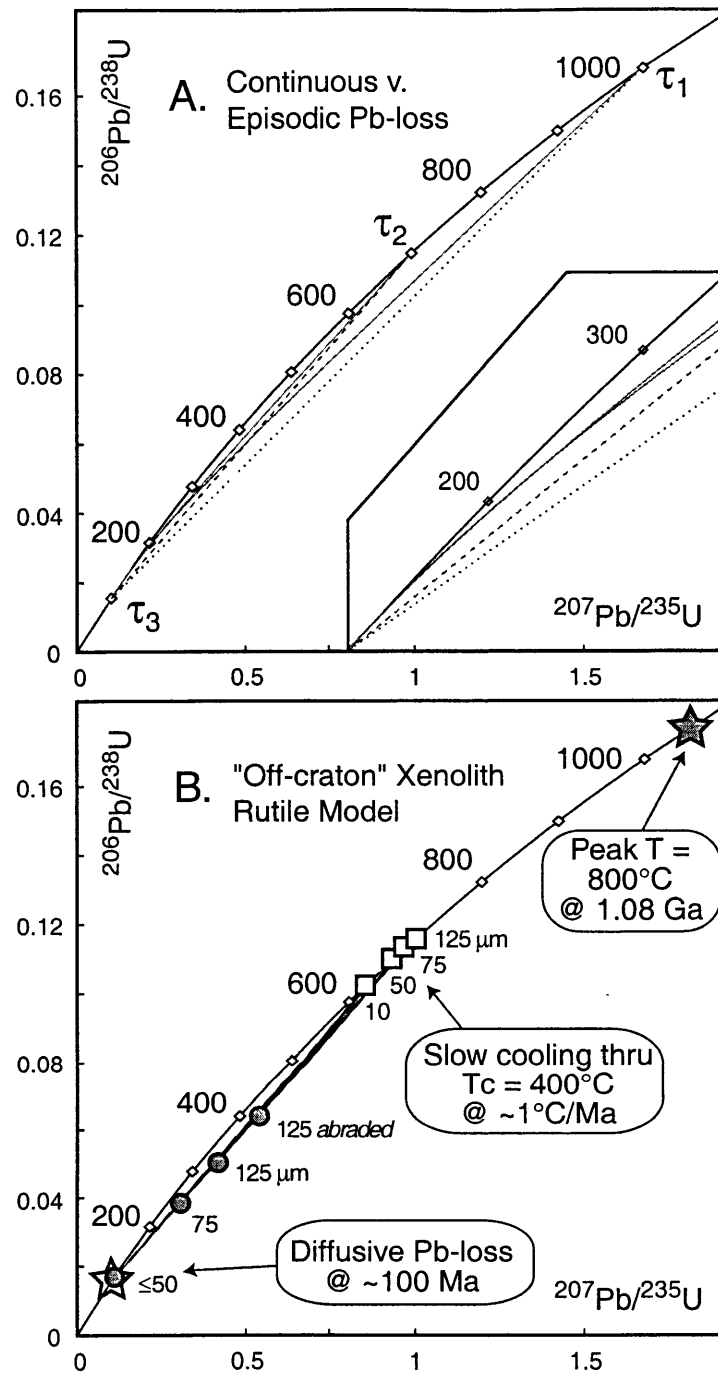


Figure 11. A) The topology of discordance for mineral systems undergoing continuous versus punctuated Pb-loss; dashed and dotted lines illustrate behaviour of minerals initially closed to diffusive loss at τ_1 and τ_2 , which underwent episodic Pb-loss at τ_3 , resulting in linear discordia. Solid lines represent continuous, constant diffusivity, Pb-loss curves for systems which began accumulating radiogenic Pb at τ_1 or τ_2 , and stopped losing radiogenic Pb at τ_3 (Tilton, 1960). B) a model of the Eastern Namaqualand data characterized by slow cooling from peak metamorphic conditions through rutile closure, followed by episodic Pb-loss during a Mesozoic thermal perturbation.

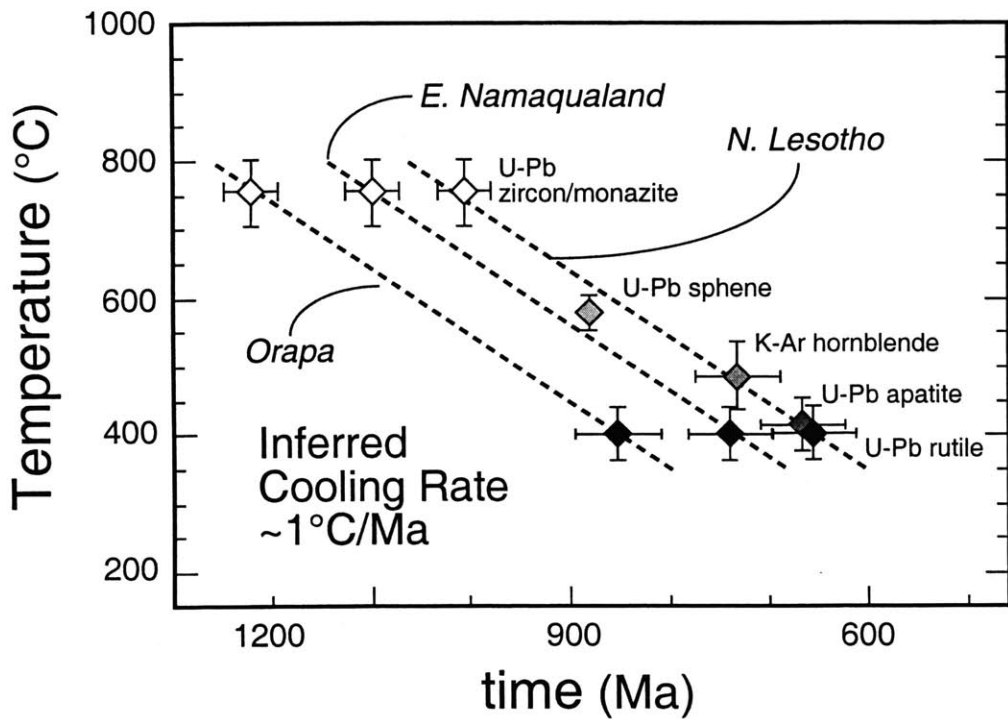


Figure 12. Temperature-time diagram illustrating integrated linear cooling rates for the lower crust beneath the Northern Lesotho, Eastern Namaqua, and Orapa kimberlite suites. These cooling rates have consistent values of approximately 1°C/m.y. following peak metamorphism during Mesoproterozoic collisional orogenesis at each of the craton's margins.

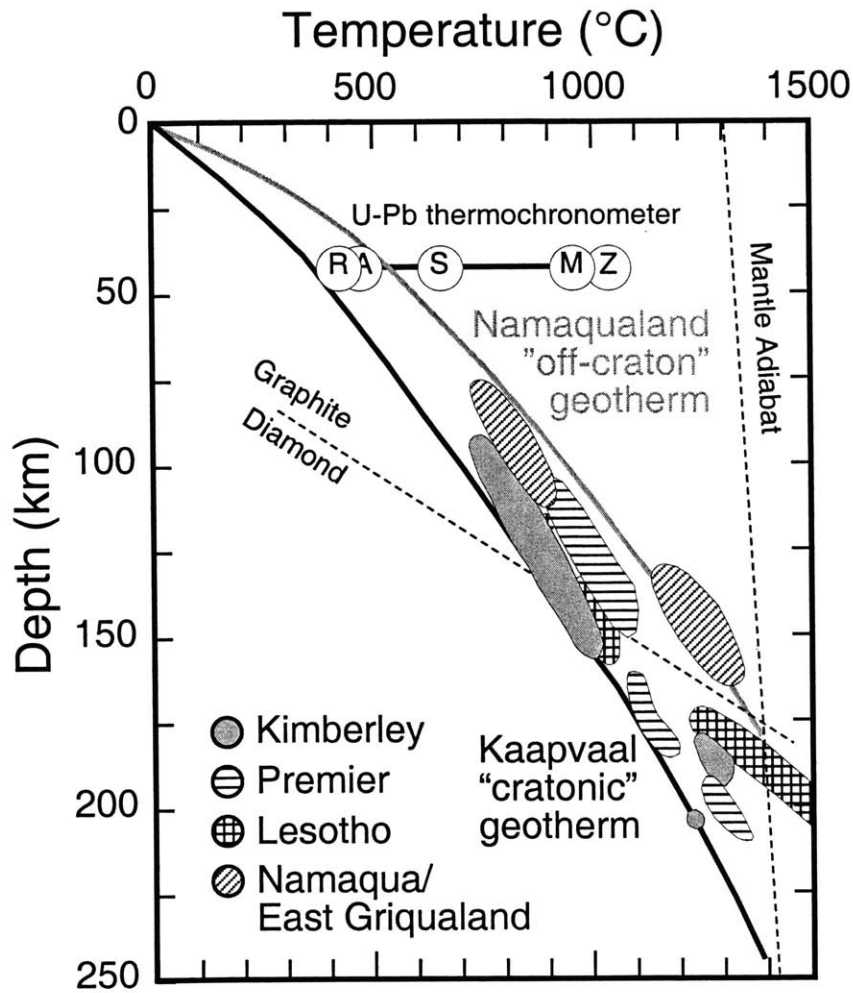


Figure 13. Pressure-temperature diagram for the southern African continental lithosphere, illustrating model geotherms based on heat flow data for cratonic and off-craton regions, fields of thermobarometric data for mantle xenolith assemblages from southern Africa, and the closure temperatures of various U-Pb accessory mineral thermochronometers. Geothermal gradients necessary to reset the rutile thermochronometer are consistent with those inferred to explain off-craton heat flow and mantle xenolith P-T data.

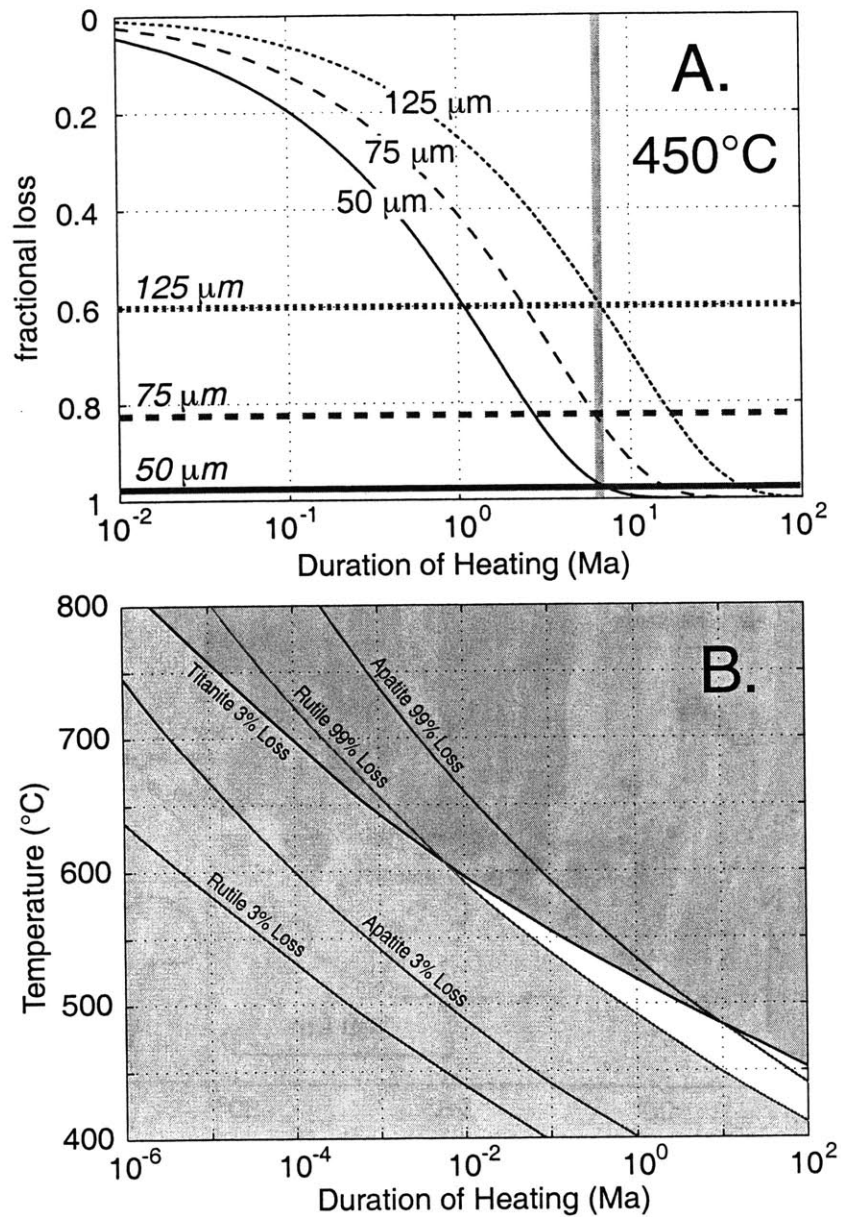


Figure 14. A) Fractional Pb loss curves for rutile (using Ti-self diffusion diffusivity parameters) as a function of duration of heat at 450°C . Each curve is labeled by the effective diffusion radius. The solid vertical line is drawn through the intersections of these model loss curves with observed losses for rutile grains from Eastern Namaqualand and Northern Lesotho lower crustal xenolith suites (horizontal lines, e.g. amount of discordance in Figures 7-9). The reproducibility of the loss curve intersections at a single duration of heating is consistent with a volume diffusion mechanisms of loss. B) Curves of % loss in 50 μm diffusive radius systems as a function of temperature and duration of heating for various accessory minerals. Unshaded region between titanite 3% loss curve and rutile 99% loss curve is allowable region of T-t space for producing the observed accessory mineral systematics.

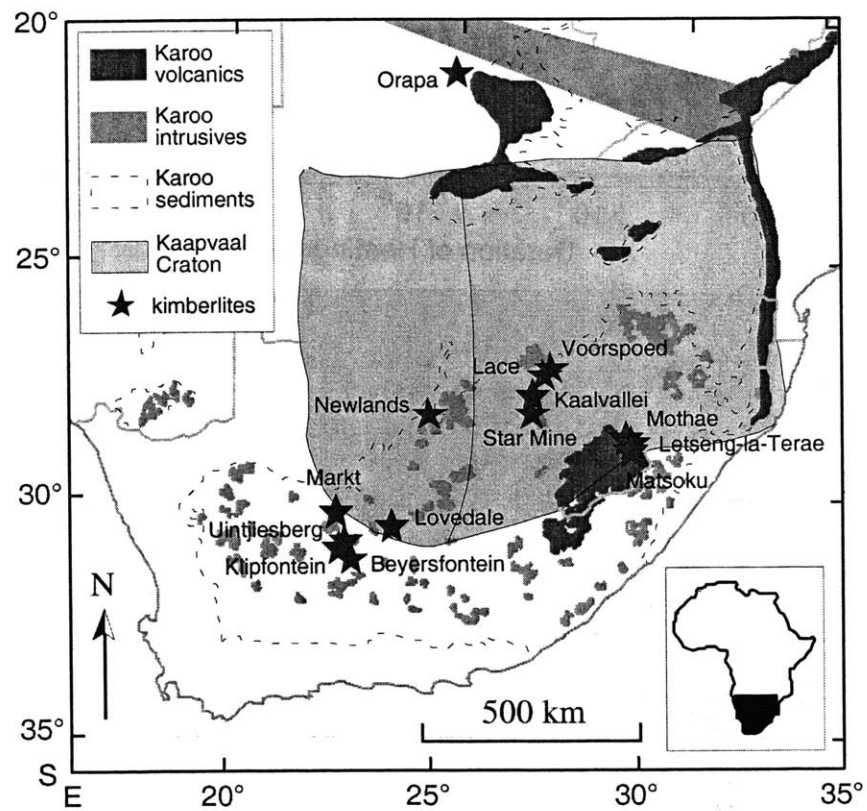


Figure 15. Map of southern Africa illustrating the geographic distribution of sediments of the Karoo Supergroup, with associated intrusive basalts of the Karoo magmatic province and overlying extrusive lavas, relative to the kimberlite-borne lower crustal xenolith suites under scrutiny.

Chapter 5.

Stabilization of the western Kaapvaal Craton: implications for Witwatersrand basin subsidence and the formation of continental lithosphere

Keywords: Kaapvaal craton, Kimberley, Kraaipan belt, U-Pb geochronology, zircon, Witwatersrand basin, Limpopo, Pietersburg belt, Murchison belt

Abstract— New U-Pb zircon geochronological data for high grade gneisses of the Kimberley area of South Africa, and a rhyolitic volcanic unit from the Kraaipan greenstone belt in the northwestern sector of the Kaapvaal craton, are combined with previously published data to refine a model for the crustal evolution of the western domain of the craton, and its Neoproterozoic juxtaposition with the eastern Kaapvaal shield. These rocks record a history of *ca* 2.94 Ga arc magmatism and marginal basin sedimentation on or near the edge of a pre-existing *ca* 3.2 to 3.0 Ga crustal block comprising the present day western domain of the Kaapvaal craton. Subsequent convergence of this block (upper plate) with the 3.7 to 3.1 Ga eastern Kaapvaal shield (lower plate) resulted in initial *ca* 2.93 Ga collision, with associated pervasive deformation, high grade metamorphism, and anatexis of the western domain. This Neoproterozoic collision along the western margin of the Kaapvaal shield is near-synchronous with similar convergent tectonics on its northern ramparts, associated with accretion of a crustal block including the Murchison, Pietersburg and Giyani greenstone belts. Consequential tectonic loading at the northern and western shield margins was responsible for flexural subsidence and deposition of the West Rand Group of the Witwatersrand Supergroup between *ca* 2.97 and 2.90 Ga in a polyphase foreland basin. Continued loading during uplift and collapse of the western orogen (and continued convergence of terranes along the northern shield margin) was responsible for post-2.90 Ga syn-depositional southeast-vergent thrusting and piggyback Central Rand basin development. Our interpretation of the primary importance of western collisional orogenic loading for development of the Witwatersrand basin as a peripheral or pericratonic Himalayan-style foredeep contrasts with existing models which traditionally focus on northern margin Kaapvaal-Limpopo interaction to form the basin in a back-arc Cordilleran-style foreland setting.

Synthesis of the available high-precision geochronological constraints into this new model for the Neoproterozoic assembly of the Kaapvaal craton also has important consequences for the timing of lithospheric mantle stabilization. We propose that the apparent age dichotomy in the Kaapvaal craton between Mesoproterozoic crust formation and stabilization (from U-Pb zircon geochronology of the eastern shield) and Neoproterozoic mantle lithosphere depletion and stabilization (from Re-Os isotopes in mantle xenoliths from the western domain), is largely an artifact of sampling geography. When the systematics of lithospheric mantle xenoliths from the western domain are compared with the complementary evolution of the overlying crust of the western

domain, a strong correlation is revealed between the *ca* 2.9 Ga age of subduction convergence and accretion of the western domain to the Kaapvaal shield, and the *ca* 2.9 age of depletion of mantle peridotites, formation age of mantle eclogites, and encapsulation age of sulfide inclusions in diamonds. These correlations support an actualistic model of subduction zone processing to produce the distinctive depleted character of mantle lithosphere peridotite, and provide compelling evidence for coupling of crust and mantle lithosphere from formation through to craton stabilization.

1. Introduction

The generation and preservation of continental lithosphere are integral processes in the thermal evolution and plate tectonic organization of the Earth, and provide our most direct record of ancient planetary evolution. In contrast to the relatively simple single-stage generation of oceanic lithosphere by adiabatic decompression melting of the mantle to produce a basaltic crust (Basaltic Volcanism Study Project, 1981), the more complex mechanisms of formation and stabilization of the continents are still incompletely understood. Among the most important questions in continental lithospheric studies is the relationship between the continental crust and its underlying lithospheric mantle section. Specific aspects of this inquiry include whether the crust and mantle are genetically complementary to each other, and to what extent the crust and mantle have been coupled to each other over their history. These relationships are particularly important to clarify as the crust is the repository of most of the geologic, structural and geochronological information bearing on the evolution of continental lithosphere, and thus provides a vital reference for the interpretation of the geophysical and rare xenolith data from the more inaccessible mantle lithosphere. Establishing the processes involved in the formation of continental lithospheric mantle to a large degree hinges on these constraints from the crustal record.

The discussion of the relationships between continental crust and its underlying lithospheric mantle has been rejuvenated by recent advancements in geophysical and geochemical methods for the probing of continental mantle lithosphere, particularly the mapping of upper mantle compositional and thermal anomalies by seismic tomography, and the application of the Re-Os isotopic system to mantle xenolith suites. Seismic tomography has produced detailed three dimensional images of velocity perturbations beneath the continents, and yielded insights into lithospheric architecture and composition (Grand, 1987; Grand et al., 1997; Simons et al., 1997; James et al., 2001). The Re-Os system is unique among radiogenic isotope schemes in its ability to record the timing of melt depletion processes in the mantle. As extreme chemical depletion of continental mantle is arguably its primary distinguishing characteristic, Re-Os ages are believed to date in some complex manner its formation (Walker et al., 1989; Pearson et al., 1995).

Mesoarchean model ages for silicate inclusions in diamonds (Richardson, 1984) and Re-Os model ages obtained for some of the first mantle xenoliths from the Kaapvaal craton (Walker et al., 1989; Pearson et al., 1995), were originally used to argue that the age structure of the Kaapvaal mantle and crust were broadly similar, implying their “coupling” over several billions years of Earth history. In contrast, recent work on a crustal section at the Vredefort Dome in the central Kaapvaal craton (Moser et al., 2000) has suggested that final stabilization of the Kaapvaal craton’s crust, *ca* 3.11 Ga, significantly post-dates the timing of mantle lithosphere stabilization necessitated by *ca* 3.2 to 3.4 Ga diamond inclusion ages and the oldest mantle xenolith Re-Os depletion ages of *ca* 3.5 Ga. Such crust-mantle “decoupling” poses obvious difficulties for establishing complementary relationships between the two parts of the lithospheric column. Another emerging complication in the relationship between crust and mantle has arisen from further analysis of Kaapvaal cratonic mantle xenoliths, which reveals a strong peak in the distribution of Re-Os model ages at *ca* 2.8 to 2.9 Ga (Carlson et al., 1999), several hundred million years *younger* than the age of the oldest crustal components of the craton, and common measures of craton stabilization like the deposition of the first supracrustal cover sequence (Dominion Group, ~3.08 Ga; Armstrong et al., 1991) on the eastern Kaapvaal shield. These data could be interpreted as supporting allochthonous crust-mantle relationships and associated models for continental lithosphere generation through slab stacking (Helmstaedt and Schulze, 1989) or diapiric accretion (Oxburgh and Parmentier, 1978; Herzberg, 1993).

Ironically however, there is a simple, if under-appreciated sampling dichotomy between the crustal and mantle geochronological data sets for the Kaapvaal craton. While the majority of high-precision geochronological data for the crust of the craton comes from the well exposed granite-gneisses and greenstone terrains of the eastern craton, for example the Barberton Mountain Land (Armstrong et al., 1990; Kamo and Davis, 1994; Kroner et al., 1996) and the Ancient Gneiss Complex (Compston and Kroner, 1988; Kroner et al., 1989) (see Figure 1), most of the Re-Os mantle geochronological data comes from the abundant xenoliths in kimberlites of the western craton (e.g. the Kimberley Pool, Newlands, Finsch). Between these regions, however, lies a profound change in the regional tectonic fabric of the craton, from predominantly east-west in the eastern domain, to predominantly north-south in the western domain. The boundary separating these domains is manifested in part by a strong N-S trending aeromagnetic anomaly, the Colesberg Lineament, which may represent an epicratonic suture separating crustal blocks of very different age and origin. The appropriateness of comparing the crustal evolution of the eastern shield with the mantle evolution of the western domain is suspect, and may be the source of apparently disparate histories in the two records.

Unfortunately, the Mesoarchean crystalline basement of the western domain of the Kaapvaal craton, which may be complementary to the mantle xenolith record, is only poorly

exposed beneath a cover of Phanerozoic through Neoproterozoic sedimentary and volcanic strata. Surface exposure of the crystalline basement are limited to isolated inliers like the Schweizer-Reneke dome, and Amalia and Kraaipan greenstone belts (Figure 1). Basement is, however, very near the surface in some regions, such that limited sections are exposed in deep boreholes and mine shafts associated with gold and diamond exploration; samples of basement lithologies are also commonly exhumed in the same kimberlites which bring the mantle xenolith suites to the surface. Taking advantage of these phenomena, the present study utilizes samples of the upper and middle crust available as xenolithic blocks in the mine dumps of Kimberley. U-Pb zircon geochronological and Nd isotopic data are used to elucidate protolith ages, as well as the history of metamorphism, deformation, and plutonism of the crust at Kimberley. In addition we present U-Pb zircon data for a volcanic tuff interbedded in banded iron formation and mafic volcanics of the Kraaipan Group of the Kraaipan Greenstone Belt north of Kimberley, which provides the first precise constraint on the age of extrusion and deposition of this greenstone sequence.

These data, together with existing geochronological, field, structural, and petrologic data, are used to establish, to first order, the tectonic evolution of the western domain and the history of its accretion to the eastern Kaapvaal shield. These western margin tectonics are then placed within a temporal framework of coeval accretion along the northern margin of the shield, as well as the cratonic response recorded in the Witwatersrand basin repositories. We argue that flexure related to *ca* 2.9 Ga continental collision along the western margin of the shield is a primary driving mechanism for Witwatersrand basin subsidence, which existing foreland basin models for Witwatersrand sedimentation fail to quantify. Finally, the timing of Neoproterozoic assembly of the Kaapvaal craton is compared with mantle xenolith and diamond geochronological data to hypothesize on the applicability of various models for the formation and stabilization of continental lithosphere.

2. Archean Evolution of the Kaapvaal Craton

The locations of exposed Paleoproterozoic to Neoproterozoic crystalline basement throughout the Kaapvaal craton are illustrated in Figure 1, as are the present distributions of sediments and volcanics of the Meso- to Neoproterozoic Dominion, Pongola, and Witwatersrand basins. Also drawn as inferred from aeromagnetics is the Colesberg lineament, a hypothesized epicratonic suture zone separating the craton into eastern and western domains (Corner et al., 1990). Similarly, the E-W trending Thabazimbi-Murchison Line (TML) is drawn to separate the southern portion of the eastern domain from a northern block containing the Murchison, Pietersburg, and Giyani greenstone belts and intervening gneisses. Following De Wit et al. (1992), the eastern domain of the craton south of the TML is termed the Kaapvaal shield, while crust north of the TML is referred

to as the northern domain. Only once the northern and western domains were sutured to the eastern shield area is the extant Kaapvaal craton recognized as a coherent entity.

The past decade has seen dramatic changes in our understanding of the Archean geologic evolution of the Kaapvaal Craton, in large part due to the availability of increasingly precise and accurate timing constraints obtained from single-crystal U-Pb zircon geochronology. In the following section, a survey of the available high-precision U-Pb zircon geochronological data for the various domains of the Kaapvaal Craton is set forth in concert with corresponding geological and structural data. In complement to Sections 2.2 and 2.3, Figure 2 presents schematic cartoons of the greenstone belts of the northern and western domains illustrating the relationships between supracrustal lithologies, deformation, and intrusive phases. Geochronological constraints on subsidence and sediment deposition in the Archean basins developed on the Kaapvaal craton are also presented and placed within the framework of development for the underlying basement. This summary provides a reference for comparison with our new U-Pb zircon geochronological data for the western domain, and subsequent discussions regarding the Meso- to Neoproterozoic assembly of the Kaapvaal Craton.

2.1 Eastern Kaapvaal Shield

The highest density of U-Pb zircon geochronological data for the Neo- to Mesoproterozoic basement of the eastern domain is available for rocks of the Barberton Greenstone Belt and the Ancient Gneiss Complex of Swaziland. These regions host the oldest rocks of the craton, and have revealed a complex history of crust formation and amalgamation between *ca* 3.7 and 3.1 Ga (Armstrong et al., 1990; Kamo and Davis, 1994; Kroner and Brandl, 1993). The earliest period of crust formation and associated deformation, between 3.70 and 3.51 Ga, is apparently restricted to the Ancient Gneiss Complex and proximal rocks of the southern Barberton belt, including trondhjemitic gneisses and volcanosedimentary sequences of the Theespruit and Sandspruit Formations of the lower Onvervacht Group. Following a 40 Ma hiatus, extrusion and deposition of the structurally overlying Komati and Hooggenoeg Formations are constrained to have occurred between 3.47 and 3.45 Ga, and tectonic juxtaposition of these formations with the underlying Theespruit Formation is constrained by the 3.45 Ga age of small post-deformational plutons (Kroner et al., 1996). A tectonic and/or unconformable contact is developed between the 3.42 to 3.30 Ga Kromberg Formation of the Upper Onvervacht Group (Byerly et al., 1996) and the overlying volcano-sedimentary Fig Tree and Moodies Groups. Fig Tree Group deposition was apparently rapid as constrained by 3.243 ± 0.004 to 3.225 ± 0.003 Ga ages for dacitic tuffs (Kroner et al., 1991) and a 3.226 ± 0.001 Ga age for an ignimbrite near the top of the formation (Kamo and Davis, 1994). Thrusting and recumbent folding of Fig Tree lithologies, and subsequent regional upright folding of both the Fig Tree and rapidly deposited Moodies Groups, occurred between

3.229 and 3.227, and later than 3.226 Ga respectively. Emplacement of pre- and post-deformational volcanics and intrusives, including porphyry stocks, tonalite dikes and the Kaap Valley and Nelshoogte plutons, bracket this primary compressional deformation in the Barberton belt (de Ronde and Kamo, 2000). The 3.216 ± 0.002 Ga age for the Dalmein pluton provides a minimum age for both deposition of the last supracrustal rocks and all compressional deformation. Following a hiatus of over 100 Ma, the Barberton belt was again subjected to a major influx of potassic magmatism at *ca* 3.10 Ga, resulting in emplacement of the Nelspruit and Mpuluzi batholiths and number of other smaller plutons. Magmatism apparently accompanied transtensional deformation which openly refolded earlier structures in the last substantive deformational episode in the belt. Finally, younger, *ca* 2.7 Ga plutons make up a minor part of the Barberton area (e.g. Mpangeni pluton) but are volumetrically more significant to the south in Swaziland (e.g. Mbabane, Kwetta, Nzimane granites: Hunter and Wilson, 1988; Maphalala and Kroner, 1993; Thomas et al., 1997).

To the south of Barberton and the Ancient Gneiss Complex, a lack of modern high-precision geochronological data limits an understanding of the stabilization of the crust of the Kaapvaal shield to its present southern contact with the Proterozoic Natal belt. Greenstone belt fragments of the region include the Assegaai, De Kraalen, Comondale and Nondweni greenstones. A singular date of 3.406 ± 0.003 Ga for a felsic unit in the Nondweni Greenstone belt at the southern edge of the craton gives an indication of the antiquity of this crust (Wilson and Versfeld, 1994). An Rb-Sr errorchron for the enclosing Anhalt Leucotonalite suggests a likely minimum stabilization age of *ca* 3.2 Ga for much of the region (Farrow et al., 1990), however detailed mapping and structural analysis are insufficient to hypothesize on the timing and modes of deformation which resulted in the assembly of the southeastern shield. To the north of Barberton, again very little high-precision geochronological data is available for a large swath of tonalitic and granitic gneisses stretching for nearly 300 km to the TML. Kamo and Davis (1994) report 3.30 to 3.33 Ga xenocrystic zircons in the 3.106 Ga Nelspruit Batholith north of the BGB. Single-zircon ages of 3.16 to 3.18 Ga are reported for granitoid gneisses and migmatites in the southern Kruger National Park (Kroner et al., 1998). South of the Murchison belt, Poujol and Robb (1999) present data for a tonalitic sample of the Makhutswi Gneiss indicating an age of 3.06 ± 0.01 Ga, as well as data for a trondhjemitic gneiss of the Harmony Granite suggesting an age from *ca* 3.04 to 3.09 Ga. Finally, a trondhjemitic gneiss sampled just south of the Murchison belt at French Bob's Mine yielded zircons suggesting an age of *ca* 3.22 Ga (Poujol et al., 1996). There appears to be a distinctly younger history in this region relative to the evolution recorded in the Barberton belt, however the available geological, geochronological and structural data are insufficient to establish its detailed crustal evolution.

Two significant basement inliers representing crust of the Kaapvaal shield to the west of Barberton are recognized in the Johannesburg and Vredefort domes. Recent geochronological investigations (Barton et al., 1999; Poujol and Anhaeusser, 1999) have begun to reveal the tectonic and plutonic evolution of these packages of Mesoarchean crust. In the Johannesburg dome, the record of crustal evolution begins with the *ca* 3.34 Ga crystallization age of trondjhemitic gneisses in the northwestern sector of the dome. While the relationship of these gneisses to mafic greenstone belt fragments in the southern margin of the dome is equivocal, a clearer intrusive relationship with 3.20 Ga tonalitic gneisses is apparent and constrains the minimum age of the supracrustal rocks. A subsequent, voluminous potassic granitoid suite intrudes much of the dome; ages for two granodiorites of 3.11 and 3.12 Ga constrain the timing of this magmatism. The striking synchronicity of *ca* 3.20 and 3.11 Ga granitoid plutonism in both the Johannesburg dome and the BGB indicates, to first order, a similar tectonic evolution for these geographically disparate sections of crust.

The second substantial inlier, the Vredefort dome, was the locus of deformation and metamorphism associated with a 2.023 ± 0.004 Ga meteorite impact (Kamo et al., 1996; Moser, 1997; Gibson et al., 1997), which to varying degree has occluded the isotopic record of the pre-impact crustal evolution in the dome. However recent mapping and single-grain U-Pb zircon and monazite geochronological studies have substantially improved the Mesoarchean geological and chronological framework. The crystalline basement core of the dome is traditionally divided into an outer annulus of amphibolite facies rocks dominated by the batholithic Outer Granite Gneiss (OGG), and an inner core of granulite facies rocks dominated by the monotonous Inlandsee Leucogranofels (ILG), but also containing significant panels of tonalitic gneisses, mafic igneous rocks, and supracrustal rocks best exposed in the Steynskraal Mafic Complex (SMC). While attempting to date the age of impact using clasts from pseudotachylite breccia developed in the OGG, Kamo et al. (1996) obtained concordant zircon dates of 3.06 to 3.08 Ga in charnockitized host rocks, interpreted to indicate a minimum age for the OGG and/or the time of charnockitization. Similarly, both Kamo et al. (1996) and Moser (1997) demonstrated primary ages >3.3 Ga for shocked zircons in both the OGG and ILG, giving an indication of the antiquity of portions of the crust in the dome. Some attention has also been given to high-T, low-P granulites in the SMC, including mafic granulites and garnet-cordierite paragneisses. Stevens (1997) presented evidence for an M1 anticlockwise P-T path for garnet-cordierite migmatites in the SMC, with peak conditions reaching 850-900°C and 5 kbar followed by near-isobaric cooling. M1 metamorphism is constrained by cross-cutting pseudotachylite veins to predate impact, and was conclusively demonstrated to be Mesoarchean in age by Hart et al. (1999), who dated 3.107 ± 0.009 Ga metamorphic monazite and zircon from both metapelites and mafic granulites in the SMC. Moser et al. (2001) also dated 3.094 ± 0.007 Ga foliated tonalitic to granitic dikes which cut deformed

tonalitic and charnockitic gneisses of the ILG complex, and tentatively correlate these phases to the batholithic OGG. While further field and geochronological studies are necessary to resolve the detailed Mesoproterozoic crustal evolution in the Vredefort dome, it is clear that a major episode of metamorphism and crustal melting leading to the intrusion of batholithic scale granitoids into the middle crust occurred *ca* 3.1 Ga, which correlates with similar intrusive activity throughout the eastern Kaapvaal shield.

Finally, there have been a limited number of U-Pb zircon dates measured for granitic gneisses exposed in the basement inliers along the northern ramparts of the Witwatersrand basin, or subcropping in boreholes of the gold fields at the margins of the basin. Armstrong et al. (1990) dated a gneissic granitoid flooring the Dominion Group in a borehole near Klerksdorp, obtaining an age of 3.120 ± 0.005 Ga. Robb et al. (1992) presented high-precision U-Pb zircon geochronological data for granitoid samples from surface outcrop and borehole intersections. The oldest granodiorite-ademellite gneisses, overlain by Dominion Group sediments and dated at 3.174 ± 0.009 Ga, was drilled on the southeast margin of the Hartbeesfontein dome; two samples from the nearby Westerdam dome yielded consistent ages of 3.086 ± 0.003 Ga. A leucogranite sample from the northwestern Coligny dome yielded a substantially younger age of 3.031 ± 0.010 Ga; and a basement granitoid intersected in a borehole south of the Vredefort dome yielded a crystallization age of 3.101 ± 0.002 Ga. Finally, a non-deformed granite intersected in a borehole west of Welkom yielded a quite young crystallization age of 2.727 ± 0.005 Ga, demonstrating a wider geographic distribution for *ca* 2.78 to 2.72 Ga granitic plutonism abundant in both the southeastern Kaapvaal shield (“post-Pongola granites”), and in the northern domain (Kanye volcanics, Gabarone and Turfloop batholiths).

2.2 Northern Domain

North of the Kaapvaal shield and the TML, rocks comprising the Murchison, Pietersburg, and Giyani greenstone belts have been the focus of most recent U-Pb zircon studies. Investigations within the Murchison belt have demonstrated that the metavolcanics and sedimentary sequences of the belt substantially post-date similar activity in the Barberton belt. The time of deposition of the supracrustals is constrained by consistent zircon ages of 2.967 ± 0.002 and 2.970 ± 0.002 Ga for sheared rhyolites of the Rubbervale Formation (Brandl et al., 1996; Poujol et al., 1996); zircons composited from felsic schists in the structurally underlying Weigel Formation ultramafic, mafic and intermediate volcano-sedimentary formations have yielded ages of *ca* 3.09 Ga, with single zircons as old 3.20 Ga, suggesting that this volumetrically dominant sequence in the Murchison belt may be significantly older than the felsic volcanics of the belt, and have age correlatives with granitoids exposed to the south of the Murchison belt. Granitoid plutonism into and surrounding the belt was demonstrated by Poujol et al. (1996) to have occurred episodically at *ca* 2.92 Ga

(Maranda and Discovery granites), at *ca* 2.82 Ga (Willie granite), at 2.74 Ga (Rooiwater layered intrusion), and at 2.68 Ga (Mashishimala Granite Suite) (Figure 2).

Vearncombe et al. (1988) develop a deformational history for the Murchison belt comprising a pervasive D1 episode of isoclinal folding and shape fabric development on N-dipping ENE-trending axial planes. S-C fabrics in D1 structures indicate a reverse N-over-S movement sense. D1 structures were subsequently deformed into asymmetric “S” folds along E-W D2 axial planes, steepened, and overprinted by a prominent pressure-solution cleavage axial planar to the D2 folds. Field relations indicate that the Maranda, and Discovery granites dated by Poujol et al. (1996) post-date D1 fabrics but are affected by D2 cleavage and folding. Unfortunately, precise crystallization ages of the granites remain equivocal; minimum ages for these post-D1 granites conservatively bracket D1 to between 2.97 and 2.90 Ga. The *ca* 2.82 Ga for the non-deformed Willie Granite similarly may provide a minimum age constraint on D2 deformation, although this upper intercept age from severely discordant zircons is relatively imprecise. Alternatively, the 2.74 Ga age of the internally undeformed (although tectonically juxtaposed) Rooiwater provides a more conservative lower limit on the timing of D2 deformation. The aforementioned juxtaposition of the amphibolite-facies metamorphosed Rooiwater complex (Vearncombe, 1987) with the lower grade rocks of the Murchison belt was probably accommodated along an oblique-slip D3 shear zone, perhaps a strand of the major sinistral Letaba shear zone which up the northeast margin of the belt (Fripp et al., 1980; Vearncombe, 1988). D3 deformation thus post-dates 2.74 Ga.

The Pietersburg and Giyani belts, like the Murchison belt, have been demonstrated to be at least partially composed of supracrustal rocks significantly younger than those at Barberton. A quartz porphyry from the Ysterberg Formation of the Pietersburg belt was recently dated by Kroner et al. (2000) at 2.950 ± 0.001 Ga, and interpreted to indicate a minimum age for felsic magmatism in the belt. This result is similar to an age of 2.958 ± 0.002 Ga for the foliated Lunsklip Granite (De Wit et al., 1993), which cuts the mafic greenstones of the belt, providing a minimum age for these rocks. This or similar granitoids were also an important source for detrital zircons in the Uitkyk Formation cover sequence of coarse clastic sediments which contain a predominant population of 2.958 Ga grains. Non-deformed granitoids in the vicinity of the Pietersburg belt include the northerly 2.687 ± 0.002 Ga Uitloop Granite, and the southerly batholithic Turfloop Granite, which was recently dated by U-Pb zircon methods at 2.777 ± 0.010 Ga (Henderson, 2000). Deformation in the Pietersburg belt was interpreted by De Wit et al. (1992) to comprise a predominant D2 SE-NW compressive phase evidenced by S-over-N thrusting, tight folding along S-dipping NE-SW oriented axial planes, and local development of a concordant penetrative fabric. Deposition of the Uitkyk Formation sediments was interpreted to be synchronous with D2 thrusting and deformation; a maximum age for D2 deformation is thus provided by the *ca* 2.90 Ga age of the youngest detrital zircon in the Uitkyk sediments. A minimum age constraint for D2

deformation is given by the *ca* 2.78 Ga age of the post-tectonic Turfloop Granite. D2 structures were subsequently steepened and disrupted by subvertical oblique-slip D3 shear zones, which must post-date intrusion of the Turfloop Granite (Figure 2).

While no direct age exists for the mafic volcanics of the Pietersburg belt, recent dating of a deformed meta-andesite of the central Giyani greenstone belt yields an age of 3.203 ± 0.001 Ga, establishing an older period of ultramafic to mafic volcanism (Kroner et al., 2000). Deformation in the Giyani belt was described by McCourt and van Reenan (1992) and de Wit (1992), who established a very similar deformational history to that of the southwestern Pietersburg belt. South-over-north thrusting during D2 was inferred to have developed the predominant ENE-WSW trending foliation and axial planes of tight folds. A weakly-foliated quartz porphyry dike cross-cutting ultramafic schists in the southern Lwaji arm of the belt dated at 2.874 ± 0.001 Ga has been suggested to post-date a significant amount of D2 deformation. These fabrics are subsequently steepened and overprinted along the Hout River shear zone, which overthrusts by oblique-slip granulite-facies rocks of the Southern Marginal Zone of the Limpopo Belt to the south over greenschist-facies greenstones of the Giyani belt; similarly oriented low-grade shear zones internal to the belt manifest the same D3 kinematics. Finally, a variety of granitoid gneisses surrounding the Giyani belt were dated by Kroner et al. (2000); two gneisses to the north of Giyani yielded ages of 3.283 ± 0.001 and 2.810 ± 0.001 Ga, while two gneissic granitoids to the south, an unnamed migmatitic augen gneiss and the foliated monzogranitic Groot Letaba gneiss, yielded inferred crystallization ages of 3.171 ± 0.001 and 2.953 ± 0.060 Ga respectively (Figure 2).

Attempts may be made utilizing new geochronological data to correlate the different deformational histories in the three greenstone belts of the northern domain (Figure 2). If parallels are drawn between the kinematic evolution of the Pietersburg and Giyani belts (de Wit, 1992), then north-directed D2 thrusting in the belts may be conservatively bracketed between 2.90 and 2.78 Ga, the ages of youngest detrital zircons in the syn-D2 Uitkyk sediments of the Pietersburg belt and intrusion of the Turfloop granite, respectively. Attractive targets for further bracketing D2 deformation include additional quartz porphyries within, and non-deformed granites to the south of, the Giyani belt (Shamiriri and Padi Granites), and the pre- to syn-D2 Melkboomfontein and Mosokgome Granites in the Pietersburg belt (Kroner et al., 2000). D2 deformation in the Murchison Belt is again poorly bracketed, however the available geochronological data are consistent with a hypothesized correlation to D2 phases in the more northerly Pietersburg and Giyani belts, and the *ca* 2.82 Ga age of the post-tectonic Willie granite may more tightly bracket D2 deformation across the northern domain. On the other hand, the pervasiveness of D1 deformation in the Murchison belt appears unique relative to the other greenstone belts, and is demonstrably older, between 2.97 and 2.90 Ga. Again, post-D1, pre-D2 intrusives in the Murchison belt are

attractive targets for precise dating in order to further constrain the timing of these deformation phases.

2.3 Western Domain

Large-scale N-S structural trends in the crustal block west of the Colesberg magnetic lineament are orthogonal to, and truncate those in the eastern Kaapvaal Shield. Sediments of the Dominion and Witwatersrand Supergroups are similarly absent from the western domain. These observations have led a number of synthesists (de Wit et al., 1992; Thomas et al., 1993; McCourt, 1995) to conclude that the juxtaposition of the western domain was a relatively young phenomenon in the evolution of the craton. A minimum age for the suturing of the western domain to the eastern Kaapvaal shield is obtained from the first cover sequence to onlap the western domain, the 2.71 Ga Platberg Group of the Ventersdorp Supergroup. The timing of juxtaposition is further refined by the 2.880 ± 0.002 Ga age for the non-deformed granite of the Schweizer-Reneke dome, which intrudes and cross-cuts the older Amalia greenstone belt fragments and the pervasive deformation fabric of the western domain. A similar age of 2.853 ± 0.004 Ga for the Draghoender granite at the southwestern margin of the western domain (McCourt and Armstrong, 2000), intrusive into the Marydale greenstone supracrustals, suggests that the western domain was a coherent amalgamated block sutured to the eastern Kaapvaal shield by this time.

The best exposures of crystalline basement occur in the northern part of the western domain, where three N-S trending linear belts of the Archean Kraaipan Group greenstone belts, defined by resistant banded iron formation, provide most of the available crystalline basement outcroppings. The stratigraphy of the Kraaipan Group is divided into a basal Goldridge Formation, consisting of outcropping magnetite quartzites and poorly exposed mafic schists/volcanics. These are overlain by the Ferndale Formation, comprising fine grained magnetite-rich banded iron formations and some mafic schists, which is in turn overlain by the Khunwana Chert Formation, which consists of banded iron formation, ferruginous cherts, mafic volcanic schists, and greywacke. Outcroppings of Kraaipan Group rocks are generally fault bounded, or engulfed by intrusive granitoids, like the previously noted Schweizer-Reneke granite in the southern Amalia region.

Until very recently, little high-precision geochronological data could be brought to bear on the age of the greenstone fragments and associated granitoids and basement gneisses of the western domain, or the timing of pervasive N-S fabric development. Exceptions were unpublished ion probe ages of *ca* 3.25 and 2.94 Ga respectively for cores and rims of zircons from gneisses in the Kimberley diamond mines reported by Drennan et al. (1990), and two *ca* 2.93 Ga zircons in migmatitic gneisses from a borehole west of the Schweizer-Reneke dome, interpreted to indicate the age of metamorphism and migmatization of this region (Robb et al., 1992). Unpublished data

for likely detrital zircons in felsic schists of the Gold Ridge and Ferndale Formations of the Kraaipan Group also yielded four $^{207}\text{Pb}/^{206}\text{Pb}$ dates of *ca* 3.02 to 3.16 Ga (Anhaeusser, 1991).

More recently, Anhaeusser and Walraven (1999) presented zircon Pb-evaporation model ages for tonalite-trondhjemite basement gneisses in a borehole at Setlagole, in the central Kraaipan belt, indicating the presence of crustal components as old as 3.07 to 3.16 Ga. Poujol and Anhaeusser (2000) presented U-Pb zircon data for a tonalitic gneiss platform west of the Amalia belt, which indicate a minimum age of the gneiss of *ca* 3.01 Ga, with individual zircon ages as old as *ca* 3.18 Ga. A cross-cutting tonalite dike in this same platform yielded a precise zircon crystallization age of 2.939 ± 0.010 Ga, while in the vicinity of the Kraaipan belt, three distinct episodes of granitoid emplacement were dated at 2.915 ± 0.012 Ga, 2.878 ± 0.008 Ga, and 2.791 ± 0.008 Ma. The youngest granitoid in the Kraaipan belt, the Mosita Adamellite, has been correlated with the batholithic Gabarone Granite and Turfloop Granites to the north and west; all of these *ca* 2.78 Ga granites are aligned along the E-W trending TML, which is likely related in some complex manner to their genesis. Similarly, Poujol and Anhaeusser (2000) noted the synchronicity of emplacement of 2.88 Ga non-deformed granites in a N-S alignment through the Amalia and Kraaipan belts.

Due to the sparse and discontinuous outcrop in the Kraaipan-Amalia region, a comprehensive deformational history has not been established. From the available literature (e.g. Anhaeusser, 1991; Vearncombe, 1986), the Kraaipan Group formations are generally subvertical in attitude, steeply dipping both E and W, lack a consistent younging direction, display rapid thickness variations and boudinage, and contain internal disharmonic folding— all of which suggest pervasive tight to isoclinal folding along generally N-S to NE-SW trending axial planes throughout the belt. Similarly striking shear zones and mylonites are also reported as pervasive. Map patterns suggest the presence of ubiquitous asymmetric S-folds at the outcrop and larger scale, and point to at least two discordant deformation phase. A clearer picture of the deformational history of the Kraaipan belt rocks from detailed mapping and geochronology is a necessary, if daunting prerequisite to an enhanced understanding of the evolution of the region. Geochronological bracketing of the deformation in the western domain is discussed further in Sections 4.1.2 and 5.2.

2.4 Witwatersrand sedimentation

The development of sedimentary basins on the Mesoproterozoic basement of the Kaapvaal shield provide important evidence for the stabilization of the crust. Subsidence, sedimentation, and subsequent deformation of these basins are a response to local and far-field stresses (Beaumont, 1981; Cloetingh, 1988; Peper et al., 1992), and thus basin studies provide important constraints on

tectonic models for the formation of the Kaapvaal craton. The sedimentary and volcanic strata of the Dominion Group, Witwatersrand and Ventersdorp Supergroups (collectively termed the Witwatersrand triad), and the correlative Pongola Supergroup, provide a rich record of cratonic evolution from *ca* 3.1 to 2.7 Ga. The available geochronological constraints on deposition of these sequences are summarized below.

The eruption ages of four volcanic horizons in the Witwatersrand triad, determined by U-Pb zircon geochronology (Armstrong et al., 1990), provide important constraints on the timing of deposition of the sediments. A quartz-porphyry from the Syferfontein Lava Formation of the upper Dominion Group has an age of 3.074 ± 0.006 Ga, and thus constrains the end of Dominion Group deposition; combined with the previously noted age for unconformably underlying granitoids of the Westerdam dome, sedimentation in the Dominion basin is confined to a brief interval between 3.086 and 3.074 Ga. A tentative age of 2.914 ± 0.008 Ga for the Crown Lava Formation of the upper West Rand Group provides a time marker near the end of West Rand sedimentation, and a maximum age for Central Rand Group deposition. In the Ventersdorp Supergroup, ages of 2.714 ± 0.008 Ga and 2.709 ± 0.004 Ga for the Alberton Porphyry Formation of the Klipriviersburg Group, and the Makwassie Quartz Porphyry Formation of the Platberg Group, constrain a minimum age of deposition of the Central Rand Group, as well as marking the time of effusive outpourings of mafic to intermediate volcanics associated with major rifting in the central craton.

Detrital zircon studies also play an important role in bracketing the timing of basin formation. Barton et al. (1989), Robb et al. (1990), and Poujol et al. (1999) have presented SHRIMP ion microprobe and conventional ID-TIMS U-Pb zircon data for several quartzites of the Dominion, West Rand and Central Rand Groups. The youngest detrital zircons in basal conglomerates of the Dominion Group are 3.105 Ga, consistent with Dominion Group sedimentation between 3.086 and 3.074 Ga. Similarly, the youngest detrital zircons in quartzites of the lower West Rand Group are 2.970 Ga, constraining the bulk of deposition in the West Rand basin to between 2.970 and 2.914 Ga. Finally, the youngest detrital zircons in quartzites of both the lower Johannesburg and upper Turffontein Subgroups of the Central Rand are 2.894 Ga, constraining deposition in the Central Rand basins to between 2.894 and 2.714 Ga.

The recognition of strong correlations between the sequence stratigraphy of the Mozaan Group of the Pongola Supergroup (Figure 1), and that of the Witwatersrand Supergroup (Beukes and Cairncross, 1991; Nelson et al., 1995) allows geochronological constraints on the deposition of the Mozaan Group to be applied to the West Rand and Central Rand Groups. Hegner et al. (1994) reported a U-Pb zircon age of 2.985 ± 0.011 Ga for a rhyolite in the volcanic Nsuzze Group underlying the Mozaan Group, providing a maximum age for Mozaan deposition. This estimate agrees well with previously noted detrital zircon constraints for West Rand deposition of < 2.970

Ga, supporting the Pongola-Witwatersrand correlation. Gutzmer et al. (1999) dated a quartz porphyry sill intrusive into the Mozaan Group at 2.837 ± 0.005 Ga which was deformed with those sediments. Maphalala and Kroner (1993) reported a precise Pb evaporation zircon age of 2.824 ± 0.006 Ga for the Mooihoek granite, which cross-cuts all strata of the Mozaan Group, providing a minimum age for its deposition and by inference, deposition of the Central Rand Group. The Central Rand Group is thus constrained to have been deposited between 2.89 and 2.82 Ga, implying a significant hiatus in deposition and likely erosion during emergence of the craton between 2.84 Ga and the onset of Ventersdorp rifting and subsidence at *ca* 2.72 Ga.

3. Analytical Techniques

Zircons were isolated from xenoliths by standard crushing, heavy liquid, and magnetic separation techniques, and separated into different populations based on crystal morphology, color, and grain size. The most transparent, inclusion-poor and crack-free grains were air-abraded with pyrite after the method of Krogh (1982), and acid rinsed in warm 3M HNO₃ for 12 hours, followed by ultrasonication. Selected zircons were subsequently loaded into Teflon FEP microcapsules and washed again in 3M HNO₃ at 50°C for 2-4 hours, followed by rinsing with several capsule volumes of water. Samples were spiked with a mixed ²⁰⁵Pb-²³³U-²³⁵U tracer and dissolved in 28M HF at 220°C for 48-120 hours, followed by conversion to 6M HCl at 180°C for 18-24 hours. Pb and U were separated using miniaturized HCl-based anion exchange chromatography procedures modified after Krogh (1973).

Pb and U were analyzed on the MIT VG Sector 54 thermal ionization multicollector mass spectrometer. Lead was loaded on single Re filaments with a dilute silica gel-0.1M H₃PO₄ emitter solution. Pb isotopes were measured either dynamically with four high-mass Faraday cups and an axial ion-counting Daly detector, peak-switching ²⁰⁵Pb into the axial position to obtain an internal Daly-Faraday gain calibration, or by peak-switching all ion beams into the Daly detector for very small amounts of lead. An ion beam of $>0.1 \times 10^{-13}$ A was maintained for ²⁰⁷Pb during data acquisition. Uranium was loaded on single Re filaments either with colloidal graphite and measured as metal ions, or with silica gel and measured as UO₂⁺ ions by one of two methods: in static mode on three Faraday cups for ²³⁸U⁺ (²³⁸U¹⁶O₂⁺) ion-beam intensities of $>0.5 \times 10^{-13}$ A, or by peak switching all ion beams into the Daly detector for smaller amounts of uranium. Details of fractionation and blank corrections are given in Table 1. Ages with propagated uncertainties were calculated using the methodology of Ludwig (1980).

For Sm-Nd isotopic analyses, 50-100 mg of powdered whole rock samples were spiked with a mixed ¹⁴⁹Sm-¹⁵⁰Nd tracer and completely dissolved with 3 ml of 29M HF and 0.5 ml of 7M HNO₃ in teflon pressure vessels at 220°C for two or five days, followed by conversion to 6M HCl

and fluxing at 120°C for 24 hours. The separation and purification of Sm and Nd were accomplished with a standard two-stage cation exchange-HDEHP reverse chromatography procedure. Sm was loaded on single Ta filaments with 1 μ l of 1M H₃PO₄ and analyzed as metal ions in static multicollector mode with a ¹⁵²Sm ion beam of 2.5x10⁻¹¹ A. Nd was loaded on triple Re filaments with 1 μ l of 0.1M H₃PO₄ and analyzed as metal ions in dynamic multicollector mode with a ¹⁴⁴Nd ion beam of 1.5x10⁻¹⁰ A. Sm and Nd data were fractionation corrected with an exponential law, normalizing to ¹⁵²Sm/¹⁴⁷Sm = 1.783 and ¹⁴⁶Nd/¹⁴⁴Nd = 0.7219 respectively. Details of data internal and external reproducibility are given in the caption to Table 2.

4. Analytical Results

4.1 U-Pb isotopic data

4.1.1 Kraaipan greenstone belt

Sample WKC00-26: This crystal-rich quartz-feldspar phenocrystic rhyolite, interbedded with banded iron formation, ferruginous cherts, and silicified mafic volcanics of the Khunwana Chert Formation of the Kraaipan Group, was sampled from a borehole approximately 2 km northwest of Khunwana. Approximately two kilograms of sample yielded several dozen pink, transparent to translucent, euhedral, prismatic, internally structureless zircons with sharp terminations, including a subpopulation of delicate, highly elongate, needle-shaped grains. A subset of these grains was severely abraded resulting in the removal of approximately 40% by mass of most grains, and significant fragmentation of larger crystals. Three of the largest remaining clear ellipsoidal abraded fragments were analyzed, yielding variably discordant U-Pb isotopic ratios which define a linear discordia with an upper intercept of 2.940±0.002 Ga and a lower intercept of 1.02±0.05 Ga (MSWD = 0.69) (Figure 2). The upper intercept of the discordia is interpreted as the crystallization and eruption age of the rhyolitic tuff. As the rhyolite is interbedded within the Khunwana Chert Formation, it provides the first precise datum for the deposition age of the supracrustal packages of the Kraaipan Group.

4.1.2 Kimberley basement

All samples of the Archean basement complex underlying Kimberley were obtained as crustal xenoliths from the Boshof Road tailings dump, which was sourced primarily from the Bultfontein Mine. Three samples comprise discrete homolithic xenoliths of amphibolite (KX14-8), peraluminous banded tonalite (KX14-20), and biotite granite (KX14-19), while the other three samples (KX14-18, KX14-21, KX14-22) comprise discrete components of a large banded gneiss block, which were isolated with a diamond saw prior to crushing.

Sample KX14-20: This ~15 cm subangular block of foliated tonalite gneiss is distinctive for its peraluminous composition, evidenced by the presence of garnet porphyroblasts. On a hand sample scale the gneiss is essentially compositionally homogeneous, although mineralogically anisotropic. The metamorphic fabric is defined by aligned biotite grains and a gneissose layering of mica-rich and mica-poor domains. Abundant small (<100 μm), colorless, variably transparent to cloudy translucent zircons have blunt prismatic morphology with consistently rounded edges and terminations. Six single grains were abraded and analyzed, all yielding discordant isotopic ratios; $^{207}\text{Pb}/^{206}\text{Pb}$ dates ranged from 3.069 to 3.246 Ga. Excluding the oldest grain, the other five zircons scatter about a discordia with an upper and lower intercepts of 3.17 and 1.03 Ga (Figure 3). The zircon systematics of this gneiss are clearly affected by ancient Pb loss, and possibly secondary 2.93 Ga metamorphic overgrowth as documented below in other Kimberley gneisses. From the available data, the zircons of this sample are unlikely to represent a singular initial population, perhaps reflecting an initial sedimentary protolith, or inheritance in a primary magmatic protolith. Irrespective of its precise age, this sample provides an important constraint on the minimum age of the oldest crustal components in the western domain.

Sample KX14-8: This small (<4 cm) rounded xenolith of garnet-bearing hornblende amphibolite exhibits a strong foliation defined by aligned amphiboles, which rotates around garnet porphyroblasts. There has been significant retrograde reaction of garnet and hornblende to coarse secondary blue-green amphibole. The amphibolite contains abundant round multi-faceted zircons typical of crystals grown during solid-state metamorphic reaction. Optical microscopy and cathodoluminescence imaging of these grains reveals rare, small, corroded, and spongiform-zoned cores which are overgrown by broadly sector-zoned phase of zircon. Again, such zoning is typical of zircon grown under solid-state conditions. Individual grains lacking optically visible cores were abraded; four grains yielded identical concordant isotopic ratios (Figure 4) with a weighted mean $^{207}\text{Pb}/^{206}\text{Pb}$ date of 2.932 ± 0.001 Ga, which is interpreted as the time of growth of the predominant metamorphic phase of zircon, and by inference the time of upper amphibolite-facies metamorphism synchronous with the development of a strong fabric in this rock.

Sample KX14-22: This sample comprises a six cm thick discrete layer of garnet-free hornblende amphibolite in the same large gneiss block from which samples KX14-21 and KX14-18 were also extracted. This mafic layer is dominated mineralogically by interlocking aligned lathes of hornblende; zircons from this sample are small, round, multi-faceted crystals, similar in appearance to the zircons from the garnet amphibolite, KX14-8. Three very small abraded zircons from this yielded identical concordant isotopic ratios, with a weighted mean $^{207}\text{Pb}/^{206}\text{Pb}$ date of 2.928 ± 0.002 Ga (Figure 4). This date is interpreted to represent the metamorphic crystallization of

zircon during amphibolite facies metamorphism of the banded gneisses, and is similar to, if only slightly younger than, the age of metamorphic zircon in amphibolite KX14-8.

Sample KX14-21: This sample is a second discrete ten cm thick layer from the banded gneiss block from which sample KX14-18 and KX14-22 were also taken. The composition of this band is amphibolitic to mafic tonalitic, and the layer exhibits a migmatitic texture with discrete mm- to cm-sized lenses of leucosome in an amphibole-rich melanosome. The presence of leucosomal segregations distinguishes this sample from amphibolite KX14-22, and similarly, the zircons of this sample are morphologically different, with elongate prismatic forms suggestive of crystallization from a melt. Three of these euhedral, prismatic, strongly pink-colored zircons were abraded, and yielded discordant data, with $^{207}\text{Pb}/^{206}\text{Pb}$ dates from 2.934 to 2.924 Ga. The most concordant zircon has a $^{207}\text{Pb}/^{206}\text{Pb}$ date of 2.927 ± 0.001 Ga (Figure 4). These zircon ages, which are very similar to those of metamorphic zircon in the previous two amphibolites are interpreted to again date the timing of amphibolite-facies metamorphism of the banded gneiss. The presence of apparent leucosomal melt in this layer, combined with the prismatic forms of the zircons also suggests that partial melting accompanied metamorphism.

Sample KX14-18: This sample comprises a discordant pegmatite layer cross-cutting the banded gneiss block, but which itself contains a moderate fabric and at times indistinct margins with the host gneiss. Zircons from the pegmatite have an elongate prismatic morphology with sharp terminations, and optically visible concentric interior zonation, consistent with crystallization from a melt. Isotopic data for three abraded zircons from this gneiss illustrate mixing between both inherited and magmatic components. Two zircons (Table X, not plotted in Figure 4) have discordant systematics with $^{207}\text{Pb}/^{206}\text{Pb}$ dates of 3.032 and 3.265 Ga, the latter being the oldest zircon reported in the western domain of the craton. These grains are apparently inherited from the host gneisses; the inherited component is consistent with the ages for zircons from the peraluminous tonalitic gneiss sample KX14-20. A third zircon is concordant with an age of 2.926 ± 0.002 Ga (Figure 4), which is interpreted to represent the crystallization age of the pegmatite. This interpretation is supported by the essentially identical ages for melt-related zircons in the migmatized amphibolite layer. Examined together, the 2.932 to 2.926 Ga ages for metamorphic and melt-related zircons from these foliated and banded gneisses suggest that upper-amphibolite facies metamorphism, partial melting, and fabric development are all closely linked in time.

Sample KX14-19: This final sample is a large (>20cm) subangular block of homogeneous, non-deformed biotite granite, exhibiting minor chalky alteration and sericitization of plagioclase. From the abundant euhedral prismatic, colorless zircons containing common biotite, quartz, feldspar and apatite inclusions, three abraded grains yielded near-concordant isotopic ratios,

defining a linear discordia with an upper intercept date of 2.724 ± 0.002 Ga (MSWD = 0.78) (Figure 5), essentially identical to the weighted mean $^{207}\text{Pb}/^{206}\text{Pb}$ date. This date is interpreted as the crystallization age of this non-deformed granite and is essentially identical to a similar non-deformed granite in the Marydale terrane (2.718 ± 0.008 Ga; McCourt and Armstrong, 2000), a granite encountered in borehole near Welkom (2.727 ± 0.005 Ga; Robb et al., 1992), and the post-Pongola granites of the southeastern shield (e.g. Kwetta granite, 2.722 ± 0.006 Ga; Maphalala and Kroner, 1993).

4.2 Sm-Nd isotopes

Sm/Nd and Nd isotopic compositions were measured for five of the Kimberley granite and gneiss samples examine for their U-Pb zircon systematics. Present day ϵ_{Nd} values range from -2.4 to -40.9 , with $^{147}\text{Sm}/^{144}\text{Nd}$ ratios of 0.196 to 0.089; calculated values of ϵ_{Nd} at 2.93 Ga, the time of metamorphic recrystallization and/or melt crystallization for the gneissic and pegmatitic rocks, range from -2.24 to 1.28, and the initial ϵ_{Nd} of the 2.724 Ga Kimberley granite is -3.25 . These predominantly negative values suggest a prior crustal residence for the gneisses and the source of the younger granite, quantified by the t_{DM} model ages for these rocks which range from 3.17 to 3.31. These Mesoarchean model ages are consistent with the zircon protolith and inheritance ages measured in the Kimberley gneisses.

5. Discussion

5.1 Antiquity of the western domain

As noted in Section 4.2, the *ca* 3.3 to 3.2 Ga Nd isotopic depleted mantle model ages for the Kimberley gneisses and granitoids are consistent with the oldest protolith and zircon inheritance ages for the same granitoids. The *ca* 3.25 Ga ages for the oldest zircons from the Kimberley gneisses may be combined with published ages for zircons from gneisses and granitoids in the Amalia, Kraaipan, and Marydale regions to develop an idea of the antiquity of at least portions of the crust of the western domain. Inherited zircons in the recently dated 2.85 to 2.72 Ga Draghoender and Skalkeput granites of the Marydale inlier (Mccourt and Armstrong, in prep) have been found as old as 3.17 Ga. Zircon inheritance in 2.94 Ga or older tonalites of the Amalia inlier ranges up to 3.18 Ga (Poujol et al., 2000). In the northern Kraaipan belts, preliminary examination of the oldest tonalitic-trondhjemitic gneisses have documented zircons as old as 3.16 Ga (Anhaeusser and Walraven, 1999). While no conclusive statement regarding the absolute antiquity of the crust of the western domain may be made on the basis of this sparse data, there is an apparent lack in the western domain of the >3.3 Ga crustal components which are apparent

throughout the eastern Kaapvaal shield, to the east of the Colesberg lineament. This is taken as very preliminary evidence that the western domain may comprise a crustal block with a distinct origin and evolutionary history from that of the eastern shield. Alternatively, the western domain may represent a crustal block originally coherent with the eastern Kaapvaal shield prior to *ca* 3.1 Ga, which was subsequently partially rifted away during extension associated with *ca* 3.08 to 3.07 Ga Dominion volcanism, and then rejoined with the shield during the *ca* 2.93 Ga convergence documented in Section 5.2. Further U-Pb geochronological and Nd and Pb isotopic studies of the basement of both western and eastern domains are warranted in order to confirm a contrasting crustal evolution of these blocks, and more clearly delineate whether structures like the Colesberg magnetic anomaly represent terrane boundaries and fundamental epicratonic suture zones.

5.2 Accretion of the western domain

While Mesoarchean components make up some proportion of the crust of the western domain, the geochronological data presented in Section 4.1, combined with the results of other geochronological studies summarized in Section 2.3, suggest that continental magmatic arc generation, convergence, and subsequent collisional suturing of the western domain with the eastern shield occurred in the Neoproterozoic. The most compelling datum in this regard is the new 2.940 ± 0.002 Ga age for the rhyolite tuff of the Khunwana Chert Formation of the Kraaipan Group, which demonstrates the age of mafic to felsic volcanism and coeval marine chemical and clastic sedimentation which formed the presently preserved Kraaipan greenstone belts. In this interpretation of the age of the Kraaipan Group, we diverge significantly from previous workers, who have inferred a Mesoarchean age for these supracrustals (Anhaeusser, 1991; Robb and Meyer, 1995; Anhaeusser and Walraven, 1999). While amphibolitic enclaves in the Mesoarchean tonalitic gneisses exposed in the vicinity of Kraaipan and Amalia have traditionally been viewed as metamorphosed and disrupted Kraaipan Group supracrustals, this interpretation is clearly equivocal and cannot be demonstrated on geochronological grounds; these amphibolite enclaves are more likely older rafted fragments of mafic material unrelated to the Kraaipan Group lithologies. Anhaeusser and Walraven (1999) analyzed whole rock samples of banded iron formation from the Gold Ridge and Ferndale Formations of the Kraaipan Group and obtained a linear array in the Pb evolution diagram, and interpreted the slope of this array and corresponding age of *ca* 3.41 Ga as representing the deposition age of the sediments. While a discussion of the pitfalls of geochronometry utilizing whole rock Pb isotopic systematics is beyond the scope of this paper, we consider it more likely that the data presented by Anhaeusser and Walraven represent a mixing relationship between a juvenile mantle-derived volcanogenic Pb component and older crustal basement-derived Pb; the slope of the mixing line thus holds no reliable geochronological information. The only U-Pb zircon data for the Kraaipan Group, noted in Section 2.3, consists of

four conventional analyses of “extremely small and of poor quality” zircon from felsic schists of the Gold Ridge and Ferndale Formations. These grains are considered to be of a likely detrital nature considering their description and considerable scatter in $^{207}\text{Pb}/^{206}\text{Pb}$ dates from 3.02 to 3.16 Ga. While these zircons do not precisely date the Kraaipan Group, the detrital constraint on the maximum age of deposition of ca 3.02 Ga is consistent with our results.

From the new age constraint on Kraaipan Group deposition and its relative synchronicity with voluminous calc-alkaline plutonism (Poujol et al., 2000), we infer the existence of an active Kraaipan arc, and complementary intra-arc or back-arc basins, situated between the western domain crustal block and the eastern shield at ca 2.94 Ga. There is suggestive evidence that this arc complex was developed on older continental basement, including the aforementioned Pb isotopic systematics of banded iron formation, and the >3.08 Ga detrital zircons in clastic sediments of the Kraaipan Group. A continental setting for the arc is also suggested by the presence of apparently syn-volcanic 2.94 Ga tonalite dikes in the nearby Amalia belt, which contain inherited zircons >3.1 Ga and are hosted in >3.0 Ga trondhjemitic gneisses. These abundant highly deformed Mesoarchean trondhjemitic gneisses observed throughout the Kraaipan and Amalia regions may be the basement upon which this arc was built, although a paucity of geochronological data and the severe shortening in the belts hampers a more detailed understanding of these relationships.

These admittedly poorly preserved Kraaipan volcanic arc and inter-arc basin sequences were obviously severely disrupted and deformed subsequent to their deposition ca 2.94 Ga. Although details of the deformational history in the western domain are lacking, there is a clear and pervasive N-S fabric to the domain, evident both in the low grade greenstone-banded iron formation remnants and in the higher grade gneisses proximal to these belts. This same regional tectonic fabric is also mapped in the basement gneisses in the Kimberley diamond mines (Drennan et al., 1990; H. Grutter, pers comm.). The first geochronological data bearing on the timing of development of this fabric comes from the 2.932 to 2.927 Ga metamorphic and partial melt-phase zircon ages for amphibolite and anatexite layers in the foliated banded gneisses at Kimberley. These zircons demonstrably grew during upper amphibolite-facies metamorphism, under the same P-T conditions which generated the minerals defining the fabric of these gneisses. Similarly, the 2.926 Ga zircons in the moderately deformed discordant pegmatites in the Kimberley gneisses indicate that high grade metamorphism, melting, and deformation were essentially synchronous.

A constraint on the timing of major compressive deformation in the western domain is indicated by the fairly consistent ca 2.915 Ga ages for the oldest granodioritic plutons intruding the Kraaipan belt (Poujol et al., 1999). Although a clear description of the tectonic fabric in these granitoids is not available in the literature, our own field observations suggest that these plutons are syn- to late-tectonic with respect to compressional deformation in the belt. A more conservative

minimum age bracket on the compressional deformation is given by the 2.880 Ga age for potassic granitoids like the Schweizer-Reneke adamellite, which clearly cross-cut the deformation fabrics in the Kraaipan and Amalia belts. The intrusion of these granitoids effectively constrains the timing of suturing of the western domain onto the eastern Kaapvaal shield.

To summarize, the broad picture emerging from the new geochronology of the western domain is one of subduction and arc genesis *ca* 2.94 Ga, which culminated in convergence and collision of the western and eastern domains as early as *ca* 2.93 Ga. Continued convergence over the next 40-50 Ma was responsible for variable exhumation of the western domain, and crustal melting to produce high-level granitoids as young as 2.880 Ga. The question of subduction polarity during the convergence of the western and eastern blocks must be addressed. There are dramatic differences in the manifestation of convergence between the two crustal blocks. Whereas *ca* 2.94 to 2.88 Ga magmatism is voluminous in the crust of the western domain, it is completely lacking in the eastern shield (Robb et al., 1992). Similarly, whereas pervasive deformation and mid-crustal high grade metamorphism are observed in the western domain, these characteristics are not observed east of the Colesberg anomaly. Finally, a dramatic contrast exists in the degree of exhumation across the Colesberg anomaly, with mid-crustal levels exposed in the western domain (Drennan et al., 1990), compared with contemporaneous subsidence and deposition in the West Rand basin on the eastern shield. These characteristics are interpreted as most consistent with the eastern Kaapvaal shield being the lower plate to subduction beneath the western domain upper plate. Implications of this geometry are explored in following sections.

5.3 Neoproterozoic assembly of the Kaapvaal Craton

Geological and geochronological data summarized in Section 2.1 suggest that the eastern Kaapvaal shield region was a coherent and stable entity following *ca* 3.2 Ga assembly through convergent margin tectonics (de Wit et al., 1992; de Ronde and Kamo, 2000). In large part this coherent state is inferred from the very similar subsequent 200 Ma of tectonomagmatic evolution correlated across all examined windows into the basement of the eastern Kaapvaal shield. Following *ca* 3.2 Ga assembly, a 100 Ma hiatus in tectonomagmatic activity was ended by shield-wide crustal melting and voluminous granitoid plutonism at *ca* 3.10 to 3.08 Ga. This plutonism, in a transtensional stress regime, was an apparent precursor to deposition and eruption of the volcano-sedimentary Dominion Group in a continental rift setting along the western ramparts of the shield. The ensuing *ca* 100 Ma hiatus in the geological record of the Kaapvaal shield, following Dominion Group deposition, is ended by convergent margin activity on the northern and western ramparts of the shield, which led to assembly of the presently recognized Kaapvaal craton. In order to develop the first detailed synthesized model for this Neoproterozoic assembly, the new data for the western domain presented in Section 4 have been combined with published geological and

geochronological data for the various granite-greenstone belts of the northern domain. Visualization of the timing relationships of volcanism, plutonism, metamorphism and deformation between these different domains is aided by Figure 7, which plots the U-Pb zircon geochronological constraints summarized in Sections 2 and 4 together with bracketed deformation phases in each belt.

The earliest record of Neoproterozoic convergence is present in the Murchison greenstone belt, where N-over-S D1 compressional deformation is bracketed by felsic volcanism and post-deformational plutonism to between 2.97 and 2.90 Ga (Figures 2 and 7). Similar magmatic activity is present in the Pietersburg and Giyani greenstone belts and in the intervening gneissic terrain suggesting the possibility that these belts were developed on the ramparts of a coherent Murchison-Pietersburg-Giyani terrain. Although all three greenstone belts contain similar-aged felsic magmatism, the N-over-S D1 compressional deformation phase is only pervasive in the Murchison belt. On this basis it is hypothesized that this *ca* 2.94 Ga D1 deformation in the Murchison belt is related to collision of the southern margin of this terrain with the northern margin of the Kaapvaal shield.

The synthesis of data for the western domain indicate that arc formation, convergence and compressional deformation related to suturing of the western domain onto the eastern Kaapvaal shield also occurred between 2.94 and 2.91 Ga (Figures 2 and 7). The first episodes of convergent margin tectonics and terrane accretion along the northern and western margins of the Kaapvaal shield were thus apparently near-synchronous. However, the styles and subduction polarity of this accretion may have been significantly different. The presence of *ca* 2.88 to 2.85 Ga granites across the western domain suggests that it was a large coherent block of continental lithosphere prior to its accretion with the eastern shield. The Kaapvaal shield was likely the lower plate to subduction along its western margin, and the resulting collision between the shield and the western domain has the hallmarks of a continent-continent collision. In contrast, the Murchison-Pietersburg-Giyani terrane appears to have been a smaller arc segment, and while subduction polarity is not well defined, could have dipped to the south beneath the Kaapvaal shield. While collision of the western domain with the Kaapvaal shield probably terminated subduction along the western margin (although convergence, crustal thickening and resultant orogenic collapse continued), the northern margin of the Kaapvaal apparently remained an accretionary boundary as evidenced by subsequent deformational events along the TML through the culmination of the Limpopo orogeny at *ca* 2.6 Ga.

With regard to the continued evolution of the northern margin of the growing Kaapvaal craton, a younger episode of terrane juxtaposition is evidenced in the northern domain as the tentatively correlated compressional D2 deformation in the Pietersburg, Giyani, and Murchison belts. As discussed in Section 2.2 and illustrated in Figure 7, this deformation is conservatively

bracketed between 2.900 and 2.777 Ga. This deformation is most likely related to the accretion of a terrane or set of terranes making up the block of crust north of the Pietersburg and Giyani greenstone belts and south of the Palala shear zone. Geochronological data for this terrane is sparse, but includes both ancient Mesoarchean basement gneisses as well as voluminous leucocratic tonalitic gneisses dated at *ca* 2.81 Ga (Kroner et al., 2000). Whether the latter definitively represents plutonism resulting from accretion of these northernmost domains to the Kaapvaal craton awaits further geological and geochronological studies.

We interpret deformation directly correlative with that in the Limpopo Belt *sensu stricto* (van Reenen et al., 1992) as restricted to the final D3 phase of deformation observed in all of the northern domain greenstone belts (Figure 7). This deformation phase of oblique-slip thrusting must be younger than the 2.740 Ga intrusive age of the Rooiwater Complex, which was uplifted and juxtaposed into the Murchison belt along a D3 thrust, and also younger than the 2.777 Ga Turfloop granite of the Pietersburg belt, which is cut by D3 shear zones. It is at the northern margin of the Giyani belt that D3 is most clearly related to the “retrocharriage” back-thrusting of the Southern Marginal Zone of the Limpopo Belt over the northern domain of the Kaapvaal craton along the Hout River shear zone (McCourt and van Reenen, 1992; Roering et al., 1992; de Wit et al., 1992). The age of D3 deformation is best constrained in the SMZ by the 2.671 to 2.664 Ga syn- to post-D3 intrusion of the charnoenderbites and granodiorites of the Matok Complex (Barton et al., 1992). The subsequent evolution of the northern margin of the Kaapvaal Craton becomes intimately linked with that of the Central Zone of the Limpopo Belt and the Zimbabwe Craton, and is beyond the scope of this paper, however it is pertinent to note that the major episodes of high grade metamorphism, deformation and syn-tectonic plutonism in the Central and Northern Marginal Zones of Limpopo belt are considerably younger (<2.60 Ga; Jaekel et al., 1997; McCourt and Armstrong, 1998; Frei et al., 1999) than D3 transpressional uplift in the SMZ. This timing must be considered when examining the tectonic stresses driving cratonic basin subsidence.

5.4 Tectonics of Witwatersrand Supergroup deposition

The improved framework of geochronological constraints for convergence of the northern and western domains is of substantial value for evaluating models for subsidence and deposition of the Witwatersrand basin. As noted in Section 5.3, a ~100 Ma hiatus occurs in the geologic record between deposition of the rift-related Dominion Group, and the initiation of further subsidence on the Kaapvaal shield to produce the lower West Rand Group of the Witwatersrand Supergroup, beginning at *ca* 2.97 Ga (Robb et al., 1990). This significant hiatus precludes suggestions that Witwatersrand basin development was a thermal subsidence response to Dominion rifting (Coward et al., 1995; Robb et al., 1997). As an alternative, West Rand subsidence has been attributed to marginal loading of the craton along its northwestern edge in the manner of a foreland basin (Burke

et al., 1986; Winter, 1987). Detailed sedimentological and stratigraphic characteristics of the Witwatersrand basin sediments supportive of a foreland basin model are eloquently summarized by those authors, including: pronounced asymmetric deepening of the basin in the NW, basinward-propagating synsedimentary thrust faulting into the NW foredeep, basinward (SE) migration of the depositional axis, and basin filling (in the Central Rand) by prograding deltaic fan complexes, again from the NW. All of these characters are consistent with sediment derivation from uplifts to the north and west of the basin.

When compared with the geochronological constraints on Neoproterozoic assembly of the craton, Figure 7 illustrates that West Rand basin subsidence between 2.97 and 2.90 Ga is approximately coeval with western and northern domain convergence with the Kaapvaal shield and collisional D1 deformation. In this manner, the foreland basin model for West Rand basin subsidence does possess a viable tectonic loading mechanism, consistent with the geometry and sedimentology of the basin. Lower West Rand Group (Hospital Hill Subgroup) marine sedimentation reflects the rapid subsidence of a low-standing, peneplained, stable cratonic shield early in the evolution of the northern and western collisional margins (Burke et al., 1986; Stanistreet and McCarthy, 1991). During Upper West Rand sedimentation (Government, Jeppestown Subgroups), the development of southeast verging thrust faults along the northern and western margins of the basin proceeded as marginal compressional stresses from collision-generated crustal uplifts to the north and west propagated basinward (Coward et al., 1995).

Central Rand Group deposition between 2.89 and 2.82 Ga is also clearly synchronous with continued compressional tectonics along the northern and western margins. The chronological correlation between the D2 deformation phase and syntectonic deposition of Central Rand correlatives (Uitkyk Formation) in the Pietersburg greenstone belt was pointed out by de Wit et al. (1992), and is bracketed between 2.90 and 2.77 Ga. The data synthesized in Figure 7 show that the same deformation phase may be correlated throughout the northern domain, and as hypothesized in Section 5.3, is the likely result of further terrane accretion to the north the Pietersburg and Giyani belts. This continued convergence on the northern margin of the Kaapvaal shield was a likely tectonic driver for continued subsidence and syndeformational deposition of the Central Rand Group. At the same time, synsedimentary east-vergent thrusting on the western margin of the Central Rand basin has also been demonstrated (Winter, 1987), which suggests that uplift in the western domain after initial ~2.93 Ga collision with the eastern shield continued to influence this margin. The pulse of granitoid plutonism in the western domain at *ca* 2.88 Ga may be recording decompression melting related to this uplift.

The accumulating high-precision geochronology of Neoproterozoic assembly of the northern and western regions of the Kaapvaal craton appears to broadly support previous foreland basin models for the Witwatersrand Supergroup. The geochronological synthesis presented in this

work, however, suggest several important refinements of earlier models. The primary refinement involves the fundamental importance of western domain convergence for development of the basin. While nearly all reviews of the tectonosedimentary evolution of the Witwatersrand Basin acknowledge significant east-vergent syn-depositional thrusting and westerly sediment derivation along the western margin of the basin (e.g. Winter, 1987; Coward et al., 1995), these same papers consistently portray an essentially north-to-south two-dimensional model of Witwatersrand basin subsidence as a flexural “back-arc” or “retro-arc” type response developed cratonward of an Andean-type continental arc (Figure 8a), with southward subduction developed beneath the Kaapvaal shield, attributed to the evolving Kaapvaal-Limpopo orogenic system (Burke et al., 1986; Stanistreet and McCarthy, 1991; de Wit et al., 1992; Robb and Meyer, 1995; Catuneanu, 2001). This geometry may be appropriate to the accretionary events playing out on the northern margin of the shield, and likely did drive a component of the subsidence of the Witwatersrand Basin. But such a restricted view of the Witwatersrand system must be discarded in the face of the demonstrated continent-continent style collision which was occurring along the western margin of the Kaapvaal shield at *ca* 2.9 Ga, synchronous with basin subsidence and deposition.

The observations summarized at the end of Section 5.2 point toward a geometry of west-dipping subduction of the Kaapvaal shield beneath the western domain during convergence and collision. Figure 8b presents three panels illustrating the evolution of this western convergent margin from initial convergence prior to 2.94 Ga, through collision at 2.93 to 2.91 Ga, and continued post-collisional convergence and suturing after 2.90 Ga. This type of tectonic scenario incorporates the various elements preserved in the geologic record of the western domain, including volcanic arc and forearc genesis (Kraaipan belt plutonics and supracrustals), exhumation of middle crustal high grade rocks in the upper plate (Kimberley gneisses), subsequent foreshortening of the forearc and arc along a subvertical suture zone (Colesberg lineament), and intrusion of late-collisional decompression melt-related granites (Schweizer-Reneke granites). In this tectonic regime, the Witwatersrand basin represents a peripheral or pericratonic foreland basin (Dickinson, 1974), analogous to the Cenozoic Himalayan foredeep, rather than a Cordilleran-style retroarc basin.

The influence of this western continental collision on the shape, filling, and deformation of the basin was profound. The patterns of foredeep migration and syn-depositional thrusting in the upper West Rand and Central Rand demonstrate the importance of E-W compression and loading related to this western orogeny (Burke et al., 1986; Winter, 1987). The western margin of the Witwatersrand basin is essentially defined by the suture zone (Colesberg lineament) between the western domain and the Kaapvaal shield (Figure 1), a geometry predicted by the peripheral foredeep model. As a consequence, this western collision orogen was more proximal to the Witwatersrand foredeep and was arguably an equal or greater volumetric source area for the basin

strata relative to the accretionary orogens along the northern shield margin. Paleocurrent data demonstrate the importance of sediment provenance from a western uplift (Coward et al., 1995; Robb and Meyer, 1995), in keeping with mid-crustal exhumation of much of the western domain during and following collision. The potential of a western “hinterland” as a source for much of the gold and uranium of the Central Rand was first intimated by Robb et al. (1992), although the operative tectonics in the western domain were not understood. In fact, the oft-quoted source area problem for the Witwatersrand gold and uranium deposits (Robb and Meyer, 1990) may be substantially solved by a recognition and further quantification of the amount of crust refined through magmatic differentiation, exhumed, and eroded during this western continental collisional orogen.

A secondary refinement of existing models for Witwatersrand basin development involves the relative importance of the Limpopo Orogen for its derivation. To some degree this issue is one of semantics, involving the strict definition of an orogenic cycle, and what geological features should be taken to characterize the Limpopo orogenic belt. In this respect, a consensus exists that the Limpopo Belt may be divided into three geographic regions comprising the Southern Marginal Zone, Central Zone and Northern Marginal Zone (van Reenen et al., 1992). As emphasized in Section 5.3, overthrusting of the Southern Marginal Zone over the Kaapvaal craton is constrained to have occurred at ca 2.67 Ga and is among the earliest phases of deformation and metamorphism in the Limpopo Belt. From Figure 7, it is obvious that even this earliest ca. 2.67 orogenic activity, while manifested throughout the northern domain of the Kaapvaal, significantly post-dates deposition of all of the Witwatersrand strata by as much as 150 m.y. It follows that attribution of Witwatersrand deposition to flexure associated with the “Limpopo Orogeny” fails, lacking the necessary direct geochronological correlations to metamorphism, deformation and structures of the stringently defined Limpopo belt.

More accurately, Witwatersrand deposition is a response to accretionary tectonics operative on the northern margin of the Kaapvaal shield between 2.97 and 2.78 Ga, involving the accretion of a set of continental terranes north of the Murchison belt, and south of the Palala shear zone. No geologic or geochronological evidence points to an active role for the exotic Limpopo Central Zone terrane (Barton et al., 1990), or the Zimbabwe craton. The apparent culmination of this accretion was the generation and intrusion of large granitic batholiths (Gaborone, Turfloop granites) along the Thabazimbi-Murchison lineament at 2.78 Ga. This redefinition of the northern tectonic driver for Witwatersrand basin subsidence is more than just semantic refinement of language. Compared to the rocks of the central Limpopo belt, the granite-greenstone terranes south of the Palala shear zone— whether at granulite grade in the Southern Marginal Zone or at greenschist to amphibolite grade south of the Hout River shear zone— have been relatively neglected with regard to detailed structural and modern geochronological studies. Yet it is increasingly apparent that this crustal

block holds the pertinent record of Neoproterozoic tectonic evolution responsible for the generation of economically important mineral placers in the Witwatersrand basin, and should be a focus of further analysis.

5.5 Implications for the stabilization of lithospheric mantle

It has been previously noted that as the database of whole rock mantle peridotite Re-Os model ages for the Kaapvaal craton has grown, a strong peak in the distribution of ages has resolved itself at approximately 2.8 to 2.9 Ga (Carlson et al., 1999). This median age is reflected both in Re-depletion model ages (T_{RD}), which are considered to represent minimum ages for a single-stage depletion of mantle peridotite in a basaltic component, and mantle model ages (T_{MA}), which represent maximum ages for a single stage depletion, in the light of possible subsequent Re addition. That these two model ages closely approach one another has been interpreted to indicate that subsequent Re-addition to the mantle xenoliths analyzed has been negligible, that the measured Re/Os ratios of the whole rocks are robust, and thus the T_{MA} ages are interpretable in terms of the time of primary mantle depletion (Carlson et al., 1999). The coherence of the peridotite Re-Os data set is particularly strong when the data is filtered to include only those samples derived from kimberlites in the western domain of the Kaapvaal craton, namely the Kimberley and Newlands pipes; resulting median model ages of $T_{RD} = 2.70 \pm 0.26$ and $T_{MA} = 2.86 \pm 0.29$ (n=17) are obtained (Figure 9).

These essentially indistinguishable model ages are obviously significantly younger than the *ca* 3.7 to 3.2 Ga crustal protolith ages across most of the eastern Kaapvaal shield. They are also younger than the 3.2 Ga compressional assembly of the Kaapvaal shield, best recorded in the rocks of the Barberton greenstone belt (Kamo and Davis, 1994; de Ronde and Kamo, 2000). They are also arguably younger than the *ca* 3.1 Ga crustal melting event associated with rifting, basin subsidence, deposition and eruption of the volcano-sedimentary Dominion Group on the Kaapvaal shield, which was recently purported to herald the birth of the Kaapvaal tectosphere (Moser et al., 2001). This apparent decoupling of the crust and mantle lithospheric records has prompted much discussion regarding the processes involved in establishing the architecture of Archean cratons, and taken as support for various models proposing the imbrication of younger oceanic lithospheric slabs beneath an allochthonous older crust (Helmstaedt and Schulze, 1989), or underplating of younger depleted and buoyant mantle beneath older crust via diapirs (Oxburgh and Parmentier, 1978) or plumes (Herzberg, 1993; Griffin et al., 1999).

As was emphasized in the introduction, these previous comparisons between the records of crust versus mantle lithosphere formation have been made between disparate data sets. On the one hand the framework of crustal evolution is biased toward that of the eastern Kaapvaal shield, while

the majority of mantle xenolith data are drawn from kimberlites in the western domain. One-to-one comparison of crust and mantle lithosphere is now possible with the new synthesis of crustal geochronological data for the western craton presented in Sections 5.1 and 5.2; we suggest that this more robust comparison resolves the apparent discrepancies between mantle and crustal ages.

It is first noted that there are in fact, a minority of >3.0 Ga Re-Os model ages for western domain peridotites (Menzies et al., 1999), whose antiquity are in line with silicate diamond inclusion Nd and Sr model ages of *ca* 3.3 Ga (Richardson et al., 1984). The prior discussion of the antiquity of crust in the western domain of the Kaapvaal similarly documented the consistent presence of crustal components as old as 3.25 Ga. The similarity of these oldest crust and mantle ages suggests that some volume of mantle lithosphere, formed at the same time and may have been coupled to the crust of western domain in the Mesoarchean. This coupling supports the notion that the western domain was a discrete continental entity with a diamondiferous mantle lithosphere prior to 3.0 Ga.

The striking new observation, however, is the strong correlation between the ~2.9 Ga median of the Re-Os T_{MA} model ages and the *ca* 2.9 Ga timing of subduction-convergence and suturing of the western domain to the eastern Kaapvaal shield as delineated by the crustal geochronology summarized in section 5.2 (Figure 9). On the basis of patterns of magmatism, deformation and basin subsidence, it has already been inferred that convergence was accommodated by subduction beneath the western domain, which was operative at *ca* 2.94 Ga, the age of the upper Kraaipan Group arc supracrustals, and for perhaps tens of millions of years prior. Following modern analogues, this subduction was accommodated beneath an overlying mantle wedge, which was the site of chemical depletion through partial melting associated with corner flow-driven adiabatic decompression, and flux melting above the dehydrating slab (Tatsumi et al., 1983; Davies and Stevenson, 1992; Furukawa, 1993; Stolper and Newman, 1994; Kincaid and Sacks, 1997). We note that in modern regimes of mantle melting, the subduction setting is unique with regard to the potential for high degrees of melt extraction and chemical depletion of mantle peridotite (Nye and Reid, 1986). We suggest that this 2.9 Ga subduction zone was a suitable site for the chemical depletion of mantle peridotite necessary to establish the refractory compositional and isotopic characteristics of at least some proportion of the western domain lithospheric mantle. However, we also envision that the depletion and re-enrichment processes necessary to produce the characteristics of the full spectrum of Kaapvaal cratonic mantle xenoliths were likely multi-stage in nature. An integral aspect of *ca* 2.9 Ga subduction zone processing may have been the further depletion and/or re-enrichment of pre-existing Mesoarchean lithospheric mantle stabilized with the older crust of the western block at *ca* 3.2 Ga. It must also be emphasized that preservation and continued isolation of remnants of this pre-existing Mesoarchean mantle keel, likely in the hinterland of the continental arc, are necessitated by the presence of >3.0 Ga diamonds, which

tentatively argues against shallow subduction commonly called upon in Archean plate tectonics (Abbott and Hoffman, 1984; Abbott, 1991).

Further correlations with mantle geochronological data support this actualistic subduction model for cratonic lithosphere stabilization. Re-Os isochron systematics of whole rock eclogite samples from the Roberts Victor, Bellsbank, Blaaubosch, and Newlands kimberlites, particularly diamondiferous samples, are consistent with a *ca* 2.9 Ga age of formation of their basaltic precursor (Menzies et al., 1998; Shirey et al., 1998, 2001). Some of the most compelling geochronological correlations come from analysis of sulfide inclusions in eclogite paragenesis diamonds. Pearson et al. (1998) first measured 2.7 to 2.9 Ga Re-Os model ages for eclogitic sulfide inclusions in diamonds from the Koffiefontein kimberlite of the western domain. More recently, Richardson et al. (2001) has demonstrated a 2.88 ± 0.06 Ga Re-Os isochron relationship for suites of individual sulfide diamond inclusions from Kimberley, which are consistent with 2.8 to 3.0 Ga model ages of single highly radiogenic sulfides. The authors further demonstrate that these eclogitic inclusions come from a protolith with an elevated initial Os isotopic composition consistent with generation by radiogenic ingrowth in a basalt evolving with an average MORB Re/Os ratio for 10-100 Ma. These results provide some of the strongest evidence to date that such diamonds grew in eclogite-facies oceanic lithosphere subducted and emplaced beneath the western domain at *ca* 2.9 Ga.

To conclude, these geochronological correlations revitalize earlier inferences of substantial coupling between the record of melt depletion in the mantle lithosphere and the formation and evolution of the overlying crust (Walker et al., 1989; Pearson et al., 1995). Large scale lateral juxtapositions of allochthonous crust or mantle do not appear to be necessary to explain the geochronological systematics and lithospheric structure of the Kaapvaal craton. These data also lend compelling support to an actualistic model for the simultaneous depletion of the mantle and generation and refining of continental crust through subduction zone processes. Finally, we note that the continent-continent collisional tectonic scenario envisaged for amalgamation of the western domain with the Kaapvaal shield must have involved significant advective thickening of the lithosphere, a mechanism long championed by Jordan (1978, 1988) for establishing the uniquely balanced isopycnal state of the continental tectosphere.

6. Conclusions

New U-Pb zircon geochronological data for a volcanic tuff of the Kraaipan Group, and for high-grade gneisses of the basement complex subcropping in the vicinity of Kimberley, South Africa, suggest that the crustal block comprising the western domain of the Kaapvaal Craton was juxtaposed with the eastern Kaapvaal shield by subduction convergence and continental collision between 2940 and 2880 Ma. Kraaipan Group supracrustals along the edge of the N-S suture

between the western domain and eastern shield are the attenuated remnants of volcanic arc and fore-arc and inter-arc basin sequences developed during this Neoproterozoic convergence, while the presently exposed plutonic and metamorphic rocks of the western domain represent the exhumed roots of a continental arc which was the upper plate to convergence and eventual collision with the Kaapvaal shield. Convergent margin tectonics along the western margin are also demonstrated to be coeval with similar activity along the northern margin of the Kaapvaal shield, as the granite-greenstone terranes of the northern domain were accreted. Within this three dimensional convergent tectonic framework, the polyphase Witwatersrand basin is reinterpreted as the superposition of both a pericratonic foreland basin to the western collision, analogous to the Cenozoic Himalayan foredeep, as well as a Cordilleran retroarc foreland basin to the northern accretionary margin.

Our new model for the tectonic evolution of the western domain of the Kaapvaal craton also allows for more meaningful comparisons with the petrologic, isotopic and geochronological dataset for the Kaapvaal mantle lithosphere, which is derived in large part from mantle xenoliths of the western domain. The timing of western domain subduction convergence with the Kaapvaal shield correlates with the strong peak in the Re-Os model age distributions of mantle peridotites, the apparent emplacement ages of many mantle eclogites, and eclogitic sulfide diamond inclusion ages, all of which cluster around 2.9 Ga. This multivariate geochronological correspondence supports significant crust-mantle coupling in the western domain of the Kaapvaal craton, and an actualistic model of subduction zone processing for the generation of continental lithosphere.

Acknowledgements— The authors wish to thank Dr. Tony Bloomer of the Kalahari Gold Ridge Mine for his insights into Kraaipan Belt geology, and Dr. Jock Robey for expediting studies of the Kimberley gneisses. Formulation of the ideas put forth in this manuscript was stimulated by many thoughtful discussions with colleagues at the Kaapvaal Craton workshops in South Africa, Botswana, and North America. This work was funded by a National Defense Science and Engineering Fellowship through the U.S. Army Research Office, grant DAAH049510560 to MDS, and by NSF Continental Dynamics Program grant EAR9526702 to SAB.

References

- Abbott, D., 1991. The case for accretion of the tectosphere by buoyant subduction. *Geophysical Research Letters* 18, 585-588.
- Abbott, D.A., Hoffman, S.E., 1984. Archean plate tectonics revisited- Part I: Heat flow, spreading rate, and the age of the subducting oceanic lithosphere, and their effects on the origin and evolution of the continents. *Tectonics* 2, 429-448.
- Anhaeusser, C.R., 1991. The Archean Kraaipan Group volcano-sedimentary rocks and associated granites and gneisses of the southwestern Transvaal, northwestern Cape Province and Bophuthatswana. Information Circular 244, Economic Geology Research Unit, University of Witwatersrand, Johannesburg, 45 p.
- Armstrong, R.A., Compston, W., de Wit, M.J., Williams, I.S., 1990. The stratigraphy of the 3.5-3.2 Ga Barberton Greenstone Belt revisited: a single zircon ion microprobe study. *Earth and Planetary Science Letters* 101, 90-106.

- Armstrong, R.A., Compston, W., Retief, E.A., Williams, I.S., Welke, H.J., 1991. Zircon ion microprobe studies bearing on the age and evolution of the Witwatersrand triad. *Precambrian Research* 53, 243-266.
- Barton, E.S., Compston, W., Williams, I.S., Bristow, J.W., Hallbauer, D.K., Smith, C.B., 1989. Provenance ages for the Witwatersrand Supergroup and the Ventersdorp Contact Reef: constraints from ion microprobe U-Pb ages of detrital zircons. *Economic Geology* 84, 2012-2019.
- Barton, J.M., Jr., Barton, E.S., Kroner, A., 1999. Age and isotopic evidence for the origin of the Archean granitoid intrusives of the Johannesburg Dome, South Africa. *Journal of African Earth Sciences* 28, 693-702.
- Barton, J.M., Jr., Blignaut, E., Salnikova, E.G., Kotov, A.B., 1995. The stratigraphical position of the Buffelsfontein Group based on field relationships and chemical and geochronological data. *South African Journal of Geology* 98, 386-392.
- Barton, J.M., Jr., Doig, R., Smith, B.C., Bohlender, F., van Reenen, D.D., 1992. Isotopic and REE characteristics of the intrusive charnoenderbite and enderbite geographically associated with the Matok Pluton, Limpopo Belt, southern Africa. *Precambrian Research* 55, 451-467.
- Barton, J.M., Jr., van Reenen, D.D., Roering, C., 1990. The significance of 300 Ma granulite-facies mafic dikes in the Central Zone of the Limpopo Belt, southern Africa. *Precambrian Research* 48, 299-308.
- Basalt Volcanism Study Project, 1981. *Basaltic Volcanism on the Terrestrial Planets*. Pergamon Press, New York, 1286 p.
- Beaumont, C., 1981. Foreland basins. *Geophysical Journal of the Royal Astronomical Society* 65, 291-329.
- Beukes, N.J., Cairncross, B., 1991. A lithostratigraphic sedimentological reference profile for the late Mozaan Group, Pongola Sequence: application to sequence stratigraphy and correlation with the Witwatersrand Supergroup. *South African Journal of Geology* 94, 44-69.
- Beukes, N.J., Nelson, J.P., 1995. Sea-level fluctuation and basin subsidence controls on the setting of auriferous paleoplacers in the Archean Witwatersrand Supergroup: a genetic sequence stratigraphic approach. *Ext. Abstr: Centennial Geocongress* 1, 860-863.
- Burke, K., Kidd, W.S.F., Kusky, T.M., 1986. Archean foreland basin tectonics in the Witwatersrand, South Africa. *Tectonics* 5, 439-456.
- Byerly, G.R., Kroner, A., Lowe, D.R., Todt, W., Walsh, M.M., 1996. Prolonged magmatism and time constraints for sediment deposition in the early Archean Barberton greenstone belt: evidence from the Upper Onverwacht and Fig Tree groups. *Precambrian Research* 78, 125-138.
- Carlson, R.W., Hunter, D.R., Barker, F., 1983. Sm-Nd age and isotopic systematics of the Bimodal Suite, Ancient Gneiss Complex, Swaziland. *Nature* 305, 701-704.
- Carlson, R.W., Pearson, D.G., Boyd, F.R., Shirey, S.B., Irvine, G., Menzies, A.H., Gurney, J.J., 1999. Re-Os systematics of lithospheric peridotites: implications for lithosphere formation and preservation. In: *The J.B.Dawson Volume: Proceedings of the 7th International Kimberlite Conference, Volume 1* Gurney, J.J., Gurney, J.L., Pascoe, M.D., Richardson, S.H. (Eds.), pp. 99-108. Red Roof Design, Cape Town, S.A..
- Catuneanu, O., 2001. Flexural partitioning of the Late Archean Witwatersrand foreland system, South Africa. *Sedimentary Geology* 141-142, 95-112.
- Cloetingh, S., 1988. Intraplate stresses: a new element in basin analysis. In: *New Perspectives in Basin Analysis*. Kleinspehn, K., Paola, C. (Eds.), pp. 205-230. Springer, New York.
- Compston, W., Kroner, A., 1988. Multiple zircon growth within early Archean tonalitic gneiss from the Ancient Gneiss Complex, Swaziland. *Earth and Planetary Science Letters* 87, 13-28.
- Corner, B., Durrheim, R.J., Nicolaysen, L.O., 1990. Relationships between the Vredefort structure and the Witwatersrand basin within the tectonic framework of the Kaapvaal craton as interpreted from regional gravity and aeromagnetic data. *Tectonophysics* 171, 49-61.
- Coward, M.P., Spencer, R.M., Spencer, C.E., 1995. Development of the Witwatersrand Basin, South Africa. In: *Early Precambrian Processes*. Coward, M.P., Ries, A.C. (Eds.), Geological Society Special Publication 95, Geological Society of London, London, 243-269.
- Davies, J.H., Stevenson, D.J., 1992. Physical model of source region of subduction zone volcanics. *Journal of Geophysical Research* 97, 2037-2070.
- de Ronde, C.E.J., Kamo, S.L., 2000. An Archean arc-arc collisional event: a short-lived (ca 3 Myr) episode, Weltevreden area, Barberton greenstone belt, South Africa. *Journal of African Earth Sciences* 30, 219-248.
- de Wit, M.J., Armstrong, R.A., Kamo, S.L., Erlank, A.J., 1993. Gold-bearing sediments in the Pietersburg Greenstone Belt: age equivalents of the Witwatersrand Supergroup sediments, South Africa. *Economic Geology* 88, 1242-1252.
- de Wit, M.J., Jones, M.G., Buchanan, D.L., 1992. The geology and tectonic evolution of the Pietersburg Greenstone Belt, South Africa. *Precambrian Research* 55, 123-153.
- de Wit, M.J., Roering, C., Hart, R.J., Armstrong, R.A., de Ronde, C.E.J., Green, R.W.E., Tredoux, M., Peberdy, E., Hart, R.A., 1992. Formation of an Archaean continent. *Nature* 357, 553-562.

- de Wit, M.J., van Reenen, D., Roering, C., 1992. Geologic observations across a tectono-metamorphic boundary in the Babangu area, Giyani (Sutherland) Greenstone Belt, South Africa. *Precambrian Research* 55, 111-122.
- Dickinson, W.R., 1974. Tectonics and sedimentation. In: *Tectonics and Sedimentation*. Dickinson, W.R. (Eds.), Special Publication 22, Society of Economic Paleontologists and Mineralogists, Tulsa, Oklahoma, 1-27.
- Drennan, G.R., Robb, L.J., Meyer, F.M., Armstrong, R.A., de Bruijn, H., 1990. The nature of the Archean basement in the hinterland of the Witwatersrand Basin: II. A crustal profile west of the Welkom Goldfield and comparisons with the Vredefort crustal profile. *South African Journal of Geology* 93, 41-53.
- Farrow, D.J., Harmer, R.E., Hunter D.R., Eglinton, B.M., 1990. Rb-Sr and Pb-Pb dating of the Anhalt leucotonalite, northern Natal. *South African Journal of Geology* 93, 696-701.
- Frei, R., Blenkinsop, T.G., Schonberg, R., 1999. Geochronology of the late Archean Razi and Chilimanzi suites of granites in Zimbabwe: implications for the late Archean tectonics of the Limpopo Belt and Zimbabwe Craton. *South African Journal of Geology* 102, 55-63.
- Fripp, R.E.P., van Nierop, D.A., Callow, M.J., Lilly, P.A., du Plessis, L.U., 1980. Deformation in part of the Archean Kaapvaal craton, South Africa. *Precambrian Research* 13, 241-251.
- Furukawa, Y., 1993. Magmatic processes under arcs and formation of the volcanic front. *Journal of Geophysical Research* 98, 8309-8319.
- Gibson, R.L., Armstrong, R.A., Reimold, W.U., 1997. The age and thermal evolution of the Vredefort impact structure: a single-grain U-Pb zircon study. *Geochimica et Cosmochimica Acta* 61, 1531-1540.
- Grand, S.P., 1987. Tomographic inversion for shear velocity beneath the North American plate. *Journal of Geophysical Research* 92, 14065-14090.
- Grand, S.P., van der Hilst, R.D., Widiyantoro, S., 1997. Global seismic tomography; a snapshot of convection in the Earth. *GSA Today* 7, 1-7.
- Griffin, W.L., Doyle, B.J., Ryan, C.G., Pearson, N.J., O'Reilly, S.Y., Davies, R., Kivi, K., van Achtebergh, E., Natapov, L.M., 1999. Layered mantle lithosphere in the Lac de Gras area, Slave Craton: composition, structure and origin. *Journal of Petrology* 40, 706-727.
- Gutzmer, J., Nhleko, N., Beukes, N.J., Pickard, A., Barley, M.E., 1999. Geochemistry and ion microprobe (SHRIMP) age of a quartz porphyry sill in the Mozaan Group of the Pongola Supergroup: implications for the Pongola and Witwatersrand Supergroups. *South African Journal of Geology* 102, 139-146.
- Hart, R., Moser, D., Andreoli, M., 1999. Archean age for the granulite facies metamorphism near the center of the Vredefort structure, South Africa. *Geology* 27, 1091-1094.
- Hegner, E., Kroner, A., Hunt, P., 1994. A precise U-Pb zircon age for the Archean Pongola Supergroup volcanics in Swaziland. *Journal of African Earth Sciences* 18, 339-341.
- Helmstaedt, H., Schulze, D.J., 1989. Southern African kimberlites and their mantle sample: implications for Archean tectonics and lithosphere evolution. In: *Kimberlites and Related Rocks Vol.1: Their Composition, Occurrence, Origin, and Emplacement* Ross, J. (Eds.), Geological Society of Australia Special Publication 14, Blackwell, Carlton, Australia, 358-368.
- Henderson, D.R., Long, L.E., Barton, J.M., Jr., 2000. Isotopic ages and chemical and isotopic compositions of the Archean Turfloop batholith, Pietersburg granite-greenstone terrane, Kaapvaal Craton, South Africa. *South African Journal of Geology* 103, 38-46.
- Herzberg, C.T., 1993. Lithosphere peridotites of the Kaapvaal craton. *Earth and Planetary Science Letters* 120, 13-29.
- Hunter, D.R., 1974. Crustal development in the Kaapvaal Craton, I. The Archean. *Precambrian Research* 1, 259-294.
- Hunter, D.R., Wilson, A.H., 1988. A continuous record of Archean evolution from 3.5 Ga to 2.6 Ga in Swaziland and northern Natal. *South African Journal of Geology* 91, 57-74.
- Jackson, M.C., 1992. A review of the Late Archean volcano-sedimentary Dominion Group and implications for the tectonic setting of the Witwatersrand Supergroup, South Africa. *Journal of African Earth Sciences* 15, 169-186.
- Jaekel, P., Kroner, A., Kamo, S.L., Brandl, G., Wendt, J.I., 1997. Late Archean to early Proterozoic granitoid magmatism and high-grade metamorphism in the central Limpopo belt, South Africa. *Journal of the Geological Society of London* 154, 25-44.
- James, D.E., Fouch, M.J., VanDecar, J.C., van der Lee, S., Kaapvaal Seismic Group, 2001. Tectospheric structure beneath southern Africa. *Geophysical Research Letters* 28, 2485-2488.
- Jordan, T.H., 1978. Composition and development of the continental tectosphere. *Nature* 274, 544-548.
- Jordan, T.H., 1988. Structure and formation of the continental tectosphere. In: Menzies, M.A., Cox, K.G. (eds.), *Oceanic and Continental Lithosphere: Similarities and Differences*. *Journal of Petrology Special Issue*, 11-37.
- Kamo, S.L., Davis, D.W., 1994. Reassessment of Archean crustal development in the Barberton Mountain Land, South Africa, based on U-Pb dating. *Tectonics* 13, 167-192.

- Kamo, S.L., Reimold, W.U., Krogh, T.E., Colliston, W.P., 1996. A 2.023 Ga age for the Vredefort impact event and a first report of shock metamorphosed zircons in pseudotachylitic breccias and Granophyre. *Earth and Planetary Science Letters* 144, 369-387.
- Kincaid, C., Sacks, I.S., 1997. Thermal and dynamical evolution of the upper mantle in subduction zones. *Journal of Geophysical Research* 102, 12295-12315.
- Kroner, A., Compston, W., Williams, I.S., 1989. Growth of early Archean crust in the Ancient Gneiss Complex of Swaziland as revealed by single zircon dating. *Tectonophysics* 161, 271-298.
- Kroner, A., Hegner, E., Wendt, J.I., Byerly, G.R., 1993. The oldest part of the Barberton granitoid-greenstone terrain, South Africa: evidence for crust formation between 3.5 and 3.7 Ga. *Precambrian Research* 78, 105-124.
- Kroner, A., Jaeckel, P., Brandl, G., 2000. Single zircon ages for felsic to intermediate rocks from the Pietersburg and Giyani greenstone belts and bordering granitoid orthogneisses, northern Kaapvaal Craton, South Africa. *Journal of African Earth Sciences* 30, 773-793.
- Kroner, A., Jaeckel, P., Brandl, G., Nemchin, A.A., Pidgeon, R.T., 1998. Evolution of the northeastern Kaapvaal craton and the central Limpopo belt, South Africa, based on single-zircon ages (extended abstract). *Geologie en Mijnbouw* 76, 361-364.
- Maphalala, R.M., Kroner, A., 1993. Pb-Pb single zircon ages for younger Archean granitoids of Swaziland, southern Africa. In: *Ext. Abst. 16th Colloquium on African Geology*. pp. 201-206. Mbabane, Swaziland.
- McCourt, S., 1995. The crustal architecture of the Kaapvaal crustal block South Africa, between 3.5 and 2.0 Ga. *Mineralium Deposita* 30, 89-97.
- McCourt, S., Armstrong, R.A., 1998. SHRIMP U-Pb zircon geochronology of granites from the Central Zone, Limpopo Belt, southern Africa: Implications for the age of the Limpopo Orogeny. *South African Journal of Geology* 101, 329-338.
- McCourt, S., Hilliard, P., Armstrong, R.A., 2000. SHRIMP U-Pb zircon geochronology of granitoids from the western margin of the Kaapvaal Craton: implications for crustal evolution in the Neoproterozoic (abs.). *Journal of African Earth Sciences* 31A, 48.
- McCourt, S., van Reenen, D., 1992. Structural geology and tectonic setting of the Sutherland Greenstone Belt, Kaapvaal Craton, South Africa. *Precambrian Research* 55, 93-110.
- Menzies, A.H., Carlson, R.W., Shirey, S.B., Gurney, J.J., 1999. Re-Os systematics of Newlands peridotite xenoliths: implications for diamond and lithosphere formation. In: *The P.H.Nixon Volume: Proceedings of the 7th International Kimberlite Conference, Volume 2* Gurney, J.J., Gurney, J.L., Pascoe, M.D., Richardson, S.H. (Eds.), pp. 566-573. Red Roof Design, Cape Town, S.A.
- Menzies, A.H., Shirey, S.B., Carlson, R.W., Gurney, J.J., 1998. Re-Os isotope systematics of diamond-bearing eclogites and peridotites from Newlands kimberlite (abs.). In: *Extended Abstracts, 7th International Kimberlite Conference*. pp. 579-581. University of Cape Town, South Africa.
- Moore, M., Davis, E.W., Robb, L.J., Jackson, M.C., Grobler, D.F., 1993. Archean rapakivi granite-anorthosite-rhyolite complex in the Witwatersrand basin hinterland, southern Africa. *Geology* 21, 1031-1034.
- Moser, D.E., 1997. Dating the shock wave and thermal imprint of the giant Vredefort impact, South Africa. *Geology* 25, 7-10.
- Moser, D.E., Flowers, R.M., Hart, R.J., 2001. Birth of the Kaapvaal tectosphere 3.08 billion years ago. *Science* 291, 465-468.
- Nelson, J.P., Beukes, N.J., Cairncross, B., 1995. Tectonostratigraphic setting of the ~2.9 Ga Mozaan Group of the Pongola Supergroup and correlation with the Witwatersrand Supergroup. *Ext. Abstr: Centennial Geocongress 1*, 838-840.
- Nye, C.J., Reid, M.R., 1986. Geochemistry of primary and least fractionated lavas from Okmok volcano, central Aleutians: implications for arc magmagenesis. *Journal of Geophysical Research* 91, 10271-10287.
- Oxburgh, E.R., Parmentier, E.M., 1978. Thermal processes in the formation of continental lithosphere. *Philosophical Transactions of the Royal Society of London A* 288, 415-429.
- Pearson, D.G., Carlson, R.W., Shirey, S.B., Boyd, F.R., Nixon, P.H., 1995. Stabilisation of Archean lithospheric mantle: a Re-Os isotope study of peridotite xenoliths from the Kaapvaal craton. *Earth and Planetary Science Letters* 134, 341-357.
- Pearson, D.G., Shirey, S.B., Harris, J.W., Carlson, R.W., 1998. Sulphide inclusions in diamonds from the Koffiefontein kimberlite, S. Africa: constraints on diamond ages and mantle Re-Os systematics. *Earth and Planetary Science Letters* 160, 311-326.
- Peper, T., Beekman, F., Cloetingh, S., 1992. Consequences of thrusting and intraplate stress fluctuations for vertical motions in foreland basins and peripheral areas. *Geophysical Journal International* 111, 104-126.
- Poujol, M., Anhaeusser, C.R., 2001. The Johannesburg Dome, South Africa: new single zircon U-Pb isotopic evidence for early Archean granite-greenstone development within the central Kaapvaal Craton. *Precambrian Research* 108, 139-157.

- Poujol, M., Anhaeusser, C.R., Armstrong, R.A., 2000. Episodic Archean Granitoid emplacement in the Amalia-Kraaipan terrane, South Africa: new evidence from single zircon U-Pb geochronology with implications for the age of the western Kaapvaal Craton. *Information Circular 346, Economic Geology Research Unit, University of Witwatersrand, Johannesburg*, 21p.
- Poujol, M., Respaut, J.P., Robb, L.J., Anhaeusser, C.R., 1997. New U-Pb and Pb-Pb data on the Murchison Greenstone Belt, South Africa and their implications for the origin of the Witwatersrand Basin. *Information Circular*, 21 p..
- Poujol, M., Robb, L.J., 1999. New U-Pb zircon ages on gneisses and pegmatite from south of the Murchison greenstone belt, South Africa. *South African Journal of Geology* 102, 93-97.
- Poujol, M., Robb, L.J., Respaut, J.-P., Anhaeusser, C.R., 1996. 3.07-2.97 Ga greenstone belt formation in the northeastern Kaapvaal Craton: implications for the origin of the Witwatersrand Basin. *Economic Geology* 91, 1455-1461.
- Poujol, M., Robb, L.J., Respaut, J.P., 1999. U-Pb and Pb-Pb isotopic studies relating to the origin of gold mineralization in the Evander Goldfield, Witwatersrand Basin, South Africa. *Precambrian Research* 95, 167-185.
- Richardson, S.H., Shirey, S.B., Harris, J.W., Carlson, R.W., 2001. Archean subduction recorded by Re-Os isotopes in eclogitic sulfide inclusions in Kimberley diamonds. *Earth and Planetary Science Letters* 191, 257-266.
- Robb, L.J., Charlesworth, E.G., Drennan, G.R., Gibson, R.L., Tongu, E.L., 1997. Tectono-metamorphic setting and paragenetic sequence of Au-U mineralization in the Archean Witwatersrand Basin, South Africa. *Australian Journal of Earth Sciences* 44, 353-371.
- Robb, L.J., Davis, D.W., Kamo, S.L., 1991. Chronological framework for the Witwatersrand Basin and environs: towards a time-constrained depositional model. *South African Journal of Geology* 94, 86-95.
- Robb, L.J., Davis, D.W., Kamo, S.L., 1990. U-Pb ages on single detrital zircon grains from the Witwatersrand Basin, South Africa: constraints on the age of sedimentation and on the evolution of granites adjacent to the basin. *Journal of Geology* 98, 311-328.
- Robb, L.J., Davis, D.W., Kamo, S.L., Meyer, F.M., 1992. Ages of altered granites adjoining the Witwatersrand Basin with implications for the origin of gold and uranium. *Nature* 357, 677-680.
- Robb, L.J., Meyer, F.M., 1995. The Witwatersrand Basin, South Africa: Geological framework and mineralization processes. *Ore Geology Reviews* 10, 67-94.
- Roering, C., van Reenen, D.D., Smit, C.A., Barton, J.M., Jr., de Beer, J.H., de Wit, J.M., Stettler, E.H., van Schalkwyk, J.F., Stevens, G., Pretorius, S., 1992. Tectonic model for the evolution of the Limpopo Belt. *Precambrian Research* 55, 539-552.
- Shirey, S.B., Carlson, R.W., Gurney, J.J., van Heerden, L., 1998. Re-Os isotope systematics of eclogites from Robers Victor: implications for diamond growth and Archean tectonic processes (abs.). In: *Ext. Abstr., 7th International Kimberlite Conference*. pp. 808-810. University of Cape Town, South Africa.
- Shirey, S.B., Carlson, R.W., Richardson, S.H., Menzies, A., Gurney, J.J., Pearson, D.G., Harris, J.W., Weichert, U., 2001. Archean emplacement of eclogitic components into the lithospheric mantle during formation of the Kaapvaal craton. *Geophysical Research Letters* 28, 2509-2512.
- Simons, F.J., Zielhuis, A., van der Hilst, R.D., 1999. The deep structure of the Australian continent from surface wave tomography. *Lithos* 48, 17-43.
- Stanistreet, I.G., McCarthy, T.S., 1991. Changing tectono-sedimentary scenarios relevant to the development of the Late Archean Witwatersrand Basin. *Journal of African Earth Sciences* 13, 65-81.
- Stolper, E., Newman, S., 1994. The role of water in the petrogenesis of Mariana trough magmas. *Earth and Planetary Science Letters* 121, 293-325.
- Tatsumi, Y., Sakuyama, S., Fukuyama, H., Kushiro, I., 1983. Generation of arc basalts and thermal structure of the mantle wedge in subduction zones. *Journal of Geophysical Research* 88, 5815-5825.
- Thomas, R.J., Von Veh, M.W., McCourt, S., 1993. The tectonic evolution of southern Africa: an overview. *Journal of African Earth Sciences* 16, 5-24.
- Treloar, P.J., Coward, M.P., Harris, N.B.W., 1992. Himalayan-Tibetan analogies for the evolution of the Zimbabwe Craton and Limpopo Belt. *Precambrian Research* 55, 571-587.
- van Reenen, D.D., Roering, C., Ashwal, L.D., de Wit, M.J., 1992. Regional geologic setting of the Limpopo Belt. *Precambrian Research* 55, 1-5.
- Vearncombe, J.R., 1986. Structure of veins in a gold-pyrite deposit in banded iron formation, Amalia greenstone belt, South Africa. *Geological Magazine* 123, 601-609.
- Vearncombe, J.R., 1988. Structure and metamorphism of the Archean Murchison belt, Kaapvaal Craton, South Africa. *Tectonics* 7, 761-774.
- Vearncombe, J.R., Barton, J.M. Jr., Walsh, K.L., 1987. The Rooiwater Complex and associated rocks, Murchison granitoid-greenstone belt terrane, Kaapvaal Craton. *South African Journal of Geology* 90, 361-377.

- Vearncombe, J.R., Cheshire, P.E., De Beer, J.H., Killick, A.M., Mallinson, W.S., McCourt, S., Stettler, E.H., 1988. Structures related to the Antimony line, Murchison schist belt, Kaapvaal craton, South Africa. *Tectonophysics* 154, 285-308.
- Walker, R.J., Carlson, R.W., Shirey, S.B., Boyd, F.R., 1989. Os, Sr, Nd, and Pb isotope systematics of southern African peridotite xenoliths: implications for the chemical evolution of subcontinental mantle. *Geochimica et Cosmochimica Acta* 53, 1583-1595.
- Wilson, A.H., Versfeld, A.J., 1994. The early Archean Nondweni greenstone belt, souther Kaapvaal Craton, South Africa; Part I. Stratigraphy, sedimentology, mineralization and depositional environment. *Precambrian Research* 67, 243-276.
- Winter, H. de la R., 1987. A cratonic foreland model for Witwatersrand Basin development in a continental back-arc, plate-tectonic setting. *South African Journal of Geology* 90, 409-427.

Table 1. Zircon U-Pb isotopic data for Kimberley and Kraaipan Belt samples

#	Frac ^a	Composition						Isotopic Ratios						corr. coef.	Dates (Ma)				
		Wt. (mg) ^b	[U] (ppm)	Th ^c U	[Pb] (ppm)	Pb* ^d Pbc	Pbc ^d (pg)	²⁰⁶ Pb/ ²⁰⁴ Pb ^e	²⁰⁸ Pb/ ²⁰⁶ Pb ^f	²⁰⁶ Pb/ ²³⁸ U ^f	% err ^g	²⁰⁷ Pb/ ²³⁵ U ^f	% err ^g		²⁰⁷ Pb/ ²⁰⁶ Pb ^f	% err ^g	²⁰⁶ Pb ^h / ²³⁸ U	²⁰⁷ Pb ^h / ²³⁵ U	²⁰⁷ Pb ^h / ²⁰⁶ Pb ^h
KX14-8, garnet-bearing amphibolite																			
1	z1	0.82	326	0.073	199	116.5	1.4	7084.1	0.020	0.576362	(.12)	16.9526	(.12)	0.21332	(.05)	0.930	2933.9	2932.2	2931.0 ± 0.7
2	z2	0.82	259	0.109	168	12.4	10.6	668.6	0.030	0.577029	(.52)	16.9934	(.52)	0.21359	(.06)	0.994	2936.6	2934.5	2933.0 ± 0.9
3	z3	0.82	285	0.067	174	116.0	1.2	7062.8	0.018	0.575660	(.31)	16.9442	(.31)	0.21348	(.07)	0.973	2931.0	2931.7	2932.1 ± 1.2
4	z4	0.82	181	0.083	111	41.1	2.2	2508.4	0.023	0.575970	(.14)	16.9492	(.19)	0.21343	(.12)	0.750	2932.3	2932.0	2931.7 ± 2.0
KX14-18, weakly deformed pegmatite cross-cutting banded gneiss																			
5	z1	0.58	114	0.220	79	5.7	7.3	315.7	0.060	0.574503	(1.51)	16.8476	(1.52)	0.21269	(.14)	0.995	2926.3	2926.2	2926.1 ± 2.3
6	z2	0.40	179	0.678	141	18.8	3.0	988.1	0.190	0.630201	(.30)	22.8598	(.31)	0.26308	(.08)	0.968	3150.4	3221.0	3265.3 ± 1.2
7	z3	0.62	155	0.381	118	4.9	12.9	254.18	0.107	0.578823	(1.20)	18.12702	(1.22)	0.22713	(.21)	0.985	2943.9	2996.5	3032.0 ± 3.4
KX14-19, non-deformed biotite granite																			
8	z2	1.73	65	1.363	51	6.4	12.3	285.0	0.381	0.520130	(1.08)	13.4672	(1.15)	0.18779	(.35)	0.951	2699.7	2713.0	2722.9 ± 5.8
9	z3	5.43	38	1.149	26	30.1	4.7	1444.8	0.318	0.525662	(.52)	13.6221	(.53)	0.18795	(.08)	0.988	2723.1	2723.8	2724.3 ± 1.3
10	z4	11.1	41	1.158	28	91.2	3.4	4536.1	0.320	0.52486	(.10)	13.59147	(.15)	0.18781	(.11)	0.699	2719.7	2721.7	2723.1 ± 1.8
KX14-20, peraluminous tonalitic layer in banded gneiss																			
11	z1	0.58	305	0.296	175	13.7	7.2	702.3	0.101	0.483016	(.66)	15.4822	(.67)	0.23247	(.10)	0.988	2540.4	2845.4	3069.1 ± 1.6
12	z2	1.01	418	0.434	276	42.3	6.5	2079.6	0.134	0.550012	(.26)	18.5289	(.27)	0.24433	(.07)	0.965	2825.2	3017.6	3148.4 ± 1.1
13	z3	0.83	234	0.412	157	40.3	3.2	2222.2	0.123	0.568640	(.26)	19.1943	(.27)	0.24481	(.07)	0.964	2902.2	3051.6	3151.5 ± 1.1
14	z4	1.56	193	0.415	138	26.9	7.8	1310.3	0.120	0.596030	(.34)	20.5308	(.35)	0.24982	(.09)	0.967	3013.8	3116.7	3183.7 ± 1.4
15	z6	1.07	160	0.576	124	118.7	1.1	6271.8	0.159	0.637552	(.22)	22.8409	(.23)	0.25983	(.06)	0.970	3179.4	3220.2	3245.7 ± 0.9
16	z7	0.70	135	0.561	115	5.2	13.7	246.2	0.157	0.616286	(.93)	21.4099	(.93)	0.25196	(.09)	0.996	3095.1	3157.3	3197.1 ± 1.4
KX14-21, migmatitic amphibolite layer in banded gneiss																			
17	z1	13.3	307	0.337	188	714.1	3.5	40731	0.098	0.542336	(.06)	15.9857	(.07)	0.21378	(.04)	0.844	2793.2	2875.9	2934.4 ± 0.7
18	z2	1.74	296	0.209	202	6.4	48.1	327.0	0.060	0.542851	(.31)	15.8949	(.42)	0.21236	(.24)	0.820	2795.4	2870.5	2923.6 ± 4.0
19	z3	3.95	192	0.291	121	122.0	3.9	6923.1	0.080	0.568437	(.19)	16.6818	(.20)	0.21284	(.07)	0.935	2901.4	2916.7	2927.3 ± 1.2
KX14-22, competent amphibolite layer in banded gneiss																			
20	z1	0.29	190	0.473	152	3.3	11.1	175.5	0.129	0.573265	(1.74)	16.8191	(1.75)	0.21279	(.19)	0.994	2921.2	2924.6	2926.9 ± 3.1
21	z2	0.74	136	0.413	92	10.9	6.0	582.9	0.113	0.574773	(.97)	16.8721	(.99)	0.21290	(.16)	0.987	2927.4	2927.6	2927.7 ± 2.5
22	z3	0.74	82	0.242	53	8.4	4.6	485.2	0.066	0.574250	(1.60)	16.8611	(1.60)	0.21295	(.13)	0.997	2925.2	2927.0	2928.2 ± 2.2
WKC00-26, crystal-rich rhyolitic tuff, Kraaipan Group																			
23	z1	3.70	76	0.007	45	150.2	1.1	9261.4	0.002	0.569507	(.23)	16.7733	(.23)	0.21361	(.06)	0.968	2905.8	2922.0	2933.1 ± 1.0
24	z2	2.30	91	0.264	54	69.1	1.8	4036.3	0.076	0.537486	(.22)	15.5641	(.23)	0.21002	(.05)	0.973	2772.9	2850.4	2905.7 ± 0.9
25	z3	1.11	109	1.158	80	35.8	2.5	1753.1	0.330	0.548946	(.47)	15.9856	(.47)	0.21120	(.07)	0.987	2820.8	2875.9	2914.8 ± 1.2

^a All fractions composed of single abraded grains. ^b Sample weights were estimated to within 40% using measured grain dimensions and a nominal density of 4.5 g/cm³. ^c Th contents calculated from radiogenic ²⁰⁸Pb and the ²⁰⁷Pb/²⁰⁶Pb date of the sample, assuming concordance between U-Th-Pb systems. ^d Pb* and Pbc represent radiogenic Pb and common Pb respectively. ^e Measured ratio corrected for fractionation and spike contribution; Pb fractionation was 0.12 ± 0.04 ‰/a.m.u. for Faraday detector or 0.15 ± 0.04 ‰/a.m.u. for Daly detector analysis, based on daily analysis of NBS-981. ^f Measured ratios corrected for fractionation, spike, blank, and initial common Pb; nominal Pb blank = 3.5 pg ± 50% (2₋); nominal U blank = 0.1 pg ± 50% (2₋); measured laboratory blank composition: ²⁰⁶Pb/²⁰⁴Pb = 19.10, ²⁰⁷Pb/²⁰⁴Pb = 15.72, ²⁰⁸Pb/²⁰⁴Pb = 38.65 ± 0.01 (2₋); initial common Pb composition from model of Stacy and Kramers (1972) at 2.9 Ga. ^g Numbers in parentheses are the % errors reported at the 2₋ confidence interval, propagated using the algorithms of Ludwig (1980). ^h Isotopic ages calculated using the decay constants of Jaffey et al. (1971): λ(²³⁵U) = 9.8485x10⁻¹⁰ yr⁻¹ and λ(²³⁸U) = 1.55125x10⁻¹⁰ yr⁻¹; error in ²⁰⁷Pb/²⁰⁶Pb date reported at the 2σ confidence interval

Table 2. Sm-Nd isotopic data for selected Kimberley gneisses and granitoids

Sample ^a	[Sm] ^a	[Nd] ^a	$\frac{^{147}\text{Sm}}{^{144}\text{Nd}}^{\text{b}}$	$\frac{^{143}\text{Nd}}{^{144}\text{Nd}}^{\text{c}}$	$\epsilon_{\text{Nd}}^{\text{c}}$	$\epsilon_{\text{Nd(t)}}^{\text{c}}$	$t_{\text{CHUR}}^{\text{c}}$	t_{DM}^{d}
KX14-18	1.42	6.5	0.1322	0.511388 ±4	-24.39	-0.09	2.97	3.27
KX14-19	15.39	79.05	0.1177	0.511051 ±3	-30.96	-3.25	3.07	3.31
KX14-20	0.81	5.49	0.0893	0.510543 ±4	-40.86	-0.36	2.98	3.17
KX14-21	9.4	28.97	0.1963	0.512516 ±5	-2.38	-2.24	****	****
KX14-22	2.95	10.97	0.1626	0.512045 ±5	-11.57	1.28	2.66	3.27

^a Concentrations in ppm, as determined by isotope dilution.

^b Internal errors in measured $^{147}\text{Sm}/^{144}\text{Nd}$ are $\leq 0.1\%$ (2σ s.d.).

^c Measured $^{143}\text{Nd}/^{144}\text{Nd}$ with internal error (2σ s.e.); long-term reproducibility of Nd isotopic standards is ≤ 20 ppm (2σ s.d.)— analyses ($n=12$) of USGS standard BCR-1 during the course of the study yielded $^{143}\text{Nd}/^{144}\text{Nd} = 0.512643 \pm 9$ and $^{147}\text{Sm}/^{144}\text{Nd} = 0.1383 \pm 3$ (2σ s.d.), which propagate into an average reproducibility for $\epsilon_{\text{Nd(t)}}$ of approximately ± 0.5 epsilon units; present-day ϵ_{Nd} and t_{CHUR} (Ga) calculated with $(^{147}\text{Sm}/^{144}\text{Nd})_{\text{CHUR}} = 0.1967$ and $(^{143}\text{Nd}/^{144}\text{Nd})_{\text{CHUR}} = 0.512638$; $\epsilon_{\text{Nd(t)}}$ calculated at age of 2.7 Ga plutonism (KX14-19) or 2.9 Ga metamorphism (all other samples).

^d t_{DM} (Ga) = $(1/\lambda_{^{147}\text{Sm}}) * \ln[(((^{143}\text{Nd}/^{144}\text{Nd})_{\text{sample}} - (^{143}\text{Nd}/^{144}\text{Nd})_{\text{DM}}) / ((^{147}\text{Sm}/^{144}\text{Nd})_{\text{sample}} - (^{147}\text{Sm}/^{144}\text{Nd})_{\text{DM}}) + 1)]$; present-day $(^{143}\text{Nd}/^{144}\text{Nd})_{\text{DM}} = 0.513151$, $(^{147}\text{Sm}/^{144}\text{Nd})_{\text{DM}} = 0.2137$.

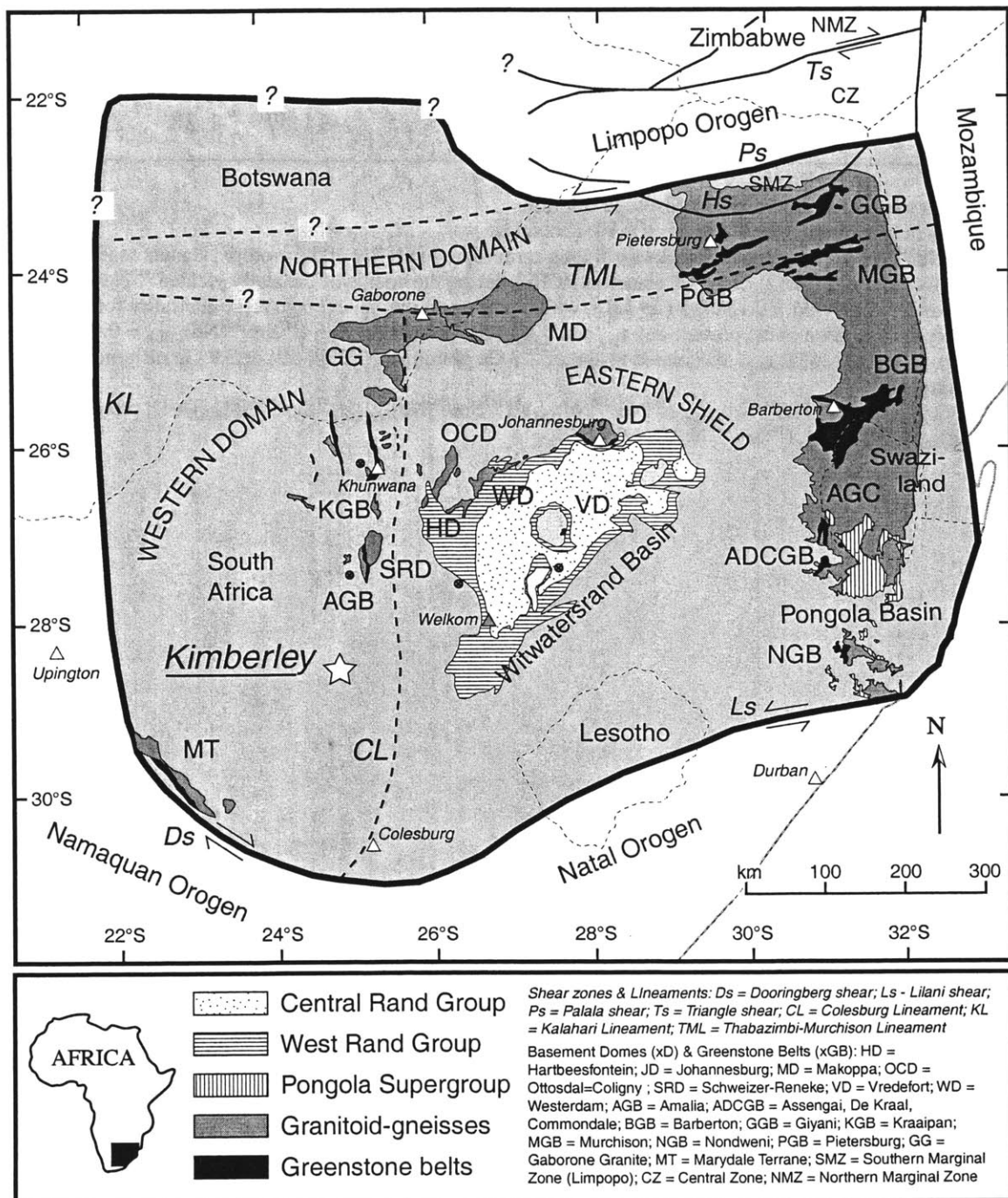


Figure 1. Geological map of Kaapvaal craton illustrating the locations of exposed Paleo- to Neoproterozoic crystalline basement throughout the Kaapvaal craton, and the present distributions of sediments and volcanics of the Meso- to Neoproterozoic Dominion, Pongola, and Witwatersrand basins. The Colesburg Lineament (CL) separates the eastern Kaapvaal shield from a western domain, while the Thabazimbi-Murchison Line (TML) separates the Kaapvaal shield from a northern domain comprising the Murchison, Pietersburg, and Giyani greenstone belts and intervening granitoid gneiss terranes.

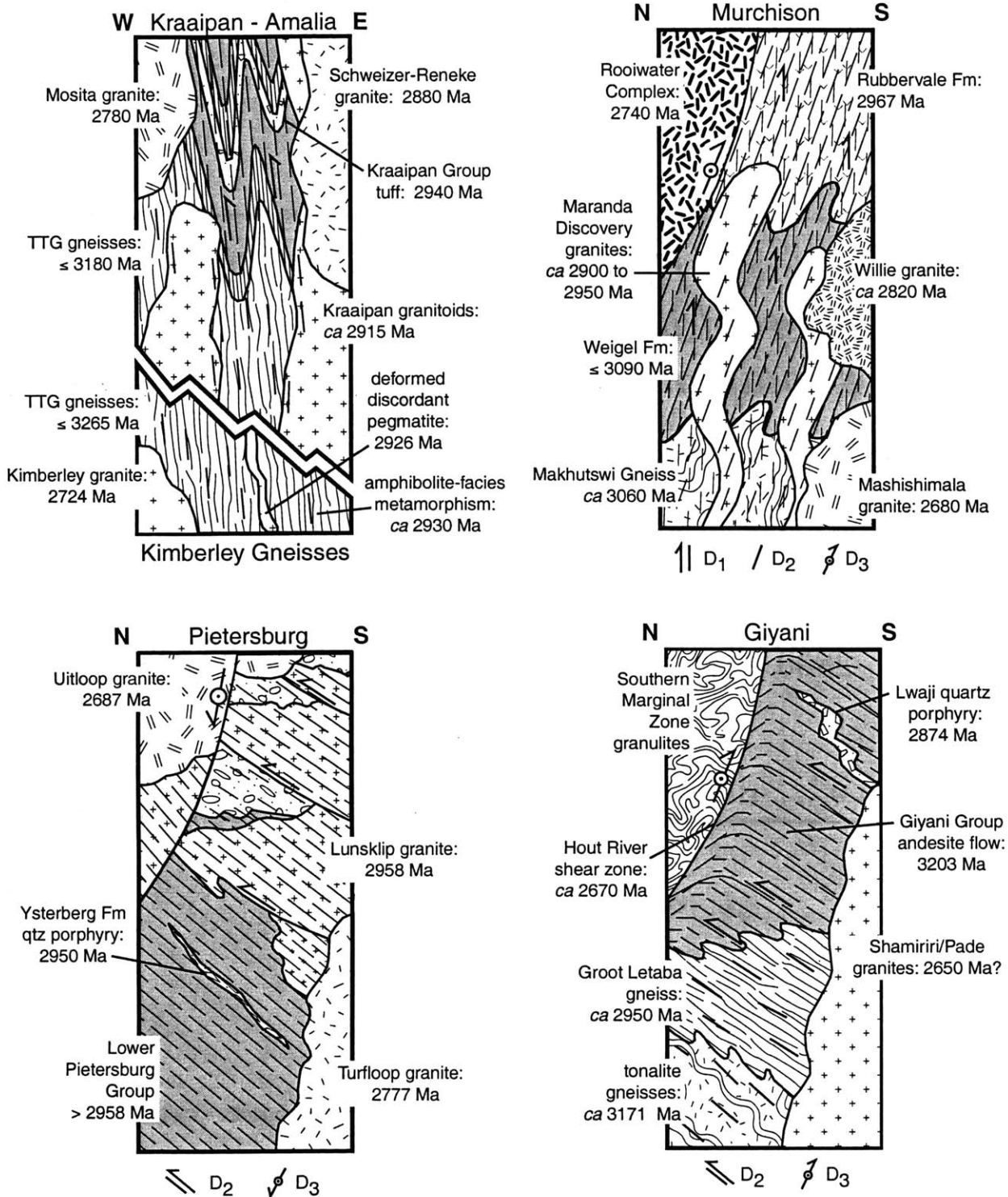


Figure 2. Interpretive geological sections for greenstone belts of the northern and western domains of the Kaapvaal craton illustrating relationships between basement and supracrustal lithologies, plutonic intrusives, and deformation phases in each belt. Geochronological, structural and lithological data constraining these representations are summarized in Section 2 and compiled in Figure 7.

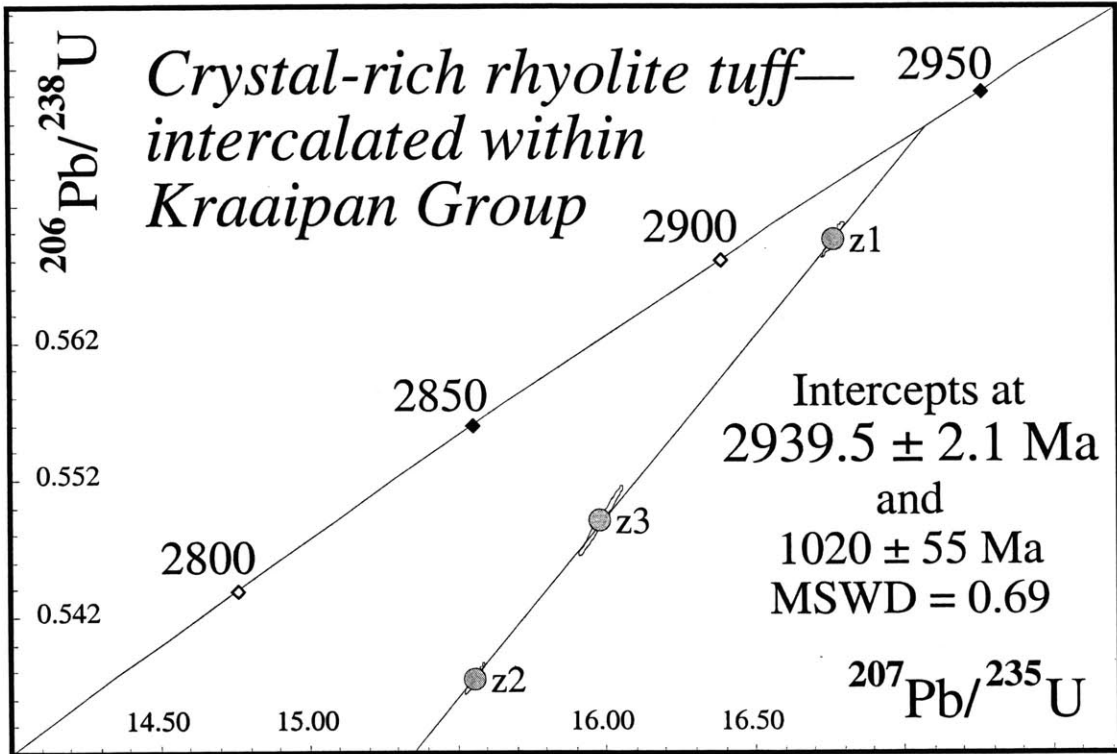


Figure 3. U-Pb concordia diagram for an interbedded rhyolite, Khunwana Chert Formation, Kraaipan Group.

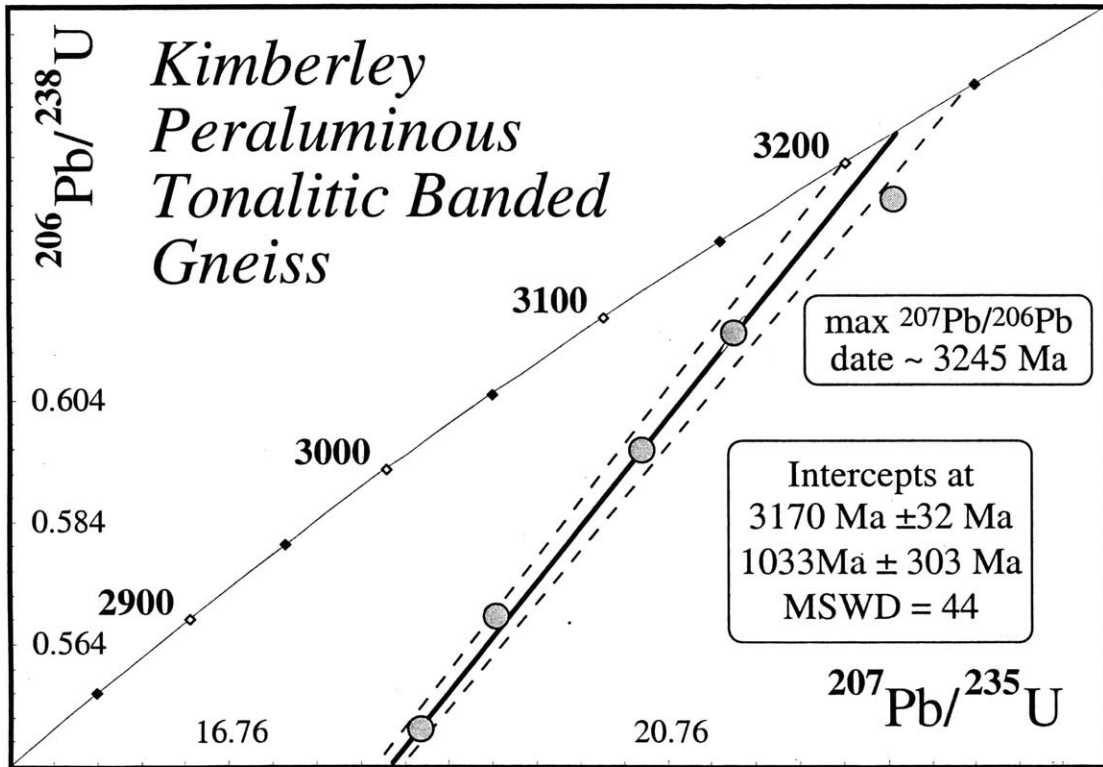


Figure 4. U-Pb concordia diagram for a Kimberley peraluminous tonalite gneiss.

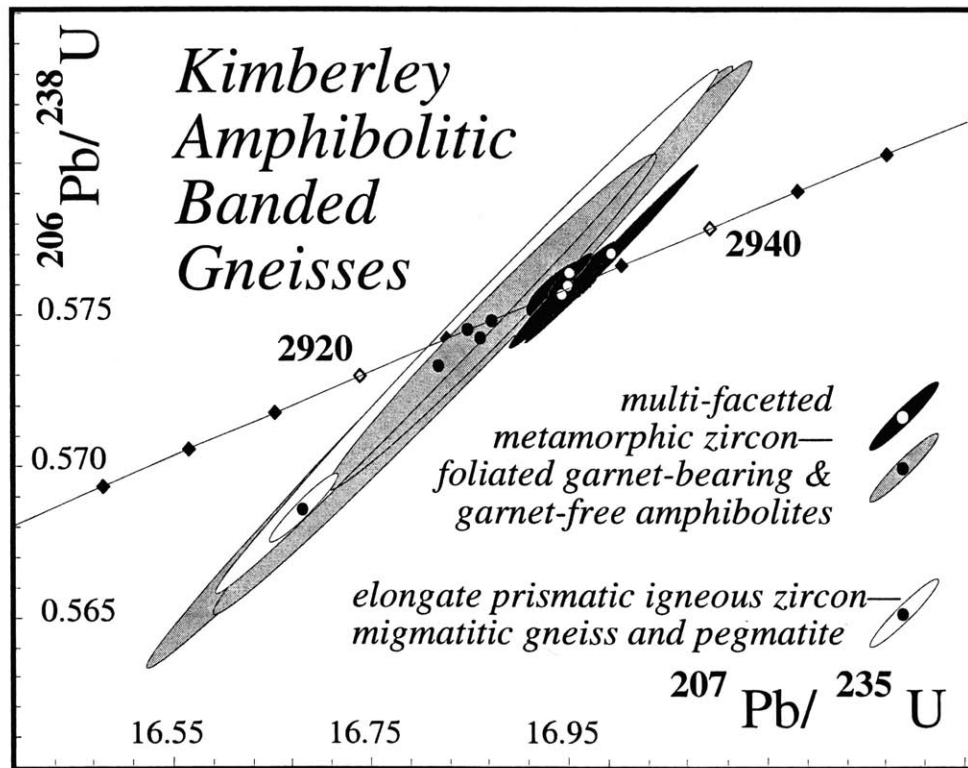


Figure 5. U-Pb concordia diagram for metamorphic and igneous zircons from Kimberley banded gneisses and cross-cutting pegmatite.

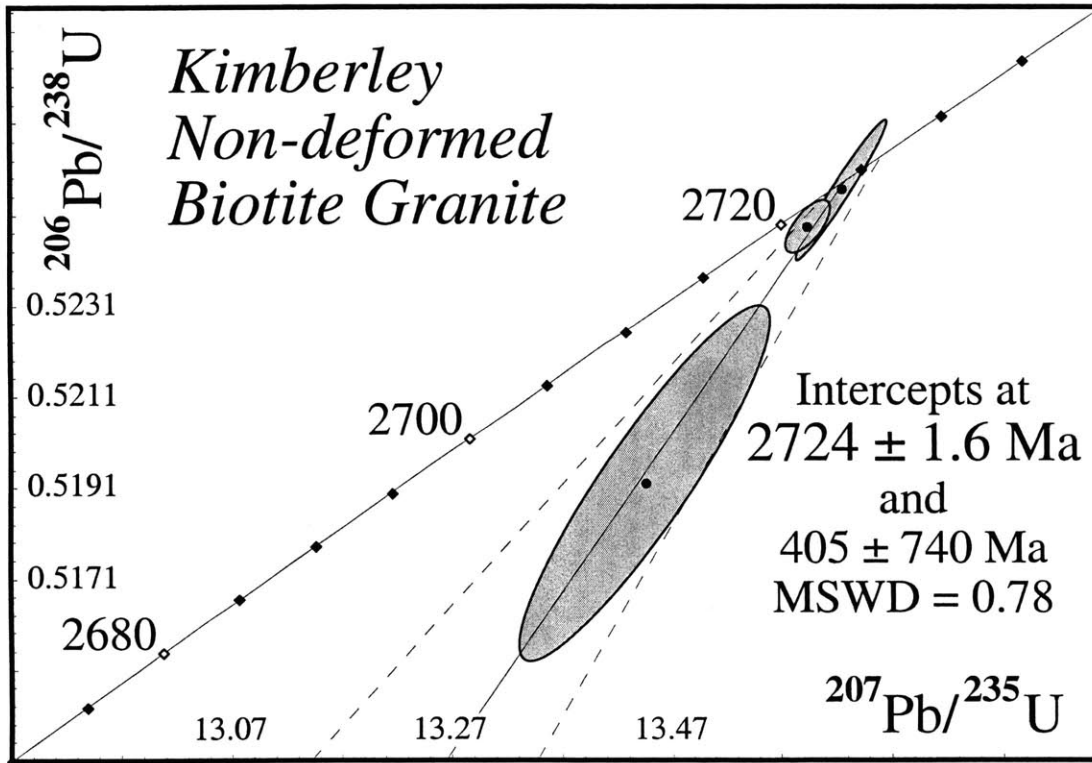


Figure 6. U-Pb concordia diagram for non-deformed biotite-bearing Kimberley granite.

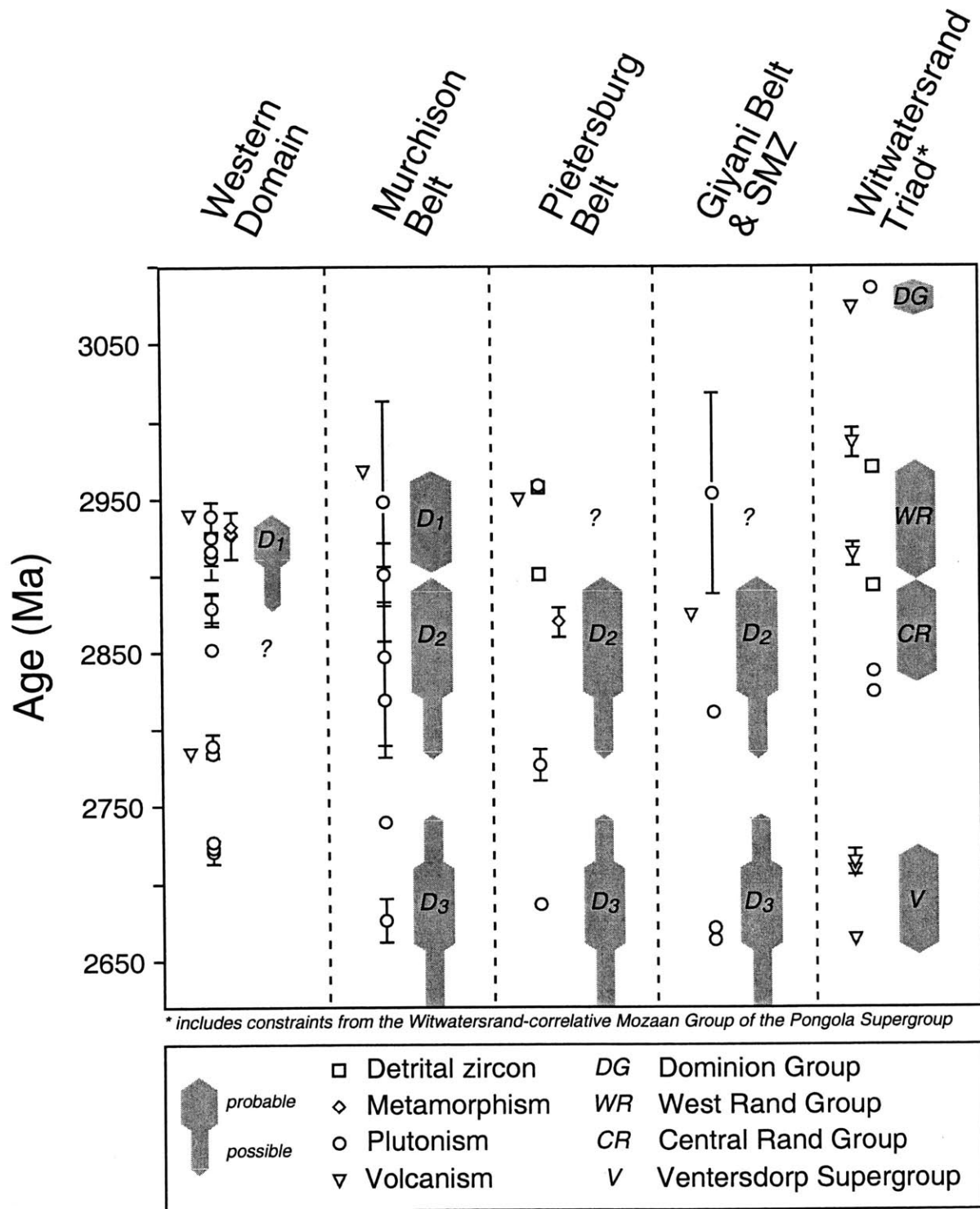


Figure 7. Compilation of U-Pb zircon geochronological constraints on the evolution of the northern and western domains, and deposition of the Witwatersrand triad, with inferred brackets (gray bars) on deformation phases in each belt and sediment deposition on the eastern shield.

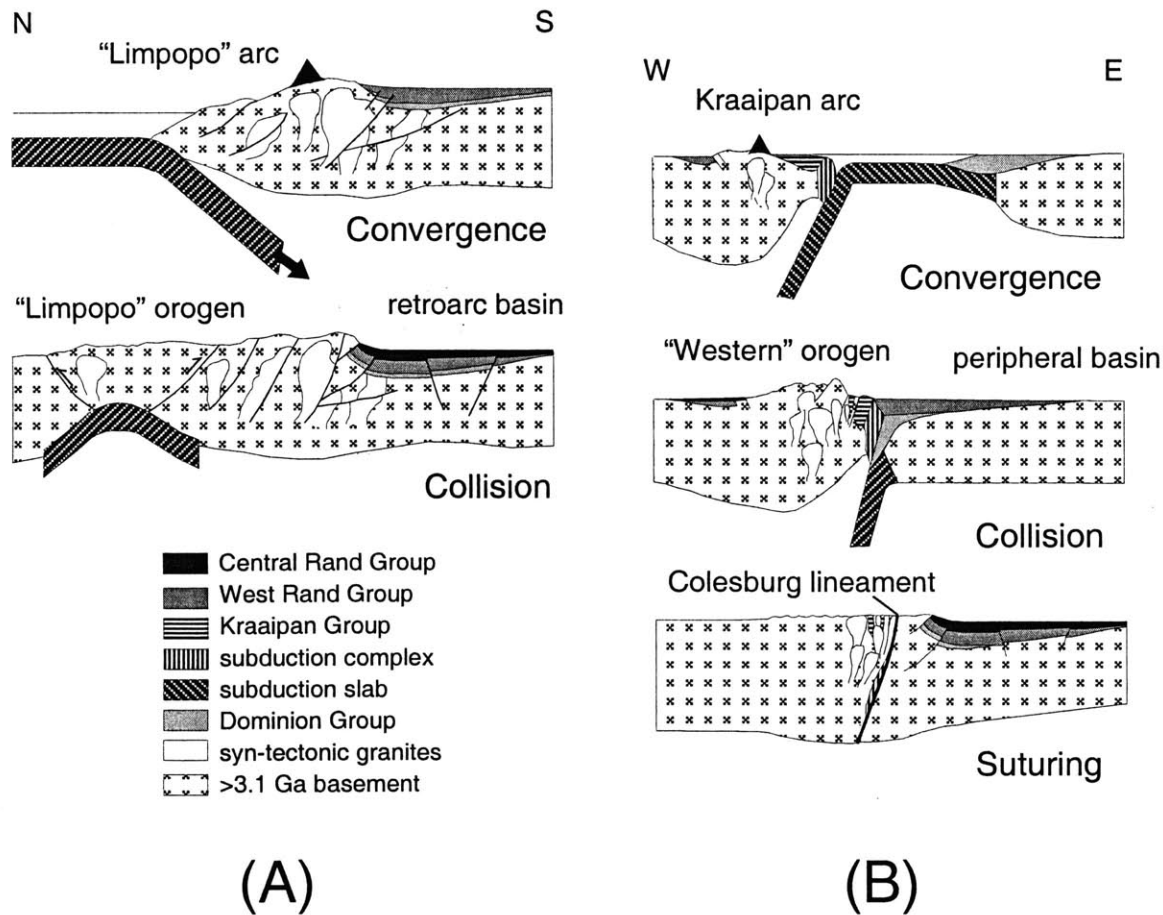


Figure 8. N-S and E-W cross sections through the Kaapvaal shield and its convergent margins at 2.97 to 2.82 Ga: A) N-S cross section through "Limpopo" orogen and Kaapvaal shield illustrating subduction beneath the Kaapvaal craton, formation of an Andean-style arc, cratonic flexural subsidence and deposition of the Witwatersrand Supergroup as a retroarc foreland basin. B) E-W cross sections through the western domain and Kaapvaal shield, illustrating west-dipping subduction-convergence and collision of the western domain, with flexural subsidence and deposition of the Witwatersrand Supergroup in a peripheral, or pericratonic basin akin to the Cenozoic Himalayan foredeep.

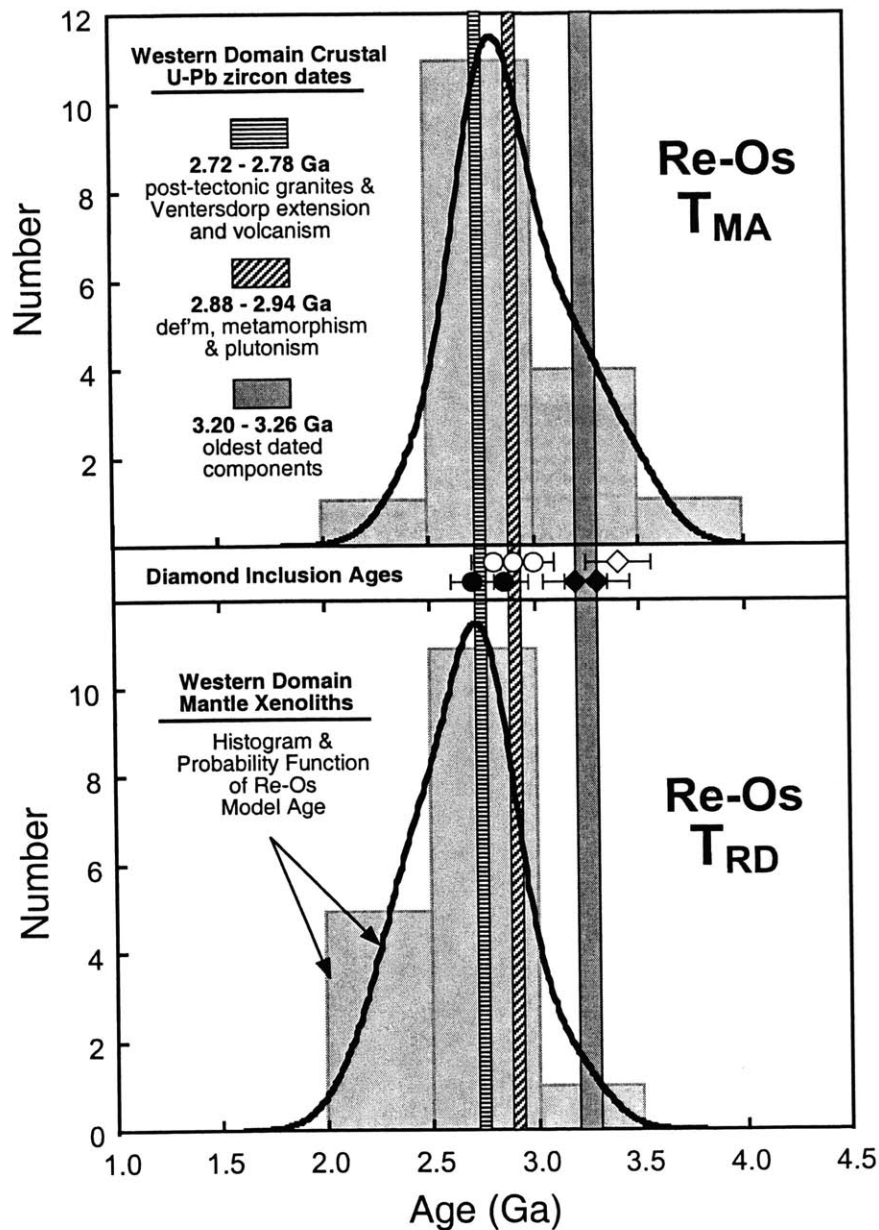


Figure 9. Histograms for Re-Os model ages of mantle peridotites from the western domain of the Kaapvaal craton (Carlson et al., 1999; Menzies et al., 1999), with associated probability density functions (calculated assuming ± 0.3 Ga error for model ages). Superimposed are crustal geochronological events in the western domain constrained from U-Pb zircon systematics. Also plotted are silicate and sulfide diamond inclusion model ages from Pearson et al. (1998) and Richardson et al. (2001) [diamonds are silicate inclusion Nd model ages, open = Kimberley, closed = Finsch; circles are sulfide inclusion Re-Os model and isochron ages, open = Kimberley, closed = Koffiefontein].



Chapter 6.
 PII S0016-7037(01)00616-0

U-Pb zircon and titanite systematics of the Fish Canyon Tuff: an assessment of high-precision U-Pb geochronology and its application to young volcanic rocks

MARK D. SCHMITZ,^{1,*} and SAMUEL A. BOWRING¹

¹Department of Earth, Atmospheric and Planetary Sciences, M.I.T., Cambridge, MA, USA

(Received December 12, 2000; accepted in revised form March 19, 2001)

Abstract—A large data set of single and multi-grain zircon and titanite analyses from a sample of the Oligocene Fish Canyon Tuff (FCT), a voluminous ash flow from the San Juan Mountains of Colorado and widely used ⁴⁰Ar/³⁹Ar geochronological standard, has been used to evaluate the influence of various sources of analytical and geological uncertainty on the calculated age of this tuff by the isotope dilution U-Pb zircon method. Twenty-three single zircon grains and seven small multi-grain fractions of the FCT yield an inverse-variance weighted mean ²⁰⁶Pb/²³⁸U date of 28.402 ± 0.023 Ma (2σ; MSWD 0.93) and a slightly older weighted mean ²⁰⁷Pb/²³⁵U date of 28.529 ± 0.030 Ma (MSWD 0.74), which are insensitive to common Pb corrections. Initial ²³⁰Th disequilibria calculated from a newly measured Th/U = 2.2 for FCT pumice shards indicate Th-deficiency for these zircons; its correction brings the weighted mean ²⁰⁶Pb/²³⁸U date to 28.478 ± 0.024 (MSWD 0.97), minimizing the discordance of the FCT zircon analyses. These calculations culminate in Concordia ages (Ludwig, 1998) for the crystallization of the FCT zircons of 28.476 ± 0.029 Ma (MSWD 1.50) without propagating decay constant errors, or 28.498 ± 0.035 Ma (MSWD 1.03) with propagated decay constant errors.

These results are in close agreement with a previous single-grain ²⁰⁶Pb/²³⁸U zircon date of 28.41 ± 0.05 Ma for the FCT (Oberli et al., 1990), however they do not corroborate the discordia lower intercept date of 27.52 ± 0.09 put forth by Lanphere and Baadsgaard (2001). The 28.476 ± 0.064 Ma Concordia age for FCT zircons (including systematic decay constant errors and uncertainty in Pb/U tracer calibration) is substantially older than all published ⁴⁰Ar/³⁹Ar sanidine ages, which range from 27.5 to 28.05 Ma (Lanphere and Baadsgaard, 1997; Renne et al. 1998). A lengthy period (~400 k.y.) of zircon residence in the magma chamber before eruption is commonly called upon to explain the age discrepancy. However, FCT titanite, which may remain open to Pb diffusive exchange until quenching upon eruption, yield a minimum ²³⁰Th-disequilibrium corrected weighted mean ²⁰⁶Pb/²³⁸U age of 28.395 ± 0.049 Ma (± 0.078 with tracer uncertainty), weakening residence time arguments, and supporting recent calls for re-evaluation of the ⁴⁰K decay constant and the accepted ages for commonly used ⁴⁰Ar/³⁹Ar mineral standards. The FCT zircon Concordia age also provides an empirical constraint on the decay constants of the U isotopes, indicating the relative accuracy of the currently accepted decay constants to within the original counting statistic errors of Jaffey et al. (1971). Copyright © 2001 Elsevier Science Ltd

1. INTRODUCTION

U-Pb zircon ages are among the most precise and accurate absolute chronometers for the study of geological and evolutionary processes, and have thus been used to measure time at increasingly fine scales throughout the geologic record. Recent applications of high-precision U-Pb zircon geochronology to Phanerozoic volcanic ash beds, for example, have pushed the limits of current analytical capability and challenged the traditional means of assessing analytical and geological uncertainty in U-Pb zircon age determinations (Mundil et al., 1996; Bowring et al., 1998; Tucker et al., 1998; Ludwig et al., 1999). The present study investigates the precision and accuracy of modern isotope dilution U-Pb zircon geochronology, applied particularly to Phanerozoic volcanic rocks, by developing a large data set of single and multi-grain zircon and titanite analyses from the well-studied Oligocene Fish Canyon Tuff (FCT) (Lipman et al., 1970; Steven and Lipman, 1976). With these data, we have attempted to assess the various sources of uncertainty in U-Pb zircon analysis, including geological factors like Pb-loss, inheritance, accurate initial common Pb

corrections, and intermediate daughter product disequilibria, as well as analytical factors including instrumental fractionation, tracer calibration, and blank estimation. The results provide the most accurate and precise estimator of the FCT zircon crystallization age currently available.

The U-Pb zircon and titanite data for the FCT in turn provide a potential benchmark for the intercalibration of isotopic ages obtained from different radioisotopic decay schemes. A previous single-grain ²⁰⁶Pb/²³⁸U zircon age of 28.41 ± 0.1 Ma for the FCT (Oberli et al., 1990) is resolvably older than published ⁴⁰Ar/³⁹Ar sanidine and biotite ages, which range from 27.5 to 28.05 Ma (Renne et al. 1994; Lanphere and Baadsgaard, 1997; Renne et al., 1998). Two contrasting explanations for this discrepancy have emerged, one challenging the accuracy of the ⁴⁰Ar/³⁹Ar method due to decay constant and age standard uncertainties, and the second suggesting several hundred k.y. of magma chamber residence to bias the zircon crystallization age from the volcanic eruption age (Renne et al., 1994; Renne et al., 1998). The number and quality of zircon analyses in the present study, when combined with data for titanite—a lower Pb closure temperature mineral, allow a more rigorous analysis of magma chamber residence than previously available.

*Author to whom correspondence should be addressed (mschmitz@mit.edu).

The comparison of ages obtained from different radioisotopic systems demands an understanding of systematic errors stemming from decay constant uncertainties. Continued evaluation and refinement of the precision and accuracy of decay constants, in particular for ^{40}K , ^{235}U , and ^{238}U is a pressing issue at the heart of modern high-precision geochronology. U-Pb isotopic measurements of geological samples demonstrated to have remained closed systems can provide constraints on U decay constants (Nier, 1939; Banks and Silver, 1966; Mattinson, 1973), in complement to alpha counting studies (Jaffey et al., 1971). In this vein, we have inverted the FCT U-Pb zircon data set to evaluate the precision and accuracy of the currently utilized uranium decay constants.

2. ANALYTICAL PROCEDURES

Zircon and titanite were separated by standard crushing, heavy liquid, and magnetic separation techniques from a sample of Fish Canyon Tuff, FC-2, an $^{40}\text{Ar}/^{39}\text{Ar}$ geochronological standard distributed by the New Mexico Geochronology Research Laboratory at New Mexico Tech. Only zircons exhibiting the lowest magnetic susceptibilities were chosen for further study. The resulting concentrates were hand-picked in ethanol under a binocular microscope, and separated into different populations based on crystal morphology, color, clarity and inclusion characteristics. From these populations representative crystals were reserved for photomicrography. Grains were mounted in epoxy, polished, carbon-coated, and imaged by back-scattered electrons (BSE) and cathodoluminescence (CL) at the MIT JEOL 733 Superprobe electron microprobe facility. Both imaging techniques used an accelerating voltage of 15 keV, 10 nA beam current, and a 1 μm beam spot size. The CL image was collected with the secondary electron detector mounted in place of the optical microscope ocular.

All zircons were air-abraded, washed in 3M HNO_3 at 50°C for 2 h, and ultrasonicated for an additional 30 min. After photographing to estimate sample weights, zircons were loaded into 300 μL Teflon FEP microcapsules, washed again in 150 μL 3M HNO_3 at 50°C for 12 h, and finally rinsed with four capsule volumes of high-purity H_2O . Zircons were dissolved in 120 μL 29M HF with a trace of HNO_3 at 220°C for 48 h with a mixed ^{205}Pb - ^{233}U - ^{235}U tracer, dried to salts, and redissolved in 120 μL 6M HCl at 180°C overnight. Some fractions of titanite were also air-abraded, followed by rinsing in 3M HNO_3 for 15 min; other fractions were not abraded or acid-rinsed. Titanite dissolution followed that for zircon, modified to include a second HF step. Pb and U were separated using HCl-based (zircon) and two stage HBr-HCl-based (titanite) anion-exchange procedures modified after Krogh (1973).

Milligram sized fractions of hand-picked optically clear sanidine feldspar were progressively leached following methods modified from Housh and Bowring (1991). All leaching was carried out in savillex PFA Teflon beakers on a hot plate at 50°C, and each leach step was followed by rinsing with two aliquots of 500 μL high-purity H_2O which was subsequently added to the leachate. After leaching with 500 μL 7M HNO_3 and 6M HCl for 5 min each, sanidine separates were subjected to three sequential treatments of 500 μL of 1M HF for 5 min. Residues were then dissolved in 500 μL of 29M HF. All leachates were dried and redissolved in 1.1M HBr for separation of Pb by conventional HBr-HCl-based anion-exchange

chemistry. Total procedural blanks are estimated as <20 pg, and thus represent a negligible contribution to the sample Pb.

Separated Pb and U were analyzed by conventional thermal-ionization mass spectrometry on the MIT VG Sector 54 multicollector mass spectrometer. Lead was loaded with a silica gel-phosphoric acid mixture (Gerstenberger and Haase, 1997) on previously degassed single Re filaments, and its isotopes measured either: (1) for ^{207}Pb ion beams $>10^{-13}$ A (all titanites), in a two-cycle dynamic "Faradaly" routine with ^{204}Pb in the axial Daly detector and ^{205}Pb through ^{208}Pb in H1-H4 Faraday cups, followed by ^{205}Pb in the axial Daly and ^{206}Pb through ^{208}Pb measured on H1-H3 Faraday cups, providing real-time Daly gain measurement; or (2) for ^{207}Pb ion beams $<10^{-13}$ A (all zircons), by peak-jumping all ion beams into the axial Daly detector in ion-counting mode. Uranium was loaded with colloidal graphite and 0.1M H_3PO_4 on previously degassed single Re filaments, and its isotopes measured in static mode on axial through L2 Faraday cups with an average ^{235}U ion beam of 3×10^{-13} A. Pb isotopic fractionation was monitored throughout the course of the study by daily analysis of the NBS-981 common Pb standard; uranium fractionation was monitored and corrected using the double spike. A total of 19 zircon procedural Pb blanks ranged from 0.87 to 2.86 pg during the course of the study; a mean and 2σ s.d. of 1.71 pg \pm 40% was used to reduce all zircon data. Six total procedural Pb blanks for titanite ranged from 4.8 to 12.8 pg, with a mean and 2σ s.d. of $8.0 \pm 50\%$ used to reduce all titanite data. U blanks were negligible relative to sample contents, with a nominal value of 0.5 pg \pm 50% used in error propagation for each analysis, following the algorithms of Ludwig (1980).

Trace element concentration measurements for pumice fragments from the Fish Canyon Tuff were obtained by solution ICP-MS on the VG PQ 2+S at M.I.T. Three 50 mg fractions of hand-picked phenocryst-free glassy pumice fragments were dissolved in HF- HNO_3 , spiked with internal standards of Se, In, and Bi, diluted, and analyzed in triplicate. Following internal and external instrumental drift corrections, blank and isobaric interference corrections, concentrations were calibrated against the USGS RGM-1 standard and are inferred to be accurate and precise to $\pm 2\%$ based on replicate analyses of blind standards.

3. RESULTS

3.1. Zircon Systematics

Zircons in the Fish Canyon Tuff comprise abundant clear to slightly pink prismatic and euhedral crystals ranging from <50 μm to 250 μm in their longest dimension, with aspect ratios from 2 to 10. The majority of zircons have colorless round to vermicular inclusions of glass, minor apatite and pyrrhotite inclusions. BSE images of polished grains are monotonous, while CL images reveal fairly simple growth zonation dominated by thick mantles of fine oscillatory-zoned zircon (Fig. 1a–e). Zoning is commonly disturbed around inclusions of glass and other minerals (e.g., Fig. 1d). The centers of some zircons exhibit broader diffuse zonation patterns (Fig. 1e), however it is difficult to pinpoint truncations of zonation indicative of resorption or inherited cores. The tips of some zircons of high aspect ratio are composed of luminescent, relatively homogeneous zircon which truncates the oscillatory-zoned zircon (Fig. 1c); this phenomenon may represent healing of crystal tips broken in the magma chamber before eruption.

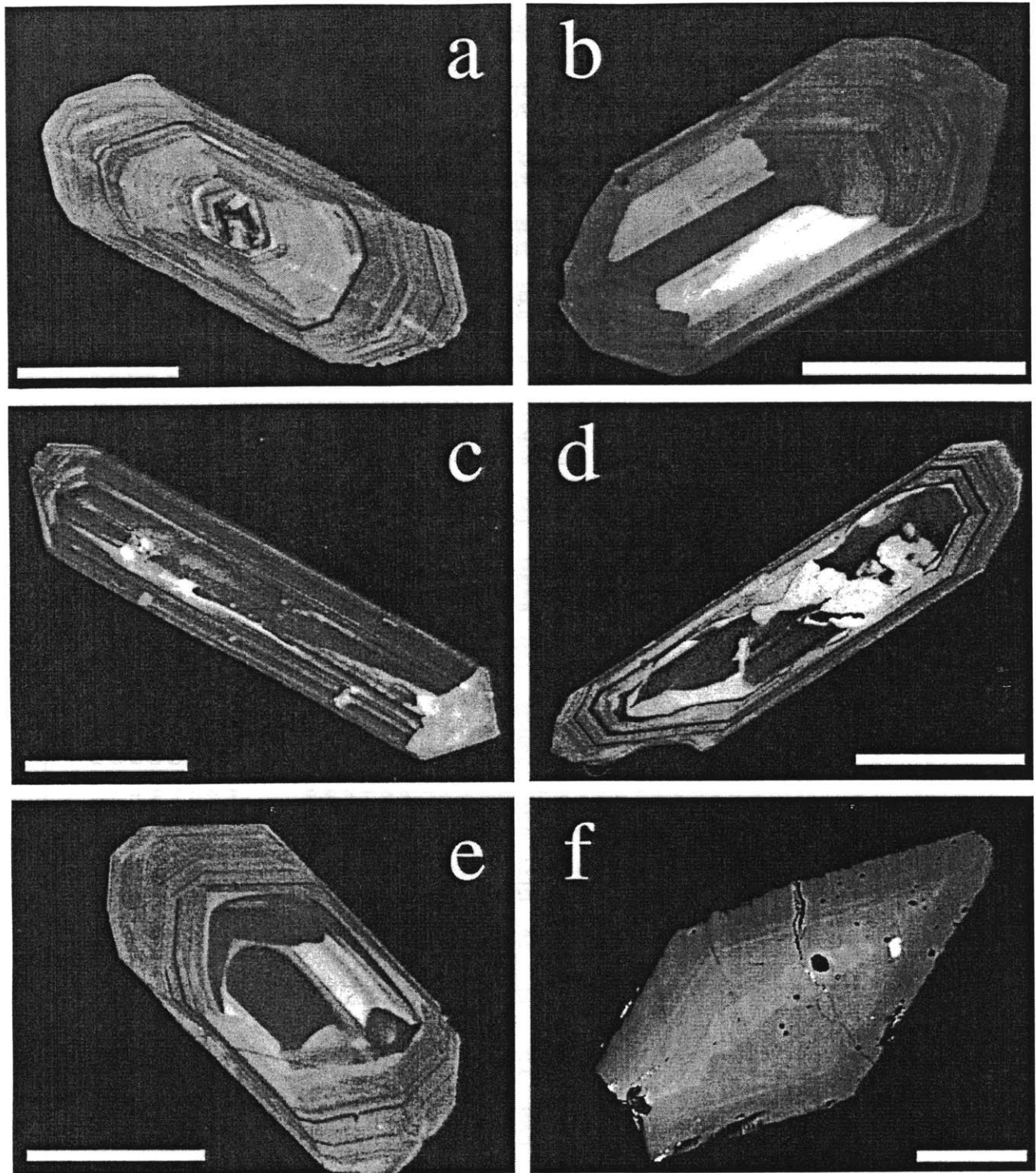


Fig. 1. Cathodoluminescence images of Fish Canyon Tuff zircons (a–e), and a back-scattered electron image of Fish Canyon Tuff titanite (f). White scale bars represent 100 μm .

Data for twenty-four single grains of zircon analyzed by conventional ID-TIMS U-Pb geochronology are summarized in Table 1. The single grains of zircon were some of the largest in the FC-2 sample (4–16 μg), and contained between 200 to 850 ppm U, and from 1 to 6 ppm total Pb. Pb^*/Pb_c (radiogenic Pb/common Pb) ratios for individual zircons ranged from 1.9 to

16.7; a single analysis yielded an extremely low Pb^*/Pb_c of 0.4, and because of its high total common Pb (45 pg) was disregarded from further study. Total common Pb in the remaining 23 zircons ranged from 1.1 to 10.7 pg, of which 1.7 ± 0.6 pg was inferred to be laboratory blank. Excess common Pb over blank was visually correlated with the presence of glass and

Table 1. U-Pb isotopic data for zircon and titanite.

Fractions ^a	Weight (μg) ^b	Composition					Isotopic Ratios							Isotopic Ages (Ma)					
		[U]	Th ^c	[Pb]	Pb* ^d	Pbc ^d	²⁰⁶ Pb ^e	²⁰⁸ Pb ^f	²⁰⁶ Pb ^f	²⁰⁷ Pb ^f		²⁰⁷ Pb ^f		corr.	²⁰⁶ Pb ^b	²⁰⁶ Pb* ¹	²⁰⁷ Pb ^h	²⁰⁷ Pb ^h	
		(ppm)	U	(ppm)	Pbc	(pg)	²⁰⁴ Pb	²⁰⁶ Pb	²³⁸ U	%err ^g	²³⁵ U	%err ^g	²⁰⁶ Pb	%err ^g	coef.	²³⁸ U	²³⁸ U	²³⁵ U	²⁰⁶ Pb
Single zircons																			
z1	6.3	845	0.509	4.06	8.6	2.8	546.8	0.1636	0.004411	(.44)	0.02842	(.64)	0.04673	(.45)	0.712	28.37	28.46	28.45	35.4
z2	5.1	676	0.690	3.59	4.9	3.4	302.4	0.2220	0.004405	(.65)	0.02837	(1.08)	0.04670	(.82)	0.653	28.34	28.41	28.40	33.9
z3	7.4	421	0.570	2.04	6.9	2.1	434.7	0.1836	0.004438	(.73)	0.02864	(.83)	0.04681	(.38)	0.892	28.54	28.62	28.67	39.5
z4	9.8	375	0.579	6.23	0.4	44.5	42.42	0.2043	0.004602	(.38)	0.03259	(1.95)	0.05135	(1.83)	0.419	29.60	29.68	32.56	257
z5	5.8	527	0.811	2.67	7.6	2.0	449.5	0.2618	0.004413	(.75)	0.02853	(.86)	0.04689	(.40)	0.888	28.38	28.45	28.57	43.9
z6	7.0	619	0.565	4.17	1.9	10.7	131.9	0.1826	0.004424	(.48)	0.02864	(1.28)	0.04696	(1.13)	0.477	28.46	28.54	28.68	47.0
z7	8.7	670	0.527	3.62	4.3	6.3	277.9	0.1704	0.004416	(.39)	0.02857	(1.28)	0.04692	(1.16)	0.445	28.40	28.49	28.60	45.1
z8	13	367	0.536	1.81	7.2	3.1	455.3	0.1730	0.004415	(.47)	0.02855	(.75)	0.04690	(.58)	0.643	28.40	28.48	28.58	44.2
z9	4.4	449	0.643	2.26	4.2	2.3	265.0	0.2068	0.004401	(1.15)	0.02835	(1.65)	0.04672	(1.12)	0.733	28.31	28.39	28.38	34.7
z10	7.4	418	0.666	2.22	4.4	3.3	279.0	0.2149	0.004412	(.72)	0.02852	(.93)	0.04687	(.56)	0.800	28.38	28.46	28.55	42.8
z12	5.7	650	0.593	3.40	4.7	3.7	298.4	0.1909	0.004399	(.61)	0.02838	(.92)	0.04680	(.65)	0.704	28.30	28.37	28.42	39.0
z13	5.1	378	0.798	1.90	5.1	1.9	313.3	0.2574	0.004400	(1.19)	0.02843	(1.36)	0.04687	(.60)	0.897	28.30	28.37	28.47	42.6
z14	6.8	604	0.809	3.18	7.1	2.9	421.6	0.2603	0.004428	(.55)	0.02854	(.67)	0.04675	(.36)	0.845	28.48	28.55	28.58	36.5
z15	5.4	439	0.478	2.13	4.6	2.4	300.9	0.1542	0.004414	(.95)	0.02852	(1.14)	0.04687	(.59)	0.857	28.39	28.48	28.56	42.6
z17	5.1	501	0.858	2.84	3.9	3.3	235.1	0.2767	0.004416	(.86)	0.02853	(1.25)	0.04685	(.85)	0.733	28.41	28.47	28.56	41.7
z18	4.5	214	1.085	1.13	3.2	1.6	190.4	0.3505	0.004388	(2.24)	0.02838	(2.51)	0.04691	(.99)	0.919	28.23	28.28	28.42	44.8
z1(2b)	13	499	0.640	2.53	8.7	3.7	530.7	0.2058	0.004435	(.35)	0.02857	(.71)	0.04673	(.58)	0.571	28.53	28.60	28.61	35.3
z2(2b)	16	582	0.593	2.96	8.6	5.1	530.8	0.1907	0.004427	(.25)	0.02853	(.38)	0.04674	(.28)	0.683	28.48	28.56	28.57	35.9
z4(2b)	10	409	0.681	2.15	5.6	3.5	343.5	0.2198	0.004419	(.55)	0.02855	(.68)	0.04686	(.39)	0.822	28.42	28.50	28.58	42.0
z5(2b)	5.4	559	0.588	2.73	6.1	2.3	386.1	0.1905	0.004397	(.77)	0.02854	(1.24)	0.04708	(.92)	0.672	28.28	28.36	28.58	53.3
z7(2b)	8.5	413	1.101	2.19	16.7	1.1	909.1	0.3534	0.004400	(.43)	0.02829	(.54)	0.04664	(.30)	0.827	28.30	28.36	28.33	30.6
z8(2b)	10	433	0.506	2.20	5.3	3.8	341.4	0.1638	0.004423	(.51)	0.02869	(.82)	0.04704	(.61)	0.665	28.45	28.53	28.72	51.2
z9(2b)	4.7	594	0.457	2.80	5.6	2.3	368.4	0.1469	0.004403	(.82)	0.02835	(1.14)	0.04670	(.75)	0.752	28.32	28.41	28.39	34.1
z17(2b)	8.6	308	0.754	1.51	9.7	1.3	582.3	0.2430	0.004416	(.68)	0.02852	(.80)	0.04684	(.39)	0.872	28.41	28.48	28.56	41.3
Multi-grain zircon fractions																			
z18(2b) 3,n,p	10	270	0.712	1.31	11.7	1.1	706.2	0.2299	0.004408	(.56)	0.02853	(.74)	0.04694	(.45)	0.789	28.35	28.43	28.56	46.3
z19(2b) 7,n,c	20	472	0.658	2.27	22.1	2.0	1328.3	0.2115	0.004411	(.25)	0.02842	(.39)	0.04672	(.28)	0.700	28.37	28.45	28.45	35.1
z20(2b) 11,e,c	15	445	0.585	2.09	23.6	1.4	1445.9	0.1887	0.004412	(.33)	0.02852	(.53)	0.04688	(.40)	0.664	28.38	28.45	28.55	42.9
z21(2b) 11,e,c	17	445	0.486	2.74	17.7	2.6	1095.9	0.1707	0.005733	(.28)	0.04058	(.47)	0.05134	(.37)	0.635	36.85	36.93	40.39	256
z22(2b) 10,q,p	21	318	0.785	1.59	15.7	2.1	916.6	0.2539	0.004413	(.35)	0.02858	(.45)	0.04697	(.26)	0.807	28.38	28.43	28.61	47.7
z24(2b) 11,q,p	21	307	0.674	1.48	19.4	1.6	1167.1	0.2170	0.004421	(.34)	0.02851	(.42)	0.04677	(.25)	0.816	28.43	28.45	28.54	37.6
z25(2b) 7,e,c	22	375	0.515	1.77	13.8	2.7	864.6	0.1661	0.004406	(.28)	0.02847	(.37)	0.04685	(.23)	0.787	28.34	28.46	28.50	41.8
z26(2b) 14,e,c	26	367	0.668	1.78	20.3	2.3	1214.8	0.2152	0.004411	(.44)	0.02848	(.53)	0.04682	(.28)	0.851	28.37	28.45	28.51	40.1

(Continued)

Table 1. (Continued).

Fractions ^a	Weight (μg) ^b	Composition					Isotopic Ratios								Isotopic Ages (Ma)				
		[U]	Th ^c	[Pb]	Pb* ^d	Pbc ^d	²⁰⁶ Pb ^e	²⁰⁸ Pb ^f	²⁰⁶ Pb ^f	²⁰⁷ Pb ^f		²⁰⁷ Pb ^f		corr.	²⁰⁶ Pb ^h	²⁰⁶ Pb* ⁱ	²⁰⁷ Pb ^h	²⁰⁷ Pb ^h	
		(ppm)	U	(ppm)	Pbc	(pg)	²⁰⁴ Pb	²⁰⁶ Pb	²³⁸ U	%err ^g	²³⁵ U	%err ^g	²⁰⁶ Pb	%err ^g	coef.	²³⁸ U	²³⁸ U	²³⁵ U	²⁰⁶ Pb
Titanite																			
s1	726	47	4.92	1.38	0.54	655	33.09	1.6491	0.004449	(.26)	0.02990	(2.98)	0.04875	(2.82)	0.637	28.61	28.48	29.92	136
s2	176	50	5.16	1.52	0.51	182	32.01	1.6780	0.004448	(.68)	0.02898	(2.85)	0.04725	(2.64)	0.417	28.61	28.46	29.01	62.0
s3	183	44	5.12	1.34	0.50	169	31.81	1.6960	0.004439	(.73)	0.02947	(2.62)	0.04814	(2.39)	0.430	28.56	28.41	29.49	106
s4	183	66	5.04	1.94	0.53	239	32.59	1.6661	0.004457	(.51)	0.02951	(2.69)	0.04801	(2.52)	0.424	28.67	28.53	29.53	99.8
s5	437	49	5.25	1.48	0.52	433	32.21	1.6791	0.004437	(.32)	0.02843	(2.94)	0.04648	(2.78)	0.520	28.54	28.39	28.47	22.3
s6	181	43	5.37	1.34	0.48	169	31.42	1.6480	0.004433	(.74)	0.02724	(3.04)	0.04456	(2.82)	0.409	28.51	28.36	27.29	-79
s7	191	53	5.00	1.36	0.62	165	35.41	1.6047	0.004420	(.67)	0.02844	(2.26)	0.04666	(2.06)	0.430	28.43	28.29	28.47	31.9
s8	220	49	4.92	1.25	0.64	172	35.96	1.5964	0.004429	(.65)	0.02877	(3.69)	0.04712	(3.46)	0.427	28.49	28.35	28.80	55.2
s9	147	63	4.99	2.22	0.39	240	29.14	1.5900	0.004430	(.72)	0.02829	(8.03)	0.04632	(7.62)	0.605	28.49	28.36	28.33	14.3
s10	98	69	4.98	2.02	0.50	137	32.16	1.6379	0.004406	(.90)	0.02906	(3.43)	0.04783	(3.18)	0.408	28.34	28.20	29.08	90.8
s11	75	58	5.62	1.94	0.44	106	29.95	1.7279	0.004455	(1.28)	0.02742	(6.74)	0.04465	(6.33)	0.404	28.65	28.48	27.47	-75
s13	462	36	4.84	1.08	0.50	338	32.26	1.5719	0.004425	(.39)	0.02880	(2.98)	0.04720	(2.82)	0.473	28.46	28.33	28.83	59.3
s14	396	60	4.87	1.61	0.60	403	34.80	1.6074	0.004420	(.31)	0.02924	(2.47)	0.04798	(2.33)	0.491	28.43	28.30	29.26	98.3
s16	102	65	4.63	1.90	0.47	136	32.04	1.4881	0.004453	(.91)	0.02868	(4.14)	0.04670	(3.88)	0.384	28.64	28.53	28.71	33.9

^a Multi-grain fraction descriptors: #=number of grains in fraction, n = needles, e = elongate, q = equant, p = pinkish, c = colorless.

^b Sample weights were estimated to within 40% using measured grain dimensions, an ellipsoidal geometry, and nominal density of 4.5 g/cm³ for zircon, or weighed to within 1- μg for titanite.

^c [Th] calculated from radiogenic ²⁰⁸Pb and the ²⁰⁷Pb/²³⁵U date of the sample, assuming concordance between U-Th-Pb systems; $\lambda(^{232}\text{Th}) = 4.9475 \times 10^{-11} \text{ yr}^{-1}$.

^d Pb* and Pbc represent radiogenic Pb and common Pb respectively.

^e Measured ratio corrected for fractionation and spike contribution; Pb fractionation correction is 0.12 \pm 0.04 % per a.m.u. (2 σ) for multicollector analyses (titanite) and 0.15 \pm 0.04 % per a.m.u. (2 σ) for single collector analyses (zircon) based on repeated daily analysis of NBS 981.

^f Measured ratios corrected for fractionation, spike, blank, and initial common Pb; nominal U blank = 0.5 pg \pm 50% (2 σ); total procedural Pb blanks measured during the course of this study averaged 1.7 pg \pm 40% (2 σ) (n = 19) for zircon, and 8.0 \pm 50% (2 σ) (n = 6) for titanite; measured laboratory blank composition: ²⁰⁶Pb/²⁰⁴Pb = 19.10 \pm 0.05, ²⁰⁷Pb/²⁰⁴Pb = 15.72 \pm 0.05, ²⁰⁸Pb/²⁰⁴Pb = 38.65 \pm 0.1 (2 σ); initial common Pb composition from leached sanidine feldspars: ²⁰⁶Pb/²⁰⁴Pb = 18.44 \pm 0.05, ²⁰⁷Pb/²⁰⁴Pb = 15.57 \pm 0.05, ²⁰⁸Pb/²⁰⁴Pb = 37.68 \pm 0.1 (2 σ).

^g Numbers in parentheses are the % errors reported at the 2 σ confidence interval, propagated using the algorithms of Ludwig (1980).

^h Isotopic ages calculated using the decay constants recommended by Steiger and Jager (1976): $\lambda(^{235}\text{U}) = 9.8485 \times 10^{-10} \text{ yr}^{-1}$ and $\lambda(^{238}\text{U}) = 1.55125 \times 10^{-10} \text{ yr}^{-1}$.

ⁱ ²⁰⁶Pb/²³⁸U date corrected for initial ²³⁰Th disequilibria, using the calculated [Th/U]_{mineral}: [Th/U]_{magma} = 2.2 as measured in Fish Canyon Tuff pumice glass; $\lambda(^{230}\text{Th}) = 9.195 \times 10^{-6} \text{ yr}^{-1}$.

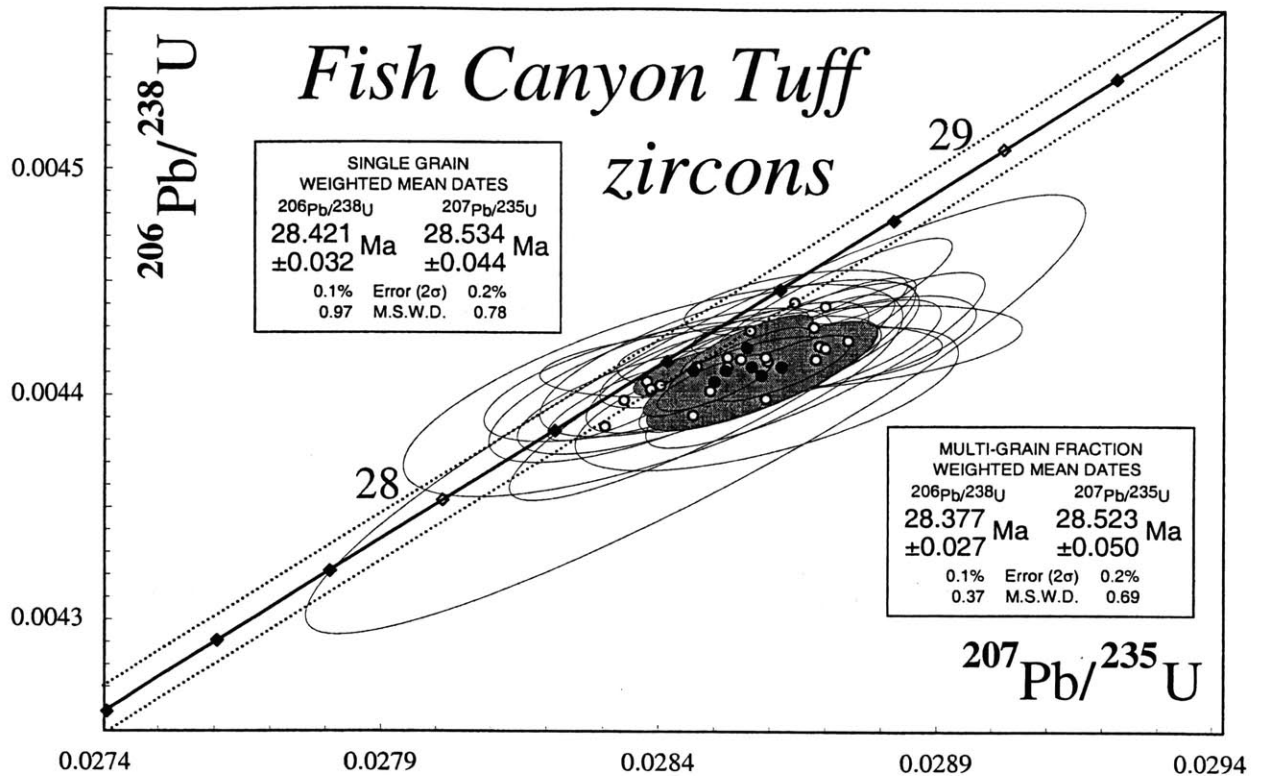


Fig. 2. U-Pb concordia diagram of single (open points, open ellipses) and multi-grain (filled points, shaded ellipses) zircon analyses from the Fish Canyon Tuff, with leached sanidine initial common Pb correction, but without initial daughter disequilibrium correction. Thin dotted lines represent the concordia error envelope resulting from propagation of decay constant counting statistic errors (2σ) of Jaffey et al. 1971.

mineral inclusions in the zircons. While further discussion of initial common Pb composition is to follow, the data in Table 1 and the following summary are corrected using the composition of leached FCT sanidine feldspars.

$^{206}\text{Pb}/^{238}\text{U}$ dates of twenty-three single grains range from 28.23 to 28.54 Ma; $^{207}\text{Pb}/^{235}\text{U}$ dates range from 28.33 to 28.72 Ma (Fig. 2). Together, these analyses yield an inverse-variance weighted mean $^{206}\text{Pb}/^{238}\text{U}$ date of 28.421 ± 0.032 Ma (2σ ; MSWD 0.97) and a slightly older weighted mean $^{207}\text{Pb}/^{235}\text{U}$ date of 28.534 ± 0.044 Ma (MSWD 0.78). Errors on isotopic ratios for each zircon analysis are inversely correlated with the associated Pb^*/Pb_c ratio. To increase this ratio, eight multi-grain fractions of zircon composed of distinct morphologies of generally smaller, but optically inclusion-poor crystals (see footnotes to Table 1) were analyzed. Seven multi-grain zircon fractions yielded $^{206}\text{Pb}/^{238}\text{U}$ dates from 28.34 to 28.43 Ma with a weighted mean date of 28.377 ± 0.027 Ma (MSWD 0.37); the associated $^{207}\text{Pb}/^{235}\text{U}$ dates ranged from 28.45 to 28.61 Ma with a weighted mean date of 28.523 ± 0.050 Ma (MSWD 0.69), demonstrating the same consistent discordance as the single grain analyses (Fig. 2). An eighth multi-grain fraction yields anomalously old dates providing the only indication of inheritance in this study. Excluding this last fraction, all combined single grain and small fraction analyses yield grand weighted mean $^{206}\text{Pb}/^{238}\text{U}$ and $^{207}\text{Pb}/^{235}\text{U}$ dates of 28.402 ± 0.023 Ma (MSWD 0.93) and 28.529 ± 0.030 Ma (MSWD 0.74) respectively.

3.2. Titanite Systematics

The FCT contains large crystals of transparent honey-colored titanite, up to 0.5 mm in diameter, with characteristic wedge-shaped igneous morphology. The crystal faces of all titanite are ornamented with small tabular to dendritic ilmenite crystals, interpreted to represent decompression crystallization during eruption. In BSE, titanite shows some concentric zonation (Fig. 1f), representing variation in rare earth element content. This image also illustrates the presence of inclusions of apatite and zircon (dark and bright spots on BSE image respectively), demonstrating co-crystallization of the accessory minerals.

Fourteen clear, inclusion-free single grain and multi-grain fractions of titanite were analyzed, including abraded and unabraded crystals. The titanite fractions contain from 36 to 69 ppm U and 1 to 2 ppm total Pb, of which roughly two-thirds is common Pb; the resulting low Pb^*/Pb_c ratios of the titanite analyses make them less precise and more sensitive to the initial common Pb correction than the FCT zircons. Correcting for initial common Pb utilizing the Stacey and Kramers (1975) model, analyses of titanite form a correlated array with a narrow range in $^{206}\text{Pb}/^{238}\text{U}$, but widely variable $^{207}\text{Pb}/^{235}\text{U}$, which falls significantly to the left of concordia (Fig. 3), suggesting systematic error in this method of correction. However, when the leached FCT sanidine feldspar Pb composition is used, the titanite analyses shift along a subhorizontal vector, converging on concordia. Resulting $^{206}\text{Pb}/^{238}\text{U}$ dates for titanite

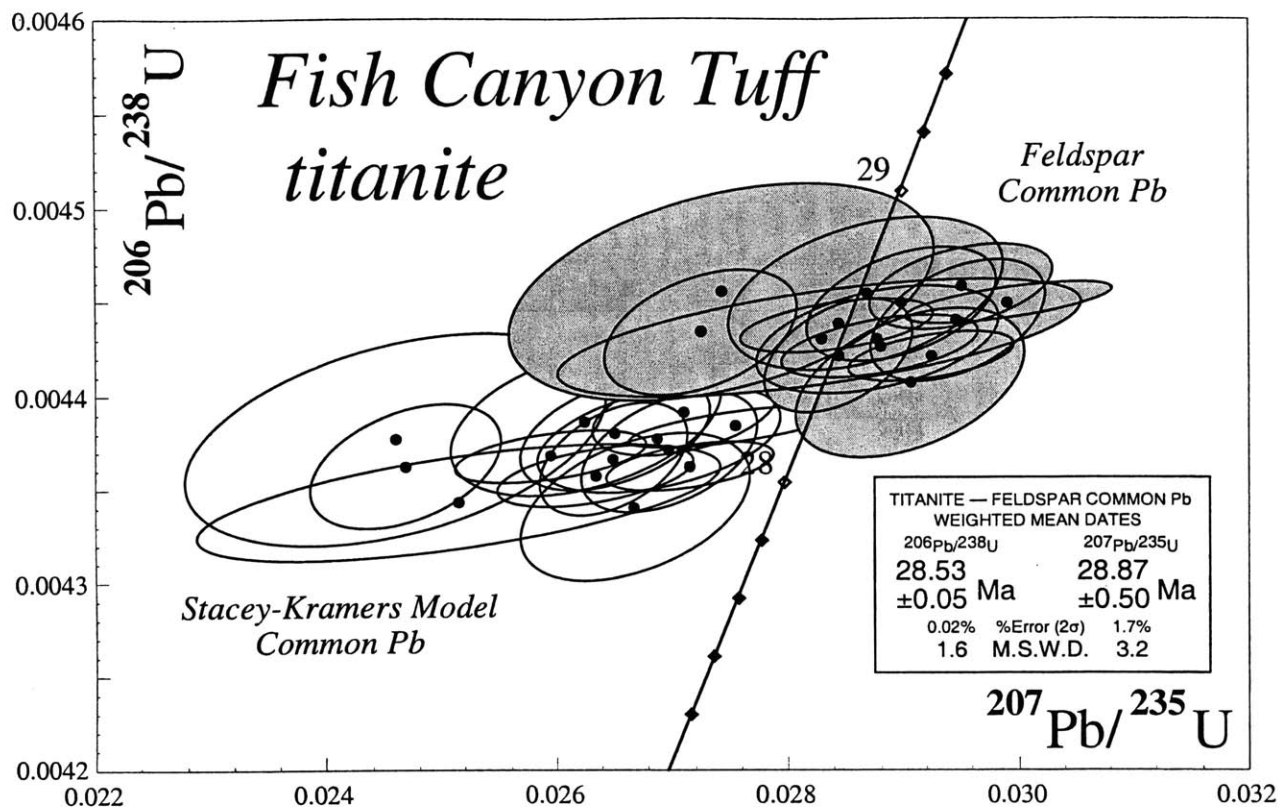


Fig. 3. U-Pb concordia diagram of titanite analyses from the Fish Canyon Tuff, calculated with initial common Pb isotopic composition estimates from leached sanidine feldspars (shaded ellipses) versus the two-stage terrestrial Pb evolution model of Stacey and Kramers (1974) at 28 My (open ellipses).

ite range from 28.34 to 28.67 Ma with a weighted mean of 28.533 ± 0.050 Ma (MSWD 1.60); $^{207}\text{Pb}/^{235}\text{U}$ dates ranged from 27.29 to 29.92 Ma, with a relatively imprecise weighted mean of 28.87 ± 0.40 Ma (MSWD 3.18).

4. AGE SENSITIVITY ANALYSIS

In this section, we explore the influences of analytical and geological uncertainties in the age calculations for the Fish Canyon Tuff zircons. This treatment has been similarly applied to the titanite data, and in the interest of brevity, those results are summarized in Table 2.

4.1. Instrumental Detector Bias and Mass Fractionation

Linearity of the Daly detector was established by single collector measurement of $^{234}\text{U}/^{235}\text{U}$ and $^{236}\text{U}/^{235}\text{U}$ ratios in CRM U-500 over a range of ^{235}U ion beam intensities from 0.5 to 1.5×10^{-13} A, normalizing for mass bias to the certified $^{238}\text{U}/^{235}\text{U}$ value of 1.000302. CRM U-500 was selected as its minor U isotope ratios have values of similar magnitude to the range of $^{206}\text{Pb}/^{204}\text{Pb}$ ratios measured for the FCT zircons. A dead time factor of 19 ns yields an external reproducibility (1σ s.d.) of the mass-bias corrected ratios at $^{234}\text{U}/^{235}\text{U} = 0.010425 \pm 0.04\%$ and $^{236}\text{U}/^{235}\text{U} = 0.001526 \pm 0.09\%$, indicating comparable or better detector linearity at count rates ≤ 1.5 MHz.

The mass-dependent isotopic fractionation of U ions during

static multi-collector analysis was monitored using the ^{233}U - ^{235}U double spike. An uncertainty (2σ) in the uranium fractionation factor of $\pm 0.01\%$ /a.m.u. was propagated through the age calculations. Instrumental fractionation of Pb ions during single-collector analysis on the ion-counting Daly detector was estimated from daily measurements of 100 pg loads of NBS-981, which indicated a magnitude and standard deviation (2σ) of $0.15 \pm 0.04\%$ /a.m.u. throughout the study period. For isotopic ratio measurements on the Faraday cups, fractionation was measured on 10 ng loads of NBS-981 as $0.12 \pm 0.04\%$ /a.m.u. The reproducibility of the fractionation measurements was applicable not only during the study period, but over the past several years of analysis. This uncertainty is propagated in the error analysis for each zircon fraction, and thus deviations within these bounds do not affect the individual calculated ages of the zircon and titanite, or the weighted mean isotopic ages, outside of the previously quoted precision.

4.2. Tracer Calibration

The mixed ^{205}Pb - ^{233}U - ^{235}U tracer spike used at the M.I.T. TIMS lab has been calibrated repeatedly against gravimetric Pb and U solutions freshly prepared from solid assay materials (originally in the early 1990s at the Geological Survey of Canada in conjunction with M. Villeneuve and R. Parrish, and subsequently at M.I.T.) and the tracer Pb/U is inferred to be accurate to within 0.1% (2σ). Pb and U isotopic compo-

Table 2. U-Pb isotopic ages for Fish Canyon Tuff zircon and titanite

	Isotopic Ages (Ma)					
	$(^{206}\text{Pb}/^{238}\text{U})$			$(^{207}\text{Pb}/^{235}\text{U})$		
	Mean	(2 σ)	MSWD	Mean	(2 σ)	MSWD
<i>Weighted Mean Zircon Ages</i>						
No Disequilibrium Corrections						
Stacey-Kramers Model Pb (28 Ma)						
Single zircons	28.411	± 0.032	0.94	28.495	± 0.041	0.66
Multi-grain fractions	28.376	± 0.028	0.40	28.517	± 0.051	0.73
All zircons	28.396	± 0.023	0.87	28.506	± 0.029	0.67
Feldspar Common Pb ^a						
Single zircons	28.421	± 0.032	0.97	28.534	± 0.044	0.78
Multi-grain fractions	28.377	± 0.027	0.37	28.523	± 0.050	0.69
All zircons	28.402	± 0.023	0.93	28.529	± 0.030	0.74
Feldspar Common Pb w/Error ^b						
Single zircons	28.421	± 0.032	0.97	28.533	± 0.044	0.77
Multi-grain fractions	28.376	± 0.027	0.37	28.523	± 0.051	0.72
All zircons	28.402	± 0.023	0.93	28.528	± 0.030	0.74
²³⁰ Th Disequilibrium Corrections (All zircons) ^{a,c}						
[Th/U] _{magma} = 3.7	28.491	± 0.024	0.95			
2.2	28.478	± 0.024	0.97			
<i>Weighted Mean Titanite Ages</i>						
No Disequilibrium Corrections						
Stacey-Kramers Model Pb (28 Ma)						
Feldspar Common Pb ^a	28.120	± 0.050	1.50	26.57	± 0.45	3.10
Feldspar Common Pb w/Error ^b	28.533	± 0.050	1.60	28.87	± 0.40	3.18
²³⁰ Th Disequilibrium Corrected ^{a,c}	28.526	± 0.055	0.76	28.84	± 0.58	0.38
[Th/U] _{magma} = 3.7	28.495	0.050	1.60			
2.2	28.395	0.049	1.60			
<i>Zircon Concordia Ages (Ma)^{a,d}</i>						
No Disequilibrium Corrections						
without λ errors						
with λ errors ^e				28.445	discordant ± 0.041	1.40
²³⁰ Th Disequilibrium Corrections ([Th/U] _{magma} = 2.2)						
without λ errors						
with λ errors ^e				28.476	± 0.029	1.50
				28.498	± 0.035	1.03
<i>Preferred FCT Zircon Age</i>						
with analytical error						
with analytical error & tracer calibration error						
with analytical error, decay constant & tracer calibration error						
				28.476 \pm ± 0.058	± 0.029 ± 0.064	Ma

^a Common Pb composition of Feldspar B in Table 3.

^b Includes propagation of (2 σ) errors in common Pb composition: 2% in $^{206}\text{Pb}/^{204}\text{Pb}$; 1% in $^{207}\text{Pb}/^{204}\text{Pb}$ & $^{208}\text{Pb}/^{204}\text{Pb}$.

^c See Section 4.4 and Table 3 for details of ²³⁰Th correction.

^d Calculated using the algorithms of Ludwig (1998).

^e Uncertainties (2 σ) in uranium decay constants: $\lambda_{235} = 0.136\%$, $\lambda_{238} = 0.107\%$, following counting statistic errors of Jaffey et al. (1971).

sitions of the tracer spike have been monitored against possible laboratory contamination and remain unchanged since mixing. A further substantial test of the accuracy of tracer calibration is the measurement of concordant Precambrian zircon ages. To this end, single zircons from the Duluth Complex Anorthositic Series zircon standard (AS-3) of Paces and Miller (1993) were analyzed. Twelve concordant single zircons yield a Concordia age of 1099.1 ± 0.2 Ma (MSWD = 0.5; Schmitz and Bowring, in prep), identical to the results of Paces and Miller (1993). These results independently support the accuracy of the M.I.T. mixed Pb-U tracer calibration as well as its intercalibration with the U.S.G.S. mixed Pb-U tracer used in the earlier study. Anticipating our conclusions, we also note the excellent reproducibility of our FCT zircon age result with that of Oberli et al. (1990), again suggesting the accuracy of the M.I.T. spike calibration relative to a third laboratory.

With regard to the effect of tracer calibration uncertainty on the FCT zircon results, an uncertainty of 0.1% in the tracer Pb/U adds a proportionate systematic uncertainty to the final age results, that is approximately ± 29 k.y. While not applicable to subsequent comparisons made between U-Pb ages measured in this study, this uncertainty must necessarily be taken into account when considering the absolute accuracy of the FCT U-Pb results, particularly with respect to comparisons with other U-Pb zircon data from other laboratories, and to data from other isotopic decay schemes like K-Ar.

4.3. Common Pb Correction

The composition of initial common Pb can be estimated using a variety of techniques. The simplest estimate is that inferred from the two-stage Pb evolution model of Stacey and Kramers (1975). The common Pb composition of leached sani-

Table 3. Fish Canyon Tuff pumice glass Th/U contents and sanidine Pb isotopic compositions

	$^{206}\text{Pb}^a$	$^{207}\text{Pb}^a$	$^{208}\text{Pb}^a$	Th ^b (ppm)	U ^b (ppm)	Th
	^{204}Pb	^{204}Pb	^{204}Pb			U
Feldspar A	18.47	15.56	37.78			
Feldspar B	18.44	15.57	37.68			
Ds28K Feldspar ^c	18.38	15.50	37.46			
S293 BK Feldspar ^c	18.42	15.54	37.60			
Stacey-Kramers (28 Ma)	18.66	15.63	38.58			
FCT pumice 1				24.82	11.26	2.20
FCT pumice 2				18.24	8.25	2.21
FCT pumice 3				18.92	8.39	2.26

^a Error in isotopic ratios estimated at ± 0.05 (2σ) based on replicate analysis of NBS-981

^b Error in Th and U concentrations estimated at $< 2\%$ (2σ) based on replicate blind standards.

^c Data from Lipman et al. (1978).

dine feldspar from the FCT may also be measured. A third method uses the three-dimensional concordia diagram, in which the third axis represents a measure of the common Pb composition ($^{204}\text{Pb}/^{206}\text{Pb}$). Regression of these data in three dimensions yields the “Total Pb/U Isochron” date of Ludwig (1998), as well as the $^{207}\text{Pb}/^{206}\text{Pb}$ of the initial common Pb; for our purposes, the FCT data are, in fact, too radiogenic to provide a precise extrapolation to the common Pb composition.

We recognize that the use of the Stacey-Kramers model Pb composition may substantially bias age calculations for unradiogenic samples, particularly for the FCT titanite, which have $\text{Pb}^*/\text{Pb}_c < 1$. To establish a better estimate for the FCT initial common Pb composition, we sequentially leached two hand-picked 99.9+ % pure sanidine feldspar separates. The Pb isotopic compositions of the least radiogenic 5% HF leach of these two samples (Feldspar A and B) are listed in Table 3, along with the Pb isotopic compositions of two feldspar mineral separates measured by Lipman et al. (1978). The correspondence between these four feldspar measurements provides some indication of the isotopic homogeneity of the initial Pb of the FCT. The composition of “Feldspar B,” the least radiogenic leach of the two feldspar splits of this study in terms of $^{206}\text{Pb}/^{204}\text{Pb}$ ratio, is used throughout this paper to describe the initial common Pb of the FCT zircon and titanite.

The isotopic ratios and ages listed in Table 1 are calculated using the feldspar common Pb composition, but without propagation of error in the initial common Pb composition. The zircon data, in fact, are radiogenic enough to be insensitive to internal propagation of initial common Pb composition measurement errors. Table 2 shows that propagating this error does not perceptibly affect the statistics of the weighted mean dates. The sensitivity of the zircon isotopic ages to systematic error in the choice of initial common Pb composition is further explored in Table 2 by comparing the mean ages resulting from use of the Stacey-Kramers model Pb composition and the leached FCT sanidine Pb composition. While the difference in composition between the Stacey-Kramers model Pb and the measured feldspar Pb is large, ranging from 0.5 to 1%, the choice of either composition makes little difference in the statistics of the zircon weighted mean dates. There is a slight shift of single grain analyses towards a higher $^{207}\text{Pb}/^{235}\text{U}$ date, however this shift is within the calculated standard error of the

mean, and it is concluded that error associated with the initial common Pb correction are insignificant for zircon.

4.4. Intermediate Daughter Product Disequilibria

The U-Th-Pb systematics of young samples may be affected by disequilibrium partitioning of intermediate daughter nuclides within the decay chains during crystallization of the mineral-isotopic system under scrutiny. Sufficiently long-lived intermediate daughter products that may significantly perturb the equilibrium systematics are ^{230}Th and ^{234}U in the ^{238}U - ^{206}Pb decay chain, and ^{231}Pa in the ^{235}U - ^{207}Pb decay chain (Mattinson, 1973; Schärer, 1984). In the former decay chain, ^{234}U is not substantively fractionated from ^{238}U during high-temperature magmatic processes, such that only ^{230}Th disequilibrium need be considered. Because of the existence of ^{232}Th , which may be considered essentially stable on time scales of $< 10^6$ years, ^{230}Th disequilibrium is amenable to quantitative treatment. Disequilibrium between minerals and magma was quantified using standard methodology; individual fractionation factors for each sample were calculated as $f = [\text{Th}/\text{U}]_{\text{mineral}}/[\text{Th}/\text{U}]_{\text{magma}}$, where the brackets indicate concentration ratios. $[\text{Th}/\text{U}]_{\text{mineral}}$ was calculated from the measured radiogenic ^{208}Pb and the uranium isotope dilution measurements for each mineral fraction, and for the FCT zircons ranged from 0.46 to 1.1. To place a firm constraint on $[\text{Th}/\text{U}]_{\text{magma}}$, three samples of phenocryst-free pumice shards were analyzed, yielding variable Th and U concentrations from 24.8 to 18.2 ppm and 11.3 to 8.3 ppm respectively, but consistent Th/U ratios of 2.2 ± 0.1 (Table 3). Using this value for $[\text{Th}/\text{U}]_{\text{magma}}$, all FCT zircons exhibit Th-deficiency, with the magnitude of the ^{230}Th correction for individual zircon analyses ranging from 50 to 90 k.y. The ^{230}Th disequilibrium-corrected $^{206}\text{Pb}^*/^{238}\text{U}$ isotopic ages for each analysis are listed in Table 1. The effect of the ^{230}Th correction is illustrated in Figure 4, where the error ellipses of the corrected zircon analyses shift upwards towards concordia.

Evaluation of the disequilibrium partitioning is limited by our knowledge of the Th/U of the melt coexisting with the crystal during growth. This ratio may evolve in the magma chamber over time, and may not correspond to the ratio in the magma at the time of eruption as captured by glass compositions. Petrologic studies of volcanic and plutonic rocks (Zie-

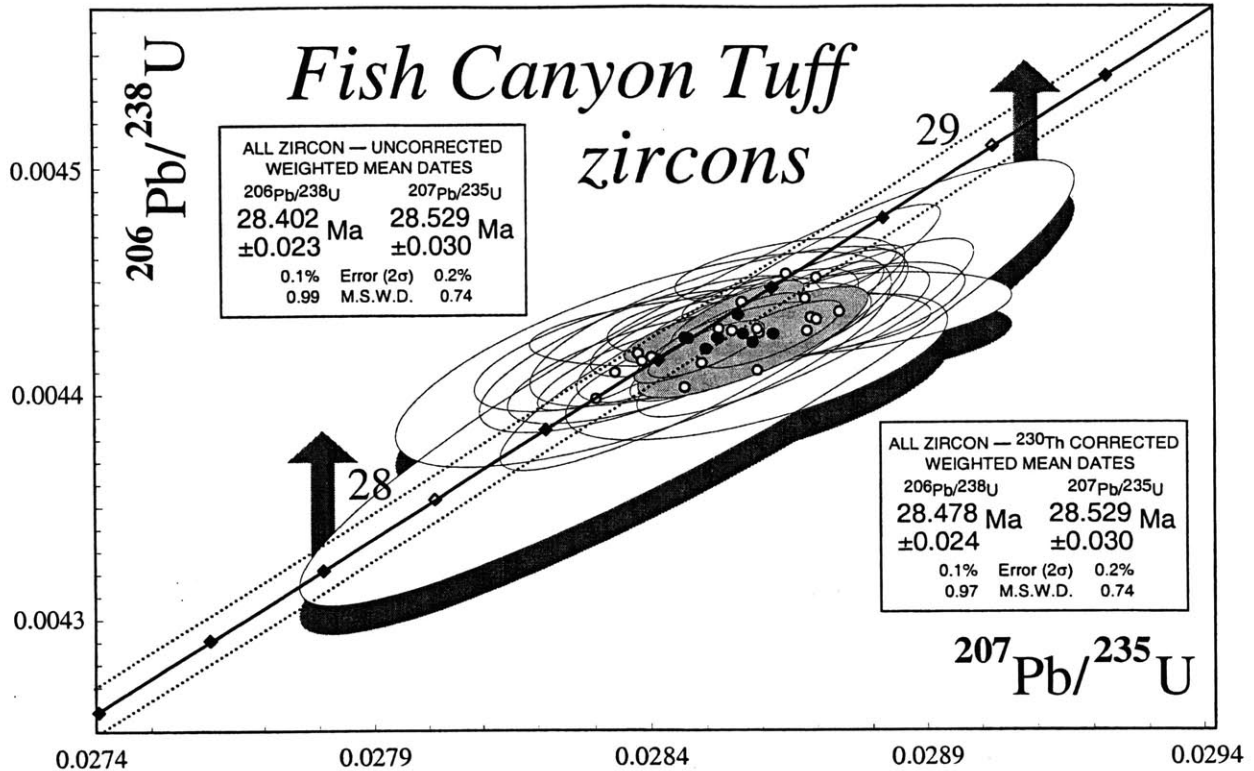


Fig. 4. U-Pb concordia diagram of all zircon fractions illustrating effect of ^{230}Th disequilibria corrections, which increase $^{206}\text{Pb}/^{238}\text{U}$, moving the error ellipses upwards toward concordia. Symbols and details of concordia envelope as in Figure 2.

linski and Lipman, 1976; Barth et al., 1989) suggest, however, that the Th/U of evolving metaluminous magmatic systems decreases with the degree of differentiation, probably by the fractionation of Th-rich phases like allanite or titanite. Specifically, the data of Zielinski and Lipman (1976) show a well-correlated trend of decreasing Th/U from 3.7 to 2.5 in alkali andesite through rhyolitic compositions in the Summer Coon volcanic series, erupted a few million years before the FCT from a nearby center in the San Juan Mts. A survey of literature data also suggests that a value of Th/U = 2.2 is at the low end of plausible metaluminous rhyolitic magmatic compositions. By inference then, the measured Th/U in pumice glass of the FCT represents the minimum Th/U of the magma in equilibrium with FCT accessory minerals over their crystallization interval.

In Figure 5, the sensitivity of the $^{206}\text{Pb}/^{238}\text{U}$ isotopic age of FCT zircon and titanite to a wide range of assumed $[\text{Th}/\text{U}]_{\text{magma}}$ is explored. It is immediately apparent that the calculated $^{206}\text{Pb}/^{238}\text{U}$ age of the zircons is very insensitive to values of $[\text{Th}/\text{U}]_{\text{magma}} > 2.2$, with only a 10 k.y. change for a very large shift in $[\text{Th}/\text{U}]_{\text{magma}}$ from 2.2 to 3.7. As we are confident that 2.2 is a *minimum* for the Th/U of the Fish Canyon Tuff magma chamber, then this analysis suggests that the ^{230}Th disequilibrium corrected $^{206}\text{Pb}/^{238}\text{U}$ age of 28.478 ± 0.024 Ma is robust to large variations in magmatic Th/U well within the measurement errors.

The Th/U ratios of the FCT titanite are ~ 5 , thus the $^{206}\text{Pb}/^{238}\text{U}$ isotopic age for the titanite is more sensitive than zircon to initial $^{230}\text{Th}/^{238}\text{U}$ disequilibria, in this case toward Th-

excesses. Figure 5 also demonstrates the greater sensitivity of the titanite $^{206}\text{Pb}/^{238}\text{U}$ isotopic age to the assumed $[\text{Th}/\text{U}]_{\text{magma}}$. While no phase equilibria studies of the FCT extend to titanite, other experimental studies (Green and Pearson, 1986) demonstrate that in general Ti-rich accessory phase saturation is achieved near the liquidus in intermediate to silicic magmas. Titanite thus may have entered the paragenetic sequence earlier than zircon in the magmatic evolution of the FCT, and by inference seen a wider spectrum of $[\text{Th}/\text{U}]_{\text{magma}}$ than that recorded in the FCT glassy pumice compositions. However, again assuming that the FCT $[\text{Th}/\text{U}]_{\text{magma}}$ has a *minimum* of 2.2, yielding the *maximum* titanite disequilibrium correction, the resulting weighted mean $^{206}\text{Pb}/^{238}\text{U}$ date of 28.395 ± 0.049 Ma (Table 2), is a robust *minimum* estimate of the isotopic age of the FCT titanite.

In the ^{235}U - ^{207}Pb decay chain, a quantitative knowledge of the partitioning of ^{231}Pa between accessory minerals and melts is lacking. Qualitative assessments of Pa partitioning relative to U and Th, based on relative ionic radii, suggest that Pa^{4+} depletion in zircon would be less than that of Th^{4+} (Mattinson, 1973; Barth et al., 1989), following the order of relative ionic radii of $\text{Zr}^{4+} < \text{U}^{4+} < \text{Pa}^{4+} < \text{Th}^{4+} = 0.84 < 1.00 < 1.01 < 1.05$ (Shannon, 1976). However Barth et al. (1989) discuss the possibility that in relatively oxidizing magmatic conditions, protactinium is present as Pa^{5+} (i.r. 0.91), in which case enrichment of Pa^{5+} relative to U^{4+} may occur in zircon, due to its closer similarity in ionic radius to Zr^{4+} . In a subsequent study of elemental partitioning between immiscible silicate and carbonate melts, Jones et al. (1995) noted that, from limited

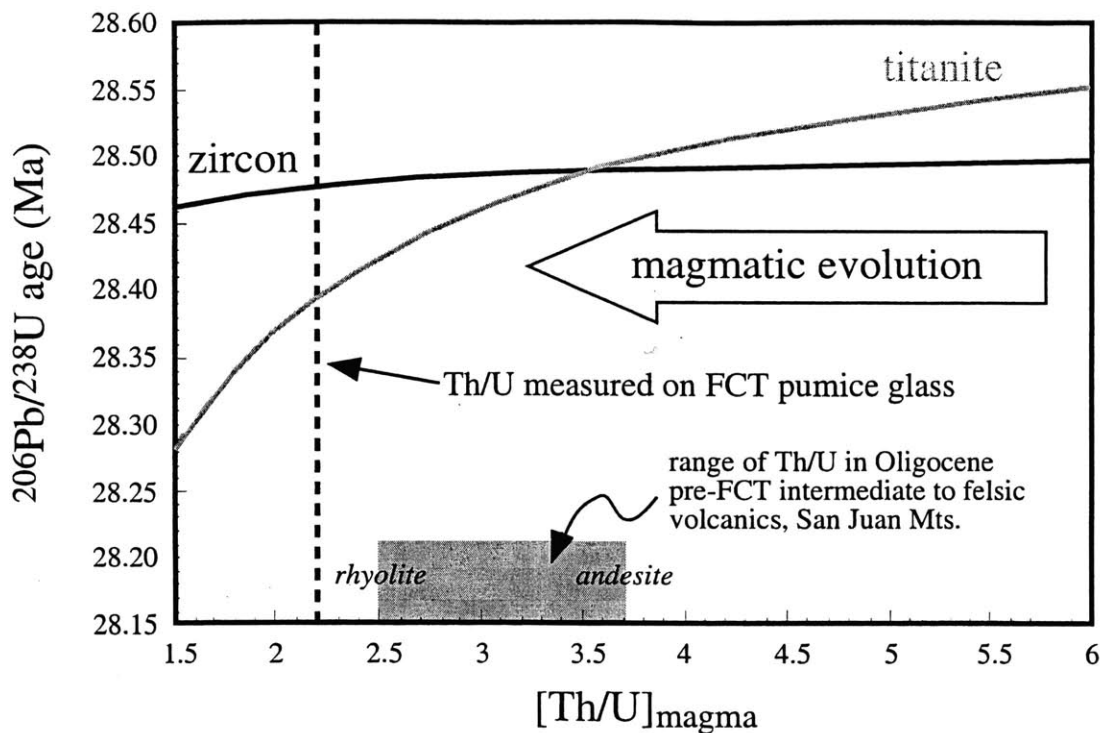


Fig. 5. Effect of varying $[Th/U]_{magma}$ on ^{230}Th -disequilibrium corrected $^{206}Pb/^{238}U$ ages for zircon and titanite. Calculation follows standard methodology, using median measured $[Th/U]_{mineral}$ values of 0.643 and 4.99 for zircon and titanite, respectively. Negligible sensitivity of corrected zircon age for $[Th/U]_{magma}$ greater than the measured value for FCT pumice glass is consistent with an inferred lowering of magmatic Th/U during metaluminous silicic magma petrogenesis (Zielinski and Lipman, 1976). By similar arguments, the titanite age calculated using the FCT pumice Th/U is a robust minimum age.

data, Pa partitioning was consistent with correlations between ionic field strength ($z/r = \text{ionic charge/ionic radius}$) and partition coefficient noted for other elements, provided Pa was present in the 5+ valence state.

A specific assessment of ^{231}Pa disequilibrium effects in the FCT zircons follows for the two cases of tetravalent versus pentavalent protactinium. Assuming that $(^{231}Pa/^{235}U)_{magma} = 1$, where the parentheses now indicate activity ratios, then $f_{Pa/U} = (^{231}Pa/^{235}U)_{zircon}$ and $f_{Th/U} = (^{230}Th/^{238}U)_{zircon}$. If tetravalent ^{231}Pa was excluded from zircon to the same degree as Th^{4+} , then the change in the weighted mean zircon $^{207}Pb/^{235}U$ date is approximately equal to the product of $(\lambda_{230}/\lambda_{231})$ and the median $(^{230}Th/^{238}U)_{zircon}$, or approximately 32 k.y. older. The previously cited ionic radius arguments, however, suggest initial $(^{231}Pa/^{235}U)_{zircon}$ substantially closer to unity than $(^{230}Th/^{238}U)_{zircon}$, such that it is likely that tetravalent ^{231}Pa deficiency would only shift the weighted mean $^{207}Pb/^{235}U$ date by < 10 k.y., which is well within measurement uncertainties and would not substantially affect assessment of concordance between $^{207}Pb/^{235}U$ and $^{206}Pb/^{238}U$ ages.

On the other hand, pentavalent ^{231}Pa excess in the FCT zircons would shift the disequilibrium corrected $^{207}Pb/^{235}U$ dates to younger values. Accordingly, excess ^{231}Pa could explain the slight residual normal discordancy of the FCT zircon data set (following ^{230}Th corrections) if the zircons had a median initial $(^{231}Pa/^{235}U)_{zircon} \approx 2$. While such an initial activity ratio may be crystal-chemically reasonable, it remains

speculative until such time as quantitative measurements of $(^{231}Pa/^{235}U)$ in young zircons and/or further thermodynamic or experimental constraints on protactinium valency in silicate melts as a function of fO_2 are achieved. However, regardless of the details of ^{231}Pa partitioning, it does not appear that its associated disequilibrium effects in zircon can cause a resolvable *greater* degree of discordance of the FCT zircon data set.

4.5. Concordia Age

The "Concordia Age" algorithms of Ludwig (1998) allow the quantitative assessment of errors and probabilities of both age equivalence and *concordance* for sets of U-Pb isotopic analyses. In addition, they provide a means of propagating decay constant uncertainties into the error associated with a U-Pb or Pb-Pb age. The Concordia ages for the combined single- and multi-grain zircon data set, for a variety of cases, are listed in Table 2. Ages were first calculated for the data set without ^{230}Th disequilibrium corrections. In this case, without decay constant uncertainties, the data set is discordant. However, introducing the decay constant counting statistic errors (2σ) of Jaffey et al. (1971) ($\lambda_{235} = 0.136\%$ and $\lambda_{238} = 0.107\%$) the FCT zircon data set yields a Concordia age of 28.445 ± 0.041 with a small probability of concordance and equivalence ($MSWD = 1.4$).

When appropriate ^{230}Th disequilibrium corrections ($[Th/U]_{magma} = 2.2$) are applied to the FCT zircon data set, its

apparent concordance improves dramatically. Even without decay constant uncertainties, the FCT data set has a small probability of concordance, with a Concordia age = 28.476 ± 0.029 Ma (MSWD = 1.5). Propagating decay constant errors yields a statistically indistinguishable Concordia age of 28.498 ± 0.035 Ma with a high probability of concordance and equivalence (MSWD = 1.03). This latter Concordia age is apparently slightly more leveraged by the $^{207}\text{Pb}/^{235}\text{U}$ age of the zircons, and because of the aforementioned uncertainties in the behaviour of ^{231}Pa and its effect on the $^{207}\text{Pb}/^{235}\text{U}$ age, we take our preferred crystallization age of the FCT zircons for inter-comparison of within-laboratory U-Pb data to be the former Concordia age of 28.476 ± 0.029 Ma, which is essentially equal to the ^{230}Th disequilibrium corrected weighted mean $^{206}\text{Pb}/^{238}\text{U}$ date. For purposes of comparison with isotope dilution U-Pb data from other laboratories, the addition of a 0.1% uncertainty in tracer Pb/U calibration (see Section 4.2) brings the FCT zircon age and error to 28.476 ± 0.058 Ma. Finally, for comparisons with other radioisotopic decay schemes, further addition of decay constant uncertainty yields a preferred age and error for the FCT zircons of 28.476 ± 0.064 Ma, which may serve as a precise and accurate benchmark for decay scheme intercalibration.

5. DISCUSSION

5.1. FCT Zircon Age Distributions

The median propagated error in individual FCT zircon ages is about 150 k.y., which approaches commonly quoted time-scales of silicic magmagenesis (Christensen and DePaolo, 1993; Davies et al., 1994; Davies and Halliday, 1998; Reid et al. 1997; Reid and Coath, 2000). The resolution of single zircon ages thus opens up the possibility of constraining the preeruptive residence time of zircon-saturated magma within the FCT caldera system if it can be shown that the range of single zircon ages exceeds analytical uncertainty. Alternatively, if magma chamber residence is minimal, then the very small standard error statistics of the inverse variance weighted mean age of the FCT zircons should place tight constraints on the eruption age of the tuff. Either scenario requires a closer examination of both the distribution of single zircon ages, as well as the applicability of the applied sample statistics. The relatively large size of the FCT zircon data set allows us to explore these issues through probability density functions.

Histograms and probability density functions of FCT zircon ages are illustrated in Figure 6. These sample functions are overlain upon normal distributions calculated from the median uncertainty of individual zircon ages, scaled (equal area) and centered on the means of the respective sample distributions. Examination shows that all sample age functions are in fact well-described by the gaussian distribution of a singular-valued mean, and do not display minor peaks, or substantial asymmetry. Slight skewing of the probability functions to younger age, particularly in the $^{206}\text{Pb}/^{238}\text{U}$ ages, is due wholly to the relatively high imprecision of the single youngest zircon grain, $z18$. The slightly greater tailing of the sample distributions relative to the model distributions is not considered significant.

Two conclusions are drawn from this analysis. First, all of the data points lie within two standard deviations of the weighted mean as defined by the analytical uncertainty of

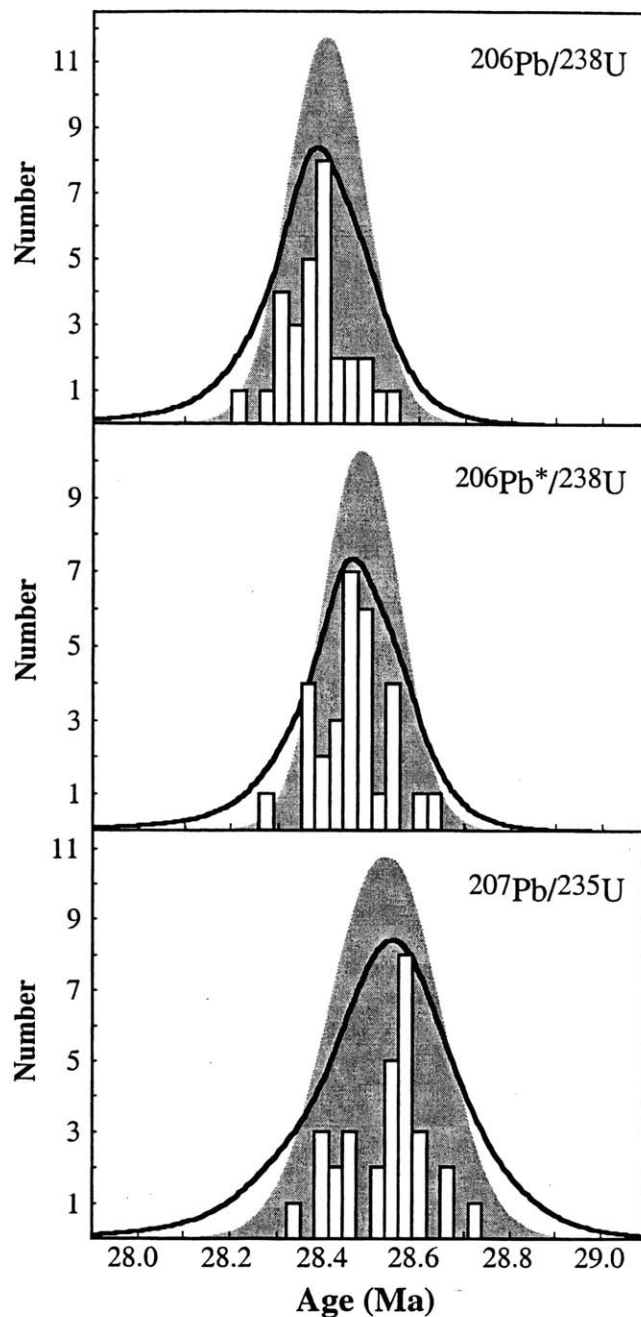


Fig. 6. Histograms and probability density functions (thick black lines) of zircon $^{206}\text{Pb}/^{238}\text{U}$, $^{206}\text{Pb}^*/^{238}\text{U}$ (^{230}Th -disequilibrium corrected), and $^{207}\text{Pb}/^{235}\text{U}$ ages from the Fish Canyon Tuff. Probability density functions are constructed by summing the probability distributions of each datum with normally distributed errors. Each sample probability density function is overlaid upon a similarly scaled (equal area) normal probability function calculated from the median uncertainty of individual zircon analyses and the inverse-variance weighted average of all fractions.

individual analyses (150 k.y.). This result demands a fairly rapid, uniform period of growth, likely <200 k.y. for the sampling of zircons analyzed. Second, as the assumption of normally distributed errors around a singular valued mean appears to hold for this data set, the precision of the Concordia

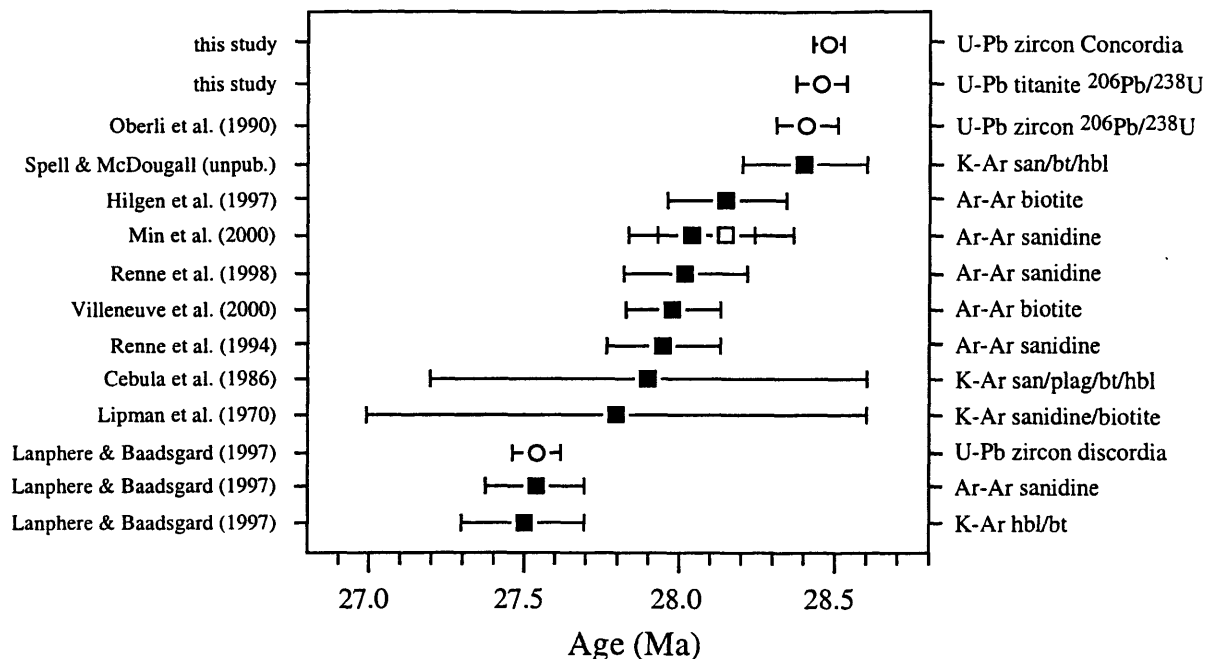


Fig. 7. Comparison of "ages" of the Fish Canyon Tuff derived by various mineral-isotopic systems. All data plotted with 2σ errors. Measurements based on the U-Pb isotopic systems are designated with circles, and those on the K-Ar decay scheme by squares. All ages were calculated using decay constants recommended by Steiger and Jäger (1977), with the exception of the data of Min et al. (2000) which contrast ages obtained with the ^{40}K decay constants of Steiger and Jäger (1977) (filled square) versus Audi et al. (1997) (open square).

age for the zircon data set is statistically, if not geologically justified.

5.2. Intercalibration of U-Pb and $^{40}\text{Ar}/^{39}\text{Ar}$ Geochronometers

The "true" age of the FCT eruption is an important parameter for $^{40}\text{Ar}/^{39}\text{Ar}$ geochronology, which uses FCT sanidine as a common neutron fluence monitor and laboratory intercalibration standard. Thus the age assumed for FCT sanidine is the foundation of much of the modern $^{40}\text{Ar}/^{39}\text{Ar}$ geochronological database. Measuring the "true" eruption age of the FCT by U-Pb geochronology is also of considerable value for establishing the absolute intercalibration of the U-Pb and $^{40}\text{Ar}/^{39}\text{Ar}$ isotopic geochronometers. This latter need is especially acute considering the increasing comparison of the two systems in applications ranging from the tempo of mass extinction (Bowring et al., 1998) to the age of meteorites (Renne et al., 2000).

Figure 7 shows various estimates of the eruption age of the Fish Canyon Tuff by both U-Pb and $^{40}\text{Ar}/^{39}\text{Ar}$ methods, clearly illustrating the discrepancy between the two radiometric systems. Of the three attempts to date the FCT by U-Pb zircon methods, two—this study and that of Oberli et al. (1990) agree within analytical uncertainty. The third determination of Lanphere and Baadsgard (2001) relies on the lower intercept of a discordia array to define a significantly younger age for the FCT zircons. Considering systematic errors associated with Pb-loss and inheritance which clearly influenced the large bulk zircon fractions used in that study, the young lower intercept age is not considered a robust estimator of the crystallization age of the zircons. Additionally, a profound lack of inheritance

in the zircons analyzed in the present study suggests either that inherited zircons are quite heterogeneously distributed within the FCT, or that inherited components are easily avoided during the sample selection stage of analysis.

Measurements of the age of the FCT using the K-Ar and $^{40}\text{Ar}/^{39}\text{Ar}$ methods mainly on sanidine and biotite span a wide range from 27.5 to 28.15 Ma (Fig. 7). Numerous $^{40}\text{Ar}/^{39}\text{Ar}$ studies in recent years have promoted an upward revision in the "accepted" age of FCT sanidine and biotite, however the highest published $^{40}\text{Ar}/^{39}\text{Ar}$ age, 28.15 ± 0.15 Ma (Hilgen et al., 1997), remains resolvable younger than the U-Pb zircon age, and the arguably most widely accepted age, approx. 28.0 Ma (Renne et al., 1998) is over 400 k.y. younger. Unpublished sanidine, hornblende and biotite K-Ar ages for the FCT of 28.4 ± 0.2 Ma (Spell and McDougall, as quoted in McDougall and Harrison, 1999) are, to our knowledge, the only results concordant with the zircon systematics. The apparent 1.3 to 1.7% discrepancy between ages calculated from the two decay systems is commonly ascribed to two contrasting lines of reasoning. The first explanation invokes systematic error in the decay constant of ^{40}K . Renne et al. (1998) noted contrasting values for the ^{40}K decay constant used in the geological and physics communities, the later being significantly lower than the value of $5.543 \times 10^{-10} \text{ yr}^{-1}$ agreed to by I.U.G.S. convention (Steiger and Jäger, 1977). Min et al. (2000) summarized the various experimental data for the ^{40}K decay constant and, in a first attempt at a systematic cross-calibration of the K-Ar system to the highly precise and accurate U-Pb decay schemes, presented coexisting $^{40}\text{Ar}/^{39}\text{Ar}$ sanidine and U-Pb zircon data for a 1.1 Ga rhyolite which they interpret as

supporting a ^{40}K decay constant-derived bias of $\sim 1\%$ between the two radiometric systems. A similar cross-calibration of the K-Ar system to U-Th-Pb chronometers has been presented by Villeneuve et al. (2000).

The second explanation for the FCT age discrepancy ascribes the older U-Pb zircon age to crystallization and residence of zircon in the magma chamber of the FCT over a period of at least several hundred thousand years before eruption of the tuff. This residence time argument hinges upon the ability of a mineral to retain radiogenic parent and daughter nuclides against diffusive loss at ambient magmatic temperatures. Diffusive loss of Ar from sanidine and biotite at magmatic conditions is widely accepted. However for zircon, experimental diffusion data and empirical observations of inherited zircons in felsic igneous rocks indicate that this mineral can quantitatively retain U, Th, and radiogenic Pb at temperatures several hundred degrees higher than that inferred for the Fish Canyon magma chamber before eruption. Thus qualitatively, the zircon magma residence argument appears tenable. However, the FCT zircon and titanite data presented in this study places unique constraints on the magma residence hypothesis, as explored in the next section.

5.3. Magma Chamber Residence Time

Bounds on the life-span of magma chambers like that which sourced the Fish Canyon Tuff may be extracted from eruption recurrence interval studies of recently active silicic volcanic centers. A survey of the literature seems to indicate two end-member situations. One extreme is represented by the Taupo Volcanic Zone of New Zealand's North Island, where geochemical and geochronological data indicate that magma batches of distinctive chemistry have a residence time of only thousands to tens of thousands of years (Houghton et al., 1995; Hochstein et al., 1993). At the other end of the spectrum, the Yellowstone volcanic center has produced three magmatic cycles culminating in large rhyolitic caldera eruptions, with a much longer recurrence interval of approximately 600 k.y. (Christiansen, 1984).

Turning to isotopic constraints, recent in situ ion microprobe dating of very young zircons by U-Pb and ^{230}Th - ^{238}U disequilibrium methods allow a direct quantification of zircon growth and magmatic residence intervals. These age determinations also demonstrate a spectrum of magma chamber residence intervals for silicic eruptives from the Long Valley caldera of California. While evidence for prolonged zircon residence times of >200 k.y. was obtained for the youngest lava domes from Long Valley (Reid et al., 1997), similar studies of the Bishop Tuff reveal a <100 k.y. residence interval between zircon crystallization and eruption of the tuff (Reid and Coath, 2000). Considering all of this data, we are left with a wide range in the possible lifetime of large silicic magma chambers, from >1 to <600 k.y.

The geologic evidence for the lifespan of the specific magma chamber resulting in the Fish Canyon Tuff is ambiguous. Steven and Lipman (1976) considered the seventeen ash flows erupted in the San Juan Mountains between 30 and 26 Ma (Lipman et al., 1970) to be sourced from cuppolas developed within a large composite batholith. FCT emplacement was preceded by at least nine caldera-forming ash flow eruptions in

the San Juans, however the FCT was only the second major ash flow tuff erupted from the central San Juan volcanic field, with most prior activity occurring to the east and west near loci of early Oligocene andesitic volcanism (Steven and Lipman, 1976). The distinctive chemistry and isotopic signature of each ash flow tuff (Lipman et al., 1978) also indicate a unique petrologic evolution for each magma batch and might suggest a life-span significantly shorter than that of the entire magmatic episode.

Knowledge of the onset of zircon crystallization during the paragenetic sequence of the FCT magma chamber is obviously important for inferring zircon residence times. The crystallization of zircon will begin as the magma cools through the temperature of zirconium saturation. This zircon saturation temperature has been constrained by experiments as a function of magma composition (Watson and Harrison, 1983). For the metaluminous Fish Canyon Tuff, a wide range of Zr concentrations from 100 to 200 ppm yield a fairly restricted range in zircon saturation temperatures of 730° to 780°C , which are well within uncertainty of the estimated eruptive temperature of $760 \pm 30^\circ\text{C}$ from Fe-Ti oxide equilibria (Johnson and Rutherford, 1989) considering systematic errors for each thermometer. These calculations may be interpreted as indicating that zircon began crystallizing near the temperature conditions extant within the Fish Canyon magma chamber immediately before eruption.

A more quantitative test of the residence time argument involves the analysis of the U-Pb isotopic systematics of a mineral which, like the K-Ar system in sanidine, remains open to diffusive exchange until eruption. The accessory mineral titanite has a nominal closure temperature for Pb diffusion of 720°C (diffusion parameters of Cherniak, 1993; spherical geometry, $500 \mu\text{m}$ diffusion dimension; $100^\circ\text{C}/\text{m.y.}$ cooling rate) for maximum grain sizes seen in the FCT, somewhat less than the temperature of last equilibration of the FCT recorded in Fe-Ti oxides. Thus, unlike zircon, titanite could have remained an open system until quenching upon explosive eruption. This interpretation is dependent however on the inferred closure temperature of titanite. Examination of the dependence of closure temperature on diffusion domain radius and cooling rate reveals that for faster cooling rates of $1000^\circ\text{C}/\text{m.y.}$, calculated closure temperatures for the largest grains (assuming grain size = diffusion dimension) approach 780°C . By these calculations, the cores of rapidly crystallized large titanite grains could conceivably preserve some fraction of radiogenic Pb at FCT eruptive conditions. However, considering that partial retention could be mitigated by higher magmatic temperatures in the FCT magma chamber before eruption, the applicability of residence time arguments to titanite seems unlikely. The isotopic date of the FCT titanite is thus reasonably assumed to represent their isotopic closure age.

The precision and accuracy of the U-Pb FCT titanite dates are affected by both initial common Pb assumptions and intermediate daughter-product disequilibria to a much greater degree than the FCT zircons. As previously noted, the Pb isotopic composition of leached FCT sanidine feldspar provides our best proxy for the initial Pb isotopic composition of the FCT magma, and does cause the titanite analyses to converge upon concordia (Fig. 3). Correction for initial ^{230}Th excess in the titanite with the same $[\text{Th}/\text{U}]_{\text{magma}}$ used for zircon results in a

robust *minimum* weighted mean $^{206}\text{Pb}/^{238}\text{U}$ date for the titanite (see Section 4.4 and Fig. 5). This date is relatively precise at 28.395 ± 0.049 Ma (MSWD 1.6). The significance of this result is that the titanite date is only slightly younger, and essentially within error of the Concordia age of the FCT zircons at 28.476 ± 0.029 Ma. If indeed titanite did not quantitatively retain radiogenic Pb before quenching upon eruption, then the correspondence of the titanite closure age and zircon crystallization age for the FCT indicate a barely resolvable residence interval for the FCT zircons of 0 to 160 k.y.

To summarize, the near-synchronicity of the U-Pb zircon and titanite systematics, combined with the extremely narrow zircon age distribution of ± 150 k.y. about the mean of 28.476 Ma, must be incorporated into any model of magmatic residence to explain the entire discrepancy between the U-Pb and $^{40}\text{Ar}/^{39}\text{Ar}$ estimates for the eruption of the FCT. If titanite remains an isotopically open system at magmatic conditions, then the U-Pb titanite systematics obviate a significant residence time rationale for the age discrepancy. Even setting aside the U-Pb titanite results, however, the FCT zircon age distribution requires rapid crystallization over a narrow time interval. This in turn necessitates a magmatic residence model in which essentially all of the zircon in the FCT crystallized rapidly in the FCT magma over perhaps 200 k.y., and then was held in stasis with no further crystallization or crystal resorption for a further 200 to 300 k.y. before eruption. Considering the ad hoc nature of such a model, magmatic residence time arguments to explain the entire discrepancy between precise U-Pb zircon and $^{40}\text{Ar}/^{39}\text{Ar}$ sanidine ages for the FCT appear considerably weakened.

5.4. U-isotope Decay Constant Uncertainties

The decay constants of ^{235}U and ^{238}U are the most precisely measured constants used by the geochronological community, with counting-statistic errors (2σ) of 0.136% and 0.108%, respectively (Jaffey et al., 1971). Nonetheless, the possibility of systematic errors exists, and recent discussions of U decay constant uncertainties applied to zircon geochronology have proposed (Mattinson, 1987) and supported (Ludwig, 1998; 2000) larger total uncertainties of 0.20% (^{235}U) and 0.16% (^{238}U). Measurement of radiogenic Pb/U ratios in closed natural systems provides another method for evaluation of the accepted U decay constants (Nier, 1939; Banks and Silver, 1966; Mattinson, 1973). Unfortunately experience has shown that the majority of natural systems are not closed, and even the refractory nature of zircon does not guarantee this necessary condition. However the FCT zircons analyzed in this study appear to provide a suitable closed system for this analysis.

The precise, concordant FCT zircon data set may be used to evaluate the precision and accuracy of the currently accepted U decay constants. The simplest and most important observation is that when ^{231}Pa and ^{230}Th -disequilibrium effects are evaluated, the FCT zircon data set is concordant to a high probability utilizing the decay constants with associated counting statistic errors of Jaffey et al. (1971), testifying to the quality and accuracy of the original counting experiments. The recent proposed revision of the ^{235}U decay constant by Mattinson (2000), while permissible, is not necessary for concordance of the FCT zircon data set. Similarly, the larger systematic U decay constant errors proposed by Mattinson (1987) are unnecessary for

concordance of the FCT zircon data. We recognize, however, that FCT zircons are not an ideal sample for evaluating the U decay constants because of their young age and corresponding sensitivity to intermediate daughter product disequilibria. Nonetheless, we believe this study illustrates the potential that further high-precision single zircon geochronological studies have for constraining the precision and accuracy of the U decay constants.

6. CONCLUSIONS

1. A precise U-Pb zircon crystallization Concordia age of 28.476 ± 0.029 Ma has been obtained for a sample of the Fish Canyon Tuff, which takes into account sources of analytical and geological uncertainty including instrumental mass fractionation, initial common Pb composition, and ^{230}Th disequilibrium effects on the $^{206}\text{Pb}/^{238}\text{U}$ decay chain. Probability density functions of the thirty individual zircon ages indicate rapid crystallization of the FCT zircon over a restricted time interval probably less than 200 k.y. When decay constant errors and uncertainty in tracer Pb/U ratio are included, the resulting FCT zircon age of 28.476 ± 0.064 Ma provides a very precise and accurate benchmark for the intercalibration of other radioisotopic decay schemes, including $^{40}\text{Ar}/^{39}\text{Ar}$.
2. U-Pb systematics of fourteen single and multi-grain fractions of co-existing titanite, when corrected for initial common Pb and ^{230}Th disequilibria, also yield a relatively precise minimum $^{206}\text{Pb}/^{238}\text{U}$ date of 28.395 ± 0.049 Ma, which is only slightly younger and essentially within error of, the FCT zircon age. If U-Pb systematics in titanite remain open at the conditions of the FCT magma chamber, then the synchronicity between titanite closure age and zircon crystallization age indicates a very short magmatic residence time for the later mineral.
3. Magmatic residence time arguments to explain the entire apparent $\sim 1.5\%$ discrepancy between the equally precise FCT U-Pb zircon and $^{40}\text{Ar}/^{39}\text{Ar}$ sanidine ages appear considerably weakened by the zircon and titanite systematics presented in this study. This conclusion supports recent calls for re-examination of the ^{40}K decay constant, and the assumed ages of primary $^{40}\text{Ar}/^{39}\text{Ar}$ age standards.
4. The concordance of the FCT zircon data set suggests the accuracy of the U decay constants of Jaffey et al. (1971) to well within their quoted 2σ counting statistic errors. While not an ideal sample for evaluating the U decay constants, due to its youth and uncertainties regarding intermediate daughter product disequilibria, these zircon data for the Fish Canyon Tuff indicate the potential value of further high precision single-zircon geochronological studies for placing tighter constraints on U decay constant uncertainties, with important consequences for the absolute precision of the $^{206}\text{Pb}/^{238}\text{U}$, $^{207}\text{Pb}/^{235}\text{U}$, and $^{207}\text{Pb}/^{206}\text{Pb}$ chronometers.

Acknowledgments—The authors wish to thank Bill Macintosh and Matt Heizler for the sample of FC-2 used in this work. Ken Ludwig is thanked for numerous discussions regarding the precision and accuracy of U-Pb zircon geochronology, as well as for providing a copy of his Isoplot/Ex software. Our appreciation is also extended to Felix Oberli, Jim Mattinson, and an anonymous reviewer for their thoughtful and thorough reviews. This material is based upon work supported in part by the U.S. Army Research Office under research agreement no.

DAAH049510560, and by NASA grant NCC 21053 and NSF grant EAR9725727.

Associate editor: K. Mezger

REFERENCES

- Audi G., Bersillon O., Blachot J., and Wapstra, A. H. (1997) The NUBASE evaluation of nuclear and decay properties. *Nucl. Phys. A.* **624**, 1–124.
- Banks P. O. and Silver, L. T. (1966) Evaluation of the decay constant of uranium 235 from lead isotope ratios. *J. Geophys. Res.* **71**, 4037–4046.
- Barth S., Oberli F. and Meier M. (1989) U-Th-Pb systematics of morphologically characterized zircon and allanite: a high-resolution isotopic study of the Alpine Renssen pluton (northern Italy). *Earth Planet. Sci. Lett.* **95**, 235–254.
- Bowring S. A., Erwin D. H., Jin Y. G., Martin M. W., Davidek K., and Wang W. (1998) U/Pb zircon geochronology and tempo of the end-Permian mass extinction. *Science*. **280**, 1039–1045.
- Cherniak D. J. (1993) Lead diffusion in titanite and preliminary results on the effects of radiation damage on Pb transport. *Chem. Geol.* **110**, 177–194.
- Christensen, J. N. and DePaolo D. J. (1993) Time scales of large volume silicic magma systems: Sr isotopic systematics of phenocrysts and glass from the Bishop Tuff, Long Valley, California. *Contrib. Mineral. Petrol.* **113**, 100–114.
- Christiansen R. L. (1984) Yellowstone magmatic evolution: its bearing on understanding large-volume explosive volcanism. In *Explosive Volcanism: Inception, Evolution, and Hazards* (eds. National Research Council Geophysics Study Committee) pp. 85–95. Studies in Geophysics, National Academy Press, Washington, D.C.
- Davies G. R. and Halliday A. N. (1998) Development of the Long Valley rhyolitic magma system; strontium and neodymium isotope evidence from glasses and individual phenocrysts. *Geochim. Cosmochim. Acta.* **62**, 3561–3574.
- Davies G. R., Halliday A. N., Mahood G. A., and Hall C. M. (1994) Isotopic constraints on the production rates, crystallization histories and residence times of pre-caldera silicic magmas, Long Valley, California. *Earth Planet. Sci. Lett.* **125**, 17–37.
- Gerstenberger H and Haase G. (1997) A highly effective emitter substance for mass spectrometric Pb isotope ratio determinations. *Chem. Geol.* **136**, 309–312.
- Green T. H. and Pearson N. J. (1986) Ti-rich accessory phase saturation in hydrous mafic-felsic compositions at high P. T. *Chem. Geol.* **54**, 185–201.
- Hilgen F. J., Krijgsman W., and Wijbrans J. R. (1997) Direct comparison of astronomical and $^{40}\text{Ar}/^{39}\text{Ar}$ ages of ash beds: potential implications for the age of mineral dating standards. *Geophys. Res. Lett.* **24**, 2043–2046.
- Hochstein M. P., Smith I. E. M., Regenauer-Lieb K., and Ehara S. (1993) Geochemistry and heat transfer processes in Quaternary rhyolitic systems of the Taupo Volcanic Zone, New Zealand. *Tectonophysics.* **223**, 213–235.
- Houghton B. F., Wilson C. J. N., McWilliams M., Lanphere M. A., Weaver S. D., Briggs R. M., and Pringle M. S. (1995) Chronology and dynamics of a large silicic magmatic system: Central Taupo Volcanic Zone, New Zealand. *Geology.* **23**, 13–16.
- Housh T. and Bowring S. A. (1991) Lead isotopic heterogeneities within alkali feldspars: implications for the determination of initial lead isotopic compositions. *Geochim. Cosmochim. Acta.* **55**, 2309–2316.
- Jaffey A. H., Flynn K. F., Glendenin L. E., Bentley W. C., and Essling A. M. (1971) Precision measurement of half-lives and specific activities of ^{235}U and ^{238}U . *Phys. Rev. C.* **4**, 1889–1906.
- Johnson M. C. and Rutherford M. J. (1989) Experimentally determined conditions in the Fish Canyon Tuff, Colorado, magma chamber. *J. Petrol.* **30**, 711–737.
- Jones J. H., Walker D., Pickett D. A., Murrell M. T., Beattie P. (1995) Experimental investigations of the partitioning of Nb, Mo, Ba, Ce, Pb, Ra, Th, Pa, and U between immiscible carbonate and silicate liquids. *Geochim. Cosmochim. Acta.* **59**, 1307–1320.
- Krogh T. E. (1973) A low contamination method for hydrothermal decomposition of zircon and extraction of U and Pb for isotopic age determination. *Geochim. Cosmochim. Acta.* **37**, 485–494.
- Lanphere M. A. and Baadsgaard H. (2001) Precise K-Ar, $^{40}\text{Ar}/^{39}\text{Ar}$, Rb-Sr, and U/Pb mineral ages from the 27.5 Ma Fish Canyon Tuff reference standard. *Chem. Geol.* **175**, 653–671.
- Lipman P. W., Steven T. A., and Mehnert H. H. (1970) Volcanic history of the San Juan Mountains, Colorado, as indicated by potassium-argon dating. *Geol. Soc. Am. Bull.* **81**, 2329–2352.
- Lipman P. W., Doe B. R., Hedge C. E., and Steven T. A. (1978) Petrologic evolution of the San Juan volcanic field, southwestern Colorado: Pb and Sr isotope evidence. *Geol. Soc. Am. Bull.* **89**, 59–82.
- Ludwig K. R. (1980) Calculation of uncertainties of U-Pb isotope data. *Earth Planet. Sci. Lett.* **46**, 212–220.
- Ludwig K. R. (1998) On the treatment of concordant uranium-lead ages. *Geochim. Cosmochim. Acta.* **62**, 665–676.
- Ludwig K. R. (2000). Decay constant errors in U-Pb concordia-intercept ages. *Chem. Geol.* **166**, 315–318.
- Ludwig K. R., Mundil R., and Renne P. R. (1999) How well can we really do timescale geochronology with zircon uranium-lead? *Ninth Ann. V. M. Goldschmidt Conference. Lunar and Planetary Institute Contribution. Houston, Texas.* **971**, 178. (abstr.).
- Mattinson, J. M. (1973) Anomalous isotopic composition of lead in young zircons. *Carneg. Inst. Wash. Yearbook.* **72**, 613–616.
- Mattinson J. M. (1987) U-Pb ages of zircons: a basic examination of error propagation. *Chem. Geol.* **66**, 151–162.
- Mattinson J. M. (2000). Revising the “gold standard,” the uranium decay constants of Jaffey et al., 1971. *EOS Trans. Am. Geophys. Union.* **81**, S444. (abstr.).
- McDougall I. and Harrison T. M. (1999) *Geochronology and Thermochronology by the $^{40}\text{Ar}/^{39}\text{Ar}$ Method*: 2nd ed. Oxford University Press, New York.
- Min K., Mundil R., Renne P. R., Ludwig K. R. (2000). A test for systematic errors in $^{40}\text{Ar}/^{39}\text{Ar}$ geochronology through comparison with U-Pb analysis of a 1.1 Ga rhyolite. *Geochim. Cosmochim. Acta.* **64**, 73–98.
- Mundil R., Brack P., Meier M., Rieber H., and Oberli F. (1996) High-resolution U-Pb dating of Middle Triassic volcanics: time-scale calibration and verification of tuning parameters for carbonate sedimentation. *Earth Planet. Sci. Lett.* **141**, 137–151.
- Nier A. O. (1939) Isotopic constitution of uranium and the half-lives of the uranium isotopes, 1. *Phys. Rev.* **55**, 150–153.
- Oberli F., Fischer H., and Meier M. (1990) High-resolution ^{238}U - ^{206}Pb zircon dating of Tertiary bentonites and the Fish Canyon Tuff: a test for age “concordance” by single-crystal analysis. Seventh International Conference on Geochronology, Cosmochronology and Isotope Geology. *Geological Society of Australia Special Publication* Canberra. **27**, pp. 74 (abstr.).
- Paces J. B. and Miller J. D. Jr. (1993) Precise U-Pb ages of Duluth Complex and related mafic intrusions, northeastern Minnesota: geochronological insights to physical, petrogenetic, paleomagnetic, and tectonomagmatic processes associated with the 1.1 Ga Midcontinent Rift System. *J. Geophys. Res.* **98**, 13997–14013.
- Reid M. R. and Coath C. D. (2000) In situ U-Pb ages of zircons from the Bishop Tuff: no evidence for long crystal residence times. *Geology.* **28**, 443–446.
- Reid M. R., Coath C. D., Harrison T. M., McKeegan K. D. (1997) Prolonged residence times for the youngest rhyolites associated with Long Valley Caldera: ^{230}Th - ^{238}U ion microprobe dating of young zircons. *Earth Planet. Sci. Lett.* **150**, 27–39.
- Renne P. R. (2000) $^{40}\text{Ar}/^{39}\text{Ar}$ age of plagioclase from Acapulco meteorite and the problem of systematic errors in cosmochronology. *Earth Planet. Sci. Lett.* **175**, 13–26.
- Renne P. R., Deino A. L., Walter R. C., Turrin B. D., Shisher C. C. III, Becker T. A., Curtis G. H., Sharp W. D., and Jaouni A. -R. (1994) Intercalibration of astronomical and radioisotopic time. *Geology.* **22**, 783–786.
- Renne P. R., Swisher C. C. III, Deino A. L., Karner D. B., Owens T. L., and DePaolo D. J. (1998) Intercalibration of standards, absolute ages and uncertainties in $^{40}\text{Ar}/^{39}\text{Ar}$ dating. *Chem. Geol.* **145**, 117–152.
- Schärer U. (1984) The effect of initial ^{230}Th disequilibrium on young

- U-Pb ages: the Makalu case, Himalaya. *Earth Planet. Sci. Lett.* **67**, 191–204.
- Shannon R. D. (1976) Revised effective ionic radii and systematic studies of interatomic distances in halides and chalcogenides. *Acta Crystallogr.* **A32**, 751–767.
- Stacey J. S. and Kramers J. D. (1975) Approximation of terrestrial lead isotope evolution by a two-stage model. *Earth Planet. Sci. Lett.* **26**, 207–221.
- Steiger R. H. and Jäger E. (1977) Subcommittee on geochronology: convention on the use of decay constants in geo- and cosmochronology. *Earth Planet. Sci. Lett.* **36**, 359–362.
- Steven T. A. and Lipman P. W. (1976) Calderas of the San Juan volcanic field, southwestern Colorado. *U.S.G.S. Prof. Paper.* **958**, United States Government Printing Office, Washington.
- Tucker R. D., Bradley D. C., Ver Straeten C. A., Harris A. G., Ebert J. R., and McCutcheon S. R. (1998) New U-Pb zircon ages and the duration and division of Devonian time. *Earth Planet. Sci. Lett.* **158**, 175–186.
- Villeneuve M., Sandeman H. A. and Davis W. J. (2000). A method for intercalibration of U-Th-Pb and ^{40}Ar - ^{39}Ar ages in the Phanerozoic. *Geochim. Cosmochim. Acta.* **23**, 4017–4030.
- Watson E. B. and Harrison T. M. (1983) Zircon saturation revisited: temperature and compositional effects in a variety of crustal magma types. *Earth Planet. Sci. Lett.* **64**, 295–304.
- Zielinski R. A. and Lipman P. W. (1976) Trace-element variations at Summer Coon volcano, San Juan Mountains, Colorado, and the origin of continental-interior andesite. *Geol. Soc. Am. Bull.* **87**, 1477–1485.